Supramolecular Pd_2L_4 self-assembled coordination metallacages for use as drug delivery system for the anti-cancer drug cisplatin

This thesis is submitted to Cardiff University in fulfilment of the requirements for the Degree of Doctor of Philosophy (Chemistry)

(June) 2019

Benjamin Woods

Contents

Declaration

This work has not previously been accepted in substance for any degree and is not concurrently submitted in candidature for any degree.

Signed …….. (Candidate)

Date ……

STATEMENT 1

This thesis is being submitted in fulfilment of the requirements for the degree of PhD

Signed …….. (Candidate)

Date ……

STATEMENT 2

This thesis is the result of my own independent work/investigation, except where otherwise stated. Other sources are acknowledged by explicit references. A bibliography is appended.

Signed …….. (Candidate)

Date ……

STATEMENT 3

I hereby give consent for my thesis, if accepted, to be available for photocopying and for interlibrary loan, and for the title and summary to be made available to outside organisations.

Signed …….. (Candidate)

Date ……

Word count ……

Signed …….. (Candidate)

Date ……

Acknowledgements

I would like to express my utmost gratitude first and foremost to my wonderful supervisor, Prof. Angela Casini, who has not only provided so much help and guidance throughout my PhD course but has also provided me with so many extra opportunities, within the University as well as opportunities abroad. I am also extremely grateful for the lovely working environment Angela has created within the group, which has led to the fun and memorable times I've had the pleasure of being part of as a member of the Casini group inside and outside of the research lab!

I'd also like to whole heartedly thank Dr Margot Wenzel for the guidance and support has given me throughout my project. The patience shown at the start of my project and the brilliant discussions we've had during are both things I'm very grateful for. I couldn't have asked for a better Postdoc supervisor!

I'd like to thank Dr. João D. G. Correia for hosting me in his group at the Instituto Tecnológico e Nuclear, and Dr. Filipa Mendes for all of her help, as well as everyone at the institute who made me feel so welcome during my stay in Lisbon. It was a wonderful experience which I will cherish forever.

I'd also like to thank the members of the Casini research group, past and present, who have made my time at Cardiff a pleasure and provided so many happy memories, as well as been instrumental in my development as a researcher with their invaluable input and advice.

Finally I'd like to thank my family for their support throughout this project, who made it all possible!

Summary

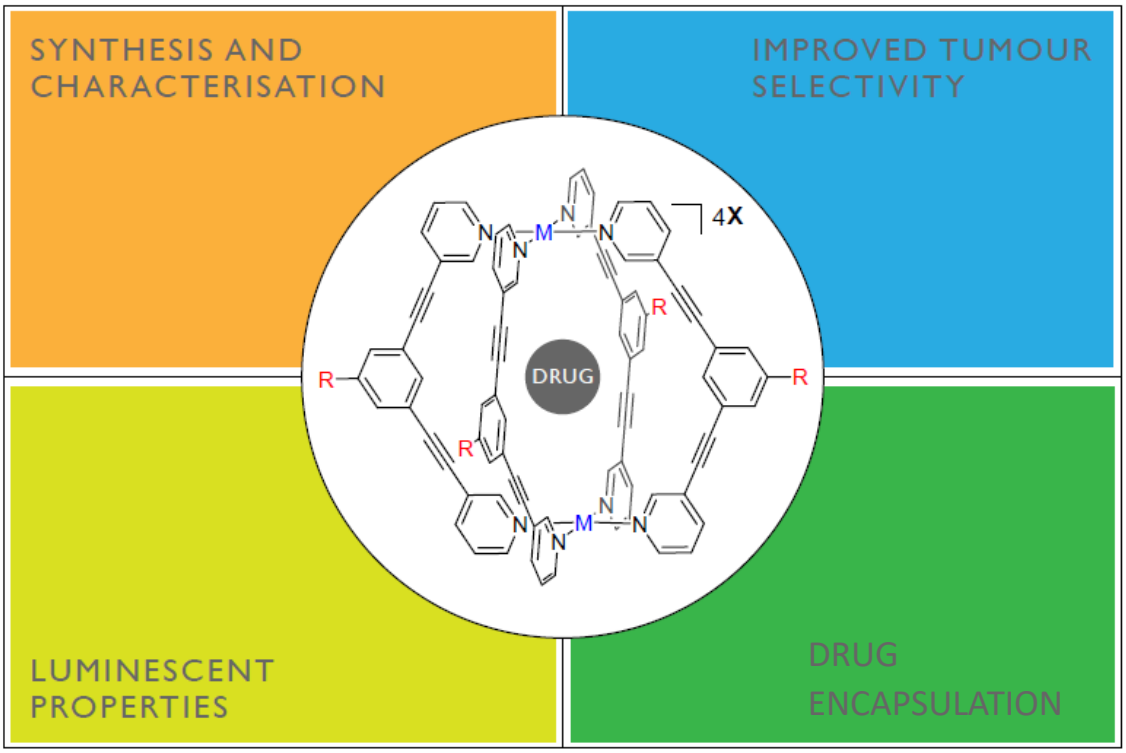

Cisplatin is a widely used anticancer drug but suffers from drawbacks and limitations, such as severe nephrotoxicity, which are still of great concern. A possible solution to these problems might lie in the optimization of new drug delivery systems able to protect the drug from metabolism (speciation) and to facilitate its uptake in cancer cells. In this context, supramolecular coordination complexes (SCCs), specifically 3D metallacages, hold great promise. These elegant supramolecular structures are well-defined discrete entities formed via self-assembly of bis-monodentate ligands with appropriate metal precursors. Interestingly, the formation of these cages creates a cavity within the structure, which can be exploited for its host-guest properties, thus allowing encapsulation of small molecules. Recently, our group reported on several Pd_2L_4 (L = 3,5-bis(3-ethynylpyridine)phenyl) metallacages as drug delivery systems for cisplatin. Notably, in vitro studies investigating the antiproliferative effect of coordination cages, with and without cisplatin encapsulated, showed an increased cytotoxicity for the combination cisplatin-cage complex [cage⊂(cisplatin)$_2$] over cisplatin alone in human cancer cells, illustrating their potential as a drug delivery systems. This research project investigated Pd_2L_4 metallacages as drug delivery systems for cisplatin in greater depth. This will include the exo-functionalisation of the cage architecture with structures such as peptides to improve tumour selectivity and to translocate the blood brain barrier, fluorophores to facilitate in vitro fluorescence microscopy, and to improve the solubility of the cage. Furthermore, the encapsulation of cisplatin in solution will be investigated.

Chapter 1: Anti-cancer platinum metallodrugs

Cancer is a disease characterised by the uncontrolled cell growth of cells, leading to a solid mass of cells known as a tumour.[1] In our modern aging population, cancer is one of the leading causes of death worldwide. There are several strategies to treat cancer, namely surgery, radiotherapy, or chemotherapy, which are often used in combination in a treatment cycle.[12] Chemotherapy involves the use of drugs to either destroy tumour cells (i.e. cytotoxic drugs) or at least limit their proliferation (antiproliferative drugs). As cancer is characterised by the uncontrolled growth of cells, cancer cells are difficult to treat as they are difficult to distinguish from healthy cells as they originate from mutations to endogenous healthy cells. Designing drugs to treat cancer is therefore challenging as the drug targets will be similar for both cancerous and healthy cells,[1,2] as opposed to the treatment of exogenous diseases such as viruses and bacterial malignancies which exhibit different characteristics owing to their exogenous origin. The disadvantages of many cytotoxic agents are related to this general lack of selectivity between healthy and cancerous cells, and include side effects such as bone marrow suppression, gastrointestinal tract lesions, hair loss and nausea, as well as the development of drug resistance which has been documented.[3] The use of chemotherapy began in the 1940s with nitrogen mustards, which are extremely powerful alkylating agents, and antimetabolites.[1] Since the early success of these initial treatments, a large number of additional small molecule organic anticancer drugs have been developed. During the 1960's it was discovered that the platinum complex *cis*-dichloro-diamineplatinum(II) (figure 1) exhibited interesting anticancer activity.[4]

1.1 Cisplatin

The anti-cancer properties of Cisplatin (*cis*-dichloro-diamineplatinum(II), figure 1) were first observed by Barnett Rosenburg in the 1960's,[5] although the initial synthesis of cisplatin is accredited to Michele Peyrone in 1844, and the elucidation of its sterical conformation was achieved by Alfred Werner in 1892. Cisplatin underwent several years of clinical trails, where it was found to exhibit excellent single agent anti-tumour activity.[4] This prompted further research interest before cisplatin was approved for clinical use against bladder, cervix, head and neck, oesophageal and small cell lung cancer, among other malignancies, in 1974.[6,7] The approval of cisplatin for clinical use marked the first instance of platinum based anti-cancer drugs, which have since become a mainstay of anti-cancer chemotherapy, used both alone but more commonly in combination therapy. However, during the several years of clinical development it was observed that cisplatin suffered from severe organ specific toxicities, namely nephrotoxicity, but also neurotoxicity.[4] The inherent toxicity of cisplatin drastically limited the

acceptable dose that could be administered to patients. Early work to limit the nephrotoxicity of cisplatin involved high volume fluid hydration and forced diuresis, which facilitated maximum safe dose of cisplatin to 1 – 3 mg/kg.[8] Since the clinical approval of cisplatin in 1978, there has been great research interest in designing cisplatin derivatives that limit the toxicity of cisplatin. The most prominent strategy is to alter the ligands which coordinate to the active platinum(II) metal ion. Although there is a vast wealth of research literature surrounding the development of cisplatin derivatives, to date there have only been two further cisplatin derivatives which have been clinically approved worldwide, Carboplatin in 1989[9] and Oxaliplatin which was approved in 2002.[10] Several other examples of cisplatin derivatives have been given country specific clinical approval (for example, Nedaplatin was approved in Japan in 1995,[11] and Lobaplatin was approved for use in China in 2010).[11]

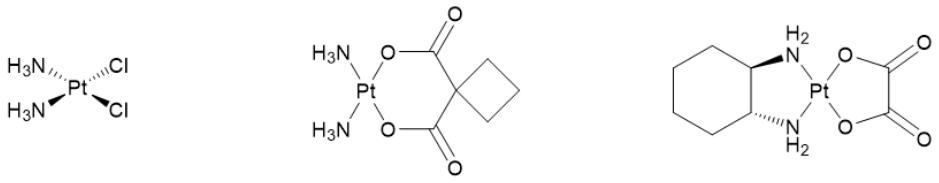

Figure 1. Chemical structures of the globally approved platinum(II) drugs with the year of clinical approval

1.2 Mechanism of action for cisplatin and cisplatin derivatives

Despite gaining clinical approval 41 years ago, the anti-cancer mechanism of action of cisplatin is still not fully understood. The widely accepted biochemical mechanism of action of cisplatin is that, upon entering the cell, cisplatin undergoes hydrolysis, forming mono- and diaquo cationic platinum complexes. The aqua platinum complexes are the activated species and can form adducts with DNA, which triggers cytotoxic processes leading to the death of the cancer cell (figure 2).

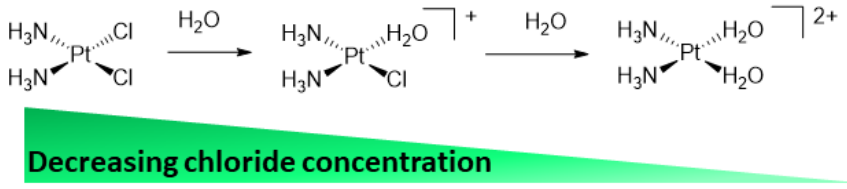

Figure 2. The process of hydrolysis forming the active mono- and diaquo platinum(II) species following the decreasing concentration of chloride upon cellular internalisation

Cisplatin is a neutral complex which is administered intravenously.[4,11] It is believed to largely remain neutral within the blood serum and thus arrives at the cancer cell as a neutral species. The mechanism of action of uptake by cells is not fully understood. It is believed that its primary mechanism of cell uptake is via passive diffusion through the lipid bilayer, although some reports have suggested that active transport mechanisms may contribute to the uptake of cisplatin as well.[12]

The process of hydrolysis is reported to be dependent on the solvent environment.[4,11,13] As cisplatin is administered intravenously, it circulates throughout the body in blood. Blood serum is known to have a high concentration of chloride (approximately 100 mMol L^{-1}),[13] and as such inhibits the substitution of chloride for water. Upon cellular uptake the concentration of chloride is reduced due to the lower concentration of chloride within the cytoplasm (2 - 30 mMol L^{-1}).[13] This facilitates the formation of mono-aquo ($[Pt(II)(NH_3)_2(H_2O)Cl]^+$) and diaquo $[Pt(II)(NH_3)_2(H_2O)_2]^{2+}$ cationic complexes,[13] which are more reactive towards nucleophilic centres of biomolecules due to water being a much better leaving group than chloride.[14]

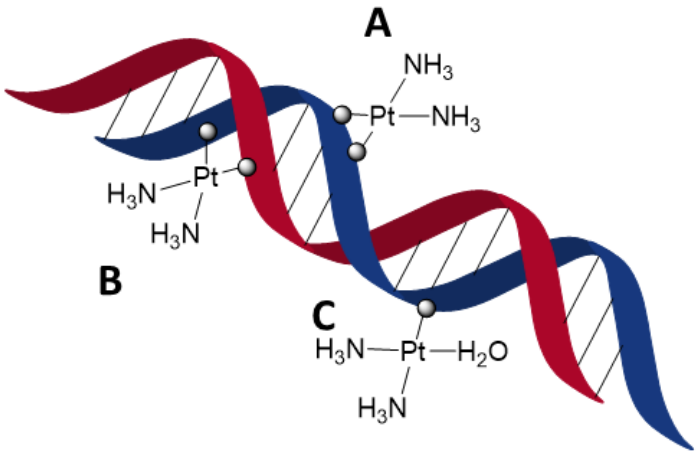

Figure 3. Cartoon diagram showing the most common cross linked adducts formed between cisplatin and DNA. A) Intra-strand cross linked adduct. B) Inter-strand cross linked adduct. C) Mono-functionalised DNA adduct

After undergoing hydrolysis, the main mechanism of action for triggering cell death occurs after the mono- and diaquo cisplatin complexes accumulate within the cell nucleus. Here, the complexes can form intra- and inter-strand adducts with DNA bases (figure 3), thus triggering cell death via either necrosis or controlled apoptosis.[14–17] The binding of the activated aquo-cisplatin complexes primarily occurs at the N7 position of guanine and adenine in the major groove, due to the higher basicity and steric accessibility of these sites compared to other sites found in DNA.[13,14] Cisplatin initially forms mono-functionalised DNA adducts, however most of these go on to form inter- or intra-strand crosslinks. Indeed, it has been reported that 60 – 65% of adducts formed by cisplatin are intra-strand cross links between two adjacent guanine

residues (1,2–d(GpG)),[18] while 20-25% of cisplatin – DNA adducts have been shown to be cross links between cisplatin with adjacent guanine and adenine residues (1,2-d(GpA)).[18] It is generally accepted that these 1,2-intra-strand crosslinks are responsible for the anticancer activity of cisplatin.[11,13] Evidence for the anticancer activity of these 1,2-intra-strand cross-links has come from the reports that high mobility group (HMG) proteins, which are a family of chromosomal proteins involved with the regulation of numerous DNA-dependent processes, recognise and process these 1,2-intra-strand cross links.[19] Further support for this assumption arises from the fact the nucleotide excision repair mechanism, an important DNA repair process, repairs 1,3-intra strand cross links most effectively, while repairing 1,2-d(GpG) cross links least efficiently.[20]

Although the anticancer activity described above is widely accepted,[4,11,13,21] and indeed the 1,2-d(GpG) cross-links have been experimentally shown to be the primary anticancer mechanism of action,[18] there are several discrepancies with this classical description of cisplatin anticancer activity. Namely, cisplatin is known to interact with several non-DNA structures.[13] These non-DNA interactions have been shown to both hinder the efficacy of the drug by forming deactivated complexes, as well as work in combination with the DNA interactions to contribute to the anti-cancer activity.[13,22]

After cisplatin has been administered intravenously, it has been found to diffuse rapidly throughout tissue.[13] This presents an immediate problem as the inherent toxicity of cisplatin will be increased due to the lack of selectivity towards cancer cells over healthy cells in the tissue it has rapidly diffused into.[11,13] Furthermore, cisplatin has also been shown to tightly bind to proteins found in blood, in particular proteins which have a high expression of sulfur-containing amino acid residues, such as cysteine, as sulfur is known to complex with platinum due to strong interactions between platinum and soft nucleophiles.[11,21,23] Indeed, approximately 90% of cisplatin present in blood is bound to proteins (in particular albumin),[24] which causes deactivation of the majority of administered cisplatin, again decreasing the efficacy of the drug.

Cisplatin molecules which do reach the cancerous cells have other physiological obstacles to overcome. Although cisplatin is believed to enter cells primarily via passive diffusion,[24] they may react with phospholipids and phosphatidylserine of the cell membrane, restricting their uptake into the cytoplasm.[25] Upon uptake into the cytoplasm there are numerous nucleophilic structures which can react with the platinum metal of cisplatin, such as microfilaments of the cytoskeleton and RNA strands,[26] as well as numerous sulfur-containing amino acid residues. Indeed, perhaps the most important sulfur-containing molecule that can interfere with cisplatin is the cysteine-containing tripeptide, glutathione (GSH).[13,27] GSH is an anti-oxidant present in high concentrations within the cytoplasm (0.5 – 10 mMol L^{-1}) and thus a potent reducing agent. It is known that GSH can form adducts with cisplatin, which deactivates

the drug. Furthermore, the GSH – cisplatin adducts are then excreted from the cell via the glutathione S-conjugate pump.[28] It has also been found that cysteine-rich proteins present in the kidneys form adducts with cisplatin, which may be the underlying reason for nephrotoxicity observed for cisplatin.[3]

1.3 Cisplatin derivatives to improve drug efficacy

As can be seen cisplatin acts as a promiscuous drug,[13] with poor selectivity for cancer cells and a lack of stability in the presence of nucleophilic moieties, in particular sulfur containing compounds.[13] As such, much research interest has been focused on the synthesis of cisplatin derivatives with enhanced stability under physiological conditions in order to avoid premature complexation to nucleophiles in the blood and thus excretion.[21] Carboplatin (*cis*-diammine-1,1-cyclobutanedicarboxylateplatinum(II), figure 1) was the first clinically approved cisplatin derivative,[3,9] gaining FDA approval in 1989.[4] Carboplatin differs from cisplatin in that the labile chloride ligands are replaced with the more stable, bis-chelating ligand, 1,1-cyclobutanedicarboxylate.[4,21] This has been reported to slow the rate of hydrolysis to the more active mono- and diaquo complex. As such, the promiscuity in the blood was reduced, which in turn led to a reduction in the toxicities associated with cisplatin, in particular nephrotoxicity. However, although carboplatin is less toxic than cisplatin it suffers from cross-resistance with cisplatin,[4] suggesting that the mechanism of action is analogous to that of cisplatin, namely triggering cell death via intra-strand cross links with DNA.

Oxaliplatin (Oxalato(1,2-diaminocyclohexane)platinum(II), figure 1) is the third cisplatin derivative to be clinically approved globally, gaining approval in 2002.[11,21] The structure differs from cisplatin in that the labile chloride ligands are replaced with the bidentate oxalate ligand, which slows the rate of hydrolysis and thus slows the rate at which it changes to the activated mono- and diaquo complex.[10] Furthermore, the coordinating ammonia ligands which are present in both cisplatin and carboplatin have been replaced by the bidentate, cyclic *trans*-1,2-diaminocyclohexane ligand.[10] It has been found that oxaliplatin can circumnavigate the cisplatin cross-resistance observed for carboplatin.[11] This lack of cross-resistance suggests that along with forming intra-strand DNA cross links to induce cell death, the mechanism of anticancer activity for oxaliplatin may also be more related to the interactions with sulfur containing proteins in the cytoplasm.[11,13,26]

Other methods of improving platinum based drugs have been explored, with several Pt(IV) prodrugs type complexes undergoing clinical trials. However, another method to improve

platinum based drugs is by forming targeted drug delivery systems. These systems would not alter the core drug structure, but instead would act as a host complex to the guest platinum drug molecule, protecting the drug from interacting with biological molecules as it circulated throughout the blood system. Moieties, such as targeting peptides or monoclonal antibodies which can target receptor molecules overexpressed in cancer cells, could be attached to the host structure to improve the selectivity of the host delivery structure and thus the guest platinum drug.[11,21]

1.4 Targeted drug delivery system for cisplatin and its derivatives

Targeted platinum drug delivery systems can be categorised into the following: host guest drug delivery systems, and platinum drug conjugates.[21,29,30] The latter typically involves conjugation of a peptide or antibody to either a platinum(II) drug or a platinum(IV) prodrug centre,[11,21] with the latter being reduced to platinum(II) under physiological conditions.[11,21] The peptide or antibody is designed to have a high selectivity for receptor proteins that are over expressed in cancer cells,[29] thus improving the selectivity of the drug conjugate.[21,29] There is a wealth of research interest into targeted platinum drug conjugates,[11,21,29] with several targeted platinum(II) and platinum(IV) currently undergoing clinical trials. However, these platinum drug conjugates involve the direct alteration of the platinum drug species by altering the ligands to include the tumour targeting moiety. This causes the chemical alteration of the active platinum drug centre, which can in itself negatively affect anticancer activity when compared to cisplatin.[21] As has been described above over the past 40 years since cisplatin, the first platinum based drug, was clinically accepted only another two platinum based drugs have been approved globally, and another three being approved in specific countries.[11]

Another method of improving platinum drug efficacy is to formulate a molecular or macromolecular “capsule” host structure, which is capable of encapsulating the platinum drug as a guest species.[21,31–33] The encapsulation process can be driven by forming favourable intermolecular interactions between the host cavity and the platinum drug,[21] by sterically trapping the drug within the cavity,[29,34] or by solvent – drug interactions, forming a host-guest structure. The host-guest structure can be further optimised by functionalisation of various groups to the external surface of the host-structure, thus negating modification of the active platinum drug, such as cisplatin. Finally, the guest can be released from the host in close proximity to cancerous cells, either by diffusion or by a stimuli responsive release mechanism.[33] Typically, two methods have been employed to achieve improved selectivity of platinum drug host-guest structures towards cancerous cells; passive targeting and active targeting.[21,35]

1.4.1 Passive targeting host-guest drug delivery systems for platinum drugs

Passive tumour targeting relies on the enhanced permeability and retention (EPR) effect, first described by Maeda in 1986.[36] The EPR effect is an observed phenomenon whereby compounds of a certain size (approximately 20-200nm) preferentially accumulate in tumour tissue rather than normal tissue.[35,37] It was suggested that this is due to larger fenestrations of poorly aligned endothelial cells in tumours, which occurs due to the rapid growth of tumours and thus the rapid and poorly structured blood vessels formed via angiogenesis.[35,37] The larger fenestrations between the endothelial cells of the blood vessels within tumours would facilitate the diffusion of larger molecules into tumour tissue, while the tight cell-cell junctions of endothelial cells of blood vessels in healthy tissue would not allow these larger structures to enter the healthy tissue. Thus, by increasing the size of the drug, via conjugation to large polymeric structures or encapsulation in large host structures, passive tumour targeting could be achieved.[37] Furthermore, the tumour environment has been found to exhibit an impaired lymphatic drainage system.[37] This causes slow clearance of compounds in the intercellular fluid from the tumour microenvironment, which in turn facilitates the accumulation of the drug conjugate or host-guest drug delivery system.

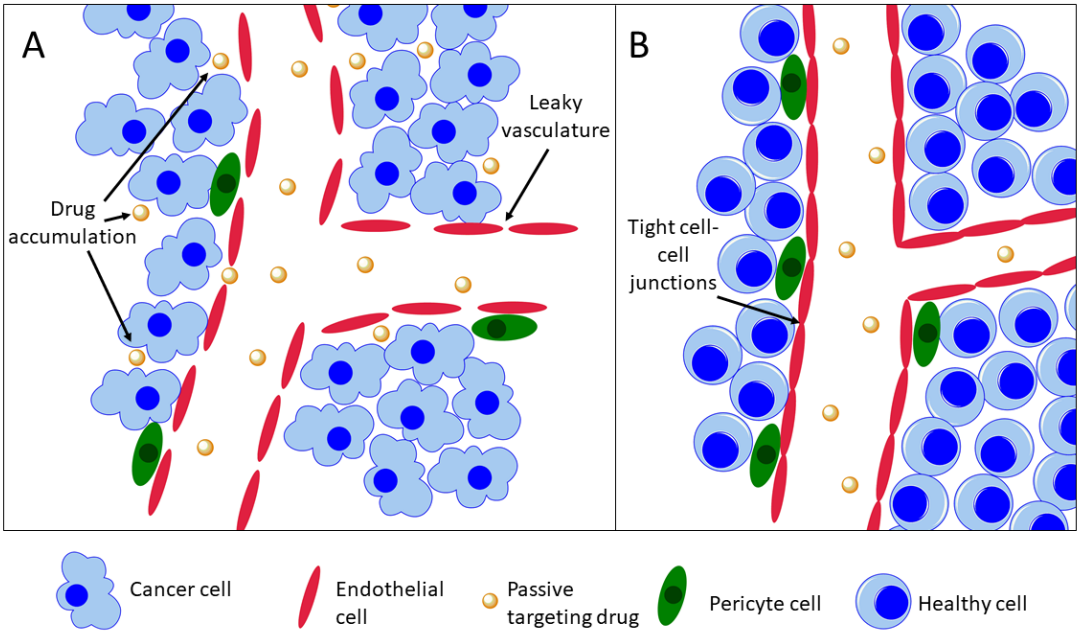

Figure 4. Schematic representation of the enhanced permeability and retention effect. Box A: The endothelial cells of the vascular system within tumours do not form tight cell-cell junctions, and thus allow drugs that exploit passive targeting to pass from the blood stream into the tumour tissue. The poor lymphatic drainage facilitates the accumulation of drug molecules within tumours. Box B: Vascular system within healthy tissue has tight cell-cell junctions and therefore do not allow drugs to pass from the blood stream to the tissue. In this way tumour targeting was hypothesised to occur

The EPR effect was thus thought to be a gateway to “magic bullet” type drugs, a concept first envisioned in 1906, by merely changing the size of the drug. However, recently it has been shown that the EPR effect is primarily observed in *in vivo* testing, and rarely translates into successes in the clinic.[38] The primary reason cited for the lack of translational success from *in vivo* to clinical trials involves the murine models used for *in vivo* experiments and the differences between tumours grown in mice and those in humans.[38] Primarily, the difference in both the rate of growth and the size of the tumour grown in murine models differs drastically from tumours found in humans. This more rapid growth causes the fenestrations in the endothelial cell line, which is not observed to the same extent in human tumours, and the larger tumour to body size ratio causes the tumour in murine models to filter a significant proportion of the injected dose of a drug and thus act as a repository for the drug, effectively accentuating the efficacy and lowering the toxicity.[38]

Although the EPR effect may not be the “magic bullet” formula it was hoped to be, several structures have been explored for their use as a drug delivery system for platinum based drugs to exploit the EPR effect.[21] For example, carbon nano-tubes have been investigated as drug delivery vectors for platinum based drugs.[39] Platinum(IV) prodrugs can be synthesised to facilitate their functionalisation to the external surface of the nano-tube. However, this requires appropriate ligands, such as those that are susceptible to amide- or ester-bond formation, to be coordinated to the platinum centre to facilitate conjugation to the nano-tube external surface,[39] which in turn are decorated with complementary amide- or ester-bond forming functional groups.[39] This principle of decorating the external surface of a large, stable nano-sized structure with platinum(IV) prodrug conjugates, which are then reduced to their active platinum(II) cisplatin-like drug, has also been explored for several inorganic nano-particle structures such as gold,[40] and other inorganic nanoparticles.[21] However, these systems do not encapsulate the drug, and thus do not shield the complex from interfering with myriad of nucleophilic biomolecules that may deactivate them. Furthermore, the platinum drug modification of the ligands, may affect the overall efficacy of the drug.[21] Carbon nano-tubes have also been explored as encapsulation based platinum drug delivery host structures.[41,42] This is due to carbon nano-tubes being stable under physiological conditions, and the ability to synthesise both single layered or multi-layered nano-tubes. Increasing the number of layers of a carbon nanotube increases the overall volume of the internal, hydrophobic cavity. It has been reported that the hydrophobic cavity can be loaded with platinum(IV) prodrug complexes, which have been coordinated to highly hydrophobic ligands. This drives the encapsulation into the cavity, and upon reduction of the platinum(IV) complex, the highly hydrophobic ligands are lost and the more hydrophilic, active platinum(II) complex is released.[39,41,42] However, the same issues as

described previously about altering the efficacy of the drug through modification of the platinum centre applies for the reported loading of carbon nano-tubes.[41,42]

A well-studied class of host systems that have been studied to exploit the EPR effect and are based on encapsulation of the unmodified cisplatin structure are liposomes (figure 5).[43] Liposomes are composed of one or more phospholipid bilayer membranes. These membranes form hollow spheres under aqueous conditions due to a combination of the hydrophobic interactions of the fatty acid "tails" and the favourable hydrophilic interactions of the phosphate "heads" and water, which results in a lipophilic membrane region and an aqueous internal core cavity thus facilitating the encapsulation of both hydrophobic and hydrophilic drug molecules.[33,43,44]

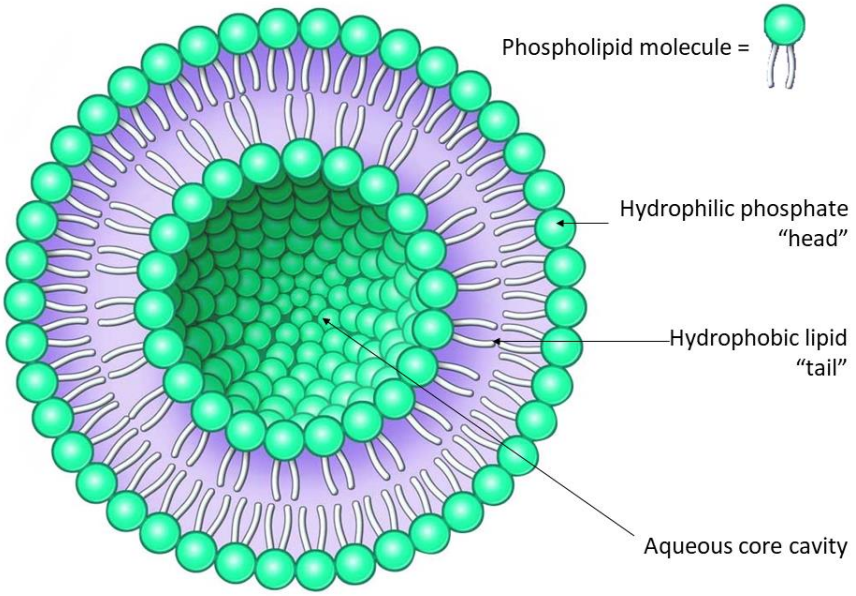

Figure 5: Cartoon representation of a unilamellar liposome highlighting the hydrophilic phosphate head and hydrophobic lipid tail of the phospholipid molecule

These structures have undergone investigation as drug delivery vehicles due to their colloidal properties and biocompatibility, and examples have made it to preclinical trials.[45] One liposome formulated host-guest drug delivery system currently undergoing preclinical trials is Lipoplatin.[46] Lipoplatin is a liposomal formula of cisplatin, whereby the active drug is camouflaged and protected from premature deactivation and metabolism by the liposome shell,[21,45] which in turn is composed of soy phosphatidyl choline, cholesterol, dipalmitoyl phosphatidyl glycerol and methoxy-poly- ethylene glycol-distearoyl phosphatidylethanolamine.[21,46] The liposomal formulation does not require the chemical alteration of cisplatin, and so the anticancer mechanism of action is not affected by the formulation. However, by being encapsulated within a liposome the host-guest system can be retained in the body longer than cisplatin alone without excretion. The circulatory time is further

improved by the decoration of the surface of the liposome with poly-ethylene glycol (PEG) units, as this aids the host-guest system to evade macrophage scavengers in the bloodstream. Furthermore, as the drug is encapsulated within a host structure, liposomal formulated cisplatin exhibits reduced nephrotoxicity and neurotoxicity, as the cytotoxic cisplatin cargo is not exposed.[21,33,46]

In summary, there are several studies of drug delivery systems which are designed to exploit passive targeting via the EPR effect. However, as very few formulations that were successful *in vivo* have found success in clinical trials, and the discrepancies between murine tumour models and tumours found in humans which were highlighted previously,[38] another strategy is needed to improve the selectivity towards cancer cells of host-guest drug delivery systems via active targeting.

1.4.2 Active targeting drug delivery systems

Active targeting of cancer cells can be achieved by first identifying a suitable feature that is overexpressed in cancer cells compared to healthy cells to target.[29] Once a suitable target has been identified, the complementary targeting molecule which exhibits high affinity for the target molecule,[11,29] and a high selectivity towards it, can be designed.[29] The targeting molecule is then functionalised with an appropriate chemical group to facilitate conjugation either directly to the drug, or to the external surface of the host structure if the drug is formulated into a host-guest drug delivery system.[29] Although the concept of an active targeting host-guest drug delivery system for known platinum(II) based drugs is being explored,[21] most examples of active targeting for platinum drugs involve the direct conjugation of the targeting species to the non-leaving group ligand of platinum(II) drugs, or to the axial position of platinum(IV) pro-drugs.[21]

Typically, the target biomolecule for drug delivery vectors will be a membrane bound protein that has been shown to be overexpressed in cancer cells, however other target molecules have been identified to exploit other upregulated characteristics of cancer cells.[11,21,29] Indeed, the production of a large range of peptide conjugated platinum(II) drugs was facilitated by the development of solid phase peptide synthesis techniques, whereby the coordination of the platinum(II) drug to the solid support bound peptide could be achieved, and the resulting platinated peptide would remain intact after cleavage from the resin.[47–50] As such, a library of peptides that could target membrane bound receptor proteins overexpressed in cancer cells could be synthesised and screened to monitor any improvements in the anticancer activity *in vitro* of the resulting platinum(II) drug conjugates,[51] however few hits were observed. An example of a platinum(II) peptide conjugate was reported for a carboplatin analogue, whereby the 1,1-cyclobutanedicarboxylate ligand of carboplatin was replaced by a malonate ligand which had been functionalised via a PEG linker to a cyclic peptide which was known to target the CD13

receptor protein.[52] CD13 is known to be overexpressed in cancers, for example prostate cancer cells.[53,54] It was found that the peptide-platinum(II) conjugate shown enhanced anticancer activity when compared to carboplatin.

Incorporation of sugar moieties to the non-leaving group ligand scaffold of carboplatin and oxaliplatin analogous platinum(II) drugs was hypothesised to improve the uptake and thus efficacy of the resulting platinum(II) complex. The hypothesis was based on the increased uptake of nutrients, in particular glucose, of cancer cells in order to sustain their unregulated cell division. However, despite numerous reports of glucose modified platinum(II) drug conjugates, so far none have produced a platinum(II) complex that has displayed enhanced anti-cancer activity compared to the analogous, non-sugar functionalised carboplatin or oxaliplatin.[55,56]

Platinum(II) based targeted drug delivery systems have also been reported by utilising different targeting molecules for different biological targets, such as the use of steroids to target receptors overexpressed in certain cancer cells. The estrogen receptor has been shown to be overexpressed in several cancer types including breast cancer.[57,58] Thus it was hypothesised that incorporation of estrogen derivatives as part of both the non-leaving group ligand or leaving group ligand of known platinum(II) drug analogues could help guide the drug conjugate towards cancer cells, thus improving the selectivity and thus efficacy of the platinum(II) drug conjugate.[59] However again this strategy of direct conjugation to the drug has seen limited success, primarily due to the steric hinderance of the large steroid moiety inhibiting the DNA binding of the active platinum(II) centre.[21,59,60] Other examples of direct conjugation of targeting molecules, such as peptides and monoclonal antibodies, have also been reported but have again not shown marked improvement in the anti-cancer activity of the resulting platinum(II) drug conjugate when compared to the known platinum(II) drugs.[21]

Active targeting of cancer cells for platinum drugs have also been explored for platinum(IV) complexes. The physicochemical properties of platinum(IV) complexes are very different to those of platinum(II) drugs. Platinum(IV) complexes generally adopt an octahedral coordination geometry, as opposed to the square planar geometry of platinum(II) complexes. Due to the saturation of the coordination sphere of platinum(IV) complexes, ligand substitution is less favourable than for platinum(II) complexes and thus platinum(IV) complexes have been reported to be more stable towards unwanted ligand substitution reactions with biological molecules in physiological conditions.[21] This stabilisation has a direct impact on the DNA binding and thus anticancer properties of platinum(IV) complexes, as although platinum(IV) can complex with DNA, the time required to form cytotoxic complexes is measured in days as opposed to hours.[61] As platinum is generally metabolised and excreted from the body within hours, platinum(IV) drugs are not considered cytotoxic in their fully oxidised form.[21,61] However,

platinum(IV) has been shown to be able to be reduced by endogenous reducing agents such as glutathione (the rate of reduction is dependent on the ligands of the platinum complex).[11,21] As such, platinum(IV) complexes are generally considered prodrugs, as they must first undergo reduction to their square planar platinum(II) analogue, which includes the loss of two axial ligands, to produce the active platinum(II) anticancer drug.

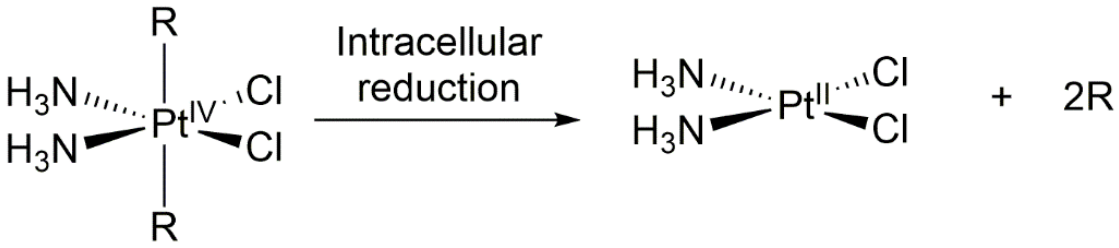

Scheme 1. Schematic representation of the reduction of a Platinum(IV) prodrug complex to a platinum(II) drug (cisplatin), upon intracellular reduction, including the loss of two axial ligands. The axial ligands (R) can be designed to improve the physiological stability, or tumour targeting moieties.

In summary, the active targeting of platinum drugs to cancer cells by direct conjugation of targeting molecules to the ligands of platinum(II) drug, or platinum(IV) prodrug, complexes has been explored, however few examples of complexes with increased anticancer activity compared to the known platinum(II) drugs have been reported.[11,21]

As previously discussed, altering the chemical structure of the anti-cancer drug may reduce the overall efficacy of the resulting drug conjugate, or sterically interfere with the mechanism of action of the platinum drug.[21] To avoid the chemical alteration of the platinum drug, a known anti-cancer drug may instead be encapsulated within a larger, host structure, as discussed for host-guest structures exploiting passive targeting via EPR effect.[39,46] Although the EPR effect does not appear to translate from the success observed *in vivo* to the clinical trials,[38] the host structure may still be exploited to protect the guest drug molecule from premature degradation and metabolism while in circulation. Furthermore, it can be envisioned that tumour targeting molecules can be functionalised to the external surface of the host structure in order to guide the overall host-guest complex towards cancerous cells, and thus improve the selectivity of the guest drug molecule.[29] Similar host systems to those exploiting passive targeting via EPR have been explored for their use as targeted drug delivery vehicles, although most studies on host-guest drug delivery systems for platinum drugs have focussed on exploiting passive targeting via the EPR effect.

An intriguing class of host systems which have recently come under investigation as host-guest drug delivery systems are supramolecular coordination complexes (SCCs).[62,63] These complexes can be formed into a diverse array of discrete supramolecular entities that can be

both two dimensional and three dimensional through the judicious choice of multi-dentate ligands that coordinate at least two different metal ion centres with complementary coordination geometry.[63,64]

Chapter 2: Biological Applications of Supramolecular Coordination Complexes

The synthesis of supramolecular coordination complexes (SCCs) has been described for several decades and has been shown to be easily predictable and reproducible through the wise choice of a combination of multidentate ligands (Lewis-basic 'donors') and metal ions (Lewis-acid 'acceptors') with different coordination geometry. Indeed, the interest in SCCs has grown steadily over the last years, although not to the same extent as their three dimensional (3D) polymer analogues, namely the metal organic frameworks (MOFs, figure 1). Furthermore, research interest into the biological applications of SCC's has also risen over the last few years but is still very much in its infancy (figure 1). Despite this, the research into biological applications of SCCs reported so far has shown that these structures hold promise in various biological applications, with particular emphasis in anti-cancer therapeutics.

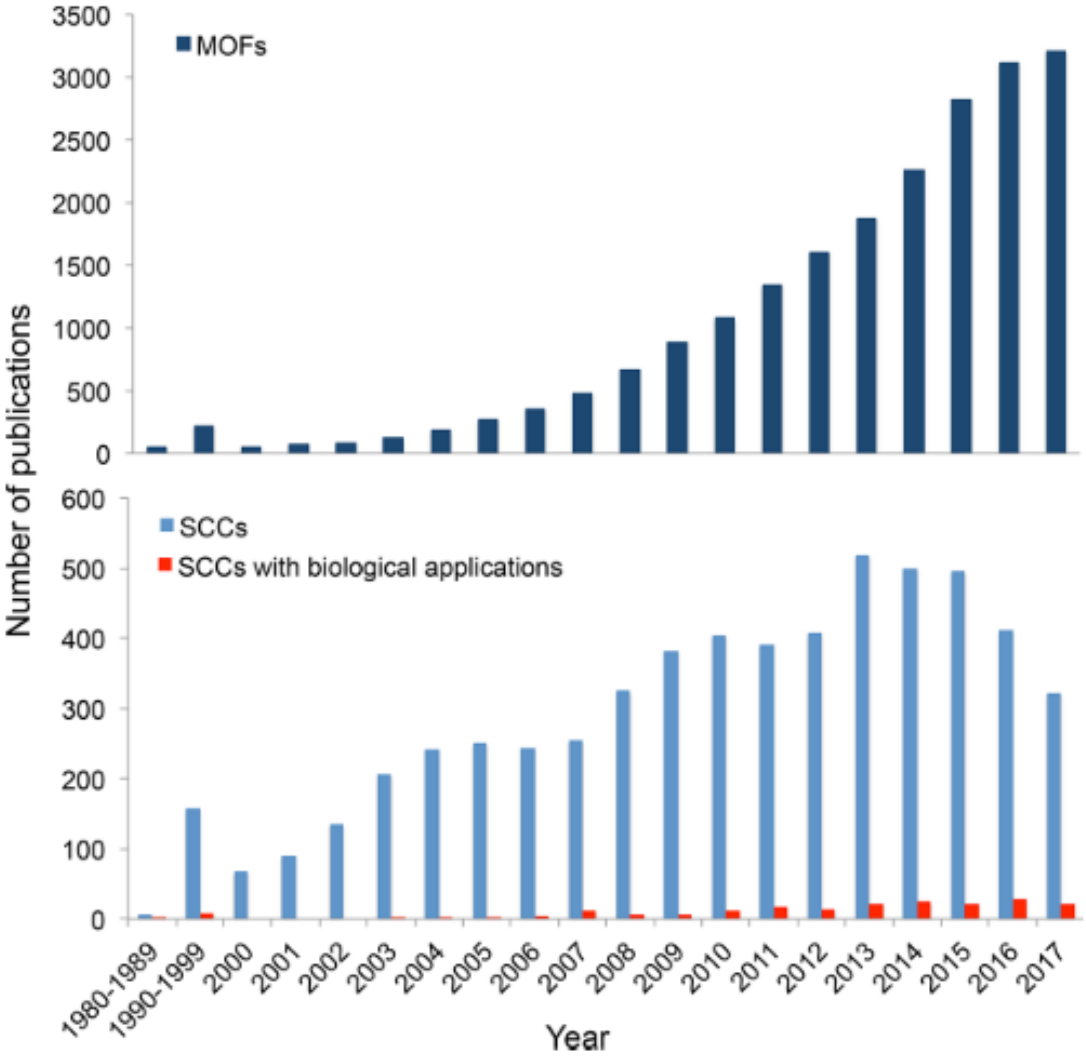

Figure 1. Graph showing the evolution of the number of publications per year between 1980 - 2017 regarding MOFs (top) and SCCs and SCCs with biological applications (bottom).

In most cases, the self-assembly of SCCs proceeds under mild conditions to form

metallacycles (2D) and metallacages (3D) of general formula $[M_xL_y]^z$ (M = metal, L = ligand, z = charge) in high yields. Various synthetic strategies to obtain SCCs of different shapes have been developed, the earliest being gathered under the theme of 'directional bonding' and including edge- and face-directed approaches, whereby a metal acceptor and a ligand donor are mixed in specific ratios to form highly symmetrical polygons and polyhedra (metallacycles and metallacages, respectively).[65] Other methodologies to form SCCs also include symmetry-adapted and weak-link approaches.[66] In the edge-directed self-assembly approach, the polyhedra are formed using stoichiometric ratios of ligand (often bidentate) to metal precursors. The symmetry-adapted method relies on the same principle but using multibranched chelating ligands (often at least tridentate), thus leading to the generation of highly symmetric architectures. In the face-directed approach, developed by Fujita in the late 90s,[67] also referred to as the 'panelling method', rigid pre-formed ligands act as 'panels' to guide coordination complex precursors to form the SCCs.[67] In this strategy, modifying the availability of the coordination sites of the metal forces an increased degree of directionality to form the final 3D-cage. Finally, the weak-link method uses a hemilabile ligand to form firstly a 'weak link' (weak metal-heteroatom bond) with a metal precursor, generating a condensed metallacycle, which can then be opened by selective introduction of an ancillary ligand with a higher binding affinity.[68]

The two main synthetic approaches, namely edge- (mainly developed by Stang *et al*.)[64,69] and face-directed (firstly reported by Fujita and coworkers),[70] have been described to form 2- and 3D nanoarchitectures based on Pd^{II}, Pt^{II} and Ru^{II} centres. For example, in the early 2000s, Fujita reported on a $[Pd(N^1,N^1,N^2,N^2\text{-tetramethylethane1,2-diamine})]_6L_4$ (L = ligand: 2,4,6-tri(pyridin-4-yl)-1,3,5-triazine) cage accessible by face-directed self-assembly between four equivalents of the planar tridentate ligand (acting as a panel) and six equivalents of the Pd(II) precursor.[71] Therrien and coworkers also used a similar type of tripyridyl-triazine ligand to form Ru(II)-based capsules of the general formula $[Ru_2]_3L_2$ by face-directed self-assembly from a dinuclear 2,5-dihydroxy-1,4-benzoquinonato complex ($[Ru_2(p\text{-}^iPrC_6H_4Me)_2(C_6H_2O_4)Cl_2]$).[72,73]

Edge-directed approaches to form metallacages have been described mainly based on bidendate 'banana-shaped' pyridyl-based ligands and Pd^{II} and Pt^{II} metal precursors.[74] In general, the simplest examples of 3D-metallacages are based on M_2L_4 type of scaffolds, but numerous other structures have been reported (M_2L_3,[75] M_4L_4,[75] M_4L_6,[75–77] M_8L_{12},[76] $M_{12}L_{24}$, [77]$M_{24}L_{48}$,[78] etc.).[74] The largest discrete self-assembled polyhedron obtained so far by edge-directed synthesis has been described by Fujita and coworkers, whereby a $Pd_{48}L_{96}$ was observed.[79] A more in depth discussion on SCC structures will be presented in chapter 3.

2.1 2D Supramolecular coordination complexes as anti-cancer agents

Several small-molecule transition metal complexes have been studied over the years for their anticancer properties, but only some of them have been approved for use as anticancer agents. Among them, the FDA approved drug cisplatin is used to treat a range of cancers such as carcinomas and germ cell tumours, amongst others.[21,80] Taking inspiration from the clinical success of cisplatin, supramolecular metal-containing complexes are also under investigation as experimental cytotoxic anticancer agents.

2.1.1 Palladium(II) and Platinum(II) SCCs metallacycles

Palladium(II) and platinum(II) ions are both d^8 transition metals which adopt a square planar geometry. In SCCs, the metal precursor can be *cis*-capped to allow only two coordination sites available for complexation to multidentate ligands to form discrete SCC architectures.[81] In this context, as representative examples, dinuclear Pt(II) and Pd(II) metallacycles, featuring both amide-based dipyridyl ligands and 1,1'-bis(diphenylphosphino) ferrocene ligands (figure 2), have been studied as anticancer agents *in vitro* in comparison to cisplatin.[82] Interestingly, both metallacycles displayed increased antiproliferative effects (IC_{50} values between ca. 4 and 36 µM depending on the various cell lines tested) compared to their metal precursor (IC_{50} values between ca. 33 and 144 µM) and organic ligand (IC_{50} values between 100 and 150 µM), suggesting that the structure of the intact metallacycle is essential for the observed activity.[82] Notably, the platinum(II)-based metallacycle was found to be a more potent inhibitor of cell proliferation against brain (IC_{50} = 4.5 µM), head and neck (IC_{50} = 13.0 µM), and thyroid (IC_{50} ca. 12 µM) cancer cell lines than cisplatin (IC_{50} > 50 µM, respectively), and yet had a lower effect against non-cancerous cell line (IC_{50} ca. 35 µM for the Pt-metallacycle *vs* IC_{50} ca.17.3 µM for cisplatin).[82] The mechanism of action of both metallacycles has been further investigated *in vitro* against the brain tumour cell line T98G.[82] The results suggest that both compounds induce oxidative stress and cell death by apoptosis. *In vitro* fluorescence microscopy studies showed that the cancer cells readily internalized both metallacycles, and that upon internalization the fluorescent ligand was released.

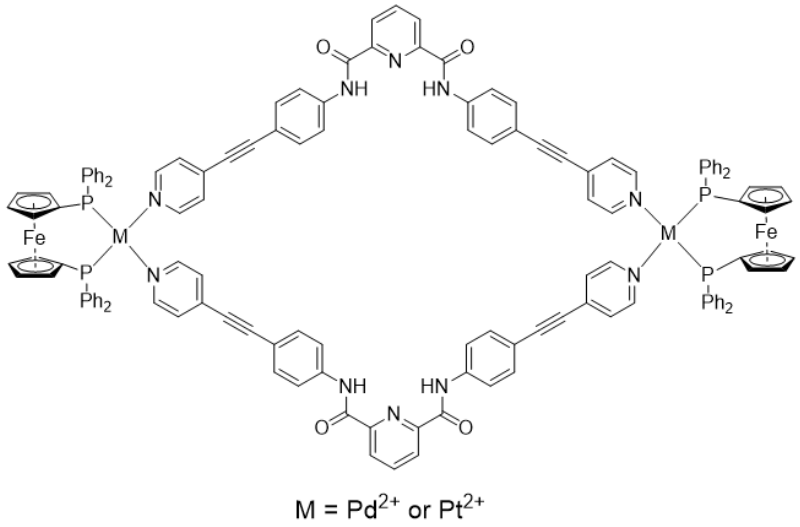

Figure 2. Chemical structure of the palladium(II) and platinum(II) metallacycle structures featuring both amide-based dipyridyl ligands and 1,1'-bis(diphenylphosphino) ferrocene ligands studied for antiproliferative effects

As well as 2D metallacycles, 3D supramolecular architectures using Pt(II) have been studied for their anticancer properties. For example, a highly charged $[Pt_6L_4]^{12+}$ metallacage was studied for its cytotoxic behaviour and mechanism of action in human ovarian cancer cells.[83] The metallacage was found in the same cytotoxicity range as cisplatin (the IC_{50} values referring to the platinum concentration) towards a range of human cancer cell lines including A2780, HT-29, A549 and MCF-7. The metallacage was, however, found to be relatively less toxic towards normal lung cells (IC_{50} = 7.2 µM for the Pt-metallacage; IC_{50} = 1.6 µM for cisplatin). Using atomic absorption spectroscopy to evaluate the intracellular Pt content, the 3D SCCs were found to be localized inside the cell nucleus.[83] In fact, it was shown that the mechanism of action involved the compound's non-covalent binding to DNA via intercalation.

$[Pd_2L_4]^{4+}$ supramolecular helicates are also promising anticancer agents. Studies by Crowley and coworkers of the effect of different ligands (functionalized trispyridyl scaffolds with rigid alkene linker vs benzotriazoles, hexane-triazoles and PEG-triazoles-bisfunctionalised phenyl rings) on the biological activity of Pd_2L_4 helicates have been carried out and showed a direct correlation between the stability of the helicate in biological media and its cytotoxicity.[84,85] Similar $[Pd_2L_4]^{4+}$ (L = 1,3-bis-hexanetriazole phenyl) helicates were also found to be up to seven-fold more toxic (IC_{50} = 6.0 µM) than cisplatin against the cisplatin-resistant MDA-MB-231 cell line.[84] Overall, these effects indicate a different mechanism of action than conventional metal-based drugs. In this case, the $[Pd_2L_4]^{4+}$ helicates were shown to induce cell death by disruption of the cell membrane.[84] Finally, examples of 3D metallacages, of the type Pd_2L_4, have also been reported as potential cytotoxic agents in cancer cells, either alone or by encapsulation of a cytotoxic agent.

2.1.2 2D Cytotoxic Ruthenium(II)-arene SCCs

Typically, Ruthenium(II) ions (d^6 electronic configuration) adopt a hexa-coordinated octahedral coordination geometry. Hence, in order to produce discrete supramolecular entities, rather than extended coordination polymers or MOFs, an auxiliary ligand is needed to block some of the several Ru^{II} coordination sites. In many cases this is achieved by forming dinuclear Ruthenium(II)-arene "clip" complexes before linking these clips together via pyridine containing multidentate ligands, to form a range of 3D and 2D supramolecular polyhedra.[86–92] Biologically active Ru-based coordination and organometallic complexes stimulated analogous studies of cytotoxic ruthenium-arene supramolecular coordination complexes.[93] Thus, a growing number of Ru cages and rectangles have been self-assembled and have shown promising results as cytotoxic agents.

Ruthenium(II) metallacycles were already reported in the late 1990's and displayed properties, such as water solubility and stability, that render them suitable for biological applications. It was initially postulated that cytotoxicity associated with supramolecular Ru(II) complexes was due to their intracellular dissociation, and subsequent binding of the released ruthenium cations to proteins and DNA, causing extensive cell damage and apoptosis.[87] However, these complexes have been shown to cause cell death also by triggering excessive autophagy, the controlled process of recycling dysfunctional or destroyed proteins and organelles via lysosome digestion.[94] Within a series of ruthenium(II)-arene metallarectangles with different panelling linkers, one has been shown to be more potent *in vitro* against multidrug resistant human colon cancer cells (HCT-15/CLO2, IC_{50} = 16.5 µM) compared to cisplatin and doxorubicin,[86] suggesting that the mechanism of cytotoxic action of these supramolecular structures is different from those of classical anticancer metallodrugs and requires further investigation.

Similarly to metallacycles, Ruthenium(II)-arene metallabowls have also been developed and tested for their antiproliferative properties *in vitro* against a range of cancer cell lines (colorectal, gastric, and liver cancer cells).[92,95,96] It was found that a ruthenium(II)-arene metallabowl featuring 8-dihydroxy-1,4-naphthaquinonato ligands was twice more active than both cisplatin and doxorubicin against HCT-15 cells (IC_{50} = 6.9 µM for the metallabowl; IC_{50} = 13.2 µM for cisplatin; IC_{50} = 15.9 µM for doxorubicin).[92] Further investigations showed that, upon metallabowl exposure, the expression of two known colorectal cancer suppressors, p53 and the Adenomatous polyposis coli (APC) gene, increased in HCT-15 cells.[92,96]

SCCs are still in the early stages of development as cancer therapeutic agents, however a few preliminary *in vivo* experiments have been carried out. The anticancer activity of two ruthenium(II)-arene metallacycles, one with a 2D rectangular geometry and one featuring a metallabowl geometry (figure 3), was studied *in vitro* against human gastric carcinoma cells (AGS) and human colon cancer cells (HCT-15).[94] The results showed that both metallacycles had comparable antiproliferative activities with respect to cisplatin and doxorubicin. Following these promising results, a hollow fiber assay was conducted, whereby a semipermeable fibre impregnated with the HCT-15 cells was implanted into the intraperitoneal and subcutaneous compartments of nude mice.[94] The two ruthenium-arene metallacycles were then administered to the impregnated nude mice, and the animals were left for 7 days before the hollow fibres were removed and the tumors examined. The study revealed that the metallabowl-type metallacycle was a more potent inhibitor of cancer cells growth than the metallarectangle. However, both these ruthenium-arene scaffolds were not as effective inhibitors of cell proliferation as the control anti-cancer drug, cisplatin, in the hollow fibres located in the intraperitoneal and subcutaneous regions of the host mice.[94] The mechanism of induced cell death was investigated and the study revealed that both metallacycles induced autophagy in HCT-15 cells, and again the metallabowl was more potent than the metallarectangle, in line with the observed anticancer activity.[94]

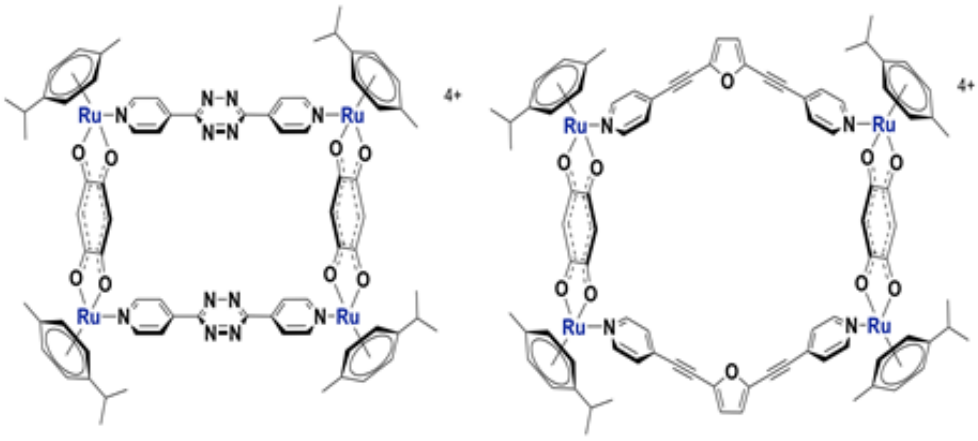

Figure 3. The chemical structures of the ruthenium(II) arene 2D SCCs studied *in vivo*; metallacycle (left) and metallabowl (right).[94] It was shown that the metallabowl had increased antiproliferative effects compared to the metallacycle, however neither structure performed as well as the known platinum(II) drug, cisplatin.

2.2 3D Supramolecular coordination complexes and their biomedical applications

Recently, 3D SCCs have been explored for biomedical applications. For example, some of these structures, due to their well-defined 3D morphology and chirality, have been exploited to target non-canonical DNA structures to achieve antiproliferative effects in cancer cells. Furthermore, as there are reported examples of 3D SCCs with well-defined and tuneable cavities, they were also exploited as drug delivery vehicles for anti-cancer drugs, rather than act as cytotoxic agents *per se*. In the next sections, we will discuss representative examples of both applications.

2.2.1 3D supramolecular coordination complexes as cytotoxic agents

Most of the cytotoxic SCCs mentioned in previous sections are non-selective for cancer cells, thus leading to possible side effects. With the aim to develop tumour directed SCCs, the initial strategy exploited the chirality of some of these scaffolds to direct molecular recognition of specific biological targets, namely nucleic acids. A first study investigated the mode of binding of a binuclear Fe(II) triple-stranded helicate (cylinder, figure 4A) to a DNA model by NMR spectroscopy and computational modelling techniques.[97] The obtained results suggested that the helicate binds to the DNA major groove. It was also revealed that although a racemic mixture of the chiral helicate was introduced to the double stranded oligonucleotide, only the *M*-enantiomer was able to bind DNA causing a change in its conformation.[97] The mode of binding of the Fe(II) cylinder was further studied and revealed that the helix preferentially binds to short (8-10 base pairs) purine-pyrimidine tracts within the DNA sequence.[98] The affinity for specific DNA sequences proved a promising feature to target cancer cells via binding of the helicates to oncogenes.[98]

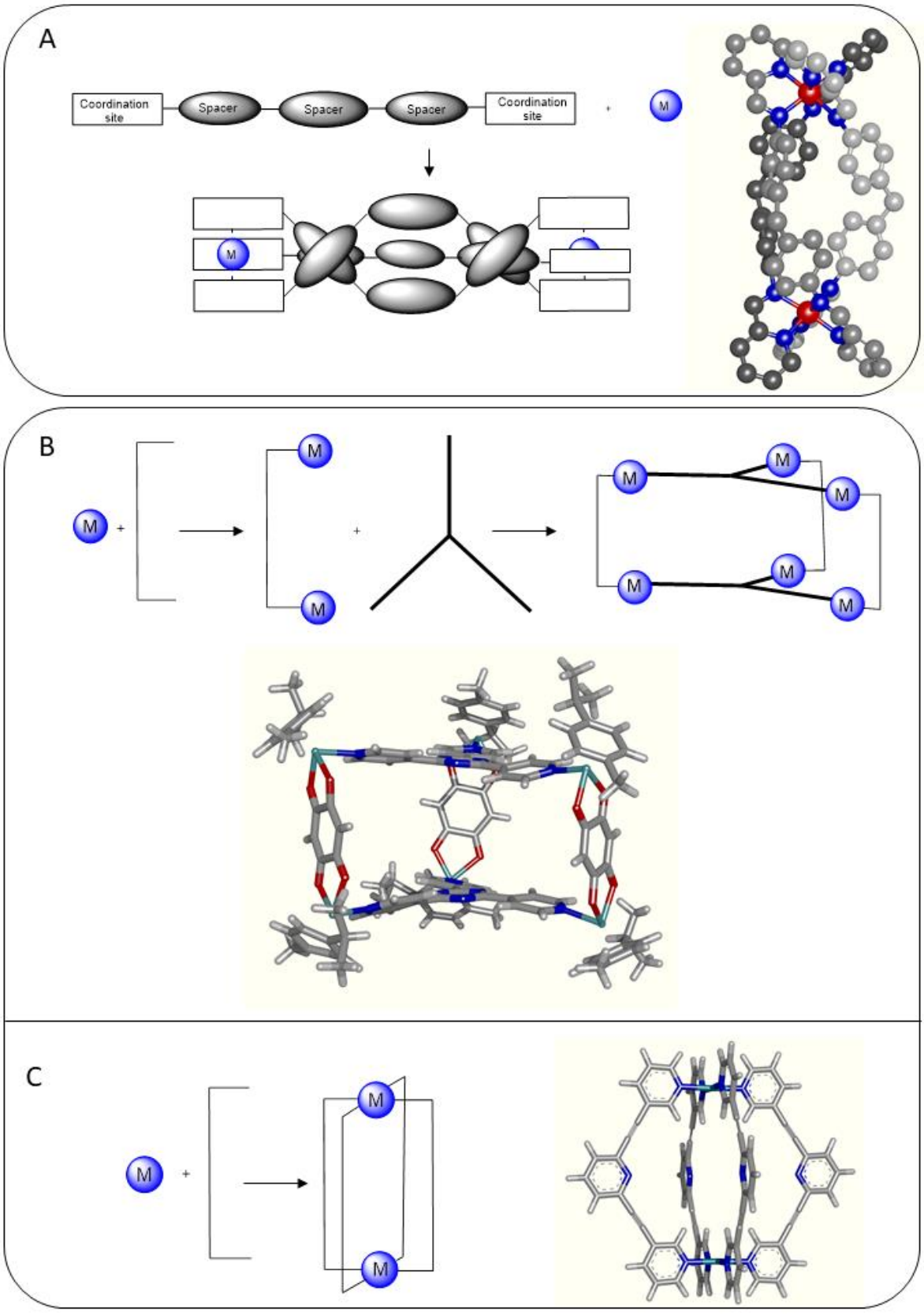

Figure 4: Cartoon representations and reported crystal structures of selected 3D SCCs which are the subject of study for use as anti-cancer therapeutics. A) Chiral $Fe^{II}_2L_3$ metallahelicate studied for its anti-cancer activity.[97] B) Hexaruthenium(II) metalallaprism which has been studied as a "trojan-horse" type drug delivery vehicle,[73] C) Pd_2L_4 type metallacage which has been studied as a drug delivery system.[99]

It was also discovered that Fe(II) cylinders have a high specificity for RNA 3-way junctions,[100] as well as for certain non-canonical secondary DNA structures, such as DNA bulges,[101,102] and G-quadruplex DNA (G4).[103] In particular, targeting telomeric G4s and stabilization of these structures has been shown to inhibit telomerase activity, leading to cell death.[104] To that end, a pair of enantiomeric Fe^{II} helicates, which were soluble in aqueous media, were synthesized and their affinity for human telomeric G4s was assessed.[103] The *P*-enantiomer Fe(II) helicate was found to bind strongly and selectively to the G4, whereas the *M*-enantiomer showed no association. Furthermore, the strong binding affinity to G-quadruplex DNA translated into strong inhibition of telomerase activity.

Another non-canonical DNA structure which has been reported as a promising target for binuclear metallahelicates (Fe(II) and Ru(II) -based) are triple stranded "Y-shaped" junctions.[98,100,105–109] These secondary structures form during DNA transcription and replication, and as such are promising targets to achieve cell cycle control. It was also shown that their stabilization severely inhibits the function of polymerase enzymes, and indeed, this has been postulated as the mode of action accounting for the cytotoxicity of the helicates.[100] Further studies of DNA binding of Fe(II) helicates revealed that, to facilitate strong binding to the major groove of duplex DNA, a rigid helicate is preferred over the analogous flexible helicates.[110] Moreover, the rigid Fe(II) helicate under investigation was found to be a potent cytotoxic agent against cisplatin-resistant human ovarian carcinoma cells.[110]

3D ruthenium-arene SCCs have also been developed as anticancer agents (figure 4B). By introducing tridentate, planar ligands to the binuclear arene Ru(II) "clips", a range of hexanuclear Ru^{II} metallacages have been reported by variation of the panelling linker ($[Ru_2(p\text{-}^{i}PrC_6H_4Me)_2(OO\cap OO)][CF_3SO_3]_2$ ($OO\cap OO$ = 2,5-dioxydo-1,4-benzoquinonato [dobq], 5,8-dihydroxy-1,4-naphthaquinonato (donq), and 6,11-dihydroxy-5,12-naphthacenedionato [dotq] etc.).[111–114] Of these 3D systems, the dinuclear "clip" containing 5,8-dihydroxy-1,4-naphthaquinonato as the bridging ligand was found to be a moderate inhibitor of cell viability against a range of cancer cell lines (IC_{50} values between 25.9 and 88.2 μM whereas all the other tested metallacages had IC_{50} values of ca. 200 μM).[87,95]

2.2.2 3D SCCs for use as drug delivery vehicles

3D SCCs have also shown promise for biomedical applications not only due to their intrinsic anticancer potential, but also for their favourable properties for use as drug delivery systems. This is particularly relevant to cancer chemotherapy, whose success rate remains limited, primarily due to scarce selectivity of drugs for the tumour tissue, often resulting in severe

toxicity and in the development of drug resistance. So far, lipid nano-systems, such as liposomes and micelles, along with virus-inspired vectors and polymeric particles,[115] dendrimers[116] as well as inorganic nanoparticles,[40] have been studied to deliver bioactive compounds to tumour sites. However, such targeted constructs have several limitations: for example, polymers and dendrimers often require considerable synthetic effort and can be plagued by low yields and largely amorphous final structures, while nanoparticles often present issues of toxicity and lack of biodegradability.[117]

In this context, supramolecular metallacages offer a number of properties that make them attractive candidates for future drug delivery systems. For example, the rigid, porous structure offers a secure cavity for small drug molecules, to protect them from metabolism, and the ability to modify the ligand structure both pre- and post- self-assembly allows for the properties of the resulting cage to be improved. Furthermore, since metallacages, at variance with MOFs, are discrete chemical entities, the issues of solubility in an aqueous environment can be potentially overcome. Despite these attractive features, SCC drug delivery is still in its infancy.[118] SCC drug delivery systems have been based on *i)* both encapsulation of a drug, driven by hydrophobicity of the cargo drug molecule and the host cavity, and non-covalent interactions within the host cavity, as well as *ii)* bonding of a pro-drug species to the SCC architecture. In the latter case, the active part of the pro-drug can then be cleaved from the SCC via external chemical stimuli to deliver the drug in a controlled manner.

Pioneering work on encapsulation based SCC drug delivery systems focused on the study of hexaruthenium metallacages (metalla-prisms, figure 4B),[73] as they were found to encapsulate lipophilic molecules. Specifically, the cationic hexanuclear metalla-prism [(*p*-cymene)$_6$Ru$_6$(tpt)$_2$(dhbq)$_3$]$^{6+}$ (tpt = 2,4,6-trispyridyl-1,3,5-triazine; dhbq = 2,5-dihydroxy-1,4-benzoquinonato) was used to encapsulate the hydrophobic Pd^{II} and Pt^{II} complexes [M(acac)$_2$] (M = metal, acac = acetylacetonato) (Figure 5).[73] The metalla-prism is water soluble and moderately cytotoxic (IC_{50} ca. 23 μM) against human ovarian A2780 cancer cells, while the [M(acac)$_2$] complexes are completely inactive due to their inherent lack of solubility in water. Interestingly, the encapsulated [Pd(acac)$_2$] ([Pd(acac)$_2$]⊂[(*p*-cymene)$_6$Ru$_6$(tpt)$_2$(dhbq)$_3$]$^{6+}$]) was 20-fold more cytotoxic (IC_{50} ca. 1 μM) than the empty metalla-prism (IC_{50} ca. 23 μM) while the effect was much less pronounced with the encapsulated [Pt(acac)$_2$] complex (IC_{50} ca. 12 μM). This initial study provided the proof-of-concept for what was defined as "*the Trojan horse strategy*" of hiding a cytotoxic agent in the cavity of a metallacage until, after internalization within the diseased cells, the drug can be released and perform its cell-killing activity.[73]

Subsequently, a hexaruthenium metallacage of the type [Ru$_6$(*p*-*i*PrC$_6$H$_4$Me)$_6$(tpt)$_2$(C$_6$H$_2$O$_4$)$_3$]$^{6+}$ was investigated for the release mechanism of encapsulated

fluorescent pyrene derivatives and for its anticancer properties *in vitro*.[72] The fluorescence of the pyrene derivatives is quenched upon encapsulation, allowing for the release of the molecule to be monitored by fluorescence spectroscopy.[72] Concerning the antiproliferative properties, while the free pyrene derivative and the cage complex alone were scarcely cytotoxic (IC_{50} >20 µM and 16 µM, respectively), the host-guest complex was considerably more active (IC_{50} ca. 6 µM).[72] Fluorescence microscopy data suggested that the increased cytotoxicity was due to an increased uptake of the poorly soluble pyrene derivative into the cancer cell after being delivered by the water-soluble cage complex.

The encapsulation properties of the hexaruthenium metallacage with a series of functionalized fluorescent pyrene derivatives was characterized using NMR (^{1}H, 2D, DOSY) spectroscopy and electrospray ionization mass spectrometry (ESI-MS).[119] The synthesis of the host-guest system proceeded via a two-step process: first the di-ruthenium half sandwich molecular "clip" reacts with silver triflate to produce a reactive intermediate; afterwards, a 2:1 solution of the tridentate tpt ligand and the pyrene derivative is introduced to form the host-guest complex via self-assembly.[119] The antiproliferative properties of the vacant cage and the pyrene-cage complexes were studied in human A2780 ovarian cancer cells. While the vacant cage had a moderate antiproliferative effect, the encapsulated host-guest complexes resulted in lower IC_{50} values.[119] Two of the host-guest complexes, namely pyrene derivatives tethered to either a carbonic anhydrase inhibitor or to a glutathione transferase inhibitor showed antiproliferative effects comparable to the anticancer drug cisplatin. The results also showed that the hexaruthenium cage complexes can help to improve the efficacy of insoluble inhibitors *in vitro.*

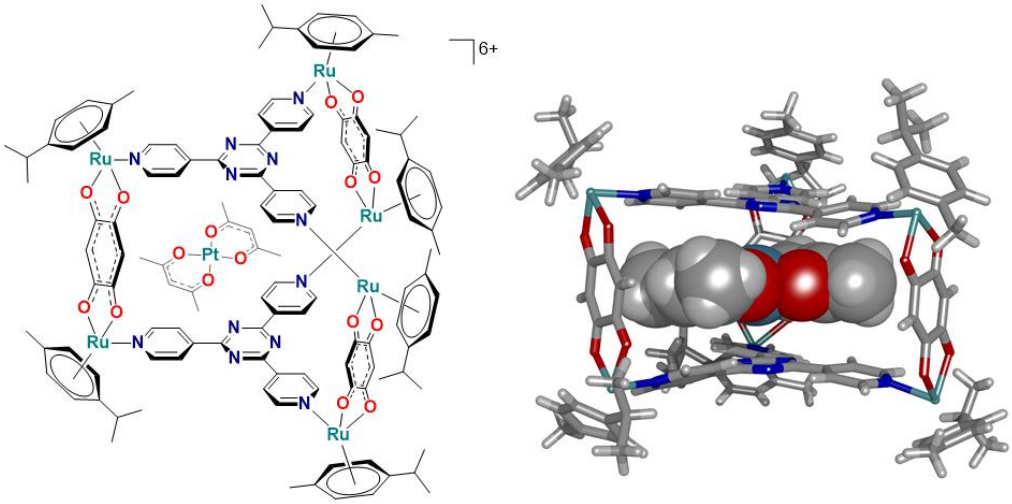

Figure 5. Chemical structure and crystal structure of a hexaruthenium metallaprism encapsulating the poorly soluble Pt(II)$(acac)_2$.[73] The release of the guest as a function of the portal size could be manipulated by extending the polycyclic aromatic system in the di-ruthenium bridging ligands.[120]

The effect of the portal size of the hexaruthenium metallacage complex on the retention of the planar guest molecules, [Pd(acac)$_2$] complex and 1-(4,6-dichloro-1,3,5-triazin-2-yl)pyrene, was also investigated.[120] Thus, three hexaruthenium cages were prepared by extending the polycyclic aromatic system in the di-ruthenium bridging ligands, using the 1,4-naphthoquinonato, 1,4-anthraquinonato, and 5,12-naphthacenedionato analogues, which progressively decreased the portal size of the cage, while the internal cavity remained largely the same. The host-guest properties of these water-soluble supramolecular drug delivery systems were studied in solution by NMR and fluorescence spectroscopy. The results showed that the complex with the largest pore size (estimated to be approximately 7.4×10.2 Å by molecular modelling) is more stable, suggesting that a larger pore size facilitates the entrance of the guest molecule in the cage, but the smaller pore size retains the guest molecule more effectively.[120] Moreover, the ability of the hosts to deliver guest molecules into cancer cells was evaluated and the uptake mechanism studied by Inductively Coupled Plasma Mass Spectrometry (ICP-MS) and fluorescence microscopy.[120] All cages delivered the host to intracellular organelles and the mechanisms of uptake involve endocytosis/macropinocytosis rather than passive diffusion across the cell membrane.[120]

Other examples of SCCs as drug delivery systems, based on other transition metals, include surface-functionalized porous coordination nanocages of Cu^{II} and 5-(prop-2-ynyloxy)isophthalic acid (pi), bearing a water solubilizing polymer (PEG5k), which have been successfully synthesized using a “click chemistry” approach.[121] The scaffold is composed of 12 di-copper paddlewheel clusters and 24 isophtalate moieties, with 8 triangular and 6 square windows that are roughly 8 and 12 Å across, respectively. The internal cavity has a diameter of ca. 15 Å and the cage has high stability in aqueous medium. In addition, the cages’ drug loading and release capacity has been evaluated using the anticancer drug 5-fluorouracil (5-FU).[121] Drug release experiments were carried out by dialyzing the drug-loaded Cu(pi)-PEG5k against phosphate buffered saline (PBS) solution, to simulate physiological conditions, at room temperature. Interestingly, around 20% of the loaded drug was released during the first 2 hours, while a flatter release curve can be observed up to 24 hours. The latter slow release has been associated to the slow diffusion rate of 5-FU caused by the strong interaction between Lewis acid sites in Cu(pi) and basic site of 5-FU.

The control of the host-guest properties of the cavity defined by the SSC is another essential feature to implement these complexes for drug encapsulation. For example, in contrast to the previously mentioned metallacages, anthracene-based Pt^{II}- and Pd^{II}-linked coordination capsules provide a characteristic spherical cavity closely surrounded by polyaromatic

frameworks.[122] The isolated cavity features a diameter of ca. 1 nm and a volume of ca. 600 Å^3.[123] These systems can accommodate various neutral molecules in the confined cavity through hydrophobic interactions, but also π-stacking, in aqueous solution. Cages of this type were recently reported to be able to encapsulate spherical (paracyclophanes, adamantanes, and fullerene), planar (pyrenes, triphenylene and caffeine), and bowl-shaped molecules (corannulene),[122–124] while fluorescence microscopy studies allowed investigation of the intracellular accumulation of these systems.[124] It is worth mentioning that the capsules – even without their guest molecules – manifest very pronounced cytotoxic effects, which may prevent their applications as "pure" drug delivery systems. The observed trends in the anticancer activity of the capsules and their host-guest complexes correlate with their different stabilities toward glutathione, estimated by NMR-based kinetic experiments.[124] The data suggest the glutathione-triggered disassembly of the capsular structures in cells as a potential activation pathway for their cytotoxic activity.

Within the M_2L_4 cage family, Crowley *et al.* have designed a cationic Pd_2L_4 cage using (2,6-bis(pyridin-3-ylethynyl)pyridine) as the bidentate ligand,[99] based on previous work by Fujita *et al.*[99] and Steel *et al..*[125] ^{1}H NMR, ESI-MS and X-ray diffraction (XRD) were used to show that a quadruple stranded cage with the internal cavity lined with nitrogen from the central pyridine of the ligand had been formed (figure 4C). Interestingly, for the first time, the encapsulation of the anticancer drug cisplatin within the cage's cavity was demonstrated by XRD studies. Moreover, ^{1}H NMR studies showed the peak corresponding to the internal proton had broadened and shifted downfield which is indicative of hydrogen bonding interactions of the host-guest system. The release of cisplatin was facilitated by the introduction of competing ligands (4-Dimethylaminopyridine or Cl^-) to disassemble the cage, as shown via ^{1}H NMR and ESI MS. The water solubility and the stability under physiological conditions are both crucial for the biological application of metalla-assemblies. Unfortunately, Pd_2L_4 cages of this type are scarcely soluble in aqueous environment, despite their overall positive charge. Improvement of their hydrophilic character may be possible via the introduction of water soluble moieties in their scaffold. As an example, PEGylation of Pd_2L_4 systems has shown to efficiently improve the stability of single nanocages in solution.[126]

Following these promising results, Casini *et al.* have recently developed a range of fluorescent *exo*-functionalised Pd_2L_4 metallacages and studied the encapsulation of cisplatin by NMR spectroscopy,[127] reporting similar downfield shifts for the protons lining the cages internal cavity, as reported previously by Crowley *et al*. for similar systems.[99] Most importantly, the cages were shown to be able to encapsulate up to two molecules of the anticancer drug cisplatin by XRD (Figure 6). Thus, the cytotoxicity of the palladium cages and cage precursor compounds

were tested against a panel of human cancer cells, including A549, SKOV-3, and HepG2 cell lines, *in vitro*. Furthermore, the activity of encapsulated cisplatin in the benzyl alcohol-derived palladium cage was evaluated against SKOV-3 cancer cells in comparison to cisplatin. Interestingly, the encapsulated cisplatin showed an important decreased IC_{50} value (1.9 ± 0.5 μM) compared to free cisplatin (15.4 ± 2.2 μM) and the vacant cage complex (11.6 ± 1.7 μM), respectively.[127] Notably, the reported metallacages were non-toxic in healthy rat liver tissue *ex vivo*.[127] Furthermore, the Pd(II) metallacages showed fluorescence properties due to the used ligand system, and fluorescence microscopy studies allowed to study their uptake in cancer cell lines.

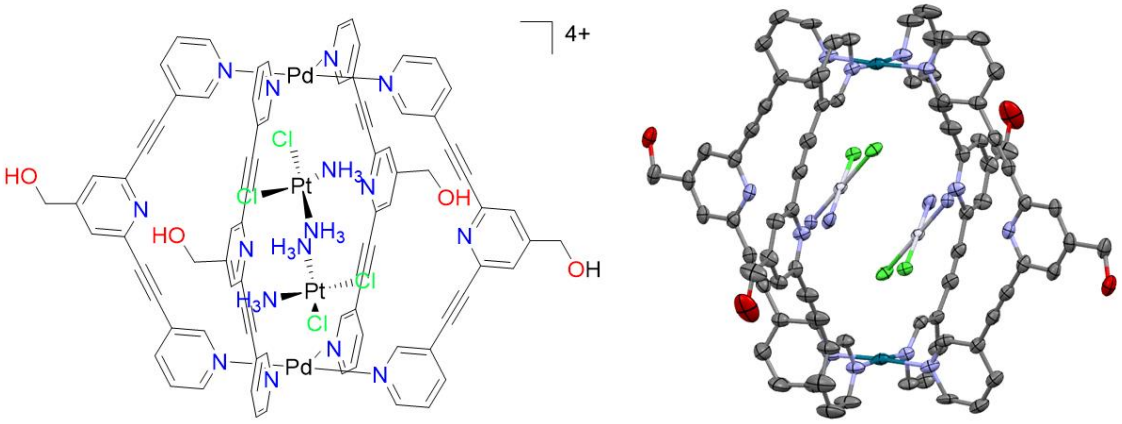

Figure 6. Chemical structure and X-ray structure of the Pd_2L_4 metallacage encapsulating two cisplatin molecules (H1-Cl: 2.786 Å; H2-Cl: 2.328 Å; N1-H3: 2.181 Å; N2-H4: 2.326 Å ; Pt1-Pt2: 3.439 Å).[127]

Selective accumulation of metallacages in tumours has been hypothesized to occur via the enhanced permeability and retention (EPR) effect,[114] which has been widely explored in cancer therapy for delivery via passive targeting.[38] In fact, the EPR effect targeting solid tumours has been predominantly shown to be involved in the passive targeting of drugs with a molecular weight of more than 40 kDa (20–200 nm in diameter) and for low molecular weight drugs presented in drug-carriers such as polymeric conjugates, liposomes, polymeric nanoparticles, as well as for micellar systems.[37] However, for supramolecular metallacages, with molecular weight of ca. 2-3 KDa and diameter of ca. 10 Å, the EPR effect is not likely to influence their delivery. Therefore, it can be assumed that successful conjugation of cell-specific ligands to the outside of the metallacage, including tumour-targeting peptides (TTPs) that are specific for tumour related surface markers such as membrane receptors,[80,128] could improve its target specificity and efficacy. However, this concept has been scarcely explored so far. For example, one study has showed non-covalent peptide coating on self-assembled $M_{12}L_{24}$ coordination spheres,[129] while encapsulation of a protein within a $Pd_{12}L_{14}$ cage (L = bidentate ligand) has been achieved

by appropriate *endo*-functionalization of the ligands.[130] In this case, ligands were first tethered to the protein. Afterwards, following the addition of metal ions and other ligands, coordination nanocages self-assembled around the protein. The latter was the first example of encapsulation of a protein within synthetic host molecules and may reveal novel strategies to delivery of proteins at specific site and to control their function.

With the aim of implementing supramolecular metallacages as drug delivery systems, the first example of bioconjugation of self-assembled Pd_2L_4 cages to a model linear peptide was recently reported.[131] In this case, the approach of bioconjugation of metallacages was based on amide bond formation between the carboxylic acid (or amine) serving as *exo*-functionalized ligand/cage and the amine (or carboxylic acid) groups of the model peptide side chains. Thus, the bioconjugation was performed using two different approaches: i) direct tethering of the metallacage to the peptide (Approach 1); or ii) initial anchoring of the ligand to the peptide, followed by metallacage self-assembly (Approach 2) (Figure 7).[131] Formation of the metallacage-peptide constructs was assessed via high-resolution ESI-MS, also coupled to high performance liquid chromatography (LC-MS). So far the best results were achieved with Approach II, where first the coupling of the peptide to the ligands constituting the cages was performed, followed by *in situ* reconstitution of the Pd_2L_4 cages via self-assembly. Interestingly, improved bioconjugation efficiency was observed in the case of the *exo*-functionalization with carboxylic acids compared to amino groups. In the latter case, formation of peptide cyclic by-products prevented efficient bioconjugation under the applied reaction conditions. Nevertheless, NH_2 functionalization may still be suitable for bioconjugation of the cages with peptides of different sequences and with antibodies, and merit investigating for this application.[131] The obtained results open the possibility of efficient bioconjugation of metallacages to peptides which could be extended to targeting moieties such as peptides or affimers, and possibly also to antibodies.

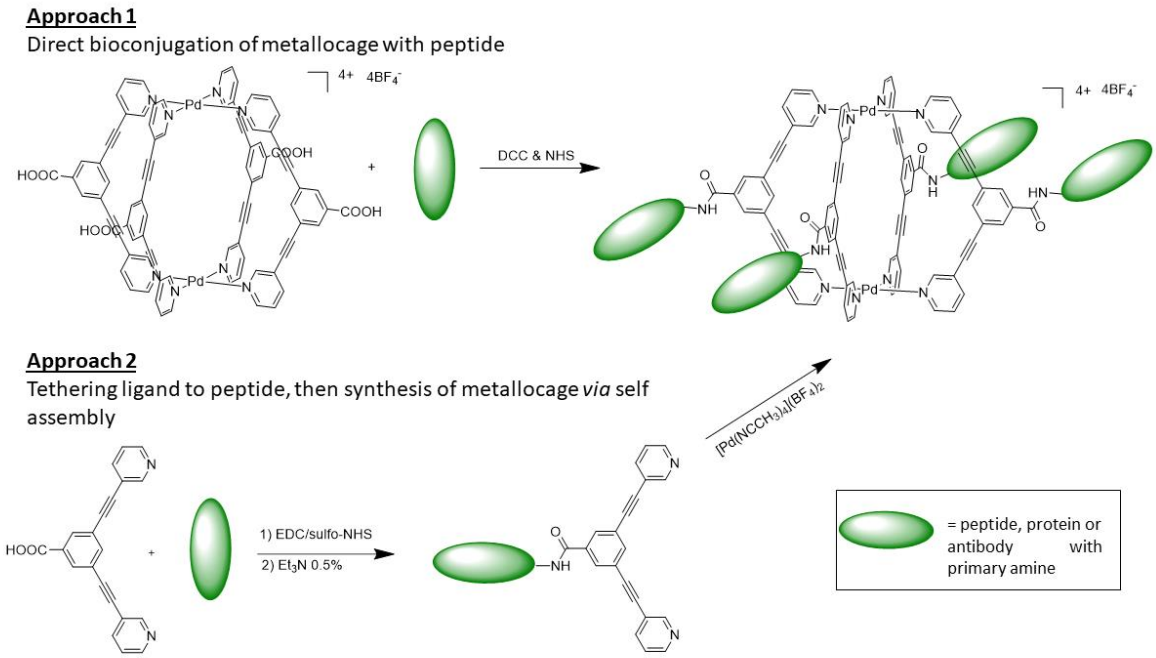

Figure 7. Scheme of the two different bioconjugation approaches applied to conjugate a Pd_2L_4 cage to a model peptide *via* amide bond formation: (i) direct tethering of the metallacage to the peptide (Approach I); or (ii) initial anchoring of the ligand to the peptide, followed by metallacage self-assembly *in situ* (Approach II).[131] Theoretically, both approaches can produce bioconjugated Pd_2L_4 cages tethered to four peptide units.

Fluorescent metallacages would be a highly desirable drug delivery system, since their fluorescence would allow to track their cellular distribution *in vitro,* and thus provide insight into their mechanisms of cellular accumulation. However, quenched photoluminescence of Pd_2L_4 metallacage systems is often observed, which can be attributed to two primary factors: i) the so called "heavy metal effect" observed upon self-assembly of luminescent ligands to the metal ion nodes,[132] and ii) the disruption of the emissive conjugated system. Therefore, in order to improve the fluorescence properties of Pd_2L_4 cages (L = fluorescent bispyridyl ligand), Casini and Kühn *et al.* have synthesized cages *exo*-functionalised *via* amide bond with either naphthalenyl or anthracenyl moieties.[132] The cages were also investigated for their anticancer properties in human lung and ovarian cancer cell lines *in vitro*. While the observed cytotoxic effects hold promise and the cages resulted to be more effective than cisplatin in both cell lines, surprisingly, it was observed that the emission properties were extremely scarce (quantum yields below 1%). To explain this unexpected observation, time dependent density functional theory (TD-DFT) was carried out on the anthracenyl-based ligand and revealed that the cause of the observed quenching was most likely due to a lower probability of emission (2%) than the corresponding carboxyl functionalised ligands (24%).[132] Further studies were carried out to determine the possible emission wavelength of the ligands by converting the calculated energy difference between the excitation energy and the relaxation energy, and converting this to a wavelength

and was found to be in the IR region (λ_{max} =2000 nm), whereas the carboxyl and amine functionalised ligands emitted in the visible range (λ_{max}= 420 nm). From this observation two reasons were given for the poor fluorescence of the ligands. Firstly, the probability of a HOMO-LUMO excitation is far less likely for the anthracenyl-based ligand. Secondly, the energy differences between the highest excited state and the non-relaxed ground level did not correlate to a wavelength within the visible range. TD-DFT calculations showed that the ground state conformation of the amide bond between the bispyridyl ligand and the anthracenyl functional group was planar with a dihedral angle of 177°. The calculated first excited state after light absorption showed that the amide bond was no longer planar, with a dihedral angle of 99°, and thus the conjugated chromophoric system is disrupted leading to a higher energy difference between the lowest point that can be reached after fluorescence and the relaxed ground state. Therefore, less energy is converted into light by emission, which explains the observed higher wavelength outside the visible range.[132]

In order to avoid disruption of the emissive conjugated fluorescent tag, the direct conjugation of highly luminescent ruthenium based fluorophores to the Pd_2L_4 metallacage scaffold *via* an unsaturated linker group (such as an amide or cycloazide) was attempted.[133] Thus, the highly luminescent fluorophore tris(bipyridine)ruthenium was conjugated to the Pd_2L_4 metallacage *via* a saturated alkyl spacer. The hypothesis proved accurate as, remarkably, the resulting cage resulted to be amongst the most emissive metallacages known to date ($\phi_{(cage)}$ = 66%).[133]

Overall, 3D SCCs with host-guest properties, including complexes based on different metal ions (Ru^{II}, Pd^{II}, Pt^{II}),[73,127,134] have been shown to be viable candidates for future drug delivery systems. In particular, the self-assembly process of M_2L_4 type SCCs (M = Pd^{II}, Pt^{II})[127,134] and their tolerance to functionalisation with numerous functionalities,[131,132,135,136] warrant further investigation into these intriguing supramolecular systems as drug delivery vehicles.

Chapter 3: Self-assembled supramolecular M_2L_4 metallacages

3D cage-like supramolecular coordination complexes (SCCs) – also defined as metal-organic polyhedra, or metallacages - are of great interest, as their 3D structure allows an internal cavity to encapsulate guest molecules. Metallacages, of the general formula M_xL_y (M: Metal; L: Ligand) form a highly diverse class of structures due to the interchangeable nature of both ligand and metallic nodes. An essential role in determining the resulting metallacage structure (geometry and size) and chemical properties is played by the metal ion, which is commonly a transition metal (*i.e.* Fe(II), Co(II), Ni(II), Cu(II), Zn(II), Mo(II), Ru(II), Rh(II), Pd(II) and Pt(II) ions have been used) or a lanthanide. Overall, the combination of the coordination geometry of the selected metal ion with different ligands can give rise to a great variety of supramolecular scaffolds for different applications.[137] Recently, numerous thematic reviews have discussed the vast progress in the design and synthesis of these attractive materials.[138–142] There are numerous methods to categorise 3D SCCs, such as the resulting cage geometry, the ratio of ligands to metals, the type of self-assembly or by the metal ion used.

3.1 Self-assembly of Pd_2L_4 metallacages

One intriguing class of metallacages, the simplest M_2L_4 metallacages, are those formed from by self-assembly of two transition metal centres, often featuring square planar coordination geometries (early studies of M_2L_4 metallacages involved octahedral *trans*-$[M(L)_4(H_2O)_2]$ metal centres)[143] bound to four bis-monodentate ligands (Scheme 1). As an important prerequisite for the polyhedral 3D structure, at least one component of the systems must show a bent geometry (with a bending angle $\theta < 180°$).[74] This provides the needed curvature for the formation of a finite metallacage structure.

Examples of M_2L_4 type metallacages include those based on Cu(II),[143] Co(II),[144] Pt(II)[134,145] and Pd(II) ions.[66,127] Within this family, M_2L_4 metallacages formed from Pd(II) (Pd_2L_4 metallacages) can self-assemble in near quantitative yields from the reaction of stoichiometric amounts of bis-monodentate ligands and Pd(II) salts (2: 1; L: Pd^{II}). Pd(II) ions are diamagnetic and therefore facilitate the cage characterisation by NMR spectroscopy; moreover, Pd(II) complexes are kinetically inert with respect to ligand exchange reactions, which prevent cage hydrolysis in aqueous environment. Thus, these Pd_2L_4 metallacages in particular have been the subject of numerous studies.[99,127,145–147] As the self-assembly can typically occur at room temperature without the aid of harsh reactants, the scope of functionalised ligands that can be used to form Pd_2L_4 metallacages is broad and, thus, several different applications have been

proposed for this family of SCCs, from molecular flasks to facilitate new catalytic reactions,[148,149] to drug delivery systems.[66,99,127]

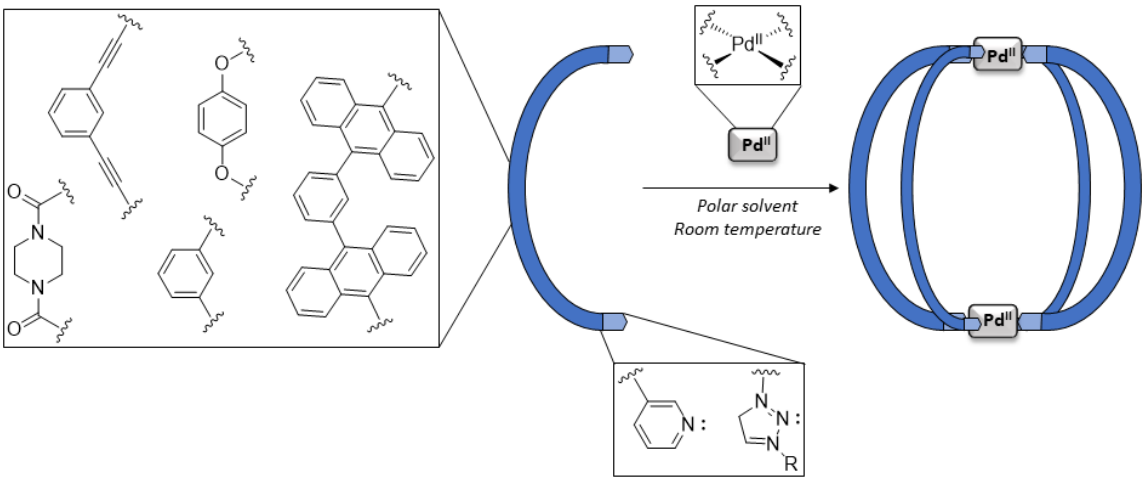

Scheme 1: Cartoon scheme highlighting the versatility of reported Pd_2L_4 metallacages all formed under similar self-assembly conditions. By utilising different ligand scaffolds able to impart a bending angle between the coordinating units of $\theta < 180°$, metallacages of different size, shape and flexibility can be obtained. Different coordinating units of the ligand can be used to alter the stability of the resulting coordination cage, such as pyridyl or triazole units. Different sources of square planar palladium(II) featuring non-coordinating counter anions can also be employed.

The self-assembly of Pd_2L_4 metallacages has been shown to occur in polar organic solvents, including acetonitrile, acetone, DMSO and DMF, and is also tolerant to numerous ligand architectures[122,125,150–153] The constituent ligands usually feature pyridyl units as the coordination sites, although other coordinating sites have been studied, for example triazoles (Scheme 1).[84154] The ligand scaffold is often composed of aromatic rings connected *via* linker units, for example amide or sp^3 linker units can impart flexibility to the corresponding Pd_2L_4 metallacage. Alkyne, or fused aromatic ring ligand systems, have also been reported for the synthesis of more rigid ligands, to restrict the degree of freedom of the corresponding cage and impart a more defined cavity within the Pd_2L_4 metallacage. There is therefore great flexibility in the design of ligands which will successfully form stable Pd_2L_4 metallacages by featuring two coordinating units separated by a ligand scaffold that forces a bending angle of $\theta < 180°$ between the two coordinating sites. This flexibility in design as led to a diverse array of final structures for Pd_2L_4 type metallacages.

The success of the self-assembly of Pd_2L_4 metallacages is also dependent on the choice of palladium precursor. The palladium salt must be square planar d^8 palladium(II) to facilitate the formation of discrete metallacage assemblies. The precursor palladium(II) salt should also contain a non-coordinating counter anion so as not to interfere with the self-assembly with the

bis-monodentate ligands.[74] Furthermore, the ligands of the palladium precursor should be labile enough to not act as competitive ligands with the coordinating units of the ligand.

3.1.1 Coordination of bis-pyridyl ligands to palladium(II)

The Pd_2L_4 metallacages that are the subject of this project are based on ligands that coordinate to Pd(II) metal ions via pyridyl units. As such, a brief synopsis on the coordination of pyridyl functional groups to square planar d^8 Pd(II) ions is presented. Pyridyl compounds are widely studied compounds,[155] and analogous to phenyl-based aromatic compounds, with one aromatic CH replaced by N. Pyridine obeys Huckels law of aromaticity,[156] with a non-hybridised *p*-orbital occupied by an electron contributing to the aromatic system. Pyridine is electron deficient when compared to phenyl derivatives due to the increased electronegativity of the heteroatom when compared to carbon. The more electronegative nitrogen will act to inductively remove electron density from the aromatic system. The heteroatom of pyridyl units, nitrogen, is sp^2 hybridised, with two of the sp^2 orbitals participating in bonding with the adjacent carbons, and the third orbital fully occupied with two electrons and protruding out from the aromatic ring. The latter fully occupied sp^2 orbital is oriented perpendicularly to the non-hybridised *p*-orbital of the nitrogen, and thus, it is also perpendicular to the plane of the delocalised electrons. As such, the occupied sp^2 orbital does not contribute to the electron density of the aromatic ring and can therefore act as a Lewis base, forming coordination bonds with Lewis acidic metals.

Palladium(II) is a third row transition metal ion with the electron configuration [Kr] $4d^8$. There are 5 *d*-orbitals that make up the valence orbitals of transition metals (figure 1). Palladium(II) has a valency of four, and adopts a square planar coordination conformation, as opposed to a tetrahedral conformation observed for d^8 transition metal ions of higher periods. The square planar geometry of palladium(II) can be shown by *d*-orbital crystal field splitting diagram (figure 1). Palladium(II) adopts a square planar conformation due to both the fact that fewer electrons occupy energetically unfavourable orbitals,[157] but also due to the lower electron pairing energy, due to the larger size of palladium(II) valence orbitals compared to the size of higher period d^8 metal ions such as nickel(II), which typically adopts a tetrahedral conformation (figure 1).[157] The square planar geometry can be experimentally demonstrated by NMR spectroscopy, as d^8 metal ions occupying a square planar geometry have no unpaired electrons and are thus, diamagnetic, which is in contrast to tetrahedral conformations which would result in unpaired electrons.

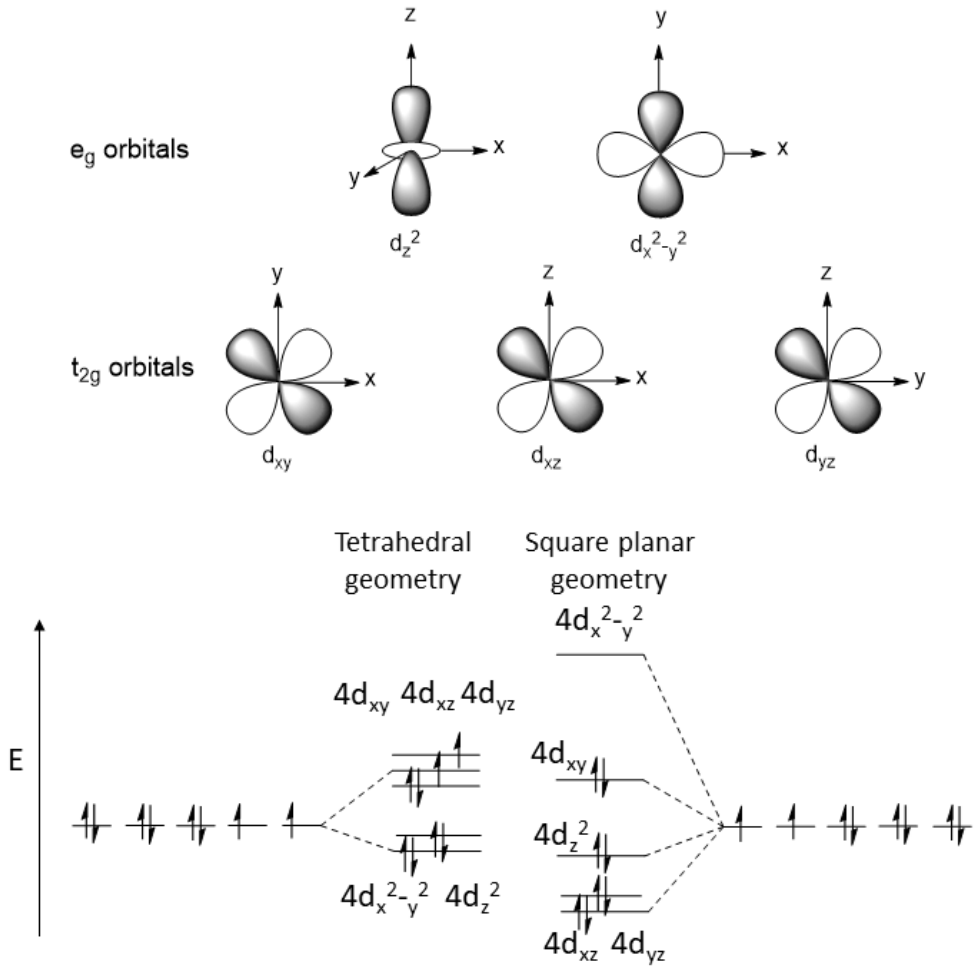

Figure 1: Top: The five d-orbitals Bottom: *d*-orbital crystal field splitting diagrams for tetrahedral and square planar geometry for Pd(II) ions. Palladium(II) adopts a square planar geometry, as the large spacial overlap of the metal ion with the ligand causes further destabilisation of the $d_{x^2-y^2}$ *d*-orbitals, and thus the energy required to pair electrons is more favourable than occupying the $d_{x^2-y^2}$ orbital.

3.1.2 Heteroleptic Pd_2L_4 metallacages

While most of the reported polyhedral complexes are homoleptic in nature (with the same type of ligands), the controlled synthesis of heteroleptic cages would be extremely attractive for biological applications in that different functional groups could be included in the overall cage scaffold (e.g. to achieve both imaging and targeted therapeutic effects). Self-assembly involving two or more different ligands has often been examined with the aim of generating more elaborate structures and functions, but a clear strategy to predict and account for the structures of mixed-ligand self-assembly does not seem to exist.[158] Although the syntheses of heteroleptic cages have been reported, the only examples to date which achieve an isolated product with a vacant internal cavity are those that follow the face directed synthesis.[65,73] First, a tightly bound organometallic precursor is synthesised, followed by the self-assembly of the metallacage upon

introduction of a multidentate Lewis basic ligand.[73] However, recently, there have been reports of the synthesis of multicomponent heteroleptic Pd_2L_4 metallacages.[146,159,160] Unfortunately, the examples reported so far do not isolate a single and pure heteroleptic cage but rather a mixture of multi-component cages. For example, Crowley *et al.* have described the controlled synthesis of heteroleptic metallacages of the general formula $Pd_2(L_a)_2(L_b)_2$ using structurally similar tripyridyl ligands, which was discovered while carrying out competitive ligand substitution experiments.[146] The study showed that the addition of an amino functional group to the terminal pyridine of the ligand would replace the original tripyridyl ligands due to the electron-donating properties of the amino substituent. Interestingly, when the amino group was functionalised in the ortho position of the terminal pyridine ring, a stable heteroleptic cage was formed.[146] DFT calculations were carried out on the new cage product and determined that the *cis* conformation was energetically more favourable than the *trans*. Furthermore, large downfield shifts for the amino protons in the ^{1}H NMR spectra of the heteroleptic cage were observed, attributable to hydrogen bonding between the adjacent amino groups, as well as further hydrogen bonding to the acidic α-H of the adjacent tripyridyl ligands.[146]

Although heteroleptic Pd_2L_4 type metallacages for use as drug delivery vehicles have not been explored to date, and are outside the scope of this project, it is worthwhile highlighting the fact that non-symmetrical, heteroleptic type, metallacages have been synthesised and observed as a mixture in solution. It can be envisioned that with further study, multi-functional drug delivery type vectors may be designed and isolated, with several *exo*-facing functionalities to facilitate both improved target selectivity, increased and varied drug cargos, both encapsulated and functionalised to the ligand, or even the design of multi-functional theragnostic metallacage vectors.

3.2 Ligand synthesis

As mentioned, a prerequisite for the formation of discreet metallacages with a well-defined overall shape, as opposed to infinite coordination polymers or MOFs, is that the ligand or metal centre must have an overall coordinating angle of $\theta < 180°$. To achieve this for SCCs formed from square planar transition metals, such as Pd_xL_y type cages, either the coordinating metal centre must be *cis*-capped to provide available coordinating sites of $\theta = \sim 90°$,[161] or the bis-monodentate ligands must have a bent overall geometry that can coordinate two different metal centres.[74,141] Typically, the coordinating sites of the ligands are pyridyl centres,[74] however examples exist of other nitrogen containing coordinating moieties which were employed to alter the stability of the final metallacage structure.[85,154] There are numerous types of bis-

monodentate ligand that can be employed to achieve differing topology and function of the resulting metallacage.[74,162] For example, flexible bis-monodentate ligands can be designed, which employ sp^3 carbon bridging units between the pyridyl centres, or more rigid but still flexible sp^2 amide bond type bridging units between the coordinating centres.[125] However, as the resulting topology of these Pd_2L_4 type metallacages has been reported to be helical, the internal cavity present is often small and unsuitable to be used in applications as a supramolecular host structure, for example as a drug delivery system. As such, more rigid bis-monodentate ligands with a bent geometry are employed in the design of Pd_2L_4 type metallacages for use as a molecular host. This is due to the more rigid metallacage produced from these ligands exhibiting a larger, well defined cavity which is suitable for the accommodation of guest molecules.[122,150–153,163] Strategies to achieve rigid ligands with a coordination angle $\theta < 180°$ include designing fused, aromatic ring ligands,[153] or using alkyne bridged coordinating moieties.[66] For the purpose of designing Pd_2L_4 metallacages suitable for drug delivery, we took inspiration from the ligands reported by Crowley and co-workers,[99] who designed bis-mono-chelating ligands by the conjugation of two terminal 3-ethynylpyridine units to a 1,3-dibromophenyl, or 2,6-dibromopyridyl precursor, using the palladium(II) catalysed Sonogashira cross coupling conditions.

3.2.1 Sonogashira cross coupling

The Sonogashira-Hagihara cross coupling protocol (more commonly known as Sonogashira cross coupling) was developed in 1975 and is used for sp^2-sp coupling of aryl- or alkynyl-halides (and triflates) with terminal alkynes.[164] Heck and Cassar both independently reported reactions to accomplish the same sp^2 – sp coupling in the same year.[164,165] Heck's procedure was adapted from the known Mizoroki-Heck palladium catalysed arylation or alkenylation of alkenes.[166] Heck employed a phosphine-palladium complex catalyst, with the reaction requiring either triethylamine or piperidine as the base/solvent.[167] Cassar similarly required a phosphine-palladium complex catalyst, but carried out the reaction in DMF with sodium methoxide as the base.[165] Both reactions required high temperatures (up to 100°C), which limited the scope for reagents as they would need to be stable at these temperatures. Sonogashira and Hagihara reported that the introduction of catalytic amounts of copper(I)iodide accelerated the reaction, by forming *in situ* copper(I) acetylides, and thus facilitated alkynylation of aryl-halides at room temperature.[164] As such, the Sonogashira cross coupling protocol has become the cornerstone of sp^2 – sp carbon coupling.

It is noteworthy that the addition of copper(I) to form *in situ* copper acetylides also accelerates homo coupling between the terminal alkynyl carbons.[168] This drives the formation of undesirable sp – sp carbon coupling when the reaction is performed in the presence of oxygen

via the so-called Glaser coupling. Although the homo-coupled product can often be separated via classic chromatography techniques, homo-coupling can provide significant issues if the alkyne used is expensive or difficult to access synthetically. It has been shown that carrying out the reaction under a reductive hydrogen atmosphere can diminish the formation of the homo-coupled product,[169] however handling hydrogen can be extremely problematic and greatly increases the risk associated with the reaction. Therefore, it is usual for the Sonogashira to be carried out under an inert atmosphere, such as nitrogen or argon, to reduce the formation of homo-coupled side product without increasing the risk associated with the reaction.

The mechanism of the Sonogashira coupling reaction involves two independent catalytic cycles, the palladium cycle, and the *in situ* formation of copper(I) acetylides (copper-cycle).[170] The palladium cycle follows the basic three steps of classic palladium catalysed coupling reactions (figure 3):

1) Oxidative addition of the aryl- or alkynyl- halide to the palladium(0) complex catalyst, which occurs quickly;

2) Transmetalation of the copper(I) acetylide (formed *in situ*) to the palladium(II) complex catalyst, which occurs slowly and is thus considered the rate determining step;

3) Reductive elimination of the sp^2 – sp coupled product from the palladium catalyst, regenerating the palladium(0) complex and closing the catalytic cycle, which occurs quickly.

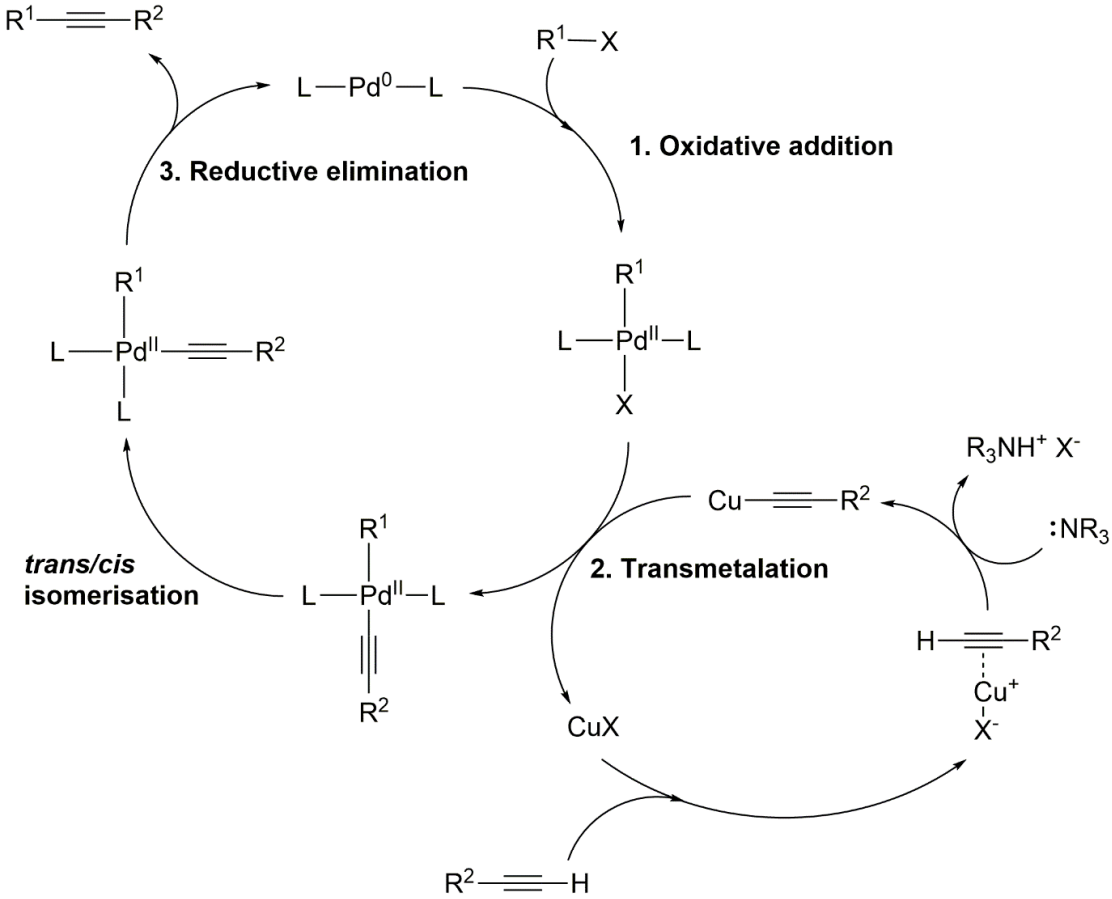

Figure 3. Mechanism for Sonogashira cross coupling showing both the palladium cycle and the copper cycle.[170] Step 1: Oxidative addition of aryl- or alkynyl- halide to palladium(0) catalyst. Step 2: Transmetalation of copper acetylide to palladium(II) catalyst complex, followed by *tran/cis* – isomerisation. Step 3: Reductive elimination of the product and the regeneration of the palladium(0) catalyst.

The activated catalytic species is the palladium(0) complex, which is usually ligated by electron rich ligands such as phosphines.[170] The rate of the oxidative addition of the aryl- or alkynyl- halide (R – X) is typically fast, however the rate is determined by the strength of the R – X bond, and the nature of the halide. Electron withdrawing groups on the aryl- or alkynyl- group weaken the R – X bond and thus increases the rate at which this addition occurs.[170] Similarly, electron donating groups on the aryl- or alkynyl- group typically strengthen the R – X bond and thus decreases the rate at which oxidative addition to the palladium complex occurs. The nature of the halide also plays a crucial role in the oxidative addition, with the strength of the R – X bond decreasing in the order $I^- > Br^- > Cl^- > F^-$. Indeed, chloride and fluoride are not typically used for palladium catalysed coupling reactions due to the strong R – X bond that these halides form, and thus slow rate of oxidative addition to the palladium catalyst.[171] The general reactivity of the R – X species can be generally considered to be vinyl iodide > vinyl bromide > vinyl chloride

> aryl iodide > aryl bromide >> aryl chloride.[170] From this reactivity it may seem obvious to use vinyl- and aryl-iodo precursor compounds for all Sonogashira coupling reactions, however these iodo- precursor compounds tend to be much more expensive than their less reactive bromo- analogues. Furthermore, due to the increased reactivity of these iodo- compounds, decomposition can occur rapidly unless stored correctly under inert conditions.

The second step of the palladium cycle connects the two catalytic cycles and is therefore usually the rate-determining step of the reaction. The copper(I) acetylide species formed in the copper cycle facilitates the coordination of the terminal alkynyl to the palladium(II) catalyst complex, with copper(I) abstracting the halide from the palladium(II) complex.[170] This leaves the sp^2 carbon (from the aryl- or alkynyl-halide) *trans*- to the sp carbon (from the terminal alkynyl precursor) across the palladium(II) centre. After *trans/cis* isomerisation, the desired sp^2 – sp coupled product is formed in the third step via reductive elimination from the palladium catalyst, which also regenerates the activated palladium(0) catalyst and thus closes the catalytic cycle.

The second cycle of the Sonogashira cross coupling protocol is the copper-cycle.[170] The terminal alkynyl group is deprotonated in the presence of a base to form the reactive copper(I)acetylide conjugate, which then participates in trans-metalation with the palladium(II) halogenated catalytic complex. Copper(I) can then abstract the halogen to regenerate a copper(I) salt, and therefore, close the cycle. However, typically the base used in the Sonogashira cross coupling protocol are tertiary amines, and thus do not have the required basicity to abstract the acetylenic proton alone to form the reactive copper(I)acetylide complex which participates in trans-metalation. As such, an initial association of the copper(I) salt with the sp – sp carbon-carbon bond, which reduces the electron density across the triple bond. This would reduce the strength of the terminal alkynyl – proton bond and facilitate the abstraction of this proton with the base (figure 3). NMR studies using silver(I) co-catalysed Sonogashira cross coupling conditions have shown that an Ag(I) – alkynyl complex is formed in solution, which supports this theory that a copper – alkynyl complex can form under copper co-catalysed Sonogashira conditions.[172]

3.2.2 Synthesis of ligands for Pd_2L_4 type metallacages under Sonogashira cross coupling conditions

The ligands used in this project are based upon either 1,3-bis(pyridin-3-ylethynyl)benzene or 2,6-bis(pyridin-3-ylethynyl)pyridine, which allowed the design of either a limited, or increased, H-bonding capacity for the cavity of the corresponding Pd_2L_4 metallacage, respectively (figure 4). The *exo*-functionalisation of the metallacage could be achieved by functionalisation of the central aryl-ring of the ligand, *para*- to the cavity facing group (CH or N, figure 4).

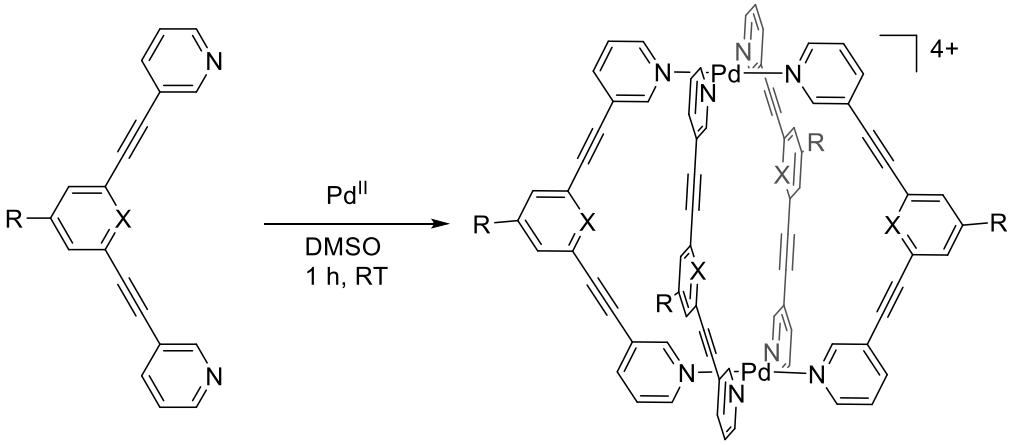

X = CH: *1,3-bis(pyridin-3-ylethynyl)benzene* based ligand scaffold
= N: *2,6-bis(pyridin-3-ylethynyl)pyridine* based ligand scaffold

Figure 4: Chemical structure of the basic bis-monodentate ligand scaffold and corresponding rigid Pd_2L_4 metallacage used throughout the project. X = *endo*- and R = *exo*-functionalization.

The synthesis of a range of *exo*-functionalised metallacages can be planned by first synthesising the appropriate 1,3-bis(pyridin-3-ylethynyl)benzene or 2,6-bis(pyridin-3-ylethynyl)pyridine scaffold by the coupling of a suitably functionalised 1,3 – dibromophenyl, or 2,6 – dibromopyridine, commercially bought starting material with 3 – ethynylpyridine, which is also commercially available. The functional group of the dibromo-aryl precursor can vary and can be judiciously chosen to offer a suitably reactive group to facilitate further conjugation of functional groups to impart desirable properties to the final Pd_2L_4 metallacage, such as luminescence or peptide conjugation. Dibromo-aryl precursors were chosen, as opposed to the more reactive diiodo-aryl precursors, as they are easier to store without degradation and still react well under Sonogashira cross coupling conditions.

The typical conditions used for the synthesis of the ligand scaffold via homogenous Sonogashira cross coupling is shown in figure 5. Triethylamine was used as both the base and the solvent due to the good solubility of the organic precursor aryl groups, as well as the final 1,3-bis(pyridin-3-ylethynyl)benzene or 2,6-bis(pyridin-3-ylethynyl)pyridine functionalised ligands. The salts formed as by-products during the reaction were poorly soluble in triethylamine, and thus could be separated from the reaction mixture easily by filtration. As dibromo-aryl precursors were used due to their improved stability under ambient conditions when compared to diiodo-aryl compounds, the coupling reaction could not be carried out at room temperature. As such, the reaction was heated to a gentle reflux at 90°C to improve the rate of the reaction. Bis(triphenylphosphine)palladium(II)dichloride was used as the palladium catalyst due to its reasonable solubility in triethylamine and improved stability.[170] Copper(I)iodide was used as the co-catalyst. As mentioned previously, the use of copper(I) salts to form copper(I) acetylides to facilitate trans-metalation also facilitates the homo-coupling of the terminal alkynyl groups (Glaser coupling) in the presence of oxidative agents, such as oxygen or even water.[170] As such, the reaction was carried out in flame dried glassware under an inert nitrogen atmosphere to minimise the formation of the homo-coupled product, 1,4-di(pyridin-3-yl)buta-1,3-diyne. In order to negate any effects on the overall yield of the reaction by the formation of 1,4-di(pyridin-3-yl)buta-1,3-diyne, an excess of 3-ethynyl pyridine was used.

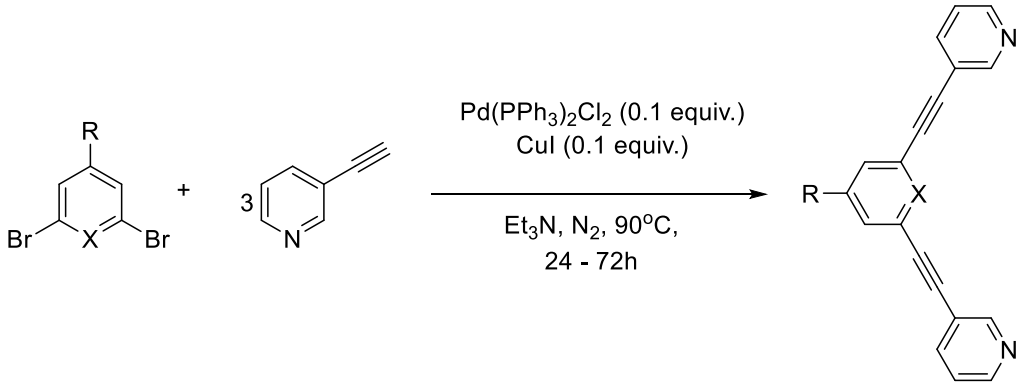

Figure 5: General synthetic conditions for the Sonogashira cross coupling protocol used to synthesise the ligand scaffolds for the formation of rigid Pd_2L_4 metallacages used throughout the study.

The final consideration for the reaction conditions was the reaction time, which was dependent on the electron withdrawing or electron donating ability of the functional group of the dibromo-aryl precursor. As described above, electron withdrawing groups reduce the electron density of the aryl carbon – halogen bond, thus increasing the initial oxidative addition step of the catalytic cycle. Thus, it was found that when using dibromo-phenyl precursors functionalised with electron withdrawing groups, or dibromo-pyridyl precursors, the reaction

could achieve good to excellent yields in 24 hours. However, when using dibromo-phenyl starting materials which were either non-functionalised (1,3-dibromobenzene) or functionalised with an electron donating group, good yields were not achieved until 72 hours reaction time (figure 5).

Due to the stability of the 1,3-bis(pyridin-3-ylethynyl)benzene and 2,6-bis(pyridin-3-ylethynyl)pyridine ligand scaffolds, the number of functional groups that can be conjugated to the ligand scaffold is extremely broad.[135] The specific strategies for functionalisation of the ligands to impart *exo*-functional groups of the corresponding homoleptic Pd_2L_4 metallacages, such as fluorophores and functional peptides, will be discussed in the next chapters.

4 Aims of this work

The aim of this project is to synthesise and characterise a library of Pd_2L_4 metallacages with the aim of studying the viability of the core Pd_2L_4 metallacage architecture as a potential drug delivery vehicle. To that end the core Pd_2L_4 metallacage scaffold will be *exo*-functionalised to bear different functional groups which have been chosen to improve the following properties of the subsequent metallacage:

1) Improved tumour targeting by functionalisation of the metallacage with integrin-binding RGD peptides

2) Translocation across the blood brain barrier (BBB) by functionalisation of the metallacage with PepH3 BBB translocating peptide

3) Exo-functionalisation of the metallacage with highly emissive fluorophores to facilitate *in vitro* cell studies to elucidate the uptake mechanism and cellular distribution

4) Improve the aqueous solubility of the metallacage drug delivery system

5) Study the encapsulation of the anti-cancer drug, cisplatin, in solution.

5 Exo-functionalisation of Pd_2L_4 metallacages for targeted drug delivery of cisplatin

(*Bioconjugation of Supramolecular Metallacages to Integrin Ligands for Targeted Delivery of Cisplatin* ***DOI: 10.1021/acs.bioconjchem.8b00682****)*

5.1 Integrin receptors for active tumour targeting

Integrins are a superfamily of heterodimeric transmembrane proteins consisting of an α- and β-subunit. To date there have been 18 α-subunits and 8 β-subunits identified in humans,[173] which can combine to generate 24 known different human integrins. It is known that the integrin superfamily is instrumental for cell-cell and cell-extracellular signalling, although the exact mechanism of action is still a controversial topic. This is in part due to a lack of solved crystal structures for this family of transmembrane proteins, and thus a lack of understanding of the active site for ligand-receptor interactions. To date only the crystal structures for the extra cellular domain of the human integrin αvβ3, α5β1 and αIIbβ3 has been solved for both the inactivated and activated state, which has allowed for a greater understanding of these integrins activation.[174–178] In fact, it has been proposed that in the inactivated state, the extracellular head-piece domains adopted a bent conformation, and thus the affinity for extracellular ligands was reduced.[179] Upon integrin activation, the extracellular headpiece domains become erect, and the ligand binding site becomes more available and thus the affinity is increased. It was also revealed that the integrin could be activated via dissociation of the intracellular "tail" domains of the α- and β-subunits.[180] First, a structural overview the heterodimeric transmembrane integrins must be addressed.

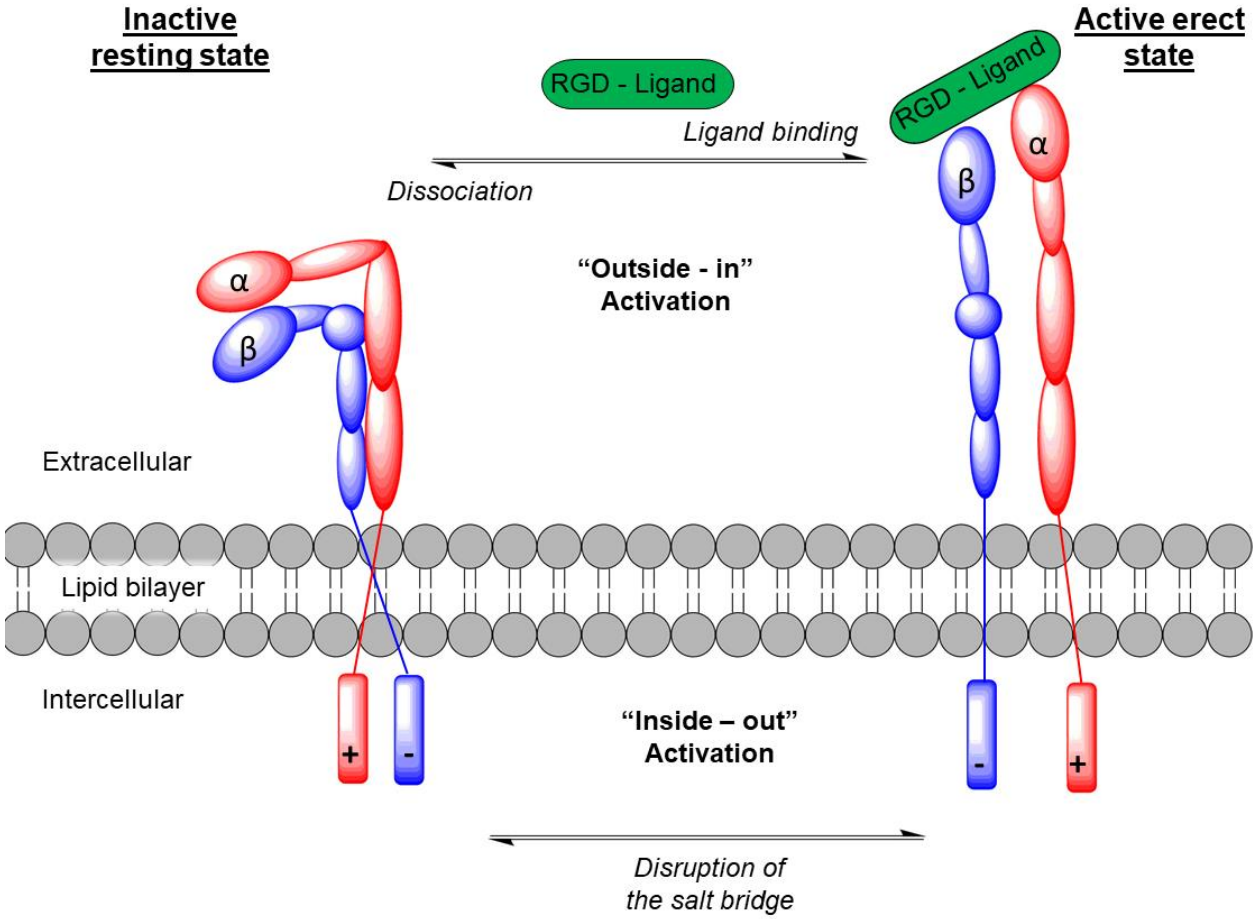

Figure 1. Schematic representation of RGD-recognising integrin activation mechanisms. Integrins show low affinity for RGD-containing ligands in their bent, inactive resting state conformation. However, conformation changes in both the α- and β- subunits cause an active, erect state.[179] This active state can be caused by the disruption of the intercellular salt bridge of the α- and β- subunits, causing an initial disruption of the trans-membrane domain, before inducing conformation changes to the extra-cellular units to the active erect state (outside – in activation). Conversely, extracellular RGD-ligand binding can induce conformational change to the active state, and subsequent oligomerization (not shown) of the integrin which can cause signal transduction from the extracellular matrix to the intercellular domain (outside – in signalling).[179]

The α- and β-subunits of the heterodimeric transmembrane integrins have distinct domain structures, however in general both are comprised of an extracellular "head-piece" domain which contains specific ligand binding sites for extracellular signalling, a transmembrane domain, and an intracellular tail domain which is connected to the cytoskeleton of the cell and is important for intracellular signalling.[174,175] The crystal structure of the human integrin αvβ3 extracellular domain revealed that the extracellular portion of the heterodimer is made up of several domains, namely the β-propeller, the plexin-semaphorin-integrin domain of the αV subunit, and the metal ion dependent adhesive site of the β-I-like domain of the β-subunit. The transmembrane domains of the α- and β-subunits are closely associated in the inactivated state. Indeed, it is the metal ion dependent I-like domain of the β-subunit that undergoes a distinct

conformational change upon ligand binding, which is responsible for the erection of the extracellular domain of the integrin and the dissociation of the transmembrane domain to form the activated state of the integrin.[174,175]

The intracellular tail domains of human integrin sub-units tend to be approximately 75-amino acid residues in length (β4 subunit is the exception with a tail length of approximately 1000 amino acid residues).[174,175] Striking similarities have been identified among the intracellular tail domains of the β-subunits of human integrins, as shown by analysis of the amino acid sequences.[174,175] In contrast, the α-subunits are highly divergent in amino acid residues, however there is a conserved GFFKR amino acid motif adjacent to the transmembrane domain that has been found to be highly important for association of the α- and β-subunits. A number of cytoskeletal and intracellular signalling proteins have been found to primarily bind to β tail domains;[181] however, some have been found to bind to specific α-tail domains. Most integrin β-tails contain at least one NPxY/F amino acid motif (x = any amino acid) which are known to be part of a recognition sequence for phosphotyrosine-binding domains, domains which are present in a large variety of signalling and cytoskeletal domains.[181] In particular, proteins that bind actin filaments within the intracellular matrix, for example talin, and thus form a connection to the cytoskeleton.[181] This connection is vital for almost all integrin mediated functions. Furthermore, the connection to the cytoskeleton and the large conformational change upon integrin activation underpins the ability of integrins to function as traction receptors and thus detect and transmit mechanical forces acting on the extracellular matrix. The tail domains of α- and β-subunits have been found to be charged, and thus can form a "salt-bridge" between the two subunits in its inactivated state.[182,183]

As these transmembrane proteins are connected to both the cytoskeleton within the cell and to components of the extracellular matrix outside of the cell, bidirectional cell signalling, i.e. "outside-in" and "inside-out", can be achieved (figure 1). Outside-in signalling allows the cell to gain information from the extracellular matrix and relay this information to specific proteins within the cytoplasm and can be achieved by activation of the integrin *via* binding of extracellular ligands.[174,175] It has been proposed that upon ligand binding, the conformation of the β I-like domain opens up, inducing the dissociation of the α and β transmembrane domains, as well as a dissociation of the "salt-bridge" formed between the tail domains of the α- and β-subunits in the intercellular region.[182,183] Upon activation of the extracellular domain of the integrin, homo-oligomerisation of the α- and β- subunits occurs which activates the intracellular binding domain, and thus allows trans-membrane signalling from the extracellular matrix to intracellular proteins.[184]

Inside-out signalling has been reported to be instrumental in regulating the affinity of specific integrins with their extracellular ligands. It is known that association of the salt-bridge in the intracellular domain of the heterodimeric integrin is essential to maintain the non-activated extracellular conformation of the integrin.[174,175] It has also been shown that intracellular guanine nucleotide binding protein (G-protein) coupled receptors can induce signals that lead to phosphorylation of the β-subunit tail which disrupts the salt bridge and causes the activation of the extracellular domain.[179] In particular, the cytoskeletal adaptor protein, talin, has been shown to interact with the tail domain of the β-subunit causing a dissociation of the salt-bridge, and thus activate the integrin via inside out signalling (figure 1).[181]

Communication between cells and with their environment is essential to their function, and integrins have been extensively studied to elucidate their roles in such mechanism of communication. In fact, several integrin subtypes have been shown to be involved in numerous cell – cell and cell – extracellular matrix communication pathways. For example, cell proliferation, cell adhesion, cell invasion and angiogenesis are regulated by integrins.[179]

Integrins can be generally categorised into the following families based on their ligand affinity; laminin-binding integrins, collagen-binding integrins, leukocyte integrins, and RGD-recognising integrins.[185] For the purpose of this study, RGD-recognising integrins were the target subsection of human integrins as the RGD motif has been widely studied for integrin binding and facilitates a readily synthetically attainable chemical motif which has been proven to bind selectively and with high affinity to integrins.

One type of chemical motif that has been found to bind selectively and with high affinity with integrin receptors is the arginine – glycine – aspartic acid (RGD) tri-amino acid sequence (figure 2), first described by Pierschbacher and Ruoslahti in 1984.[186] Numerous studies have been undertaken to elucidate the structure and mechanism of the so-called RGD recognising integrin subtypes. To date, of the 24 known human integrin families there are 7 known RGD recognising integrin subtypes,[185] and of these 3 have had the crystal structure solved for the extracellular domain (αvβ3,[174–176] α5β1,[177] and αIIbβ3).[178]

Many of the roles that integrin receptors are involved in are processes that are exacerbated in cancer cells. For example, malignant cancer cells must be able to detach from their immediate physiological environment and invade other areas of the body, without undergoing apoptosis. It has been found that integrin receptors are overexpressed in cancer cells, and therefore, offer a potential target for active tumour targeting mechanisms for drug molecules.[187–189]

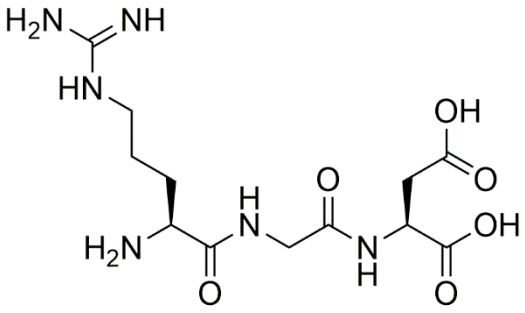

Figure 2. The arginine – glycine – aspartic acid tripeptide (RGD peptide). The sequence has a high affinity for RGD-recognising integrin proteins, and is found in numerous extracellular ligands which have a high affinity for RGD-recognising integrins

RGD-recognising integrins, such as αvβ3, α5β1 and αIIbβ3, are known to be overexpressed in several cancer types.[179,190] This is due to these transmembrane proteins being connected to important sub-cellular structures, such as the cytoskeleton, and recognising the RGD motif of several important extracellular ligands such as fibronectin, osteopontin, and vitronectin. In this way the RGD recognising integrins can facilitate communication between the cell and the extra-cellular matrix via these RGD containing ligands, which provide the capacity for several processes that are characteristic of cancer, such as cell proliferation, cell migration and invasion, and angiogenesis.[179] It has been found that the upregulation of RGD-recognising integrins correlates with metastasis and poor patient prognosis. As such, these integrins present an attractive target for cancer therapeutics.[179]

5.2 Integrin binding RGD peptides

The high affinity of the RGD motif for the extracellular domain of certain integrins was first discovered due to the high affinity of the extracellular matrix protein, fibronectin, towards integrins.[186] It was then reported that the high affinity of fibronectin for integrins was due to it containing the RGD sequence. After reporting this tri-amino acid sequence as a highly conserved, small molecule for integrin recognition, the RGD sequence was subsequently discovered in several other extracellular matrix proteins, including vitronectin, osteopontin, and laminin.[191–194]

Although the RGD motif is crucial for certain integrin recognition, the affinity of extracellular matrix proteins for specific integrin subtypes over other subtypes is governed by strict conformational and spatial arrangement of the RGD motif with respect to the extracellular protein domain.[195,196] Thus, a degree of selectivity of extracellular matrix ligands towards different integrin subtypes can be achieved. As such, synthetic RGD containing peptides and peptidomimetics have been widely studied and synthetically altered, either by the judicious choice of flanking amino acid residues to work synergistically with the RGD sequence, or by cyclisation and thus imparting a degree of rigidity to the amino acid sequence, to produce highly selective and potent integrin recognition sequences.[197]

Due to the small, highly selective and synthetically available RGD motif (figure 2), as well as the tunability of the RGD peptide selectivity towards different integrin subtypes via different flanking amino acid sequences, RGD containing peptides and peptidomimetics have been studied as targeting functionalities to improve the selectivity of a number of therapeutic or diagnostic agents towards cancer cells overexpressing RGD-recognising integrins.[190]

Amongst the numerous RGD-conjugates used for improved cancer therapy, examples of RGD-platinum(II) conjugates have been reported.[21,198] However, direct conjugation of active platinum(II) complexes to peptides comes with myriad of problems. For example, altering the ligand scaffold may affect the efficacy of the activity of the biological resulting platinum(II) species in a negative way, lowering the overall potency of the targeted complex. Furthermore, possible side-effects are still possible due to the presence of the same integrins in specific normal tissues. An intriguing strategy to partly overcome this issue, is to use platinum(IV) species conjugated to RGD containing peptides or peptidomimetics.[21,198] The platinum(IV) species is stable extracellularly and will only become activated upon reduction to its platinum(II) counterpart inside the cancer cells before it can carry out its chemotherapeutic effect.

Due to the success of integrin targeting-platinum conjugates towards improving the selectivity of platinum chemotherapy agents, it was hypothesised that conjugation of an integrin targeting peptide to the *exo*-surface of Pd_2L_4 (L = *1,3-bis(pyridin-3-ylethynyl)benzene* based ligands) metallacages would allow for the active targeting of this novel drug delivery system towards cancer cells overexpressing RGD recognising integrin types. As such, in collaboration with the group of Prof. Horst Kessler at the Technical University of Munich, a small library of cyclic and non-cyclic peptidomimetic entities was chosen which were selective for the human integrin αVβ3 (**1-3**) and a linear peptidomimetic that was selective for the integrin α5β1 (**4**) (figure 3).

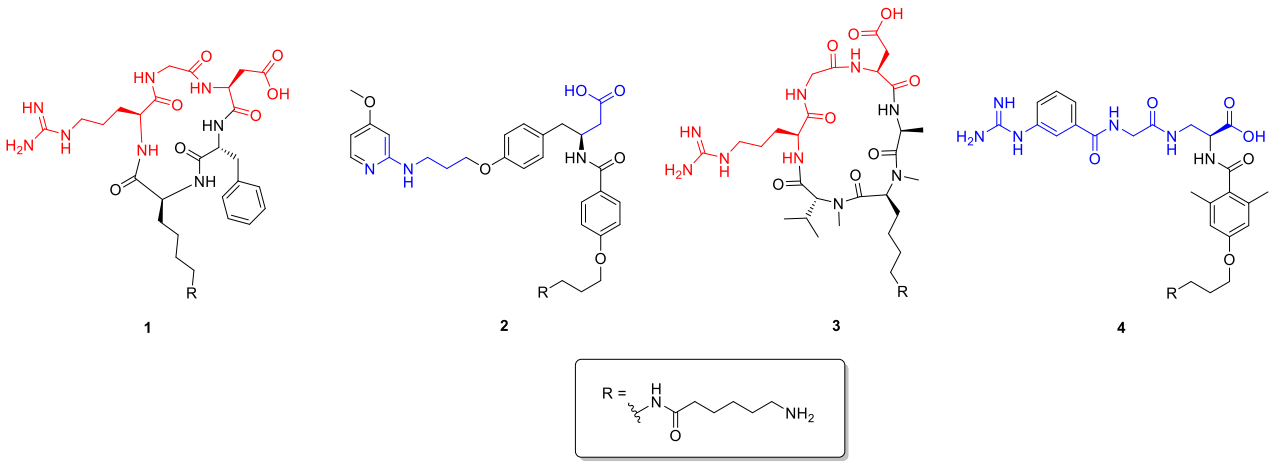

Figure 3: Chemical structure of the small library of cyclic (**1** and **3**) and linear peptidomimetic (**2** and **4**). The RGD sequence is highlighted in red for the cyclic model peptides **1** and **3**. The functionalities used to mimic the RGD motif are highlighted in blue for the linear peptidomimetics **2** and **4**.

The αvβ3 integrin is widely distributed throughout the body as they are expressed on endothelium cells.[185] It has been shown in a series of cancer entities that the expression of αVβ3 integrins correlates well with metastasis and thus poor patient prognosis.[187] It has also been shown that overexpression of αVβ3 favours tumour growth and invasion of the cancer cells to bones, which leads to metastasis. This tumour growth and invasion is exacerbated in αVβ3 upon ligation to an extra-cellular matrix ligand such as vitronectin or osteopontin. The selectivity towards cancer cells may be compromised due to the abundance of αvβ3 type integrins throughout the body. However, as the crystal structure has been solved for αvβ3 in both the ligated and non-ligated form,[174,175] there is much more known about the active site of this integrin than other integrin types. Furthermore, they are overexpressed in several cancer cell types, such as gastric,[199] brain,[200] and breast cancer,[189,201] and so will impart a degree of selectivity towards the integrin targeting drug conjugate. It has also been shown that cancer stem cells display an increased expression of αvβ3 type integrins on their membranes.[179,185] Ligation of its major extra-cellular ligand, vitronectin, to the integrin initiates a process that causes the downregulation of genes that contribute to cancer stem cell maintenance. Thus, αvβ3 type integrins offer attractive targets for designing high affinity and selective integrin targeting ligands.

α5β1 type integrins are highly expressed in oral squamous cell carcinoma and ovarian cancer cells,[202] although they can be found in other tissue types. Overexpression of α5β1 type integrins has been shown to promote metastasis in breast cancer cells, and thus overexpression is associated with poor patient prognosis. Furthermore, α5β1 integrins are strongly induced in cancer cells upon hypoxia, and overexpression of the α5β1 integrin has demonstrated a 3-fold increase in cell invasiveness compared to cancer cells with low α5β1 expression.[179,185,202] This

clearly demonstrates a crucial role of α5β1 type integrins in facilitating cell invasiveness and migration, and thus offers α5β1 as another attractive target for integrin targeting ligands.

5.3 Results and Discussion

The integrin targeting peptides and RGD-functionalised ligands used in this study were synthesised and characterised by the group of Prof. Horst Kessler from the Centre of Integrated Protein Science, Technical University of Munich.

5.3.1 Exo-functionalisation of metallacages with integrin binding peptides

It has been previously shown that the most effective strategy to exo-functionalise Pd_2L_4 metallacages with a peptide model was to functionalise the bidentate ligand via classical amide bond formation, before initiating the self-assembly of the metallacage by introducing stoichiometric amounts of Pd^{II}, as opposed to forming the Pd_2L_4 metallacage, and subsequently exo-functionalising the cage complex.[131] We therefore adopted this approach for the conjugation of the integrin targeting peptide to the metallacage. It was also hypothesised that due to the large and sterically bulky Pd_2L_4 type architecture of the metallacage, a flexible alkyl spacer moiety should be incorporated to ensure that the large metallacage does not interfere with the RGD sequence interacting with the integrin.

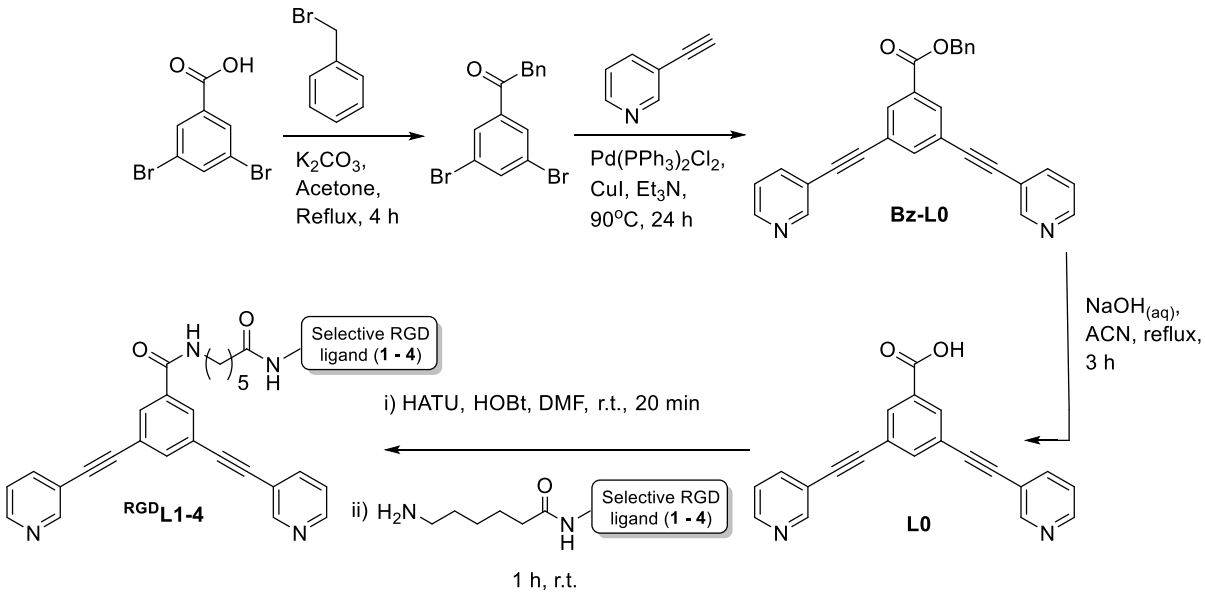

Scheme 1: Synthesis of ^{RGD}**L1-4**, with the intermediate ligands **Bz-L0** and **L0**. Benzyl protection followed by Sonogashira coupling give **Bz-L0**. Subsequent deprotection gives the carboxylic acid functionalised ligand **L0**. Finally, classical amide bond formation between **L0** and the RGD-alkyl linker conjugate produces ^{RGD}**L1-4**

In order to facilitate amide bond formation between the alkyl spacer and the ligand, a carboxylic acid functionalised ligand was synthesised via palladium catalysed Sonogashira cross coupling between the benzyl protected dibromobenzoic acid, benzyl-3,5-dibromobenzoate, and 3-ethynylpyridine. Subsequent deprotection of the benzyl group afforded the carboxylic acid exo-functionalised ligand, **L0**. **L0** could then be coupled to the appropriate RGD-peptide functionalised with a diamine alkyl spacer by first activating the acid using *O*-(7-azabenzotriazol-1-yl)-*N,N,N',N'*-tetramethyluronium-hexafluorophosphate (HATU), *N,N'*-diisopropylethylamine (DIPEA) and 1-hydroxybenzotriazole (HOBt) in DMF and stirring at room temperature for 30 min. The activated acid DMF solution was then added to a DMF solution of the appropriate RGD-peptide-spacer conjugate. The reaction was stirred for 1 hour at room temperature before the solvent was removed and the crude residue was purified via semipreparative HPLC to give the RGD-peptide exo-functionalised ligands ^{RGD}**L1**-^{RGD}**L4**.

Finally, the corresponding Pd_2L_4 metallacages, ^{RGD}**C1**-^{RGD}**C4**, were formed via self-assembly by the addition of 2 equiv. of tetrakisacetonitrilepalladium(II)tetrafluoroborate ($Pd(II)(MeCN)_4(BF_4)_2$) to a solution of 4 equivalents of the ligand in DMSO-d_6 (figure 4).

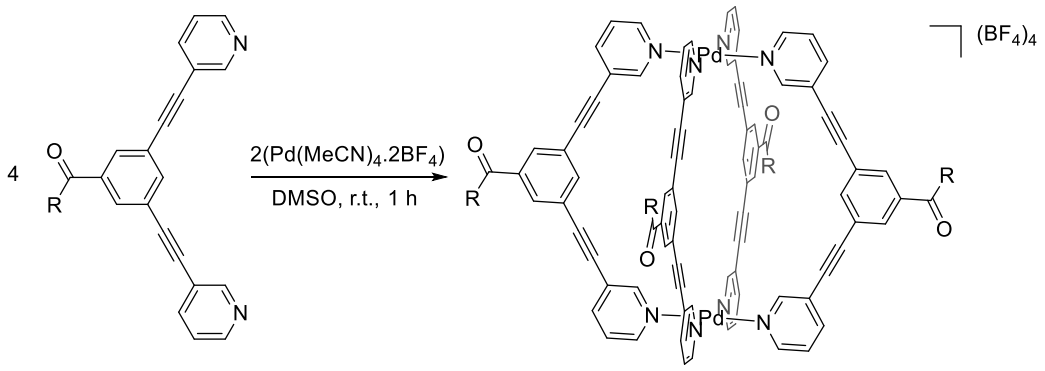

Figure 4: Scheme of the self-assembly of metallacages **C0, Bn-C0,** and ^{RGD}**C1-4** from their constituent ligands **L0, Bn-L0** and ^{RGD}**L1-4**.

After stirring at room temperature for 1 hour, quantitative formation of the Pd_2L_4 metallacage had occurred. To ensure that the self-assembly process was not compromised by the large and flexible exo-functionalised RGD-peptide, the self-assembly process of ^{RGD}**L4** to ^{RGD}**C4** was monitored via ^{1}H NMR in DMSO-d_6 (figure 5). Upon sequential addition of 0.5 equivalents of $Pd(II)(MeCN)_4(BF_4)_2$, the peaks corresponding to protons H_a and H_b of the ligand

diminish, and new peaks corresponding to H_a and H_b of the Pd_2L_4 metallacage emerge approximately $\Delta\delta$ = 1 ppm downfield from the ligand peaks. Upon addition of the full 2 equivalents of $Pd(II)(MeCN)_4(BF_4)_2$, the peaks of H_a and H_b of ^{RGD}**L4** disappear, to be replaced by the peaks further downfield corresponding to H_a and H_b of ^{RGD}**C4**, which is indicative of quantitative cage formation.

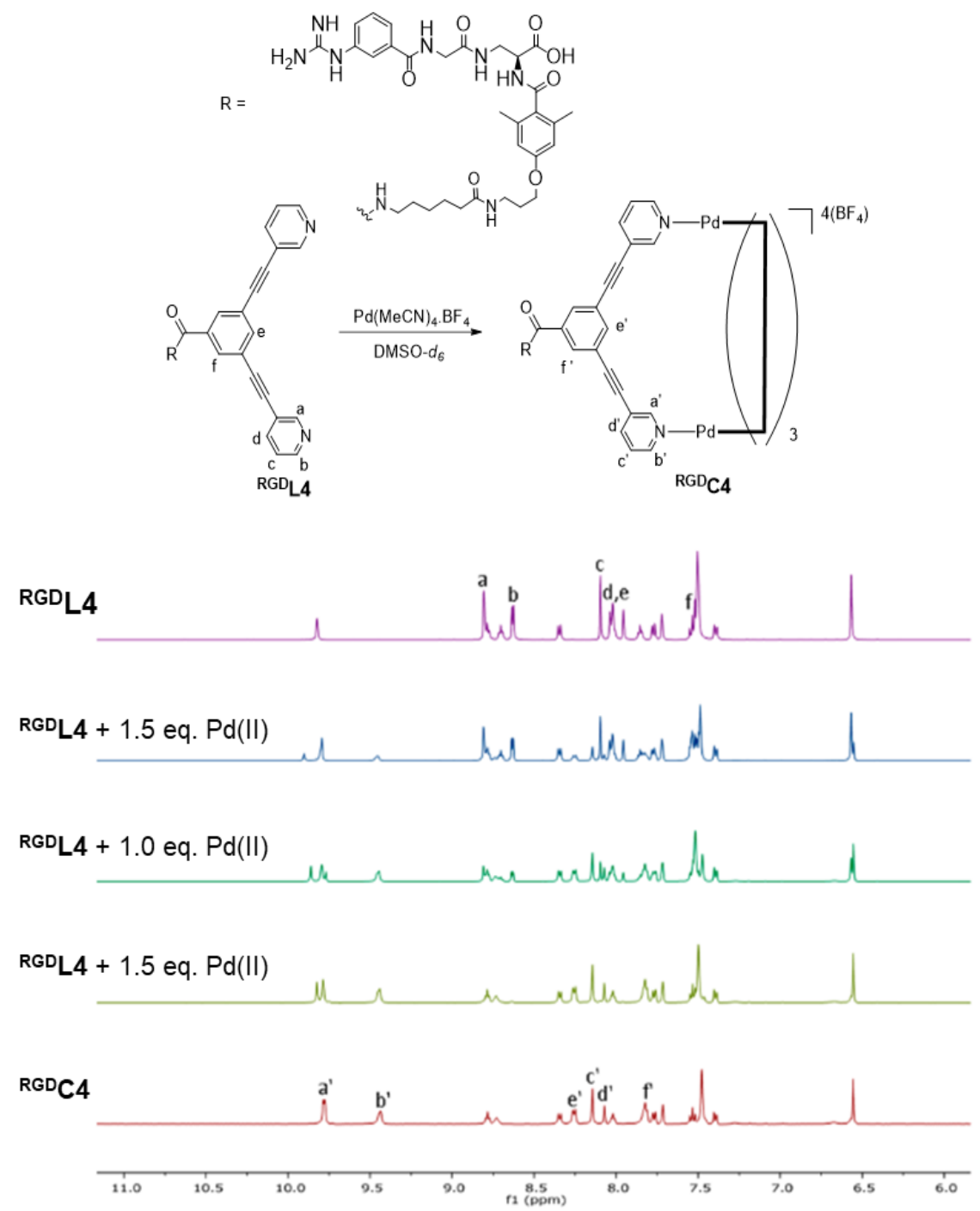

Figure 5. Titration of 0.5 eq. tetrakisacetonitrilepalladium(II) tetrafluoroborate to a DMSO-d_6 solution of ligand ^{RGD}**L4**. The quantitative self-assembly of the corresponding Pd_2L_4 metallacage, ^{RGD}**C4**, can be monitored by the appearance of the corresponding proton peaks ($H_{a'} - H_{f'}$) and the disappearance of the proton peaks of ^{RGD}**L** ($H_a - H_f$). These chemical shifts are observed for all metallacages (^{RGD}**C1** - ^{RGD}**C3**) upon the addition of 2 equiv. of tetrakisacetonitrilepalladium(II) tetrafluoroborate to a DMSO-d_6 solution of the corresponding ligand, indicating successful metallacage formation for all peptide functionalised metallacages.

5.3.2 Encapsulation of cisplatin within integrin targeting peptide exo-functionalised Pd_2L_4 metallacages

The encapsulation study was performed on a non-integrin targeting peptide exo-functionalised metallacage. A metallacage with a carbonyl exo-functional group was used as a mimic instead **(Bz-C0)** (figure 6). The exo- facing carboxylic acid was protected using a benzyl group in order to improve the solubility of the resulting metallacage in the ^{1}H NMR conditions used to study the encapsulation. Furthermore, as the benzyl protected carboxylic acid will act as an electron withdrawing group in the same way as the integrin targeting peptide exo-functional group would do the conjugated ligands of the metallacage, the electronic environment of the internal cavity of the Pd_2L_4 metallacage will be comparable to the internal cavity of the peptide functionalised Pd_2L_4 metallacages.

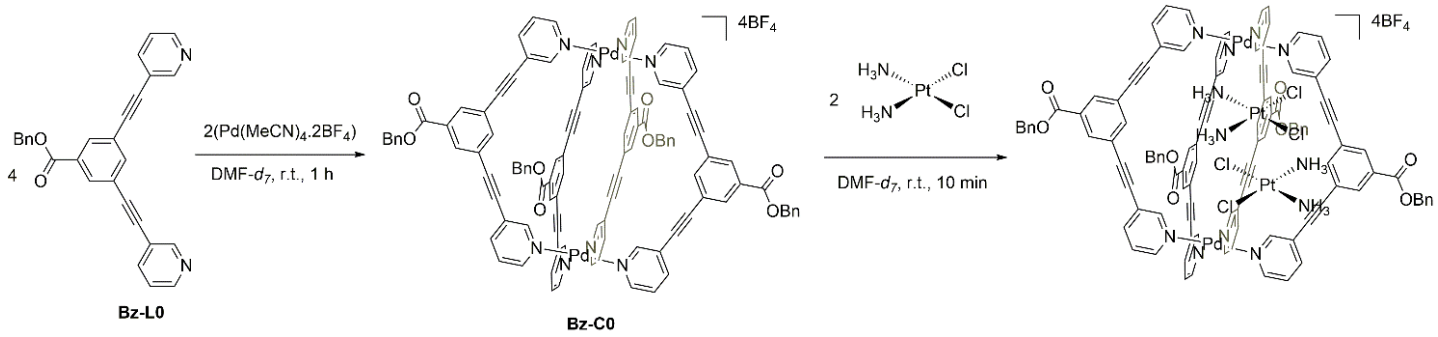

Figure 6: Self-assembly of metallacage **Bz-C0** from ligand **Bz-L0**, and encapsulation of cisplatin in DMF-d_7

The encapsulation of cisplatin within **Bz-C0** was studied using ^{1}H, ^{195}Pt, and ^{1}H DOSY NMR spectroscopy in DMF-d_7. The choice of deuterated solvent for this study was dictated by the poor solubility of Pd_2L_4 type metallacages in D_2O, which would be a better choice of solvent to replicate physiological conditions. Thus, an organic deuterated solvent that has similar properties (i.e. polarity and density) to water was needed. As DMSO-d_6 is known to form complexes with cisplatin, DMF-d_7 was chosen as an appropriate solvent for this experiment.

Previous studies have shown unequivocally via single crystal X-ray diffraction that up to two molecules of cisplatin can be encapsulated within the cage cavity of a non exo-functionalised metallacage.[99,127] As such, two equivalents of cisplatin were added to a solution of **Bz-C0** in DMF-d_7 and the solution was stirred for 10 minutes. The resulting NMR spectrum was compared to an NMR spectrum of **Bz-C0** in DMF-d_7 to observe any shift in peak position. It was observed in the ^{1}H NMR spectra that upon addition of 2 equivalents of cisplatin the peaks corresponding to the exo-facing protons of the metallacage and the benzyl protecting group did not move and the splitting patterns remained the same, indicating that their environments are unaffected by the addition of cisplatin. However, both cavity facing proton peaks (H_a and H_e) were shown to shift upon addition of cisplatin (figure 7).

H_a, the endo-facing proton alpha to the coordinating nitrogen of the ligand, exhibits a downfield shift of $\Delta\delta$ = 0.0048 ppm. H_e, the endo-facing proton of the central phenyl ring of the ligand, undergoes significant broadening of the signal. Interestingly the exo-facing proton, alpha to the coordinating nitrogen of the ligand, exhibits a downfield shift of $\Delta\delta$ = -0.0148 ppm. This would suggest that the electron density around the protons alpha to the coordinating nitrogen is reduced. Furthermore, the upfield shift of the peak corresponding to H_e indicated that more electron density is acting to shield the proton. This is in agreement with the reported crystal structure of cisplatin encapsulated within a Pd_2L_4 metallacage, as the electronegative chloride ligands of cisplatin are oriented towards H_a and may act to repel electron density away from the H_a nucleus onto the highly conjugated ligand scaffold. Furthermore, according to the crystal structure, the cationic Pt^{II} nucleus of cisplatin is located towards the centre of the metallacage. This may be why there is the peak broadening of H_e, which would be in closest proximity

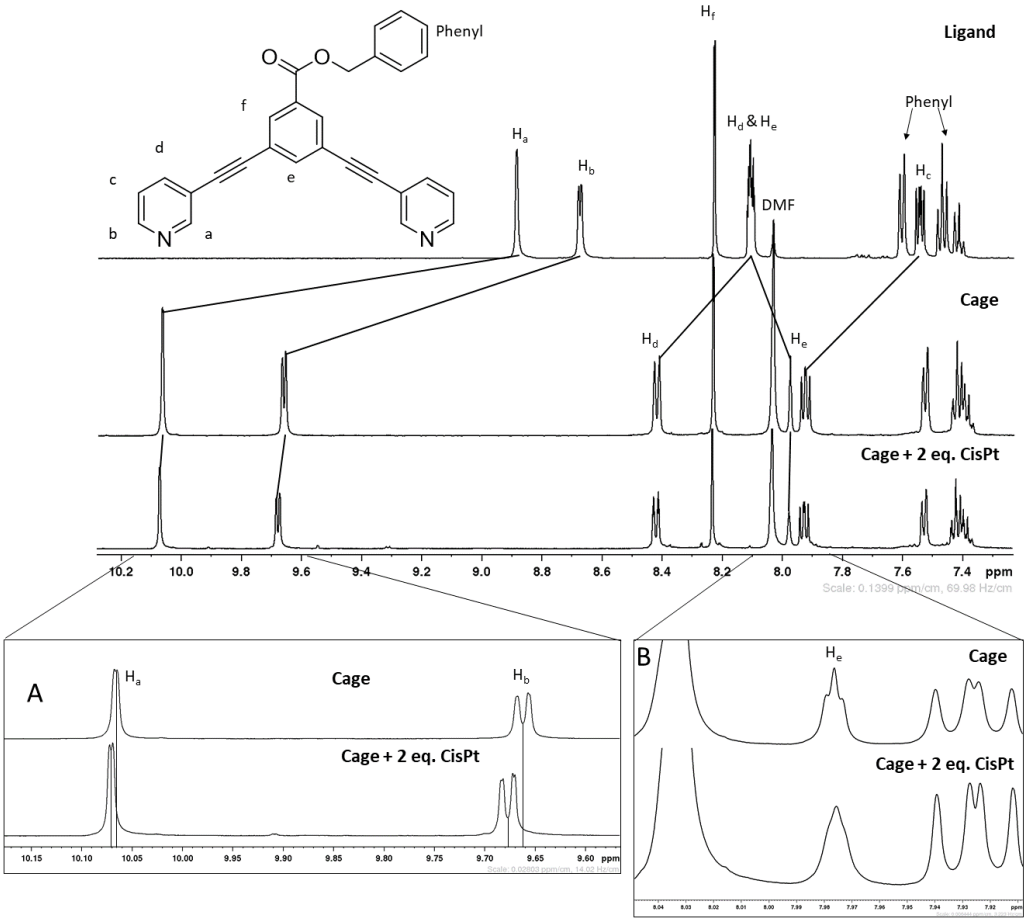

Figure 7: Stacked ^{1}H NMR spectra in DMF-d_7 showing top: Ligand **Bz-L0**; middle: metallacage **Bz-C0**; bottom: **Bz-C0** in the presence of 2 equivalents of cisplatin. Box A shows a zoom in of the proton peaks H_a and H_b, highlighting the downfield shift of H_a ($\Delta\delta$ = 0.0048 ppm) and H_b ($\Delta\delta$ = -0.0148). Box B is a zoom in of the H_e highlights the broadening of the peak.

Another method to study the encapsulation of cisplatin by metallacage **Bz-C0** was by ^{1}H DOSY NMR. It was hypothesised that by titrating cisplatin into a solution of **Bz-C0** in DMF-d_7, the

signal corresponding to NH_3 protons of cisplatin (6.22 x 10^{-5} m^2/s) would have the same diffusion coefficient as the metallacage (1.93 x 10^{-6} m^2/s), thus supporting that both the cage and cisplatin have formed a host-guest complex and so diffuse throughout the solution together. Upon addition of more than 2 equivalents of cisplatin, it was hypothesised that the cage cavity would become saturated with cisplatin and a second signal for the NH_3 protons would appear with the same diffusion coefficient as that of free cisplatin in DMF-d_7.

Interestingly this was not observed. Rather, addition of 1 equivalent of **Bz-C0** to 1 equivalent of cisplatin caused the quenching of the cisplatin signal. Addition of a second equivalent of cisplatin to the cisplatin and **Bz-C0** solution did not cause the reappearance of this signal in the resulting ^{1}H DOSY NMR spectrum. A third equivalent of cisplatin was titrated into the solution which caused the re-emergence of the signal corresponding to free cisplatin (figure 8).

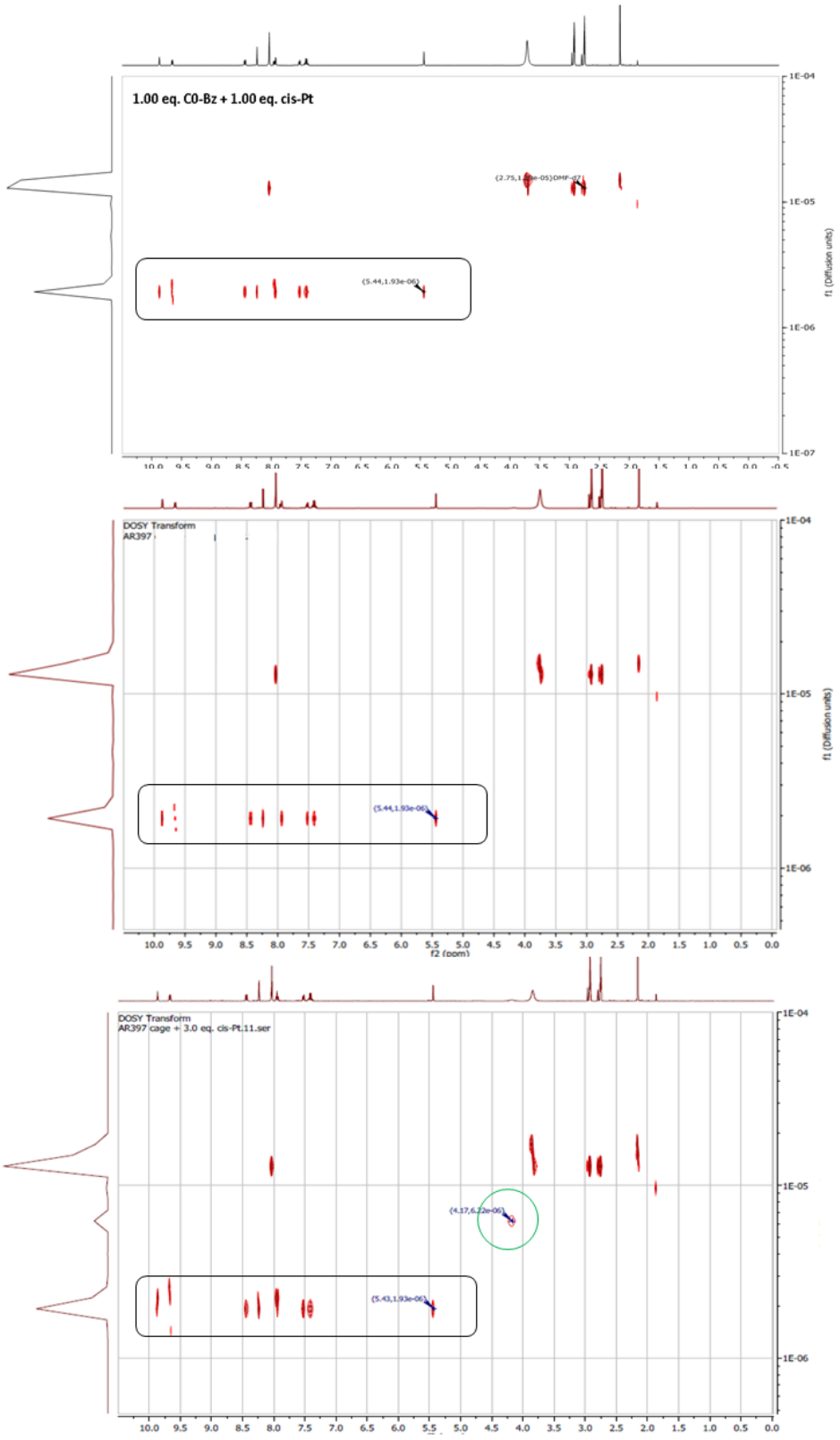

Figure 8: ^{1}H DOSY NMR spectra of; left: **Bz-C0** with 1 equiv. of cisplatin; middle: **Bz-C0** with 2 equiv. of cisplatin; right: **Bz-C0** with 3 equiv. of cisplatin. The black box highlights the signals corresponding to **Bz-C0** (diffusion coefficient = 1.93 x 10^{-6} m^2/s). Upon addition of a third equivalent of cisplatin, the signal corresponding to free cisplatin emerges (diffusion coefficient = 6.22 x 10^{-5} m^2/s)

The quenching of the cisplatin signal, as opposed to changing the diffusion co-efficient to that of the metallacage, was unexpected but may be due to ^{1}H NMR DOSY units (m^2/s). The units show that the rate of diffusion throughout the solution is based upon the movement of the surface of the diffusing compound, m^2. As cisplatin is encapsulated within the cavity of the metallacage the surface of the resulting host-guest complex corresponds to the surface of the metallacage, with the signals from the guest species therefore quenched. Upon titration of a third equivalent of cisplatin to the solution, the metallacage cavity is saturated and thus free cisplatin is present in the bulk solution, and so the signal corresponding to free cisplatin is restored. This again is in agreement with the crystal structure and suggests that up to 2 molecules of cisplatin can be encapsulated within Pd_2L_4 metallacages in DMF-d_7, however further studies are needed to confirm that the stoichiometry of cisplatin: cage is 2: 1 in solution.

Finally, ^{195}Pt NMR was used to study the effect of the guest species upon encapsulation in the metallacage **Bz-C0**. Addition of 1 equivalent of **Bz-C0** to a DMF-d_7 solution of 2 equivalents of cisplatin caused the almost complete quenching of the signal for cisplatin, which again supports the hypothesis that up to 2 molecules of cisplatin can be encapsulated within a Pd_2L_4 metallacage.

In order to ascertain that **^{RGD}C1-^{RGD}C4** maintained their specific affinity for either αvβ3 (**^{RGD}C1-^{RGD}C3**) or α5β1 (**^{RGD}C4**) the metallacages, as well as their constituent ligands **^{RGD}L1-^{RGD}L4**, were assessed via an established ELISA-like solid phase binding assay. The metallacages and ligands were screened against both αvβ3 and α5β1, as well as αvβ5 and αvβ6, to distinguish any selectivity exhibited by the metallacages. Cilengitide, a cyclic RGD containing peptidomimetic, was used as a standard, and the carboxylic acid exo-functionalised metallacage, **C0**, was also studied as a control to demonstrate that the RGD motif, and not the Pd_2L_4 type architecture, is responsible for the binding affinity. The results are summarised in table 1.

Table 1: IC_{50} values of **^{RGD}C1-^{RGD}C4** and their constituent ligands **^{RGD}L1-^{RGD}L4** for binding to RGD-recognising integrin subtypes α5β1, αvβ3, αvβ5, αvβ6, as well as the control cyclic peptide, Cilengitide, which is selective towards αv containing integrins.

	IC_{50} [nM]			
Compound	α5β1	αvβ3	αvβ5	αvβ6
C0	> 10 000	> 10 000	> 10 000	> 10 000
^{RGD}C1	20 ± 2	2.1 ± 0.8	49 ± 6	159 ± 18
^{RGD}L1	215 ± 71	24 ± 5	147 ± 9	479 ± 39
^{RGD}C2	1025 ± 331	0.98 ± 0.24	6580 ± 911	644 ± 66
^{RGD}L2	66 ± 12	3.3 ± 1.3	827 ± 118	148 ± 11
^{RGD}C3	193 ± 62	0.38 ± 0.01	24 ± 6	13 ± 2

^{RGD}**L3**	396 ± 127	0.87 ± 0.31	156 ± 20	64 ± 13
^{RGD}**C4**	1.77 ± 0.15	> 10 000	> 10 000	2370 ± 303
^{RGD}**L4**	< 1	> 10 000	> 10 000	1361 ± 151
Cilengitide	14.9 ± 3.1	0.61 ± 0.06	8.4 ± 2.1	2050 ± 640

As expected, it was shown that **C0** exhibited no affinity for any of the integrins used (IC_{50} > 10,000 nM). ^{RGD}**C1-**^{RGD}**C4** demonstrated strong binding affinity, with IC_{50} values in the low nanomolar range, for their targeted integrin (^{RGD}**C1-**^{RGD}**C3** = αvβ3, ^{RGD}**C4** = α5β1) and indeed exhibited selectivity towards their targeted integrin. Interestingly, the two cyclic RGD-peptide exo-functionalised cages (^{RGD}**C1** and ^{RGD}**C3**) were found to be more promiscuous against their non-targeted integrins (α5β1, αvβ5, αvβ6) than the linear RGD-peptides of ^{RGD}**C2** (αvβ3) and ^{RGD}**C4** (α1β5). Furthermore, the three αvβ3-targeting metallacages, ^{RGD}**C1-**^{RGD}**C3**, all displayed higher binding affinity than that of their constituent ligands. This observation is in agreement with several reports that multimerization improves the binding affinity of ligands to their receptors. This is especially important in the case of integrin binding ligands as multimerization may induce uptake of the RGD-peptide conjugate in cells via endocytosis, as has been observed for virus' such as foot and mouth disease. Conversely, the α5β1 integrin targeting ligand, ^{RGD}**L4**, exhibited a much higher binding affinity than the corresponding metallacage, ^{RGD}**C4** (IC_{50} = <1 nM and 1.77 ± 0.15 nM, respectively). This increased affinity of the ligand was not further investigated but can be attributed to non-specific interactions between the ligand scaffold of ^{RGD}**L4** and the active site of the α5β1 integrin. In summary, the successful demonstration of cisplatin encapsulation within the Pd_2L_4 metallacage scaffold was achieved; conjugation of the RGD-peptides to the bispyridyl-ligand scaffold and subsequent metallacage self-assembly was shown; the RGD-peptide affinity for specific integrins was shown to be conserved upon metallacage formation for metallacages ^{RGD}**C1-**^{RGD}**C4**. The αvβ3 targeting metallacages, ^{RGD}**C1-**^{RGD}**C3**, were taken on to be studied *in vitro* and *ex vivo* as drug delivery systems for cisplatin.

5.3.3 *In vitro* and *ex vivo* results

To validate the concept of using integrin targeting Pd_2L_4 metallacages as active tumour targeting drug delivery systems, the antiproliferative activity (EC_{50} values) of the selected metallacages, as well as the host guest systems [$(cisplatin)_2\subset$(^{RGD}**C1-**^{RGD}**C3**)], were first studied against a cancer cell line overexpressing αvβ3 integrins (human malignant melanoma cell line, A375),[203] and against a cancer cell line which does not express αvβ3 (human lung cancer cell line, A549). The non RGD-peptide exo-functionalised metallacage, **C0**, and its constituent ligand, **L0**, were also studied for their antiproliferative effects, both alone and as the host guest complex

[(cisplatin)$_2$⊂(**C0**)]. The results are summarised in table 2 and show that in all cases the EC_{50} value is >60 μM for the unoccupied metallacages ^{RGD}**C1**-^{RGD}**C3**, as well as for the host-guest complexes [(cisplatin)$_2$⊂(^{RGD}**C1**-^{RGD}**C3**)] when incubated with the αvβ3 deficient cancer cell line, A549.

Table 2: Antiproliferative activity of the αvβ3 targeting metallacages, ^{RGD}**C1**-^{RGD}**C3**, the corresponding host-guest complexes, [(cisplatin)$_2$⊂(^{RGD}**C1**-^{RGD}**C3**)], and non-peptide functionalised **L0** and **C0**.

Treatment	EC_{50} [μM]	
	A375 (*overexpressed αv*β3)	A579 (*deficient αv*β3)
L0	> 50	>100
C0	> 50	82.6 ± 15.1
[(cisplatin)$_2$⊂(^{RGD}**C0**)]	31.5 ± 3.0	>60
^{RGD}**C1**	> 50	>60
[(cisplatin)$_2$⊂(^{RGD}**C1**)]	32.4 ± 1.2	>60
^{RGD}**C2**	> 50	>60
[(cisplatin)$_2$⊂(^{RGD}**C2**)]	15.80 ± 3.35	>60
^{RGD}**C3**	> 50	>60
[(cisplatin)$_2$⊂(^{RGD}**C3**)]	29.5 ± 0.6	>60
Cisplatin	33.9 ± 2.9	63.2 ± 5.2

When incubated with A375 cancer cell line, which overexpresses αvβ3 integrins, the unoccupied metallacages ^{RGD}**C1**-^{RGD}**C3** displayed no antiproliferative activity (>50 μM). The non-RGD peptide exo-functionalised metallacage **C0**, and its constituent ligand **L0** also exhibited no anti-proliferative activity. However, for the host-guest complexes [(cisplatin)$_2$⊂(^{RGD}**C1**-^{RGD}**C3**)], there was an increase in anti-proliferative activity which, in all cases, was at least as good as free cisplatin (EC_{50} value of approximately 30 μM). In the case of the host guest complex [(cisplatin)$_2$⊂(^{RGD}**C2**)], which was exo-functionalised with the linear RGD -peptidomimetic and exhibited the strongest binding affinity for αvβ3 integrins, the EC_{50} value was approximately half of that of free cisplatin. This represents an approximate two-fold increase in potency of [(cisplatin)$_2$⊂(^{RGD}**C2**)] compared to free cisplatin. This may be interpreted as representing a much higher uptake of cisplatin within the cells when it is encapsulated within ^{RGD}**C2**, compared to free cisplatin and indeed compared to the cyclic-RGD exo-functionalised metallacages, ^{RGD}**C1** and ^{RGD}**C3**. However, this result may also be due to differences in the stability of the different metallacages under physiological conditions, especially with respect to metallacage aggregation or competitive guest encapsulation and subsequent cisplatin release, which may affect the overall antiproliferative activity of the studied [(cisplatin)$_2$⊂(^{RGD}**C1**-^{RGD}**C3**)] complexes.

Finally, an optimal drug delivery system should protect healthy tissue from its toxic drug cargo, as well as lack any intrinsic toxicity itself. As a proof of concept of this for the integrin targeting metallacages, the toxicity of the unoccupied metallacage **C0**, the host guest system [(cisplatin)$_2$⊂(**C0**)], and free cisplatin were studied *ex vivo* for their toxicity against healthy rat liver and kidney tissue, using the FDA approved precision-cut tissue slices (PCTS) technique.[204]

To summarise this *ex vivo* technique, a core of healthy, viable tissue (5 mm in diameter) is taken from the organ of choice. This is then precisely cut to either 150 µm (kidney slices) or 250 µm (liver slices). The slices are then incubated for 24 hours with the compound of interest. Afterwards, they can be analysed by different methods. By keeping the tissue as slices the cells are kept in their natural environment and can maintain their cell-cell and cell-extra cellular matrix contacts, and thus offers a more complex and true-to-life model for studying the toxicity of compounds towards organs with respect to the analogous 2D *in vitro* models.

The viability of the liver and kidney tissue slices was assessed by incubating the slices with different concentrations of the metallacage **C0**, the host-guest complex [(cisplatin)$_2$⊂(**C0**)], and free cisplatin. After 24 hours incubation, the ATP and protein content of the slices were analysed to determine the tissue viability, and thus, the toxicity of the various treatments. The results are reported in figure 9. Predictably, when incubated with cisplatin the liver and kidney slice viability was greatly reduced; in particular the liver slices showed almost complete quenching of ATP production when incubated with a solution of 50 µM cisplatin. **C0** exhibited scarce toxicity towards liver across the concentration range used in this study (5 – 25 µM), and only a small reduction in ATP production in kidney slices. The [(cisplatin)$_2$⊂(**C0**)] host guest complex showed a significant reduction in toxicity compared to the same concentration of free cisplatin used against both kidney and liver tissue slices, which would suggest that the cage is acting to protect the healthy tissue from the toxic cargo Pt(II) molecule.

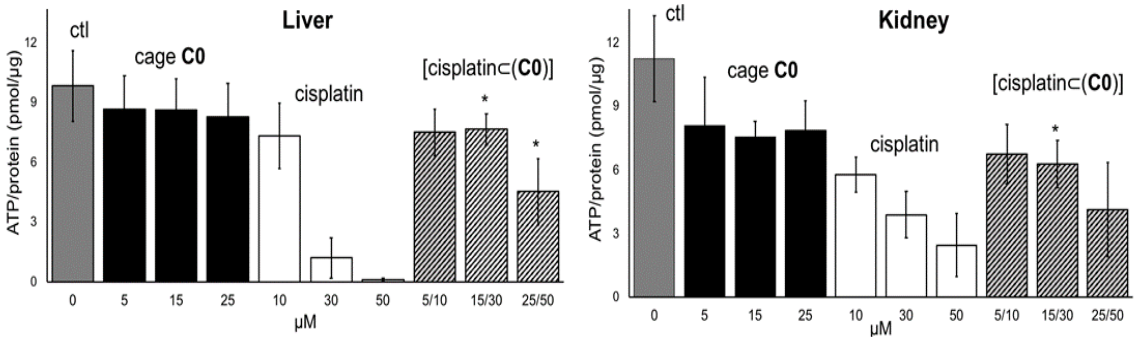

Figure 9: Bar chart showing the ATP content of left: liver slices; right: kidney slices; after 24 h incubation in the presence of increasing concentrations of **C0** (black bars), free cisplatin (white bars), and the host guest complex [(cisplatin)$_2$⊂(**C0**)] (dashed bars), and a control (grey bar).

The reduced uptake of encapsulated cisplatin by the tissues, when compared to free cisplatin, may be the reason for the observed reduced toxicity. As both the metallacage host and

cisplatin guest molecules have potentially toxic exogenous metals as part of their composition (palladium and platinum, respectively) ICP-MS was used to determine the amount of metals present in the tissue slices. As such, precision cut liver and kidney tissue slices were prepared by complete digestion using concentrated nitric acid, before the sample was monitored by ICP-MS for the $^{195}Pt^{+}$, $^{194}Pt^{+}$ and $^{104}Pd^{+}$ ion content. The results are shown in figure 10. In both liver and kidney tissue slices, the palladium content of both the unoccupied metallacage **C0** and the [(cisplatin)$_2$⊂(**C0**)] host guest system was the same, indicating that the encapsulated cisplatin does not affect the uptake of the metallacage by the tissue. It was also shown that the platinum content of the tissue slices incubated with free cisplatin was higher than the platinum content of the tissue slices that were incubated with [(cisplatin)$_2$⊂(**C0**)] for both the liver and kidney slices. Moreover, the ratio of palladium: platinum was broadly in accordance with the predicted host: guest stoichiometry of 1: 2. However, there was a much larger difference in platinum content between encapsulated and free cisplatin in kidney slices. This may be due to a high retention of the entire host-guest complex within the liver, while there may be partial excretion of the palladium metal from the kidneys, but higher retention of the platinum metal centres. However, the further investigation into the metabolism and excretion of the host-guest complex should be carried out, as retention of platinum and palladium in the liver is not usually observed. The results, however, would indicate that the lower cytotoxicity exhibited by the encapsulated cisplatin is due to a lower uptake of the metallacage, and thus the [(cisplatin)$_2$⊂(**C0**)] host-guest complex, when compared to free cisplatin.

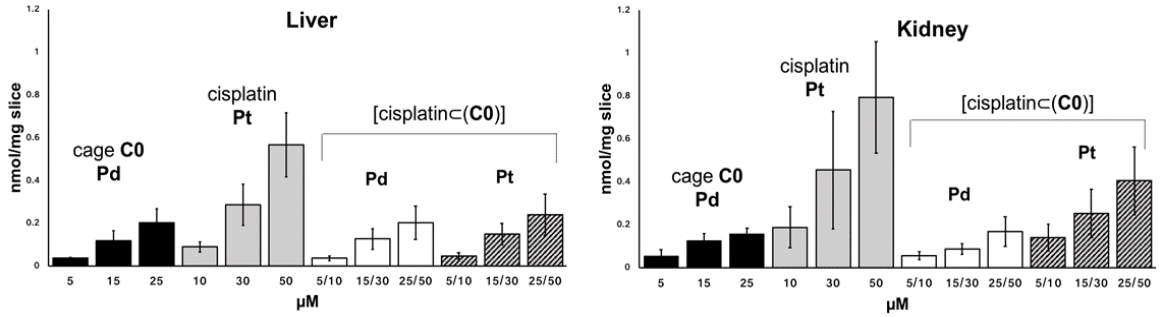

Figure 10: Bar chart showing the palladium (black and white bars) and platinum (grey and dashed bars) content of the liver (left) and kidney (right) tissue slices after 24 hours incubation with increased concentrations of **C0** (black bars), cisplatin (grey bars), and the host-guest complex [(cisplatin)$_2$⊂(**C0**)] (white and dashed bars).

In summary, we have demonstrated the first proof of concept for targeted drug delivery of cisplatin using supramolecular coordination complexes, namely the Pd_2L_4 metallacages. The encapsulation of two molecules of cisplatin in solution was demonstrated *via* NMR (^{1}H, ^{195}Pt, and ^{1}H DOSY). Furthermore, the successful conjugation of integrin targeting peptides to the metallacage ligand was achieved, and this large appendage was shown not to interfere with the Pd_2L_4 metallacage self-assembly process. The resulting integrin targeting metallacages, ^{RGD}**C1**-

^{RGD}**C4**, were shown to have a high affinity for their respective integrin types. The αvβ3 targeting metallacages, ^{RGD}**C1**-^{RGD}**C3**, were screened against a αvβ3 enriched (A375) and an αvβ3 depleted (A549) cancer cell line for their antiproliferative activity and were all found to be non-cytotoxic. Upon encapsulation of cisplatin, the [(cisplatin)$_2$⊂(^{RGD}**C1**-^{RGD}**C3**)] complexes were shown to be at least as potent as cisplatin against the αvβ3 enriched cancer cell line, with [(cisplatin)$_2$⊂(^{RGD}**C2**)] exhibiting nearly a two-fold increase in its potency when compared to cisplatin. Finally, as a proof of concept, cisplatin was encapsulated within **C0** and the resulting host-guest complex was studied for its possible toxicity *ex vivo* against healthy rat liver and kidney slices. [(Cisplatin)$_2$⊂(**C0**)] exhibited limited toxicity within both tissue slices when compared to free cisplatin, which was shown *via* ICP-MS to be due to reduced Pt uptake by the tissue of the [(cisplatin)$_2$⊂(**C0**)] host guest complex with respect to cisplatin.

Chapter 6 *Exo*-functionalisation of Pd_2L_4 metallacage for blood brain barrier translocation

6.1 Introduction

Chemotherapy for malignancies within the central nervous system (CNS), including brain tumours, remains a challenge in medicine. Reasons for this challenge are primarily due to factors such as incomplete understanding of the brain's biochemistry and physiology, limited information on appropriate biomarkers to assess the therapeutic efficacy of potential drug candidates, and the often reported undesirable side effects which occur due to a lack of selectivity towards the brain over other tissue and organs within the body.[205,206] A large hurdle in the improvement of accessing therapeutic targets within the brain is delivering drugs into the central nervous system.[207] Although there are several methods to accomplish this many, such as neurosurgical techniques, are invasive and risk compromising the integrity of the CNS.[207] Non-invasive techniques of delivering drugs to the CNS therefore offer an attractive approach in neurology. There are several strategies that have been explored to accomplish this, however these non-invasive techniques would ideally require administration of the drug to the patient either orally, or intravenously.[207–209] Indeed, the interface between the blood circulatory system and the cerebrospinal fluid is composed of a highly specialised group of closely related cells known as the neurovascular unit.[210] The neurovascular unit itself is composed of neurones, astrocytes, myocytes, pericytes, extracellular matrix components and endothelial cells with tight cell-to-cell junctions.[210] These tightly formed endothelial cells at the interface between the blood circulatory system and CNS is known as the blood–brain barrier (BBB).[211] The BBB is a highly selective semi permeable membrane which separates the blood circulatory system from the brain cerebrospinal fluid. The highly selective membrane protects the CNS by maintaining a stable environment and guards against fluctuations in composition of the blood circulatory system, as well as from toxic compounds and solutes which may also be present within the blood.[210,211]

The BBB presents a significant challenge in the delivery of drugs via non-invasive delivery methods due to its high selectivity.[210] Small, gaseous molecules, such as carbon dioxide and oxygen, and small lipophilic molecules (less than 500 Da, log P_{oct} 2–4)[210,212] that are not substrates of active efflux transporters have been reported to cross the BBB by passive diffusion.[213] Ions and water molecules are regulated and can pass through the barrier via channels. However, other molecules can only pass across the BBB into the CNS either by specialised transport proteins via receptor mediated translocation (RMT), or by adsorptive

mediated translocation (AMT).[211] Similarly, the metabolites and waste products formed within the brain must translocate across the BBB from the CNS into the blood in order to be excreted and avoid build-up of compounds within the brain.[210,211] It has been reported that approximately 98% of small molecules, and almost all large molecules and macromolecules, are unable to traverse the BBB.[214] As there are numerous proteins within the BBB which have been identified as transporter proteins (approximately 10-15% of all proteins identified within the BBB are transporter proteins),[215] these offer attractive targets for potential drugs.

One strategy to enable large molecules or molecules that are otherwise unable to translocate across the BBB by themselves is to utilise transporter proteins by the so called "trojan-horse" method.[216] This method requires the therapeutic cargo to be conjugated to a ligand, such as a protein or small peptide sequence, which is recognised and transported across the BBB (transcytosis) by transporter proteins present on the apical (blood facing side) membrane of endothelial cells of the BBB, thus carrying the therapeutic cargo across the BBB.[216] A widely explored class of transporter proteins to target for RMT of the BBB are transferrin receptor proteins.[205] Transferrin receptor proteins bind and translocate transferrin across cell membranes. Although transferrin receptors are expressed in the BBB, they are also highly expressed and broadly distributed in other cells throughout the body.[217] This wide distribution of transferrin receptor proteins throughout the body limits the selectivity of "trojan-horse" type drug conjugates that target transferrin receptor proteins, as they will interact with transferrin transporter proteins present in cells of other organs, and thus increase the risk of undesirable side effects of these so called "trojan-horse" drug conjugates. This broad distribution and high expression of transporter proteins within the BBB is not restricted to transferrin receptor proteins but is unfortunately characteristic of most known transporter proteins.[205] This limits the appeal of targeting transporter proteins to access the CNS via the BBB by RMT. Furthermore, in order to avoid build-up of the drug within the brain, the drug conjugate would need to be recognised by transporter proteins on the basolateral (brain facing side) membrane and undergo transcytosis back across the BBB.

Adsorptive mediated translocation (AMT) offers an attractive alternative to RMT in traversing the BBB. AMT requires an initial attraction between the peptide or protein and the apical membrane of the BBB.[218] This initial attraction usually occurs via electrostatic interactions,[219] whereby a positively charged peptide or protein is attracted to the negatively charged face of the lipid bilayer.[219] The peptide or protein must then be able to penetrate the lipid bilayer and translocate across the endothelial cell, before being able to pass through the basolateral membrane and thus enter the cerebrospinal fluid of the CNS. Many viruses are known to exploit the receptor independent AMT in order to enter the CNS, for example, the

trans-activating transcriptional activator from the human immunodeficiency virus 1 (HIV-1) is a known peptide vector that crosses endothelial cell lines, including the BBB, by AMT.[220]

Receptor independent AMT has been a known phenomenon that may be exploited to translocate across the BBB for the past two decades.[221] However, the discovery of novel, synthetically accessible and efficient peptide vectors to access the CNS via AMT is ongoing. Short peptide sequences from Dengue capsid protein (DEN2C) had previously been shown to be particularly efficient at cellular membrane translocation (figure 1), and indeed could transport macromolecules across cellular membranes via conjugation of the peptide sequences to the macromolecule.[222,223]

PepH1 PepH2 **PepH3** PepH4

MNDQRKKARNTPFNMLKRERNRVSTVQQLTKRFSLGMLQGRGPLKLFMALVAFLRFLTIPPT**AGILKRW**GTIKKSKAINVLRGFRKEIGRMLNILNRRRR

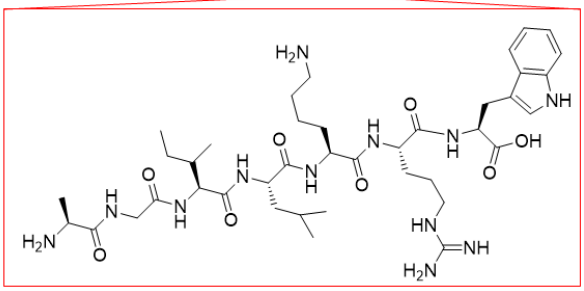

Figure 1. Dengue virus capsid protein (DEN2C) sequence, with the identified helical domains highlighted in red (PepH1-4) which were investigated for their adsorptive mediated translocation properties. PepH3 (highlighted in red and bold, with the structure shown) was shown to be the most effective translocator of the brained endothelial cells.

As such, Castanho and co-workers investigated the short peptide sequences for their ability to cross an *in vitro* model BBB.[224] The *in vitro* model consisted of a transwell assay whereby the upper apex of the setup was separated from the base well by a semipermeable filter.[224] Brain endothelial cells (bEnd.3 cells) were grown on the filter to mimic the BBB. The integrity of the endothelial cells was assessed using fluorescently labelled macromolecules of increasing size in order to ensure that the cell-cell junctions were tight enough to be a comparable *in vitro* model for the BBB.[224] The peptide vectors were radiolabelled and introduced to the apex well, before the concentration of radiolabelled peptide vector could be determined at selected time intervals.[224] The ratio of peptide to translocate across the model BBB could be determined by analysing the solution in the base well, as well as the ratio of peptide to only be associated with the apex facing membrane of the endothelial cells, as well as the amount of peptide to be retained within the cells. From the results of the *in vitro* model, two peptide vectors were selected for *in vivo* studies to analyse the biodistribution as well as the stability profiles of the peptides in blood serum and urine. It was reported that the seven amino acid peptide vector, PepH3, was efficiently taken up within the brain via AMT, was rapidly eliminated

from the brain, and was rapidly excreted from the body.[224] As such, PepH3 offers an extremely attractive peptide vector to translocate cargo across the BBB.

It has previously been shown that conjugation of peptides can be accomplished to Pd_2L_4 metallacages via exo-functionalisation without compromising the metallacage structure.[131] As Pd_2L_4 metallacages can encapsulate cisplatin,[99,127,148] it was hypothesised that conjugation of PepH3 to a Pd_2L_4 metallacage could impart the metallacage with the ability to translocate across the BBB via receptor independent AMT. In order to ensure that PepH3 could carry out its BBB translocating function without steric interference from the bulky and rigid Pd_2L_4 metallacage, a polyethylene glycol (PEG) chain was used in the design as a spacer moiety between PepH3 and the ligand of the Pd_2L_4 metallacage (figure 2). Finally, as PepH3 would be synthesised via Fmoc solid phase peptide synthesis (SPPS) (figure 3), the ligand and PEG spacer unit were designed to be amenable to amide bond formation so that the entire PepH3-PEG *exo*-functionalised ligand could be synthesised on the solid support resin, before being cleaved, purified, and finally self-assembled by introduction of stoichiometric amount of palladium(II) (Pd^{II}: L; 1: 2) into the PepH3 *exo*-functionalised Pd_2L_4 metallacage.

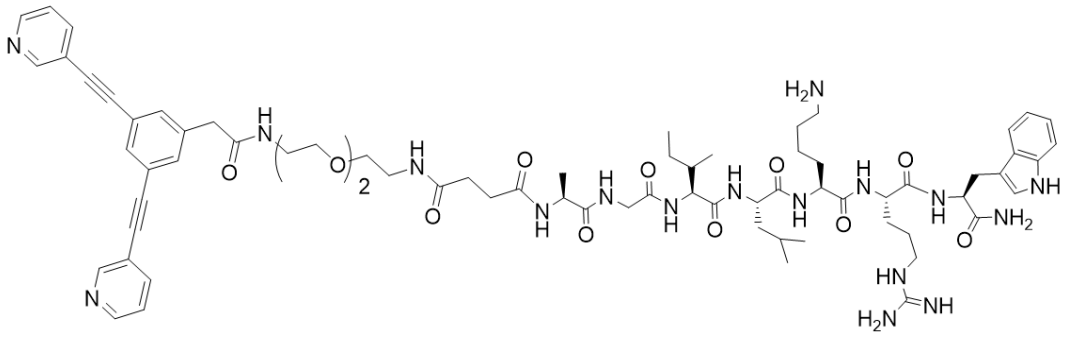

Figure 2. Chemical structure of the PepH3 *exo*-functionalised ligand (**L^{PepH3}**). A short polyethylene glycol chain was used to separate the ligand scaffold and the BBB translocating peptide to inhibit steric interference between the peptide and metallacage self-assembly, and the bulky metallacage from sterically interfering with the BBB translocation of PepH3

6.2 Synthesis of PepH3 BBB translocating peptide *exo*-functionalised ligand

PepH3 and the PepH3-PEG-functionalised ligand conjugate was synthesised as part of a two month Erasmus+ project in the laboratory of Dr. João D. G. Correia at the Instituto Tecnológico e Nuclear in Sacavém by stepwise Fmoc SPPS.

6.2.1 Synthesis of PepH3 via Fmoc-SPPS

SPPS involves the addition of N-protected amino acid residues to the deprotected N-terminal of an amino acid which has been anchored to an insoluble, solid support resin (usually a functionalised polymer) via the C-terminus. In this way, the primary structure of the peptide

can be synthesised by sequential addition of the appropriate amino acids in the C – N direction of the peptide (figure 3). The functional groups of the amino acid residues must be protected in order to avoid undesirable side reactions with the reagents used for SPPS but must also be susceptible to cleavage once the desired peptide has been synthesised (i.e. orthogonal protecting group, denoted in brackets for the protected amino acid residues). Furthermore, the N-terminal of each amino acid residue must also be protected with a suitable group which must be stable under the reaction conditions of conjugation of the amino acid to the growing peptide chain, but susceptible to cleavage under conditions that will not result in deprotection of the side groups present on the growing peptide, or cleavage from the solid support. Finally, once the desired peptide chain has been synthesised, the peptide is cleaved from the solid support and the functional groups are deprotected (often in a single reaction step), purified *via* reverse phase liquid chromatography and isolated as a solid by freeze drying the aqueous solution of the isolated peptide (lyophilisation).[225]

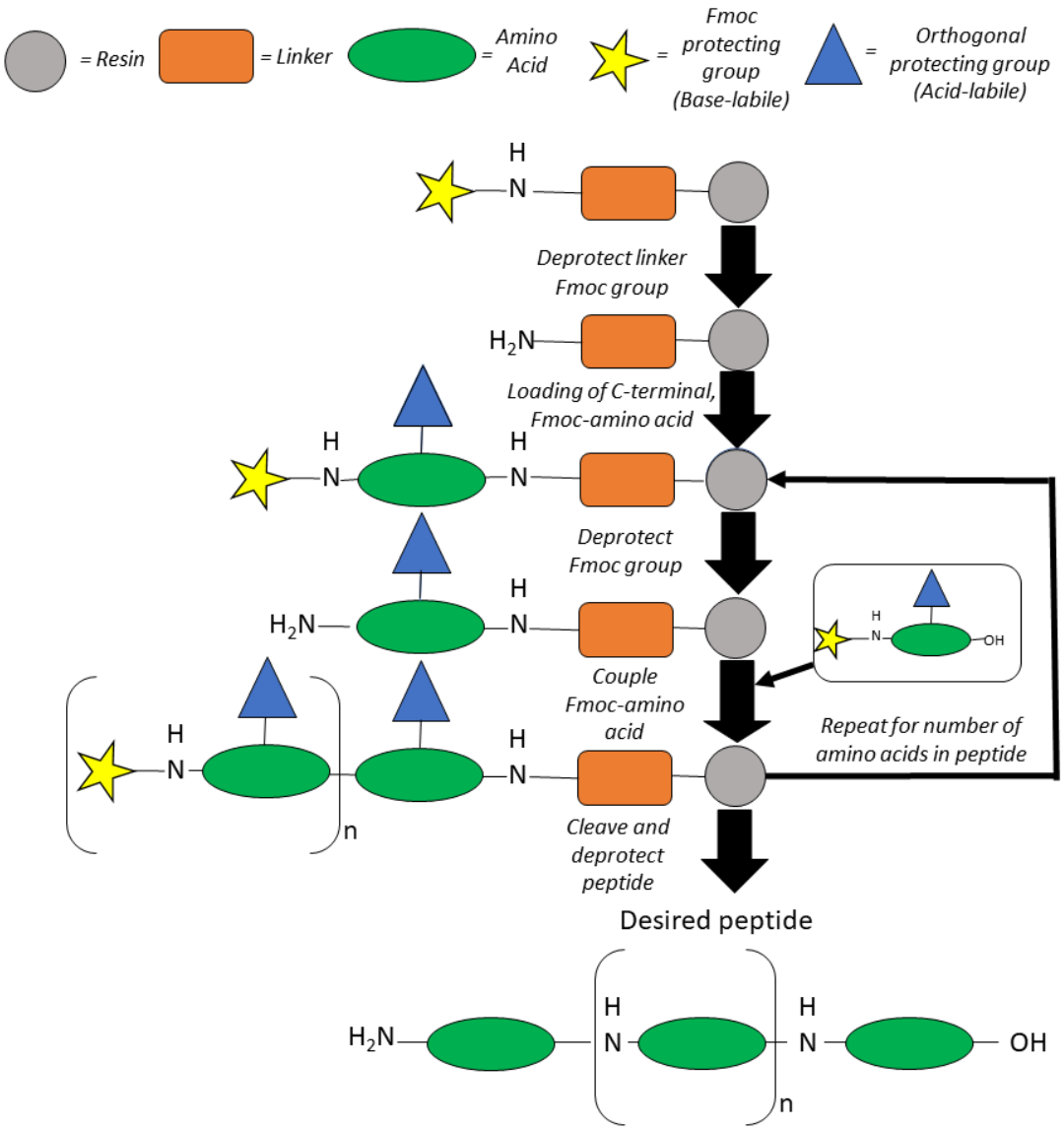

Figure 3. Schematic representation of Fmoc solid phase peptide synthesis. The sequential addition of Fmoc protected amino acid residues, with any functional groups protected by orthogonal protecting groups to limit undesirable side reactions during the synthesis, can be added to build the peptide sequence. The final peptide sequence can be cleaved from the solid support resin, and the orthogonal protecting groups removed, by use of trifluoroacetic acid.

There are two commonly used SPPS methods which are differentiated by the protecting group of the N-terminal of the amino acid residues: Fmoc-SPPS and BOC-SPPS.[225] Fmoc-SPPS is the most commonly employed method for SPPS as it requires milder reaction conditions to deprotect the N-terminal of the supported peptide chain than Boc-SPPS and does not require the use of hydrofluoric acid to cleave the peptide from the solid support and deprotect the functional groups of the peptide.[225]

Fmoc-SPPS requires the amino acid residues to have the N-terminal protected by fluorenylmethyloxycarbonyl (Fmoc) via a carbamate bond which can be cleaved *via* deprotonation using a secondary amine, such as piperidine. The C-terminal Fmoc-protected

amino acid of the peptide is tethered to the solid support resin by a bond stable under basic conditions. The amino acid loaded resin is washed to remove any unreacted reagents, before the Fmoc-protected amino acid is deprotected. The solid support resin, with the deprotected amino acid loaded onto it, is then washed to ensure there are no residual unreacted reagents present, before the next Fmoc-protected amino acid is conjugated via amide bond formation.[225] The amino acid loaded resin is washed to remove any unreacted reagents before the next Fmoc-protected amino acid is conjugated to the growing peptide chain *via* amide bond formation. This sequential process of deprotection of the Fmoc group, removing unreacted reagents and conjugation of the next Fmoc-protected amino acid is repeated until the desired peptide has been synthesised on the solid support resin (figure 3).[225] The orthogonal protecting groups of the side chain functional groups, as well as the chemical bond tethering the peptide to the solid support resin, are then cleaved using trifluoroacetic acid (TFA), and a small amount of a radical scavenger (triisopropylsilane; TIPS) to quench any radicals formed from the decomposition products of the protecting groups. The peptide is then purified *via* RP-LC and the aqueous solvent removed by lyophilisation to give the desired peptide.[225]

Due to the growing peptide being immobilised on a solid support, characterising the peptide before it has been cleaved and thus assessing whether the loading of an amino acid residue has been successful, can present a challenge. The ninhydrin-based Kaiser test, a colorimetric test based on the reaction of ninhydrin with primary amines, can be employed to assess whether the loading of an Fmoc-protected amino acid has been successful, and whether the deprotection of the amino acid has been successful, by analysing a small sample (3-5 beads) of the solid support resin.[226] The small sample of beads are removed from the bulk of the solid support resin, and the Kaiser test reagents are applied. In the presence of a primary amine, i.e. deprotected N-terminal of the supported peptide, the reagents cause the beads to turn blue. If the N-terminal amine is protected, no reaction will occur and thus the beads will remain colourless.[226] Thus, the Kaiser test can provide qualitative analysis on the success of conjugation of an Fmoc-protected amino acid, or the deprotection of the Fmoc group.

PepH3 was thus synthesised following standard stepwise Fmoc-SPPS (figure 3). Rink amide MBHA resin was used as the solid support in order to prevent cyclisation of the final, cleaved PepH3 peptide, as the cleaved peptide will be endowed with an amide group at the C-terminal, as opposed to a carboxylic acid group (figure 2). The resin was swollen using DCM and deprotected using piperidine in DMF (which was checked using the Kaiser test), before being washed using DCM. The protected C-terminal amino acid, Fmoc-Trp(boc)-OH, was loaded onto the rink amide MBHA resin using a DMF solution of DMAP and Hexafluorophosphate azabenzotriazole tetramethyl uranium (HATU). The reaction was monitored using the Kaiser

test, before the resin was washed using DCM and the second protected amino acid, Fmoc-Arg(Pbf)-OH, was conjugated *via* amide bond formation using a DMF solution of DMAP and HATU. The conjugation was monitored by the Kaiser test. This process was repeated for the next 5 protected amino acids (Fmoc-Lys(boc)-OH; Fmoc-Leu-OH; Fmoc-Ile-OH; Fmoc-Gly-OH; Fmoc-Ala-OH, respectively), with the success of the conjugation and deprotection monitored at each stage *via* the Kaiser test. The N-terminal amino acid, Alanine, was left protected with the Fmoc group, in order to improve the stability of the resin bound peptide against side reactions. In order to ensure that PepH3 had been successfully formed on the resin, a sample was cleaved from the Rink amide MBHA resin and the orthogonal protection groups removed, by immersing the resin in a solution of TFA, water and TIPS (95: 2.5: 2.5 v/v). The TFA was removed and the aqueous solution was analysed by RP-HPLC. The major peak was isolated and sent for analysis by mass spectrometry, which showed that the peptide had been formed.

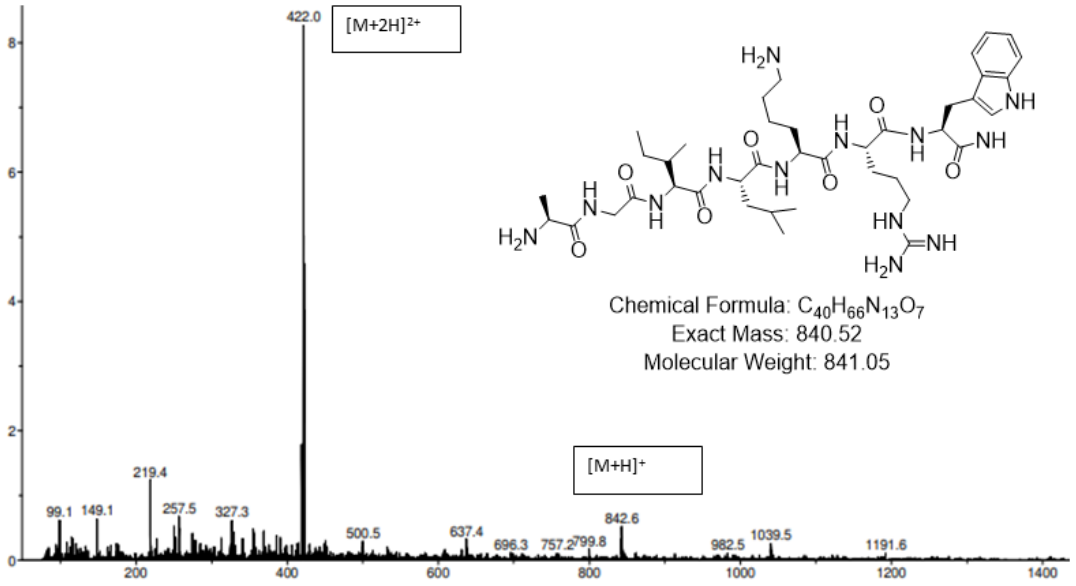

Figure 4. Mass spectrum of the cleaved and deprotected PepH3 peptide fragment from a small sample of resin beads, which was carried out to ensure that the peptide had been synthesised successfully. The conjugation of the PEG linker moiety was then carried out on the solid supported PepH3 fragment following standard SPPS protocol.

6.2.2 *Exo*-functionalisation of the ligand via PEG spacer unit

The resin bound PepH3 peptide was functionalised with a PEG spacer unit. The PEG unit was selected to be short, with two polyethylene glycol units capped by an unprotected carboxylic acid group at one end, and a Fmoc-protected amine group at the other end, (N-[8-(9-Fluorenylmethyloxycarbonyl) amino-3,6-dioxaoctyl]succinamic acid; Fmoc-NH-$(PEG)_2$-COOH, figure 5). In this way it could be treated as another Fmoc-protected amino acid residue and be conjugated to the resin bound peptide *via* standard Fmoc-SPPS. As such, the Fmoc-protected N-

terminal amino acid was deprotected using piperidine, which was confirmed using the Kaiser test.

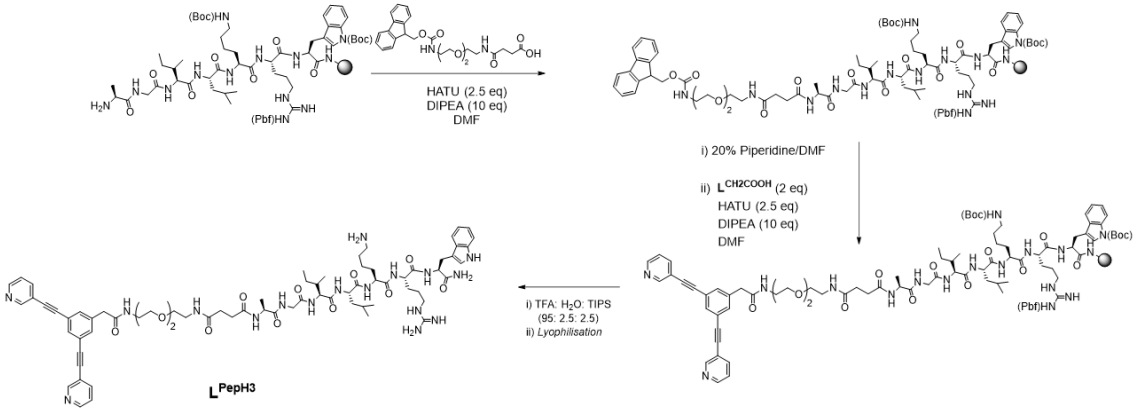

Figure 5. Conjugation of the PEG spacer unit and $\mathbf{L^{CH2COOH}}$ to the resin bound PepH3 peptide, followed by deprotection of the orthogonal protecting groups and cleavage from the resin to give the PepH3 *exo*-functionalised ligand $\mathbf{L^{PepH3}}$.

The resin was washed with DCM before a solution of Fmoc-NH-$(PEG)_2$-COOH, DMAP and HATU in DMF was added to conjugate the PEG unit via amide bond formation. The reaction was monitored by the Kaiser test, whereupon the negative result (no colour change) indicated complete saturation of the primary amine of the terminal alanine residue, and thus complete conjugation of Fmoc-NH-$(PEG)_2$-COOH to the resin bound PepH3. A small sample of the resin was separated, deprotected using piperidine and cleaved using a solution of TFA, water and TIPS (95: 2.5: 2.5 v/v). The TFA was removed and the aqueous solution was analysed by RP-HPLC. The major peak was isolated and the filtrate was analysed by mass spectrometry, which confirmed that the peak corresponded to the PepH3-$(PEG)_2$-NH_2 conjugate, which could be observed via the $[M+2H]^{2+}$ and $[M+3H]^{3+}$ mass fragment peaks (figure 6).

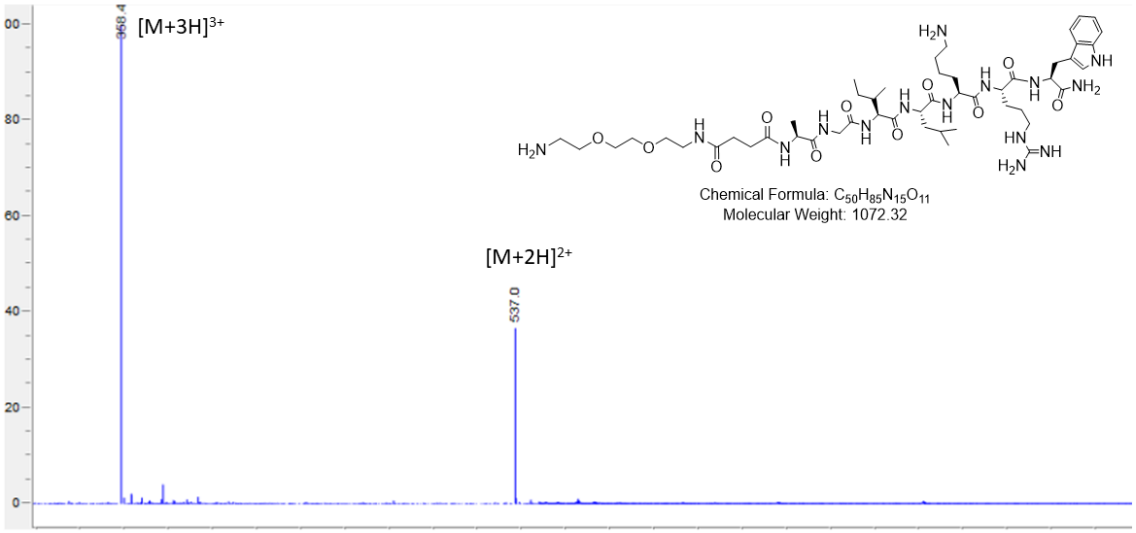

Figure 6. Mass spectrum of the PepH3 and polyethylene glycol conjugate, showing the *m/z* = $[M + 2H]^{2+}$ and $[M + 3H]^{3+}$ mass peaks.

As the peptide-PEG conjugate was confirmed to have formed on the resin, a carboxylic *exo*-functionalised ligand was synthesised to be conjugated *via* amide bond formation under standard Fmoc-SPPS conditions (figure 3). As discussed in chapter 8, the solubility of 3,5-bis(pyridin-3-ylethynyl)benzoic acid is extremely modest in almost all organic solvents, including DMF, DCM, and water. However, the solubility can be improved by separating the carboxylic acid group from the conjugated ligand scaffold by introducing an alkyl spacer. As such, 2-(3,5-bis(pyridin-3-ylethynyl)phenyl)acetic acid ($\mathbf{L^{CH2COOH}}$) was selected as the ligand (the synthesis of 2-(3,5-bis(pyridin-3-ylethynyl)phenyl)acetic acid is described in chapter 8), and was conjugated to the resin bound peptide-PEG moiety following standard Fmoc-SPPS conditions, as described above. The conjugation was initially confirmed via the Kaiser test, which gave a negative result and indicated that there were no primary amine groups present, which strongly suggests full conjugation of the ligand to the resin bound peptide-PEG moiety. The ligand-$(PEG)_2$-PepH3 conjugate was cleaved from the resin using a solution of TFA, water and TIPS (95: 2.5: 2.5 v/v), the TFA was removed by evaporation and the aqueous residue was purified *via* preparative RP-HPLC. The major peak was collected, with an aliquot analysed by mass spectrometry to determine that it was the full PepH3 *exo*-functionalised ligand (figure 7). The collected faction was dried by lyophilisation to yield the pure PepH3 *exo*-functionalised ligand, $\mathbf{L^{PepH3}}$.

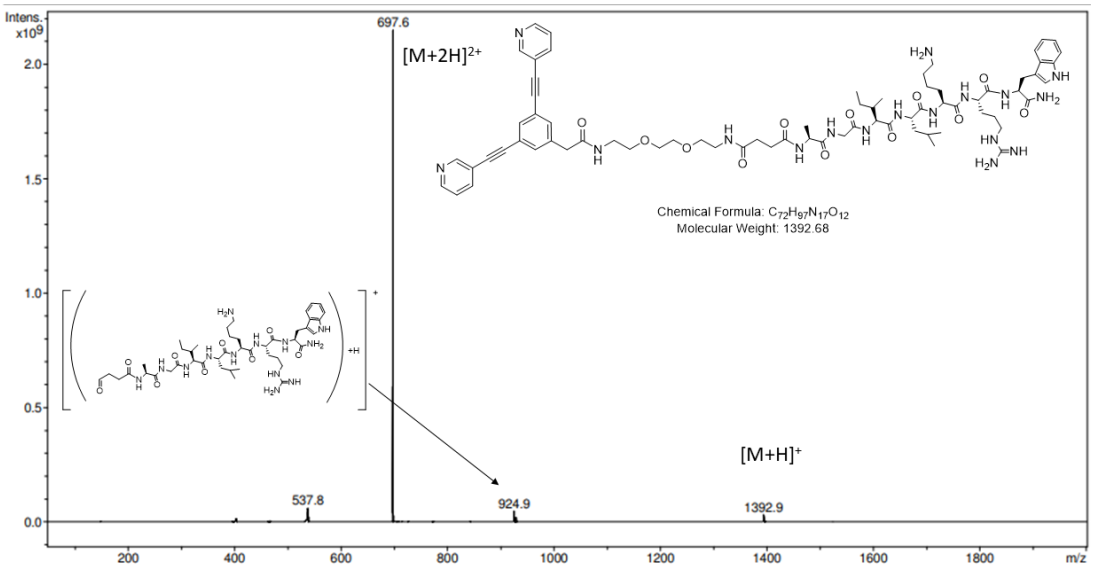

Figure 7. Mass spectrum of the PepH3 *exo*-functionalised ligand, $\mathbf{L^{PepH3}}$.

6.3 Self-assembly of Pd_2L_4 metallacage *exo*-functionalised with PepH3 BBB translocating peptide

The characterised ligand, $\mathbf{L^{PepH3}}$, was self-assembled into the corresponding Pd_2L_4 metallacage, $\mathbf{C^{PepH3}}$, by the stoichiometric addition of tetrakis(acetonitrile)palladium(II)tetrafluoroborate (1: 2; Pd^{II}: $\mathbf{L^{PepH3}}$). As the resulting metallacage, $\mathbf{C^{PepH3}}$, would be used for *in vitro* cell studies to assess its BBB translocating properties, as well as the fact that Pd_2L_4 metallacages self-assemble in quantitative yields, the synthesis of the metallacage was carried out in non-deuterated DMSO so that the sample could be directly used as a stock solution for the subsequent *in vitro* studies. The self-assembly of the metallacage can be monitored by ^{1}H NMR spectroscopy in non-deuterated DMSO by the use of a capillary insert filled with a deuterated solvent which the NMR spectrometer can lock on. Although there is inevitably a large peak corresponding to the non-deuterated DMSO solvent molecules, as the proton peaks of the ligand are in the aromatic region (approximately 7 – 10 ppm), and the solvent signal maximum is approximately 2.50 ppm, the large DMSO solvent peak does not mask the proton signals of the ligand. As such, the self-assembly of Pd_2L_4 metallacages can be successfully monitored directly in non-deuterated DMSO, and this sample can then be used directly for *in vitro* studies (figure 8).

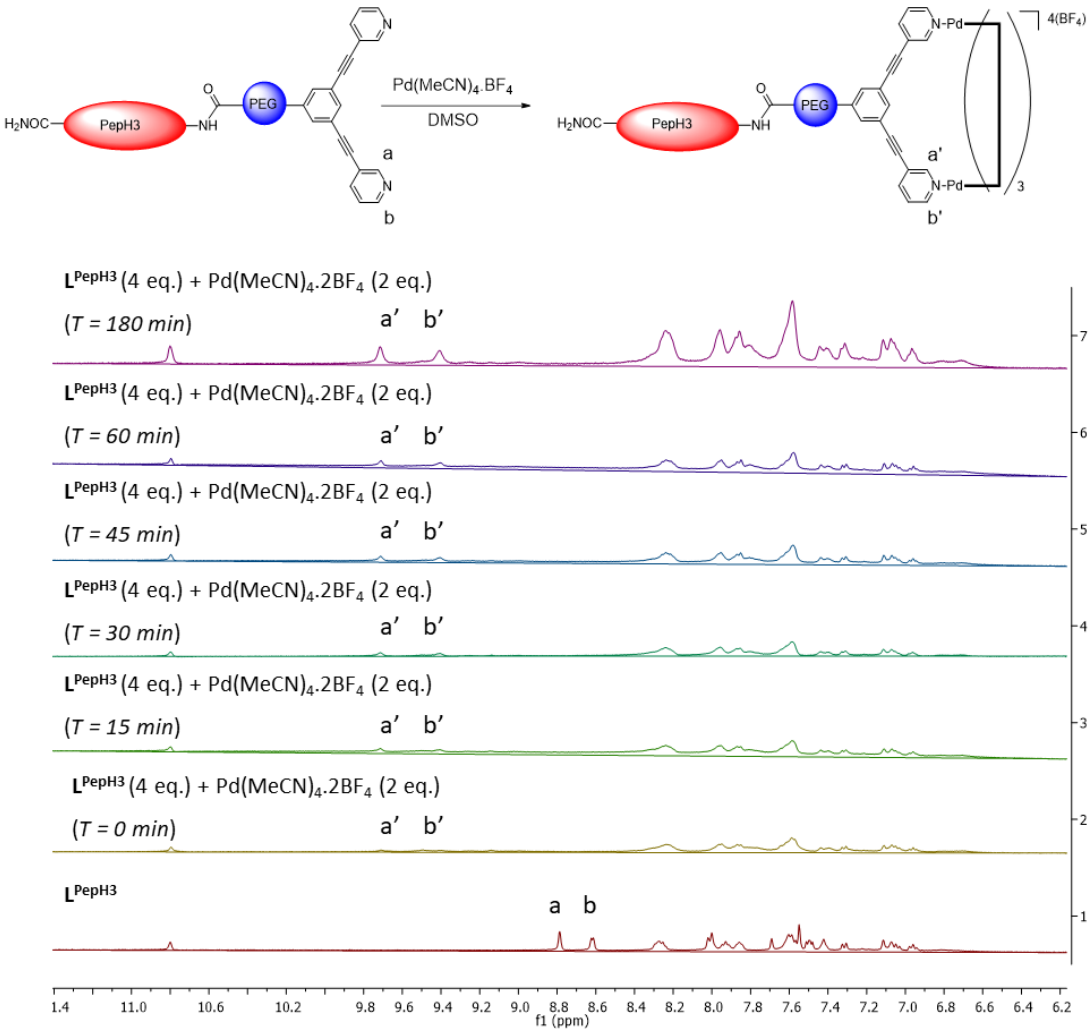

Figure 8. Stacked ^{1}H NMR spectra, which are zoomed to the aromatic region of **L^{PepH3}** (4 eq.) in the presence of tetrakisacetonitrilepalladium(II) tetrafluoroborate (2 eq.) in non-deuterated DMSO. After 15 minutes the quantitative self-assembled formation of the metallacage, **C^{PepH3}**, was observed. The reaction was monitored for 3 hours to ensure both stability and full coordination of **L^{PepH3}** to the palladium(II) metal centre.

The self-assembly of the metallacage was monitored in non-deuterated DMSO over 3 hours to ensure full coordination of the ligand, **L^{PepH3}**, to the palladium metal centres. The signals corresponding to H_a and H_b of **L^{PepH3}** (δ = 8.78 ppm and δ = 8.61 ppm, respectively) were seen to be completely quenched after 15 minutes, with two new peaks appearing which corresponded to H_a and H_b of **C^{PepH3}** (δ = 9.61 ppm and δ = 9.42 ppm, respectively, which indicated successful self-assembly to the metallacage **C^{PepH3}**.

6.4 Conclusions and future outlook

As the metallacage **C^{PepH3}** has been successfully self-assembled in non-deuterated DMSO, the transwell assay described by Castanho and coworkers will be carried out to assess whether the

PepH3 *exo*-functionalised metallacage will maintain the brain endothelial cell translocating function of PepH3. The ratio of metallacage that has crossed the endothelial cell line in the assay can be monitored by ICP-MS to assess the concentration of palladium(II), which will be attributed to the metallacage, in both the apex, cell line, and the base well cavity. However, as the presence of palladium will not conclusively show that the intact metallacage has translocated the endothelial cell line, current work in collaboration with Dr João D. G. Correia has focussed on optimising a HPLC assay to quantitatively assess the amount of intact metallacage present in a solution.

7 Highly fluorescent self-assembled Pd_2L_4 metallacages for cell imaging *in vitro*

7.1 Introduction

One method to study the intercellular distribution of molecules is fluorescence microscopy. The fluorescent sample can be incubated with the cell, after which the cell is fixed and prepared for visualisation using fluorescence microscopy. To build an image of the sample distribution within the cell, organelles can be stained with known fluorophores which selectively accumulate at a specific organelle.[227] An image of each fluorescently stained organelle can be taken by exciting the fluorophore with light (λ_{ex}) and applying a filter to the emitted light (λ_{em}). The filter will separate the strong light used to excite the sample from the weaker light emitted from the fluorophore. An image of each fluorescent stain used, and the sample fluorophore, within the cell can be collected in this way. The resulting images can then be overlaid to produce an image of the intercellular distribution of the sample fluorophore.

Fluorescence is a three-stage process that occurs for certain molecules known as fluorophores (figure 1). These molecules are usually polyaromatic, rigid heterocycles. The first stage of fluorescence is excitation, whereby a photon of energy hv_{ex} is provided by an external source (e.g. a laser of known wavelength) and absorbed by the fluorophore. This increase in energy of the molecule causes the excitation of an electron from the ground state to an excited singlet electron state ($S_0 – S_1'$) (figure 1).

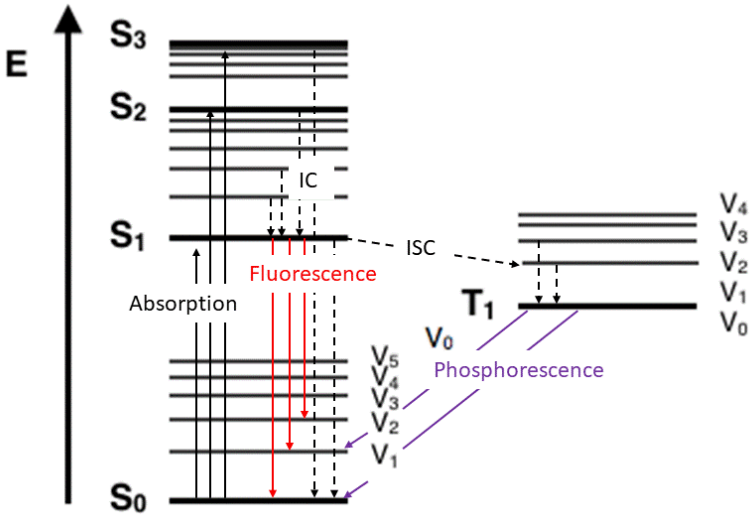

Figure 1: Jablonski diagram to visualise the three main steps of luminescence. Solid lines denote radiative transitions; dashed lines indicate non-radiative transitions.

It is important to note that numerous singlet excited states (S_2, S_3 etc) exist due to the different energies needed to promote electrons from different bonding orbitals to non-bonding orbitals (figure 1). However, as electrons promoted to higher energy levels typically dissipate energy via non-radiative internal conversion processes until they have the energy of the first excited singlet electron state (S_1), only the excitation of $S_0 – S_1$ and subsequent emission $S_1 – S_0$ are relevant to fluorescence.

The second stage of fluorescence is the excited state life-time, which is a measure of how long the new excited state (S_1') stays populated before the energy has been released and the electron returns to its ground state (S_0). The excited state life-time is typically less than 10 ns (although intersystem crossing of the first excited singlet state to the first excited triplet state (S1 – T1) can cause the lifetime to increase dramatically due to the forbidden reversal of the electron's spin during this process (phosphorescence). During this time the fluorophore can undergo conformational changes, intramolecular interactions and collisions which will dissipate the absorbed radiative energy *via* non-radiative pathways. This will reduce the energy of the singlet excited state S_1' to a relaxed singlet excited state, S_1, from which the fluorescence emission originates (figure 1).

The third stage of fluorescence is the fluorescence emission in which a photon of energy hv_{em} is emitted, returning the excited state singlet electron to the ground state (S1 – S0). As energy has been dissipated through non-radiative pathways during the fluorescence lifetime, the energy of the emitted photon will be lower and as such the emission wavelength (λ_{em}) of a fluorophore is longer than that of its excitation wavelength (λ_{ex}). The difference between λ_{em} and λ_{ex} is known as the Stokes shift. Finally, as there are numerous non-radiative pathways for the transition $S_1 – S_0$, every absorbed photon of energy hv_{ex} will not definitively produce an emitted photon of energy hv_{em}. The ratio of absorbed photons to emitted photons can be calculated experimentally and is known as the quantum yield of fluorescence (ϕ).

Previous studies have used an alcohol *exo*-functionalised Pd_2L_4 metallacage to study the intercellular distribution of the metallacage in A549 human lung cancer cells.[127] Unfortunately, despite the constituent ligands exhibiting fluorescence, the resulting metallacage was scarcely fluorescent due to the so-called 'heavy metal effect'. The localisation of the metallacage could therefore only be visualised at a concentration of 70 μM, at which point the metallacage appeared to be diffuse throughout the cytoplasm and the cell nucleus, providing limited information on uptake or sub-cellular localisation of the non-functionalised metallacage.

It was hypothesised that *exo*-functionalisation of the constituent ligands with a fluorophore would impart suitable fluorescent properties to the resulting cage and avoid

quenching upon formation of the Pd_2L_4 metallacages. Therefore, the aromatic fluorophores anthracene and naphthalene were selected and coupled to the Pd_2L_4 metallacage via amide bond formation.[132] Unfortunately, the resulting metallacages exhibited no fluorescence. This unexpected result was further studied via time dependent density functional theory (TD-DFT) and was revealed to be due to two factors: i) the probability of emission was lowered upon conjugation of the fluorophore to the ligand scaffold, and ii) the calculated wavelength of emitted light was within the IR region at 2000 nm.[132] In order to prevent the conjugation of the fluorophore to the ligand, and the resulting fluorescence quenching, it was hypothesized that insertion of a 'spacer' group between the fluorescent tag and the ligand scaffold was necessary to avoid the above mentioned conjugation.

7.2 BODIPY *exo*-functionalised Pd_2L_4 metallacages

In order to develop fluorescent metallacages suitable for *in vitro* imaging, it was thought that attaching the highly fluorescent fluorophore boron dipyrromethene (BODIPY) to the Pd_2L_4 metallacage scaffold, *via* a linker of sufficient length, would result in a metallacage with the necessary luminescent properties to be visualised in cells by fluorescence microscopy. BODIPY has been an attractive fluorophore for *in vitro* imaging due to several factors, including their ease of synthesis and structural versatility. Furthermore, the BODIPY spectroscopic properties can be altered through the judicious choice of functional group incorporation.[228] The spectroscopic features of BODIPYs include narrow, gaussian-like absorption and emission bands, high molar extinction co-efficients ($\varepsilon > 80{,}000\ M^{-1}\ cm^{-1}$), excellent quantum yields ($\phi > 50\%$) and negligible effect of the absorption and emission spectra due to solvent polarity. As such, the BODIPY fluorophore has found applications in several research fields. [229–232] Furthermore, the typical emission band of BODIPY is in the range of 470 – 530 nm, which can allow greater sensitivity when visualising as there will be less interference from endogenous fluorophores and background fluorescence due to biological components which typically emit at shorter wavelengths.

Although BODIPY does not fit Huckels rule of aromaticity (No. e^- = 4n+2, n = 1, 2, 3, etc..),[156] its properties are similar to aromatic fluorophores as the coordination of the pyrrole moieties to boron forms a cross-linked system which is cyclic, planar, highly conjugated and rigid. Indeed, without the coordination to boron, the organic BODIPY scaffold loses its rigid, planar conformation and adopts a similar conformation to cyanine dyes. Thus, it behaves in a similar way to cyanine dyes, which suffer emission quenching due to *trans-cis* isomerisation upon excitation. Due to the highly rigid, crosslinked and planar structure of BODIPY, little

intermolecular movement or vibration occur upon excitation, which allows for a low rate of non-radiative decay. Furthermore, it has been shown that there are relatively low instances of inter system crossing (ISC), although modification to the 3,5 – position has been shown to increase the rate of ISC.[233,234] As such, BODIPY derivatives tend to exhibit excellent quantum yield values.

The absorption spectra for BODIPY derivatives are dominated by an intense 0 – 0 band of the S0 – S1 excitation (480 – 530 nm). This sharp peak often has a visible shoulder peak on the shorter wavelength side of the absorption band attributed to the 0 -1 vibrational transition. Finally, due to the conjugated nature of BODIPY, weaker absorption bands observed at shorter wavelengths can be attributed to various $S_0 – S_n$ ($n \geq 2$) transitions.

7.2.1 Synthesis of BODIPY exo-functionalised Pd_2L_4 metallacages

In order to avoid quenching of the BODIPY fluorophore, the final ligand and metallacage must be rigid in order to minimise the non-radiative pathways for relaxation of $S_1 – S_0$. It was therefore proposed to link the BODIPY fluorophore to the metallacage ligand scaffold through the conjugated bonds formed formed via amide bond formation (scheme 1 route B), or by copper(I) catalysed alkyne azide [2+3] cycloaddition (CuAAC) "click" chemistry (scheme 1 route A). In order to achieve this, ligands exo-functionalised with an amine group ($\mathbf{L^{NH2}}$) (to facilitate amide bond formation), or with an azide group ($\mathbf{L^{N3}}$) to facilitate CuAAC. The BODIPY fluorophore must also be functionalised with a carboxylic acid group ($\mathbf{BDP^{COOH}}$), or functionalised with a terminal alkynyl ($\mathbf{BDP^{alkynyl}}$) to facilitate these conjugation strategies.

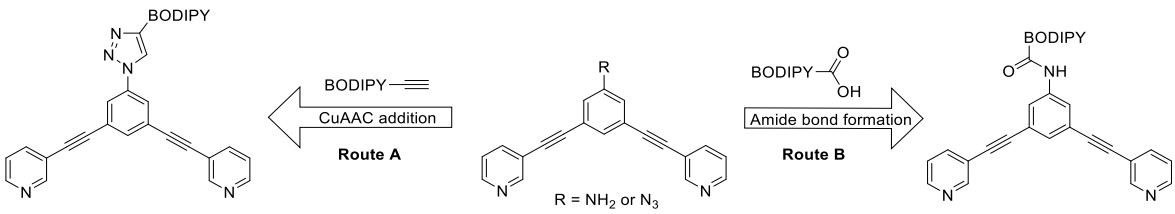

Scheme 1. Proposed synthetic routes for conjugation of BODIPY to the ligand. Route A: CuAAC addition. Route B: Amide bond formation**.**

The ligands $\mathbf{L^{NH2}}$ and could be synthesised directly via Sonogashira cross coupling between 3,5-dibromoanaline 3-ethynylpyridine to afford the bidentate ligand (figure 2). The azide *exo*-functionalised ligand could be obtained from $\mathbf{L^{NH2}}$ by addition of $NaNO_2$ under acidic conditions, followed by addition of NaN_3 and subsequent neutralisation of the solution to afford $\mathbf{L^{N3}}$.

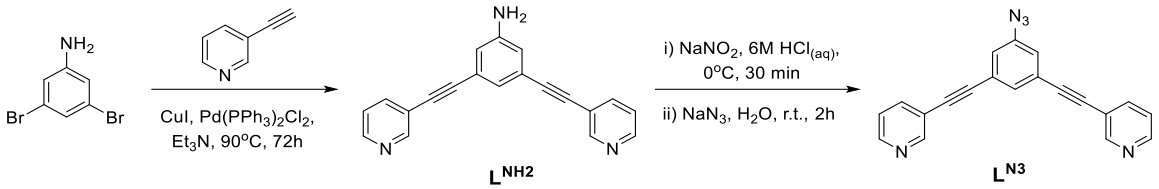

Figure 2. Synthesis of the precursor ligands $\mathbf{L^{NH2}}$ and $\mathbf{L^{N3}}$.

The BODIPY precursors were synthesised according to a previously reported procedure.[235,236] A condensation reaction between 3-ethyl-2,3-dimethylpyrrole and 4-formylbenzoic acid ($\mathbf{BDP^{COOH}}$), 4-aminobenzaldehyde ($\mathbf{BDP^{NH2}}$) or 4-ethynylbenzaldehyde ($\mathbf{BDP^{alkynyl}}$) in the presence of trifluoroacetic acid (TFA) produced the dipyrromethene organic scaffold, which was converted to the dipyrromethene analogue by treatment with DDQ. Coordination of BF_2 to the BODIPY scaffold was achieved by reacting $Et_2O.BF_3$ with the dipyrromethene scaffold in the presence of the tertiary amine, triethylamine (figure 3).

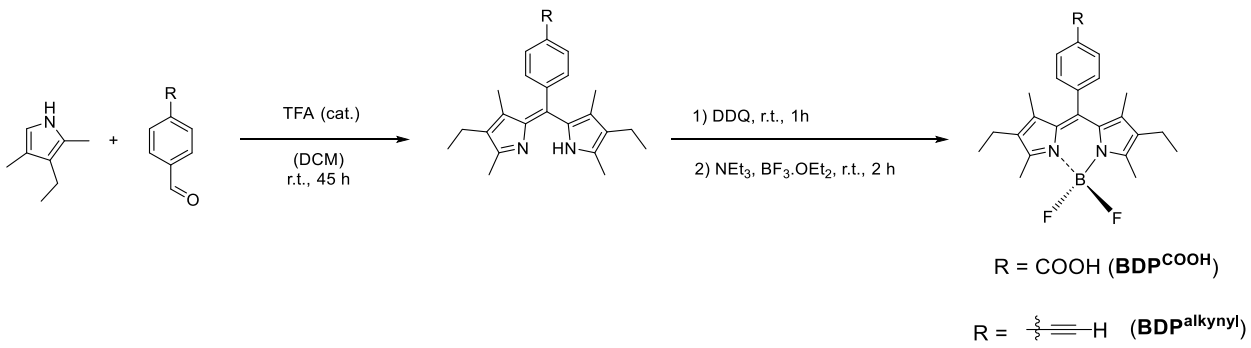

Figure 3: Synthesis of the BODIPY precursor groups, $\mathbf{BDP^{COOH}}$ and $\mathbf{BDP^{alkynyl}}$.

The conjugation of $\mathbf{BDP^{COOH}}$ to $\mathbf{L^{NH2}}$ via amide bond formation was carried out in DMF at 130°C using 2-chloro-1-methylpyridinium iodide (CMPI) and *N,N*-dimethyl-4-aminopyridine (DMAP), to activate the acid, for 24 hours. The compound could be recovered by diluting the reaction with DCM and washing with water, before purification of the crude product *via* silica chromatography to give $\mathbf{L1^{BDP}}$ (figure 4).

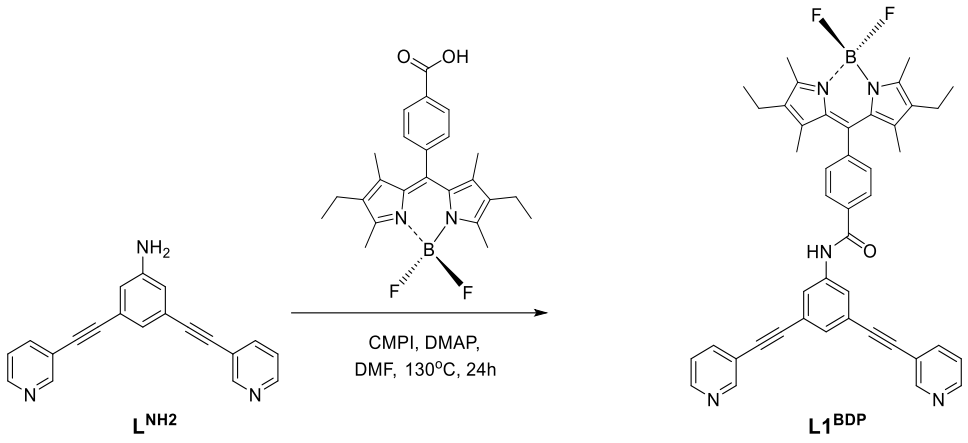

Figure 4. Synthesis of the BODIPY functionalised ligand, **L1^{BDP}**.

The conjugation of **L^{N3}** to **BDP^{alkynyl}** via CuAAC "click" chemistry was carried out in MeOH: H_2O (3: 1), with the reactants first being dissolved in minimal DCM. Copper(II)sulphate was reduced to give the Cu(I) catalyst by sodium ascorbate, which was made *in situ* by the addition of *L*-(+)-ascorbic acid and sodium hydroxide. The reaction was stirred at room temperature to avoid the formation of any *cis*-addition products (figure 5). The reaction was quenched using an excess of aqueous ammonium acetate solution, before the crude product was separated by washing the reaction solution with DCM. The crude product was purified using silica chromatography to give the ligand **L2^{BDP}**.

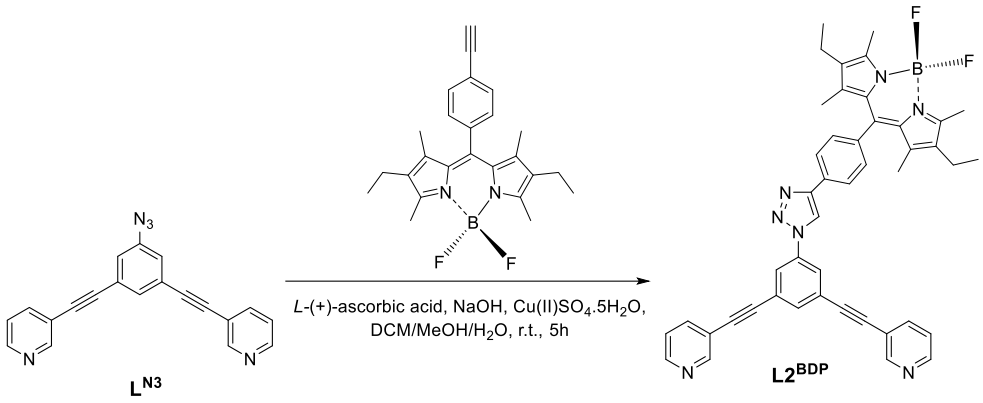

Figure 5. Synthesis of the BODIPY functionalised ligand, **L2^{BDP}**.

After successful conjugation of the BODIPY fluorophore to the ligand scaffold, Pd_2L_4 metallacages were formed via self-assembly in DMSO. The ligand and palladium(II) precursor ($[Pd(MeCN)_4.2BF_4]$ or $[Pd(NO_3)_2.5H_2O]$ depending on the desired counterion of the cage complex) were stirred at room temperature at a ratio of Pd: Ligand of 1: 2, which results in the clean and quantitative self-assembly of Pd_2L_4 metallacages (figure 6). The choice of nitrate as a counterion was used to see if the counterion played a significant role in the uptake of the metallacage as it is known to improve aqueous solubility, as well as behave differently to BF_4 in terms of location within the metallacage complex. The metallacages formed quantitatively in

under an hour and could be isolated cleanly by precipitation using acetone and diethylether. The metallacages (**C1.BF$_4$**, **C1.NO$_3$** and **C2.BF$_4$**) were characterised using NMR (^{1}H, ^{13}C, ^{11}B, ^{19}F, ^{1}H DOSY) and HR-ESI-MS to show that the metallacage complex had formed.

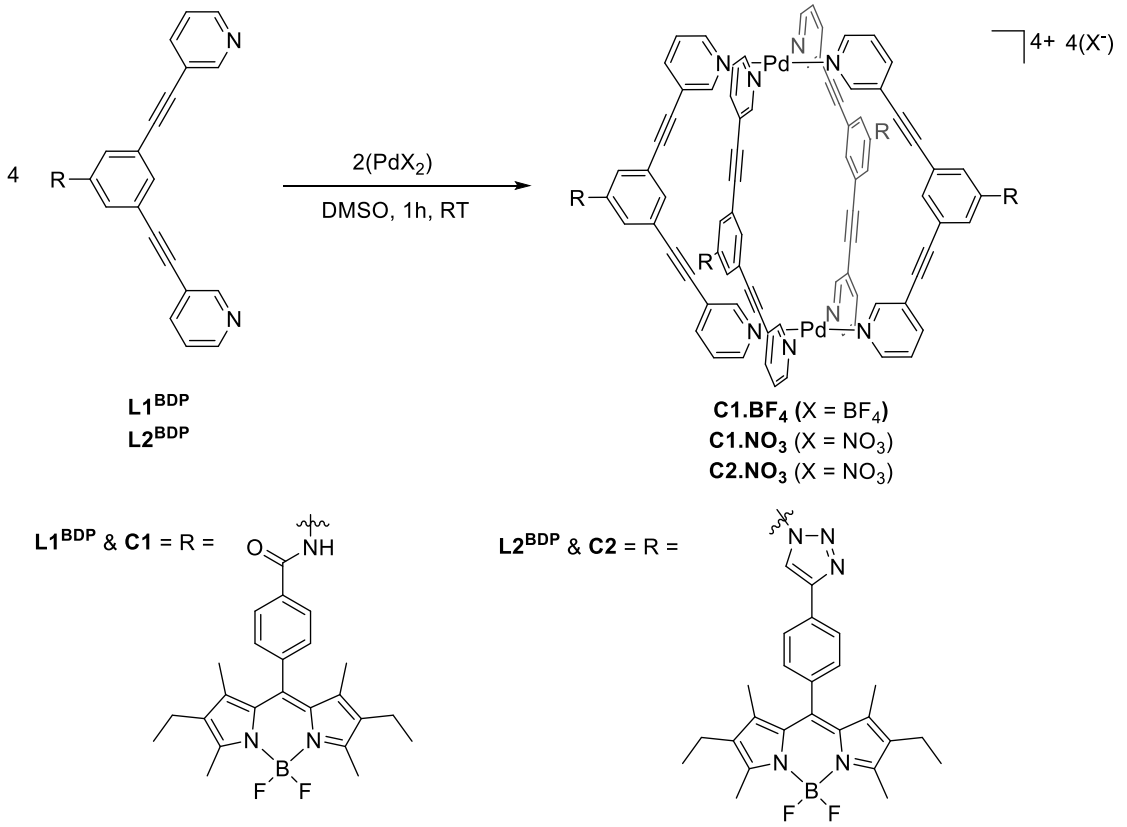

Figure 6. Self-assembly of the BODIPY exo-functionalised metallacages **C1.BF$_4$**, **C1.NO$_3$**, **C2.NO$_3$**.

7.2.2 Photophysical studies of BODIPY functionalised fluorescent Pd_2L_4 metallacages

In order to assess the suitability of the metallacages for use as *in vitro* imaging agents, the photophysical properties of the cages were studied. The UV-Vis absorption and emission spectra were recorded in degassed DMSO. The absorption spectra of **BDP^{COOH}** and **BDP^{Alkynyl}** both show a strong absorption peaks at λ_{ab} = 525 nm, consistent with 0 – 0 transition band, and both show a slight but visible "shoulder" on the high energy side of the absorption band (λ_{ab} = 495), corresponding to the 0 – 1 vibrational band (figure 7). Another small absorption band is observed for various S_0 - S_n transitions which can be associated with the phenyl "spacer" moiety and other transitions within the conjugated BODIPY scaffold. The emission profiles of **BDP^{COOH}** and **BDP^{alkynyl}** were taken by exciting the 0 – 0 band (λ_{ex} = 525 nm). As expected, both **BDP^{COOH}** and **BDP^{alkynyl}** showed strong emission profiles with a small stokes shift compared to their λ_{ab} (λ_{em} = 544 nm and 545 nm, respectively).

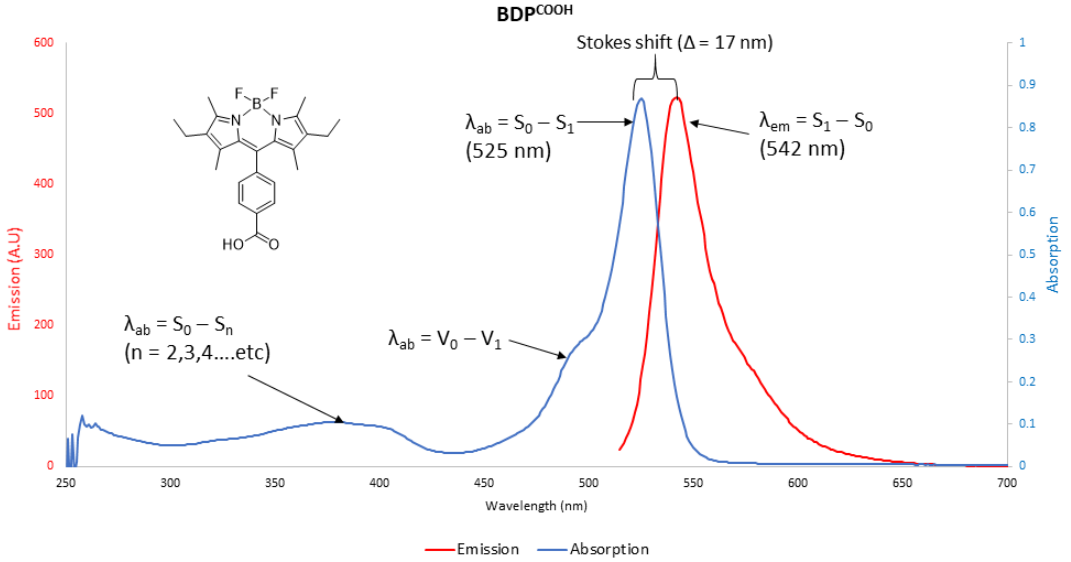

Figure 7: Representative annotated absorption (blue) and emission (red) spectra. (**BDP^{COOH}**). The absorption and emission bands are annotated to indicate their origin.

The absorption spectra for the ligands **L1^{BDP}** and **L2^{BDP}** were recorded in degassed DMSO, and both showed the same 0 – 0 excitation band as the BODIPY precursors, λ_{ab} = 525 nm, with the higher energy "shoulder" of the $S_0 - S_1$ vibrational band (figure 8). The absorption band corresponding to various $S_0 - S_n$ excitation (< 300 nm) was much stronger for **L1^{BDP}** and **L2^{BDP}** compared to their respective precursors (figure 8). The emission spectra were recorded by exciting the 0 – 0 band of the ligands (λ_{ex} = 525 nm) in degassed DMSO. The ligands **L1^{BDP}** and **L2^{BDP}** showed very similar Stokes shift as their BODIPY precursors, with λ_{em} = 544 nm and 543 nm respectively.

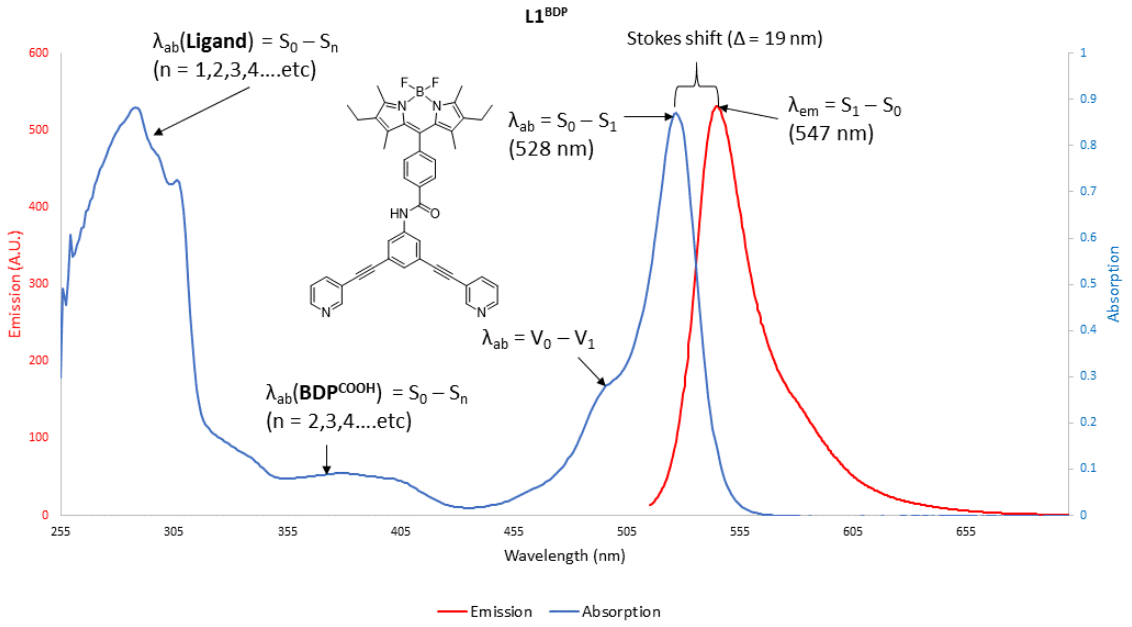

Figure 8: Representative annotated absorption (blue) and emission (red) spectra (**L1^{BDP}**). The absorption and emission bands are annotated to indicate their origin

Finally, the absorption and emission spectra of all the Pd_2L_4 metallacages (**C1.NO$_3$**, **C1.BF$_4$** and **C2.NO$_3$**) were recorded in degassed DMSO. The absorption band corresponding to the 0 – 0 excitation was prominent, however the large absorption peak corresponding to the various $S_0 – S_n$ excitations was stronger, which is to be expected due to the highly conjugated and delocalised system of the Pd_2L_4 metallacage scaffold (figure 9). The emission spectra were recorded by exciting the 0 – 0 band and again the metallacages exhibited the same λ_{em} as their precursor ligand and BODIPY fluorophore (**C1.NO$_3$** and **C1.BF$_4$** = 544 nm; **C2.NO$_3$** = 543 nm). In order to calculate the luminescence quantum yield (ϕ), a comparative method was used for the BODIPY fluorophores (**BDP^{COOH}** and **BDP^{alkynyl}**), conjugated ligands (**L1^{BDP}** and **L2^{BDP}**) and subsequent Pd_2L_4 metallacages (**C1.BF$_4$, C1.NO$_3$** and **C2.NO$_3$**), using Rhodamine 6G in ethanol as the known standard (ϕ = 94%, λ_{em} = 530 nm). The following equation was used:

$$\phi_x = \phi_{st} \cdot \frac{A_x}{A_{st}} \cdot \left(\frac{\eta_x}{\eta_{st}}\right)^2 \cdot \frac{Abs_{st}}{Abs_x}$$

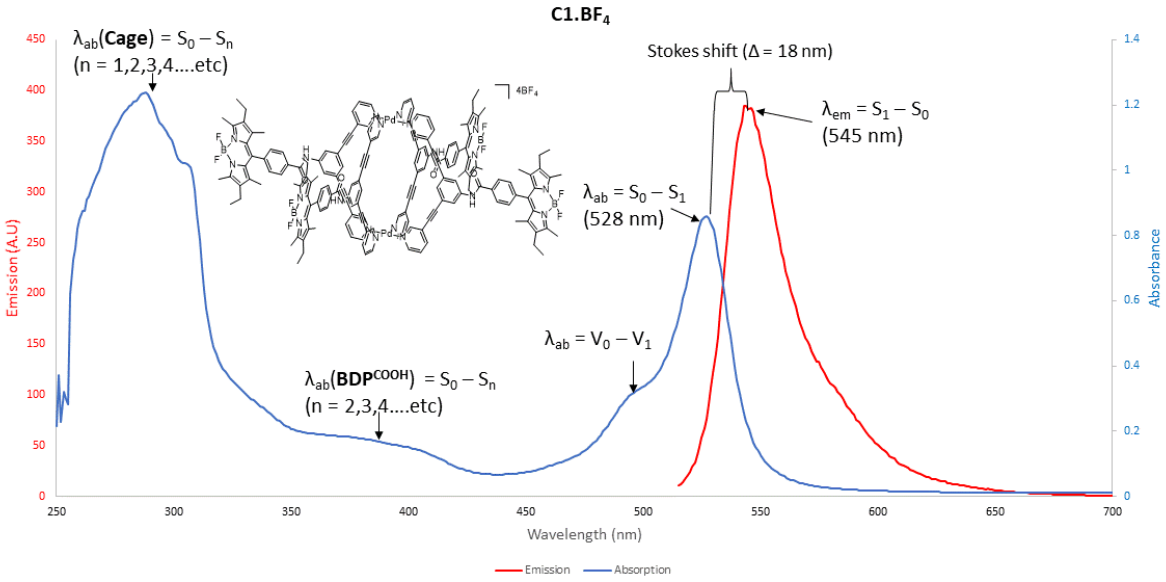

Figure 9: Annotated absorption (blue) and emission (red) spectra of the fluorescent ligand **C1.BF$_4$**. The absorption and emission bands are annotated to indicate their origin

ϕ_x = quantum yield of sample, ϕ_x = quantum yield of standard, A_x = integrated area of sample emission peak, A_{st} = integrated area of standard emission peak, η_x = refractive index of sample solvent; η_{st} = refractive index of standard solvent, Abs_{st} is the absorption intensity of the standard and Abs_x is the absorption intensity of the sample. As the quantum yield of the standard, and the refractive index of the solvents are known, the absorption intensity of the sample and the integrated area of the emission peak are the unknown variables that can be

gained easily experimentally. The concentration of both the sample and the standard was adjusted so that the absorption band corresponding to HOMO – LUMO excitation was < 0.8 A.U in order to avoid interference by re-absorption of the fluorescence. The sample and standard absorption spectra were overlaid and the wavelength of the crossing point of the two bands was recorded. This wavelength would be used as λ_{ex} for both the standard and the sample when recording the emission spectra in order to excite both fluorophores equally. The emission spectra of the standard and the sample were recorded, in each case keeping all experimental conditions the same for both (i.e. emission and excitation slit width). The emission peak could be integrated to provide the final variables, A_x and A_{st}. The experimental and known values could be inserted into equation 1 to give the quantum yield of **BDP^{COOH}**, **BDP^{alkynyl}**, **L1^{BDP}**, **L2^{BDP}**, **C1.NO$_3$**, **C1.BF$_4$** and **C2.NO$_3$**. The photophysical data for these compounds is summarised in table 1.

Table 1. Photophysical properties of the BODIPY exo-functionalised metallacages (**C1.NO$_3$**, **C1.BF$_4$**, and **C2.NO$_3$**), the constituent ligands (**L1^{BDP}** and **L2^{BDP}**) and the precursor BODIPY functional groups (**BDP^{COOH}** and **BDP^{alkynyl}**).

Compound	$\lambda_{max\ (abs)}$ [nm]	ε_{max} [L mol^{-1} cm^{-1}]	$\lambda_{max\ (ems)}$ [nm]	ϕ [%]
BDP^{COOH}	525	53,333	544	72
BDP^{alkynyl}	525	72,727	543	75
L1^{BDP}	290, 525	66,666	544	76
L2^{BDP}	290, 525	50,000	543	74
C1.NO$_3$	291, 527	42,105	544	50
C1.BF$_4$	291, 525	111,111	544	64
C2	291,525	160,000	543	70

7.2.3 Stability of BODIPY *exo*-functionalised Pd_2L_4 metallacages in aqueous and buffered solutions

After the photophysical properties of the BODIPY functionalised Pd_2L_4 metallacages (**C1.NO$_3$**, **C1.BF$_4$** and **C2.NO$_3$**) and precursors had been assessed and were suitable for *in vitro* applications, the stability of the metallacages in both aqueous and phosphate buffered saline solution (pH 7.4) was studied. The stability was assessed over 24 h by recording a UV-Vis spectrum of the solution every 15 minutes for the first hour, and then every hour after that for the next 23 hours. The resulting spectra were overlaid and compared. In each case; after 24 h, the solution was shaken, and a new spectrum was taken to confirm if the possible loss of intensity was due to precipitation. The obtained results are shown in Figures 10 – 15.

The spectrum of **BDP^{alkynyl}** shows two main absorption bands at ca. 325-410 nm and 555 nm (Figure 10), attributable to the numerous $S_0 – S_n$ ($n \geq 2$) and $S_0 – S_1$ excitations, respectively. The spectrum suffered from loss of signal intensity, as well as a bathochromic shift over time in

both PBS solution (pH 7.4) and in deionised water. In PBS solution the intensity started to decrease within the first 15 min, while in deionised water the fluorophore appeared stable for the first hour before the absorption intensity began to fall. The bathochromic shift occurred in both solutions, although it was more pronounced in deionised water than in PBS solution. Shaking each solution after 24 hours did not restore the signal intensity in either case, which suggests that the fluorophore has not only precipitated from the solution in both cases but may have undergone structural modification over the 24 hours which has resulted in a loss of absorption (figure 10).

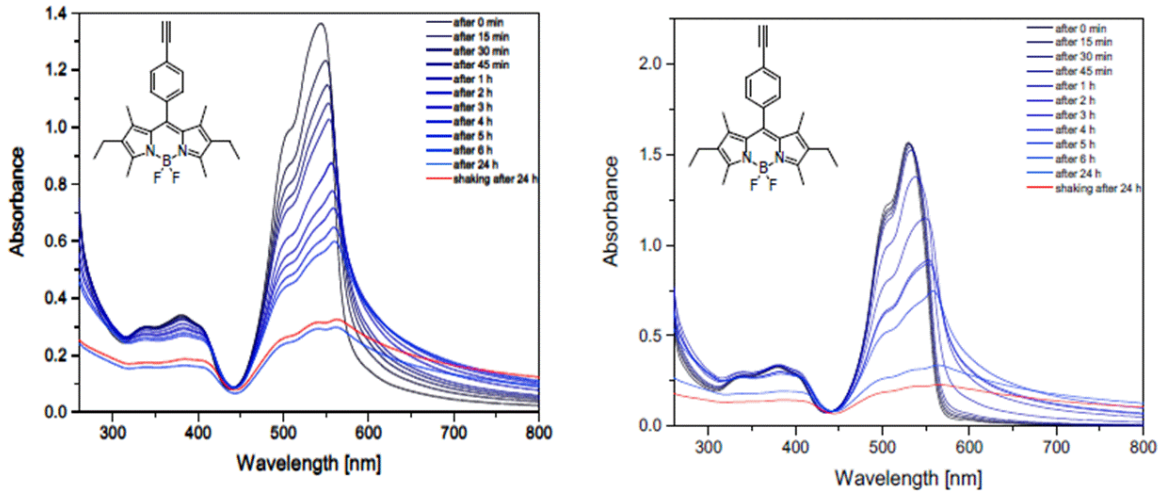

Figure 10. Stability of **BDP^{alkynyl}** over 24 hours. Left: 1 x PBS solution (pH 7.4) [60 x 10^{-6} M] . Right: Deionised water [60 x 10^{-6} M]

Concerning **BDP^{COOH},** this fluorophore was shown to be stable for 24 hours in PBS solution (pH 7.4), with no loss in signal intensity over this time, and no shift in the absorption band position (figure 11). In deionised water the fluorophore was shown to be reasonably stable over the first 2 hours. However, severe loss in signal intensity of the main absorption band was observed over time (λ_{abs} = 545 nm reduced to almost half over the 24 hours, figure 11). After shaking the solution the signal was restored to 75% of the original absorption peak (figure 11). This may suggest that the fluorophore has undergone structural modification which has decreased its solubility over time. However, as no shift in peak position is observed it is far more likely that the aggregates of **BDP^{COOH}** formed during precipitation are not fully dispersed and re-dissolved upon shaking the cuvette, and so the concentration of **BDP^{COOH}** in solution remains less than the original concentration, resulting in a still quenched signal intensity but no shift in absorption band position (figure 11).

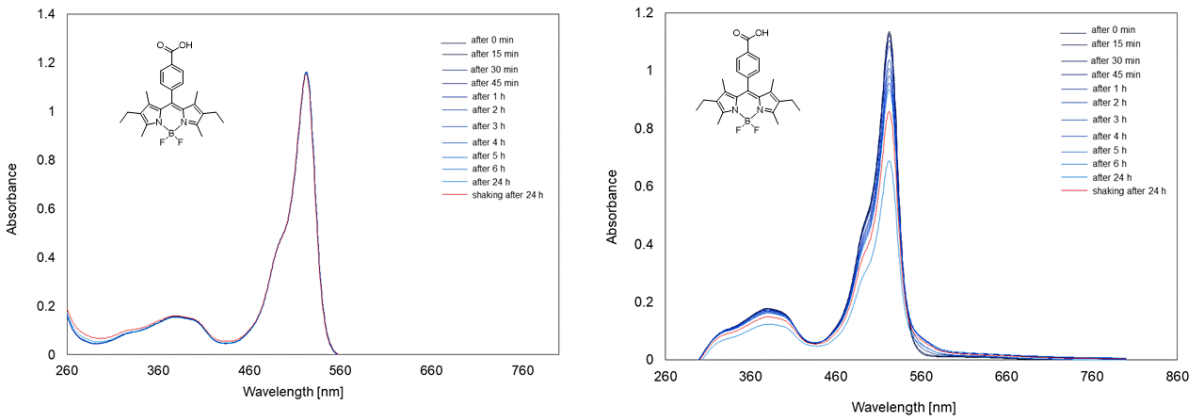

Figure 11. Stability of **BDP^{COOH}** over 24 hours. Left: 1 x PBS solution (pH 7.4) [20 x 10^{-7} M] . Right: Deionised water [20 x 10^{-7}]

The fluorescent ligand, **L1^{BDP}**, showed similar absorption bands as the BODIPY conjugate, as well as a main band at 283 nm due to the $S_0 - S_n$ transitions attributed to the highly conjugated ligand scaffold (figure 12). The compound exhibited opposite trend of stability with respect to its BODIPY precursor, **BDP^{COOH}**. In fact, the stability of **L1^{BDP}** in deionised water was excellent, with no change in absorption bands position or signal intensity over the 24 hours. However, in PBS solution (pH 7.4) the ligand was relatively stable over the first 5 hours (7% decrease in λ_{ab} = 545 nm signal intensity and no shifting of the peak position). However, the signal intensity was reduced to 12% of the original absorption peak after 24 hours, and could only be restored to 32% after vigorous shaking of the solution, which would suggest that after precipitation has started to occur the aggregates of **L1** are quite stable in deionised water and will not be re-dispersed and dissolved (figure 12).

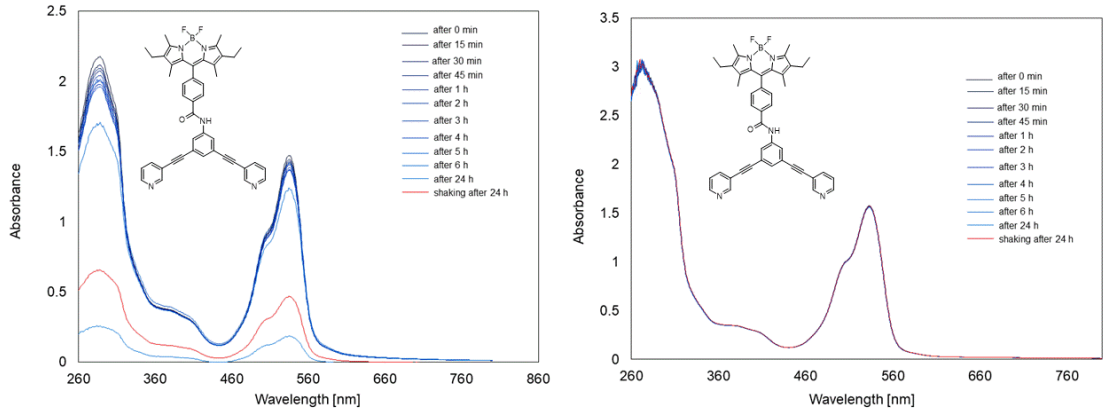

Figure 12. Stability of **L1^{BDP}** over 24 hours. Left: 1X PBS solution (pH 7.4) [5 x10^{-6} M]. Right: Deionised water [5 x10^{-6} M].

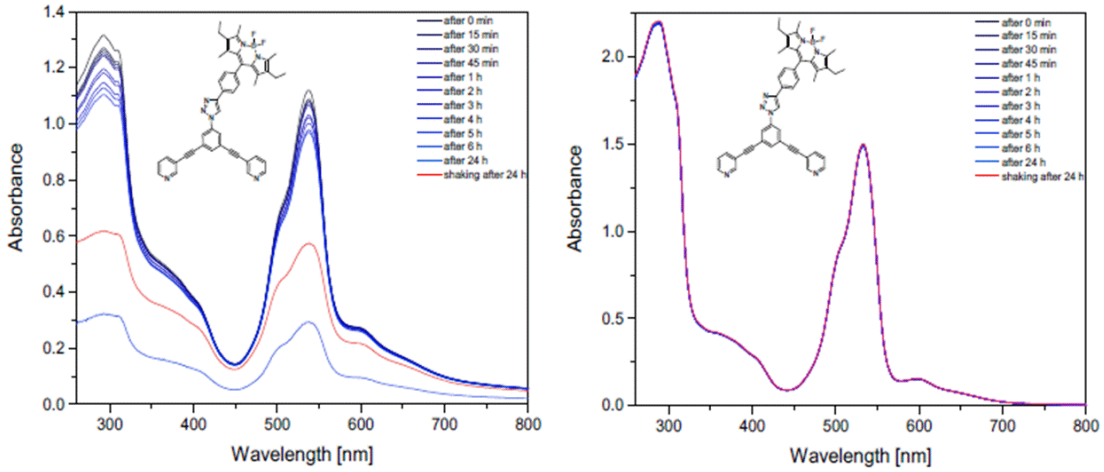

Figure 13. Stability of **L2**^{BDP} over 24 hours. Left: 1 X PBS solution (pH 7.4) [53 x 10^{-6} M]. Right: deionised water [53 x 10^{-6} M].

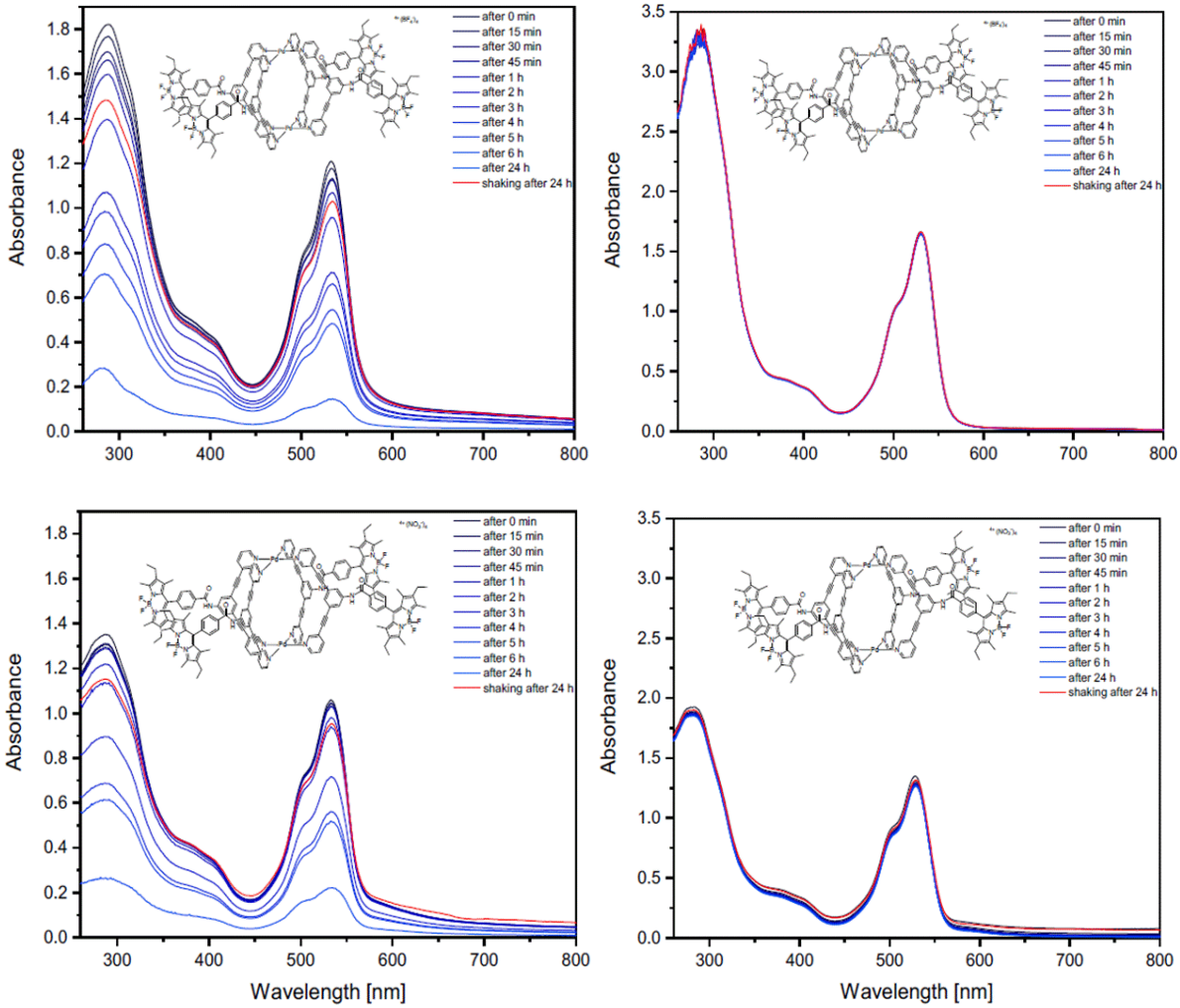

Figure 14. Stability of metallacage **C1.BF$_4$** (top row) and **C1.NO$_3$** (bottom row). All spectra recorded at a concentration of [55 x 10^{-6} M] over 24 hours. Left column: 1 x PBS solution (pH 7.4). Right column: Deionised water.

The CuAAC "click" conjugated fluorescent ligand, **L2**, was shown to be stable in PBS solution (pH 7.4) but not in deionised water (figure 13), showing a similar trend to **L1**. In both solutions, no changes in the main λ_{ab} band (545 nm) was observed, but in PBS solution the spectrum of **L2** decreases in intensity already after 2 hours, and at 24 hours only 26% of the original signal intensity at 545 nm was observed. After shaking the solution, the intensity was only restored to 51% of the original intensity, again suggesting that the aggregates of **L2** formed during precipitation are not readily dispersed in PBS solution. When the stability profiles of **L2** and its BODIPY precursor, **BDP^{alkynyl}**, are compared it is obvious that **BDP^{alkynyl}** has undergone a structural change to cause the peaks to shift so much. This may be indicative that it is the ethynyl functional group of **BDP^{alkynyl}** that is altered in aqueous and buffered solutions, and that forming the triazole linker group between **L^{N3}** and **BDP^{alkynyl}** acts to protect this group (figure 13).

The metallacages **C1.BF$_4$**, **C1.NO$_3$** and **C2.NO$_3$** were studied for their stability in PBS solution (pH 7.4) and in deionised water. As can be seen from figure 14 and figure 15, all three metallacages were stable in deionised water over 24 hours. In PBS solution, the stability of all three metallacages was reduced. Both **C1.BF$_4$** and **C1.NO$_3$** were shown to precipitate in PBS solution over 24 hours, with the signal intensity over this time reduced to 13% and 18%, respectively (figure 14). However, upon shaking the signal intensity of both **C1.BF$_4$** and **C1.NO$_3$** was restored to 86%. Furthermore, the metallacages **C1.BF$_4$** and **C1.NO$_3$** were shown to exhibit reasonable stability over the first 2 hours. It was therefore proposed that both Pd_2L_4 metallacages **C1.BF$_4$** and **C1.NO$_3$** could be studied *in vitro* to assess their intracellular distribution.

As shown in figure 15, metallacage **C2.NO$_3$** was not stable in PBS solution (pH 7.4). In fact, the absorption spectrum undergoes a small bathochromic shift of the peak λ_{ab} = 524 nm, which again may indicate some structural modification to the metallacage. The signal intensity is not severely quenched during the first 2 hours; however, the intensity falls to 31% over 24 hours and after vigorous shaking the solution, the original spectral intensity could not be reached again (only

54% intensity restored). As such, **C2.NO$_3$** was not selected to be studied *in vitro*, despite exhibiting promising luminescence properties.

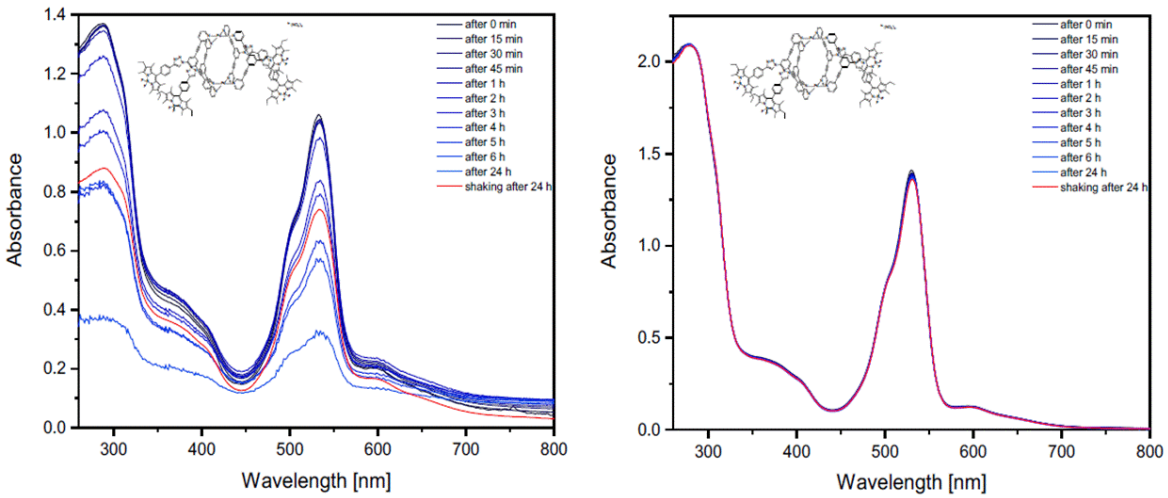

Figure 15. Stability of **C2.NO$_3$** over 24 hours. Right: 1 x PBS solution (pH 7.4) [86 x 10^6 M]. Right: Deionised water [86 x 10^6 M].

7.2.4 Encapsulation of cisplatin in BODIPY *exo*-functionalised Pd_2L_4 metallacages

Note that a full discussion on the encapsulation of cisplatin within Pd_2L_4 metallacages is presented in chapter 9.

Before studying the intracellular distribution of the metallacages *in vitro*, NMR experiments (^{1}H and ^{195}Pt) were carried out to ensure that the large, rigid BODIPY *exo*- group did not interfere with the encapsulation of cisplatin. Due to solubility issues, NMR experiments could not be carried out in D_2O. DMF-d_7 was used as a polar, deuterated solvent that could dissolve **C1.NO$_3$** and **C1.BF$_4$**, as DMSO is known to form complexes with cisplatin and thus is not suitable for encapsulation studies.[237] ^{1}H NMR studies have been reported previously to provide qualitative evidence of cisplatin encapsulation.[99,127,148]

The ^{1}H NMR spectrum of metallacages **C1.BF$_4$** and **C1.NO$_3$** were recorded in DMF-d_7. Cisplatin (2 equiv.) was added to the deuterated solution and a second ^{1}H NMR spectrum was recorded. The spectra were calibrated to the DMF carbonyl signal (δ = 8.03 ppm) and compared to see if any peaks had moved.

C1.NO$_3$ stacked ^{1}H NMR spectra show that the cavity-facing proton peaks both undergo slight upfield shifts upon introduction of 2 equiv. of cisplatin (H_a = -0.02 ppm; H_e = -0.02 ppm, figure 16). Furthermore, H_e becomes broader upon addition of cisplatin. The *exo*-facing proton, α- to the coordinating nitrogen shows a slight downfield shift (H_b = +0.07 ppm, figure 16). These results, as previously discussed, are consistent with the report that NO_3^- is encapsulated within the cavity of Pd_2L_4 metallacages in polar organic solvents,[238] and that upon introduction of cisplatin, the counterion is evacuated from the cavity and replaced with the metallodrug. In this way, the originally encapsulated anionic counterion acts to "mask" the downfield shift in peak position of the cavity facing protons in the spectra of [(cisplatin)$_2$⊂C1.NO$_3$] as it causes a more significant downfield shift than neutral cisplatin. As such, the small shifts in peak positions may be indicative of cisplatin encapsulation.

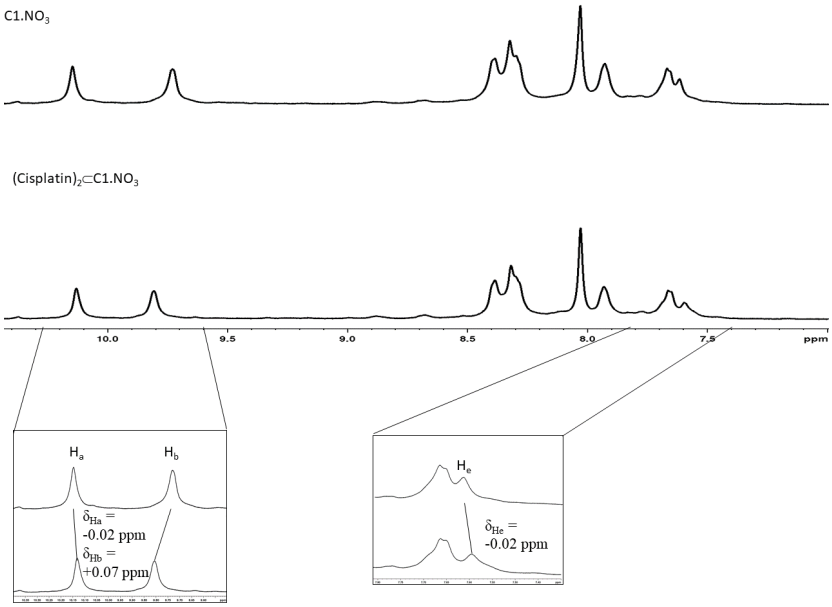

Figure 16. Zoomed aromatic region of stacked ^{1}H NMR spectra in DMF-d$_7$. Top: **C1.NO$_3$** alone. Bottom: **C1.NO$_3$** and 2 equivalents of cisplatin in DMF-d$_7$, with zoom boxes highlighting the peak shifts of the cavity facing protons H_a and H_e, as well as the exo-facing proton H_b.

C1.BF$_4$ shows a small downfield shift and signal broadening of the cavity facing proton peak of the central phenyl ring of the ligand (δH_e = +0.08 ppm, figure 17). Furthermore, the proton peaks corresponding to the protons α- to the coordinating nitrogen both undergo small downfield shifts (δH_a = +0.03 ppm; δH_b = +0.04 ppm). The remaining peaks show no broadening or peak movement upon the introduction of 2 equivalents of cisplatin. This result supports that cisplatin has occupied the cavity of the metallacage.

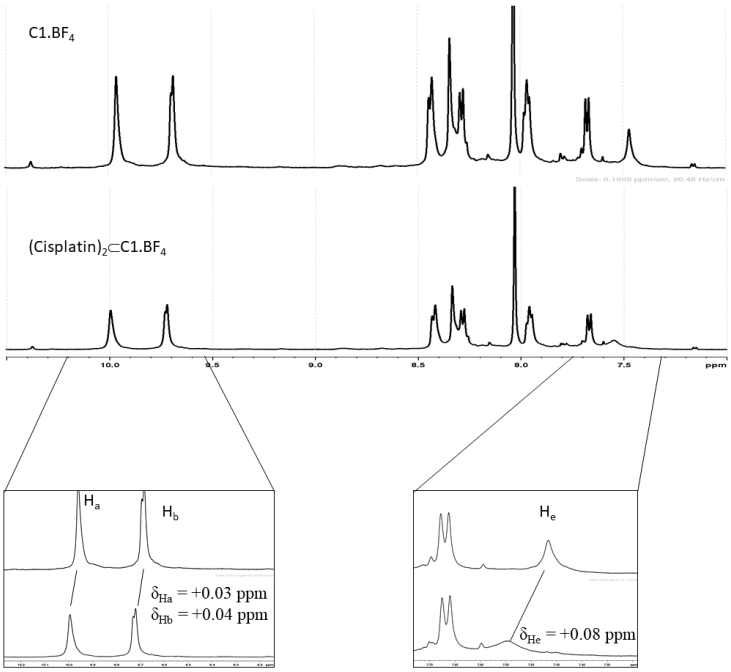

Figure 17. Zoomed aromatic region of stacked ^{1}H NMR spectra in DMF-d$_7$. Top: **C1.BF$_4$** alone. Bottom: **C1.BF$_4$** and 2 equivalents of cisplatin in DMF-d$_7$, with zoom boxes highlighting the peak shifts of the cavity facing protons H_a and H_e, as well as the exo-facing proton H_b.

^{195}Pt NMR was used to see if a complementary shift of the platinum(II) signal from the guest molecule cisplatin could be observed upon introduction of the metallacage. Unfortunately, **C1.NO$_3$** exhibited poor solubility in DMF-*d$_7$* compared to **C1.BF$_4$**. The solubility of the metallacage was sufficient to study the encapsulation by ^{1}H NMR (broad signals in figure 12 where caused by the Tyndall effect as a fine suspension formed at the required concentration), ^{195}Pt NMR was not suitable. As such, **C1.BF$_4$** was used to study the encapsulation of cisplatin *via* ^{195}Pt NMR. Cisplatin was dissolved in DMF-*d$_7$* and a ^{195}Pt NMR spectrum was recorded (figure 18). 1 equivalent of metallacage **C1.BF$_4$** was added to the DMF-*d$_7$* solution before a second ^{195}Pt NMR spectrum was recorded. Finally, a second equivalent of cisplatin was added to the DMF-*d$_7$* solution and a third spectrum was recorded. The spectra were compared to observe any shift in peak position (figure 18). As can be seen, the free cisplatin signal (δ = -2080 ppm) is shifted upfield upon addition of 1 equivalent of **C1.BF$_4$** (Δδ = -2 ppm). Upon addition of a second equivalent of cisplatin, the peak remains upfield. The upfield shift may indicate a greater degree of shielding of the Pt(II) signal upon encapsulation of cisplatin.

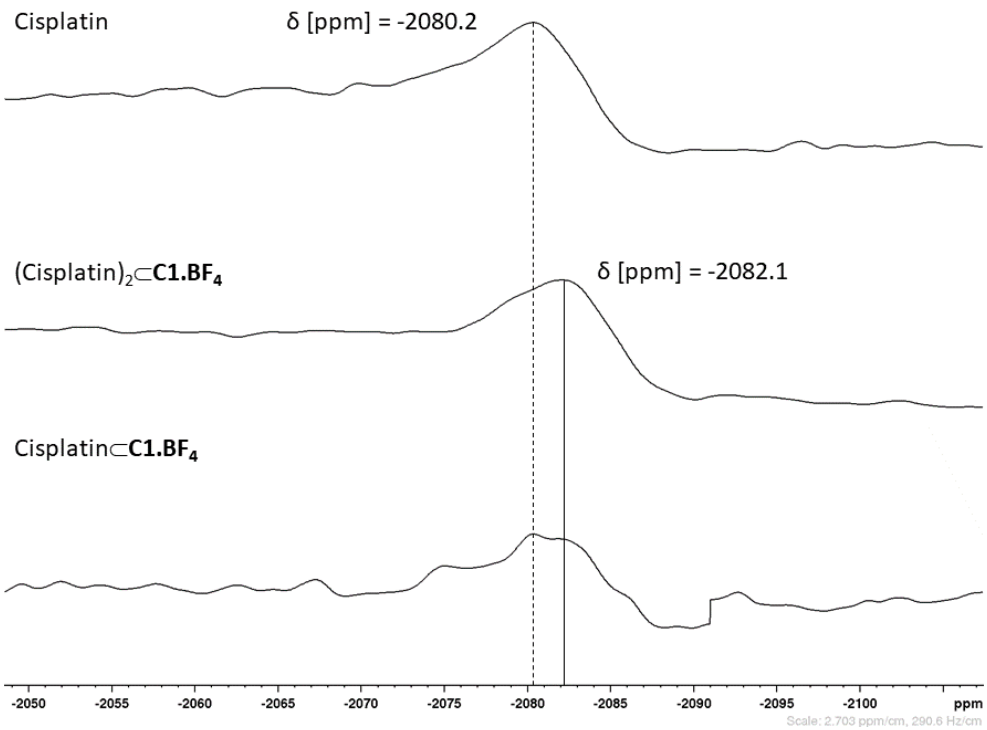

Figure 18. Stacked ^{195}Pt NMR spectra showing: Top: Cisplatin alone. Middle: 2 equiv. of cisplatin in the presence of 1 equiv. of **C1.BF$_4$**. Bottom: 1 equiv. of cisplatin in the presence of 1 equiv. of **C1.BF$_4$**.

As the counterion did not appear to affect the stability of the metallacage, and the solubility in deuterated organic solvents had not allowed both ^{1}H and ^{195}Pt NMR to study the uptake of cisplatin within **C1.NO$_3$**, only **C1.BF$_4$** was studied *in vitro*.

7.2.5 *In vitro* cellular distribution of BODIPY *exo*-functionalised metallacages

The metallacage **C1.BF$_4$** was studied first via fixed cell fluorescence microscopy against A375 human melanoma cells by another PhD student in our group, Ms. Brech Aikman. The constituent BODIPY functionalised ligand, **L1**, were also studied alongside the two metallacages, in order to determine if their sub-cellular behaviour is different, thus allowing discrimination between the ligand and metallacage. After incubation with the cells for 2 hours, the melanoma cells were fixed with formaldehyde and studied via fluorescent microscopy. The cell nuclei were stained using DAPI, a fluorophore which selectively accumulates within the cell nucleus. The images showed that indeed both the metallacage and the ligand were taken up within A375 melanoma cells. The DAPI stained nuclei highlighted that neither the metallacages nor the ligand accumulated within the nucleus, but rather appeared to localise within the cytoplasm. Furthermore, the ligand and the cage appeared to accumulate within vesicles in the cytoplasm, as the microscopy images showed discreet, intense spots of luminescence as opposed to a diffuse background luminescence which may suggest that the fluorophore would be diffuse throughout the cell cytoplasm (figure 19).

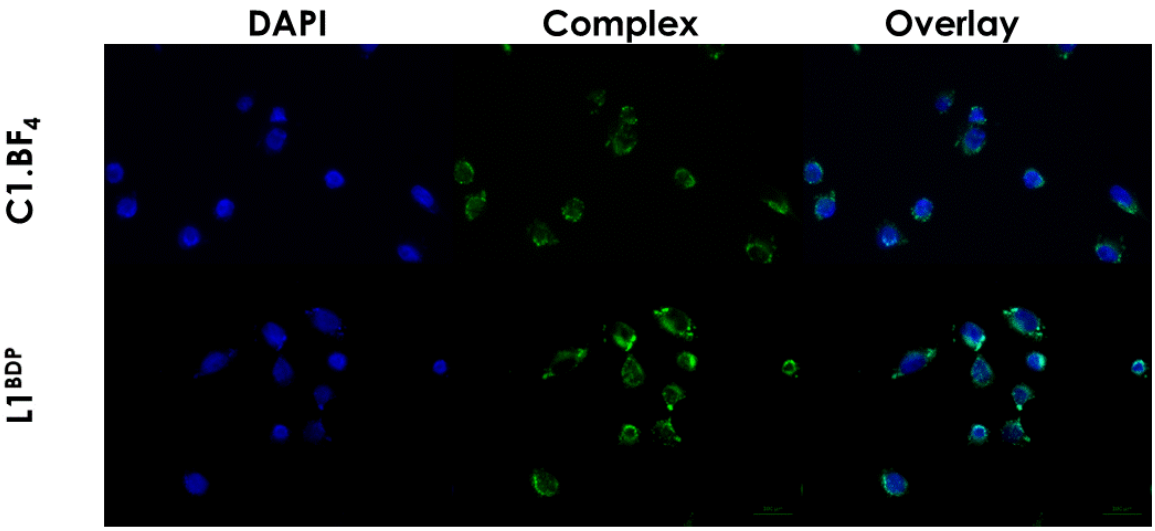

Figure 19. Fixed cell fluorescence microscopy images of **C1.BF$_4$** (top) [5 x 10^{-6} M] and **L1^{BDP}** (bottom) [5 x 10^{-6} M] incubated at 37°C for 1 hour with A375 human melanoma cells. DAPI was used to stain the cell nuclei (left column). Overlay of the images (right column).

Although the fixed cell images provided intriguing insight into the sub-cellular localisation of **C1.BF$_4$**, the bright intense spots of fluorescence could be attributed to aggregates of the metallacage and the ligand **L1**, based on both the stability studies performed in PBS solution as well as the reported phenomenon of aggregate induced emission.[239] To gain further insight into the localisation of **C1.BF$_4$** and **L1^{BDP}**, the mechanism of uptake was studied. There are numerous routes for cells to take up extracellular molecules, although the different routes can be broadly divided into two categories: passive uptake (i.e. diffusion through the lipid bilayer) or active uptake (i.e. receptor mediated endocytosis, membrane channels etc.). To discriminate between active or passive uptake, a temperature dependant *in vitro* assay was carried out, whereby **L1^{BDP}** and **C1.BF$_4$** were incubated with A375 melanoma cells at either 4°C or 37°C. At 4°C, the membrane bound receptor proteins and membrane channels will not function, and so if **C1.BF$_4$** and **L1^{BDP}** are taken up at this temperature it is strong evidence that they pass through the lipid bilayer *via* passive diffusion. However, if the fluorescent metallacage and ligand are only taken up into the cell at 37°C, then it is more probably taken up *via* an active transport mechanism. The fluorescent images were taken, and the cell nuclei were stained with DAPI to highlight the subcellular distribution. As can be seen in figure 20, no fluorescence which can be attributed to **C1.BF$_4$** or **L1^{BDP}** can be seen when the cells are incubated at 4°C. At 37°C, fluorescence attributed to **L1^{BDP}** and **C1.BF$_4$** can be seen clearly and appear again to be localised within vesicles. This is strong evidence that the mechanism of cellular uptake is *via* an active transport mechanism as opposed to passive diffusion.

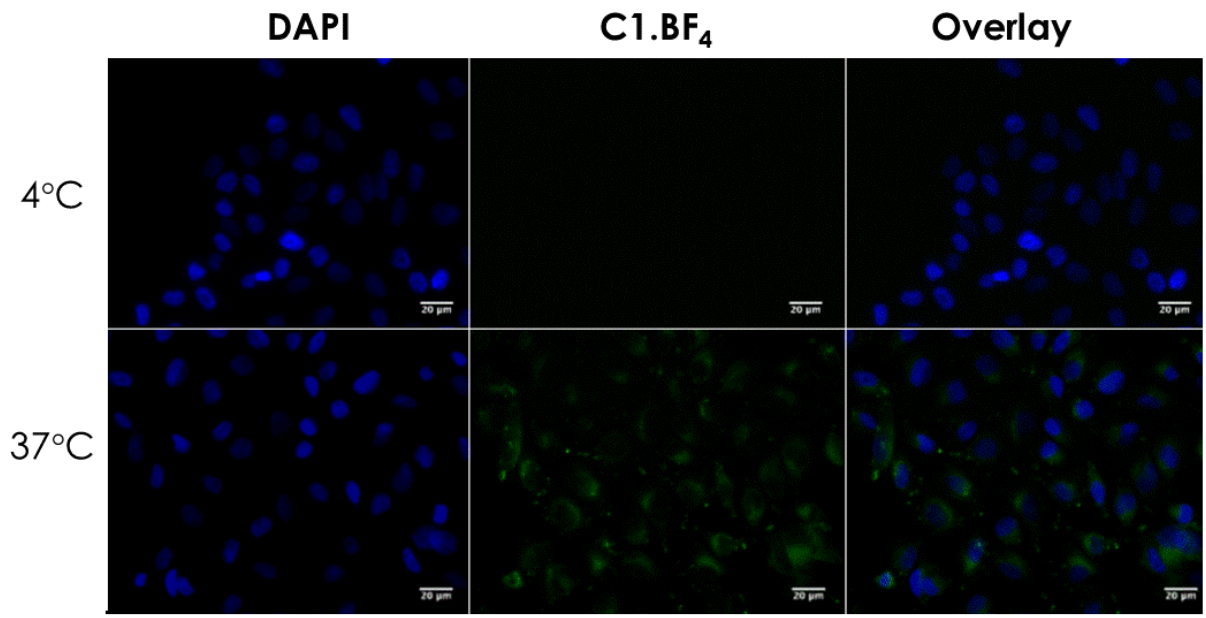

Figure 20. Temperature dependant fixed cell fluorescence microscopy images. Top: A375 human melanoma cells incubated at 4°C with **C1.BF$_4$** [5 x 10^{-6} M]. Bottom: A375 human melanoma cells incubated at 37°C with **C1.BF$_4$** [5 x 10^{-6} M].

Although the metallacage and ligand appear to localise within vesicles, the intense spots of fluorescence could be attributed to aggregates of the cage and ligand. In order to study the sub cellular distribution of the metallacage and ligand, confocal fluorescence microscopy can be used. Confocal microscopy can be employed to build a pseudo-3D image of the cell and fluorophore. In order to achieve this, the focal plane of the microscope can be adjusted in order to produce a series of 2D images capturing "slices" of the cell. These images can then be stacked to produce a Z-stack image which can give 3-dimensional information on the fluorophore within the cell. This 3D information is vital in order to show that the fluorophore is located within the cell, as opposed to aggregates forming outside the cell. Furthermore, proof that the fluorophores do not localise within the nucleus can be gained by the Z-stacked image.

As can be seen by figure 21, the Z-stack images of metallacage **C1.BF$_4$** and **L1^{BDP}** incubated with A375 cells show clearly that **C1.BF$_4$** and **L1^{BDP}** are localised within small vesicles in the cytoplasm, and do not just form aggregates around the lipid bilayer. Furthermore, neither **C1.BF$_4$** nor **L1^{BDP}** are localised within the nuclei. These results suggest that **C1.BF$_4$** is taken up via endocytosis. Endocytosis covers several uptake pathways, which can broadly be broken down into the following categories: receptor mediated endocytosis, pinocytosis, phagocytosis and caveolae. In order to try and discriminate between the possible uptake mechanisms, the lysosomes of A375 human melanoma cells were stained. The resulting images showed no

overlap of the fluorescence attributed to **C1.BF$_4$** or the stained lysosomes, which strongly suggests that the metallacage is not located within lysosomes during any stage of its uptake.

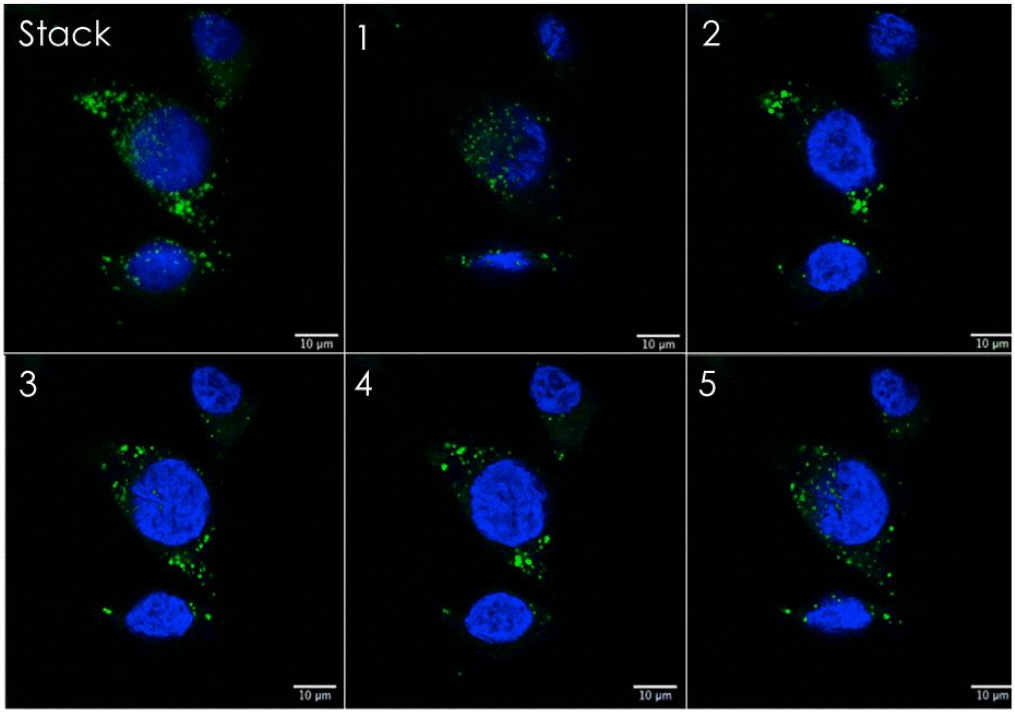

Figure 21. Confocal microscopy images of **C1.BF$_4$** [5 x 10^{-6} M] incubated with A375 human melanoma cells, with the compiled z-stack of images (top right).

Bright field images were recorded of the sample to try and get more information on the other intracellular features of the A375 melanoma cells to see if they correlated with the metallacage (figure 22). The bright field images highlight melanosomes within the cell as small black spots. Melanosomes are lysosome-related organelles found in mammalian skin melanocytes and are responsible for the storage, synthesis and transport of melanin pigments, which provide cells with photoprotection and tissues with colour.[240] As can be seen from figure 22, the metallacages appear to localise within melanosomes, as opposed to lysosomes, although the image does not provide conclusive data.

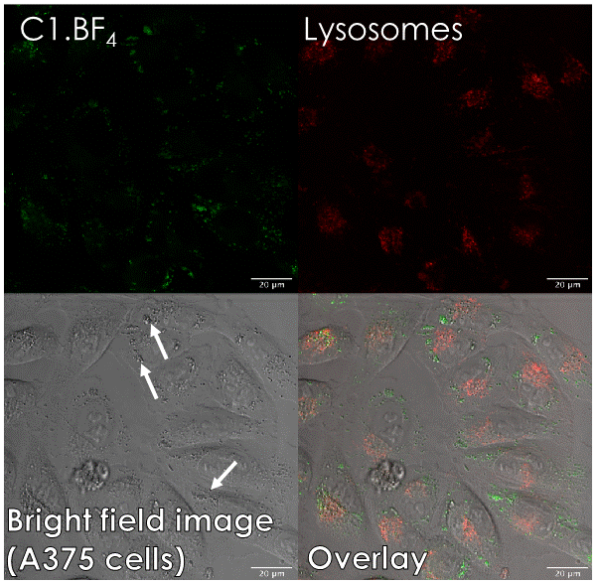

Figure 22. Fixed cell microscopy images of **C1.BF$_4$** [5 x 10^{-6} M]. Top: Fluorescence microscopy images showing the emission of **C1.BF$_4$** (left) and stained lysosomes (right). Bottom: Bright field images of A375 human melanoma cells with white arrows highlighting examples of melanosomes, which appear as dark spots (left), and an overlay of the emission of the lysosomes and **C1.BF$_4$** (right).

7.2.6 *In vitro* cytotoxicity of BODIPY *exo*-functionalised metallacages

After establishing that the metallacage **C1.BF$_4$** was taken up into A375 melanoma cells, it was necessary to establish the cytotoxicity towards these cells of the metallacage, as well as its constituent ligand to ensure that even if the metallacage breaks down, the drug delivery system is not antiproliferative by itself, and so any therapeutic effect from the host guest drug delivery complex will be attributed to the cisplatin guest.

Table 2. Antiproliferative activity of **L1^{BDP}**, **C1.BF$_4$**, cisplatin, and cisplatin encapsulated within **C1.BF$_4$** (cisplatin)$_2$⊂**C1.BF$_4$** against A375 human melanoma cells after 24 h incubation.

EC_{50} (μM)

Compound	EC_{50} [μM]
L1^{BDP}	> 50
C1.BF$_4$	> 50
Cisplatin	33.9 ± 2.9
(cisplatin)$_2$⊂**C1.BF$_4$**	29 ± 2

C1.BF$_4$, **L1^{BDP}**, (cisplatin)$_2$⊂**C1.BF$_4$**, and free cisplatin were incubated with A375 melanoma cells. As can be seen from table 2, the EC_{50} of the metallacage and constituent ligand did not display any antiproliferative activity at the concentration used (>50 μM). Free cisplatin

was scarcely cytotoxic with an EC_{50} value of 33.9 ± 2.9 μM. Cisplatin encapsulated within **C1.BF$_4$**, exhibits an EC_{50} value of 29 ± 2 μM.

7.2.7 Intracellular guest release of cisplatin from BODIPY functionalised metallacages

Various guest release mechanisms have been proposed for the release of cisplatin from M_2L_4 metallacages.[64] These include competitive guest substitution with other molecules present in solution (anions, neutral molecules) and breakdown of the metallacage via different mechanisms and subsequent guest release.[99] For example, Ahmedova and co-workers have described a ligand exchange mediated breakdown of Pd^{2+} and Pt^{2+} metallacages in the presence of excess of glutathione (GSH).[124] Glutathione is a naturally occurring anti-oxidant that is responsible for reducing oxidants intercellularly *via* its pendant thiol group. During the reductive process, glutathione forms a dimer, glutathione disulphide (GSSH), binding to itself via a disulphide bridge (figure 23).[241] The experiment from Ahmedova and coworkers was carried out in a solvent system of 1:3 D_2O: DMSO-d_6 and showed that complete breakdown and release of the guest molecule (pyrene or caffeine) from a metallacage was achieved in less than 1 hour in the presence of 10 equiv. GSH.

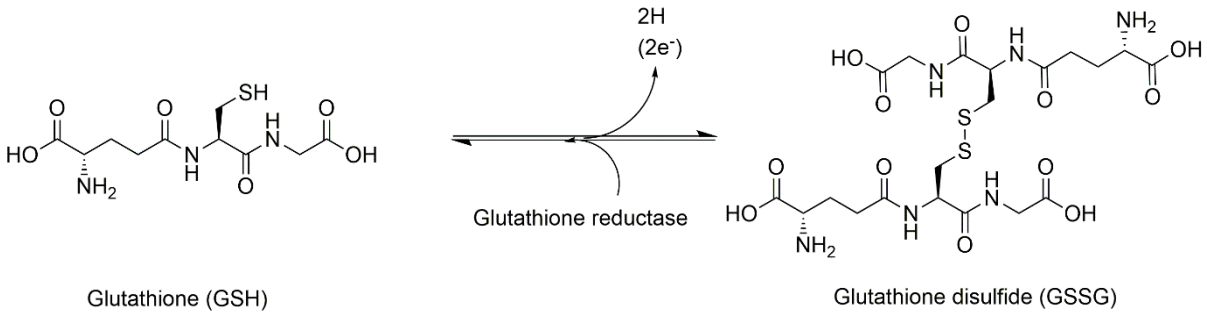

Figure 23. Scheme of the oxidation of glutathione (GSH) to the disulfide, glutathione disulfide (GSSG). In living cells, the reverse reduction of GSSG is achieved with the catalytic action of the enzyme, glutathione reductase.

It was hypothesised that breakdown of the BODIPY decorated Pd_2L_4 metallacages could be achieved in a similar way. As such, the experiment was first reproduced using the non BODIPY *exo*-functionalised metallacage, **C1^{NH2}.BF$_4$**, as well as **C1^{NH2}.NO$_3$**, to establish if the counterion would have an effect on the reduction of the metallacage. The ^{1}H NMR spectrum of the constituent ligand, **L^{NH2}**, was also recorded to help the analysis of the cage breakdown. It is worth mentioning that the solvent system used in the original paper (3: 1 DMSO-d_6: D_2O) could not be used for our cage due to poor solubility issues. Therefore, three solutions of **C1^{NH2}.NO$_3$**, **C1^{NH2}.BF$_4$** and **L1^{NH2}** in DMSO-d_6 were made, made up to a ratio of 9: 1 DMSO-d_6: D_2O. The ^{1}H NMR spectrum was recorded of the respective metallacage, before addition of 10 equiv. of GSH.

Afterwards, ^{1}H NMR spectra were recorded every 5 minutes for the first hour, followed by every hour for the next 17 hours. The spectra were stacked and compared in Figure 24.

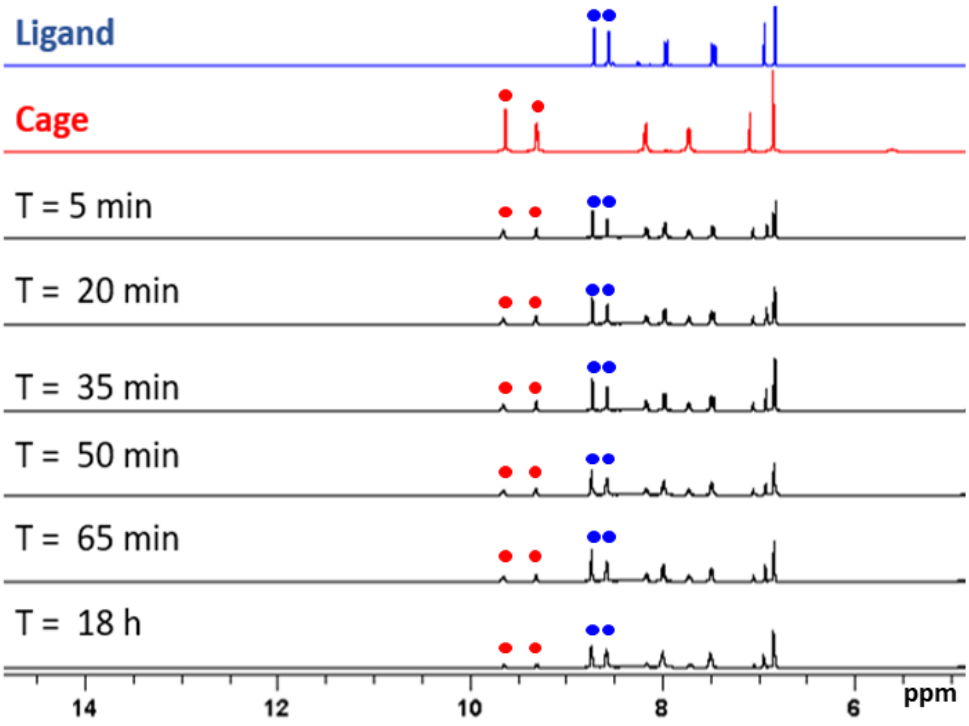

Figure 24. Stacked ^{1}H NMR spectra in DMSO-d_6 showing the clean breakdown of **C1^{NH2}.BF$_4$** (red spectra) to its constituent ligand **L^{NH2}** (blue spectra) over 18 hours after addition of GSH. The peaks that were monitored to calculate the ratio of **C1^{NH2}.BF$_4$**: **L^{NH2}** are highlighted by red and blue dots, respectively.

Following GSH addition, **C1^{NH2}.BF$_4$** was broken down to its constituent ligand within the first hour, by monitoring the disappearance of the proton peaks corresponding to H_a and H_b of metallacage **C1^{NH2}.BF$_4$** and the appearance of proton peaks H_a and H_b of the ligand, **L1^{NH2}**. As such, the integrals of the peaks from **C1^{NH2}.BF$_4$** and from **L^{NH2}** could be monitored in order to establish the ratio of cage: ligand in solution at each time point. This data could be plotted as % intact cage in solution v time, in order to visualise the breakdown of the cage (figure 25). As can be seen, after 1 hour an apparent equilibrium is achieved with approximately 10% of the metallacages still intact. During the first 5 minutes, a rapid breakdown of the metallacage occurs (100% - 29% cage intact in solution).

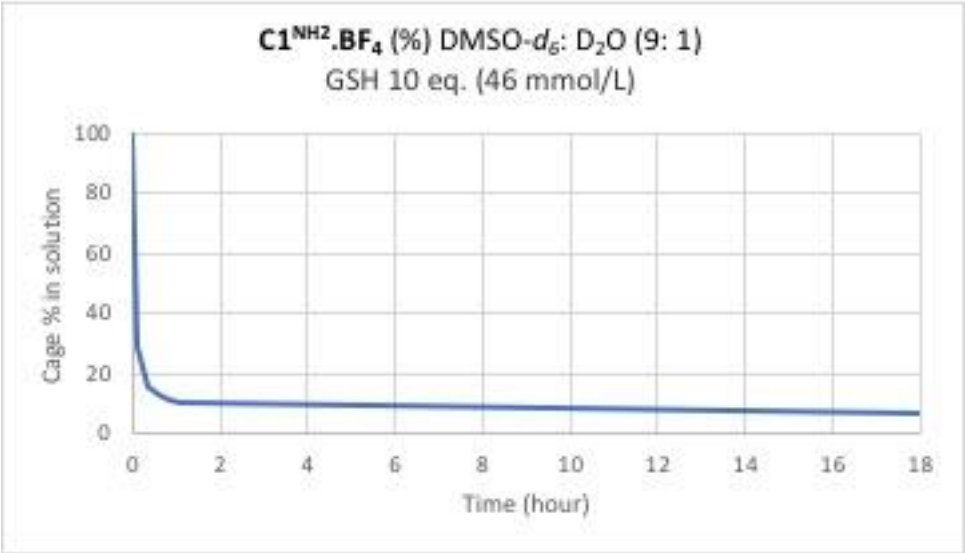

Figure 25. Plot of the amount of intact **C1^{NH2}.BF$_4$** cage present in solution over time in the presence of 10 equiv. (46 mmol/L) GSH. The peaks corresponding to the protons adjacent to the nitrogen of the terminal pyridyl groups were monitored (H_a and H_b, figure 24).

C1^{NH2}.NO$_3$ also was shown to break down into its constituent ligand, however the process was not as clean as for **C1^{NH2}.BF$_4$**. Namely, two new peaks (δ [ppm] = 8.52 (*t*, J = 5.63 Hz, 8H) and 8.25 (*d*, J = 8.31 Hz, 8H) appeared upon addition of 10 equiv. of GSH (Figure 26) indicative of the formation of new products in solution.

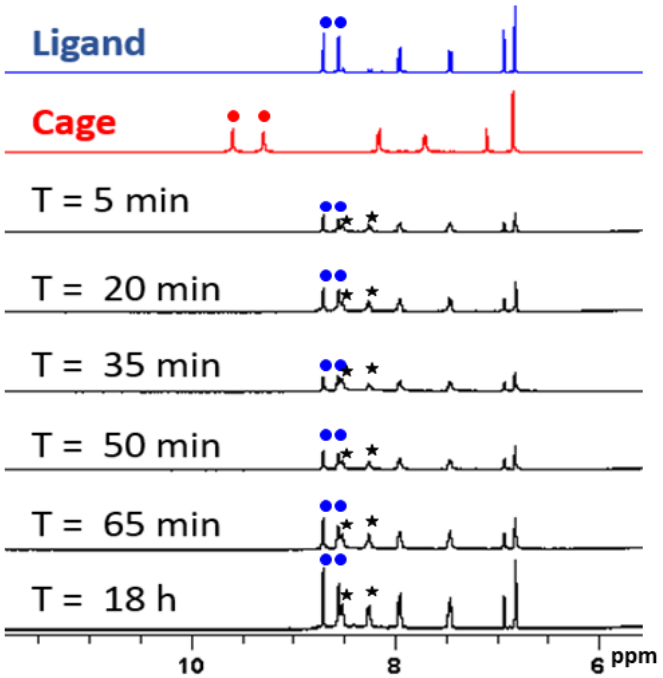

Figure 26. Stacked ^{1}H NMR spectra in DMSO-d$_6$ of **C1^{NH2}.NO$_3$** (red) in the presence of 10 equivalents of GSH. Although some peaks correspond to the constituent ligand (blue), 2 new peaks appear which suggest that the breakdown of **C1^{NH2}.NO$_3$** is not as clean as **C1^{NH2}.BF$_4$.** The peaks used to calculate the ratio of **C1^{NH2}.NO$_3$**: **L^{NH2}** are highlighted by red and blue dots, respectively. The two new peaks are identified by the black stars.

The two new peaks (figure 26) integrate to 8 protons with respect to H_a and H_b of the ligand, and the intensity does not alter over time. As such, it would appear that the breakdown of **C1^{NH2}.NO$_3$** occurs rapidly in the presence of GSH; however, further studies are necessary to investigate which type of product is formed.

In order to determine if this breakdown experiment was relevant to physiological conditions of GSH, the concentration of GSH used in the initial experiments described above was calculated to be 46 mmol/L. The concentration of GSH intracellularly is 1 – 2 mmol/L (although exceptions, such as hepatocytes, are known to have a concentration of around 10 mmol/L).[241] As the concentration of GSH was too high to be applicable to physiological conditions, a second experiment was planned using **C1.BF$_4$** in the presence of 2 mmol/L GSH in 9: 1 DMSO-d_6: D_2O. The spectrum of **C1.BF$_4$** in this solvent system was recorded, before GSH was added. Afterwards, ^{1}H NMR spectra were recorded every 5 minutes for the first hour, and then every half an hour for the next 3 hours. The integrals of the peaks identified as belonging to either **C1.BF$_4$** or **L1^{BDP}** were recorded and the ratio of cage: ligand was calculated. From this, the percentage of cage still intact in solution could be calculated and plotted as a function of time (figure 27).

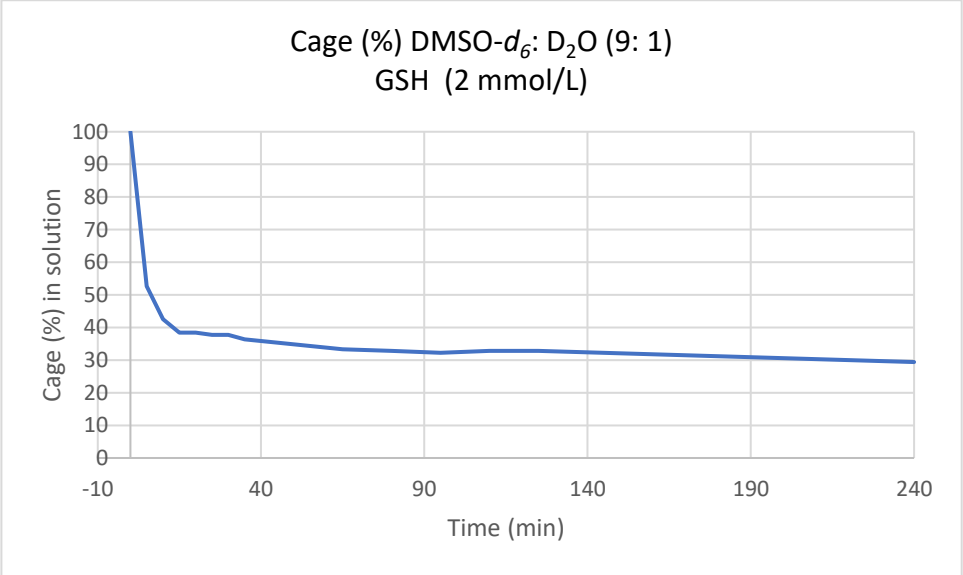

Figure 27. Plot of the amount of **C1.BF$_4$** in the solution over time in the presence of physiological concentration of GSH (2 mmol/L) (approx. 2.3: 1 ratio **C1.BF$_4$**: GSH). Comparison of the quenching of the proton signals corresponding to the protons adjacent to the coordinating nitrogen of **C1.BF$_4$** (H_a an H_b) with the emergence of the proton peaks adjacent to the nitrogen of the terminal pyridyl units of **L1** (H_a and H_b) was used to determine the cage in solution.

It was shown that **C1.BF$_4$** broke down at a slower rate compared to **C1^{NH2}.BF$_4$** over the initial 5 minutes (**C1.BF$_4$** = 9.5% cage disassembled /minute; **C1^{NH2}.BF$_4$** = 14.2% cage disassembled /minute). Furthermore, the metallacage appeared to reach an equilibrium at 30% over the 4 hours. As only the rate of disassembly was expected to be altered by altering the concentration, and not the final equilibrium reached of cage: cage disassembled, it was

suspected that the active GSH had been oxidised to the non-reductive GSSG (figure 23). As the peaks corresponding to GSH are masked by the solvent peak of DMSO and water, this could not be seen by the spectra. Furthermore, the molar ratio of **C1.BF$_4$**: GSH used was approximately 2.3: 1. A 1: 1 non-reversible reaction between the reduction of the metallacage and GSH would predict a final cage concentration of 43% in solution, which is close to the experimental value determined, and the discrepancy may be attributed to either partial reduction of the GSSG formed back to the reducing agent, GSH, or due to experimental errors attributed to working on a small scale. As such, a further 1 equivalent of GSH was added to the sample of **C1.BF$_4$** after 4 hours. The first ^{1}H NMR spectra taken (T = 5 min) showed complete breakdown of the cage to **L1^{BDP}**. This result strongly suggests that the cage does not reach an equilibrium with GSH, but rather the metallacage **C1.BF$_4$** is rapidly reduced and broken down to its ligand by the presence of GSH (concentration = 2 mmol/L) at a rate of approximately 9.5% per minute (determined by the gradient between T = 0 and T = 5 mins). The GSH is then almost quantitatively converted to GSSH, and thus cannot be recycled back to the reactive GSH without the presence of the catalysing enzyme glutathione reductase. This evidence of clean and complete metallacage breakdown in the presence of physiological concentrations of GSH is excellent proof of a viable guest release mechanism upon uptake into cells.

7.3 Red emissive *exo*-functionalised Pd_2L_4 metallacages

In order to further elucidate the mechanism of cellular uptake of Pd_2L_4 metallacages, fluorescent live cell imaging of A375 melanoma cells incubated with fluorescent Pd_2L_4 metallacages was proposed. However, in this case, a new fluorophore which would emit in the lower energy range of the visible spectrum was designed. This would minimise the effects of photobleaching and production of reactive oxygen species when the fluorophore is excited, which can harm the live cell sample and produce misleading data in terms of the toxicity of the fluorophore being studied.[233] To this end it is beneficial to use fluorophores that absorb and emit light in the near-infrared (NIR) range (λ = 700 – 1400 nm). This wavelength range is thought to be ideal as there will be no interference from endogenous chromophores or lumiphores, and thus will produce better resolution images.

Furthermore, longer wavelength light is known to exhibit better tissue penetration than shorter wavelength light (typically < 1mm tissue penetration).[242] Thus, it can be envisioned that as well as facilitating live cell imaging, *in vivo* photonic experiments can be facilitated by the use of fluorophores that both absorb and emit NIR light. Indeed, over the last few decades there has been a surge of research interest into small animal macroscopic photonic imaging techniques,

thanks to progress in both instrumentation design and the design of suitable, long wavelength absorbing and emitting probes.[242] As such, the design and synthesis of NIR absorbing and emitting Pd_2L_4 type metallacages may facilitate the live cell imaging and thus the elucidation of the cellular uptake mechanism, and even be envisioned to facilitate *in vivo* photonic imaging experiments.

7.3.1 Ru(II)(bipy)$_3$ fluorophore synthesis and photophysical studies

With the aim to achieve luminescent metallacages, an heterometallic Pd_2L_4 cage (L = bis(2,2'-bipyridine)(*N*-(3,5-bis(pyridin-3-ylethynyl)phenyl)-3-(4'-methyl-[2,2'-bipyridin]-4-yl)propenamide)ruthenium(II) tetrafluoroborate, $\mathbf{L^{Ru(II)}}$, figure 28) has been previously synthesised in our group.[133] The metallacage was *exo*-functionalised with a (Ru(II)(bipy)$_3$) type fluorophore (bipy = 2,2'-bipyridine), whose luminescence has been shown to be based on spin forbidden charge transfer, Ru(II)(bipy)$_3$ was separated from the metallacage ligand scaffold by an alkyl linker and conjugated via amide bond formation (figure 28). It was reported that despite the Pd_2L_4 metallacage exhibiting an excellent quantum yield (ϕ = 66%, DMSO), this could only be achieved by exciting the fluorophore at a high energy wavelength (λ_{ex} = 260 nm) which would not be suitable for live cell imaging. It was reported that by exciting the charge transfer band of the fluorophore (λ_{abs} = 460 nm), the quantum yield of the metallacage was severely reduced to ϕ = 4%.

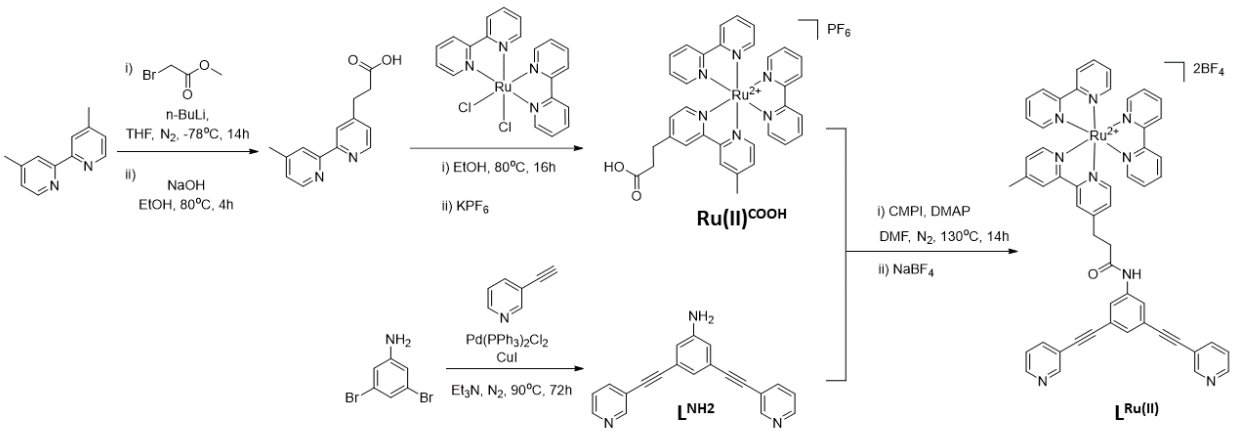

Figure 28. Synthesis of the ruthenium based fluorophore, $\mathbf{Ru(II)^{COOH}}$, and the subsequent fluorescently labelled ligand, $\mathbf{L^{Ru(II)}}$.

Despite the poor quantum yield when excited at 460 nm, the synthesis and characterisation of the Ru(II) metallacage ($\mathbf{C^{Ru(II)}}$) was carried out to test its suitability for *in vitro* tests and fluorescent live cell imaging. The carboxylic acid functionalised ligand ($\mathbf{Ru(II)^{COOH}}$) was synthesised in two steps. First, the carboxylic acid functionalised 2,2'-bipyridine ligand was synthesised by the asymmetric deprotonation of a methyl group of 4,4'-dimethyl-2,2'-bipyridine

via *n*-butyllithium followed by the addition of methyl-2-bromoacetate and subsequent *in situ* cleavage of the methyl protecting group by addition of sodium hydroxide (figure 28). This was then stirred at reflux with Ru(II)bis(bipyridine)dichloride under an inert atmosphere in ethanol for 18 hours before precipitation of the product using potassium hexafluoride. The Ru(II) *exo*-functionalised ligand ($\mathbf{L^{Ru(II)}}$) was formed via amide bond formation between $\mathbf{Ru(II)^{COOH}}$ and $\mathbf{L^{NH2}}$ in DMF at reflux, using CMPI and DMAP to activate the carboxylic acid. The solution was diluted with DCM before being washed with deionised water and the solvent removed to give the crude product. Silica chromatography was used to purify the crude product to give the ligand $\mathbf{L^{Ru(II)}}$.

The metallacage $\mathbf{C^{Ru(II)}}$ was formed via self-assembly in DMSO by addition of 2 equiv. of Pd(II)$(MeCN)_4.2BF_4$ to 4 equiv. of $\mathbf{L^{Ru(II)}}$. After stirring at room temperature for 1 hour, the cage was obtained by precipitation using diethyl ether and acetone (figure 29).

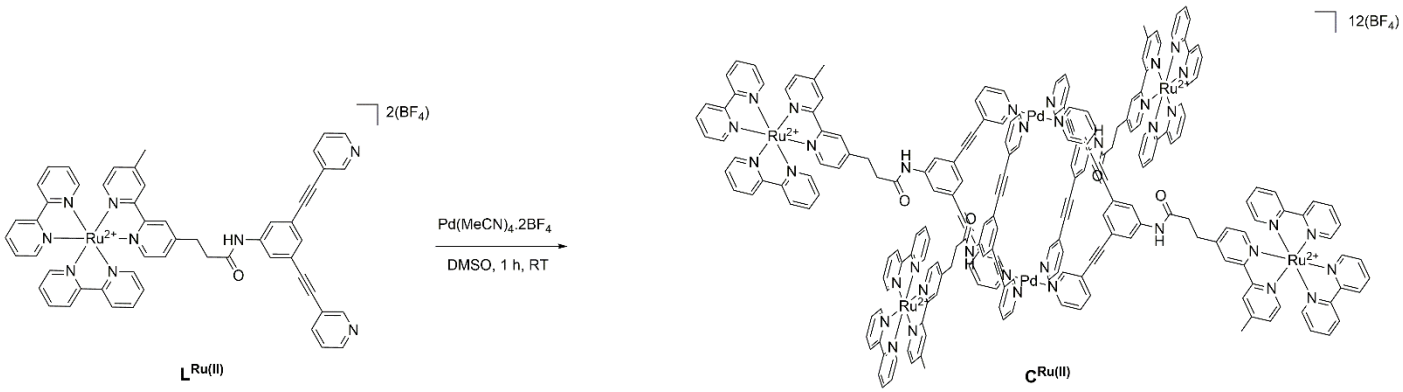

Figure 29. Self-assembly of the metallacage $\mathbf{C^{Ru(II)}}$ from ligand $\mathbf{L^{Ru(II)}}$ within 1 hour in DMSO at room temperature.

The photophysical properties of $\mathbf{Ru^{COOH}}$, $\mathbf{L^{Ru(II)}}$, and $\mathbf{C^{Ru(II)}}$ were investigated and are summarised in table 3. The UV-Vis spectra of each compound was shown to have a strong absorption below 300 nm which can be attributed to the various S_0-S_n excitation events due to the highly conjugated nature of $\mathbf{Ru^{COOH}}$, $\mathbf{L^{Ru(II)}}$, and $\mathbf{C^{Ru(II)}}$. A smaller absorption band was seen at circa. 460 nm which can be attributed to the ligand to metal charge transfer. It was confirmed that upon excitation of the charge transfer band (circa. λ_{ex} = 460 nm) $\mathbf{Ru^{COOH}}$, $\mathbf{L^{Ru(II)}}$, and $\mathbf{C^{Ru(II)}}$were found to have quantum yields equal to or below 4 % ($\phi(\mathbf{C^{Ru(II)}})$ = 4 %; $\phi(\mathbf{L^{Ru(II)}})$ = 4 %; $\phi(\mathbf{Ru(II)^{COOH}})$ = 3 %).

Table 3. Photophysical properties of **Ru(II)^{COOH}**, **L$^{Ru(II)}$** and **C$^{Ru(II)}$**.

Compound	λ_{ab} [nm]	λ_{em} [nm]	ε [mol^{-1} dm^{-1} cm^{-1}]	ϕ [%]
Ru(II)^{COOH}	459	628	12,900	3
L$^{Ru(II)}$	459	625	14,400	4
C$^{Ru(II)}$	459	625	53,800	4

C$^{Ru(II)}$ was confirmed not to exhibit a high enough quantum yield to facilitate live cell images. As such, a different fluorophore which would emit light at longer wavelengths but retain a higher quantum yield to facilitate fluorescence microscopy studies was necessary.

7.3.2 NIR-BODIPY fluorophore synthesis and photophysical studies

BODIPY fluorophores typically emit light in the region of 470-530 nm.[228] However, through the judicious choice of additional functional groups and their placement on the BODIPY scaffold, the energies of the BODIPY HOMO and LUMO can be altered.[234,243] For example, it has been shown that by substituting the *meso*-carbon of BODIPY for an aza-nitrogen (to produce an aza-BODIPY) the wavelength of emission can be bathochromically shifted. Furthermore, substitution of the 3,5 and 1,7- positions with aryl or styryl substituents has also been shown to alter the energy of the HOMO and LUMO, which can be made to have a smaller band gap and thus emit lower energy light. Following this, a collaboration with the group of Dr. Darren Griffith of the University of Dublin was established, which provided us a sample of the previously reported near infrared emitting *aza*-BODIPY based fluorophore, **BDP^{NIR}**.[244] **BDP^{NIR}** has been substituted at the 1,7-position with phenyl groups, the 3,5- position was functionalised with phenol groups, and the meso-carbon was substituted for an *aza*-nitrogen.

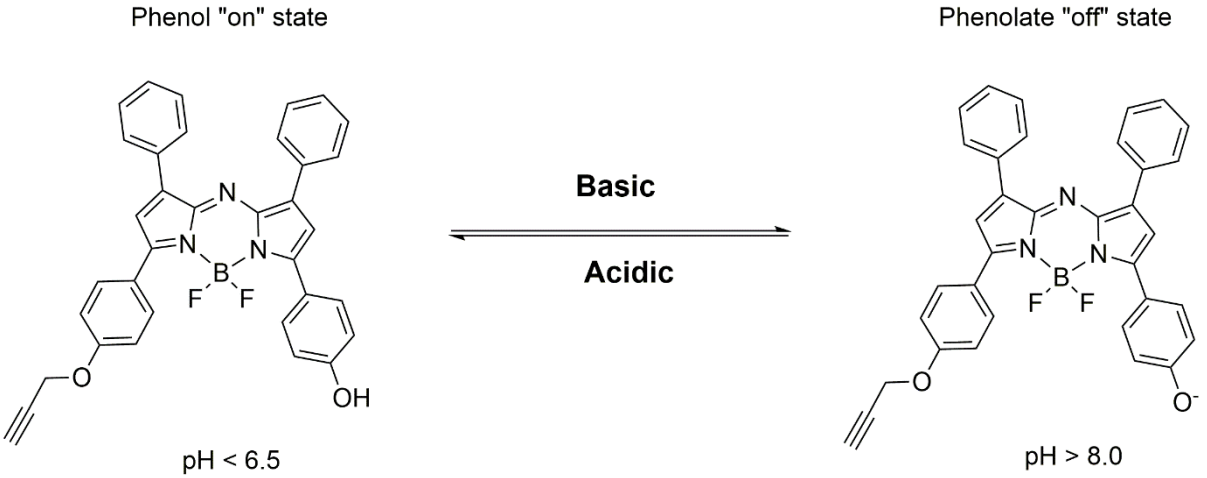

Figure 30. Structure of **BDP^{NIR}** under basic and acidic conditions. Conversion of the phenol group to a phenolate causes complete quenching of the emission for **BDP^{NIR}**

Furthermore, the fluorophore had been asymmetrically functionalised by forming an ether bond between one of the functionalised phenol groups and propargyl to give a pendant primary alkynyl group which can be conjugated to other moieties via CuAAC click chemistry. The remaining phenol group has also been shown to be able to act as a fluorescence "switch", whereby the pH-dependent phenol – phenolate interconversion triggers a complete quenching, with a pKa = 6.9, and complete quenching of the fluorescence signal at pH 8.0 and above (figure30).

Conjugation of **BDP^{NIR}** to **L^{N3}** was carried out following standard CuAAC click conditions (figure 31). Unlike the conjugation of **L^{N3}** to **BDP^{alkynyl}**, the reducing agent, sodium ascorbate, could not be produced *in situ* and so was added in catalytic amounts to the solution of **L^{N3}**, **BDP^{NIR}**, Cu(II)SO_4.5H_2O and stirred in THF at room temperature for 16 hours. The reaction mixture was diluted with excess water and extracted using DCM. The solvent was removed, and the crude residue was purified *via* silica chromatography to give the near-infrared BODIPY exo-functionalised ligand, **L^{NIR}**. The metallacage, **C^{NIR}**, was then formed via self-assembly after 2 equivalents of Pd(II)$(MeCN)_4$.2BF_4 were stirred with 4 equivalents of **L^{NIR}** in DMSO at room temperature for 1 hour. Precipitation of the cage was achieved by addition of acetone and diethyl ether (figure 31).

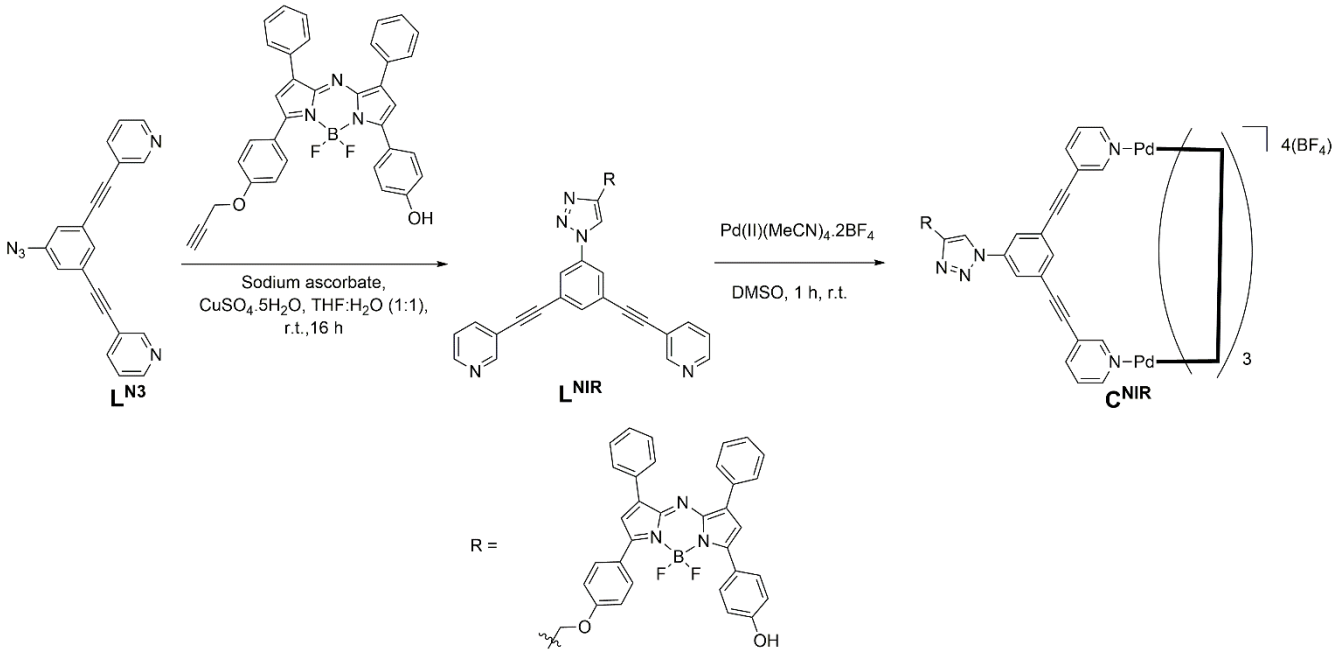

Figure 31. Synthesis of **L^{NIR}** and **C^{NIR}** from the precursor ligand **L^{N3}** and the fluorophore **BDP^{NIR}** using standard CuAAC conditions.

The spectral properties of **L^{NIR}** and **C^{NIR}** were studied via uv-vis and emission spectroscopy and are summarised in table 4. Both **L^{NIR}** and **C^{NIR}** show an intense absorption band below 350 nm, indicative of numerous $S_0 - S_n$ excitation events. Furthermore, a small absorption band can be seen for both **L^{NIR}** and **C^{NIR}** at circa. 460 nm, and a final absorption band, attributed

to the $S_0 – S_1$ excitation, is found at 704 nm for **L^{NIR}** and 709 nm for **C^{NIR}** in DMSO. The emission profile of **L^{NIR}** and **C^{NIR}** was taken in degassed DMSO by excitation at λ_{ex} = 704 nm and 709 nm, respectively. The emission profiles both show a peak at λ_{em} = 747 nm, due to relaxation of an electron from $S_1 – S_0$. The quantum yield of **L^{NIR}** and **C^{NIR}** could be calculated by comparison to a suitable standard. Due to the lack of known available quantum yield standards which have an excitation and emission band that would overlap to a suitable degree with the excitation and emission bands of **L^{NIR}** and **C^{NIR}**, the previously reported **BDP^{NIR}** was used as a standard (ϕ = 37 %; 5 x 10^{-7} M; $CHCl_3$) as it had suitable spectral properties for this use (λ_{ex} = 680 nm¸ λ_{em} = 708 nm). The fluorescence quantum yield for **L^{NIR}** and **C^{NIR}** was collected in degassed DMSO and calculated to be ϕ = 22% and ϕ = 20%, respectively.

Table 4. Photophysical properties of **L^{NIR}** and **C^{NIR}**

Compound	λ_{ab} [nm]	λ_{em} [nm]	ε [L mol^{-1} cm^{-1}]	ϕ [%]
L^{NIR}	475, 710	747	322,593	22
C^{NIR}	475, 710	746	190,400	20

7.3.3 Stability of NIR emitting BODIPY functionalised metallacage

The stabilities of **C^{NIR}** and **L^{NIR}** were studied in both PBS solution (pH 7.4) and deionised water by recording the UV-Vis spectrum of the sample in either solvent over a period of 24 hours and monitoring any shift to the peak position (figure 32). The stability of **L^{NIR}** was found to be excellent in both deionised water and PBS solution (pH 7.4). There was no quenching of the peaks at 475 and 710 nm which would indicate precipitation of the sample, and no bathochromic or hypsochromic shifts over the selected time period. However, metallacage **C^{NIR}** was shown to precipitate in both deionised water and PBS solution (pH 7.4) after 2 hours. Although this is not ideal for a fluorophore for *in vitro* imaging, we considered the cage sufficiently stable to study its cell uptake in the first hour by fluorescence live cell imaging.

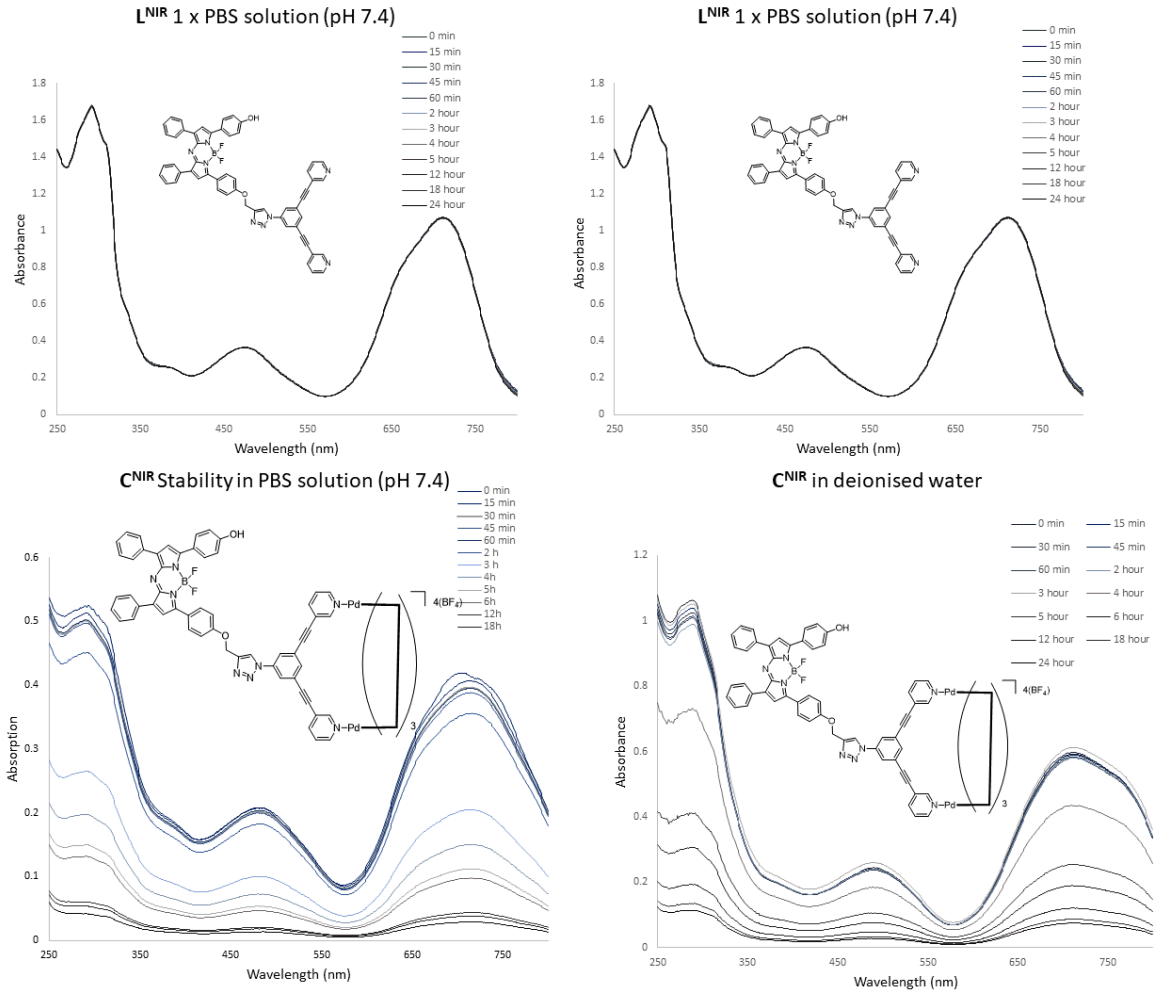

Figure 32. Stability of **L^{NIR}** (top row), both recorded at [5 x 10^{-6} M] and **C^{NIR}** (bottom row), both recorded at [1 x 10^{-5} M] in 1 x PBS solution (pH 7.4) (left column) and in deionised water (right column).

7.3.4 *In vitro* cellular distribution of NIR-BODIPY Pd_2L_4 metallacage

After finding that the fluorophore had suitable spectral properties to be used for live cell *in vitro* imaging. The EC_{50} value was calculated for the metallacage **C^{NIR}** and found to be >50 µM against A375 human melanoma skin cells. **C^{NIR}** was initially incubated with A375 melanoma cells at a concentration of 15 µM in 2-(*N*-morpholino)ethanesulfonic acid (MES) to achieve a pH of 6.5. This was done to ensure that the fluorophore was predominantly in its protonated form, and thus exhibited fluorescence, while causing the cells minimum stress due to the acidic environment. A fixed cell fluorescence microscopy image was recorded in both non-MES buffered pH 7.4 solution, and MES buffered pH 6.4 and to ensure that fluorescence was observed (figure 33).

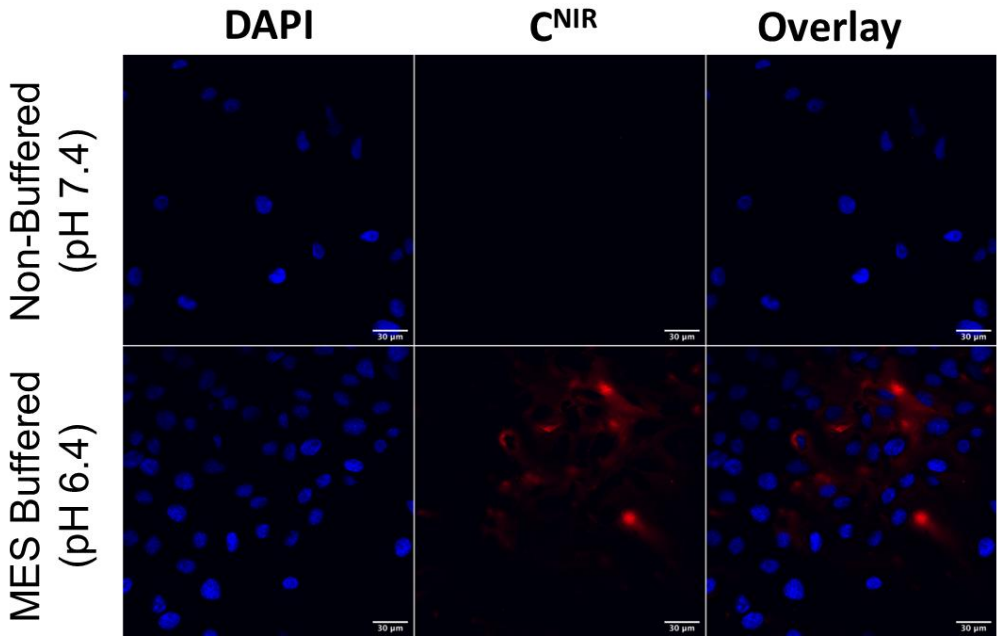

Figure 33. Fixed cell fluorescent microscopy images of **C^{NIR}** [15 x 10^{-6} M] incubated at 37°C with A375 human melanoma cells for 1 hour. Left: DAPI nuclei stain. Middle: **C^{NIR}**. Right: Overlay. Top row: non-MES buffered solution (pH 7.4). Bottom row: MES buffered solution (pH 6.4).

The initial fixed cell fluorescence microscopy images (figure 33) highlighted that the cells were viable at pH 6.4, and that **C^{NIR}** exhibited a high enough fluorescence to be monitored by fluorescence microscopy. However, the initial images showed that the distribution of **C^{NIR}** was not homogenous throughout the sample. Furthermore, the initial images could not determine whether **C^{NIR}** had been taken up within the A375 cells or whether they were associated with the cellular membrane. In order to determine if **C^{NIR}** had been taken up within the cells, and thus determine the sub-cellular distribution, confocal microscopy studies were carried out (figure 34).

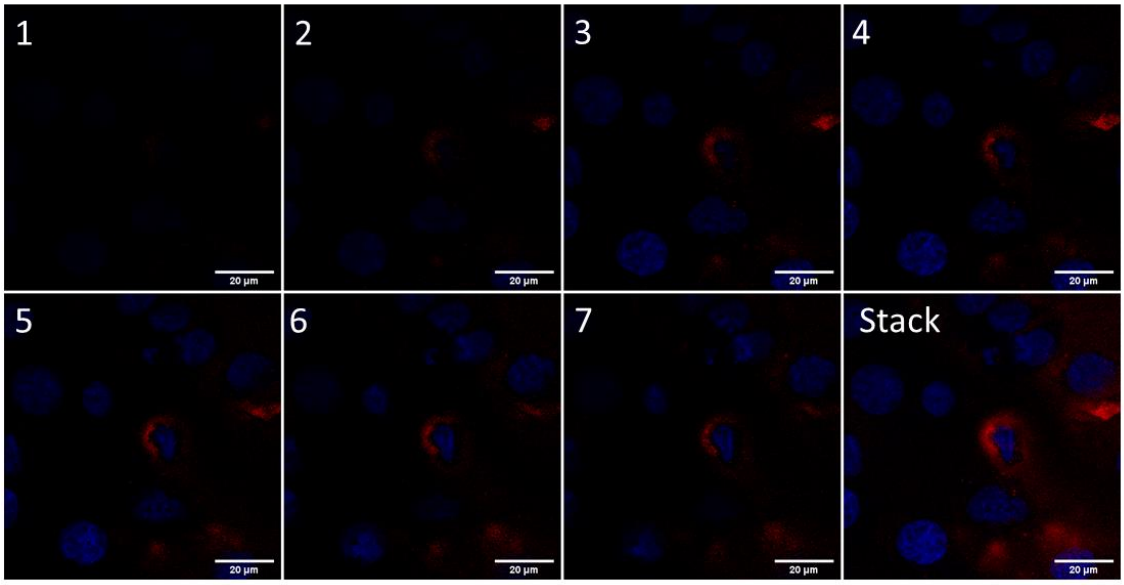

Figure 34. Confocal microscopy images of A375 human melanoma cells incubated with **C^{NIR}** [15 x 10^{-6} M] at 37°C for 1 hour (pH 6.4). The cell nuclei is stained with DAPI. Bottom right: Z-stack of images 1-7.

Figure 34 again shows that **C^{NIR}** is not evenly spread throughout the cell sample, but appears to be localised around a small, poorly formed cell, which is evidenced by the deformed cell nucleus of the cell. The deformation of the cell would indicate that it is unhealthy. As **C^{NIR}** was shown to be non-toxic to A375 cells (EC_{50} > 50 µM), and that the other cells appear to be viable, **C^{NIR}** was thought to associate with a feature of the unhealthy cell, as opposed causing distress to the cell. Furthermore, the images show that **C^{NIR}** is not taken up within the cell in vesicles, but instead seems to be associated with the cell membrane of the deformed cell. This would indicate that **C^{NIR}** does not enter cells by the same mechanism as **C1.BF$_4$**, if indeed it does enter the cell at all. To gain further insight into the location of **C^{NIR}**, bright field images were recorded and overlaid with the fluorescence images recorded (figure 35).

Figure 35 confirms the unviability of the cell which has the highest intensity of **C^{NIR}**, as shown by the small cytoplasmic area and deformed shape of the cell membrane. Furthermore, the bright field images indicate that the other areas of fluorescence attributed to **C^{NIR}** correspond to folds and crevices from the A375 cells, which are formed during the fixation of the cells using formaldehyde. Indeed, the bright field images indicate that **C^{NIR}** is not taken up within A375 cells, nor associate with the cell membrane. Instead, it appears that small amounts of **C^{NIR}** remain within the folds and crevices of the fixed cell sample after washing the cells before recording the fluorescence microscopy images. This strongly suggests that **C^{NIR}** is not taken up within the cells, or within the cell membrane of A375 human melanoma cells, and thus cannot be used to elucidate the mechanism of cellular uptake for Pd_2L_4 metallacages.

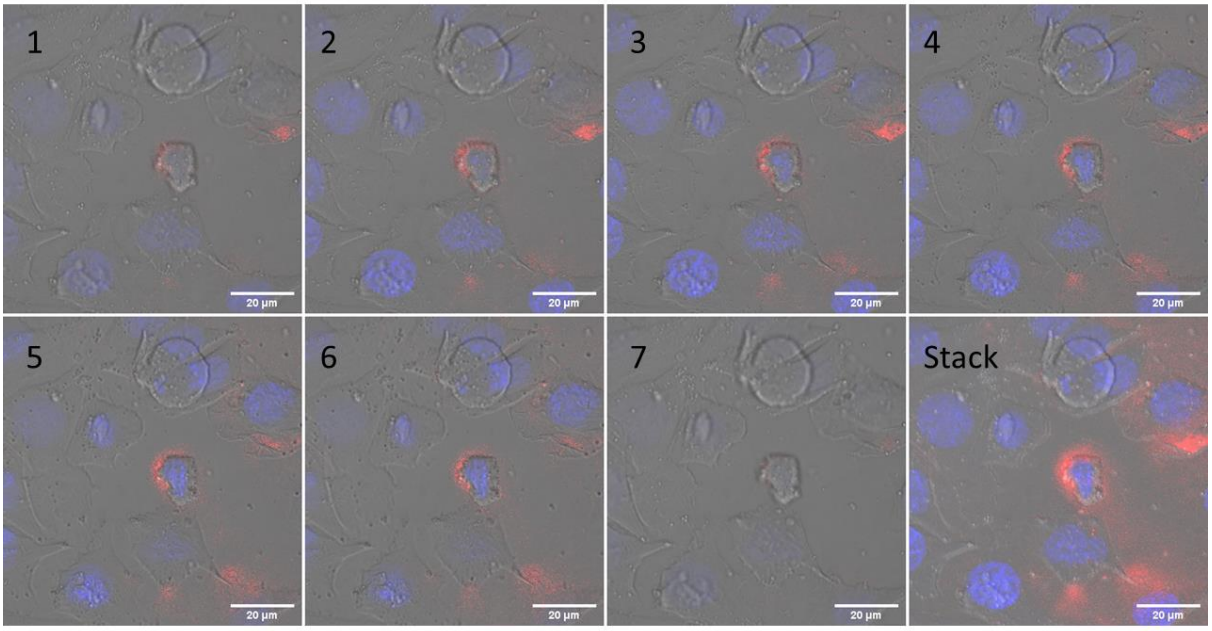

Figure 35. Bright field microscopy image of A375 human melanoma cells incubated for 1 hour with $\mathbf{C^{NIR}}$ [15 x 10^{-6} M] at 37°C (pH 6.4). The bright field image is overlaid with the corresponding confocal images 1 – 7 from figure 34. Bottom right: overlay of the Z-stack image from figure 34 and the bright field microscopy image.

7.4 Summary and future outlook

The synthesis of a library of metallacages *exo*-functionalised with BODIPY based fluorophores has been reported (**C1.BF$_f$**, **C1.NO$_3$**, **C2.NO$_3$**, $\mathbf{C^{NIR}}$), as well as their corresponding ligands ($\mathbf{L1^{BDP}}$, $\mathbf{L2^{BDP}}$, $\mathbf{L^{NIR}}$) and the BODIPY based fluorophore groups ($\mathbf{BDP^{COOH}}$, $\mathbf{BDP^{alkynyl}}$). Furthermore, the synthesis of a ruthenium(II) based fluorophore ($\mathbf{Ru(II)^{COOH}}$), the ruthenium fluorophore functionalised ligand ($\mathbf{L^{Ru(II)}}$) and the ruthenium fluorophore *exo*-functionalised metallacage ($\mathbf{C^{Ru(II)}}$) has also been reported.

The photophysical properties of the fluorophores, fluorescently functionalised ligands, and Pd_2L_4 metallacages were recorded via UV-vis absorption and emission spectroscopy. The stability in both aqueous and PBS solution was recorded over 24 hours via UV-vis spectroscopy for the fluorophores, ligands and metallacages reported, to assess the suitability for *in vitro* studies. **C1.NO$_3$** was not deemed suitable for *in vitro* studies as the stability in PBS solution was not as good as **C1.BF$_4$**, despite showing promising photophysical properties.

The encapsulation of cisplatin was studied via ^{1}H NMR for **C1.BF$_4$** and **C1.NO$_3$**, and via ^{195}Pt NMR for **C1.BF$_4$**, and suggests encapsulation of cisplatin in both cages (*further discussion on the encapsulation of cisplatin in Pd_2L_4 metallacages can be found in chapter 8*). The stability of **C1.BF$_4$** and **C1.NO$_3$** analogues ($\mathbf{C^{NH2}.BF_4}$ and $\mathbf{C^{NH2}.NO_3}$) were studied in the presence of the

reducing agent glutathione (GSH) via ^{1}H NMR spectroscopy. Both $\mathbf{C^{NH2}.BF_4}$ and $\mathbf{C^{NH2}.NO_3}$ were found to degrade rapidly in the presence of GSH. $\mathbf{C^{NH2}.BF_4}$ was found to cleanly disassociate back to its corresponding ligand, $\mathbf{L^{NH2}}$, however $\mathbf{C^{NH2}.NO_3}$ did not disassociate cleanly back to $\mathbf{L^{NH2}}$. $\mathbf{C1.BF_4}$ was therefor tested for its stability in the presence of GSH via ^{1}H NMR and was shown to cleanly disassociate to its corresponding ligand, $\mathbf{L1^{BDP}}$, which suggests a viable guest release mechanism upon cellular internalisation.

$\mathbf{C1.BF_4}$, which was *exo*-functionalised with a green light emitting (λ_{ems} = 544 nm) BODIPY fluorophore, was selected for *in vitro* studies due to its photophysical properties, its stability in water and that it does not structurally deform in PBS solution, its ability to encapsulate cisplatin, and its clean disassociation to its constituent ligand in the presence of GSH.

The uptake mechanism of $\mathbf{C1.BF_4}$ in A375 human melanoma cells was studied via fluorescent microscopy. $\mathbf{C1.BF_4}$ was found to be taken up by active transport and appeared to localise in sub-cellular vesicles. The bright field images strongly suggest that the vesicles $\mathbf{C1.BF_4}$ are taken up in are melanosomes and not lysosomes. To investigate this mechanism further, it was envisioned that Pd_2L_4 metallacages *exo*-functionalised with NIR-emitting fluorophores could be synthesised ($\mathbf{C^{Ru(II)}}$ and $\mathbf{C^{NIR}}$) and used in live cell microscopy assays to determine the cellular uptake mechanism of Pd_2L_4 type metallacages. $\mathbf{C^{Ru(II)}}$ did not exhibit a high enough quantum yield to be used *in vitro*. $\mathbf{C^{NIR}}$ exhibited suitable photophysical properties for *in vitro* fluorescence microscopy tests. The stability of the ligand, $\mathbf{L^{NIR}}$, and $\mathbf{C^{NIR}}$ was assessed in water and PBS solution via UV-Vis spectroscopy over 24 hours. $\mathbf{L^{NIR}}$ was shown to be stable in both solutions over 24 hours, however $\mathbf{C^{NIR}}$ was not stable in either solution over 24 hours. Despite this, preliminary *in vitro* fixed cell fluorescent microscopy images were recorded against A375 human melanoma cells, as well as confocal and bright field images. Combined, these images showed that $\mathbf{C^{NIR}}$ is not taken up within A375 human melanoma cells, and thus was unsuitable to determine the uptake mechanism of Pd_2L_4 metallacages. Further work can be done on designing a NIR-emitting Pd_2L_4 metallacage to facilitate live cell *in vitro* microscopy studies to elucidate the mechanism of cellular uptake of Pd_2L_4 type metallacages.

Chapter 8: Improved Pd_2L_4 metallacage solubility in aqueous solution

*(Woods, B. et. al, (**2019**) Exo-Functionalized Metallacages as Host-Guest Systems for the Anticancer Drug Cisplatin**. Front. Chem.** 7:68. doi: **10.3389/fchem.2019.00068**)*

8.1 Introduction

Despite their tetra-cationic charge, discrete architecture and relatively small size of the core Pd_2L_4 metallacage structure (cavity volume = 1.12 x 1.11 x 1.13 nm^3),[127] Pd_2L_4 metallacages suffer from extremely scarce solubility in most polar protic, aprotic and non-polar organic solvents, with the exception of DMSO, DMF and acetonitrile. The only metallacage of this type having the required solubility to facilitate ^1H NMR studies in D_2O,[135] was based on a Pd_2L_4 scaffold, where L = 2,6-bis(pyridine-3-ylethynyl)pyridine. Unfortunately, this type of cage is unsuitable as a drug delivery system for neutral drugs (e.g. cisplatin) due to the preferential encapsulation of water molecules over neutral guests.[99]

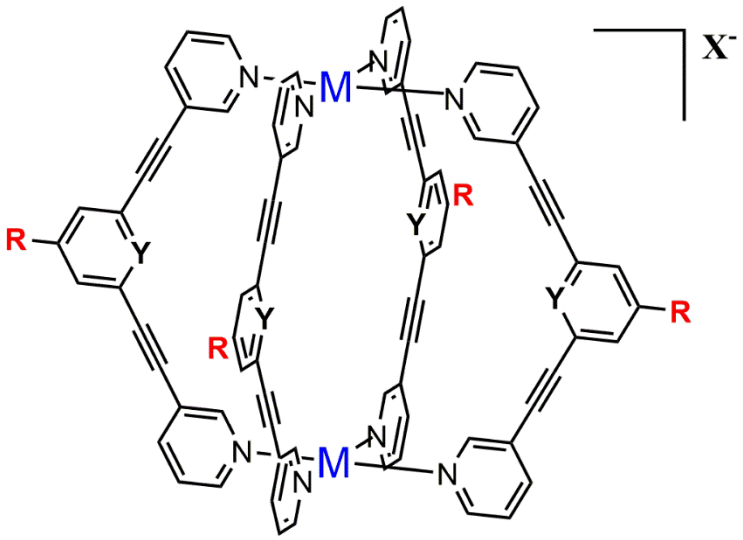

Figure 1: Chemical structure of the core M_2L_4 type metallacage, highlighting several sites for synthetic modification to optimise the final physical properties of the structure. M = d^8 metal such as Pd(II) or Pt(II);[134] Y = *endo*-functionalisation site;[99] R = *exo*-functionalisation site;[135,136] X = counterion.[238]

The poor aqueous solubility of Pd_2L_4 metallacages (L = 1,3-bis(pyridin-3-ylethynyl)benzene) has fortunately not limited their study in cells *in vitro* as they may be first dissolved in DMSO to form a stock solution of the metallacage, before dilution in aqueous media to the required concentration to carry out *in vitro* tests.[127,132,134] Most importantly, the aqueous solubility can be improved sufficiently via the *exo*-functionalisation of the metallacage with peptides.[131] However, it would be still desirable to achieve highly water soluble Pd_2L_4 metallacages, to facilitate the study of their stability and host-guest properties in aqueous

media by a range of analytical techniques that require concentrations unattainable by current metallacages scaffolds, including NMR spectroscopy and calorimetric methods.

Within this framework, there are numerous strategies to improve the solubility of compounds in water.[245] Typically, functionalisation of the insoluble compound with a known water solubilising group has proved to be a successful approach.[245] In this chapter we describe a series of attempts to improve the hydrophilic character of the Pd_2L_4 via the exo-functionalization of the 1,3-bis(pyridin-3-ylethynyl)benzene ligand with a highly water-soluble group, including sugars, carboxylic acids and PEG moieties. Another simple and successful strategy that has previously been used to improve the solubility of charged compounds in solution is to exchange the counterion for one which is known to be soluble in water,[246] which was also investigated.

8.2 Results and discussion

8.2.1 *Exo*-functionalisation of Pd_2L_4 metallacage with water soluble groups

A small library of 1,3-bis(pyridin-3-ylethynyl)benzene based ligand scaffolds, *exo*-functionalised with a series of moieties envisioned to improve the water solubility of the resulting ligand, were synthesised and characterised by different methods (**L_{aq}1-7**, figure 2).

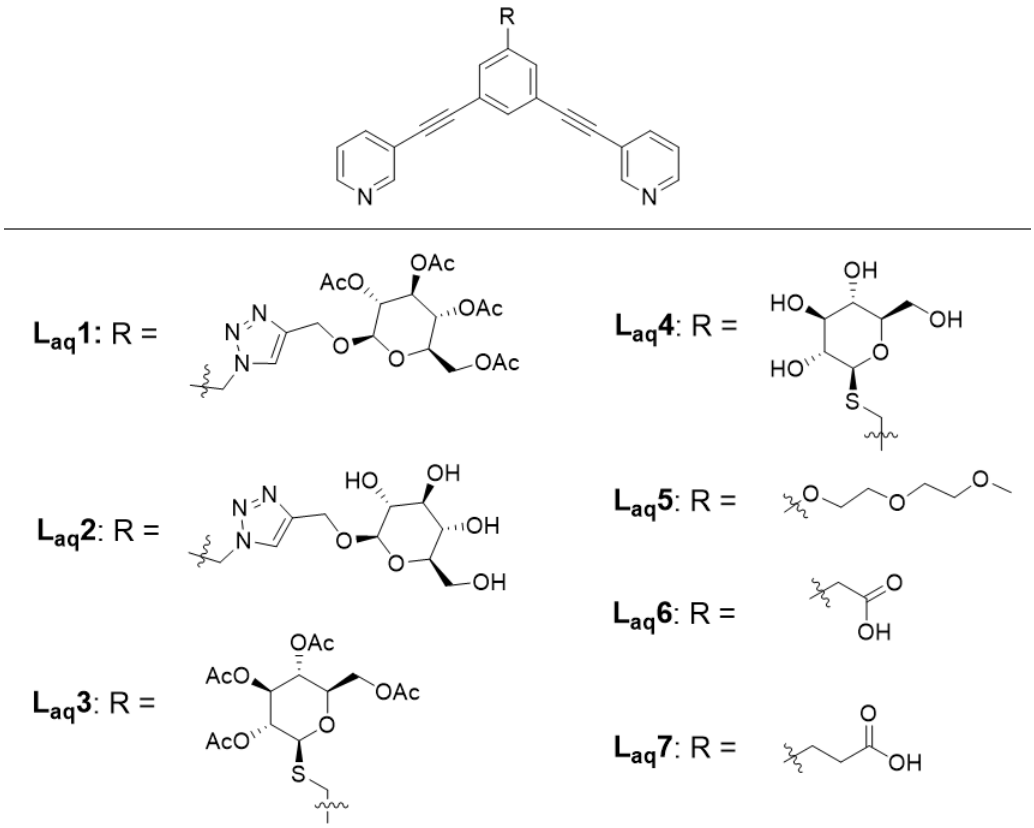

Figure 2: Chemical structures of the library of ligands selected to improve water solubility (**L_{aq}1-7**).

As a water soluble tris-pyridyl ligand based Pd_2L_4 metallacage has previously been reported,[135] the bis-pyridyl ligand analogue, with D-glucose functionalised to the bis-pyridyl ligand scaffold via copper-catalysed alkyne azide [2+3] cycloaddition (CuAAC) was chosen as a starting target molecule (**L_{aq}1**). The synthetic route to this molecule involved the acetylated-D-glucose intermediate, which was also tested for its water solubility (**L_{aq}2**).

The synthesis of **L_{aq}1** and **L_{aq}2** followed a modified previously reported procedure.[135] Initially, the alcohol functionalised bis-pyridyl ligand ((3,5-bis(pyridin-3-ylethynyl)phenyl)methanol, **L^{CH2OH}**) was formed *via* Sonogashira cross-coupling of 3-ethynylpyridine and 3,5-dibromobenzylalcohol. The alcohol group was brominated *via* the Appel reaction to form the corresponding alkyl bromide functionalised ligand (3,3'-((5-(bromomethyl)-1,3-phenylene)bis(ethyne-2,1-diyl))dipyridine, **L^{CH2Br}**). Finally, this was converted to the alkyl azide functionalised ligand, (3,3'-((5-(azidomethyl)-1,3-phenylene)bis(ethyne-2,1-diyl))dipyridine **L^{CH2N3}**), via S_N2 type nucleophilic addition by introduction of sodium azide. The 2-propyl-tetra-O-acetyl-β-D-glucopyranide decorated ligand could then be formed *via* CuAAC click chemistry to give **L_{aq}2** (scheme 1). The deprotection of the acetate groups was then achieved by stirring under ambient conditions with the ion exchange resin, Amberlite 401 (OH^-), to produce the ligand **L_{aq}1** (scheme 1).

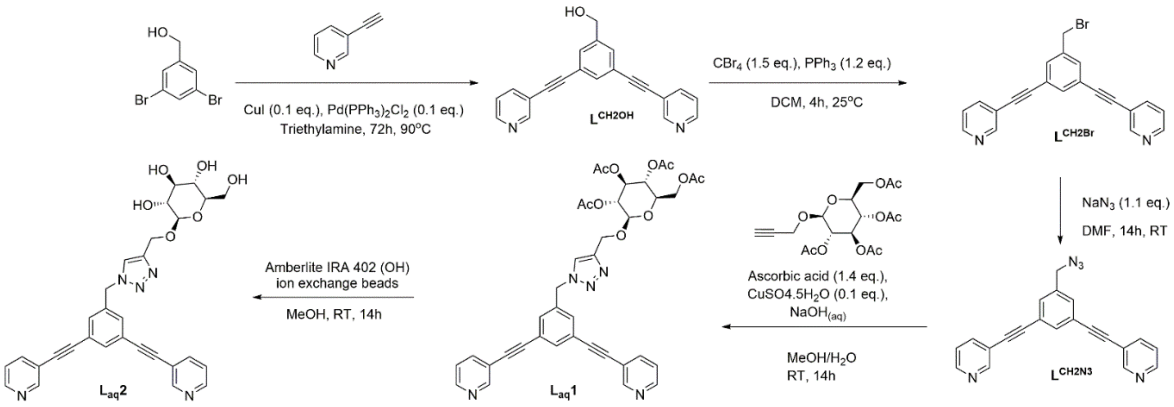

Scheme 1: Synthesis of ligands **L_{aq}1** and **L_{aq}2** adapted from the reported synthesis of the tris-pyridyl based ligand scaffold.[135] The alcohol functionalised ligand precursor (**L^{CH2OH}**) was formed *via* Sonogashira cross coupling, which was then brominated via the Appel reaction to afford precursor ligand **L^{CH2Br}**. The bromide was substituted for the azide (**L^{CH2N3}**) which could then be functionalised with 2-propyl-tetra-O-acetyl-β-D-glucopyranide via CuAAC click chemistry to afford **L_{aq}1**, which could then be deacetylated with ion exchange resin to afford **L_{aq}2**.

Conjugation of both D-glucose and acetylated-D-glucose was also achieved by the formation of a thioether bridge between the glucose moiety and the ligand scaffold (L_{aq}**3** and L_{aq}**4**, respectively). The synthesis of L_{aq}**3** and L_{aq}**4** could be achieved in a similar manner to L_{aq}**1** and L_{aq}**2**. Precursor ligand L^{CH2Br} was conjugated directly with 1-thio-β-D-glucose tetraacetate in the presence of triethyl amine via S_n2 type nucleophilic addition at reflux in acetonitrile to produce the ligand L_{aq}**3**. L_{aq}**3** was then stirred in the presence of Amberlite 401 (OH^-) ion exchange resin in methanol to deprotect the acetate groups and produce L_{aq}**4** (scheme 2).

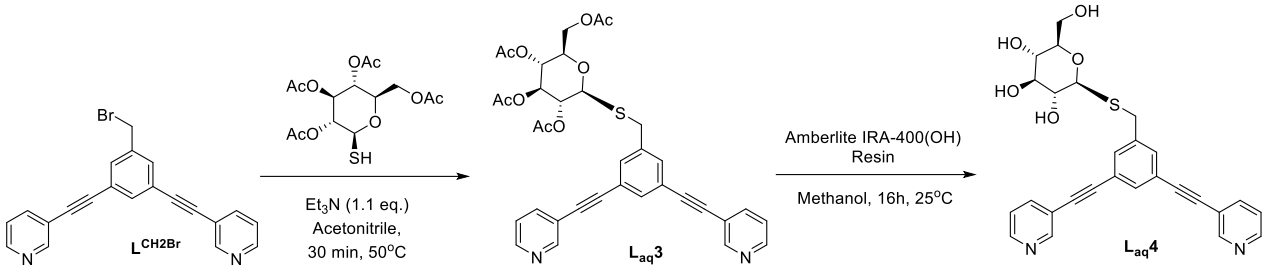

Scheme 2: Synthesis of ligands L_{aq}**3** and L_{aq}**4**. Precursor ligand L^{CH2Br} was reacted with 1-thio-β-D-glucose tetraacetate in the presence of triethylamine to afford L_{aq}**3**. L_{aq}**3** was then stirred with ion exchange resin in methanol to deacetylate the sugar moiety to produce L_{aq}**4**.

Polyethylene glycol (PEG) is the lineal polymer of ethylene glycol. It has been shown to improve the solubility of numerous conjugates and has been used in medicinal and formulation chemistry. Therefore, conjugation of a PEG chain to the ligand was also achieved. The length of PEG chain was chosen to be short enough so as not to act as a steric hinderance to the encapsulation process, as steric hinderance has been shown to affect the encapsulation and release profiles of a ruthenium based SCCs.[120] Therefore, a PEG chain consisting of two ethylene glycol units (dimer) was selected and conjugated to the ligand *via* an ether bridge (L_{aq}**5**) (figure 2). L_{aq}**5** was synthesised by first forming a reactive diethylene glycol monomethyl ether to facilitate conjugation to the bis-pyridyl ligand scaffold. Diethylene glycol monomethyl ether was heated to reflux with thionylchloride in chloroform in the presence of an excess of pyridine under an inert atmosphere to afford the chlorinated diethylene glycol monomethyl ether, 1-chloro-2-(2-methoxyethoxy)ethane. The phenol functionalised ligand, L^{OH}, was formed *via* Sonogashira cross coupling with 3,5-dibromophenol and 3-ethynylpyridine and was

subsequently conjugated to 1-chloro-2-(2-methoxyethoxy)ethane under basic conditions in DMF to afford the PEG *exo*-functionalised ligand, $\mathbf{L_{aq}5}$ (scheme 3).

Scheme 3: Synthesis of ligand $\mathbf{L_{aq}5}$. Precursor ligand $\mathbf{L^{OH}}$ was synthesised *via* Sonogashira cross coupling between 3,5-dibromophenol and 3-ethynylpyridine. 1-chloro-2-(2-methoxyethoxy)ethane was then refluxed under basic conditions with $\mathbf{L^{OH}}$ in DMF to produce $\mathbf{L_{aq}5}$.

Finally, carboxylic acid moieties are known to improve the water solubility of insoluble compounds. However, direct conjugation of the carboxylic acid group to the highly conjugated ligand, 3,5-bis(pyridin-3-ylethynyl)benzoic acid ($\mathbf{L^{COOH}}$, *chapter 5*) resulted in an extremely poorly soluble ligand in all common laboratory solvents, with only scarce solubility in DMSO. It was

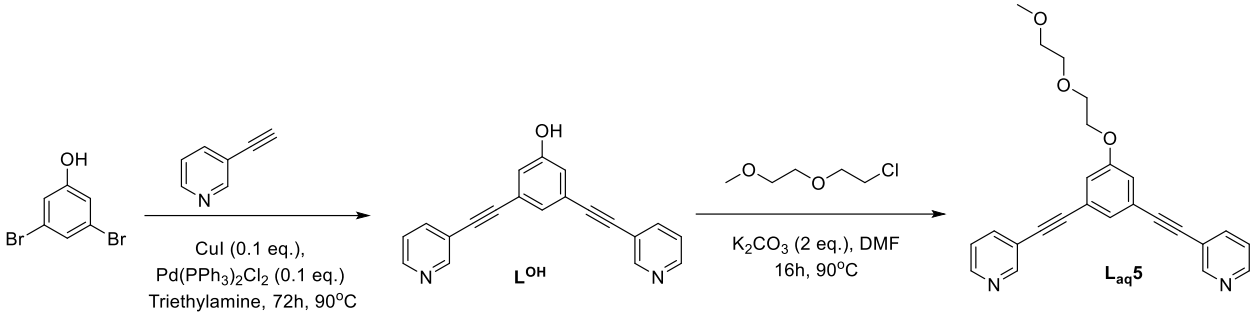

proposed that the aqueous solubility of the ligand could be improved by functionalisation with a carboxylic acid linked to the ligand scaffold *via* an alkyl bridge, thus, breaking the conjugated system and the electron withdrawing nature of the carboxylic acid on the aromatic phenyl ring. As such, the bis-pyridyl based ligand scaffold was synthesised with a carboxylic acid group separated from the ligand scaffold *via* a methyl ($\mathbf{L_{aq}6}$) and ethyl ($\mathbf{L_{aq}7}$) group and tested for their aqueous solubility (figure 2).

The carboxylic acid functionalised ligands, $\mathbf{L_{aq}6}$ and $\mathbf{L_{aq}7}$, were synthesised by first protecting the reactive acid functional group of the precursors 3,5-dibromobenzylacetic acid and 3-(3,5-dibromophenyl)propionic acid, respectively, using benzyl bromide. The dibromophenyl benzoate precursor could then be coupled to 3-ethynylpyridine via Sonogashira cross coupling, before deprotection of the benzyl group *via* sodium hydroxide and subsequent acidification to afford the alkyl carboxylic acid functionalised ligands, $\mathbf{L_{aq}6}$ and $\mathbf{L_{aq}7}$ (scheme 4).

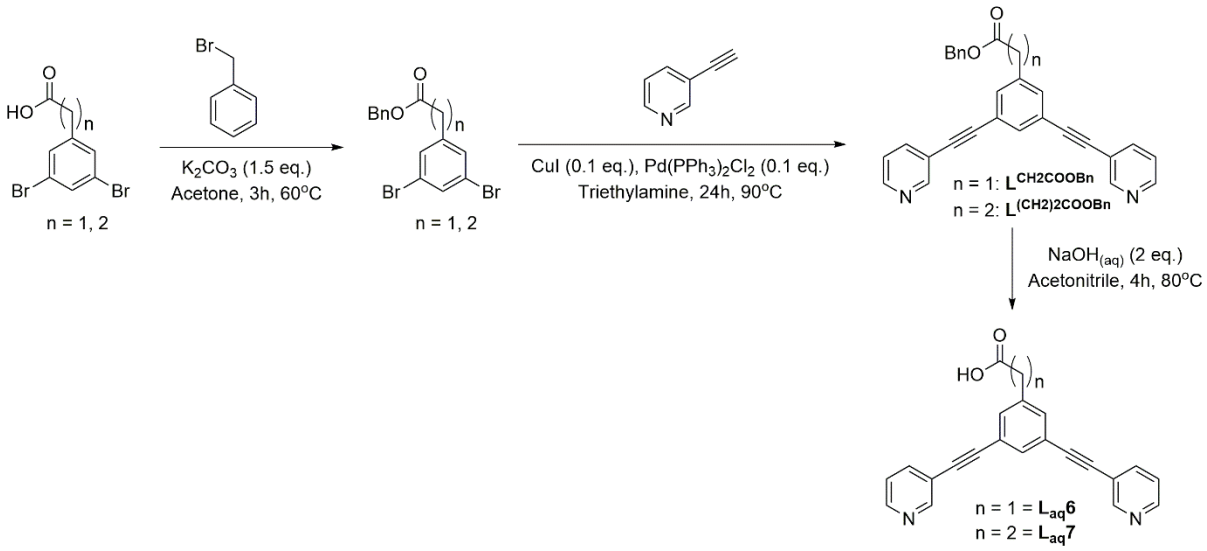

Scheme 4: Synthesis of water soluble ligands $\mathbf{L_{aq}6}$ and $\mathbf{L_{aq}7}$. The dibromophenyl carboxylic acid precursor was first protected using benzyl bromide. The protected dibromophenyl benzoate was then coupled with 3-ethynylpyridine via Sonogashira cross coupling conditions to afford the protected ligands $\mathbf{L^{CH2COOBn}}$ and $\mathbf{L^{(CH)2COOBn}}$. The protected ligands were then deprotected using sodium hydroxide before being acidified to afford the alkyl carboxylic acid functionalised ligands, $\mathbf{L_{aq}6}$ and $\mathbf{L_{aq}7}$.

The ligands $\mathbf{L_{aq}1\text{-}7}$ were initially tested for their aqueous solubility before self-assembly into the corresponding Pd_2L_4 metallacages. The improvement to the solubility of the ligands and corresponding Pd_2L_4 metallacages was primarily to facilitate further analytical techniques to elucidate guest binding in aqueous media. As such, experimentally determining the Log *P* of the ligands and corresponding metallacages to compare to other pharmaceuticals was not performed. The solubility of the ligands $\mathbf{L_{aq}1\text{-}7}$ was assessed by sonicating the metallacage overnight at 40°C in D_2O, and then filtering the resulting mixture through a 450 µm filter. The filtrate was then analysed *via* ^{1}H NMR to assess whether any of the ligands $\mathbf{L_{aq}1\text{-}7}$ could achieve a sufficient concentration to be studied by ^{1}H NMR spectroscopy. Unfortunately, ligands $\mathbf{L_{aq}1\text{-}5}$ could not be distinguished from the baseline showing that their solubility in water had not been improved sufficiently. Pleasingly, the alkyl carboxylic acid functionalised ligands, $\mathbf{L_{aq}6\text{-}7}$, were found to exhibit reasonable solubility in D_2O, with neither $\mathbf{L_{aq}6}$ nor $\mathbf{L_{aq}7}$ requiring sonication overnight to achieve a suitable concentration in D_2O solution for ^{1}H NMR spectroscopy (figure 3). The solubility of $\mathbf{L_{aq}6}$ and $\mathbf{L_{aq}7}$ was further investigated by titrating water into a dry sample of each ligand. It was found that the solubility of $\mathbf{L_{aq}6}$ was 10 mg/mL and $\mathbf{L_{aq}7}$ was found to be in

excess of 100 mg/mL, supporting the hypothesis that separation of the electron withdrawing carboxylic acid group from the conjugated ligand scaffold results in improved aqueous solubility.

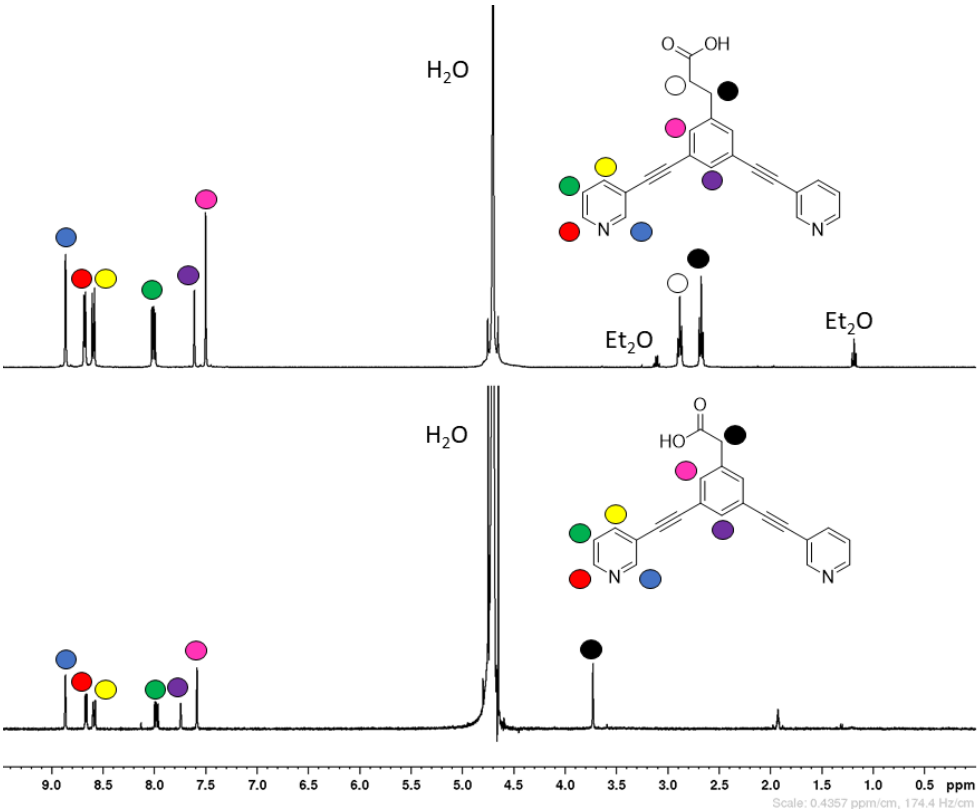

Figure 3: ^{1}H NMR spectra water soluble ligands $\mathbf{L_{aq}6}$ (bottom) and $\mathbf{L_{aq}7}$ (top) recorded in D_2O. The spectra were recorded of the filtrate of the samples after overnight sonication at 40°C in D_2O and subsequent filtration through 450 µm filter.

Although only ligands $\mathbf{L_{aq}6\text{-}7}$ were found to exhibit enhanced water solubility compared to the non-functionalised bis-pyridyl ligand scaffold, all the ligands were self-assembled into their corresponding metallacages ($\mathbf{C_{aq}1\text{-}7}$, scheme 5). As the only reported water soluble Pd_2L_4 (L = 1,3-bis(pyridin-3-ylethynyl)pyridine) metallacage was formed using nitrate as the counterion,[135] we selected this anion for the cage synthesis. Thus, the metallacages $\mathbf{C_{aq}1\text{-}7}$ were synthesised via self-assembly in DMSO by stirring the corresponding ligand, $\mathbf{L_{aq}1\text{-}7}$, and stoichiometric amounts of palladium(II)nitrate pentahydrate (1: 2, Pd^{II}: L) for 1 hour at room temperature (scheme 5). The metallacages were isolated first by precipitation using diethyl ether and acetone followed by filtration. Afterwards, the products were fully characterised using NMR (^{1}H, ^{13}C) and HR-ESI-MS. Thus, the solubility of the metallacages $\mathbf{C_{aq}1\text{-}7}$ was tested by sonicating the sample in D_2O overnight at 40°C, before filtering through a 450 µm filter and analysing the filtrate by ^{1}H NMR spectroscopy. Disappointingly, none of the formed Pd_2L_4 metallacages exhibited any discernible water solubility as no trace of the proton signals could be observed in the resulting ^{1}H NMR spectra.

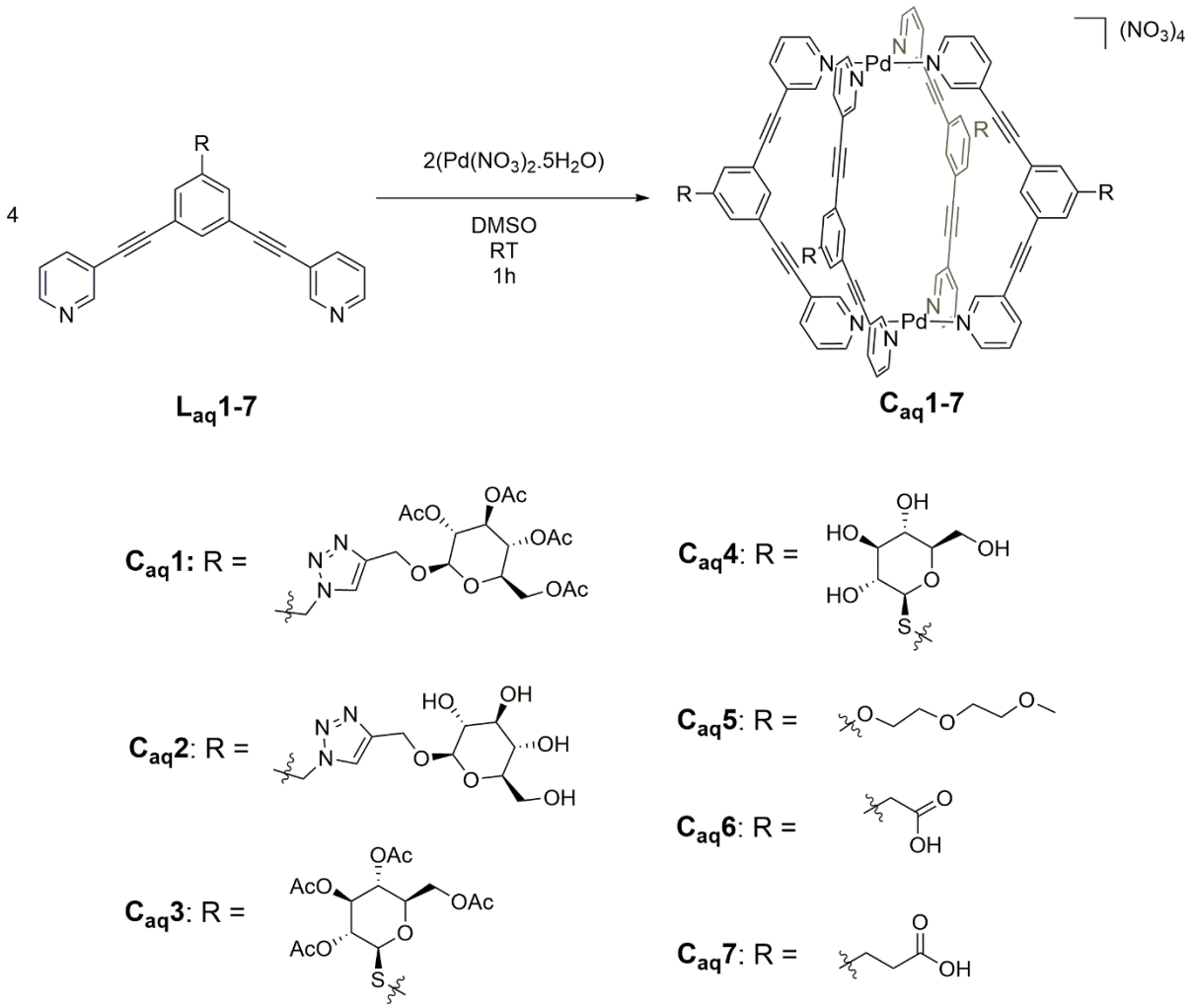

Scheme 5: Synthesis of metallacages **C_{aq}1-7** from the corresponding ligands **L_{aq}1-7** via self-assembly by the stoichiometric introduction of Pd(II)nitrate pentahydrate (1: 2; Pd^{II}: L) in DMSO.

8.2.2 Counterion exchange of Pd_2L_4 metallacages

Another strategy that has been employed in order to improve water solubility of poorly soluble, charged complexes is to alter the counterion.[247] An obvious consideration in the selection of counterion for charged metallacages with potential applications in biology is the biocompatibility of the counterion.[248] However, another more subtle consideration is the resulting geometry of the metallacage. The geometry of metallacages is primarily dictated by the coordinating metal ions coordination sphere and the design of the ligand scaffold.[74,81,161] For example, Amouri and coworkers have reported that tetrafluoroborate can act as a weakly coordinating anion for a Co_2L_4 type metallacage.[144] The counterion was shown to be encapsulated within the metallacage cavity by X-ray diffraction studies and thus, act as a template to dictate the resulting shape of the metallacage.[144] Further examples of encapsulated anions acting as templates of their cationic metallacages have also been reported.[81,162]

Crowley and coworkers have reported a comprehensive investigation into the *exo*- and *endo*-hederal effect of weakly-coordinating, pharmaceutically acceptable counterions (tetrafluoroborate, BF_4^-; nitrate, NO_3^-; triflate, OTf^-; mesylate, OMs^-; and tosylate, OTs^-) on Pd_2L_4 type metallacages (L = 2,6-bis(pyridine-3-ylethynyl)pyridine). The effect of the counterion on the resulting Pd_2L_4 metallacage structure was studied via ^1H NMR in DMSO-d_6 and single crystal X-ray diffraction (from crystals grown in either DMSO or DMF).[238] It was shown that only the nitrate and mesylate counterions were shown to be encapsulated, despite the cavity being large enough to accommodate several other counterions studied.[238] It was suggested that for the fluorine containing counterions (BF_4^- and OTf^-), the electrostatic repulsion of the cavity facing lone electron pairs may cause the encapsulation to be unfavourable, while for the larger, aromatic tosylate counterion steric hinderance, along with electrostatic repulsion, may be the cause for the anion to not be encapsulated. It was also shown by ^1H NMR and X-ray diffraction that that the choice of counterion did not alter the resulting geometry of the Pd_2L_4 metallacage.[238] However, disappointingly none of the counterions were shown to improve the water solubility of the resulting metallacage, which suggests that the choice of counterion does not have a strong effect on the resulting water solubility of Pd_2L_4 metallacages.

Crowley and coworkers have also studied the effect of the coordinating counterion chloride.[148] The study reported the degradation of the Pd_2L_4 (L = 2,6-bis(pyridine-3-ylethynyl)pyridine based ligand scaffold) to a $Pd_2L_2Cl_4$ macrocycle and non-coordinated ligand upon introduction of an excess of $[NBu_4]Cl$ to the metallacage in DMF-d_7. Although the study suggested that this degradation may be a viable guest release mechanism for a Pd_2L_4 based drug delivery system, it was conclusive proof that chloride was not appropriate to use as a counterion for Pd_2L_4 metallacages.[148]

Similarly, the tetrafluoroborate anion (BF_4^-), which is typically used to form Pd_2L_4 metallacages,[99,127,132,133,135,136,146] is not ideal for improving water solubility. Tetrafluoroborate is a small, hard anion with a symmetrical tetrahedral geometry. As such, the negative charge associated with it is evenly distributed over the molecule, which results in the stable and unreactive nature of tetrafluoroborate. Although this is desirable in many ways for a counterion of a metallacage species, and that tetrafluoroborate salts often exhibit reasonable solubility in polar organic solvents, the solubility of tetrafluoroborate salts is often poor in aqueous media. To this end, salts formed with the trigonal planar nitrate ion, which consists of electron dense oxygen atoms and a tetravalent, electron deficient nitrogen may improve the solubility of cationic species in aqueous media,[238,248] and thus may be employed to improve the solubility of Pd_2L_4 type metallacages. However, as discussed in section 8.2.1, the metallacages $\mathbf{C_{aq}1\text{-}7}$ were

formed featuring nitrate as the counterion, but unfortunately none of them exhibited solubility in D_2O.

Acetate has been reported to drastically improve the aqueous solubility of a class of Au(I) pillarplex type supramolecular coordination complexes.[246] The scaffold of the Au(I) pillarplex complex is considerably different from the Pd_2L_4 metallacages use in this study, with different transition metals of both different coordination geometry and oxidation state used, as well as different coordinating ligand entities, and considerably different final morphologies. In fact, Au(I) pillarplexes form open ended "hour glass" type architectures,[246] (whereas Pd_2L_4 metallacages form closed, "lantern shaped" type architectures, scheme 5).[64] Remarkably, the aqueous solubility of the Au(I) pillarplexes featuring acetate counerions reached over 1 g/mL.

In an attempt to apply the same strategy to our cages, ligands $\mathbf{L_{aq}1\text{-}7}$ were reacted in stoichiometric amounts with Pd(II)acetate (1: 2, Pd^{II}: L) in DMSO for 1 hour at room temperature. Unlike previous examples of metallacage self-assembly, a dark precipitate formed over the first 30 min for each ligand and Pd(II)acetate mixture. This precipitate was isolated for characterisation, but unfortunately could not be dissolved in any common laboratory solvents. Indeed, it was found that the precipitate could only be dissolved by the use of concentrated mineral acids such as HCl or HNO_3. The self-assembly process was also carried out in DMF under the same conditions as before, to assess whether DMSO was responsible for the formation of the insoluble dark precipitate upon mixing Pd(II)acetate and ligands $\mathbf{L_{aq}1\text{-}7}$. However, the same results were observed whereby a dark precipitate formed within the first 30 min in each case. This precipitate could also be isolated but not dissolved in any common laboratory solvents but was dissolved by the use of the concentrated mineral acids HCl and HNO_3.

8.3 Summary and conclusions

With the aim to improve the water solubility of Pd_2L_4 metallacages to primarily facilitate encapsulation studies of cisplatin in water (for example *via* ^{1}H NMR spectroscopy or isothermal titration calorimetry), different exo-functionalized 1,3-bis(pyridin-3-ylethynyl)benzene based ligands were synthesised and characterised. ^{1}H NMR spectroscopy showed that two of them, featuring carboxylic acid groups separated from the highly conjugated and aromatic ligand scaffold *via* alkyl spacer moieties, $\mathbf{L_{aq}6}$ (2-(3,5-bis(pyridin-3-ylethynyl)phenyl)acetic acid) and $\mathbf{L_{aq}7}$ (3-(3,5-bis(pyridin-3-ylethynyl)phenyl)propanoic acid), are sufficiently water soluble. Unfortunately, none of the ligands formed water soluble Pd_2L_4 type metallacages when nitrate was employed as the counterion. Furthermore, attempts to improve the water solubility using

acetate as the counterion were not successful and only achieved a dark precipitate that would not dissolve in any common laboratory solvents.

In any case, the solubility of Pd_2L_4 metallacages could be sufficiently improved by the *exo*-functionalisation of tumour targeting peptides for the envisioned future application as a drug delivery system (see chapters 5 and 6). As such, the poor solubility of the core Pd_2L_4 metallacage was not investigated further in this project. E*xo*-functionalisation at both terminal coordinating pyridyl rings of the ligand may be attempted to sufficiently improve aqueous solubility.

Chapter 9 Encapsulation of the anti-cancer drug cisplatin in self-assembled Pd_2L_4 metallacages

9.1 Introduction

Crowley and co-workers initially used SPARTAN molecular force field (MFF) energy minimised molecular modelling to show that cisplatin could be encapsulated within the cavity of a Pd_2L_4 metallacage.[99] In the study, it was also hypothesised that in order to stabilise the host-guest complex, $[(cisplatin)_n \subset Pd_2L_4]$, favourable interactions between the drug and the functional group present in the host cavity should be present. As such, a Pd_2L_4 (L = 2,6-bis(pyridin-3-ylethynyl)pyridine; *tris-pyridyl ligand*) metallacage was synthesised featuring an internal cavity lined with electron pairs, at the endo-nitrogen atom, which would improve favourable H-bonding interactions between the metallacage and cisplatin itself (figure 1).

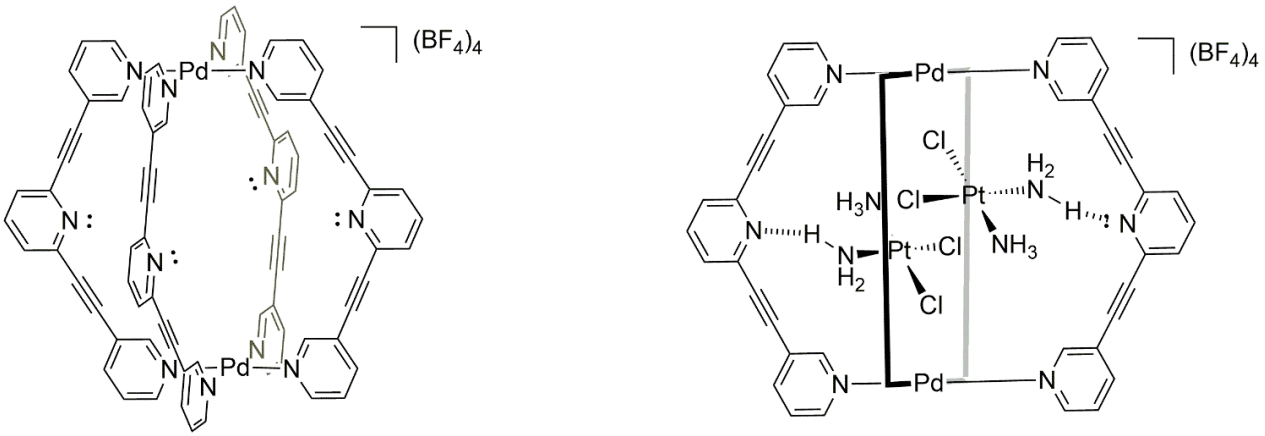

Figure 1. Chemical structure of the Pd_2L_4 (L = 2,6-bis(pyridin-3-ylethynyl)pyridine) used to first study the encapsulation of cisplatin.[99] **Left**: Full chemical structure highlighting the cage central cavity endo-functionalized with N donors. **Right**: Simplified drawing of the metallacage highlighting the hydrogen-bonding interactions between the lone electron pairs and the amine groups of cisplatin.

Unfortunately, the validation of the drug encapsulation was hampered by the extremely modest solubility of the Pd_2L_4 metallacages and cisplatin in most common organic solvents, and almost complete lack of solubility of the metallacage in water. Furthermore, as the introduction of cisplatin to the metallacage caused no observable change to the overall absorption/emission properties of the metallacage, studying the encapsulation of cisplatin *via* UV-vis and fluorescence spectroscopy was not feasible. Therefore, ^{1}H NMR was employed to monitor the small shifts in peak position of the metallacage upon encapsulation of cisplatin. The metallacage was found to be suitably soluble in acetonitrile-d_3, DMSO-d_6 and DMF-d_7 . The obtained results showed that encapsulation studies carried out in DMSO-d_6 were unsuccessful as this solvent

caused disruption to the H-bond interactions between the host metallacage and guest cisplatin due to the two H-bond acceptor sites.[99] In acetonitrile-d_3 the cavity facing proton peak (H_a, Figure 2) underwent a downfield shift ($\Delta\delta$ = ~0.11 ppm) and peak broadening, indicative of guest binding within the metallacage. The *exo*-facing proton peak H_b adjacent to the coordinating nitrogen of the ligand, was also shown to undergo a slight downfield shift upon introduction of cisplatin ($\Delta\delta$ = 0.05 ppm). No other peaks were shown to undergo a chemical shift upon cisplatin addition, which further supported the idea that the small downfield shifts observed were due to interactions between cisplatin and the cavity of the tris-pyridyl ligand-based metallacage. High resolution electrospray ionization mass spectrometry (HR-ESI-MS) was also used to provide evidence of cisplatin encapsulation, showing signals for two host-guest complexes corresponding to the encapsulation of one or two equivalents of cisplatin.[99] To establish the importance of the cavity facing lone electron pairs on the encapsulation of cisplatin, the same group synthesised the analogous Pd_2L_4 (L = 1,3-bis(pyridine-3-ylethynyl)benzene; *bis-pyridyl ligand*) metallacage and studied the encapsulation of cisplatin in acetonitrile-d_3.[99] It was found that there was no shift in any of the cage's peak positions upon addition of cisplatin in acetonitrile-d_3, and as such the cavity facing lone electron pairs were believed to be instrumental for guest encapsulation *via* functional group based host-guest interactions.

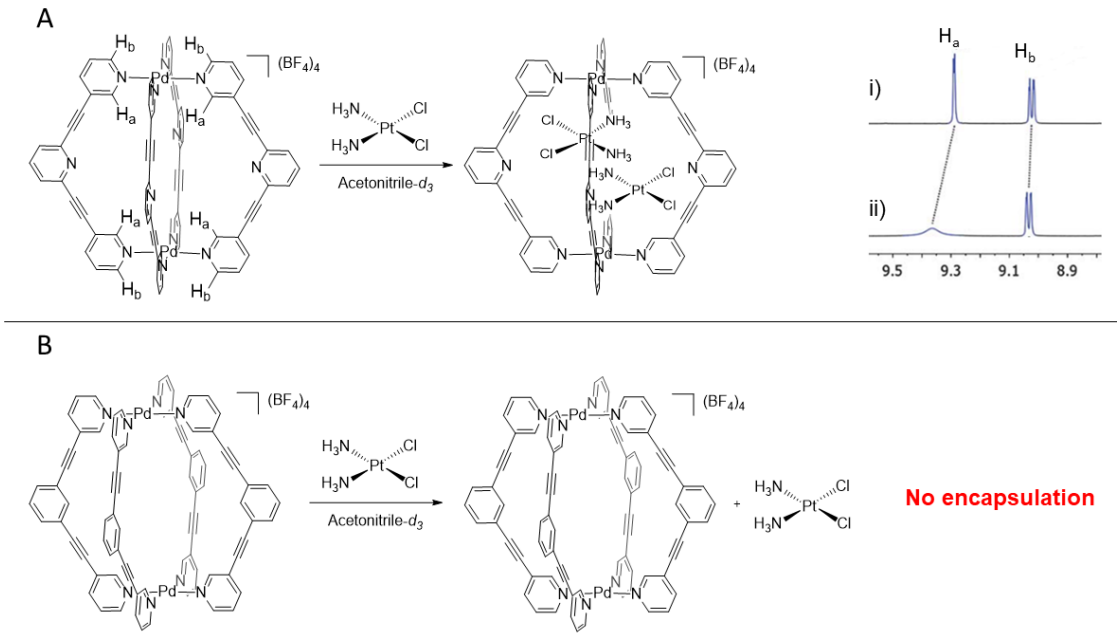

Figure 2. Encapsulation of cisplatin as reported by Crowley and coworkers.[99] **A**: Scheme of successful cisplatin encapsulation in acetonitrile-d_3 and excerpt from the reported ^{1}H NMR spectrum showing: i) Tris-pyridyl ligand-based cage alone; ii) cage with two equiv.of cisplatin. The downfield shift of both the *endo*-facing proton (H_a, $\Delta\delta$ = ~0.11 ppm) and the *exo*-facing proton (H_b, $\Delta\delta$ = 0.05 ppm). **B**: Scheme highlighting that no encapsulation of cisplatin was observed for the bis-pyridyl ligand-based cage in acetonitrile-d_3.

Crowley and coworkers continued to study the exact nature of the host-guest complex for the *tris-pyridyl* based-cage in the solid state via single crystal XRD studies of [(cisplatin)$_2$⊂Pd$_2$L$_4$] (L = 2,6-bis(pyridin-3-ylethynyl)pyridine based ligands) grown by vapour diffusion of diethyl ether into a solution of [(cisplatin)$_2$⊂Pd$_2$L$_4$] in 1: 1 DMF: acetonitrile.[99] The XRD results showed that two molecules of cisplatin were encapsulated within the Pd$_2$L$_4$ metallacage, and that these complexes were stabilised by favourable host-guest interactions such as H-bonding between the cavity facing electron pairs and the hydrogen of the amine groups coordinated to cisplatin (figure 3).[99] The study also showed that the acidic, *endo*-facing protons adjacent to the coordinating nitrogen of the terminal pyridine rings were engaged in H-bonding with the chloride ligands of cisplatin, further stabilising the encapsulation.

Finally, the importance of the H-bonding interactions between the metallacage and cisplatin by introducing D$_2$O to the acetonitrile-*d$_3$* solution of [(cisplatin)$_2$⊂Pd$_2$L$_4$] and comparing the position of the cavity facing proton peaks was investigated.[99] It was found that upon introduction of D$_2$O, the two proton peaks affected by the encapsulation of cisplatin were shifted back upfield, and the cavity facing proton peak became sharper. This evidence supported the evacuation of cisplatin from the cavity upon introduction of D$_2$O and this effect was hypothesised to be due to the D$_2$O forming stronger H-bonds with the cavity facing lone electron pairs of the pyridyl nitrogen in the *endo* position. Due to the preference of D$_2$O to occupy the cage cavity of the *tris-pyridyl* ligand-based metallacage in acetonitrile-*d$_3$*, the authors concluded that Pd$_2$L$_4$ type metallacages are in general unsuitable for drug delivery due to the preference to encapsulate water over cisplatin.[99]

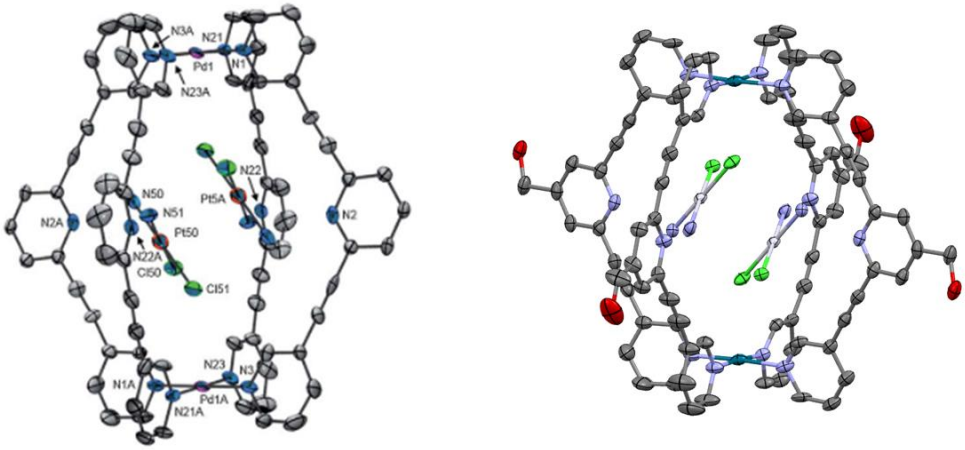

Figure 3. Single crystal XRD structures of tris-pyridyl based Pd$_2$L$_4$ metallacages encapsulating two equivalents of cisplatin. **Left**: Resolved crystal structure reported by the Crowley group (Grey: carbon; Blue: nitrogen; Green: chloride; orange: platinum; purple: palladium).[99] **Right**: Resolved crystal structure reported by Casini and coworkers (Grey: carbon; Blue: nitrogen; Green: chloride; Silver: platinum; Teal: palladium; Red: oxygen).[127]

A more recent study of the encapsulation of cisplatin within Pd_2L_4 metallacages has been reported by Casini and coworkers where L was (3,5-bis(pyridin-3-ylethynyl)phenyl)methanol or (2,6-bis(pyridin-3-ylethynyl)pyridin-4-yl)methanol.[127] The study was largely concurrent with the results of the Crowley group, with a similar single crystal XRD experiment showing the same 1:2 stoichiometry of the metallacage: cisplatin adduct when the tris-pyridyl ligand scaffold is used (figure 3). Furthermore, our group carried out the ^{1}H NMR encapsulation experiment in DMF-d_7 using the bis-pyridyl ligand scaffold, 3,5-bis(pyridin-3-ylethynyl)phenyl)methanol.[127] It should be noted that the bis-pyridyl ligand-based metallacage lacks any cavity facing electron pairs, or other hydrogen bond acceptor functional groups, and yet exhibited a downfield shift of the peak corresponding to the cavity facing proton peak adjacent to the coordinating nitrogen of the ligand ($\Delta\delta$ = 0.06 ppm), albeit smaller than the chemical shift reported by Crowley and co-workers. Of note, as the central phenyl ring also has a cavity facing proton, this peak could be analysed and was shown to undergo a small upfield shift ($\Delta\delta$ = -0.04 ppm) and peak broadening upon introduction of 2 equiv. of cisplatin to a DMF-d_7 solution of the metallacage. It was also noticed that, unlike the metallacage with the constituent tris-pyridyl ligand, the Pd_2L_4 metallacage with the bis-pyridyl ligand forms a host-guest complex that appeared to be stable in the presence of water for at least 72 hours.[127]

The ability of Pd_2L_4 metallacages (L = bis-pyridyl ligand scaffold) to encapsulate cisplatin in DMF-d_7 has since been supported by a subsequent report that highlighted the slight shift in peak position of the cavity facing proton peaks in the ^{1}H NMR spectra of the metallacage and host-guest complex.[134] However, as the shift in peak position is relatively small ($\Delta\delta$ < 0.5 ppm) and is often accompanied by broadening of the signal, elucidating data such as the binding affinity and the stoichiometry in solution of the host: guest system is not feasible. Overall, although it has been demonstrated that Pd_2L_4 metallacages can encapsulate the anticancer drug cisplatin, there has not been quantitative data reported for the host-guest complex in solution, but only when formed in the solid state *via* resolved single crystal XRD structures of [(cisplatin)$_2\subset Pd_2L_4$].[99,127] In both cases the Pd_2L_4 metallacages were formed from tris-pyridyl-based ligands. The cavity facing lone electron pairs of the tris-pyridyl ligand, which can act as H-bond acceptor sites to stabilise the host-guest complex (cisplatin)$_2\subset Pd_2L_4$), preferentially form H-bonds with water rather than cisplatin. and thus, replace cisplatin as the guest. Conversely, preliminary ^{1}H NMR data show that Pd_2L_4 metallacages with a more 'hydrophobic' cavity (bis-pyridyl-based scaffold) may be suitable as a future drug delivery system.[127,134] However, further studies are necessary to fully validate this hypothesis.

9.2 Host-guest interactions of Pd_2L_4 metallacages

As mentioned above, Pd_2L_4 metallacages (L = 2,6-bis(pyridin-3-ylethynyl)benzene based ligands; bis-pyridyl ligands) have no reported quantitative data demonstrating the formation of [(cisplatin)$_2$⊂Pd_2L_4] host-guest complexes, either in solution or in the solid state. However, in DMF-d_7, the ^{1}H NMR spectra show chemical shifts in peak position of the cavity facing proton peak which are analogous to those of Pd_2L_4 metallacages formed from tris-pyridyl ligands, which suggests that there is encapsulation of cisplatin despite the lack of formal H-bond acceptor sites to stabilise the host-guest complex. This may suggest that either subtle changes to the electron density of the cavity facing proton (achieved by *exo*-functionalisation of the ligand with suitable electron donating or withdrawing groups) is enough to stabilise cisplatin within the Pd_2L_4 metallacage cavity, without providing a formal functional group able to form strong hydrogen bonds with competing water, or that there is a different mechanism of encapsulation between Pd_2L_4 metallacages formed from bis-pyridyl ligands compared to cages based on tris-pyridyl ones. In order to elucidate the encapsulation mechanisms, several hypotheses were explored in this thesis work, as detailed in the sections below, according to which various non-specific supramolecular interactions could be responsible for the stabilisation of cisplatin within these Pd_2L_4 metallacages.

9.2.1 Altering the electron density of the metallacage cavity via *exo*-functionalisation

As previous studies suggested that a H-bond acceptor site facing the cavity is needed for encapsulation of cisplatin, but yet similar behaviour is observed for cisplatin encapsulation in Pd_2L_4 metallacages with no formal H-bond acceptor site within the cavity, it was hypothesised that merely altering the electron density of the central ring lining the metallacage cavity may be sufficient to stabilise the guest drug. This effect could be achieved by the introduction of an appropriate electron withdrawing group (EWG), or electron donating group (EDG) in the central phenyl ring of the metallacage. The EDG or EWG would alter the electron density at the *para*-position with respect to the *exo*-functionalised group, which corresponds to the central, cavity facing proton of the subsequent metallacage. The effect of the encapsulation of cisplatin by altering the electron density could then be monitored by ^{1}H NMR spectroscopy.

As such the *exo*-functionalized ligands reported in scheme 1 were synthesized, $\mathbf{L^{E1}}$ (EWG), $\mathbf{L^{E2}}$ (EDG), as well as the non-functionalised ligand ($\mathbf{L^{E3}}$) with the aim of altering the electron density around the *endo*-facing group of the central aromatic ring. It is worth noting

that for ligand $\mathbf{L^{E1}}$ the *exo*-functionalised carboxylic acid group (EWG) was protected with a benzyl group in order to improve the solubility of the resulting metallacage ($\mathbf{C^{E1}}$) in DMF-d_7.

The *tris-pyridyl* ligand, $\mathbf{L^{E4}}$, was also synthesised to synthesize the corresponding cage, with the cavity *endo*-functionalized with nitrogen lone pairs to facilitate H-bonding.

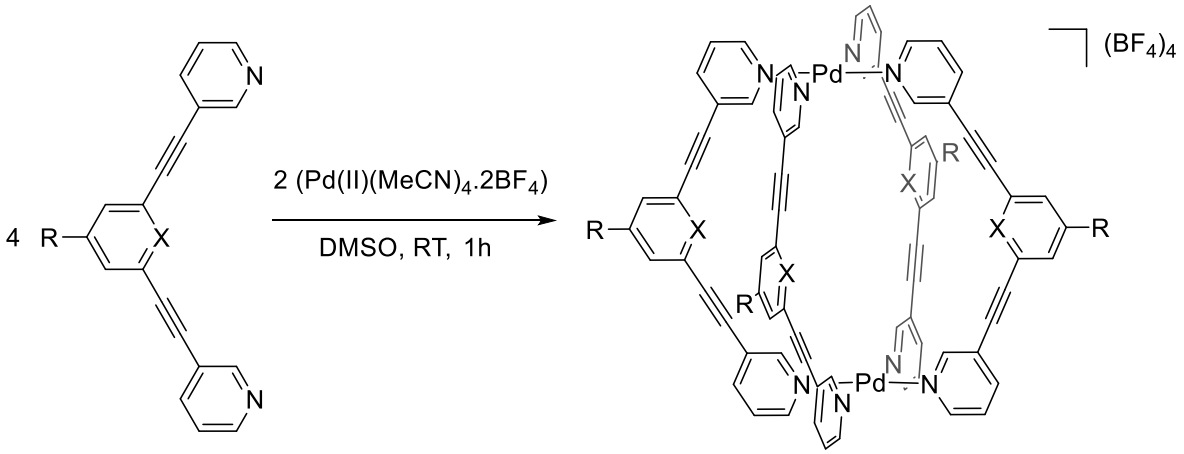

$\mathbf{L^{E1}}$: R = COOBn X = CH
$\mathbf{L^{E2}}$: R = NH_2; X = CH
$\mathbf{L^{E3}}$: R = H X = CH
$\mathbf{L^{E4}}$: R = H X = N

$\mathbf{C^{E1}}$: R = COOBn X = CH
$\mathbf{C^{E2}}$: R = NH_2; X = CH
$\mathbf{C^{E3}}$: R = H X = CH
$\mathbf{C^{E4}}$: R = H X = N

Scheme 1. Self-assembly of metallacages $\mathbf{C^{E1\text{-}4}}$ from the precursor ligands $\mathbf{L^{E1\text{-}4}}$ with labelled *exo*-functionalised R groups, and *endo*-X groups.

The synthesis of $\mathbf{L^{E1}}$, $\mathbf{C^{E1}}$, $\mathbf{L^{E2}}$ and $\mathbf{C^{E2}}$ have been described previously (*chapter 5* and *chapter 7* respectively). $\mathbf{L^{E3}}$ was designed to be "neutral", with no *exo*-functional group and no *endo*-facing functionality, whereas $\mathbf{L^{E4}}$ has no *exo*-facing functional group but features a central pyridine ring to facilitate H-bond interactions. The synthesis of $\mathbf{L^{E3}}$ and $\mathbf{L^{E4}}$ was achieved *via* Sonogashira cross coupling between either 1,3-dibromobenzene ($\mathbf{L^{E3}}$) or 3,5-dibromopyridine ($\mathbf{L^{E4}}$), and 3-ethynylpyridine in the presence of $[Pd(PPh_3)_2Cl_2]$ and CuI in triethyl amine at 90°C for 48 hours. Afterward, the various metallacages, $\mathbf{C^{E1}}$-$\mathbf{C^{E4}}$, were formed *via* self-assembly by introduction of 2 equiv. of $[Pd(MeCN)_4](BF_4)$ to four equiv. of the respective ligands (scheme 2) according to previously reported procedures.[99,132,133]

9.2.2 Effect of counterion on Pd_2L_4 type metallacages

It has been previously shown that the tetrafluoroborate counterion is not encapsulated within $\mathbf{C^{E4}}$ in DMSO-d_6, as evidenced by ^{19}F NMR studies in solution,[238] whereby the ^{19}F signal for $\mathbf{C^{E4}}$ corresponded to that of free BF_4^-, which strongly suggests that the counterion is not encapsulated within the cage, but is loosely associated with the *exo*-face of the metallacage in solution.[238] In addition, single crystal XRD studies showed that although the exact location of the BF_4^- counterions could not be resolved it could be proved that they were not encapsulated within

the cavity.[238] It was suggested that this was due to electrostatic repulsion of the *endo*-facing lone electron pairs from the central pyridine ring of $\mathbf{C^{E4}}$. However, as metallacages $\mathbf{C^{E1-3}}$ do not feature lone electron pairs facing the cage cavity, the BF_4^- counterion may be encapsulated by these metallacages. In fact, previous studies by Lusby and coworkers suggested that for bis-pyridyl ligand-based cages, which indicates that the stronger coordinating anions, including OTf^- and BF_4^-, are likely to reside within the cavity of the cage in CD_3NO_2.[249]

In our case, the ^{19}F NMR spectra of metallacages $\mathbf{C^{E1-4}}$ in DMSO-d_6 showed one environment per cage (a large peak corresponding to $^{11}B^{19}F_4$ and a smaller peak corresponding to $^{10}B^{19}F_4$), between δ = -149.8 and -150.4 ppm (Figure 4). The chemical shift range is in accordance with free BF_4^- and one signal suggests that the counterion either does not enter the cavity, or if it does enter the cage cavity it disassociates fast enough to not be resolved within the NMR timeframe at the temperature of the experiment.

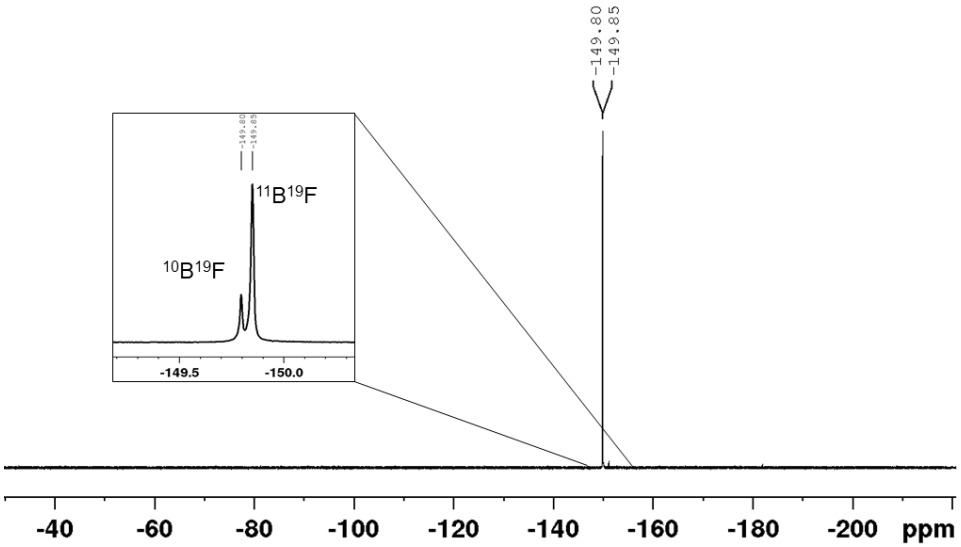

Figure 4: Representative ^{19}F NMR spectrum for cage $\mathbf{C^{E1}}$ DMSO-d_6

Conversely, it has been demonstrated via ^1H NMR that the nitrate counterion (NO_3^-) is encapsulated in the metallacage cavity of Pd_2L_4 (L = 2,6-bis(pyridin-3-ylethynyl)pyridine) metallacages in DMSO-d_6.[238] The study used the metallacage analogous to $\mathbf{C^{E4}}$, with the tris-pyridyl based ligand but with a nitrate counterion ($\mathbf{C^{E4}.NO_3}$). The study concluded that counterion binding inside the cavity is not as strong when the cavity of the cage is lined with electron donor groups due to electrostatic repulsion,[238] although NO_3^- (along with mesylate)[238] were found to be encapsulated within the cage cavity. It can thus be hypothesised that counterion encapsulation could be stronger within $\mathbf{C^{E1-3}}$ used in this study due to the lack of the *endo*-facing N. Therefore, it may be anticipated that our cages may prefer encapsulation of the counterion over the neutral cisplatin molecule. In order to validate this hypothesis, a new series of metallacages analogues of $\mathbf{C^{E1-4}}$ were synthesised ($\mathbf{C^{E1}.NO_3}$, $\mathbf{C^{E2}.NO_3}$, $\mathbf{C^{E3}.NO_3}$ and $\mathbf{C^{E4}.NO_3}$) with nitrate as counterion using palladium(II)nitrate dihydrate as the precursor for the self-assembly.

The ^{1}H NMR results for the bis-pyridyl ligand based metallacage were concurrent with the previously reported study,[238] whereby the distance between peaks H_a and H_b was larger for the metallacages $\mathbf{C^{E1\text{-}3}.NO_3}$ compared to metallacages $\mathbf{C^{E1\text{-}3}}$, and both peaks were further downfield for $\mathbf{C^{E1\text{-}3}.NO_3}$ compared to $\mathbf{C^{E1\text{-}3}}$ (figure 5 and table 1). The shift of the proton peaks adjacent to the coordinating nitrogen of the ligand indicates counterion encapsulation, which is responsible for pushing the signal of the *endo*-facing proton H_a downfield (figure 5). Furthermore, for metallacages $\mathbf{C^{E1\text{-}3}.NO_3}$, the *endo*-facing proton H_e also exhibited a downfield shift, albeit smaller than that of the *endo*-facing proton H_a (table 1). Surprisingly, the tris-pyridyl ligand based metallacages, $\mathbf{C^{E4}}$ and $\mathbf{C^{E4}.NO_3}$, did not show as prominent chemical shift differences between the spectra (figure 6, table 1), suggesting that the counterion is not encapsulated due to the electrostatic repulsion between the anion and the lone electron pairs of the constituent ligand in DMF-d_7. As the Crowley group have shown that the NO_3^- counterion is encapsulated within the cage cavity for $\mathbf{C^{E4}.NO_3}$ in DMSO-d_6,[238] this result strongly suggests that the solvent plays a crucial role in counterion encapsulation.

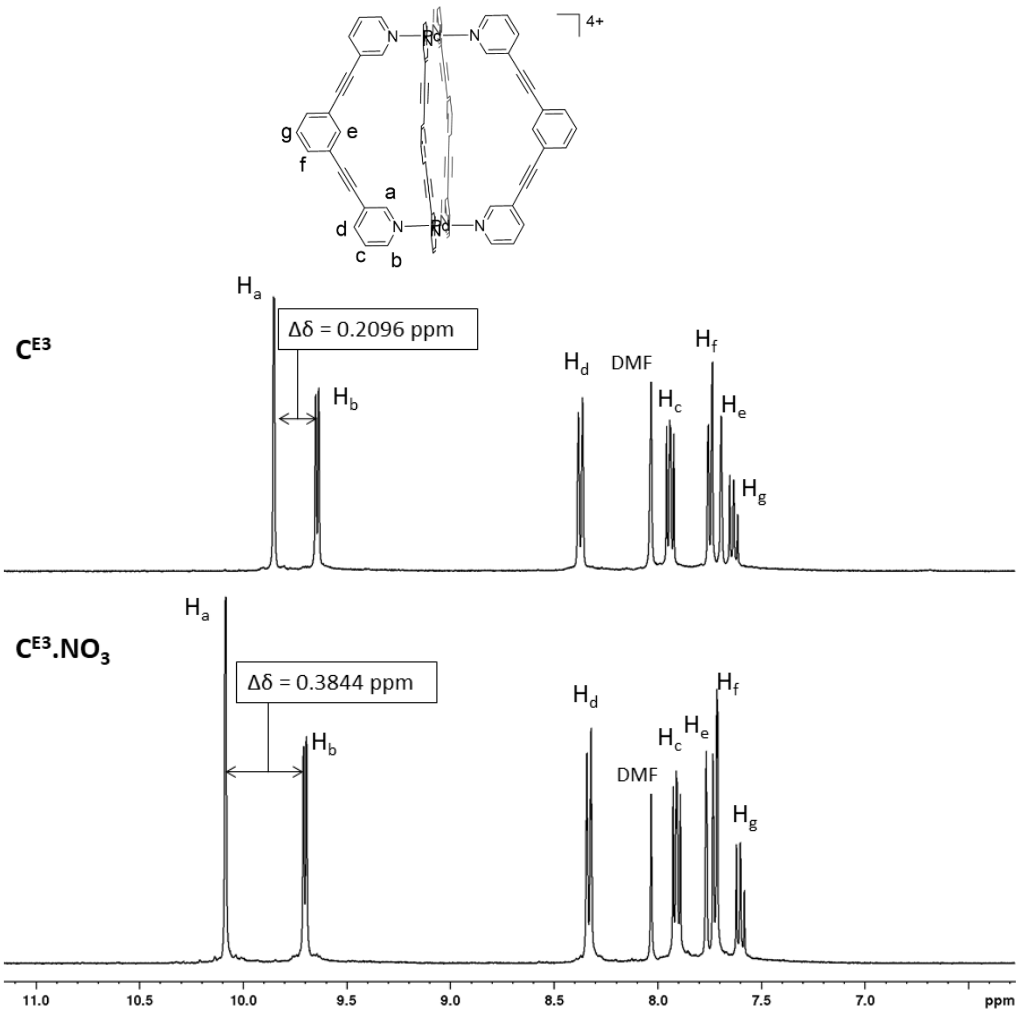

Figure 5. Stacked ^{1}H NMR spectra of **C^{E3}** (top) and **C^{E3}.NO$_3$** (bottom) in DMF-*d*$_7$. The figure shows the larger Δδ ppm between proton H_a and H_b of **C^{E3}.NO$_3$** compared to **C^{E3}**, which is concurrent with reported studies that NO_3^- is encapsulated within the cage cavity. This is also observed between the bis-pyridyl ligand based metallacages **C^{E1}** and **C^{E1}.NO$_3$**, as well as **C^{E2}** and **C^{E2}.NO$_3$**, but not between the tris-pyridyl ligand based **C^{E4}** and **C^{E4}.NO$_3$**. On top, the **C^{E3}.X** metallacage scaffold with the proton peaks labelled H_a-H_g. This peak labelling system will be used throughout the chapter when describing the chemical shifts of the *endo*- (H_a and H_e) and *exo*-facing protons (H_b, H_c, H_d, H_f, H_g).

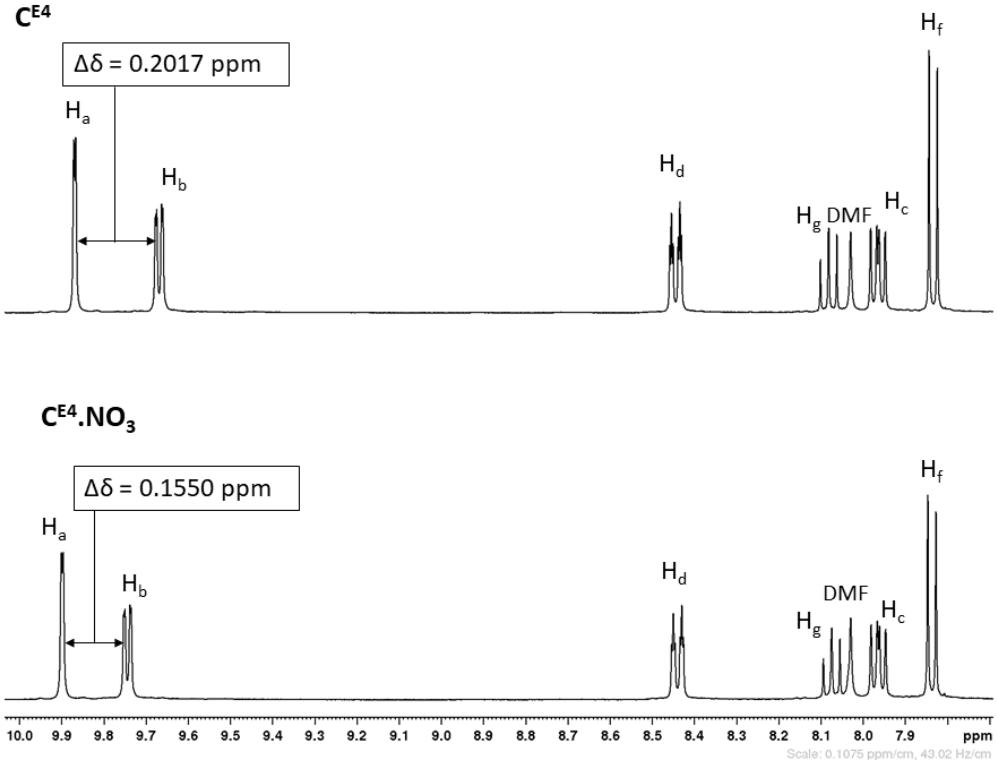

Figure 6 Stacked ^{1}H NMR spectra of $\mathbf{C^{E4}}$ (top) and $\mathbf{C^{E4}.NO_3}$ (bottom) in DMF-d_7, with a smaller Δδ ppm of $\mathbf{C^{E4}.NO_3}$ compared to $\mathbf{C^{E4}}$. This is due to the downfield shift of H_b for $\mathbf{C^{E4}.NO_3}$ compared to $\mathbf{C^{E4}}$ (Δδ = 0.0765 ppm) paralleled by a smaller downfield shift of the cavity facing proton peak, H_a, (Δδ = 0.0297 ppm), indicative of no NO_3^- encapsulation.

Table 1: Comparison of chemical shifts of the protons of metallacages $\mathbf{C^{E1\text{-}4}}$ with $\mathbf{C^{E1\text{-}4}.NO_3}$

	Δδ ppm						
	H_a	H_b	H_c	H_d	H_e	H_f	H_g
$\mathbf{C^{E1}}$	9.8808	9.6606	7.9487	8.4441	7.8945	8.2371	N/A
$\mathbf{C^{E1}.NO_3}$	10.1075	9.7298	7.9246	8.4121	7.9434	8.2286	N/A
Δδ($\mathbf{C^{E1}.NO_3}$-$\mathbf{C^{E1}}$)	***0.2267***	***0.0692***	***-0.0241***	***-0.032***	***0.0489***	***-0.0085***	***N/A***
$\mathbf{C^{E2}}$	9.8180	9.6160	7.9016	8.3152	6.8226	6.9843	N/A
$\mathbf{C^{E2}.NO_3}$	10.0208	9.6464	7.8631	8.2681	6.9897	6.9617	N/A
Δδ($\mathbf{C^{E2}.NO_3}$-$\mathbf{C^{E2}}$)	***0.2028***	***0.0304***	***-0.0385***	***-0.0471***	***0.1671***	***-0.0226***	***N/A***
$\mathbf{C^{E3}}$	9.8180	9.6426	7.9379	8.3718	7.6922	7.7461	7.6317
$\mathbf{C^{E3}.NO_3}$	10.0850	9.7007	7.9066	8.3307	7.7642	7.7214	7.5993
Δδ($\mathbf{C^{E3}.NO_3}$-$\mathbf{C^{E3}}$)	***0.2670***	***0.0581***	***-0.0313***	***-0.0411***	***0.0720***	***-0.0247***	***-0.0324***
$\mathbf{C^{E4}}$	9.8695	9.6682	7.9655	8.4451	N/A	7.8342	8.0827
$\mathbf{C^{E4}.NO_3}$	9.8992	9.7447	7.9644	8.4409	N/A	7.8373	8.0752
Δδ($\mathbf{C^{E4}.NO_3}$-$\mathbf{C^{E4}}$)	***0.0297***	***0.0765***	***-0.0011***	***-0.0042***	***N/A***	***0.0031***	***-0.0075***

Unfortunately, a single crystal XRD structure has not been obtained to provide insight into the exact location of the NO_3^- counterion within Pd_2L_4 metallacages. However, the nature of NO_3^- encapsulation may be elucidated from the ^{1}H NMR data in DMF-d_7. As the signals for all the proton peaks are sharp and well resolved for metallacages $\mathbf{C^{E1-3}}$, it can be presumed that the metallacages maintain their D_{4h} point group symmetry, which would imply that the nitrate encapsulation maintains this symmetry. The chemical shifts are not significantly different between $\mathbf{C^{E1-4}}$ and $\mathbf{C^{E1-4}.NO_3}$ for the *exo*-facing proton peaks, although for cages $\mathbf{C^{E1-3}.NO_3}$ there was slight upfield shifts of these peaks when compared to their corresponding $\mathbf{C^{E1-3}}$ metallacages, which suggests that NO_3^- does not interact significantly with the *exo*-facing protons of the metallacage. Similarly, the BF_4^- counterion has been shown to only loosely associate with the metallacage complex, as evidenced by both XRD and ^{19}F NMR spectroscopy studies.[238] However, downfield chemical shifts could be observed for protons H_a and H_b of cages $\mathbf{C^{E1-3}}$ and $\mathbf{C^{E1-3}.NO_3}$, as well as for the *endo*-facing proton H_e. Of note, the *endo*-facing proton peak H_a exhibits the most significant downfield shift in all cases ($\Delta\delta$ ~ 0.2 ppm, table 1).

Overall, the ^{1}H NMR data discussed suggests that the nitrate counterion is encapsulated within metallacages $\mathbf{C^{E1-3}.NO_3}$ in a manner that maintains D_{4h} point symmetry, whereby the counterion is in close proximity to both H_a, H_b, and to a lesser extent H_e. The downfield shift can be attributed to the repulsion of the counterion 'pushing' the electron density away from protons in close proximity to the counterion, thus de-shielding the nucleus. The proposed encapsulation of NO_3^- counterions in metallacages is shown in figure 7.

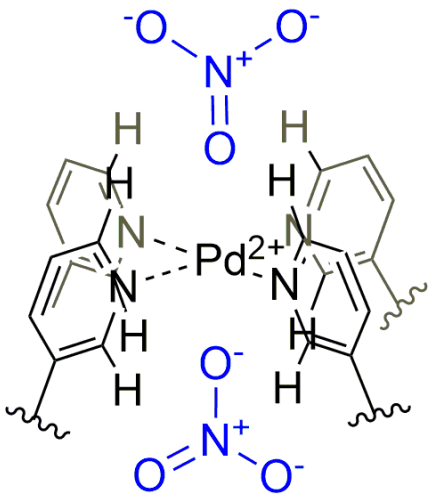

Figure 7: Cropped chemical structure showing one of the two coordinating Pd(II) centres. The proposed location of the nitrate counterions surrounding the coordinating Pd(II) within metallacages $\mathbf{C^{E1-3}.NO_3}$ is shown, which maintains the D_{4h} point symmetry and has the nitrate counterion in close proximity with protons H_a (*endo*- facing) and H_b (*exo*-facing).

9.2.3 Effect of *exo*-functionalization on Pd_2L_4 type metallacages

After having elucidated the possible interaction of the two counterions on the ^{1}H chemical shifts of the various cages, we proceeded with the observation of the effects of the *exo*-functionalization on the same signals. The electron density of the central aromatic ring of ligands $\mathbf{L^{E1-4}}$ and corresponding metallacages $\mathbf{C^{E1-4}}$ could be analysed by the position of the proton peaks of the central aromatic ring (H_e, H_f, H_g). Ligand $\mathbf{L^{E3}}$ was designed to be electron neutral. Therefore, the chemical shifts of the protons of the central phenyl ring, H_e, H_f and H_g, for ligands $\mathbf{L^{E1}}$, $\mathbf{L^{E2}}$, and $\mathbf{L^{E4}}$ could be compared to $\mathbf{L^{E3}}$ to determine if the electron density had increased (corresponding to an upfield shift) or decreased (downfield shift), respectively. Similarly, $\mathbf{C^{E3}}$ was used as a control to monitor the *endo*-facing proton, H_e, as well as the *exo*-facing protons, H_f and H_g, of the central aromatic ring of the ligand of cages $\mathbf{C^{E1}}$, $\mathbf{C^{E2}}$, and $\mathbf{C^{E4}}$. Table 2 summarizes the chemical shift of the protons of the *exo*-functionalised metallacages ($\mathbf{C^{E1}}$ and $\mathbf{C^{E2}}$) and the *endo*-functionalised metallacage ($\mathbf{C^{E4}}$) with respect to the non-functionalised metallacage ($\mathbf{C^{E3}}$) obtained in DMF-d_7.

Table 2: Comparison of the ^{1}H NMR peak position for functionalised metallacages $\mathbf{C^{E1}}$, $\mathbf{C^{E2}}$, and $\mathbf{C^{E4}}$ with respect to the non-functionalised metallacage, $\mathbf{C^{E3}}$ in DMF-d_7.

	Δδ (ppm)						
	H_a	H_b	H_c	H_d	H_e	H_f	H_g
$\mathbf{C^{E3}}$	9.8180	9.6426	7.9379	8.3718	7.6922	7.7461	7.6317
$\mathbf{C^{E1}}$	9.8808	9.6606	7.9487	8.4441	7.8945	8.2371	N/A
Δδ($\mathbf{C^{E1}}$-$\mathbf{C^{E3}}$)	***0.0628***	***0.018***	***0.0108***	***0.0723***	***0.2023***	***0.4910***	***N/A***
$\mathbf{C^{E2}}$	9.8180	9.6160	7.9016	8.3152	6.8226	6.9843	N/A
Δδ($\mathbf{C^{E2}}$-$\mathbf{C^{E3}}$)	**0**	**-0.0266**	**-0.0363**	**-0.0566**	**-0.8696**	**-0.7618**	**N/A**
$\mathbf{C^{E4}}$	9.8695	9.6682	7.9655	8.4451	N/A	7.8342	8.0827
Δδ($\mathbf{C^{E4}}$-$\mathbf{C^{E3}}$)	**0.0515**	**0.0256**	**0.0276**	**0.0733**	**N/A**	**0.0881**	**0.4510**

As expected, the electron deficient metallacage $\mathbf{C^{E1}}$, exhibited downfield chemical shifts for all the protons when compared to the electron neutral metallacage, $\mathbf{C^{E3}}$ (table 2). As expected, the electron density was shown to be the lowest for the proton peaks located on the central aromatic ring of the ligand scaffold ($\mathbf{C^{E1}}$ = H_e and H_f). This is shown by these peaks exhibiting the largest downfield shifts with respect to $\mathbf{C^{E3}}$ (table 2). The metallacage featuring the *exo*-EDG group NH_2, $\mathbf{C^{E2}}$, showed the opposite trend, whereby all the peaks exhibited upfield

chemical shifts (with the exception of H_a which displayed no chemical shift). Again, the largest chemical shifts were exhibited by the protons located on the central phenyl ring of the metallacage ligand (H_e and H_f). The comparison of the chemical shifts of the ^{1}H NMR spectra of metallacages $\mathbf{C^{E1-3}}$ highlights the difference in electron density surrounding the protons of the metallacage scaffold, and thus, that the electron density lining the cage cavity will be altered as predicted.

Concerning $\mathbf{C^{E4}}$, featuring the central pyridyl ring, the electron withdrawing nature of the unoccupied *p*-orbital in the plane of aromaticity causes an electron withdrawing effect on the aromatic ring. Due to resonance effects, the largest downfield chemical shift, indicating the least electron density, occurs for H_g when compared to the non-functionalised metallacage $\mathbf{C^{E3}}$. Furthermore, the other proton peaks are all shifted downfield, indicating lower electron density over the ligand scaffold which correlates with the EWG *exo*-functionalised metallacage, $\mathbf{C^{E1}}$.

A similar comparison of the chemical shift in the proton peaks for the functionalised metallacages $\mathbf{C^{E1}.NO_3}$ and $\mathbf{C^{E2}.NO_3}$ with the non-functionalised metallacage $\mathbf{C^{E3}.NO_3}$ was carried out (table 3). Although similar results were anticipated to those reported in table 2 for $\mathbf{C^{E1-4}}$, the comparison was necessary to ensure that altering the counterion did not affect the anticipated electron density of the resulting metallacages $\mathbf{C^{E1-3}.NO_3}$.

Table 3: Comparison of the ^{1}H NMR peak position for functionalised metallacages $\mathbf{C^{E1}.NO_3}$, $\mathbf{C^{E2}.NO_3}$, and $\mathbf{C^{E4}.NO_3}$ with respect to the non-functionalised metallacage, $\mathbf{C^{E3}.NO_3}$.

	Δδ (ppm)						
	H_a	H_b	H_c	H_d	H_e	H_f	H_g
$\mathbf{C^{E3}.NO_3}$	10.0850	9.7007	7.9066	8.3307	7.7642	7.7214	7.5993
$\mathbf{C^{E1}.NO_3}$	10.1075	9.7298	7.9246	8.4121	7.9434	8.2286	N/A
Δδ($\mathbf{C^{E1}.NO_3}$- $\mathbf{C^{E3}.NO_3}$)	***0.0225***	***0.0291***	***0.0180***	***0.0814***	***0.1792***	***0.5072***	***N/A***
$\mathbf{C^{E2}.NO_3}$	10.0208	9.6464	7.8631	8.2681	6.9897	6.9617	N/A
Δδ($\mathbf{C^{E2}.NO_3}$- $\mathbf{C^{E3}.NO_3}$)	***-0.0642***	***-0.0543***	***-0.0435***	***-0.0626***	***-0.7745***	***-0.7597***	***N/A***
$\mathbf{C^{E4}.NO_3}$	9.8992	9.7447	7.9644	8.4409	N/A	7.8373	8.0752
Δδ($\mathbf{C^{E4}.NO_3}$- $\mathbf{C^{E3}.NO_3}$)	***-0.1858***	***0.044***	***0.0578***	***0.1102***	***N/A***	***0.1159***	***0.4759***

The electron rich metallacage, $\mathbf{C^{E2}.NO_3}$, exhibited upfield chemical shifts of all the proton peaks with respect to the electron neutral metallacage, $\mathbf{C^{E3}.NO_3}$, and the largest chemical shifts corresponded to the protons of the central phenyl ring, H_e and H_f (Δδ = -0.7745 and -0.7597 ppm, respectively). The electron deficient metallacage, $\mathbf{C^{E1}.NO_3}$, exhibited downfield chemical

shifts of all the protons with respect to the electron neutral metallacage **$C^{E3}.NO_3$**, with the largest chemical shifts again occurring for the protons of the central phenyl ring, H_e and H_f ($\Delta\delta$ = 0.1792 ppm and 0.5072 ppm, respectively). The metallacage, **$C^{E4}.NO_3$**, also exhibited downfield chemical shifts of the proton peaks with respect to **$C^{E3}.NO_3$**, with the proton peaks of the central aromatic ring, H_f and H_g, exhibiting the largest chemical shifts ($\Delta\delta$ = 0.1159 ppm and 0.4759 ppm, respectively). The notable exception for **$C^{E4}.NO_3$** was the *endo*-facing proton peak adjacent to the coordinating nitrogen of the terminal pyridyl ring, H_a, which displayed a distinct upfield shift in comparison to **$C^{E3}.NO_3$**. This is supportive of the idea that the NO_3^- counterion is not encapsulated within the cage cavity of **$C^{E4}.NO_3$** in DMF-d_7, which is most likely due to the electrostatic repulsion between the counterion and the endo-facing electron pairs. The comparison of the chemical shifts of the ^{1}H NMR spectra of metallacages **$C^{E1\text{-}4}.NO_3$** highlights the difference in electron density surrounding the protons of the metallacage scaffold, and thus that the electron density lining the cage cavity will be altered as predicted.

9.2.4 Cisplatin encapsulation in *exo*-functionalized Pd_2L_4 metallacages

^{1}H NMR experiments were initially used to study the shift in ^{1}H peak position of **$C^{E1\text{-}4}$**, with BF_4^- as counterion, upon introduction of two equiv. of cisplatin in DMF-d_7 solution (figure 8). A fixed ratio of cisplatin: cage (2: 1) was used. As mentioned above, a precise stoichiometry of encapsulated cisplatin molecules could not be determined using classic NMR titrations due to the very small shifts in peak position. In any case, upon addition of cisplatin, only the proton peaks adjacent to the nitrogen of the palladium coordinating pyridyl units (H_a (*endo-facing*) and H_b (*exo-facing*)) underwent a shift for **$C^{E1\text{-}4}$** (see figure 8), as well as the cavity facing proton peak of the phenyl group of the ligands of **$C^{E1\text{-}3}$** (H_e). The chemical shifts of H_a and H_b, as well as H_e (**$C^{E1\text{-}3}$**) are presented in table 4. The remaining peaks (H_c, H_d, H_f, and H_g), all corresponding to *exo*-facing protons, did not undergo any shift in peak position upon addition of cisplatin, but underwent a slight broadening of the respective signals. While the shift of proton H_e may be due to the interaction with encapsulated cisplatin, the proton peaks H_a and H_b are in very close proximity to the coordinating metal centre. In this case we hypothesized that this effect is due to possible rearrangements of the counterion around the positive Pd(II) ions upon cisplatin encapsulation.[238]

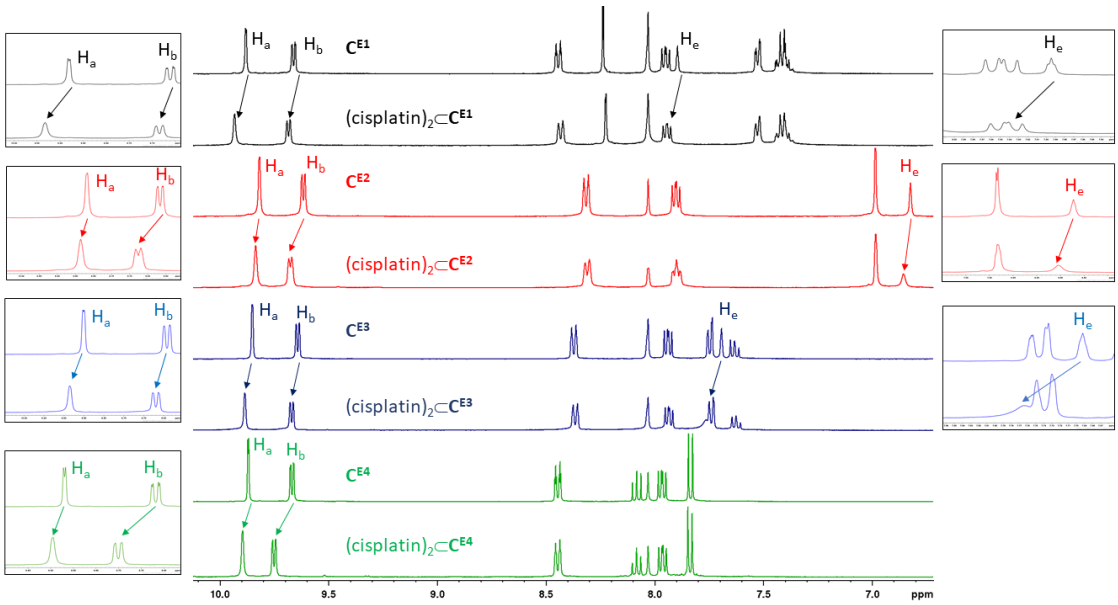

Figure 8. Stacked ^{1}H NMR spectra (DMF-d_7) for metallacages $\mathbf{C^{E1-4}}$, and the ^{1}H NMR spectra (DMF-d_7) of the host-guest complexes formed upon introduction of 2 equiv. cisplatin ((cisplatin)$_2$⊂$\mathbf{C^{E1-4}}$), with boxes highlighting the chemical shifts of protons H_a, H_b, and H_e.

Table 4. Chemical shift of ^{1}H NMR signals of selected protons (H_a H_b and H_e) of cages $\mathbf{C^{E1-4}}$ upon encapsulation of cisplatin in DMF-d_7.

	Δδ ppm		
Metallacage	H_a (*endo*-facing)	H_b (*exo*-facing)	H_e (*endo*-facing)
$\mathbf{C^{E1}}$	+ 0.053 (*broadening*)	+ 0.025	*N/R (possible downfield shift*)
$\mathbf{C^{E2}}$	+ 0.018 (*broadening*)	+ 0.060	+ 0.031 (*broadening*)
$\mathbf{C^{E3}}$	+ 0.034 (*broadening*)	+ 0.028	+ 0.072 (*broadening*)
$\mathbf{C^{E4}}$	+ 0.027 (*broadening*)	+ 0.083	N/A

Unfortunately, the chemical shift of H_e for $\mathbf{C^{E1}}$ could not be accurately recorded as it was masked by the signal for H_c. However, it can be assumed to behave similarly to signal H_e of $\mathbf{C^{E2}}$ and $\mathbf{C^{E3}}$ based on the behaviour of H_a and H_b as well as on the position of the signal that masks it, H_c. Furthermore, in all cases where the cavity facing proton peaks (H_a and H_e) could be recorded, a distinct broadening of both peaks was observed; although for $\mathbf{C^{E2}}$ and $\mathbf{C^{E3}}$ the broadening of H_e was more pronounced than for H_a. Broadening of the signal in ^{1}H NMR spectra is typically indicative of intermolecular interactions,[238] such as hydrogen bond formation, and strongly suggests that the cavity of the metallacages $\mathbf{C^{E1-3}}$ are occupied upon introduction of

cisplatin. Furthermore, for cage $\mathbf{C^{E4}}$ the chemical shifts for H_a (+ 0.027 ppm) and H_b (+ 0.083 ppm) are also attributable to the interactions with the encapsulated cisplatin. However, our values did not match a previously reported study on the same cage,[238] but that was conducted in a different solvent (acetonitrile-d_3) and showed chemical shifts for H_a of Δδ = +1 ppm and H_b of Δδ = +~0.05 ppm, respectively.

Overall, the comparison of $\mathbf{C^{E1\text{-}E4}}$ NMR spectra suggests that in all cases cisplatin is encapsulated using DMF-d_7 as solvent. Furthermore, it would appear that by increasing the electron density of the cavity facing proton H_e, using a *para*-EDG ($\mathbf{C^{E2}}$) causes the largest shift of the *exo*-facing peak (H_b), but the smallest shift of the *endo*-facing ones (H_a and H_e). The electron 'neutral' metallacage, $\mathbf{C^{E3}}$, exhibited the largest downfield shift of cavity facing peak H_e, and the second largest shift of H_a. As the chemical shifts for the *endo*- facing protons are downfield, this would suggest that the electron density has been 'pushed' away from the cavity facing protons; thus, de-shielding H_e and H_a, which would result in the downfield chemical shift that is observed. This may be indicative of a closer proximity of the guest molecule to these cavity facing protons, and thus suggest a higher affinity of the guest, cisplatin, to the cavity of $\mathbf{C^{E3}}$ in DMF-d_7.

The obtained results demonstrate that encapsulation of cisplatin occurs within each cage cavity of $\mathbf{C^{E1\text{-}4}}$, independently of the electron density of the cage cavity, although to different extents. Therefore, while the encapsulation process may not be primarily driven by subtle differences in the electron density of the cage cavity facilitating host-guest binding, different *exo*-functional groups (EWG, EDG, H) do cause slight differences in the chemical shifts values of proton peaks H_a, H_b, and H_e between metallacages $\mathbf{C^{E1\text{-}4}}$ upon addition of cisplatin. However, further studies are necessary to fully characterise this process: for example, two dimensional (2D) NMR spectroscopy techniques, such as Nuclear Overhauser Effect Spectroscopy (NOESY) NMR, may be able to improve our understanding of the environment around the protons H_a, H_b and H_e.

Afterward, the same cisplatin encapsulation studies were performed for the metallacage series $\mathbf{C^{E1\text{-}4}.NO_3}$. As shown in table 5 and figure 9, upon introduction of two equiv. of cisplatin to metallacages $\mathbf{C^{E1\text{-}4}.NO_3}$ the cavity facing protons H_a and H_e undergo small shifts, as does the *exo*-facing proton peak H_b. However, unlike the case of metallacages $\mathbf{C^{E1\text{-}4}}$, the shift in peak positions does not follow the same pattern across all cage architectures. In fact, while for the metallacages formed from the bis-pyridyl ligand scaffold ($\mathbf{C^{E1\text{-}3}.NO_3}$) the *endo*-facing peak H_a undergoes a small upfield shift upon introduction of cisplatin, and the *exo*-facing peak H_b undergoes a small downfield shift, the cavity facing proton, H_e, does not follow a pattern across the cages.

It is also worthwhile highlighting the anomalous result of $\mathbf{C^{E3}.NO_3}$ (highlighted in table 5 by the asterisk, and ^{1}H NMR spectrum shown in figure 9). In this case, the *exo*-facing peaks of the central phenyl ring are all shifted slightly downfield upon addition of cisplatin (H_g: Δδ = +0.0062 ppm, H_f : Δδ = +0.0051 ppm), which is in contrast to all the other investigated cages (figure 9). Furthermore, the peak corresponding to H_f appears to be split into a doublet and a broad singlet (ratio 1:1), and this splitting is maintained upon encapsulation of cisplatin.

Instead, the metallacage based on the *tris-pyridyl* based ligand, $\mathbf{C^{E4}.NO_3}$, follows a similar trend of peak shifts compared to $\mathbf{C^{E4}}$, whereby both peaks adjacent to the coordinating nitrogen of the terminal pyridine groups undergo small downfield shifts, which may be indicative of cisplatin encapsulation, with the *exo*-facing proton peak, H_b, exhibiting a larger shift in both cases. As the trend for both $\mathbf{C^{E4}}$ and $\mathbf{C^{E4}.NO_3}$ are similar, this result supports the idea that NO_3^- is not encapsulated within this metallacage in DMF-d_7, and that the cage cavity is vacant, hence the downfield shift of both H_a and H_b.

Instead, the small upfield shifts exhibited by metallacages $\mathbf{C^{E1\text{-}3}.NO_3}$ can be attributed to a "masking" effect due to the encapsulation of the anionic NO_3^- counterion prior cisplatin addition (figure 10). The overall negative charge of the encapsulated NO_3^- counterion would cause a repulsion of the electron density around the cavity facing protons, causing the electron density to be "pushed" away from the ^{1}H nucleus onto the highly conjugated ligand, thus de-shielding the nucleus and causing the signal to shift downfield. Upon introduction of the neutral drug cisplatin, the anionic NO_3^- counterion is evacuated from the metallacage cavity of the cages $\mathbf{C^{E1\text{-}3}.NO_3}$ and thus, the repulsive effect on the electron density surrounding the cavity facing ^{1}H nucleus would be reduced and would thus explain the observed upfield shift for H_a for metallacages $\mathbf{C^{E1\text{-}3}.NO_3}$. The small upfield shifts observed for the cavity facing proton peak H_e for metallacages $\mathbf{C^{E1}.NO_3}$ and $\mathbf{C^{E3}.NO_3}$ can be rationalised in a similar manner. Of note, the proton peak H_e for metallacage $\mathbf{C^{E2}.NO_3}$ undergoes a small downfield shift (Δδ = + 0.0067 ppm) (table 5; figure 9), which suggests a different mode of encapsulation than the other metallacages.

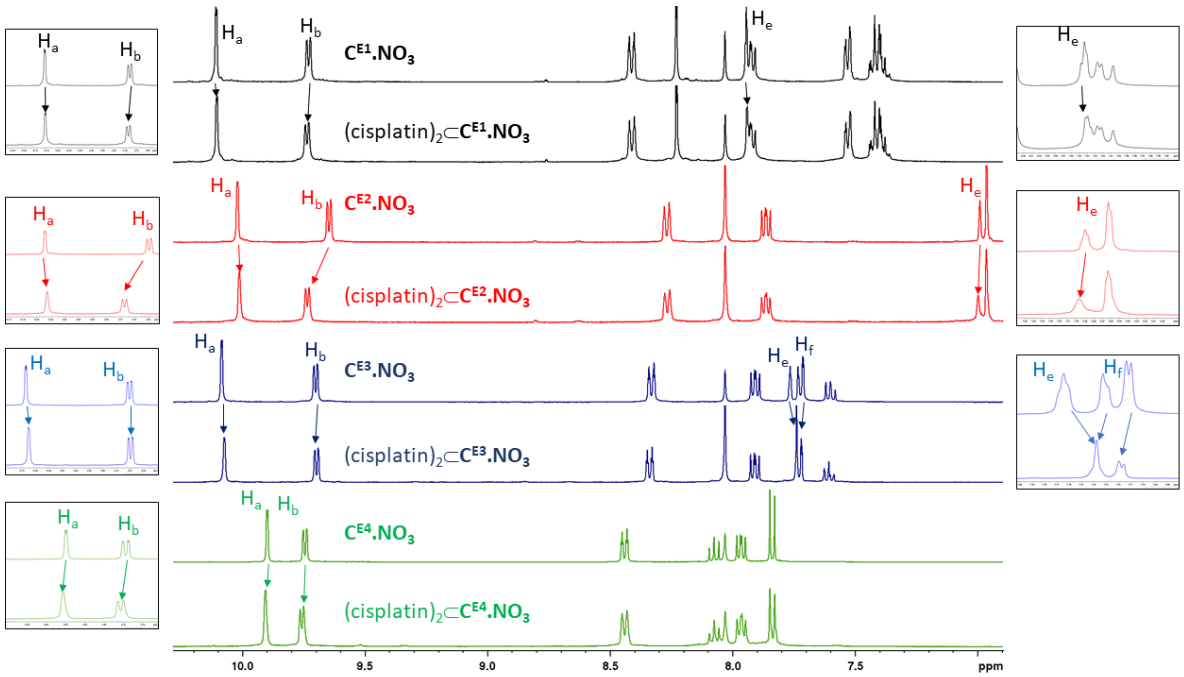

Figure 9. Stacked ^{1}H NMR spectra (DMF-d_7) for metallacages **$C^{E1-4}.NO_3$**, and the ^{1}H NMR spectra (DMF-d_7) of the host-guest complexes formed upon addition of 2 equiv. cisplatin ((cisplatin)$_2$⊂**$C^{E1-4}.NO_3$**), with boxes highlighting the chemical shifts of protons H_a, H_b, and H_e (and H_f for **$C^{E3}.NO_3$**).

Table 5. Chemical shift of ^{1}H NMR signals of selected protons of **$C^{E1-4}.NO_3$** upon encapsulation of cisplatin in DMF-d_7.

	Δδ ppm		
Metallacage	H_a (*endo*-facing)	H_b (*exo*-facing)	H_e (*endo*-facing)
$C^{E1}.NO_3$	-0.002	+0.006	-0.012
$C^{E2}.NO_3$	-0.0076	+0.09	+0.0067
$C^{E3}.NO_3$*	-0.0085	+0.0042	-0.0268
$C^{E4}.NO_3$	+0.0083	+0.0125	N/A

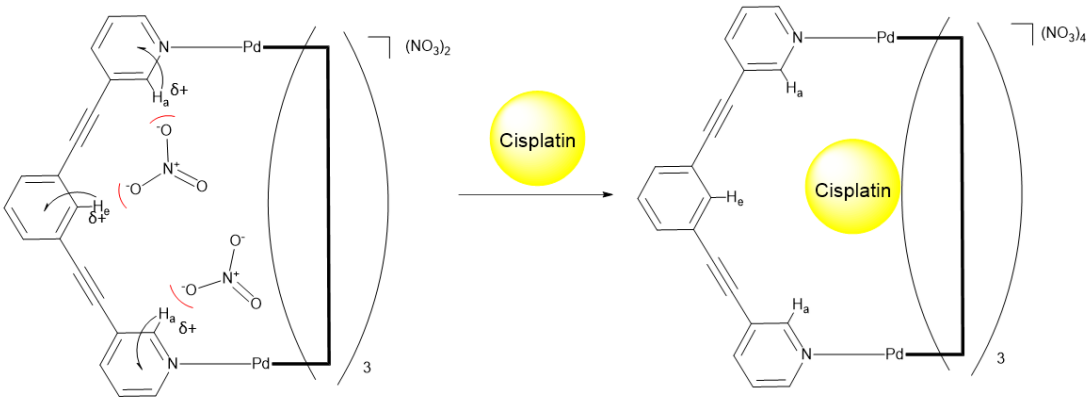

Figure 10. Schematic representation of the "masking" effect proposed for **C^{E1-3}.NO$_3$**. The red parentheses represent the repulsion of the electron density surrounding the anionic oxygen of the nitrate counterion, on the cavity facing protons H_a and H_e. The arrows do not represent the movement of electron pairs, but rather the more subtle shifting of the electron density away from the nucleus of protons H_a and H_b onto the conjugated ligand scaffold, causing H_a and H_e to become less shielded (*δ+*). Upon introduction of the neutral molecule cisplatin, the repulsive effect is reduced which results in the apparent upfield shift of the peaks H_a and H_e.

Although the *exo*-facing proton peaks of metallacage **C^{E3}.NO$_3$** also underwent slight downfield shifts upon encapsulation of cisplatin, due to the unusual splitting of the proton peak H_f, this shift may be due to rearrangement of the counterion lying outside of the cage cavity. However, it must be acknowledged that the scope of this study is limited, and that in DMF-d_7 the encapsulation of the nitrate counterion may prevent or limit the encapsulation of cisplatin as the shifts observed are much smaller than those observed for metallacages **C^{E1-4}**. In order to further elucidate the exact nature of the encapsulation of anionic species such as NO_3^-, further studies may be appropriate, such as 2D NMR analysis or calorimetric techniques, and a more thorough screening process against other anionic species.

To summarise, the ^{1}H NMR experiments presented so far strongly suggest that encapsulation of cisplatin does occur in DMF-d_7 for metallacages that do not have lone pairs of electrons lining the metallacage cavity. The downfield shift of H_a for **C^{E4}.NO$_3$**, along with the results obtained by Crowley and coworkers previously,[238] suggests that encapsulation of cisplatin does occur in DMF-d_7, however the mechanism of encapsulation may be driven by host-guest interactions, such as H-bond formation, rather than solvent effects.[238] The results also show that electrostatic interactions between the metallacage and the anionic guest NO_3^- do not appear to be sufficient to oppose the displacement of NO_3^- by the neutral molecule cisplatin. However, the scope of the study was limited and further analysis is needed to elucidate the exact affinity of anionic species for the cavity of cationic Pd_2L_4 metallacages. Furthermore, it would appear that while altering the electron density of the constituent ligand of the

metallacages does have a subtle effect on the encapsulation of cisplatin, due to the cavity facing proton peaks exhibiting different chemical shifts depending on the different electron density, it is unlikely to be the driving force of encapsulation as previously suggested as cisplatin encapsulation occurs for each metallacage, regardless of the cavity environment.

9.3 Encapsulation of guest molecules via the non-classical hydrophobic effect

It has been proposed that water-soluble supramolecular coordination complexes (SCCs) could be used as a tool to help elucidating the mechanism of binding between ligands and complex biomolecules.[250] It has been hypothesised that the ability to alter the cavity morphology of different classes of SCCs, as well as the ability to synthetically introduce *endo*-facing functionalities to the SCC cavity would allow for the creation of simple 3D models that mimic the environment of the binding site of much more complex biomolecules.[251] These simplistic, SCC models would be much easier to analyse than the biomolecules they mimic, and thus, provide a valuable complementary analytical tool for studying ligand receptor interactions in aqueous media.

Leung and co-workers reported the first systematic study on the effect of different solvents (D_2O, MeOD-d_4 and DMSO-d_6) on the encapsulation of various, structurally different guests within a water soluble, anionic $Na_{12}[Ga_4L_6]$ tetrahedral SCC.[250] Leung and co-workers studied the binding affinity of a range of structurally different iridium complexes within the cavity of a $Na_{12}[Ga_4L_6]$ metallacage. The results showed that the binding constants for the guests were remarkably similar to each other ($K_a \sim 10^{-3}$).[250] The enthalpic and entropic contributions for the encapsulation process were also reported for encapsulation of the guest species in the polar, protic solvents D_2O and MeOD-d_4. The results show a trend whereby as the guest becomes larger and more hydrophobic, the entropic contributions decrease while the enthalpic contributions increase. This is in direct contradiction of the classical hydrophobic effect whereby, as guests become larger and less water soluble, the de-solvation of the molecule causes an increase in entropy of the system as the water molecules of the solvation sphere are released into the bulk solution, and a decrease in the enthalpy of the system.[250,252] Conversely in the aprotic polar solvent, DMSO-d_6, the opposite trend was observed, in that as the guest molecule increased in size, the overall encapsulation process becomes more entropically driven, as the guest displaces more solvent molecules from the cavity into the bulk solution.[250] The group went on to demonstrate that the encapsulation process is more likely to be driven by the non-classical hydrophobic effect, in which the water molecules are released from the cage cavity upon

introduction of a poorly water-soluble guest molecule.[250] The released water molecules are free to form stabilising hydrogen bond networks with the bulk solution, and this effect decreases the overall enthalpy of the system. In parallel, this process causes a loss in entropy of the system due to the newly formed hydrogen bond networks that restrict the degree of freedom of the water molecules within the bulk solution.

More recently, Ward and co-workers have studied a similar encapsulation process for several poorly water-soluble cyclic ketone guest molecules, based on the release of water molecules from the cavity of a cubic $[Co_8L_{12}](BF_4)_{16}$ metallacage.[253] Using a combination ^{1}H NMR spectroscopy and crystallography, it was shown that water molecules encapsulated within the metallacage can form less hydrogen bonds than those in the bulk solution, and thus, can be termed "high energy" or "frustrated" water molecules. Upon introduction of a series of cyclic ketones, which could be sequentially enlarged by the addition of CH_2 groups, the water molecules were released from the cavity and thus form enthalpically favourable hydrogen bond networks.[253] The study showed that the larger the guest molecule, the more enthalpically favourable the contribution to the system upon encapsulation, as more water molecules could be displaced to form the stabilising hydrogen bond networks, at the expense of a loss of entropy due to the lower degree of freedom of these hydrogen bond "locked" water molecules. Several other studies have also described the non-classical hydrophobic effect as the driving force for ligand and guest molecule recognition by host structures.[253–256]

9.3.1 Encapsulation of cisplatin in Pd_2L_4 metallacages based on the non-classical hydrophobic effect studied by NMR spectroscopy

The non-classical hydrophobic effect appears to be a good hypothesis for the driving force of cisplatin into bis-pyridyl ligand based Pd_2L_4 type metallacages, which lack the cavity facing lone electron pairs and so do not exhibit any functional group based molecular recognition interactions. Unfortunately, Pd_2L_4 type metallacages are poorly water soluble, despite synthetic efforts to improve this feature (*see chapter 8*). As such classical methods used to elucidate the binding constants of host-guest systems (such as ^{1}H NMR in D_2O) were unsuitable to study cisplatin encapsulation within Pd_2L_4 metallacages. On the other hand, as described in the previous chapters, the chemical shifts of the cavity facing peaks of Pd_2L_4 metallacages are too small in DMF-d_7 to elucidate any quantitative data for the encapsulation process. Furthermore, as DMF-d_7 cannot form extended hydrogen bond networks and that these networks are crucial for the non-classical hydrophobic effect, the use of this solvent is not so meaningful to validate our hypothesis. However, as the DMF-d_7 used for the experiments was stored under atmospheric conditions on the benchtop, small amounts of water were present within the

solution (as can be seen from the large signal at circa. 3.5 ppm in the ^{1}H NMR spectra, see experimental section). Therefore, it was hypothesised that the small amount of water present in the deuterated solution was forming small hydrogen bond networks with DMF-d_7, which features two hydrogen bond acceptor sites, and that these interactions could mimic a pseudo non-classical hydrophobic effect. This effect explains the apparent lack of binding of cisplatin with Pd_2L_4 type metallacages in acetonitrile-d_3, since this solvent is not able to form extended hydrogen bonding networks with the present residual amount of water. Furthermore, if indeed the encapsulation of cisplatin within Pd_2L_4 metallacages in DMF-d_7 is based on the non-classical hydrophobic effect it can be presumed that the binding affinity in water, and by extension in physiological conditions, will be stronger than that measured in DMF-d_7.

As the encapsulation was believed to be driven by the release of "frustrated" solvent molecules from the cage cavity, which are then stabilised by extended hydrogen bonding networks in the bulk solution,[250,253] it was appropriate to first investigate the maximum concentration of water in DMF that could be achieved without $\mathbf{C^{E1}}$ precipitating. This preliminary study provides the thermodynamic profile that would be closer to that of the one under physiological conditions.

DMSO-d_6 was initially used in place of DMF-d_7 (due to the lower cost of DMSO-d_6) to study the optimal concentration of water for the solvent system to be used for the ITC experiment. DMSO-d_6 shares similar properties to DMF-d_7, as both have two hydrogen bond acceptor sites, similar polarity indexes (P'_{DMSO} = 7.2, P'_{DMF} = 6.4), high dielectric constants (ε_{DMSO} = 47; ε_{DMF} = 38.25) and similar densities (ρ_{DMSO} = 1.092 g/cm^3, ρ_{DMF} = 0.9445 g/cm^3).[257]

Therefore, DMSO-d_6 was dried over molecular sieves (4 Å) and a series of solvent mixtures of DMSO-d_6: D_2O were prepared (0 – 50% v/v, 0 – 27 M). $\mathbf{C^{E3}}$ was added to the solution and a ^{1}H and ^{19}F NMR spectra were recorded for each sample. It was expected that the peaks would not shift in either the recorded ^{1}H or ^{19}F NMR spectrum, but would start to broaden upon precipitation of $\mathbf{C^{E3}}$, indicating the maximum concentration of water in DMSO-d_6. This concentration could then be tested in the more expensive solvent DMF-d_7 to ensure that precipitation did not occur, and eventually the optimal water/DMF ratio could be used for the proposed ITC experiment.

The obtained stacked ^{1}H NMR spectra are shown in figure 11. At a concentration of 16.65 M D_2O (30% v/v) the distinct peak broadening and a loss of signal splitting can be observed, which is consistent with precipitation of metallacage $\mathbf{C^{E3}}$ from the solution. Indeed, the Tyndall effect was observed in the NMR tube, indicative of a colloid suspension having formed, which indicates that 16.6 M concentration of water is the limit to facilitate a fully dissolved cage

solution. Interestingly, the cavity facing proton peaks, H_a and H_e, as well as the *exo*-facing proton peak H_b undergo significant shifts ($\Delta\delta_{Ha}$ = -0.0859 ppm, $\Delta\delta_{Hb}$ = +0.0529 ppm, $\Delta\delta_{He}$ = +0.0661 ppm) upon introduction of only 2% v/v D_2O (1.11 M). Furthermore, the remaining *exo*-facing protons do not exhibit any shifts. This trend in chemical shift for protons H_a, H_b, and H_e continues up until a concentration of 10% D_2O v/v (5.55 M) and strongly suggest that $\mathbf{C^{E3}}$ has encapsulated a guest molecule, possibly the counterion, BF_4^-. The complementary ^{19}F NMR spectra supports that the BF_4^- counterion has been encapsulated, as there is an upfield shift ($\Delta\delta$ = -0.223 ppm) of the ^{19}F signal up to 10% D_2O v/v (5.55 M) (figure 11D). It is worth noting that the observed upfield shift is also concurrent with the ^{195}Pt NMR experiments described in chapters 5 and 8, whereby the ^{195}Pt signal underwent a slight upfield shift ($\Delta\delta$ = -2 ppm) upon cisplatin encapsulation in selected Pd_2L_4 type metallacages.

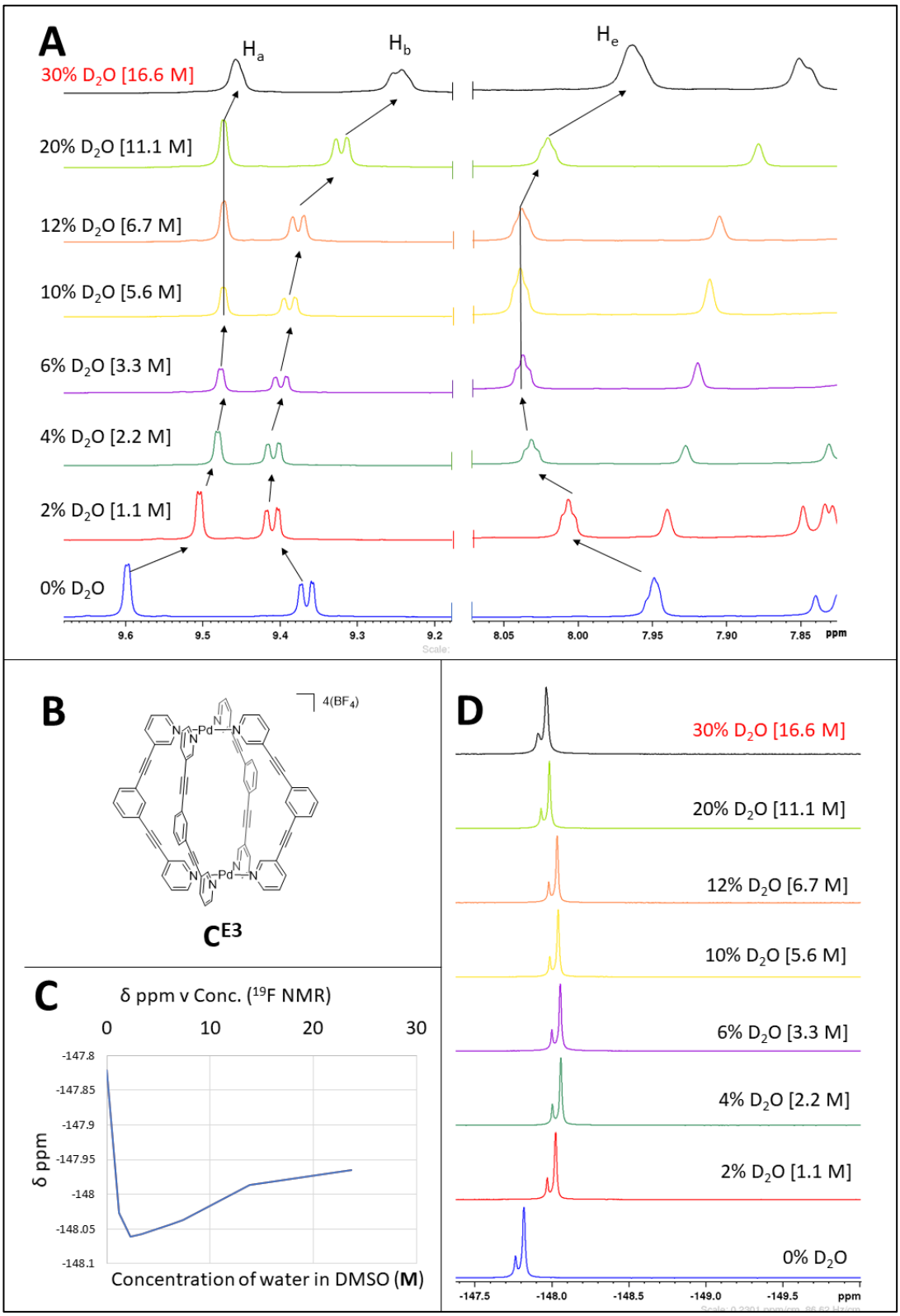

Figure 11. Compiled ^{1}H and ^{19}F NMR data for the titration of D_2O into a DMSO-d_6 solution of metallacage $\mathbf{C^{E3}}$. **Box A**: stacked ^{1}H NMR spectra, focused on the protons H_a, H_b and H_e, with increased concentration of D_2O (30% [16.6 M] D_2O causes the metallacage to precipitate). **Box B**: Chemical structure of the metallacage $\mathbf{C^{E3}}$. **Box C**: Plot of the chemical shift of the ^{19}F signal against concentration of water. **Box D**: Stacked ^{19}F NMR spectra with increase concentration of D_2O (30% [16.6 M] D_2O causes the metallacage to precipitate)

Above 10% v/v D_2O in DMSO-d_6, the *exo*-facing proton peaks begin to shift upfield as the concentration of D_2O increases. However, the cavity facing protons H_a and H_e do not undergo any further significant shifts. The upfield shifts of the *exo*-facing protons is due to the solvent composition changing, namely becoming more polar and thus causing shielding of the *exo*-facing peaks due to the altering composition of the solvation sphere. The fact that the cavity facing protons do not follow this trend demonstrates that the different solvent systems do not have an impact on the internal cavity environment, which provides further indirect evidence that the solvent molecules do not occupy the cavity of $\mathbf{C^{E3}}$ above 10% v/v D_2O in DMSO-d_6.

To further support the theory that cisplatin is encapsulated within the bis-pyridyl ligand based Pd_2L_4 metallacage scaffold, the experiment was repeated for the tris-pyridyl ligand based metallacage, $\mathbf{C^{E4}}$, whereby the concentration of D_2O in DMSO-d_6 was increased and a ^1H and ^{19}F NMR spectrum was recorded for each concentration (figure 12). Unlike the case of $\mathbf{C^{E3}}$ the cavity facing proton peak, H_a, does not shift upfield upon addition of D_2O, which suggests that no encapsulation of the counterion has occurred. This can be confirmed by the complementary ^{19}F NMR spectra which show no upfield shift upon addition of D_2O. It can be seen that the *exo*-facing proton peak, H_b, has been shifted downfield slightly upon addition of 10% D_2O v/v, which may be indicative of a closer association of the counterion to the *exo*-side of the palladium ion. All other *exo*-facing proton peaks undergo the same pattern of shifting upfield as was seen for $\mathbf{C^{E3}}$ (figure 11), which supports the theory that this upfield trend is due to the difference in solvent properties of the various solvent systems interacting with the external side of the metallacage. Furthermore, the only cavity facing proton peak, H_a, does not undergo any significant shifts upon addition of up to 30% v/v D_2O in DMSO-d_6 (16.65 M) , which is consistent with the idea that the cavity of the cage does not behave in the same manner as the bulk solution. The slight shift and broadening of the spectra at 30% concentration of D_2O can be attributed to the cage precipitating out of solution, as evidenced by the observation of the Tyndall effect. The obtained results are concurrent with previous studies that state that the lone electron pairs on the *endo*-pyridyl nitrogen repulse anionic counterions, and so do not allow them to be encapsulated.[238] The difference in the chemical shift patterns of both the ^1H and ^{19}F NMR spectra for $\mathbf{C^{E3}}$ and $\mathbf{C^{E4}}$ support the theory that the BF_4^- counterion is encapsulated within the cage cavity of $\mathbf{C^{E3}}$ as the size of the hydrogen bond networks of the bulk solvent are increased, but not in $\mathbf{C^{E4}}$ due to the more electron rich cavity environment.

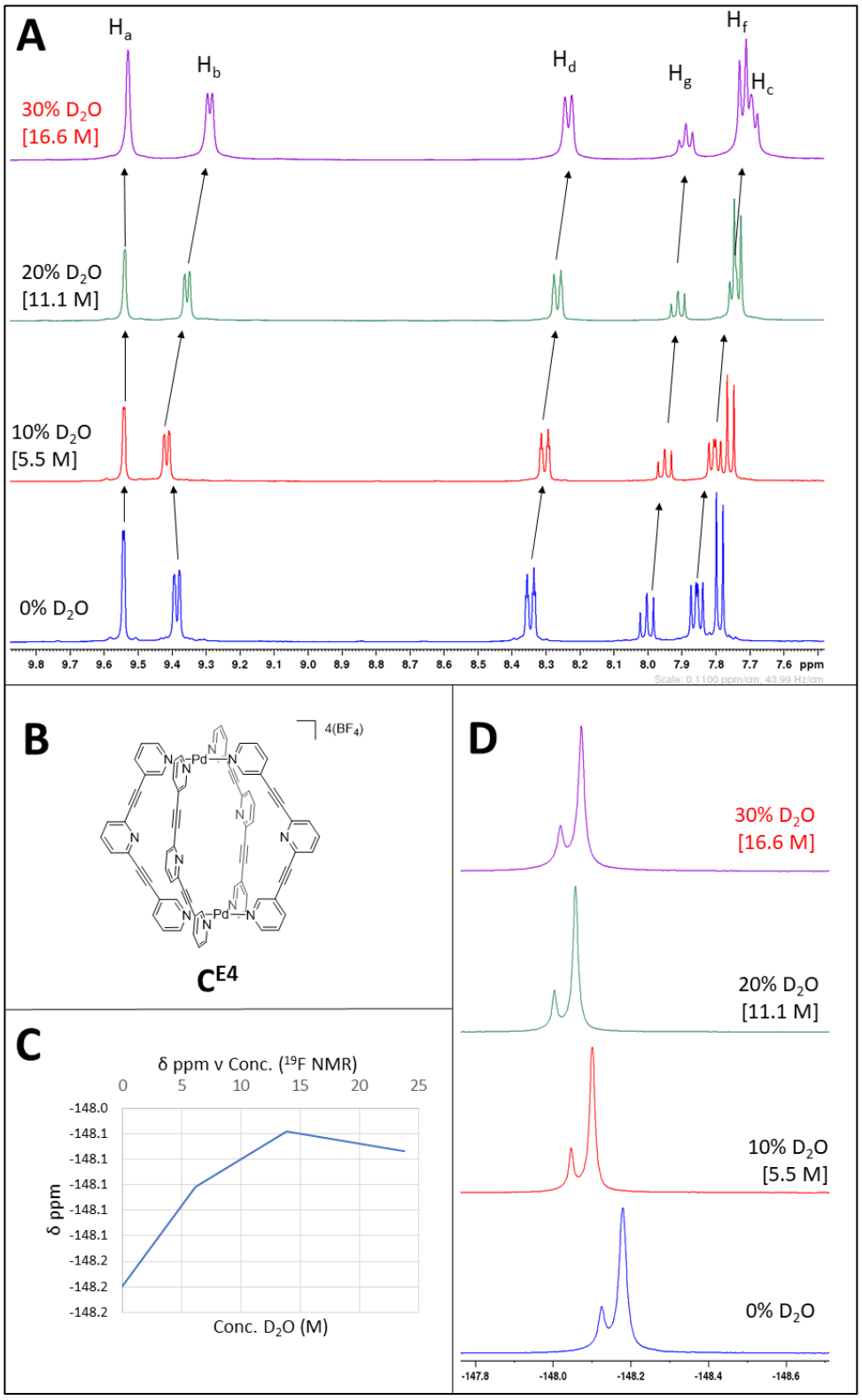

Figure 12. Compiled ^{1}H and ^{19}F NMR data for the titration of D_2O into a DMSO-d_6 solution of metallacage $\mathbf{C^{E4}}$. **Box A**: stacked ^{1}H NMR spectra of $\mathbf{C^{E4}}$ (30% [16.6 M] D_2O causes the metallacage to precipitate). **Box B**: Chemical structure of the metallacage $\mathbf{C^{E4}}$. **Box C**: Plot of the chemical shift of the ^{19}F signal against concentration of water. The lack of upfield shift of the signal suggests that BF_4^- is not encapsulated upon increased concentration of D_2O. **Box D**: Stacked ^{19}F NMR spectra with increase concentration of D_2O (30% [16.6 M] D_2O causes the metallacage to precipitate).

Following the initial experiments of $\mathbf{C^{E3}}$ in D_2O: DMSO-d_6 solvent systems, the experiment was repeated for $\mathbf{C^{E3}}$ in DMF-d_7 as the latter does not alter cisplatin coordination sphere *via* ligand exchange reactions. Four concentrations of D_2O in DMF-d_7 were selected based on the previous experiments in DMSO-d_6 (concentration of D_2O = 0 M, 2.2 M, 6.7 M, 7.8 M and 14 M) The stacked ^1H and ^{19}F NMR spectra are shown in figure 13. The concentration of 14 M D_2O in DMF-d_7 caused immediate precipitation and so the data is not shown. It can be seen that the cavity facing proton peak H_a undergoes a downfield shift, whereas the cavity facing proton peak H_e undergoes an upfield shift upon increased concentration of D_2O in DMF-d_7, which is suggestive of encapsulation of the counterion. Furthermore, the *exo*-facing proton peaks follow the same upfield trend observed for $\mathbf{C^{E3}}$ in DMSO-d_6. The ^{19}F NMR spectra supports that BF_4^- is encapsulated, as there is an initial downfield shift of the ^{19}F signal upon introduction of D_2O. At a concentration of D_2O in DMF-d_7 above 6.7 M, the signal starts to shift downfield, which can again be attributed to the changing solvent polarity of the solvent system. From the NMR results it appears that the BF_4^- counterion becomes fully encapsulated between 6 – 7 M concentration of D_2O.

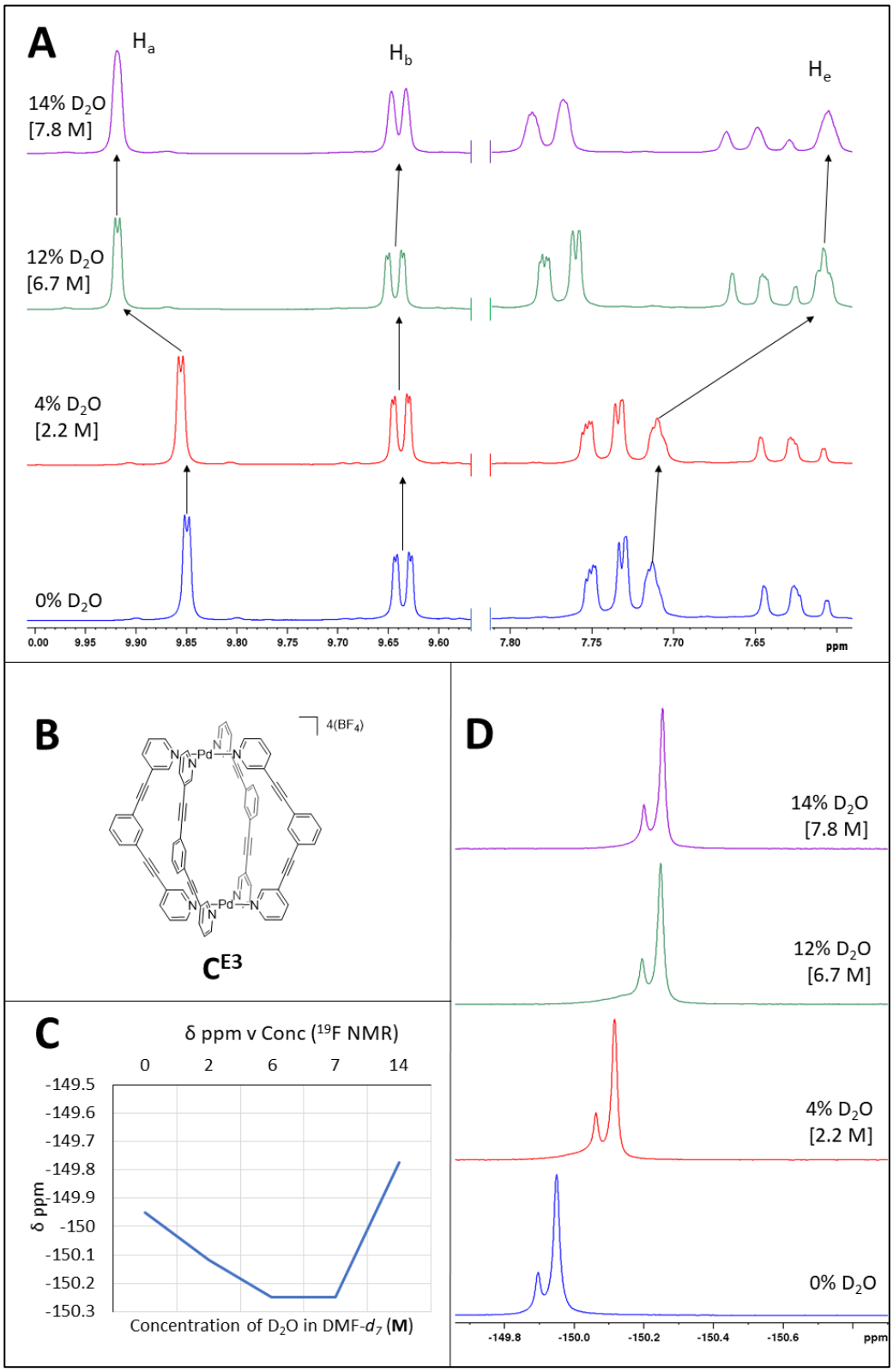

Figure 13. Compiled ^{1}H and ^{19}F NMR data for the titration of D_2O into a DMF-d_7 solution of metallacage $\mathbf{C}^{E3}$. **Box A**: stacked ^{1}H NMR spectra, focused on the protons H_a, H_b and H_e, with increased concentration of D_2O. **Box B**: Chemical structure of the metallacage $\mathbf{C}^{E4}$. **Box C**: Plot of the chemical shift of the ^{19}F signal against concentration of water. The signal at 14 M D_2O is shifted much further downfield due to precipitation of the metallacage. **Box D**: Stacked ^{19}F NMR spectra with increase concentration of D_2O.

Finally, before future studies of the encapsulation process of cisplatin within $\mathbf{C^{E3}}$ in 6 M H_2O in DMF by ITC, the encapsulation of cisplatin was studied in 6 M D_2O in DMF-d_7 *via* ^1H and ^{19}F NMR to ensure that representative chemical shifts can be observed. As such, cisplatin was titrated into the solution of $\mathbf{C^{E3}}$ in 6 M D_2O in DMF-d_7 and a ^1H and ^{19}F NMR spectra were recorded (figure 14 and figure 15, respectively). Upon introduction of one equiv. of cisplatin, the ^1H NMR spectra show that the peaks corresponding to the cavity facing proton H_a exhibit a small upfield shift (Δδ = -0.033). The other cavity facing proton peak exhibits a larger downfield shift (Δδ = +0.06 ppm). Interestingly, all the *exo*-facing proton peaks, except for H_c, also undergo small chemical shifts upon introduction of one equiv.of cisplatin (±0.01 – 0.02 ppm), which has not been observed in the previous ^1H NMR encapsulation studies. These shifts are most probably due to rearrangement of the released BF_4^- counterion and the subsequent alteration of the solvation sphere surrounding the solvated $\mathbf{C^{E3}}$. Upon addition of the second equivalent of cisplatin to $\mathbf{C^{E3}}$, the cavity facing proton peak H_a undergoes a downfield shift of Δδ = +0.0445 ppm with respect to one equivalent of cisplatin encapsulated within $\mathbf{C^{E3}}$, and Δδ = +0.0143 ppm with respect to the cage alone. The cavity facing proton peak H_e underwent an upfield shift of Δδ = -0.0764 ppm with respect to the one equiv. of cisplatin encapsulated within $\mathbf{C^{E3}}$, and Δδ = -0.021 ppm with respect to $\mathbf{C^{E3}}$ alone (figure 14). Furthermore, upon introduction of two equiv. of cisplatin to $\mathbf{C^{E3}}$, both cavity facing proton peaks exhibited peak broadening, which is indicative of intermolecular interactions, such as hydrogen bonding or other non-specific supramolecular interactions.

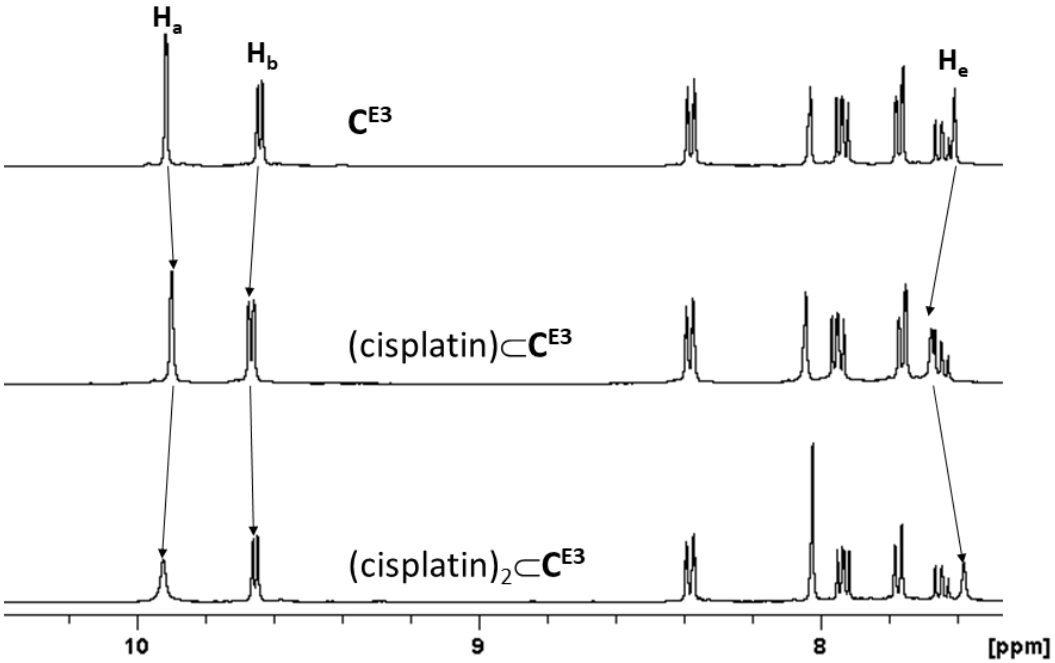

Figure 14. Stacked ^{1}H NMR spectra of $\mathbf{C^{E3}}$ in 6 M D_2O in DMF-d_7. **Top**: Metallacage $\mathbf{C^{E3}}$ **Middle**: One equivalent of cisplatin with one equivalent of $\mathbf{C^{E3}}$. **Bottom**: Two equivalents of cisplatin with one equivalent of $\mathbf{C^{E3}}$.

The ^{19}F NMR spectra (figure 15) show a similar trend as the ^{1}H NMR spectra. Upon introduction of one equiv. of cisplatin, the ^{19}F NMR signal undergoes a downfield shift of Δδ = +0.25 ppm. However, upon introduction of a second equiv. of cisplatin, the ^{19}F signal undergoes an upfield shift with respect to the one equiv. of cisplatin encapsulated of Δδ = -0.179 ppm. However, the signal remains downfield with respect to the ^{19}F signal corresponding to $\mathbf{C^{E3}}$ alone (Δδ = +0.072 ppm). The compiled NMR results of the encapsulation of cisplatin in 6 M D_2O in DMF-d_7 in metallacage $\mathbf{C^{E3}}$ suggest that encapsulation of two equiv. of cisplatin occurs, while addition of one equiv. of cisplatin results in an intermediate species with both BF_4^- and cisplatin occupying the cage cavity, before the introduction of a second equiv. of cisplatin causes complete release of BF_4^- counterions from the cavity. However, this hypothesis needs further validation.

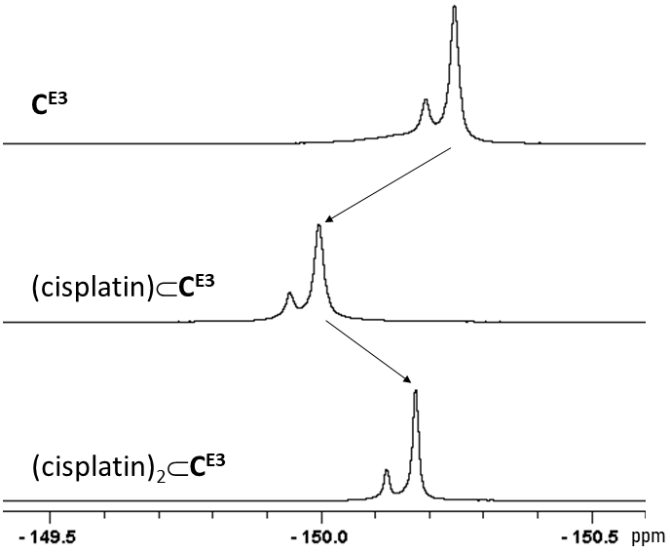

Figure 15. Stacked ^{19}F NMR spectra of $\mathbf{C^{E3}}$ in 6 M D_2O in DMF-d_7. **Top**: Metallacage $\mathbf{C^{E3}}$ **Middle**: One equivalent of cisplatin with one equivalent of $\mathbf{C^{E3}}$. **Bottom**: Two equiv. of cisplatin with one equivalent of $\mathbf{C^{E3}}$.

9.4 Summary, conclusions and future outlook

The synthesis of a small library of *exo*-functionalised of Pd_2L_4 type metallacages with EWG ($\mathbf{C^{E1}}$) and EDG ($\mathbf{C^{E2}}$), as well as non *exo*-functionalised metallacage ($\mathbf{C^{E3}}$) and an *endo*-functionalised metallacage ($\mathbf{C^{E4}}$), with the aim of altering the electronic environment of the internal cavity, have been reported. The electron density surrounding the cavity facing proton peaks for the *exo*- and *endo*- functionalised metallacages was analysed in comparison to the non-functionalised metallacage to establish that the electron density had been altered.

The encapsulation of the anti-cancer drug, cisplatin, by ^1H NMR spectroscopy in DMF-d_7 was been reported. In each case, the internal cavity facing proton peaks underwent small chemical shifts in the ^1H NMR spectra, which were concurrent with previous studies of cisplatin encapsulation in Pd_2L_4 metallacages. This would suggest that for each metallacage cisplatin was encapsulated, although binding affinities could not be elucidated. The shift in ^1H peak position of the cavity facing protons for each metallacage suggests that altering the electronic nature of the internal cavity does contribute to the internalisation of cisplatin, however it does not appear to be the driving force for encapsulation.

The effect of the counter anion on the encapsulation of cisplatin was studied. Namely, the counter anion, NO_3^-, was used to synthesise analogues metallacages to the ($\mathbf{C^{E1}.NO_3}$, $\mathbf{C^{E2}.NO_3}$, $\mathbf{C^{E3}.NO_3}$ and $\mathbf{C^{E4}.NO_3}$) as NO_3^- has been reported to be encapsulated within the cavity of Pd_2L_4 type metallacages, and thus the electrostatic attraction between the positive Pd_2L_4 metallacage

and negative NO_3^- counterion may inhibit encapsulation of the neutral complex, cisplatin. In each case, it was found that cisplatin was encapsulated within the metallacage cavity in DMF-d_7 (it is worth highlighting that NO_3^- was not encapsulated within $\mathbf{C^{E4}.NO_3}$ in DMF-d_7, despite being reported to be encapsulated in acetonitrile-d_3.)[238] Electrostatic attraction was therefore not the driving force of encapsulation, as the neutral cisplatin complex was preferentially encapsulated in each metallacage rather than NO_3^-.

Solvent effects were then studied as the driving force of encapsulation, namely solvent rearrangement effects (non-classical hydrophobic effect). As such, the effect of increasing volume of water in a DMF-d_7 solution was studied on $\mathbf{C^{E3}}$ and $\mathbf{C^{E4}}$ via ^{1}H and ^{19}F NMR spectroscopy. The results suggested that increasing the water content of the solution caused encapsulation of the BF_4^- counterion in $\mathbf{C^{E3}}$, but not in $\mathbf{C^{E4}}$ due to electrostatic repulsion between the cavity facing electron lone pairs and the counter anion. Furthermore, it was shown via ^{1}H and ^{19}F NMR that cisplatin would be preferentially encapsulated in the water-DMF-d_7 solution of $\mathbf{C^{E3}}$, by evacuating the counter anion from the cavity.

In order to elucidate quantitative data on the encapsulation process in solution, isothermal titration calorimetry (ITC) studies should be performed. ITC is a very sensitive technique which is typically employed to study the binding of ligands to biological receptors.[258,259] The technique directly measures the heat released or absorbed during a binding event, which allows for the accurate determination of thermodynamic parameters such as the binding constant (K_d) stoichiometry (n), change in entropy (ΔS) and the change in enthalpy (ΔH) in solution. As such, a well-designed ITC experiment can provide a complete thermodynamic profile of a binding event in solution.[259] The data provided in this study provides a good foundation for the design of a suitable ITC experiment to elucidate quantitative data for the encapsulation of cisplatin in Pd_2L_4 metallacages in solution.

Chapter 10: Conclusions

In conclusion, the synthesis and characterisation of a diverse range of exo-functionalised Pd_2L_4 (L = 1,3-bis(3-ethynylpyridine)benzene or 2,6-bis(3-ethynylpyridine)pyridine based ligands) has been described.

Several peptides have been successfully conjugated to the ligands of Pd_2L_4 metallacage. The peptides were selected to impart either improved tumour selectivity, via the conjugation of integrin binding RGD containing peptides, or with the aim of translocating the blood brain barrier via the conjugation of the helical peptide, PepH3.

It was shown that when *exo*-functionalised with integrin-targeting peptides, the selectivity for cancer cell lines overexpressing the specific integrin was increased *in vitro*, which supports that the metallacage may benefit from improved tumour selectivity as a drug delivery system. Furthermore, it was shown that the sterically bulky RGD peptides do not hinder the encapsulation of the anti-cancer drug, cisplatin. It was also shown that the toxicity of cisplatin is reduced in healthy liver and kidney tissue *ex vivo*, when encapsulated within the Pd_2L_4 type metallacage. This lower toxicity was shown to be due to a lower uptake of the encapsulated cisplatin, compared to the unencapsulated cisplatin, as shown by ICP-MS.

The synthesis of the blood brain barrier translocating peptide, PepH3, and successful conjugation of the peptide to a 1,3-bis(3-ethynylpyridine)benzene type ligand was shown. The self-assembly of the PepH3 *exo*-functionalised metallacage formation was shown via ^{1}H NMR in non-deuterated DMSO. The solution is awaiting study via *in vitro* transwell assay to determine if the metallacage can translocate brain endothelial cells *in vitro*.

The synthesis and characterisation of a library of fluorescently labelled Pd_2L_4 metallacages has been reported, and their photophysical properties analysed. The stability of the metallacages in water and PBS solution were also studied, and the breakdown of the Pd_2L_4 type metallacage, with either nitrate or tetrafluoroborate as the counterion, in the presence of glutathione was studied using ^{1}H NMR. The study showed that when tetrafluoroborate is used as the counterion, a clean breakdown of the metallacage to its constituent ligand is observed, which provides excellent proof of concept for a viable guest release mechanism upon cellular internalisation. Finally, fluorescence microscopy studies were used to determine the cellular uptake mechanism of a suitably stable, fluorescently labelled Pd_2L_4 metallacage. The results show that the Pd_2L_4 type metallacage entered cells via receptor mediated means, as opposed to adsorptive mediated cell entry. Furthermore, it appeared the metallacage localised within

melanosomes rather than lysosomes upon internalisation by the cell, although further studies are needed to confirm this hypothesis.

The encapsulation of the anti-cancer drug, cisplatin, in Pd_2L_4 type metallacages was studied using a variety of NMR experiments (^{195}Pt, ^{1}H, ^{1}H DOSY, ^{19}F). The data obtained suggests that the encapsulation process is predominantly solvent dependent, although the electronic environment of the internal cavity can also contribute to the overall encapsulation process. In particular, the ability for the bulk solvent to be able to form H-bonding networks appears to play a crucial role in the encapsulation process. The data obtained provides the basis for well designed isothermal titration calorimetry experiments to elucidate quantitative data for the encapsulation of cisplatin in solution and to determine the driving force of encapsulation of cisplatin in solution for Pd_2L_4 metallacages.

Overall, the project has demonstrated the Pd_2L_4 type metallacages hold promise as future drug delivery systems. The metallacage scaffold can encapsulate the anti-cancer drug, cisplatin, and reduce the toxicity of the drug against healthy liver and kidney tissue. Furthermore, Pd_2L_4 metallacages have been shown to be tolerant to exo-functionalisation by numerous functional groups, thus offering great versatility in the design of a drug delivery system. The conjugation of integrin targeting peptides to the metallacage enhanced the selectivity towards the specific integrin, thus providing excellent support that this strategy can be used to improve selectivity towards tumours overexpressing these integrin types. Finally, the fluorophore functionalised Pd_2L_4 metallacage enters human melanoma cells via receptor mediated endocytosis and appears to localise in melanosomes.

Appendix

Monitoring cage synthesis via ^{1}H NMR spectroscopy

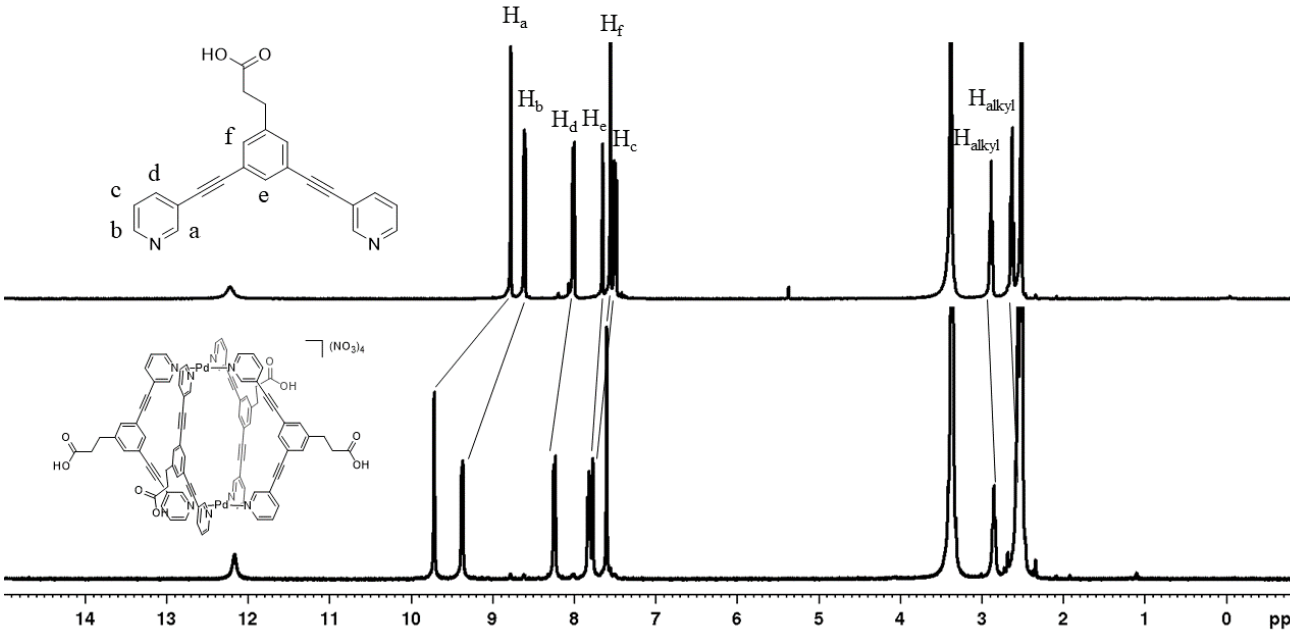

Figure S0: Representative example of monitoring metallacage formation. Stacked ^{1}H NMR (DMSO-d_6) spectra of a ligand (e.g. $\mathbf{L_{aq}7}$) (top) and the corresponding metallacage (e.g. $\mathbf{C_{aq}7}$) (bottom) demonstrate the clear downfield shift of peaks H_a and H_b indicative of quantitative cage formation. This is seen for all metallacages formed via self-assembly.

Chapter 5: Supporting information

Cage synthesis

Synthesis of cage C0

A solution of $[Pd(NCCH_3)_4](BF_4)_2$ (22.2 mg, 0.05 mmol, 2.00 equiv.) and ligand $\mathbf{L^{COOH}}$ (32.4 mg, 0.10 mmol, 4.00 equiv.) in DMSO was stirred for 1 h at 90 °C (**Scheme S1**). Following precipitation by addition of acetone and diethyl ether, the solid was then filtrated and washed with diethyl ether to yield the cage compound as an off-white solid (42.0 mg, 23.0 µmol, 92%). See also **Figures S9-S10**.

^{1}H NMR (400 MHz, DMSO-d_6): δ [ppm] = 9.60 (s, 2H, H_a), 9.40 (d, *J* = 5.8 Hz, 2H, H_b), 8.35 (d, *J* = 8.8 Hz, 2H, H_d), 8.20 (s, 2H, H_f) 8.15 (s, 1H, H_e), 7.85 (dd, *J* = 6.1, 8.2 Hz, 2H, H_c).

^{13}C{^{1}H} NMR (400 MHz, DMSO-d_6): δ [ppm] = 165.9, 153.2, 151.3, 143.6, 137.9, 134.0, 133.1, 127.9, 122.9, 122.6, 93.3, 86.5.

^{11}B{^{1}H} NMR (128 MHz, DMSO-d_6): δ [ppm] = -1.18.

^{19}F{^{1}H} NMR (376 *MHz,* DMSO-d_6*):* δ [ppm] = *-147.8.*

HRMS (ESI) calcd. for $C_{84}H_{44}N_8O_8Pd_2$ [M-4(BF_4)]$^{4+}$: *m/z* = 377.5426; found: 377.5406; δ= 5.3 ppm).

Synthesis of cages C1-C4

The starting material (compounds ^{RGD}**L1**-**4**, ~2 µmol, 4.00 eq.) was weighed into an NMR-tube, respectively, and solubilized in DMSO-d_6 (0.4 mL). A solution of $Pd(MeCN)_4(BF_4)_2$ in DMSO-d_6 (20.54 mM, 2.00 eq.) was added to the solution in the NMR-tube and homogenized. In the ^{1}H-NMR, the starting material was completely converted to the corresponding metallacage (^{RGD}**C1**-**4**). For the ligands ^{RGD}**L1**, ^{RGD}**L3** and ^{RGD}**L4** the molecular weight was calculated as one fold TFA-salts, for ligand ^{RGD}**L2** a calculation without TFA-salt gave full consumption of the starting material. Due to their chromatographic instability, the formation procedure was optimized in NMR-solvent (DMSO-d_6) and analyzed without isolating the product. Hereafter cell- and ELISA-assays were performed directly with these solutions.

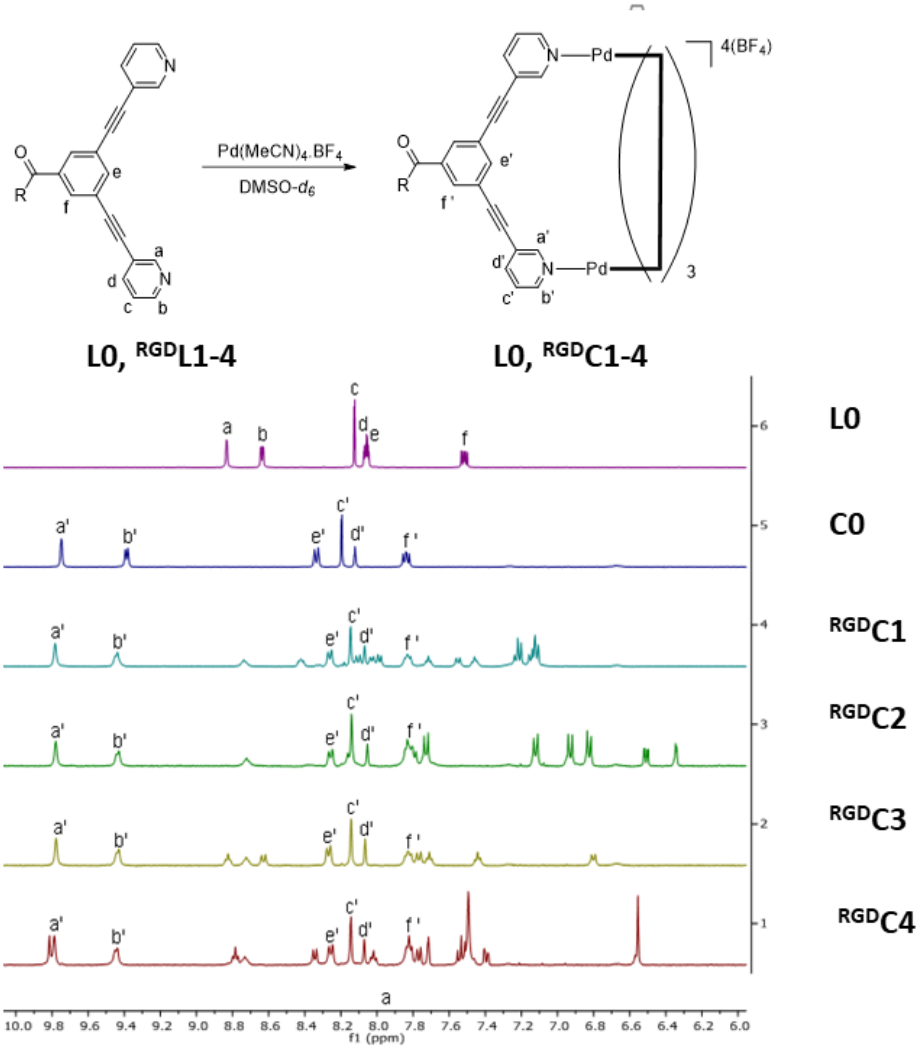

Figure S1. Stacked ^{1}H NMR spectra (DMSO-d_6), zoomed to the aromatic region, of RGD-peptide functionalised metallacages, **^{RGD}C1-4**, showing the downfield shift of protons H_a and H_b, which is indicative of successful Pd_2L_4 metallacage formation

Synthesis of ligand L0

The starting compound benzyl 3,5-dibromobenzoate was synthesised according to a previously reported procedure by benzyl protection of 3,5-dibromobenzoic acid

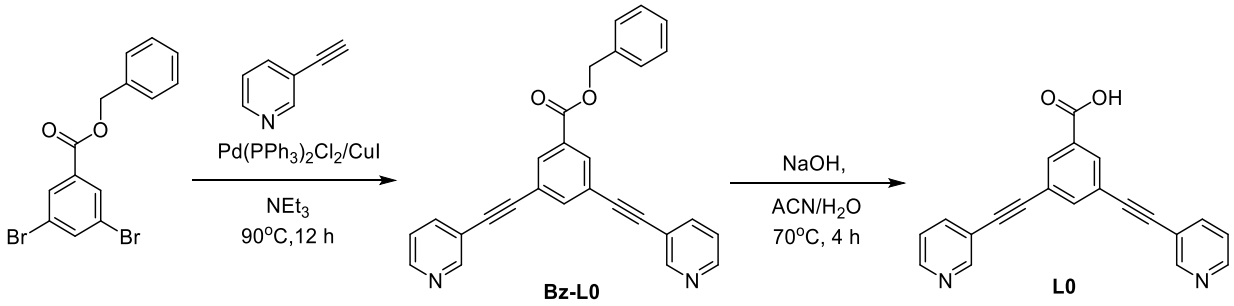

Figure S2. Synthesis of ligand **L0** *via* Sonogashira cross-coupling.

Benzyl 3,5-bis(pyridin-3-ylethynyl)benzoate (Bz-L0)

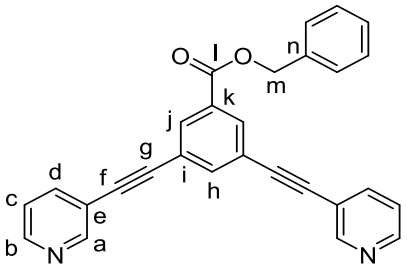

A mixture of benzyl 3,5-dibromobenzoate (370 mg, 1.00 mmol, 1.00 eq.), 3-ethynylpyridine (309 mg, 3.00 mmol, 3.00 eq.), $[Pd(PPh_3)_2Cl_2]$ (68.1 mg, 0.10 mmol, 0.10 eq.), and CuI (18.5 mg, 0.10 mmol, 0.10 eq.), was suspended in distilled triethylamine (15 mL) and stirred under a nitrogen atmosphere at 90°C. After 24 h, the reaction mixture was diluted with ethylacetate (50 mL) and filtered over glass-fritted funnel (por. 3). The solvent was removed under vacuum and the crude residue further purified by column chromatography on silica gel (Ethylacetate: Methanol = 100: 5, R_f = 0.57) to give the product **Bz-L0** as an off white solid (311 mg, 0.75 mmol, 75%).

^{1}H-NMR (400 MHz, DMSO-d_6): δ[ppm] = 8.80 (d, *J* = 1.4 Hz, 2H, H_a), 8.61 (dd, *J* = 1.6, 5.0 Hz, 2H, H_b), 8.12 (d, *J* = 1.6 Hz, 2H, H_f) 8.06 (t, *J* = 1.6, 1H H_e) 8.02 (dt, *J* = 1.8, 8.0 Hz, 2H, H_d) 7.64-7.35 (m, 7H, phenyl, H_c), 5.39 (s, 2H, H_g).

^{13}C{^{1}H}-NMR (101 MHz, DMSO-d_6): δ[ppm] = 164.5 (C_l), 152.3 (C_a), 149.9 (C_b), 139.3 (C_h), 138.7 (C_d), 136.1 (C_k), 132.5 (C_j), 131.9 (C_{phenyl}), 131.4 (C_n) 129.2 (C_{phenyl}), 129.1 (C_{phenyl}), 128.8 (C_{phenyl}), 128.7 (C_{phenyl}), 124.1 (C_c), 123.3 (C_i), 119.2 (C_e), 90.5 (C_f/C_g), 88.6 (C_f/C_g), 67.4 (C_m).

HRMS (ESI) calcd. for $C_{28}H_{19}N_2O_2$ $[M+H]^+$: *m/z* = 415.1447; found: 415.1448; δ = 0.2 ppm.

3,5-bis(pyridin-3-ylethynyl)benzoic acid (L0)

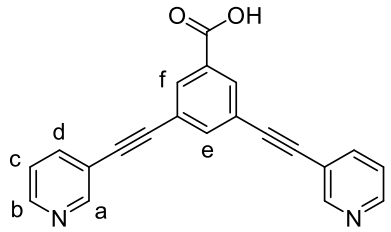

Benzyl 3,5-bis(pyridin-3-ylethynyl)benzoate (**Bz-L0**) (415 mg, 1.00 mmol, 1.00 eq.) was dissolved in acetonitrile (5 mL). To the yellow solution, deionised water (2 mL) was added and the solution was heated to 70°C before sodium hydroxide (100 mg, 2.50 mmol, 2.50 eq.), was added. The resulting orange solution was stirred at 70°C for 4 h. 1 M HCl was added to acidify the solution (~pH 6). The resulting yellow precipitate was collected by filtration, washed with diethyl ether and re-suspended in methanol. The solvent was removed under vacuum to give the product **L0** as a white powder (301 mg, 0.93 mmol, 93%) (Overall yield 66%).

^{1}H-NMR (400 MHz, DMSO-d_6): δ = 8.82 (dd, *J* = 0.89, 2.2 Hz, 2H, H_a), 8.63 (dd, *J* = 1.7, 4.8 Hz, 2H, H_b), 8.12 (d, *J* = 1.6, 2H, H_f), 8.08-8.01 (m, 3H, H_e, H_d), 7.50 (ddd, *J* = 0.90, 4.9, 8.2 Hz, 2H, H_c).

^{13}C{^{1}H}-NMR (101 MHz, DMSO-d_6): δ = 166.2(C_l), 152.3(C_a), 150.0(C_b), 139.3(C_h), 138.1(C_d/C_k), 132.8(C_j), 124.2(C_c), 123.5(C_i), 119.3(C_e), 90.7(C_f/C_g), 88.3(C_f/C_g).

HRMS (ESI) calcd for $C_{21}H_{13}N_2O_2$ [M+H]$^+$: *m/z* = 324.0899; found: 324.0901; δ = 0.6 ppm.

Encapsulation studies

^{1}H-NMR spectroscopy

The benzoate protected Pd_2L_4 cage **C0-Bz** (8 mg, 36 µmol, 1.00 eq.) was dissolved in DMF-d_7 (1mL) and the ^{1}H-NMR (500 MHz, 64 scans) spectrum was recorded. Cisplatin (2 mg, 72 µmol, 2.00 eq.) was added and the yellow solution was stirred for 10 min. The ^{1}H-NMR (400 MHz, 64 scans) spectrum of the sample was recorded and compared with the previous one.

^{1}H-DOSY NMR spectroscopy

The benzoate protected ligand **L0-Bz** (15.7 mg, 37.9 µmol, 4.00 eq.) was dissolved in DMF-d_7 (2.63 mL, 14.4 mM) and a solution of $Pd(MeCN)_4(BF_4)_2$ (8.41 mg, 18.9 µmol, 2.00 eq.) in DMF-d_7 (461 µL, 41.1 mM) was added and a ^{1}H-NMR (400 MHz) spectrum was measured to ensure cage-formation. For each ratio, cisplatin was exactly measured out in a glass vial and the previously prepared cage solution was added to get a final cage: cis-Pt ration of 1: 1, 1: 2, 1:3. The solution was mixed for about 5 min to guarantee complete dissolution of the cis-Pt, subsequently a ^{1}H-NMR and a DOSY-NMR was measured

NMR Spectroscopy

^{1}H and ^{13}C NMR Spectra

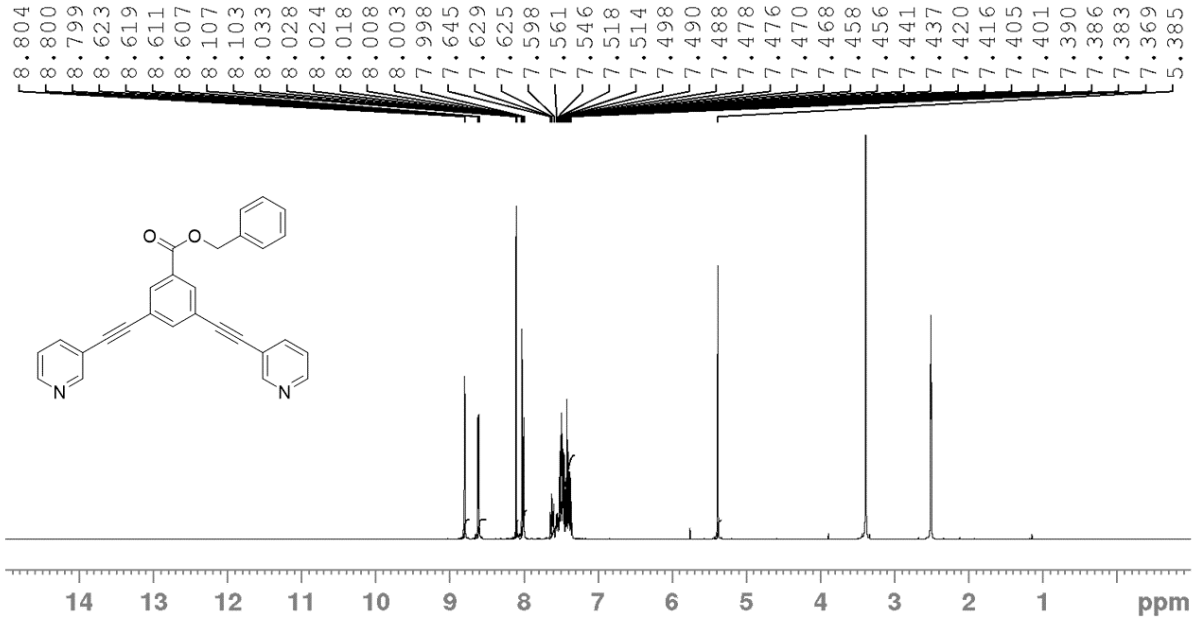

Figure S3 ^{1}H NMR (400 MHz, [DMSO-d_6) of Benzyl 3,5-bis(pyridin-3-ylethynyl)benzoate (**Bz-L0**)

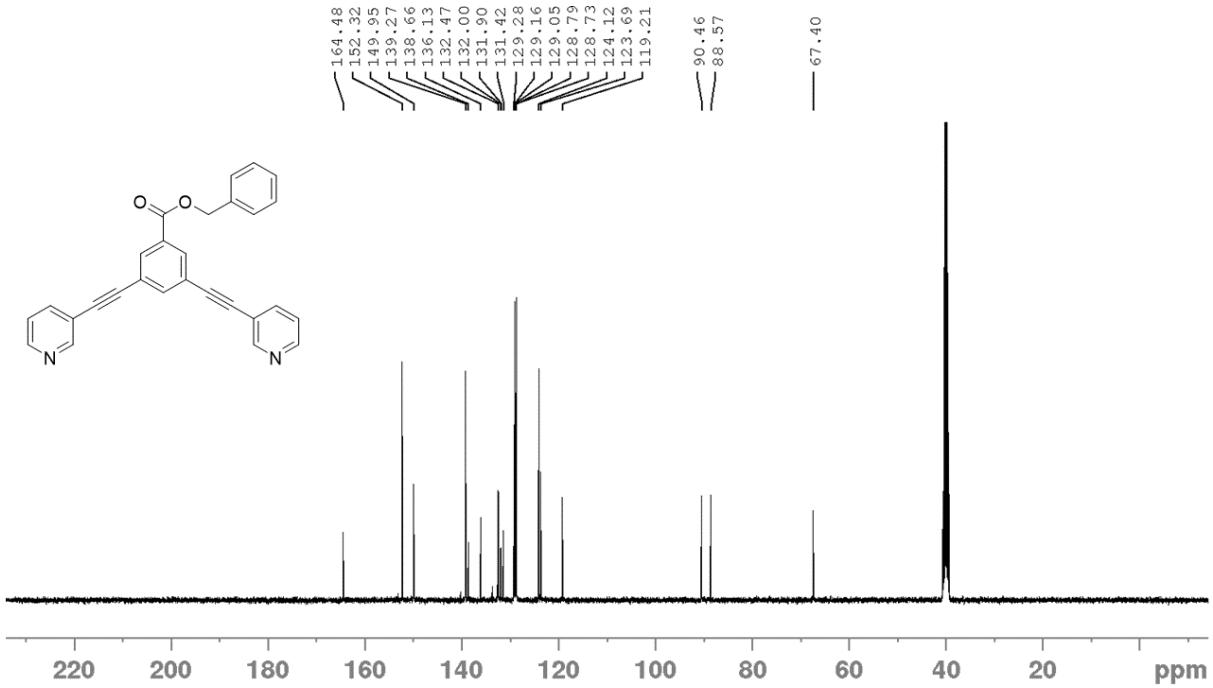

Figure S4. $^{13}C\{^{1}H\}$ NMR (400 MHz, DMSO-d_6) of Benzyl 3,5-bis(pyridin-3-ylethynyl)benzoate (**Bz-L0**)

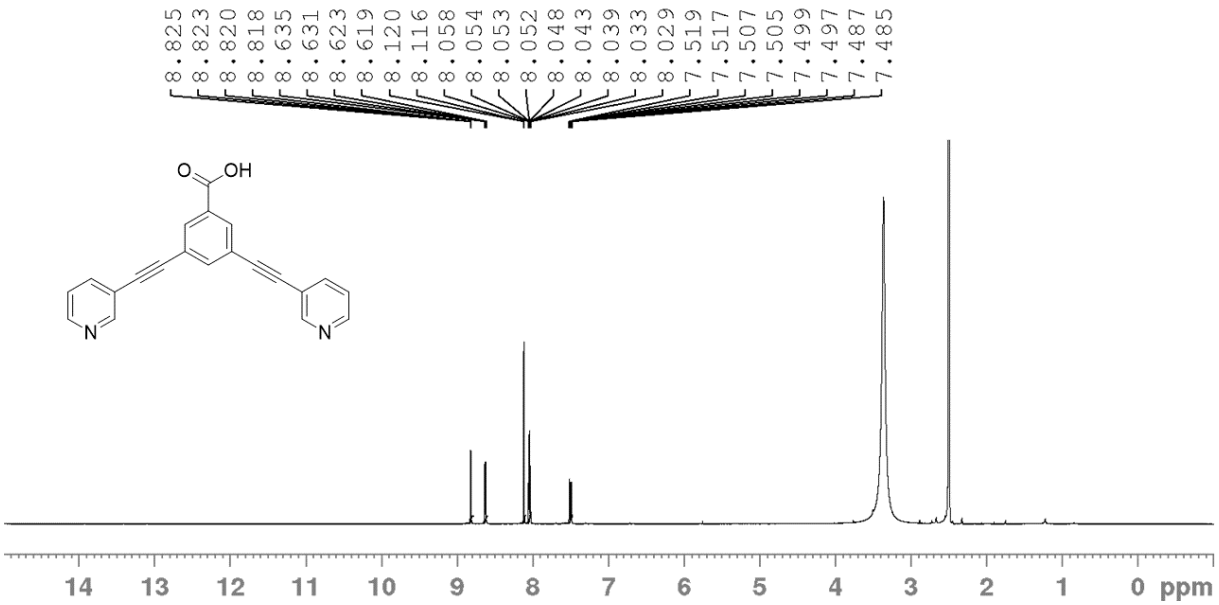

Figure S5. ^{1}H NMR (400 MHz, DMSO-d_6) of ligand **L0**.

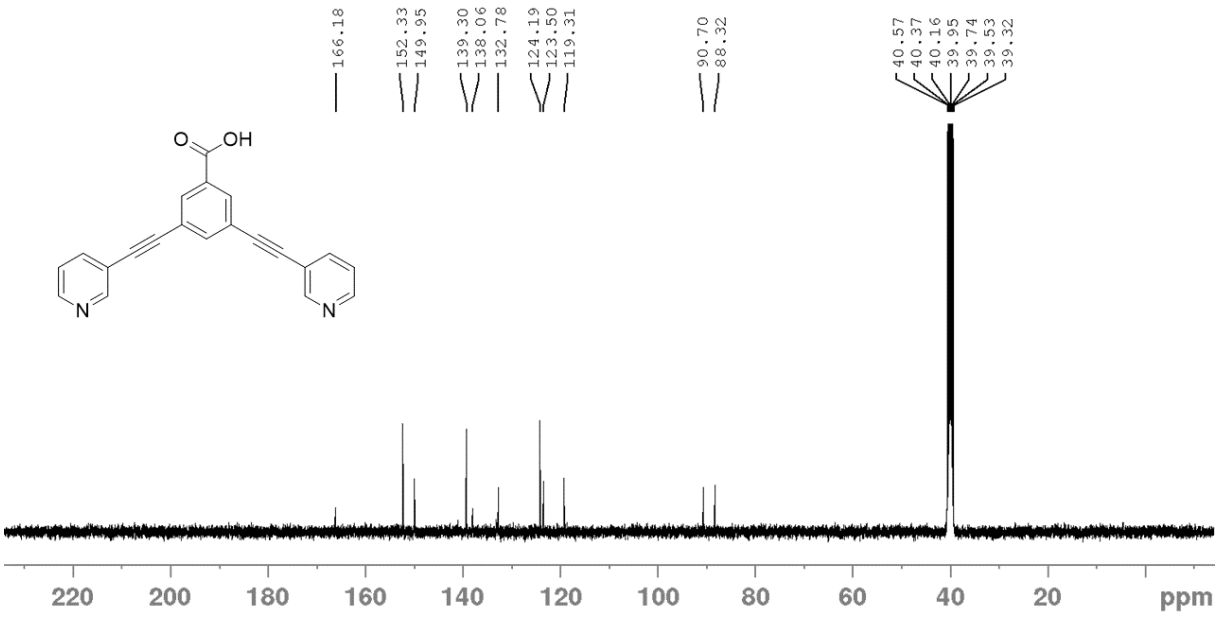

Figure S6. ^{13}C NMR (400 MHz, DMSO-d_6) of ligand **L0**.

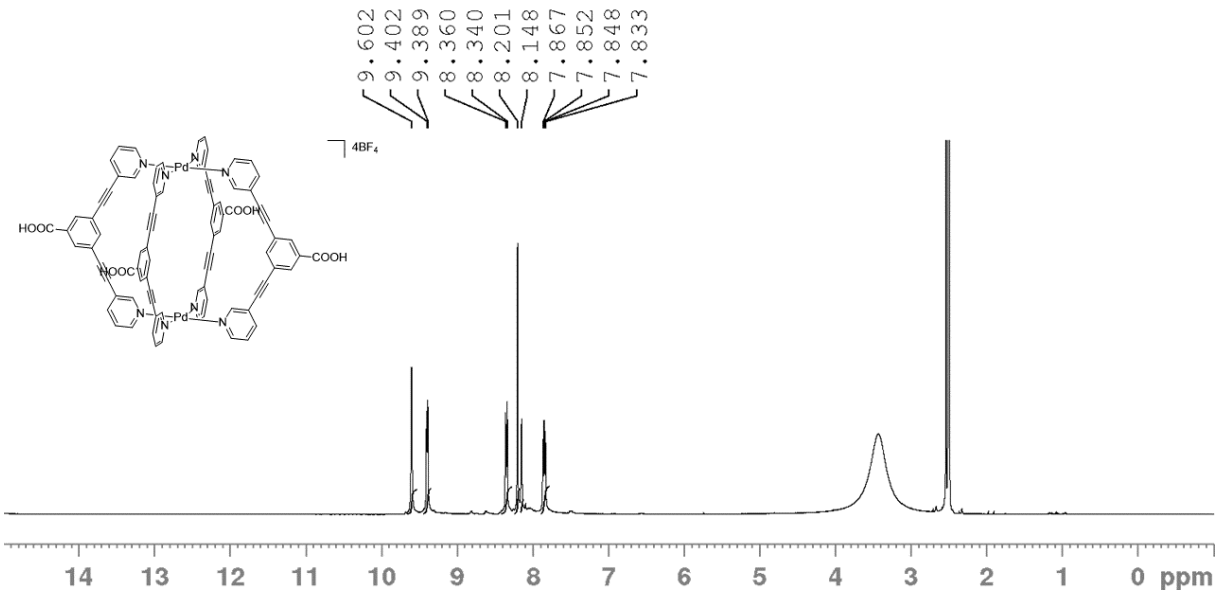

Figure S7^{1}H NMR (400 MHz, DMSO-d_6) of cage **C** (bottom) and related zoom (top).

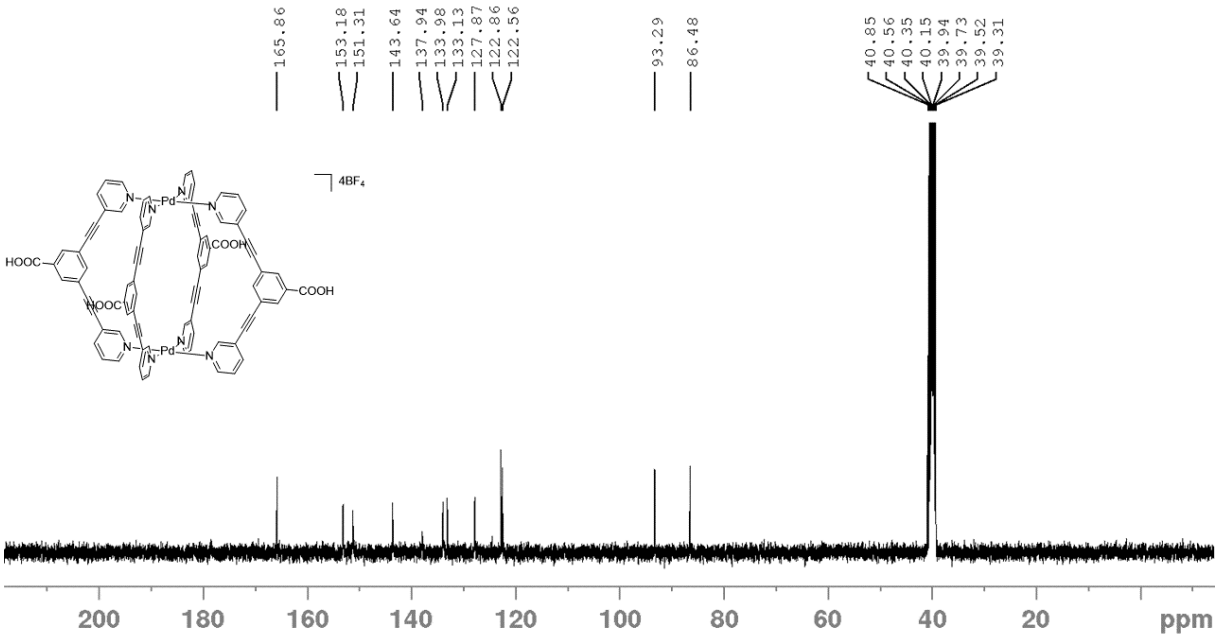

Figure S8. ^{13}C NMR (400 MHz, DMSO-d_6) of cage **C0**.

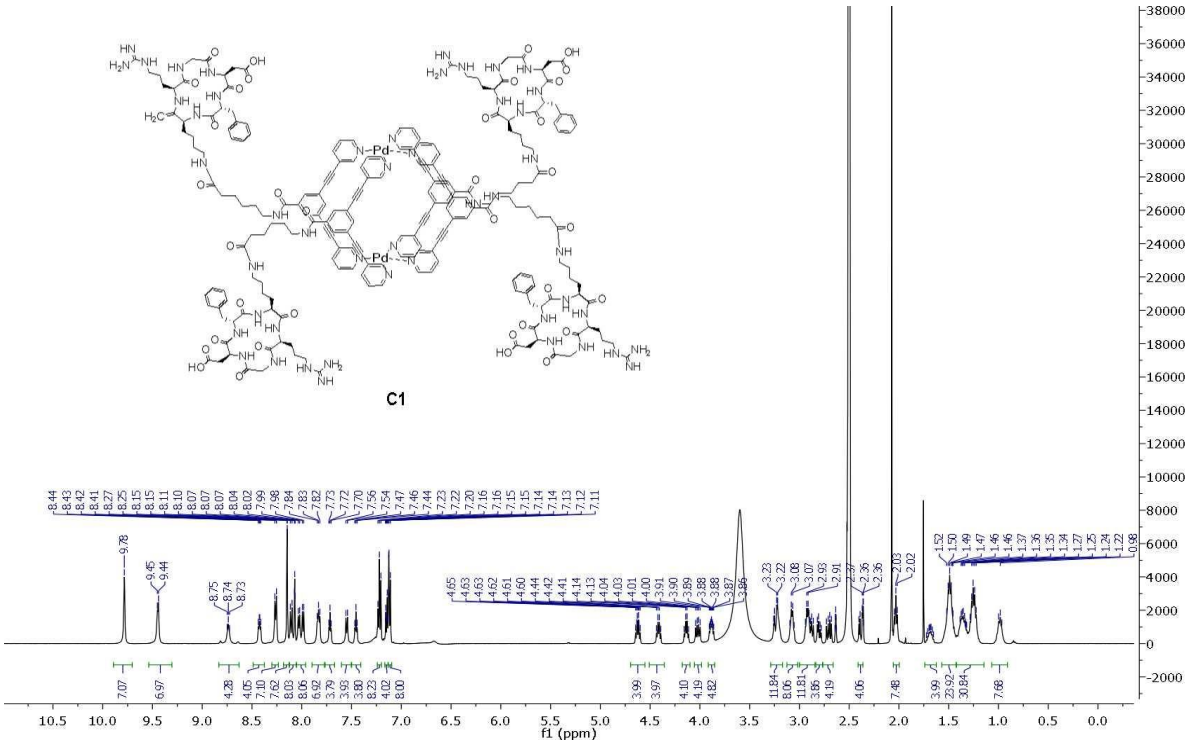

Figures S9. ^{1}H NMR (400 MHz, DMSO-d_6) spectrum of cage ^{RGD}**C1**.

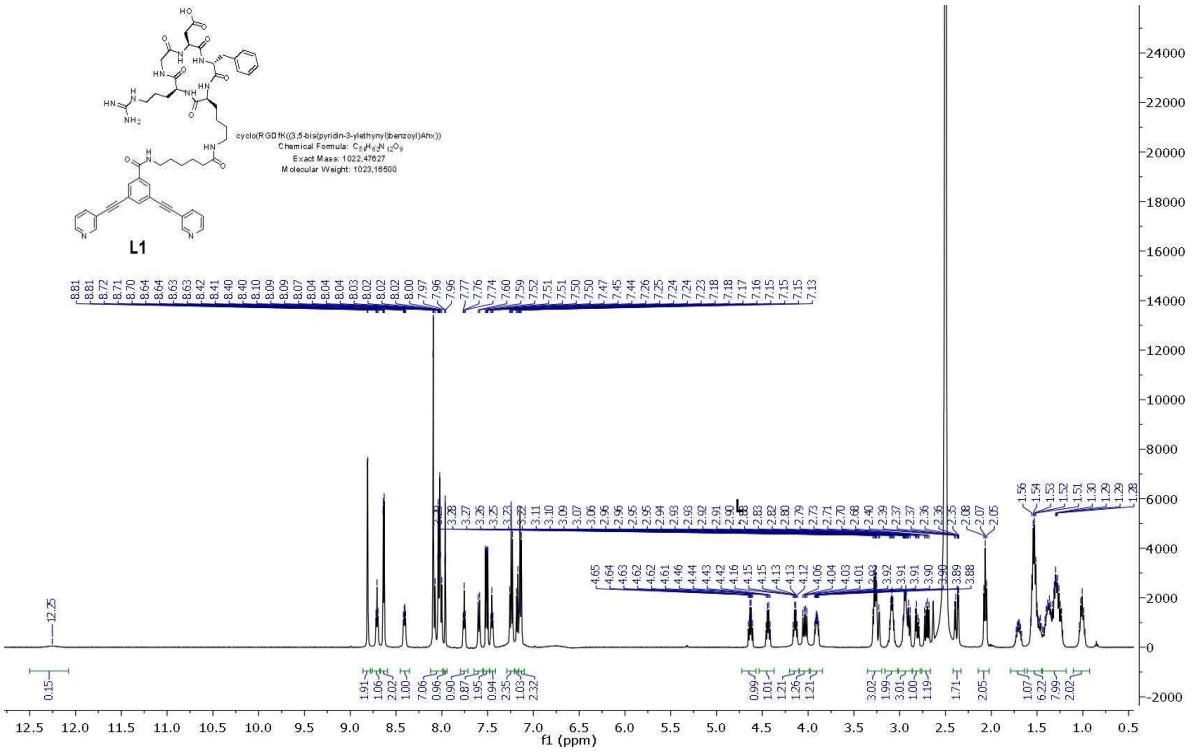

Figures S10. ^{1}H NMR (500 MHz, DMSO-d_6) spectrum of ligand ^{RGD}**L1**.

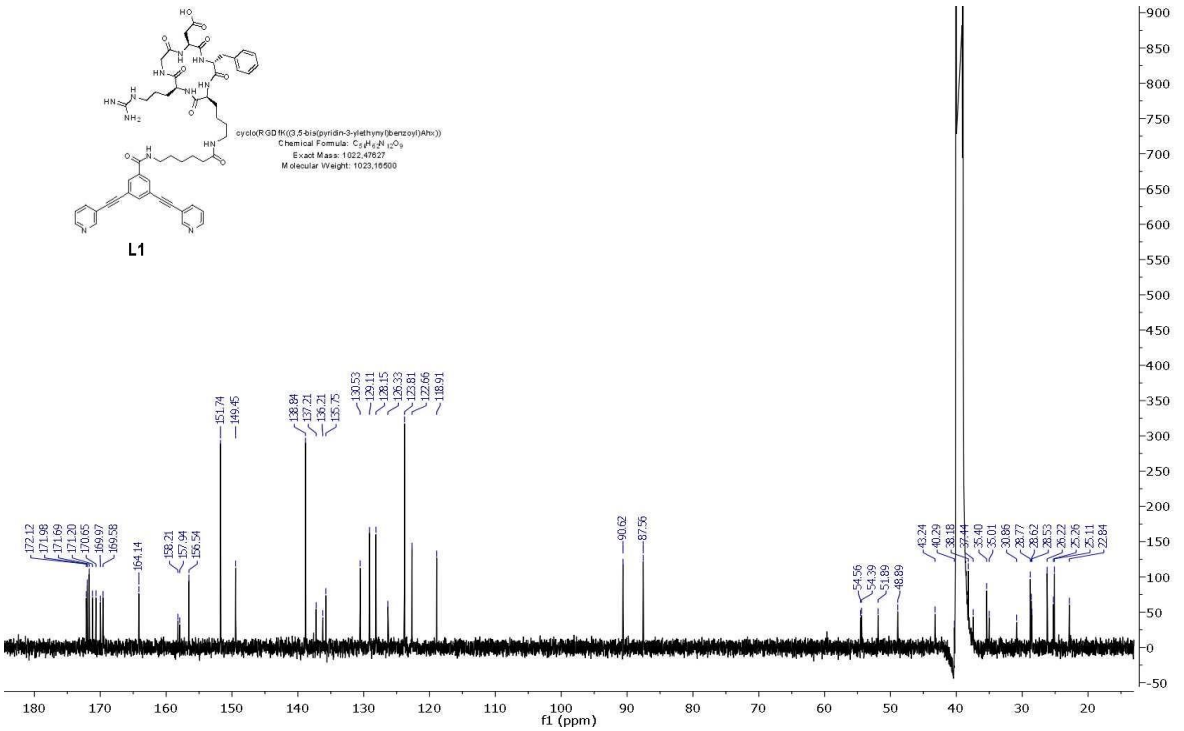

Figures S11. ^{13}C NMR (126 MHz, DMSO-d_6) spectrum of ligand ^{RGD}**L1**.

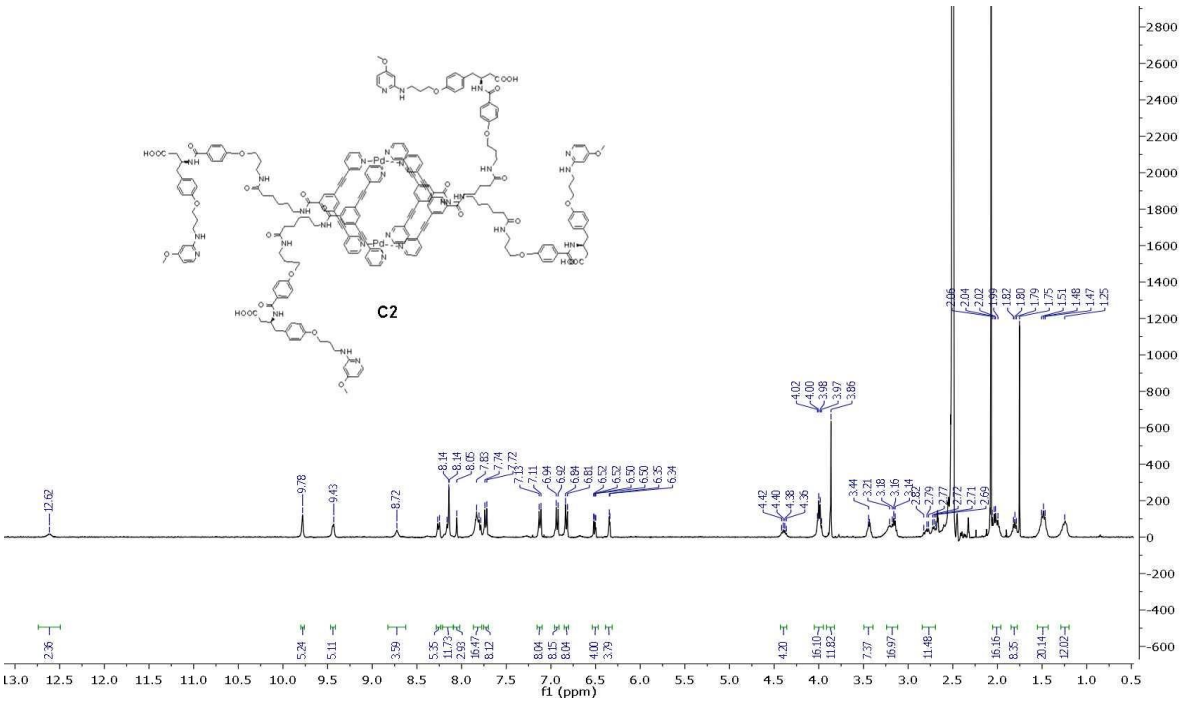

Figures S12. ^{1}H NMR (500 MHz, DMSO-d_6) spectrum of cage ^{RGD}**C2**.

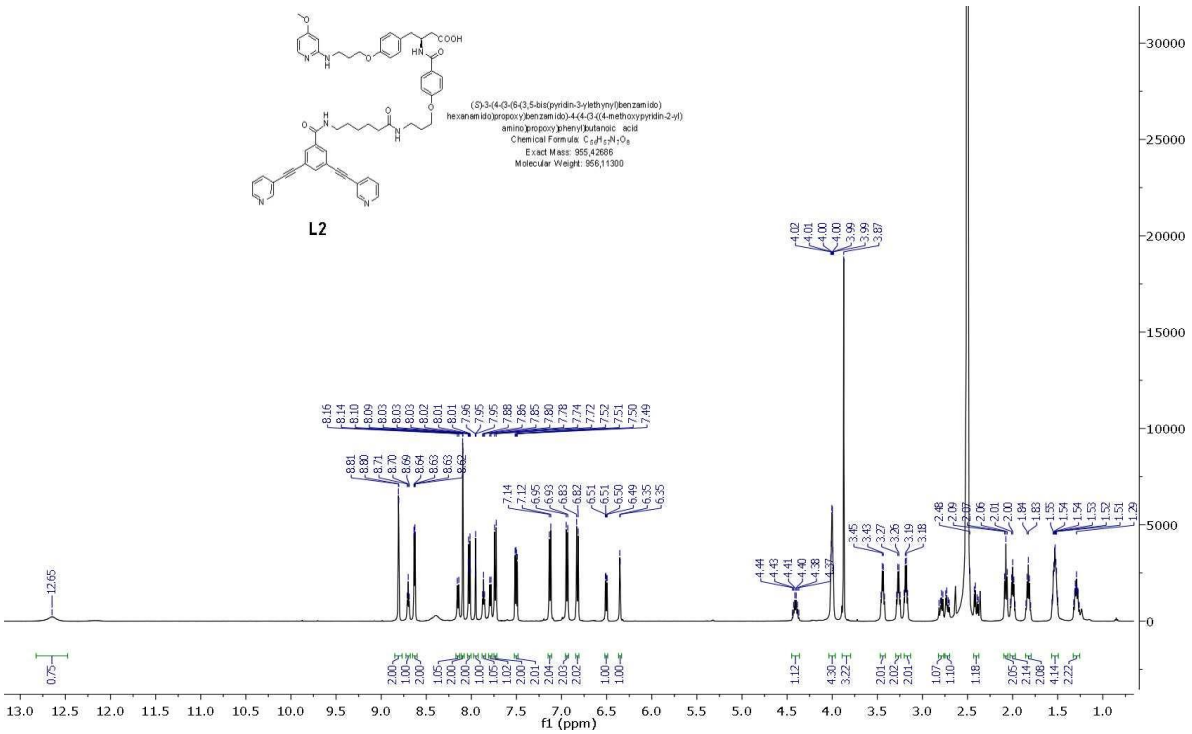

Figures S13. ^{1}H NMR (500 MHz, DMSO-d_6) spectrum of ligand ^{RGD}**L2**.

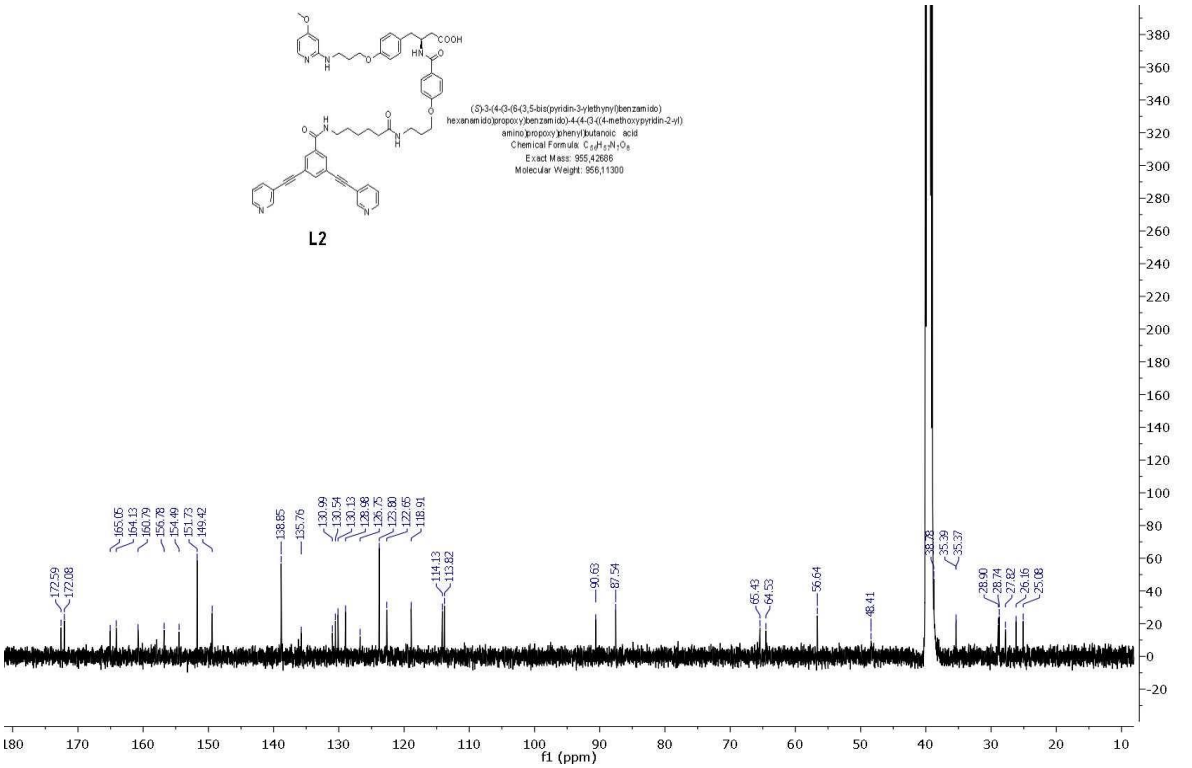

Figures S14. ^{13}C NMR (126 MHz, DMSO-d_6) spectrum of ligand ^{RGD}**L2**.

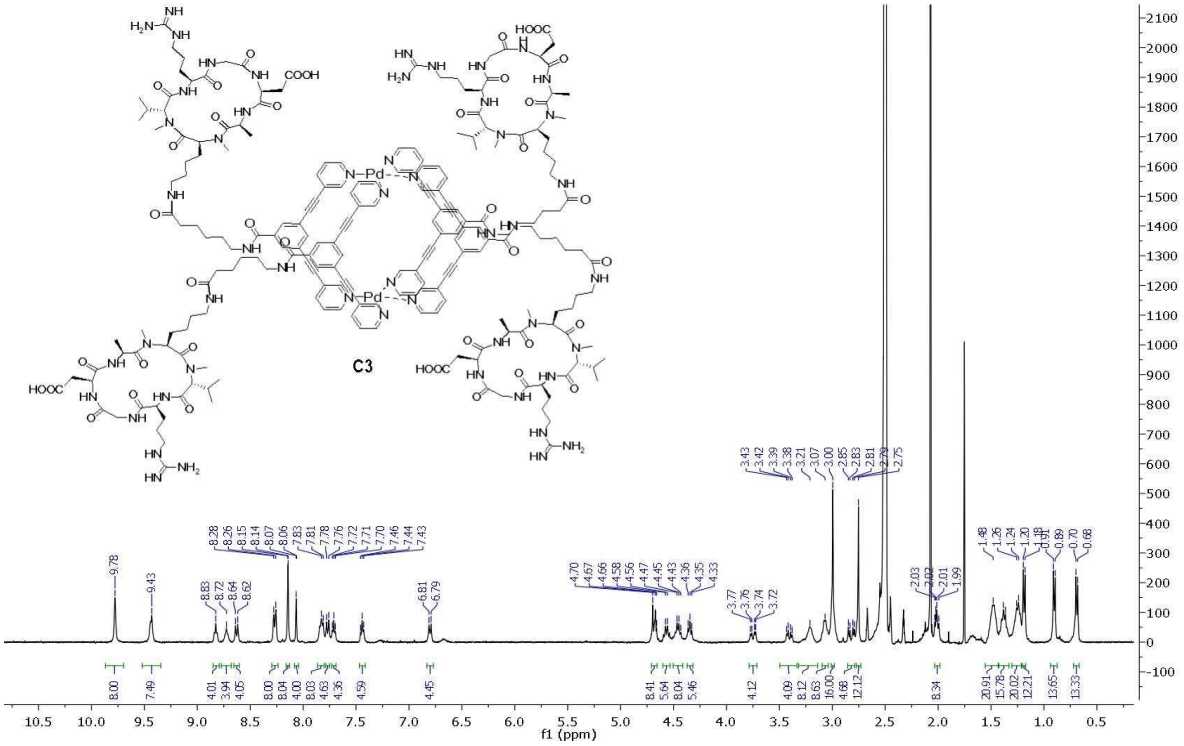

Figures S15. ^{1}H NMR (500 MHz, DMSO-d_6) spectrum of cage ^{RGD}**C3**.

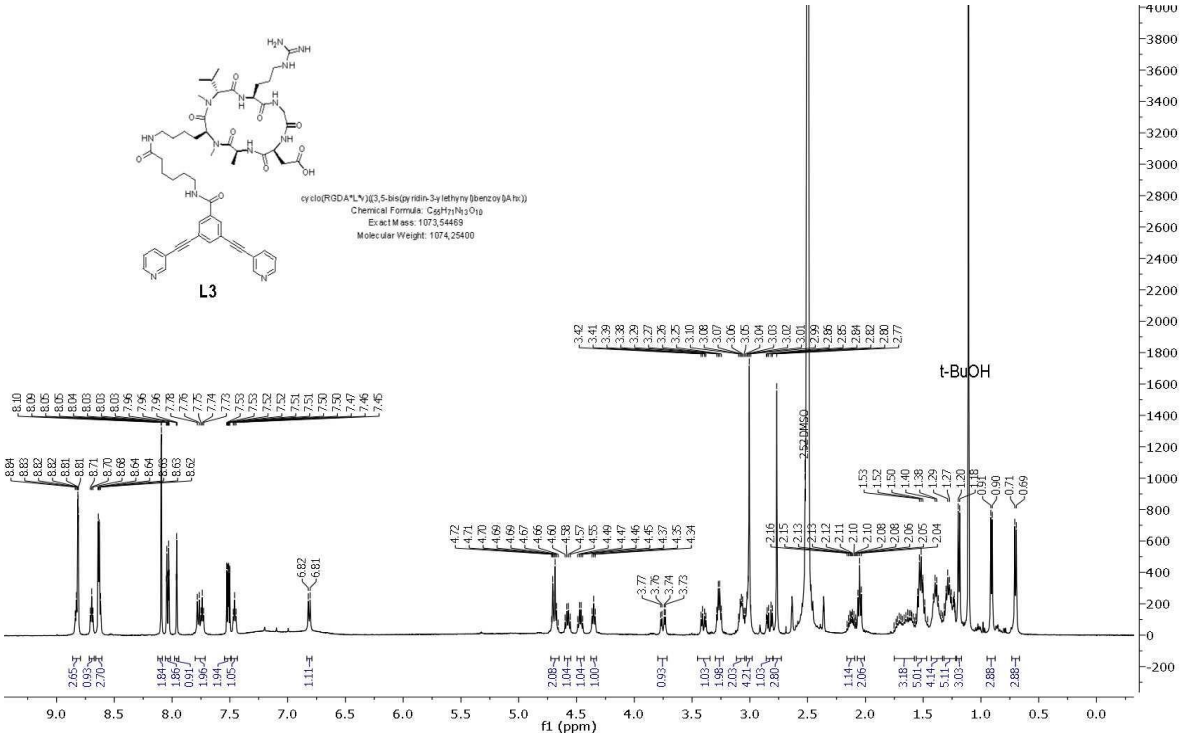

Figures S16. ^{1}H NMR (500 MHz, DMSO-d_6) spectrum of ligand ^{RGD}**L3**.

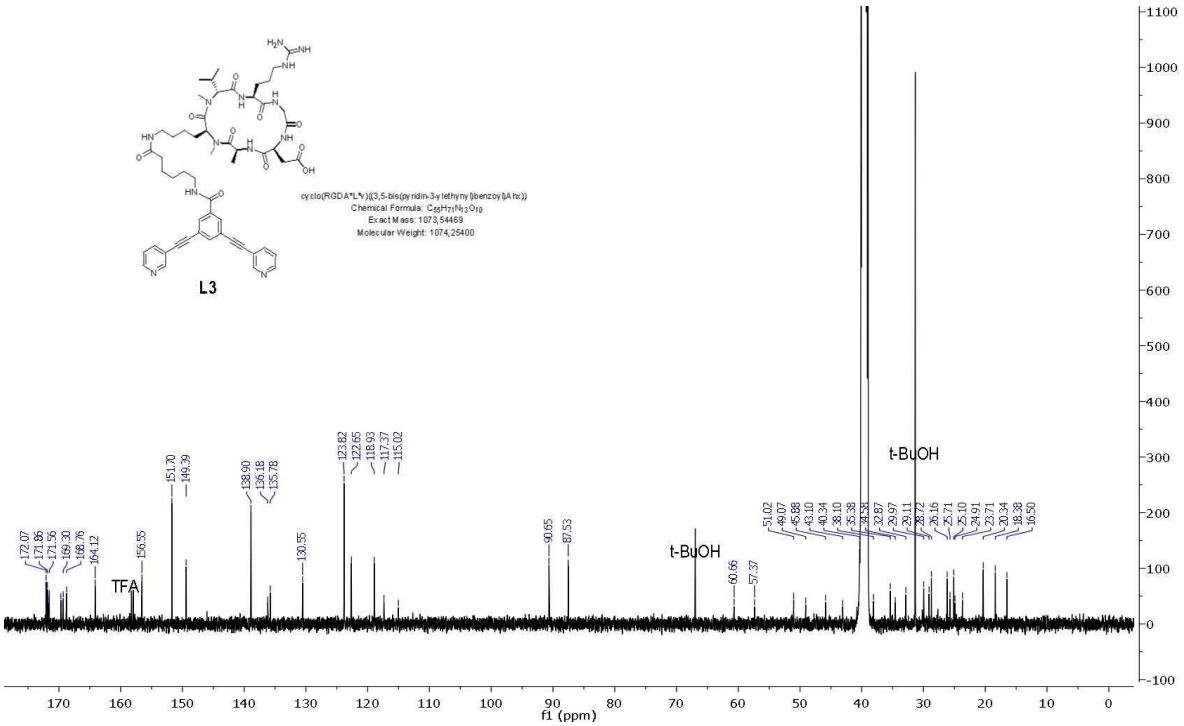

Figures S17. ^{13}C NMR (126 MHz, DMSO-d_6) spectrum of ligand ^{RGD}**L3**.

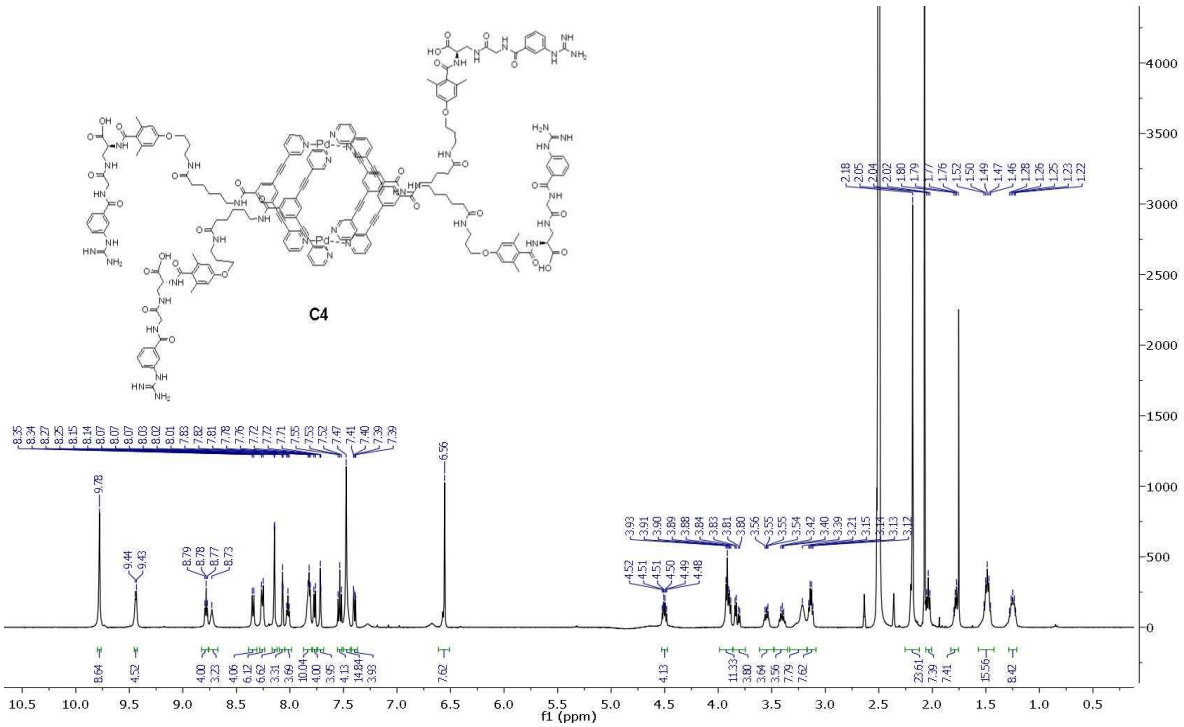

Figures S18. ^{1}H NMR (500 MHz, DMSO-d_6) spectrum of cage ^{RGD}**C4**.

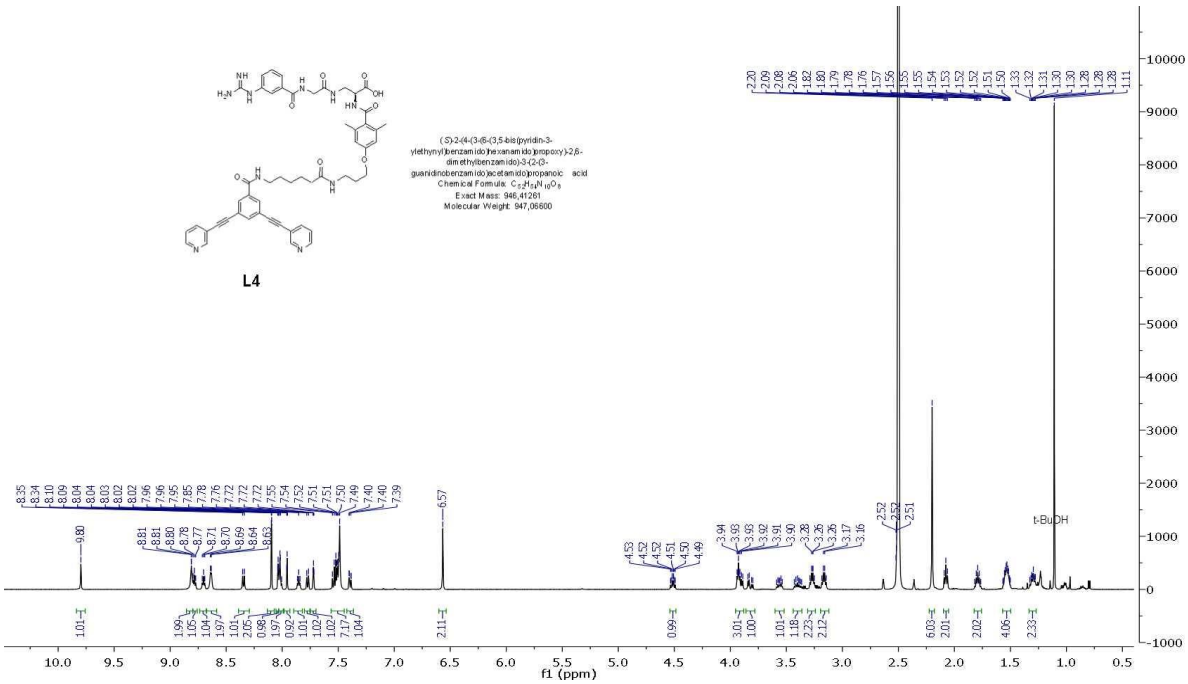

Figures S19. ^{1}H NMR (500 MHz, DMSO-d_6) spectrum of ligand ^{RGD}**L4**.

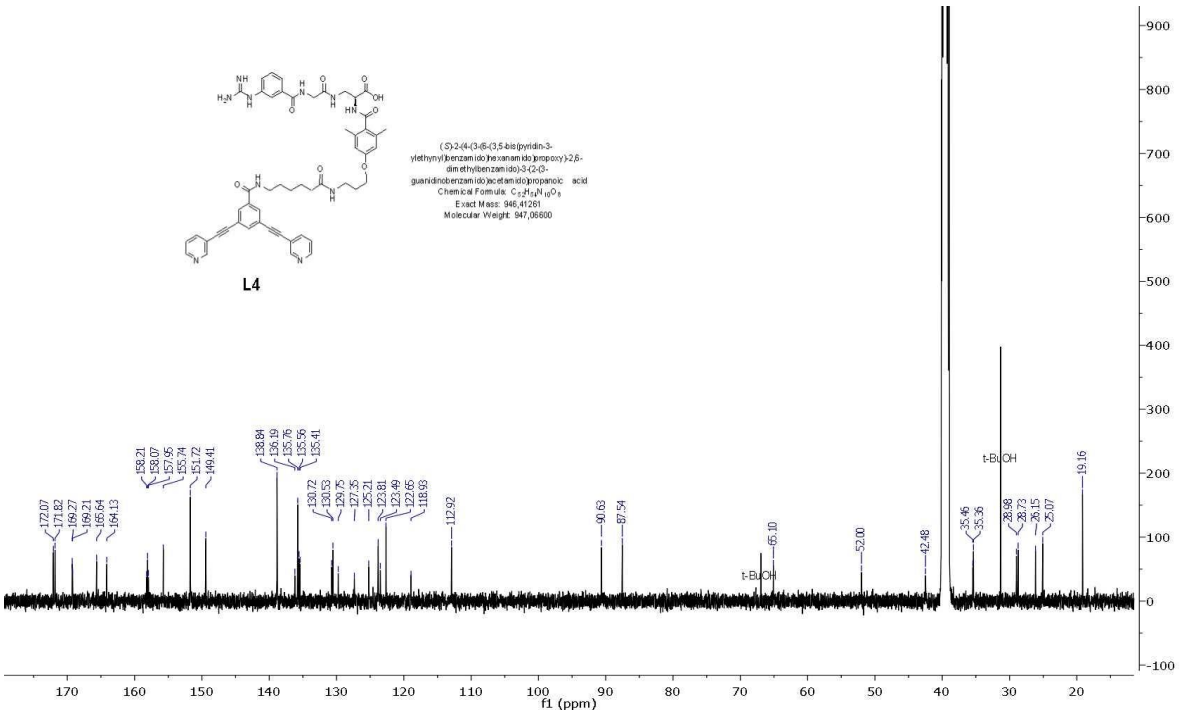

Figures S20. ^{13}C NMR (126 MHz, DMSO-d_6) spectrum of ligand ^{RGD}**L4**.

^{1}H DOSY NMR Spectra

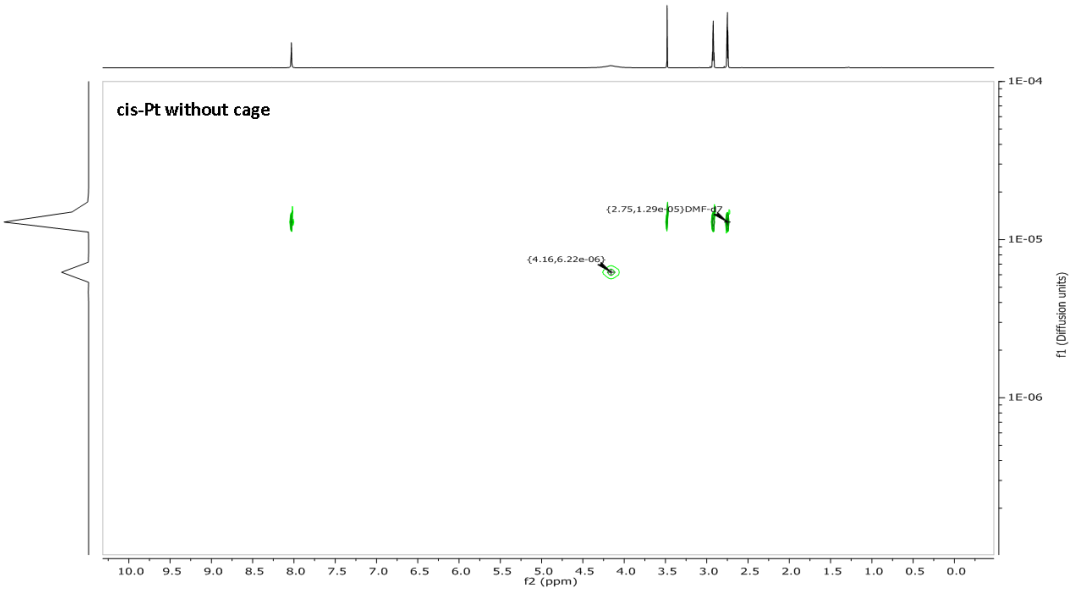

Figure S21: ^{1}H-DOSY-NMR of Cisplatin (1 eq.) in DMF-d_7.

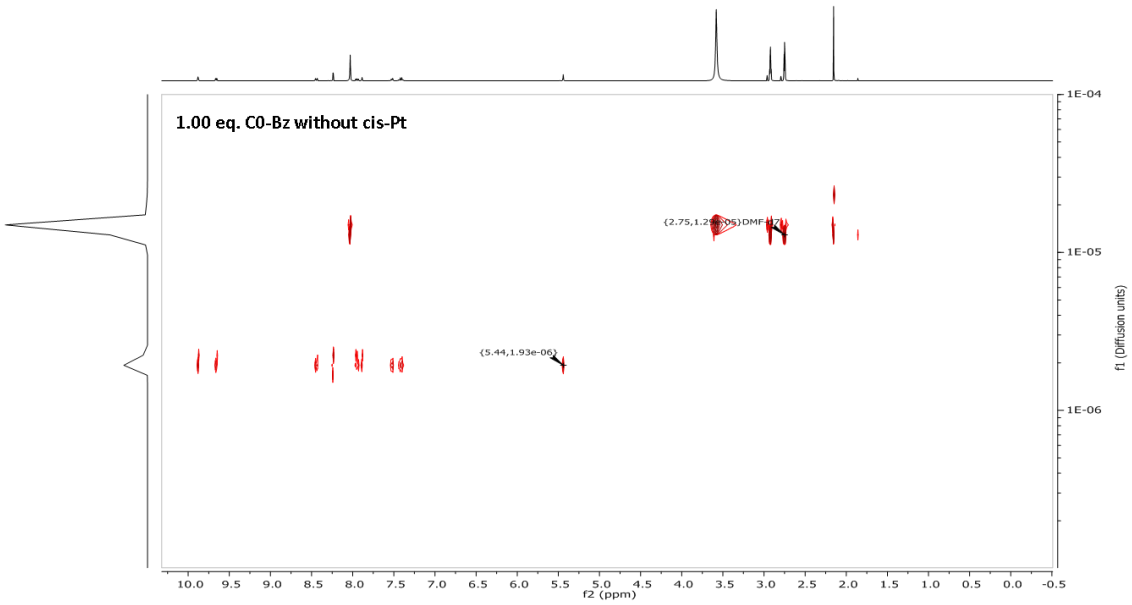

Figure S22: ^{1}H-DOSY-NMR of **Bz-C0** in DMF-d_7.

Chapter 6: Supporting information

Synthesis of L^{PepH3} via standard Fmoc solid phase peptide synthesis (SPPS) protocol

Loading of Rink Amide MBHA resin.
Peptide synthesis was carried out using Rink amide MBHA resin (0.78 mmol/g) following standard Fmoc-strategy. The resin was swollen using DCM (20 mL/g, 30 min). The DCM was removed and the resin was treated with 20% (*v/v*) piperidine in DMF twice (10 min + 5 min) and subsequently washed with DMF (3x).Fmoc-Trp(Boc)-OH (2.5 eq.) was attached to the resin with *O*-(7-azabenzotriazol-1-yl)-*N*,*N*,*N*',*N*'-tetramethyluronium-hexafluorphosphate (HATU) (2.5 eq.), DMAP (2.5 eq.) and DIPEA (5 eq.) in DMF (20 mL/g resin) for 4 h at rt. The resin was then filtered and washed with DMF (3x) and then CH_2Cl_2 (3x). The loading capacity was estimated to be 0.78 mmol/g (100 %).

On-Resin Fmoc Deprotection.
The resin-bound Fmoc peptide was treated with 20% (*v/v*) piperidine in DMF twice (10 min + 5 min) then washed with DMF (3x) and DCM (3x)

Standard Amino Acid Coupling.
A solution of Fmoc-Xaa-OH (Xaa = arginine, lysine, leucine, isoleucine, glycine, alanine) (2.5 eq.), HATU (2.5 eq.), and DIPEA (5.0 eq.) in DMF (10 mL/g resin) was added to the resin-bound free amine peptide and agitated with nitrogen for 2 hours at rt. The resin was then washed with DMF (3x) and DCM (3x).

Coupling with PEG linker on resin.
N-[8-(9-Fluorenylmethyloxycarbonyl)amino-3,6-dioxaoctyl]succinamic acid (**PEG**) (2.00 eq.) HATU (2.00 eq.) and HOBt (2.00 eq.) were dissolved in DMF (40 mL) and DIPEA (4.00 eq.) was added. The solution was stirred at room temperature for 4 hours, or until complete coupling had been observed, and subsequently added to the suspension of the free amine PepH3 bound resin in DMF (1.00 eq.). The reaction mixture was stirred for 1 h at rt, the solvent removed and the resin washed with DMF (3x) and DCM (3x)

Coupling with $L^{CH2COOH}$ on resin.
3,5-bis(pyridin-3-ylethynyl)benzoic acid (**$L^{CH2COOH}$**) (2.00 eq.) HATU (2.00 eq.) and HOBt (2.00 eq.) were dissolved in DMF (40 mL) and DIPEA (4.00 eq.) was added. The solution was stirred at room temperature for 4 hours, or until complete coupling had been observed, and subsequently added to a solution of the corresponding amine (1.00 eq.) in DMF (50 mm). The reaction mixture was stirred for 1 h at rt, the solvent removed *in vacuo* and the crude product purified via RP-HPLC.

Coupling with $L^{CH2COOH}$ on resin.
3,5-bis(pyridin-3-ylethynyl)benzoic acid (**$L^{CH2COOH}$**) (2.00 eq.) HATU (2.00 eq.) and HOBt (2.00 eq.) were dissolved in DMF (40 mL) and DIPEA (4.00 eq.) was added. The solution was stirred at room temperature for 4 hours, or until complete coupling had been observed, and subsequently added to a solution of the resin bound PepH3-PEG free amine (1.00 eq.). The

reaction mixture was agitated with nitrogen for 4 hours, the solvent was removed and the resin washed with DMF (3x) and DCM (3x).

Cleavage of Peptide conjugate from the Resin.

For complete cleavage from the resin, the peptide conjugate was treated with a solution of trifluoroacetic acid, water and triisopropylsilane (TFA: H_2O: TIPS; 95: 2.5: 2.5 *v/v*) for 30 min at rt (2x). The solvent was removed, and the resin was washed with DCM (5x), before the solvent was evaporated under nitrogen, and the crude residue was purified via semi-preparative HPLC.

Analytical control by RP-HPLC

Analytical control of PepH3 and PepH3-PEG conjugate was carried out on a Supelco Discovery BioWide Pore C18 column (250 mm × 4.6 mm, 5 μm) with a flow rate of 1.0 mL min^{-1}.
UV detection: λ = 220 and 280 nm.
Eluents: A = 0.1% TFA in H2O; B = 0.1% TFA in CH_3CN.
HPLC Gradient: 0−5 min, 100% eluent B, 5 - 25 min, 0−50% eluent A; 25−27 min,50-100% eluent A; 27−28 min 100% eluent A

Purification by semipreparative RP-HPLC

Semipreparative purifications of $\mathbf{L^{PepH3}}$ were achieved on a Supelco Discovery BioWide Pore C18 column (250 mm × 4.6 mm, 5 μm) with a flow rate of 2.0 mL min^{-1}. UV detection: λ = 220 and 280 nm.
Eluents: A, 0.1% TFA in H2O; B, 0.1% TFA in CH_3CN.
HPLC Gradient: 0−25 min, 10−50% eluent A; 25−27 min, 100% eluent B; 27−28 min 100% eluent B

Chapter 7 Supporting information

General

Synthesis of ligands

BODIPY **B1**,[235] **B2**[236] and ligand **L1** have been synthesized adapting previously reported procedures and the analytical data is in accordance with the literature.

3,3'-((5-azido-1,3-phenylene)bis(ethyne-2,1-diyl))dipyridine (L^{N3}):

$\mathbf{L^{NH2}}$ (136 mg, 459 μmol, 1.00 eq.) was dissolved in 6M HCl (4.5 mL) and cooled down to 0 °C (water/ice). $NaNO_2$ (39.7 mg, 575 μmol, 1.20 eq.) was dissolved in water (3 mL) and added dropwise to the reaction. After 30 min, the reaction was allowed to warm to r.t. and NaN_3 (59.3 mg, 912 μmol, 2.00 eq.) dissolved in water (3 mL) was added dropwise and stirred for 2 h. The pH-value was adjusted to 8 with 2M NaOH, the formed precipitate filtered over a glass-fritted funnel (pore 3) and washed with a small amount of water, EtOH and Et_2O to give **L2** as a pale brown solid (96.3 mg, 300 μmol, 65%).

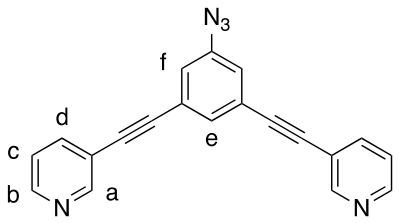

^{1}H NMR (400 MHz, $CDCl_3$): δ [ppm] = 8.78 (d, *J* = 1.3 Hz, 2H, H_a), 8.59 (dd, *J* = 1.7, 4.9 Hz, 2H, H_b), 7.82 (dt, *J* = 1.9, 7.9 Hz, 2H, H_d), 7.51 (t, *J* = 1.4 Hz, 1H, H_e), 7.31 (dd, *J* = 4.9, 7.9 Hz, 2H, H_c). 7.19 (s, 2H, H_f)

^{13}C NMR (101 MHz, DMSO-d_6): δ [ppm] 151.8. 149.5, 141.0, 138.8, 130.7, 123.9, 123.7, 122.5, 118.8, 90.3, 87.8.

HRMS (ESI, MeCN): calcd. for $C_{20}H_{12}N_5$ $[M+H]^+$: *m/z* = 322.1094; found: 322.1112, δ = 5.9 ppm.

N-(3,5-bis(pyridin-3-ylethynyl)phenyl)-4-(2,8-diethyl-5,5-difluoro-1,3,7,9-tetramethyl-5H-4λ^4,5λ^4-dipyrrolo[1,2-c:2',1'-f][1,3,2]diazaborinin-10-yl)benzamide ($L1^{BDP}$):

A mixture of $\mathbf{BDP^{COOH}}$ (152 mg, 357 μmol, 1.00 eq.), $\mathbf{L^{NH2}}$ (105 mg, 356 μmol, 1.00 eq.), CMPI (360 mg, 1.41 mmol, 4.00 eq.) and DMAP (433 mg, 3.54 mmol, 10.0 eq.) was dissolved in *anhydrous* DMF (18 mL) and stirred under a nitrogen atmosphere at 130 °C. After 18 h, the solvent was removed under reduced pressure, the residue dissolved in DCM (50 mL) and washed with water (3x 40 mL) and brine (1x 40 mL). The organic layer was dried over $MgSO_4$ and filtered over a glass-fritted funnel (pore 3). The solvent was removed under reduced pressure and the crude compound purified via silica column chromatography (EtOAc:*n*-hexane = 1:1 → 3:1; EtOAc:*n*-hexane = 1:1, R_f = 0.21) to give the product as a red/pink solid (108 mg, 154 μmol, 43%).

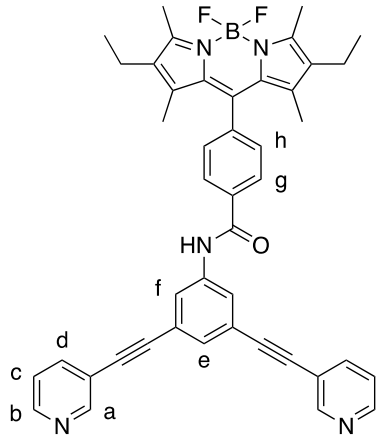

^{1}H NMR (400 MHz, acetone-d_6): δ [ppm] = 9.97 (s, 1H, N*H*), 8.80 (d, *J* = 1.3 Hz, 2H, H_a), 8.61 (dd, *J* = 1.7, 4.9 Hz, 2H, H_b), 8.30 (d, *J* = 8.3 Hz, 2H, H_g), 8.21 (d, *J* = 1.5 Hz, 2H, H_f), 7.99 (dt, *J* = 1.9, 7.9 Hz, 2H, H_d), 7.61 (d, *J* = 8.2 Hz, 2H, H_h), 7.57 (t, *J* = 1.4 Hz, 1H, H_e), 7.47 (dd, *J* = 4.9, 7.9 Hz, 2H, H_c), 2.51 (s, 6H, NCCH_3), 2.36 (q, *J* = 7.5 Hz, 4H, CH_2CH$_3$), 1.36 (s, 6H, CCH_3), 0.99 (t, *J* = 7.5 Hz, 6H, CH$_2$CH_3).

^{13}C NMR (101 MHz, acetone-d_6): δ [ppm] = 165.4. 156.0, 154.8, 152.9, 150.1, 148.3, 141.0, 140.2, 139.3, 139.0, 133.8, 130.5, 129.7, 129.4, 124.4, 124.3, 124.2, 120.6, 96.1, 91.8, 87.5, 17.5, 14.9, 12.7, 12.1.

^{11}B NMR (128 MHz, acetone-d_6): δ [ppm] = 0.76.

^{19}F NMR (376 MHz, acetone-d_6): δ [ppm] = -145.1.

HRMS (ESI, MeCN): calcd. for $C_{44}H_{38}BFN_5O$ $[M\text{-}F]^+$: *m/z* = 682.3125; found: 682.3139, δ = -2.1 ppm.

10-(4-(1-(3,5-bis(pyridin-3-ylethynyl)phenyl)-1H-1,2,3-triazol-4-yl)phenyl)-2,8-diethyl-5,5-difluoro-1,3,7,9-tetramethyl-5H-4λ^4,5λ^4-dipyrrolo[1,2-c:2',1'-f][1,3,2]diazaborinine (L2^{BDP}):

L^{N3} (15.8 mg, 49.2 μmol, 1.00 eq.) was dissolved in DCM (0.5 mL) and diluted with MeOH:water (3:1, 6 mL). **BDP^{Alkynyl}** (54.5 mg, 135 μmol, 3.00 eq.), DCM (1 mL) and a solution of *L*-(+)-ascorbic acid (11.6 mg, 65.9 μmol, 1.35 eq.), NaOH (3.10 mg, 77.5 μmol, 1.60 eq.) and $CuSO_4 \cdot 5\ H_2O$ (1.10 mg, 4.41 μmol, 0.10 eq.) in water (2 mL) was added to the reaction mixture and stirred at room temperature. After 5 h, the reaction was quenched with a saturated NH_4OAc solution (20 mL) and stirred for 1 h. The reaction solution was washed with DCM (3x 20 mL) and the combined organic layers with brine (1x 30 mL). The organic layer was dried over Na_2SO_4, filtered over a glass-fritted funnel (pore 3) and the solvent removed under reduced pressure. The crude compound was purified *via* silica column chromatography (DCM:MeOH = 100:5, R_f = 0.34) to give product **L2^{BDP}** as a purple solid (19.7 mg, 27.1 μmol, 55%).

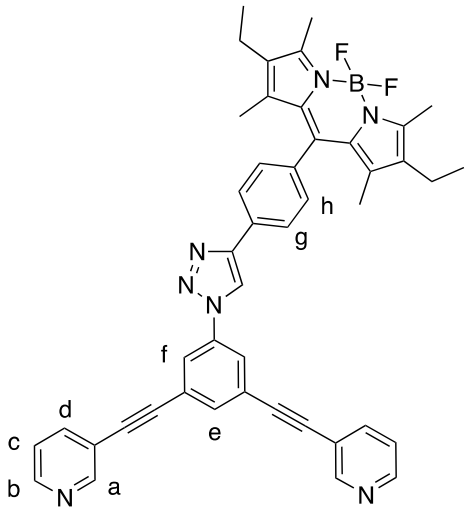

^{1}H NMR (400 MHz, acetone-d_6): δ [ppm] = 9.34 (s, 1H, C*H*), 8.84 (d, *J* = 1.2 Hz, 2H, H_a), 8.64 (dd, *J* = 1.6, 4.9 Hz, 2H, H_b), 8.20 – 8.35 (m, 4H, H_f, H_g), 8.04 (dt, *J* = 1.9, 8.0 Hz, 2H, H_d), 7.92 (t, *J* = 1.4 Hz, 1H, H_e), 7.55 (d, *J* = 8.3 Hz, 2H, H_h), 7.50 (dd, *J* = 4.9, 7.9 Hz, 2H, H_c), 2.52 (s, 6H, NCCH_3), 2.37 (q, *J* = 7.5 Hz, 4H, CH_2CH$_3$), 1.44 (s, 6H, CCH_3), 1.00 (t, *J* = 7.5 Hz, 6H, CH$_2$CH_3).

^{13}C NMR (126 MHz, acetone-d_6): δ [ppm] = 154.5. 153.0, 150.5, 148.4, 139.4, 139.1, 138.7, 136.5, 134.9, 132.2, 130.0, 127.2, 126.5, 125.7, 125.7, 124.4, 123.8, 123.6, 120.5, 120.2, 90.7, 89.1, 17.5, 15.0, 12.6, 12.1.

^{11}B NMR (160 MHz, acetone-d_6): δ [ppm] = 0.83.

^{19}F NMR (471 MHz, acetone-d_6): δ [ppm] = -145.1.

HRMS (ESI, MeCN): calcd. for $C_{45}H_{38}BFN_7$ [M-F]$^+$: *m/z* = 706.3281; found: 706.3214, δ = -7.7 ppm.

Synthesis of metallacages C1.BF$_4$, C2.BF$_4$, C1.NO$_3$

A solution of Pd precursor (2 eq.) and ligand (4 eq.) in DMSO was stirred at r.t. for 1 h (Scheme S4). Afterwards, precipitation by addition of acetone and diethyl ether and consecutive filtration gave the respective cages **C1.BF$_4$**, **C1.NO$_3$** and **C2.NO$_3$**.

C1.BF$_4$

A solution of Pd(MeCN$_4$)$_4$(BF$_4$)$_2$ (6.00 mg, 14.3 µmol, 2.00 eq.) and **L1^{BDP}** (20.0 mg, 28.5 µmol, 4.00 eq.) in DMSO (1.5 ml) was stirred for 1 h at r.t.. Following precipitation by addition of acetone (3 ml) and diethyl ether (excess), the solid was filtered over a glass-fritted funnel (pore 4) to give cage **C1.BF$_4$** as a red solid (19.0 mg, 5.56 µmol, 78%).

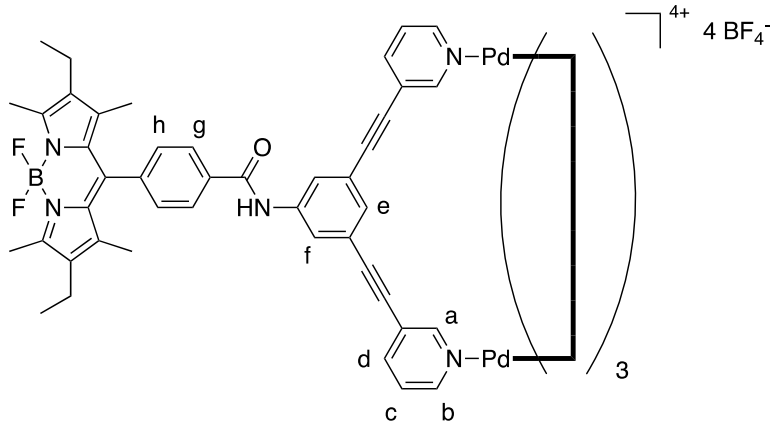

^{1}H NMR (400 MHz, acetone-d_6): δ [ppm] = 9.95 (s, 1H, N*H*), 9.91 (s, 2H, H_a), 9.55 (d, J = 4.9 Hz, 2H, H_b), 8.39 – 8.13 (m, 6H, H_d, H_g, H_h,), 7.96 (s, 1H, H_e), 7.88 – 7.73 (m, 2H, H_c), 7.57 (s, 2H, H_f), 2.52 (s, 6H, NCCH_3), 2.48 (s, 4H, CH_2CH$_3$), 1.30 (s, 6H, CCH_3), 0.96 (t, J = 6.94 Hz, 6H, CH$_2$CH_3).

^{13}C NMR (101 MHz, acetone-d_6): δ [ppm] = 165.1, 161.8, 153.9, 153.5, 150.6, 143.0, 139.5, 138.0, 134.9, 132.9, 130.2, 129.3, 128.9, 128.5, 127.4, 124.5, 123.4, 122.7, 116.3, 93.9, 84.5, 16.5, 14.0, 11.7, 11.2.

^{11}B NMR (128 MHz, acetone-d_6): δ [ppm] = 0.66 (BF$_2$), -0.38 (BF$_4$).

^{19}F NMR (376 MHz, acetone-d_6): δ [ppm] = -145.1 (d, J = 33.2 Hz, BF_2), -145.3 (d, J = 33.2 Hz, BF_2), -149.9 (s, BF_4).

HRMS (ESI, MeCN): calcd. for $C_{180}H_{159}B_4F_7N_{22}O_4Pd_2Na$ $[M\text{-}4BF_4\text{-}F+H+2MeCN+Na]^{2+}$: *m/z* = 1552.0696; found: 1552.0424.

C1.NO$_3$:

A solution of $Pd(NO_3)_2 \cdot 2\ H_2O$ (4.60 mg, 17.3 µmol, 2.00 eq.) and **L1^{BDP}** (23.1 mg, 32.9 µmol, 4.00 eq.) in DMSO (1.5 mL) was stirred for 2 h at r.t. Following precipitation by addition of acetone (2 mL) and diethyl ether (excess), the solid was filtered over a glass-fritted funnel (pore 4) to give cage **C1.NO$_3$** as a red solid (24.6 mg, 7.53 µmol, 91%).

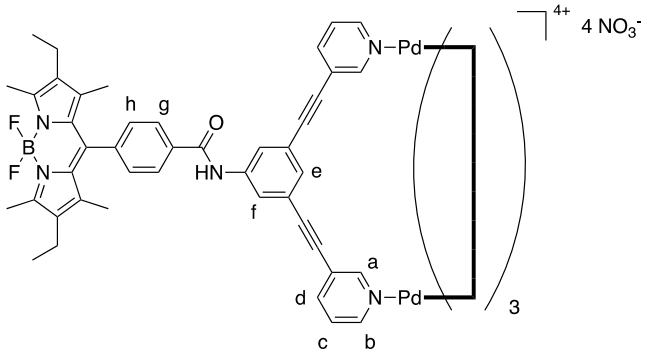

^{1}H NMR (500 MHz, DMSO-d_6): δ [ppm] = 10.69 (s, 1H, N*H*), 9.69 (s, 2H, H_a), 9.42 (s, 2H, H_b), 8.30 (d, J = 7.9 Hz, 2H, H_g), 8.24 (s, 2H, H_f), 8.16 (d, J = 7.4 Hz, 2H, H_d), 7.84 (s, 2H, H_h), 7.72 (s, 1H, H_e),

7.59 (d, *J* = 7.8 Hz, 2H, H_c), 2.44 (s, 6H, NCCH_3), 2.28 (s, 4H, CH_2CH$_3$), 1.25 (s, 6H, CCH_3), 0.93 (s, 6H, CH$_2$CH_3).

^{13}C NMR (126 MHz, DMSO-d_6): δ [ppm] = 183.5. 165.1, 157.9,153.6, 153.0, 150.6, 143.0, 140.2, 139.3, 138.5, 137.9, 132.8, 129.6, 128.6, 127.4, 122.2, 122.1, 93.7, 86.8, 85.9, 85.1, 16.4, 14.5, 12.3, 11.5.

^{11}B NMR (128 MHz, DMSO-d_6): δ [ppm] = 0.65.

^{19}F NMR (376 MHz, DMSO-d_6): δ [ppm] = -142.9.

HRMS (ESI, MeOH): calcd. for $C_{178}H_{161}B_4F_7N_{20}O_6Pd_2Na_2$ [M-4NO$_3$-F+H+2MeOH+2Na]$^{2+}$: *m/z* = 1554.5469; found: 1554.5005.

C2.NO$_3$:

A solution of Pd(NO$_3$)$_2$ · 2 H$_2$O (4.10 mg, 15.4 μmol, 2.00 eq.) and **L2^{BDP}** (22.3 mg, 30.7 μmol, 4.00 eq.) in DMSO (1.5 mL) was stirred for 1 h at r.t.. Following precipitation by addition of acetone (3 mL) and diethyl ether (excess), the solid was filtered over a glass-fritted funnel (pore 4) to give cage **C2.NO$_3$** as a dark purple solid (24.0 mg, 7.14 μmol, 93%).

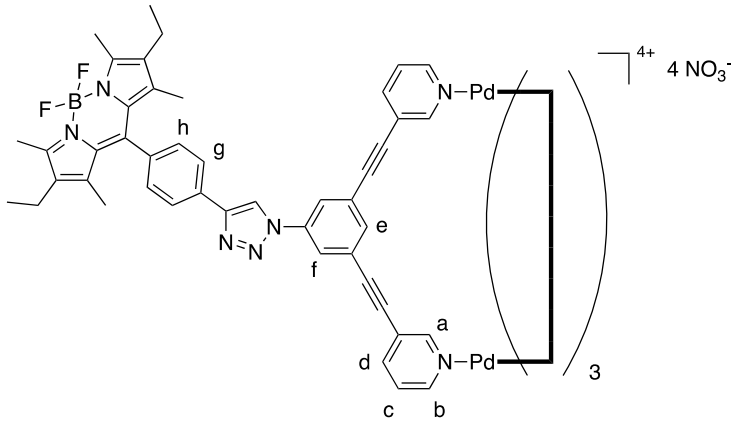

^{1}H NMR (500 MHz, DMSO-d_6): δ [ppm] = 9.83 (s, 2H, H_a), 9.59 (s, 1H, C*H*), 9.45 (s, 2H, H_b), 8.38 (s, 2H, H_f), 8.31 (d, *J* = 8.3 Hz, 2H, H_d), 8.30 (d, *J* = 7.9 Hz, 2H, H_g), 8.05 (s, 1H, H_e), 7.89 (s, 2H, H_c), 7.51 (d, *J* = 8.1 Hz, 2H, H_h), 2.44 (s, 6H, NCCH_3), 2.22 – 2.32 (m, 4H, CH_2CH$_3$), 1.31 (s, 6H, CCH_3), 0.93 (t, *J* = 7.4 Hz, 6H, CH$_2$CH_3).

^{11}B NMR (128 MHz, DMSO-d_6): δ [ppm] = 0.77.

^{19}F NMR (376 MHz, DMSO-d_6): δ [ppm] = -142.9.

HRMS (ESI, MeOH): calcd. for $C_{180}H_{152}B_4F_8N_{28}Pd_2$ [M-4NO$_3$]$^{2+}$: *m/z* = 1556.5469; found: 1556.5500.

L$^{Ru(II)}$ synthesis

3-(4'-methyl-[2,2'-bipyridin]-4-yl)propanoic acid was synthesised according to a previously reported procedure.[260]

4'-methyl-[2,2'-bipyridin]-4-yl)propenamide)ruthenium(II) tetrafluoroborate (**Ru(II)^{COOH}**): $[RuCl_2(bipy)_2]$ (484 mg, 1 mmol, 1 equiv.) and 4'-methyl-2,2'-bipyridine-4-propionic acid (242 mg, 1 mmol, 1 equiv.) were dissolved in dry ethanol (15 mL). The mixture was heated to reflux under a nitrogen atmosphere for 16 h. After cooling to r.t., the solvent was removed under reduced pressure and the residue dissolved in water. The red solution was treated with KPF_6, and the resulting precipitate was filtered, washed with water and diethyl ether, and dried under reduced pressure to obtain the Ru complex **Ru^{COOH}** as an orange solid (566 mg, 0.6 mmol, 60%).

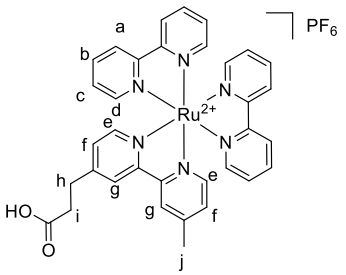

^{1}H NMR (400 MHz, CD_3CN) δ[ppm] = 8.48 (d, J = 7.9 Hz, 4 H, H_a), 8.39-8.35 (m, 2 H, H_g), 8.08-8.00 (m, 4 H, H_b), 7.75-7.67 (m, 4 H, H_d), 7.54 (dd, J = 14.1, 5.9 Hz, 2 H, H_e), 7.43-7.34 (m, 4 H, H_c), 7.29-7.20 (m, 2 H, H_f), 3.06 (t, J = 7.1 Hz, 2 H, H_i), 2.74 (t, J = 7.4 Hz, 2 H, H_h),2.53 (s, 3 H, H_j).

bis(2,2'-bipyridine)(*N*-(3,5-bis(pyridin-3-ylethynyl)phenyl)-3-(4'-methyl-[2,2'-bipyridin]-4-yl)propenamide)ruthenium(II) tetrafluoroborate (**L$^{Ru(II)}$**):

A mixture of **Ru(II)^{COOH}** (378 mg, 0.4 mmol, 1 equiv.), **L^{NH2}** (118 mg, 0.4 mmol, 1 equiv.), CMPI (409 mg, 1.6 mmol, 4 equiv.) and DMAP (489 mg, 4.0 mmol, 10 equiv.) in dry DMF (15 mL) was stirred under an argon atmosphere at 130 °C for 24 h. Dichloromethane (50 mL) was added to the reaction mixture and the organic phase was extracted five times with water (40 mL). The organic phase was dried over $MgSO_4$ and concentrated under reduced pressure. After precipitation by addition of diethyl ether to the DMF residue, the red solid was filtered, dissolved in acetonitrile and further purified by column chromatography (acetonitrile/H_2O/KNO3(sat.) = 100: 10: 1). The collected band was reduced in volume and treated with NaBF4 to precipitate the product. The precipitate was filtered, washed with water and diethyl ether and dried under reduced pressure to give the product as an orange solid (177 mg, 0.16 mmol, 40%)

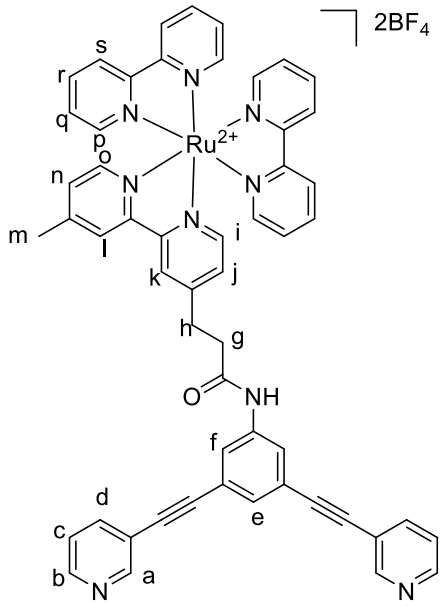

^{1}H NMR (400 MHz, CD_3CN): δ [ppm] = 8.95 (s, 1 H, N*H*), 8.72 (d, J = 1.6 Hz, 2 H, H_a), 8.58 (dd, J = 4.7, 1.6 Hz, 2 H, H_b), 8.48-8.43 (m, 4 H, H_s), 8.42 (s, 1 H, H_k), 8.35 (s, 1 H, H_l), 8.04- 7.97 (m, 4 H, H_r), 7.87 (dt, J = 7.8, 1.6 Hz, 2 H, H_d), 7.74-7.69 (m, 6 H, H_f/H_p), 7.57 (d, J = 5.8 Hz, 1 H, H_i), 7.50 (d, J = 5.8 Hz, 1 H, H_o), 7.44 (s, 1 H, H_e), 7.41-7.34 (m, 6 H, H_c/H_q), 7.31 (dd, J = 1.6, 5.8 Hz, 1 H, H_j), 7.20 (dd, J = 1.6, 5.4 Hz, 1 H, H_n), 3.18 (t, J = 7.1 Hz, 2 H, H_g), 2.82 (t, J = 7.0 Hz, 2 H, H_h), 2.50 (s, 3 H, H_m).

^{13}C NMR (101 MHz, CD_3CN): δ [ppm] 170.9, 157.6, 157.5, 157.2, 157.0, 153.6, 152.4, 152.3,152.2,152.1,152.0, 151.6, 151.3, 151.1, 149.7, 140.0, 139.2, 138.2, 130.0, 128.9, 128.3, 128.1, 128.0, 125.5, 124.9, 124.8, 124.7, 124.1, 124.0, 122.9, 91.3, 87.2, 65.8, 36.9, 30.8, 20.8

^{11}B NMR (128 MHz, CD_3CN): δ [ppm] = -1.211

HRMS (ESI, MeOH): calcd. for $C_{54}H_{39}N_9ORu$ $[M\text{-}2BF_4]^{2+}$: *m/z* = 466.6246; found: 466.6248

C$^{Ru(II}$

A solution of $[Pd(NCCH_3)_4](BF_4)2$ (6.7 mg, 15 µmol, 2 equiv.) and **L$^{Ru(II)}$** (33 mg, 30 µmol, 4 equiv.) in DMSO (1 mL) was stirred at r.t. for one hour. After precipitation by addition of acetone and diethyl ether, the solid was filtered and washed with diethyl ether to yield the cage compound **C$^{Ru(II)}$** as an orange solid (24 mg, 5.2 µmol, 65%).

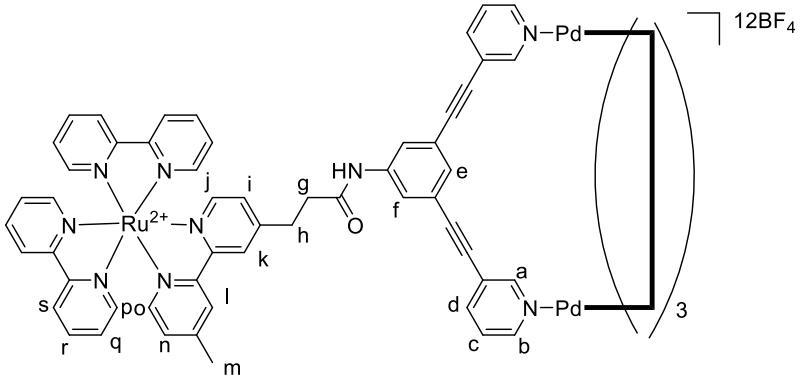

^{1}H NMR (400 MHz, CD_3CN): δ [ppm] = 9.56 (s, 2 H, H_a), 9.21 (d, J = 5.3 Hz, 2 H, H_b), 9.01 (s, 1 H, N*H*), 8.47-8.39 (m, 6 H, H_s/H_k/H_l), 8.08 (d, J = 8.1 Hz, 2 H, H_d), 8.04-7.97 (m, 4 H, H_r), 7.87 (s, 2 H, H_f), 7.69-7.60 (m, 7 H, H_c/H_e/H_p), 7.53 (d, J = 5.9 Hz, 1 H, H_i), 7.48 (d, J = 5.9 Hz, 1 H, H_o), 7.38-7.32 (m, 4 H, H_q), 7.26 (d, J = 5.9 Hz, 1 H, H_j), 7.19 (d, J = 5.7 Hz, 1 H, H_n), 3.12 (t, J = 7.5 Hz, 2 H, H_g), 2.78 (t, J = 7.5 Hz, 2 H, H_h), 2.49 (s, 3 H, H_m).

^{13}C NMR (101 MHz, CD_3CN): δ [ppm] = 171.5, 158.0, 157.9, 157.6, 157.4, 154.2, 153.9, 152.6, 152.5, 152.4, 152.0, 151.6, 151.5, 151.2, 143.8, 140.9, 138.5, 130.2, 129.3, 128.6, 128.5, 128.4, 128.3, 128.2, 125.9, 125.2, 125.1, 125.1, 124.4, 123.6, 94.7, 85.4, 37.2, 31.1, 21.2.

^{11}B NMR (128 MHz, CD_3CN): δ [ppm] = -1.06.

^{19}F NMR (377 MHz, CD_3CN): δ [ppm] = -151.3

Synthesis of **L^{NIR}**

***BDP^{NIR}** was synthesised by the group of Dr. Darren Griffith of the University of Dublin*

To a solution of fluorophore **BDP^{NIR}** (18.2 mg, 0.032 mmol) dissolved in THF (4 mL) was added to **L^{N3}** (9.9 mg, 0.031 mmol) in H_2O (2 mL) and THF (2 mL). $CuSO_4.5H_2O$ (2 mg, 40% mole equiv.) and sodium ascorbate (1.6 mg, 40% mole eq.) in water (1 mL) was added and the reaction was stirred at r.t. for 1 h. The THF was removed under reduced pressure and the residue diluted with H_2O (10 mL) and extracted into EtOAc (2 x 25 mL). The organic layer was washed with brine (20 mL), H2O (20 mL), dried over Na_2SO_4, filtered and concentrated under reduced pressure. The crude product was subject to column chromatography on silica using 85:15 DCM:EtOAc gradually increasing to 1:1 to yield **L^{NIR}** as a brown-green solid (11.9 mg, 43 %).

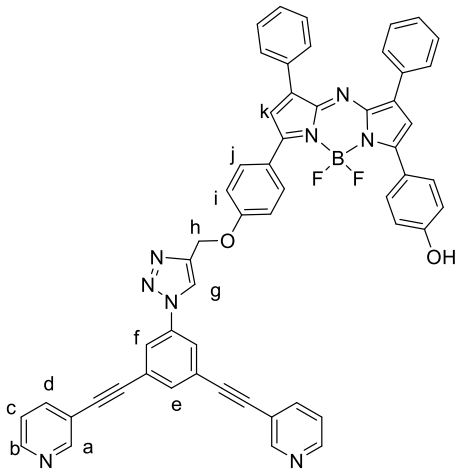

^{1}H NMR (400 MHz, DMSO-d_6) δ [ppm]: 9.27 (s, 1H, H_g), 8.90 (s, 2H, H_a), 8.71 (s, 2H, H_b), 8.35 (d, J = 1.4 Hz, 2H, H_f), 8.27 – 8.18 (m, 10H, H_{phenyl}), 8.12 (dt, J = 8.1, 1.9 Hz, 2H, H_d), 8.02 (t, J = 1.4 Hz, 1H, H_e), 7.74 (s, 1H, O*H*) 7.65 – 7.33 (m, 10H, H_c/H_i/H_j) 7.00 (d, J = 9.0 Hz, 2H, H_k) 5.49 (d, J = 5.7 Hz, 2H, H_h)

^{11}B NMR (128 MHz, DMSO-d_6): δ [ppm] = -1.07

^{19}F NMR (377 MHz, DMSO-d_6): δ [ppm] = -130.2

Synthesis of **C^{NIR}**

A solution of [Pd(MeCN)$_4$.2BF$_4$] (5 mg, 7.5 μmol, 2.00 eq.) and **L^{NIR}** (13.3 mg, 15 μmol, 4.00 eq.) in DMSO (5 mL) was stirred for 1 h at r.t.. Following precipitation by addition of acetone (3 mL) and diethyl ether (excess), the solid was collected by centrifugation, eluent was discarded and the pellet was washed with diethyl ether to yield **C^{NIR}** (6 mg, 3 μmol, 40 %)

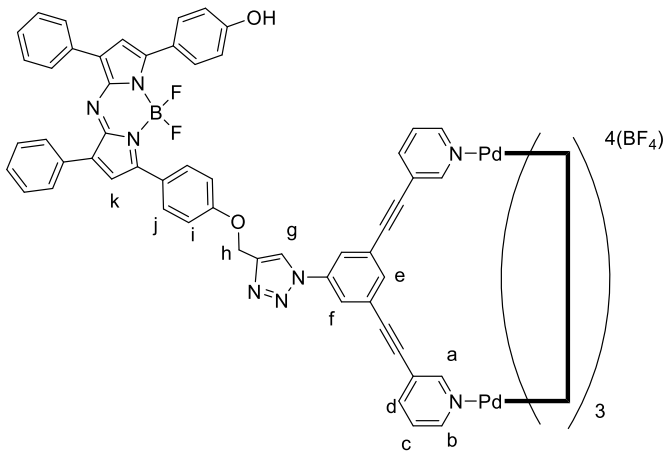

^{1}H NMR (400 MHz, DMSO-d_6): δ [ppm] = 10.57 (s, 1H, H_g), 9.74 (s, 2H, H_s), 9.43 (s, 2H, H_b), 9.16 (s, 1H, O*H*), 8.38 (s, 2H, H_f), 8.30 – 8.09 (m, 10H, H_{phenyl}), 8.02 (s, 1H, H_e), 7.87 (s, 2H), 7.66 (s, 2H), 7.60 – 7.26 (m, 6H), 6.93 (d, J = 8.6 Hz, 2H) 5.40 (s, 2H, H_h)

^{11}B NMR (128 MHz, DMSO-d_6): δ [ppm] = -1.07

^{19}F NMR (377 MHz, DMSO-d_6): δ [ppm] = -130.2

Quantum Yield Determination

Quantum yield was calculated by comparison to a reference standard (Rhodamine 6G in ethanol, ϕ = 94%). UV-Visible absorption spectra were recorded on a Cary 60 UV-Vis spectrometer from *Agilent Technologies*. Emission spectra were recorded on a Cary Eclipse Fluorescence Spectrophotometer from *Agilent Technologies*. The selected fluorophore was dissolved in degassed DMSO to a concentration corresponding to UV-Vis absorbance 0.8 A.U. The solution

was transferred to a fluorescence spectrophotometer and an emission spectrum was recorded (excitation wavelength 595 nm).

Stability studies by UV-Visible Spectroscopy

UV-visible absorption spectra to investigate the stability of the metallacages in solution were recorded on a Cary 60 UV-Vis spectrometer from *Agilent Technologies*. For each compound, stock solutions at a concentration of $3 \cdot 10^{-3}$ M were prepared. An aliquot was diluted either with 1x PBS (pH 7.4) or deionized water and the UV-Vis spectra measured at different times immediately after dilution at room temperature over 24 h. The cuvette was then shaken, and another spectrum recorded, to determine if the compound was altered during the 24 h or if the reduction in absorption was only due to precipitation.

Cisplatin encapsulation studies

^{1}H NMR spectroscopy

Each metallacage (4.4 µM, 1.00 eq.) was dissolved in 1 mL DMF-d_7 and a ^{1}H NMR spectrum was recorded. Afterwards, Cisplatin (8.8 µM, 2.00 eq.) was added to the NMR tube and the deuterated solution was stirred for 10 min before ^{1}H NMR spectrum was recorded. Finally, NMR spectra were compared to evaluate any chemical shifts due to the encapsulation of cisplatin. Both spectra were calibrated to the residual solvent signal of the carbonyl proton of DMF (8.03 ppm).

^{195}Pt NMR spectroscopy

Cisplatin (2 mg, 6.7 µM, 1 eq.) was dissolved in DMF (0.5 ml) and transferred to a NMR tube with a capillary insert filled with DMF-d_7. Thus, the ^{195}Pt NMR spectra was recorded. To this sample, the selected metallacage (**C1.BF$_4$** or **C1.NO$_3$**) (6.7 µM, 1 eq.) was added and the solution stirred for 10 min before another ^{195}Pt NMR spectra of 1 equivalent of metallacage and 1 equivalent of cisplatin was recorded. A second equivalent of cisplatin (2 mg, 6.7 µM, 1 eq.) was added to the metallacage and cisplatin containing solution and a final ^{195}Pt NMR spectra was recorded of 2 equivalents of cisplatin and 1 equivalent of metallacage. The resulting spectra were compared to observe any chemical shifts between the free cisplatin and metallacage complex.

Fluorescence microscopy assays

Fluorescence microscopy assays were performed by Ms Brech Aikman

Round glass coverslips (Ø 13mm, VWR) sterilized by UV-light were inserted in 24-well tissue culture-treated plates (Corning). Cells were seeded at a concentration of 125.000 cells/mL and incubated at 37°C under humidified atmosphere with 5% CO_2 for 48h. Afterwards, medium was discarded and cells fresh medium containing 5 µM of either cage or ligand was added. Following 2 h of incubation, the glass coverslips were removed from the wells, washed 4x with 1x

Phosphate Buffered Saline (PBS, Corning) and fixed with 4% formaldehyde (Alfa-Aesar) for 20 min at room temperature (r.t.). The coverslips were washed 3x with 1x PBS and incubated for 1 minute with 40 µL 1:1000 from a 1 mg/mL stock solution of 4',6-Diamidino-2-phenylindole dihydrochloride (DAPI, Sigma-Aldrich/ MERCK) at r.t. protected from light. After washing the coverslips thrice with 1x PBS they were mounted on glass microscope slides (VWR) using Mowiol® 4-88 (Sigma-Aldrich). Fluorescence images were obtained using a Leica SP5 confocal laser-scanning microscope. Two laser lines were used: 405 Blue Diode (excitation wavelength 405 nm, laser intensity 30%) for DAPI and Argon (excitation wavelength 514 nm, laser intensity 30%) for the complexes. A HCX PL APO 63x 1.4 NA oil immersion objective was used for all images with Leica Type F immersion oil. Captured "XYZ" images were analysed using ImageJ.

NMR spectra

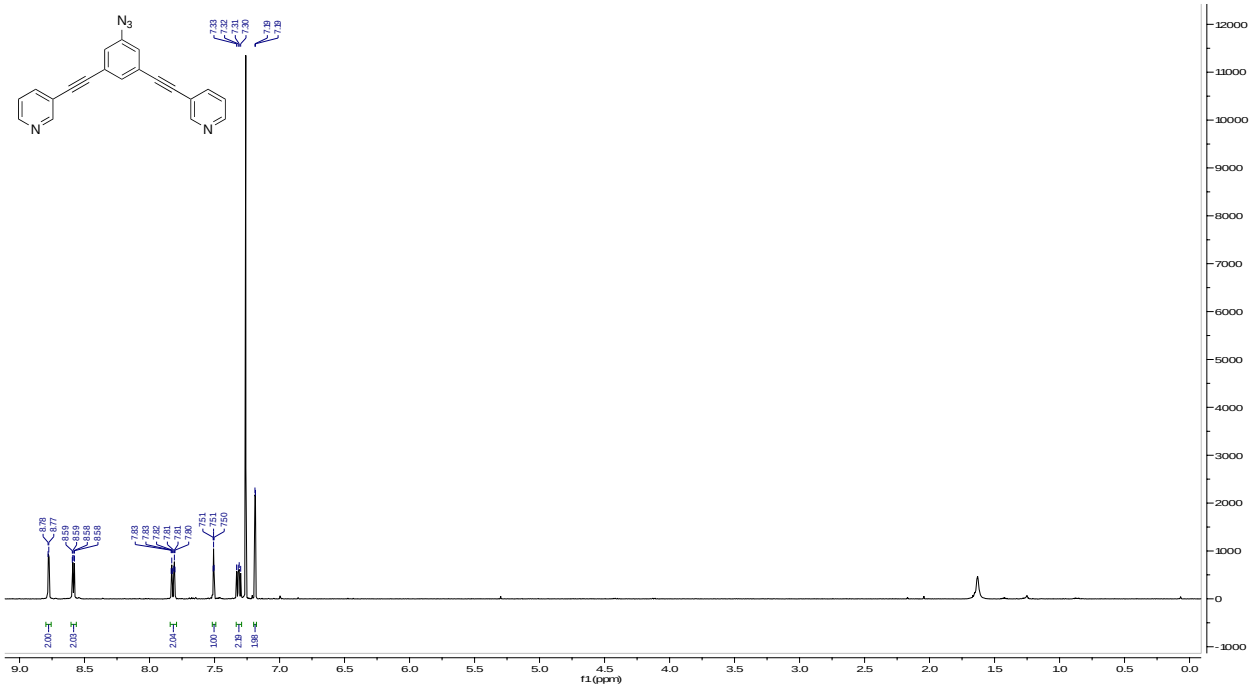

Figure S24. ^{1}H NMR (400 MHz, $CDCl_3$) spectrum of $\mathbf{L^{N3}}$.

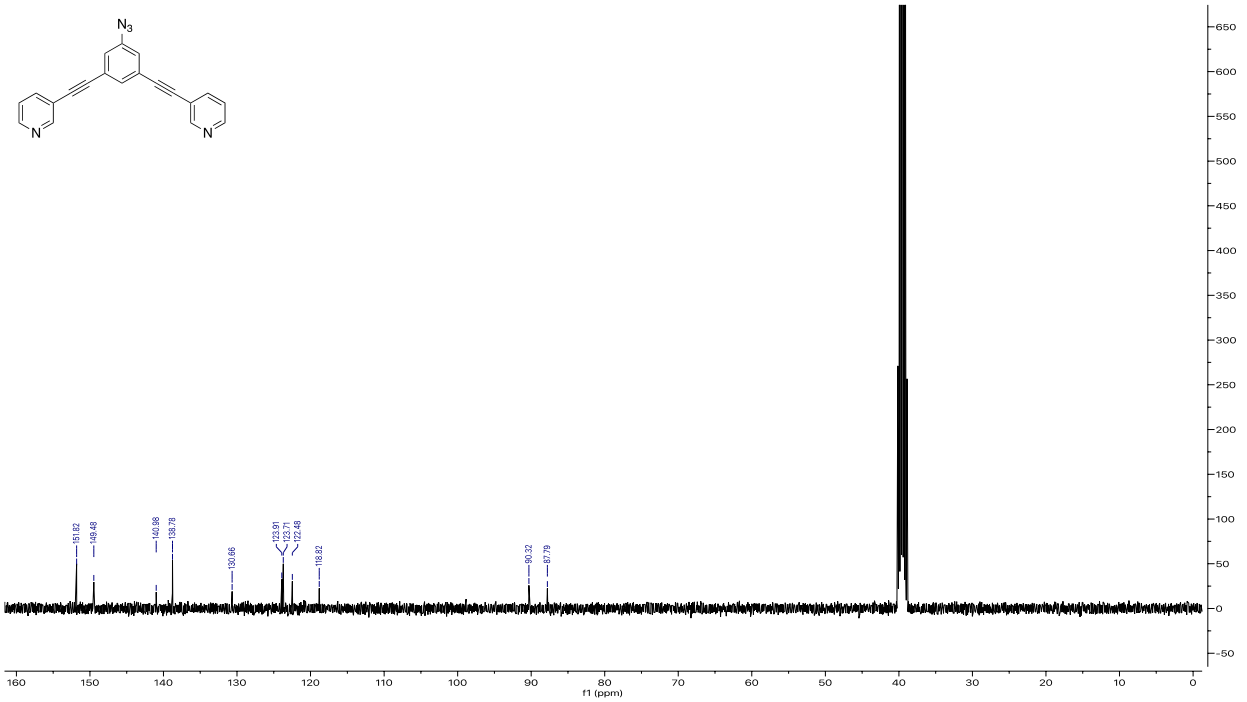

Figure S25. ^{13}C NMR (101 MHz, DMSO-d_6) spectrum of **L^{N3}**.

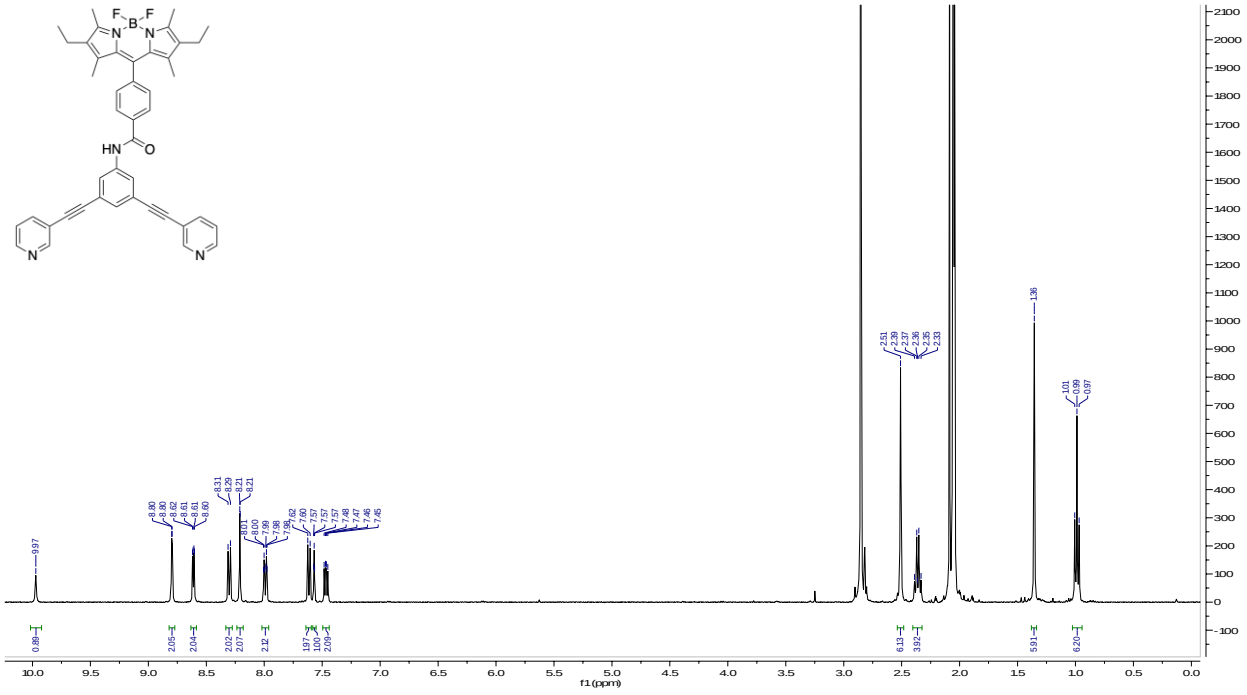

Figure S26. ^{1}H NMR (400 MHz, acetone-d_6) spectrum of **L1^{BDP}**.

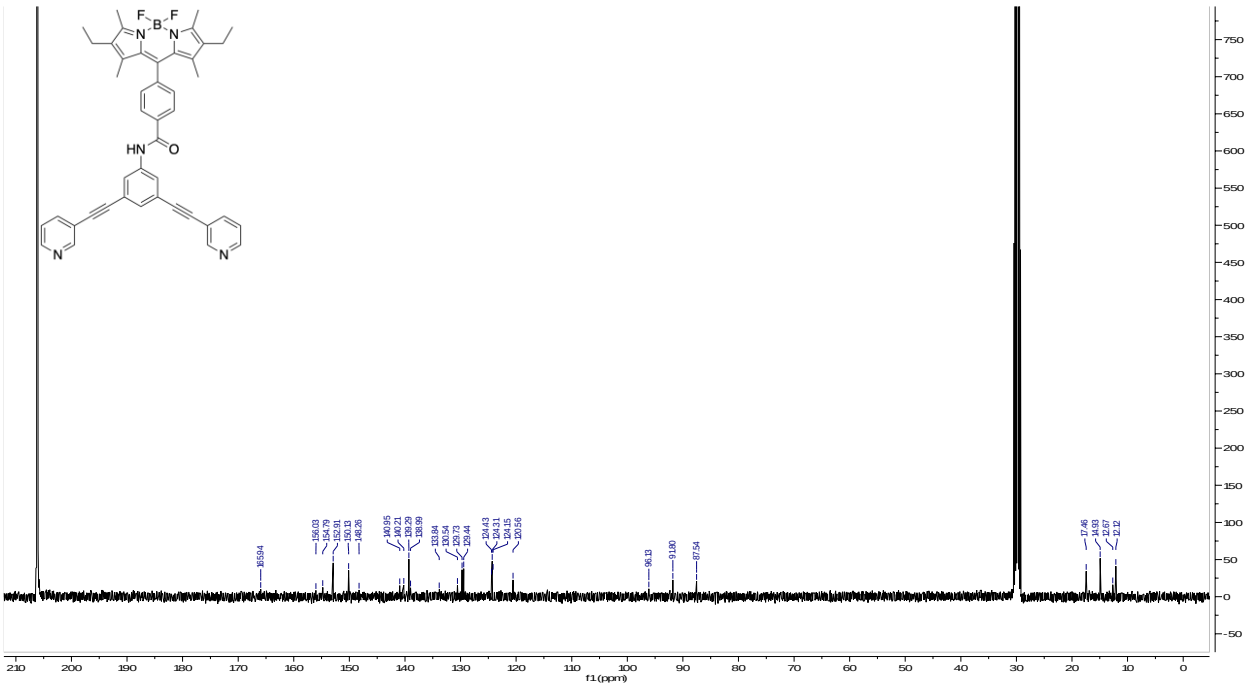

Figure S27. ^{13}C NMR (101 MHz, acetone-d_6) spectrum of **L1^{BDP}**.

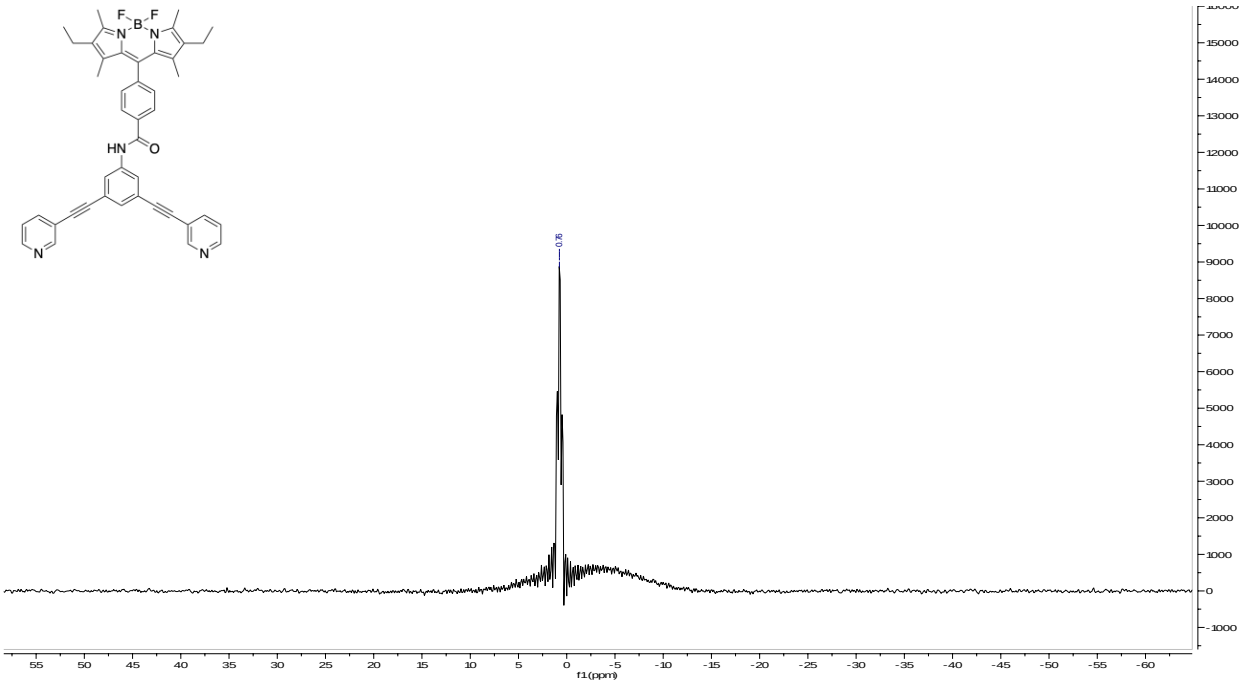

Figure S28. ^{11}B NMR (128 MHz, acetone-d_6) spectrum of **L1^{BDP}**.

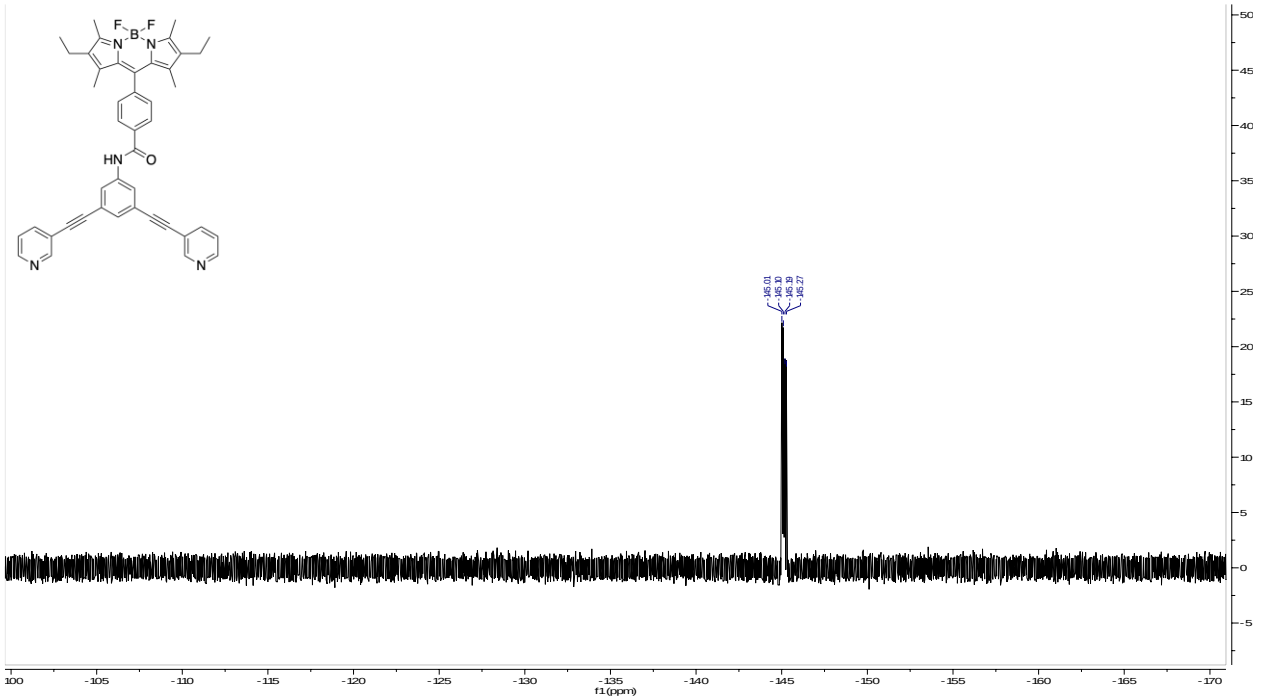

Figure S29. ^{19}F NMR (376 MHz, acetone-d_6) spectrum of **L1^{BDP}**.

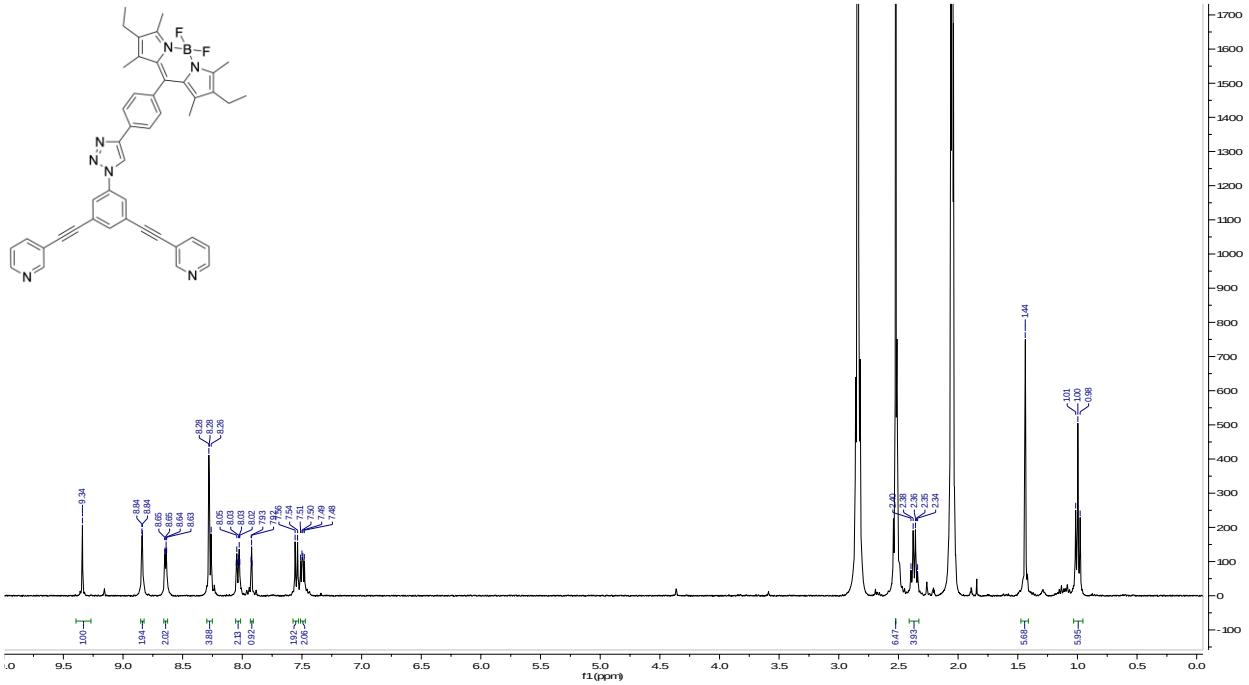

Figure S30. ^{1}H NMR (400 MHz, acetone-d_6) spectrum of **L2^{BDP}**.

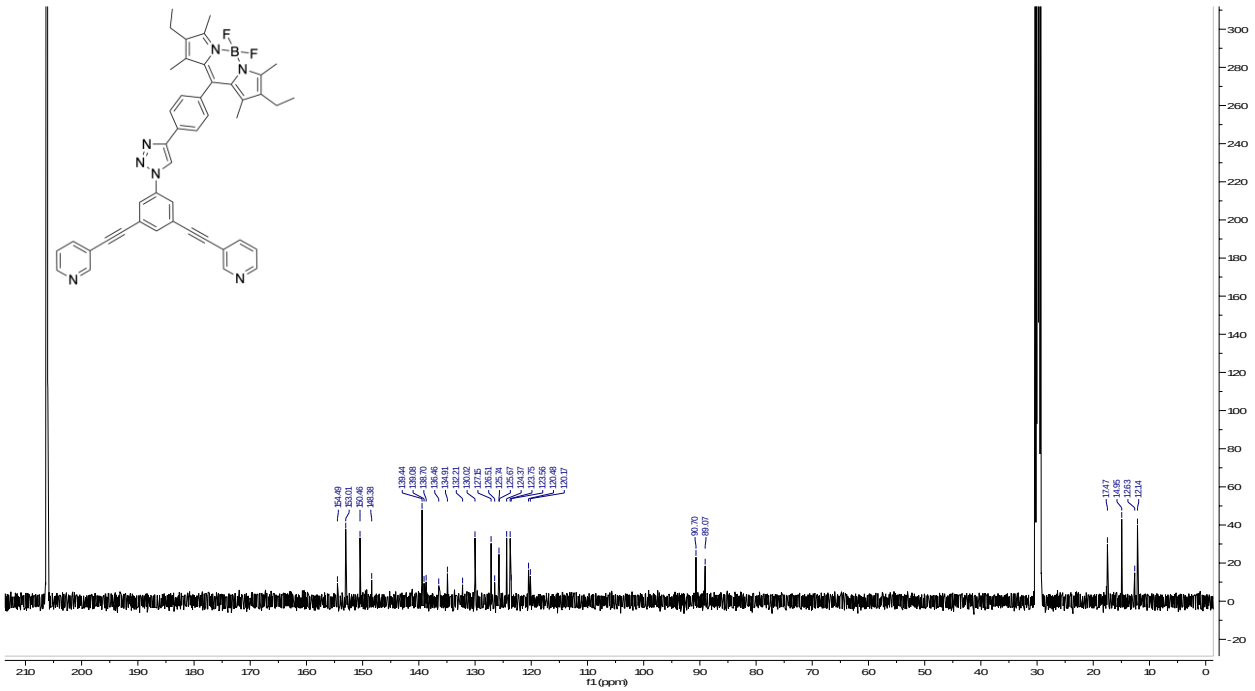

Figure S31. ^{13}C NMR (126 MHz, acetone-d_6) spectrum of **L2^{BDP}**.

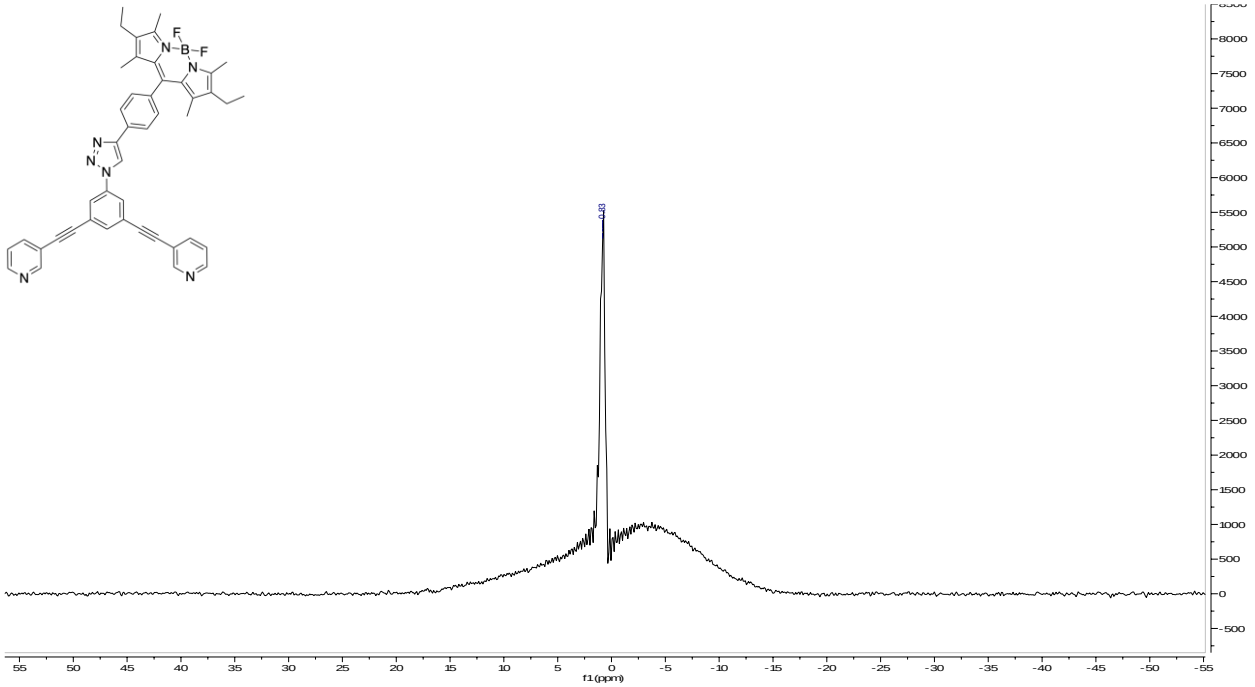

Figure S32. ^{11}B NMR (160 MHz, acetone-d_6) spectrum of **L2^{BDP}**.

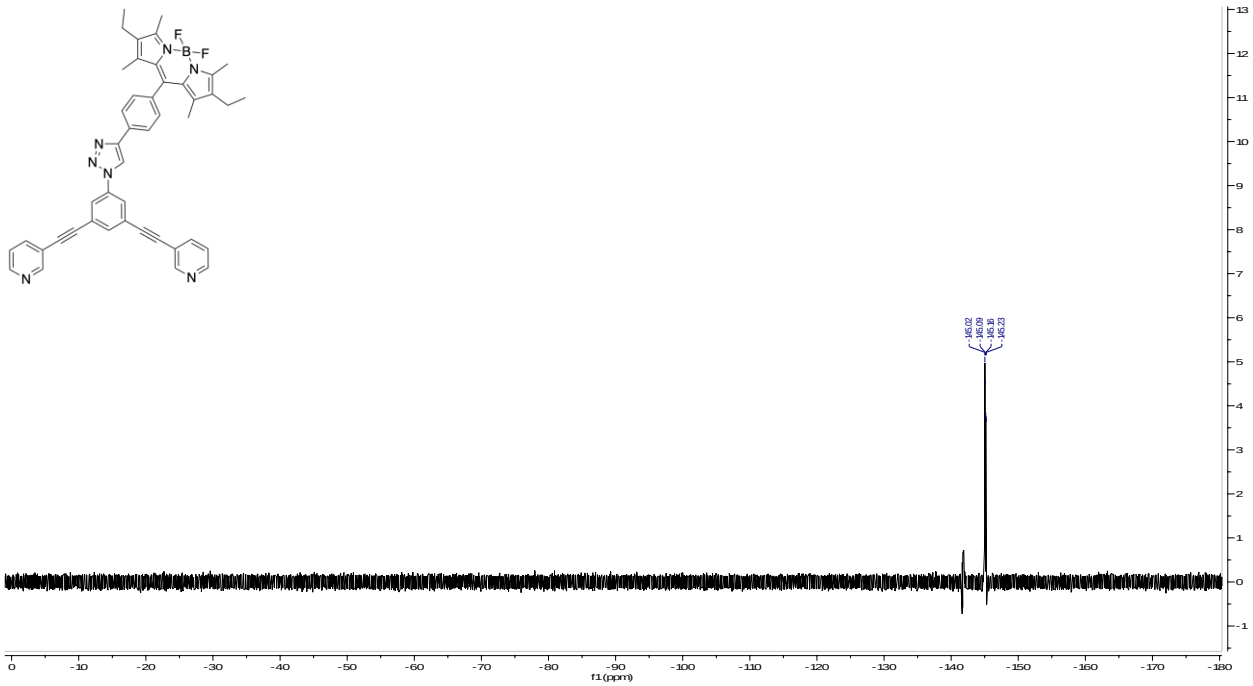

Figure S33. ^{19}F NMR (471 MHz, acetone-d_6) spectrum of **L2^{BDP}**.

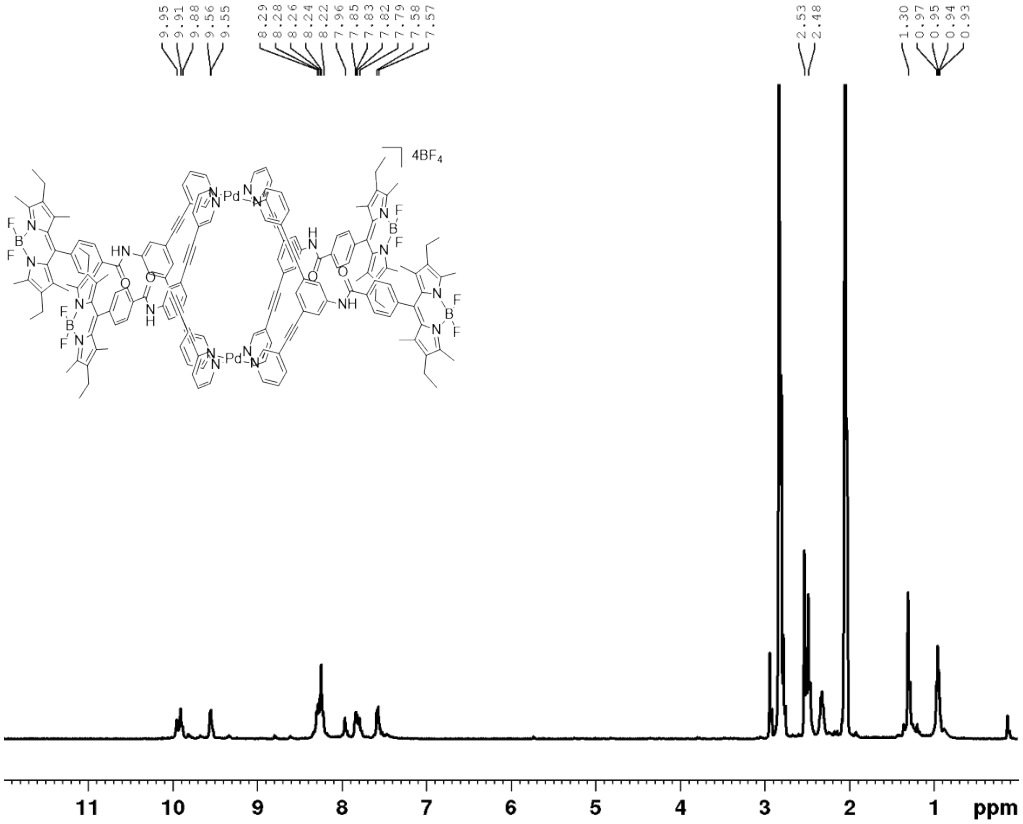

Figure S34. ^{1}H NMR (400 MHz, acetone-d_6) spectrum of **C1.BF$_4$**.

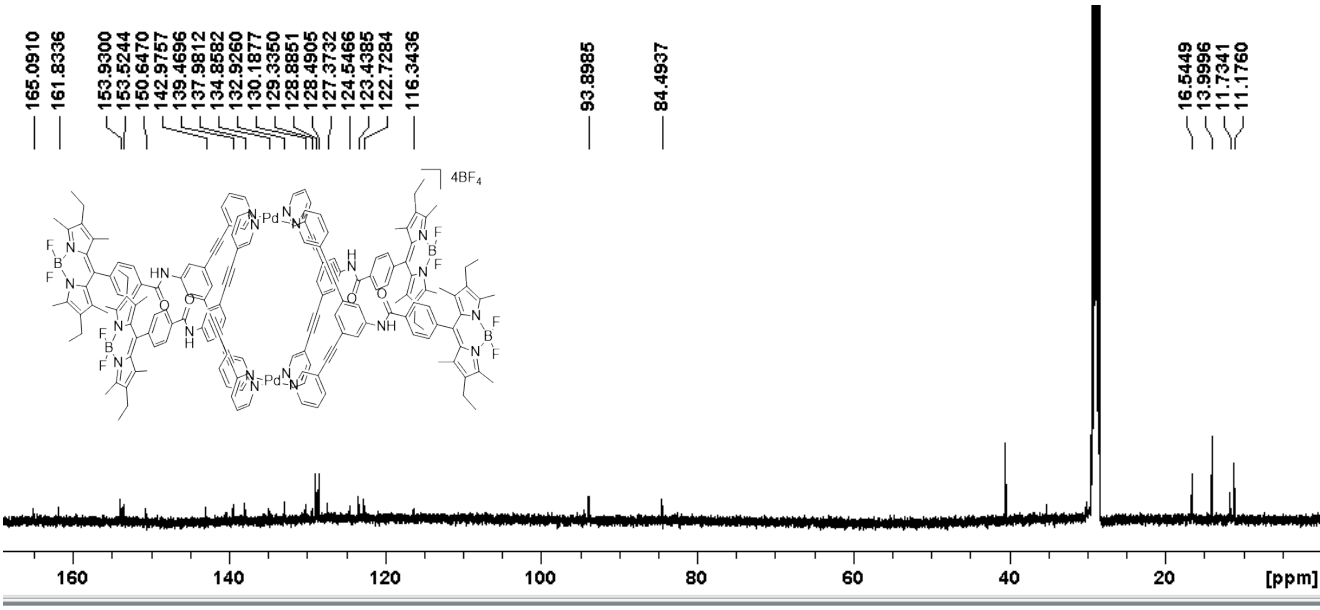

Figure S35. ^{13}C NMR (126 MHz, acetone-d_6) spectrum of **C1.BF$_4$**.

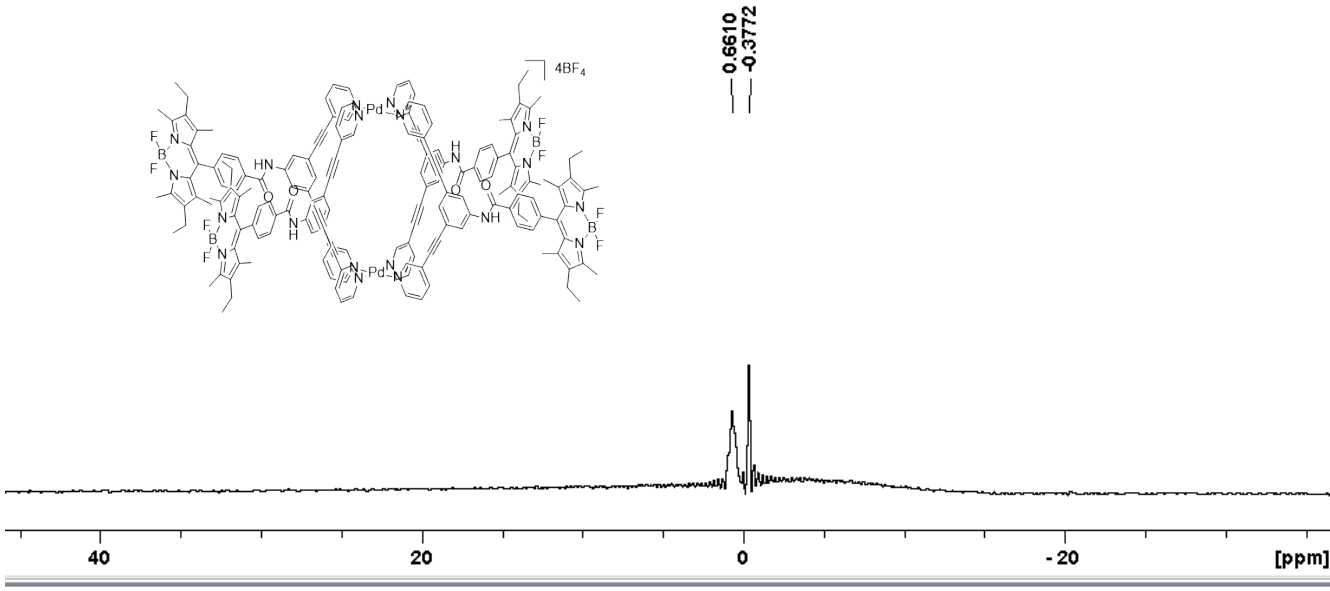

Figure S36. ^{11}B NMR (160 MHz, acetone-d_6) spectrum of **C1.BF$_4$**.

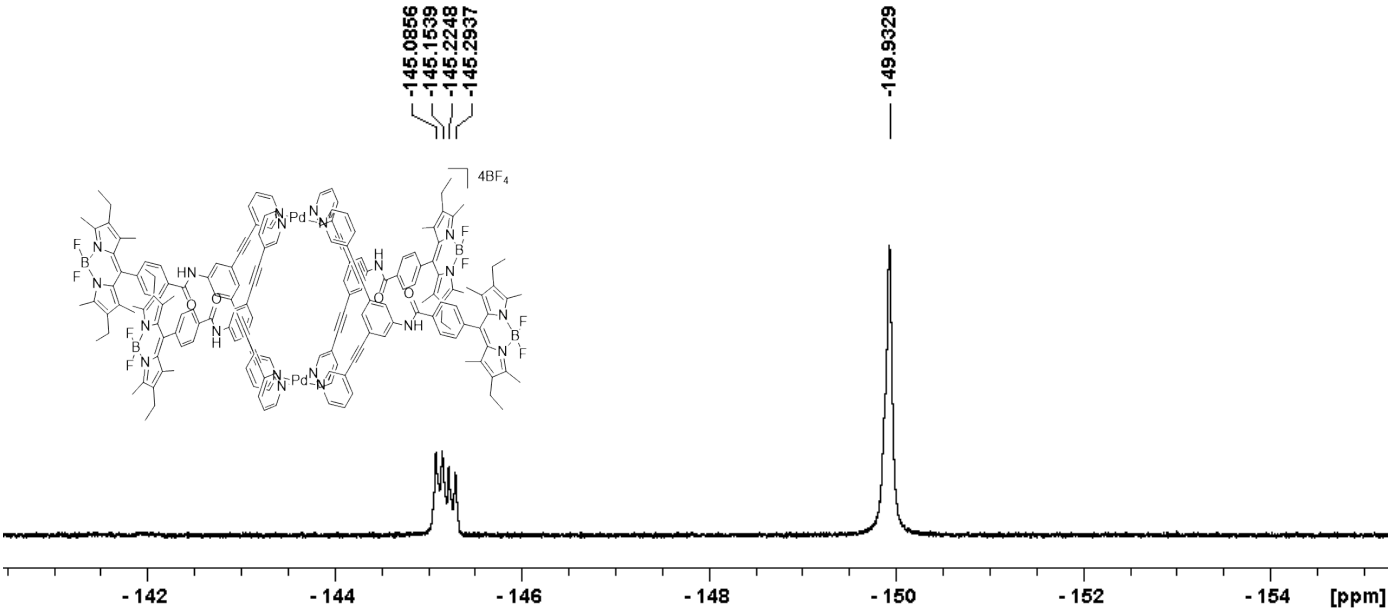

Figure S37. ^{19}F NMR (471 MHz, acetone-d_6) spectrum of **C1.BF$_4$**.

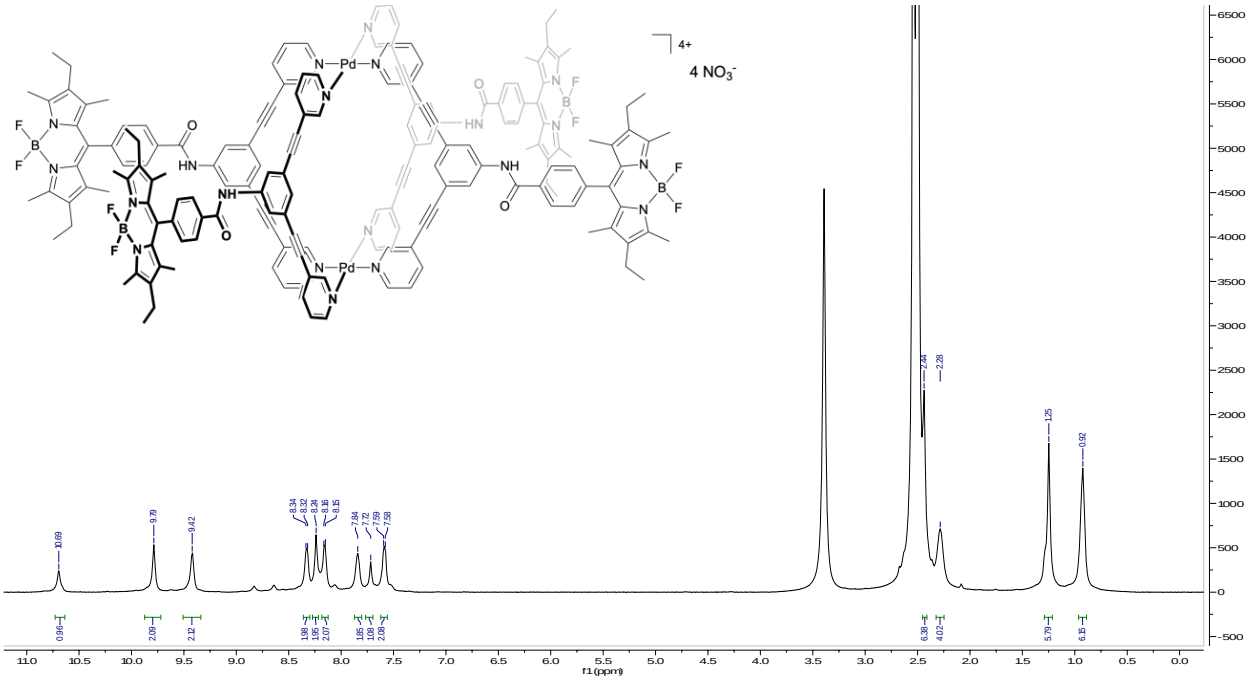

Figure S38. ^{1}H NMR (500 MHz, DMSO-d_6) spectrum of **C1.NO$_3$**.

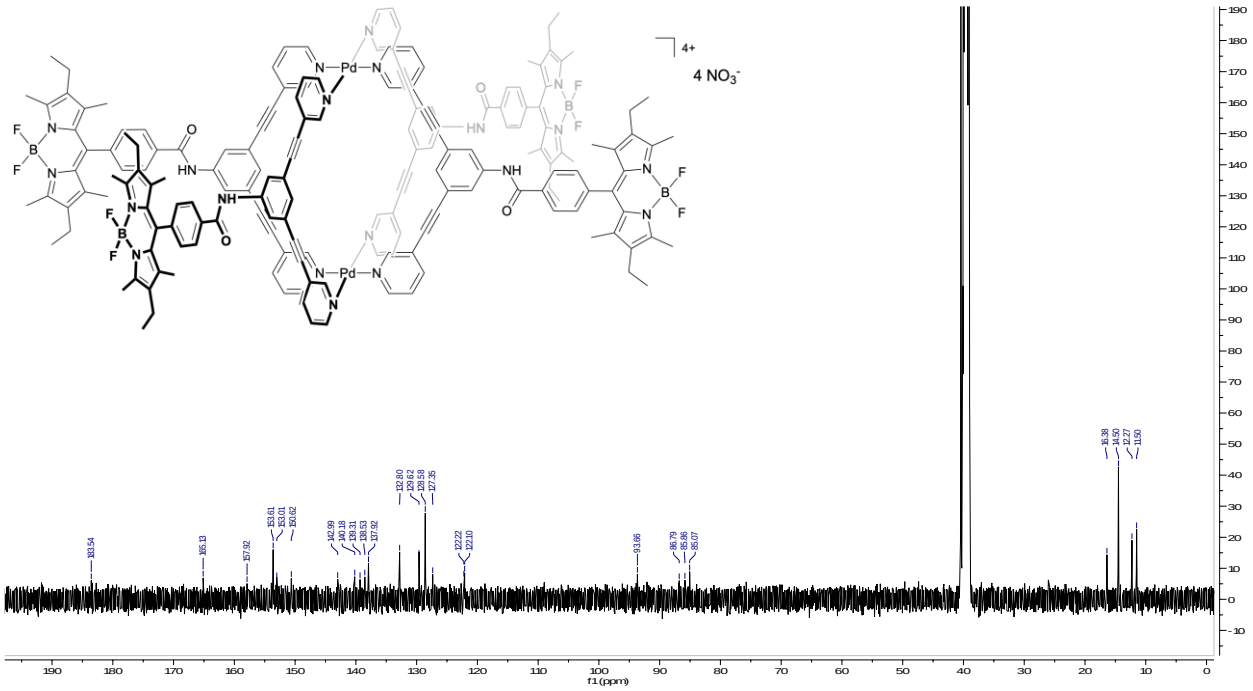

Figure S39. ^{13}C NMR (126 MHz, DMSO-d_6) spectrum of **C1.NO$_3$**.

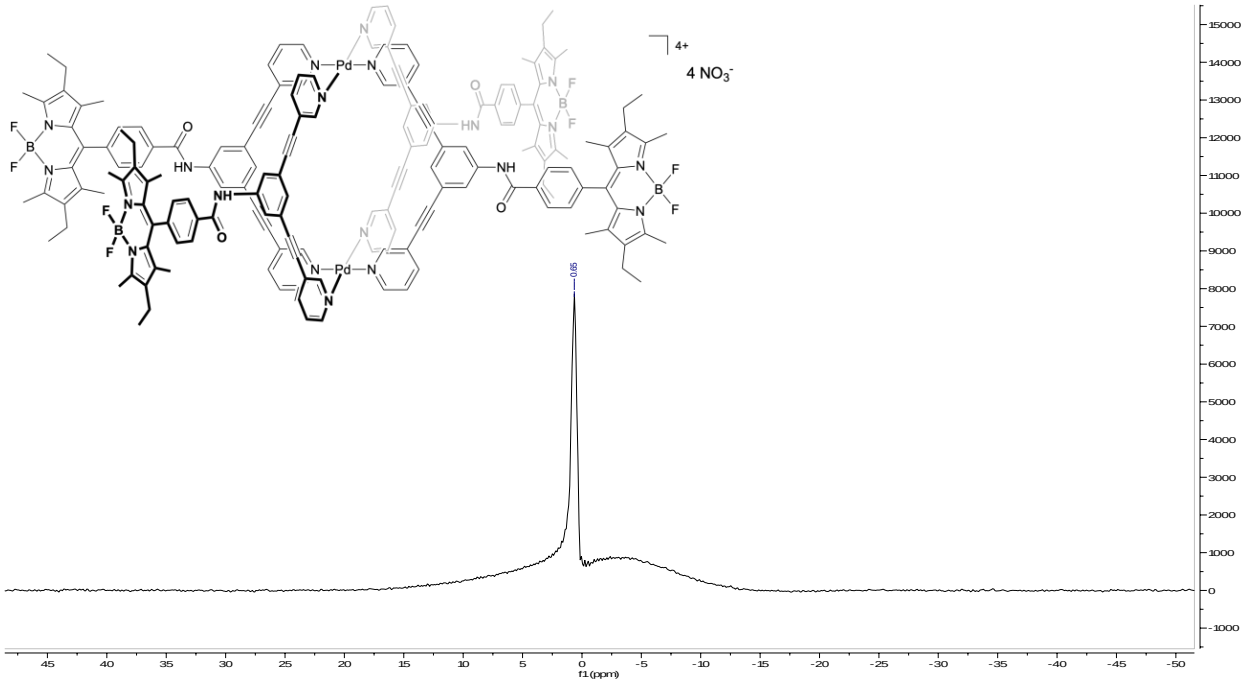

Figure S40. ^{11}B NMR (160 MHz, DMSO-d_6) spectrum of **C1.NO$_3$**.

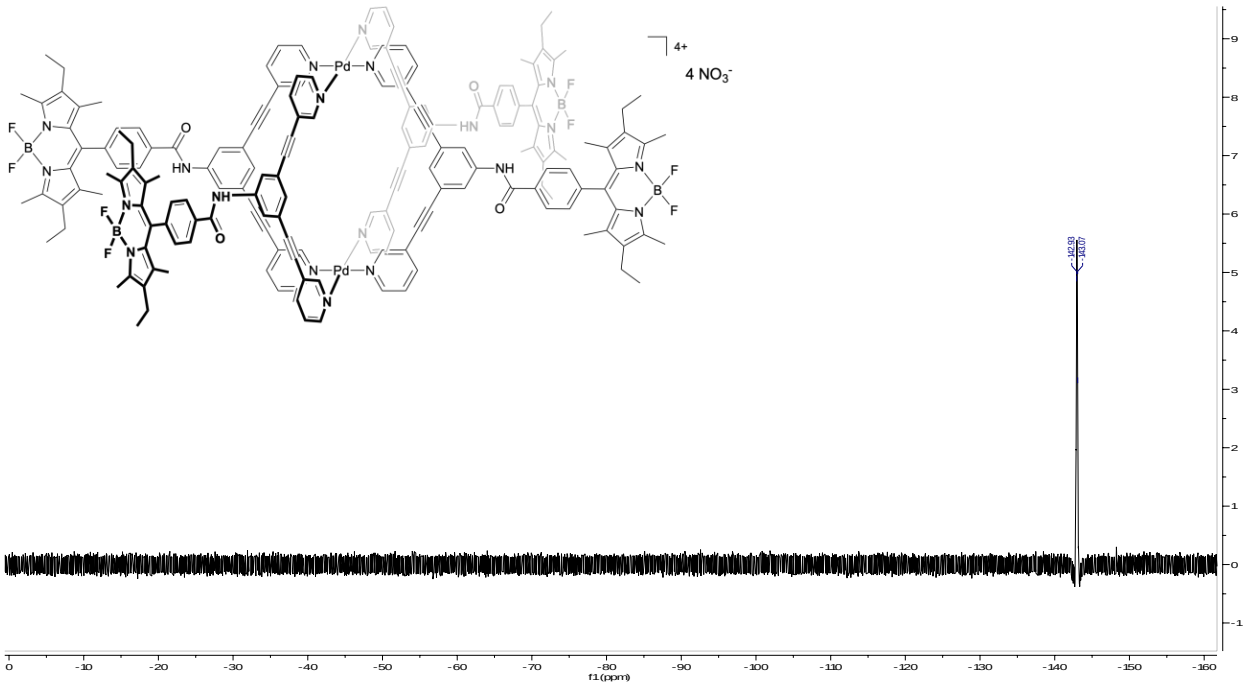

Figure S41. ^{19}F NMR (471 MHz, DMSO-d_6) spectrum of **C1.NO$_3$**.

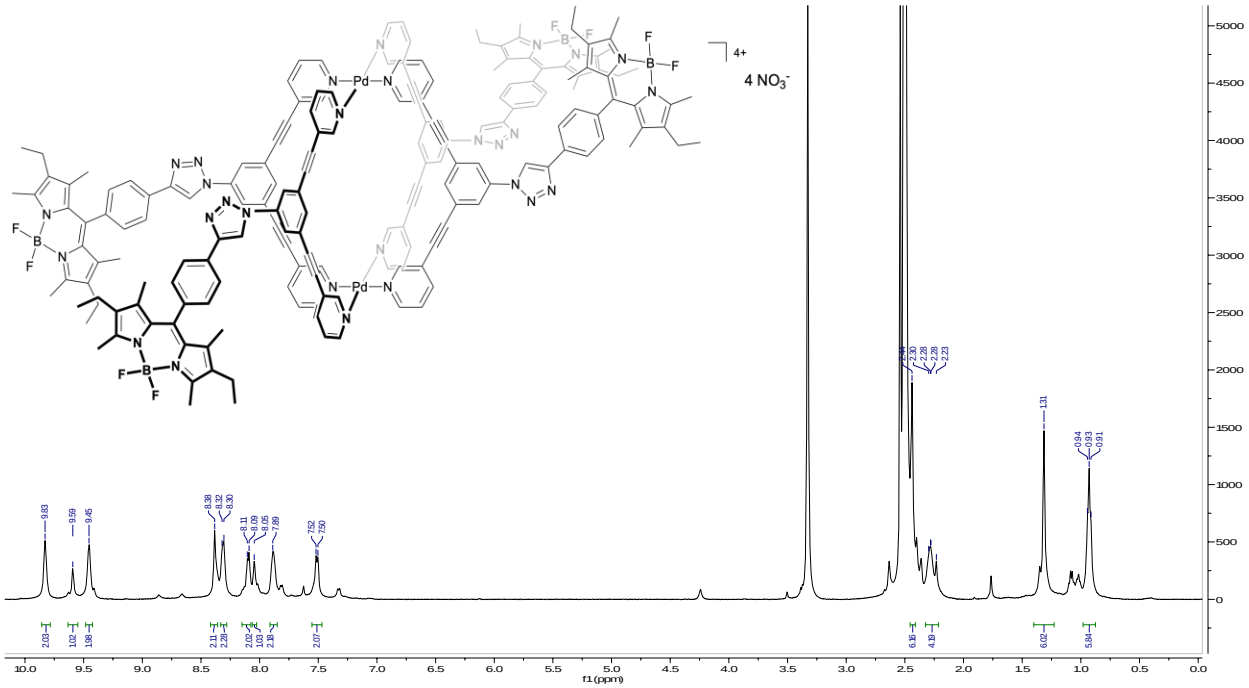

Figure S42. ^{1}H NMR (500 MHz, DMSO-d_6) spectrum of **C2.NO$_3$**.

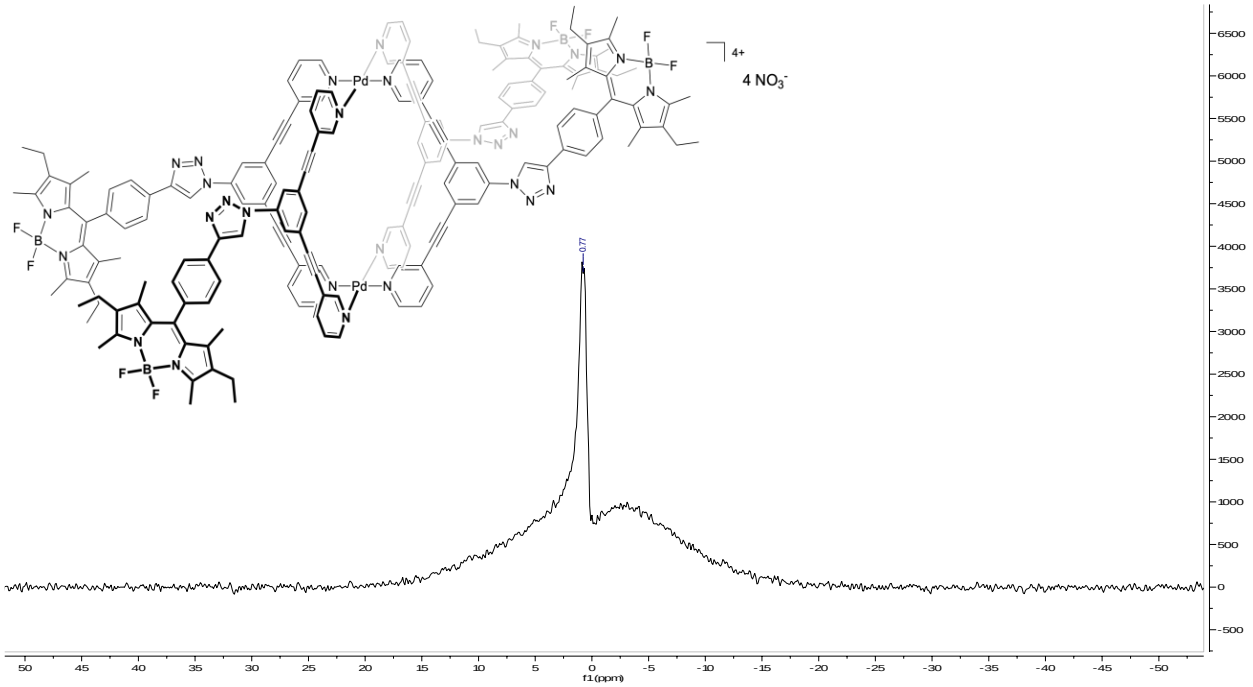

Figure S43. ^{11}B NMR (128 MHz, DMSO-d_6) spectrum of **C2.NO$_3$**.

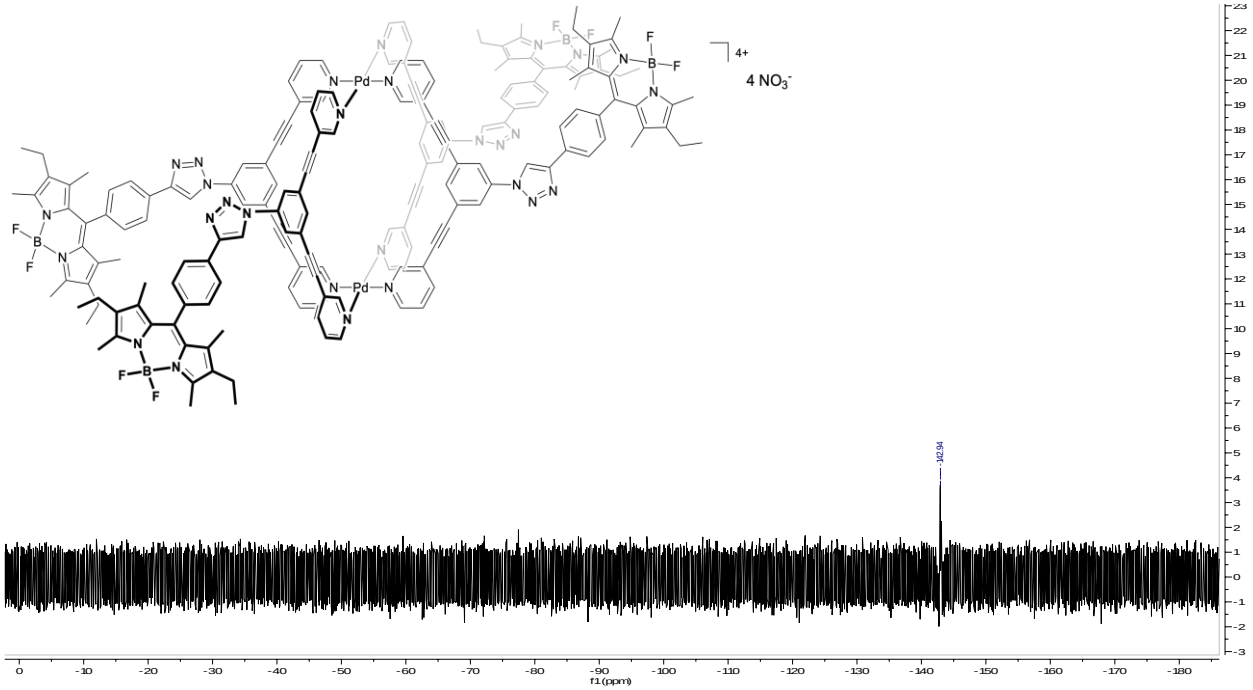

Figure S44.^{19}F NMR (376 MHz, DMSO-d_6) spectrum of **C2.NO$_3$**.

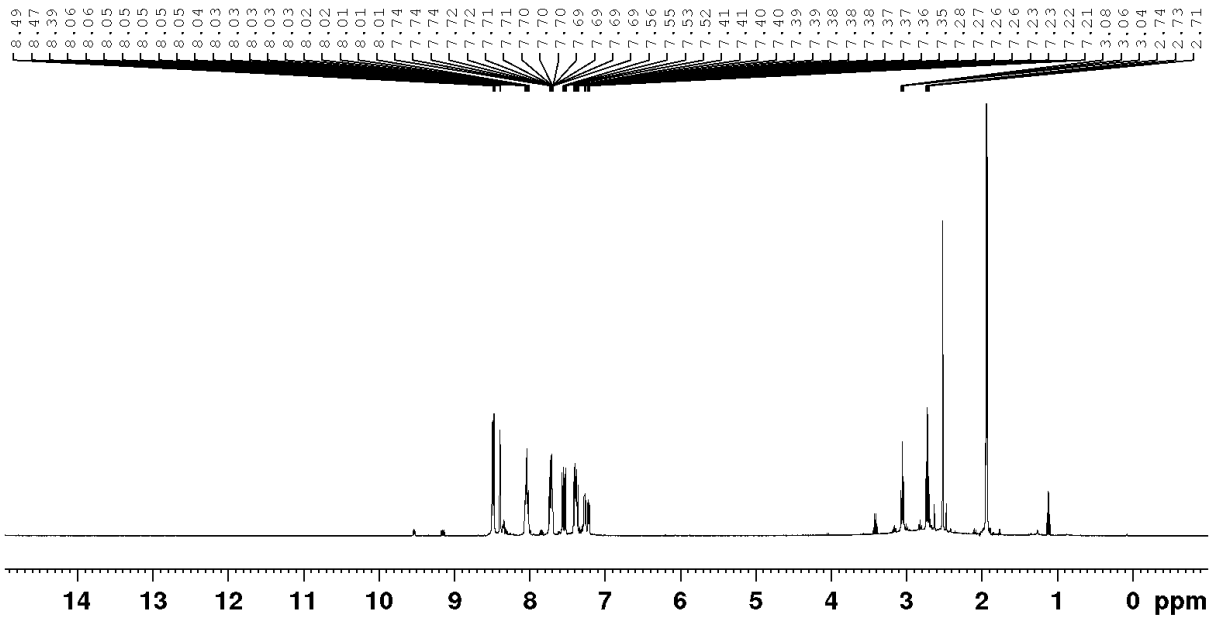

Figure S45: ^{1}H NMR (400 MHz, CD_3CN) spectrum of **Ru^{COOH}**

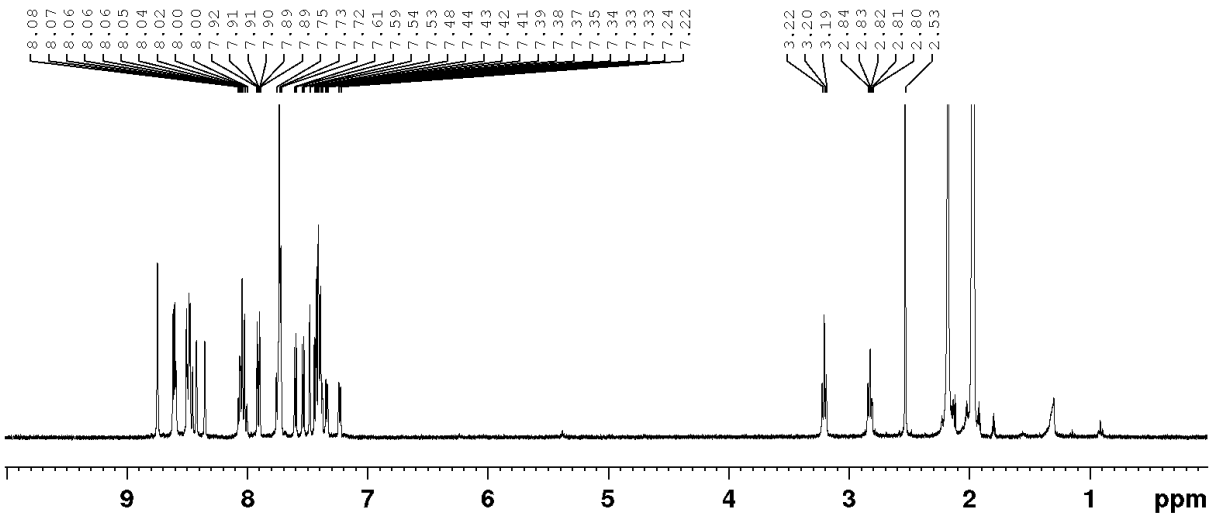

Figure S46: ^{1}H NMR (400 MHz, CD_3CN) spectrum of **L$^{Ru(II)}$**

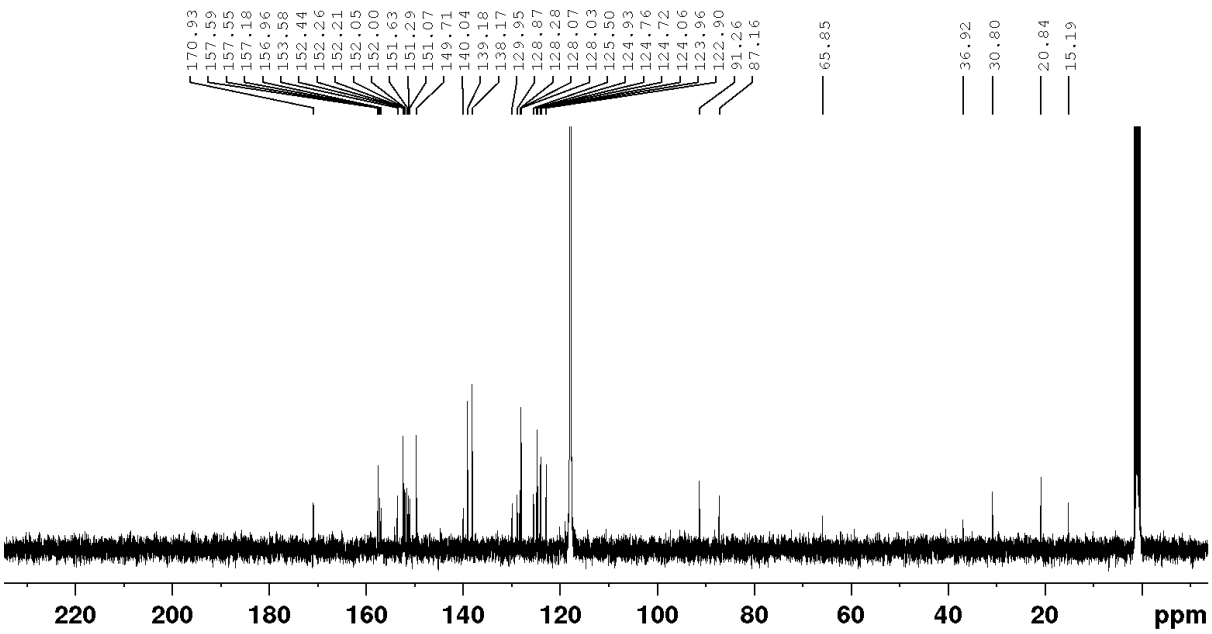

Figure S47 ^{13}C NMR (101 MHz, CD_3CN) spectrum of $\mathbf{L^{Ru(II)}}$

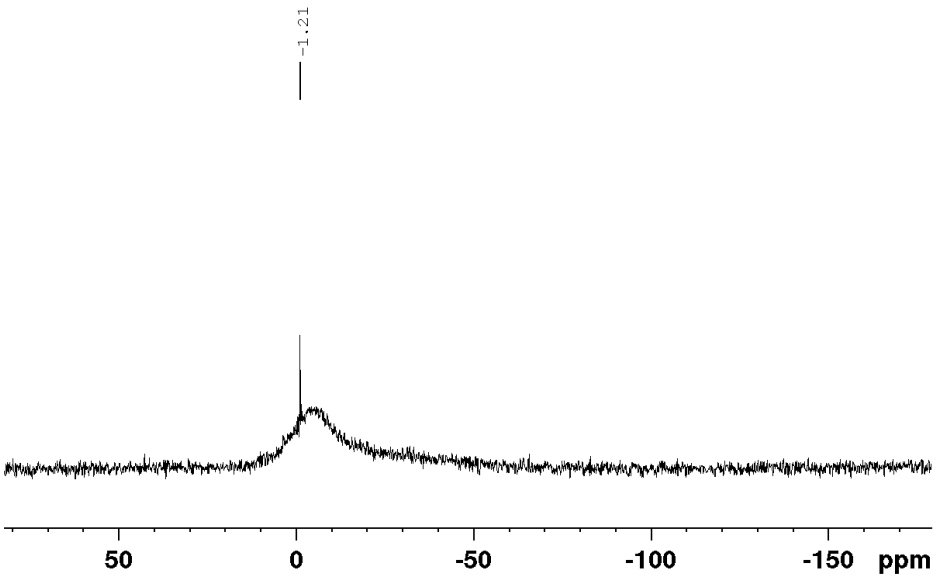

Figure S48: ^{11}B NMR (128 MHz, CD_3CN) spectrum of $\mathbf{L^{Ru(II)}}$

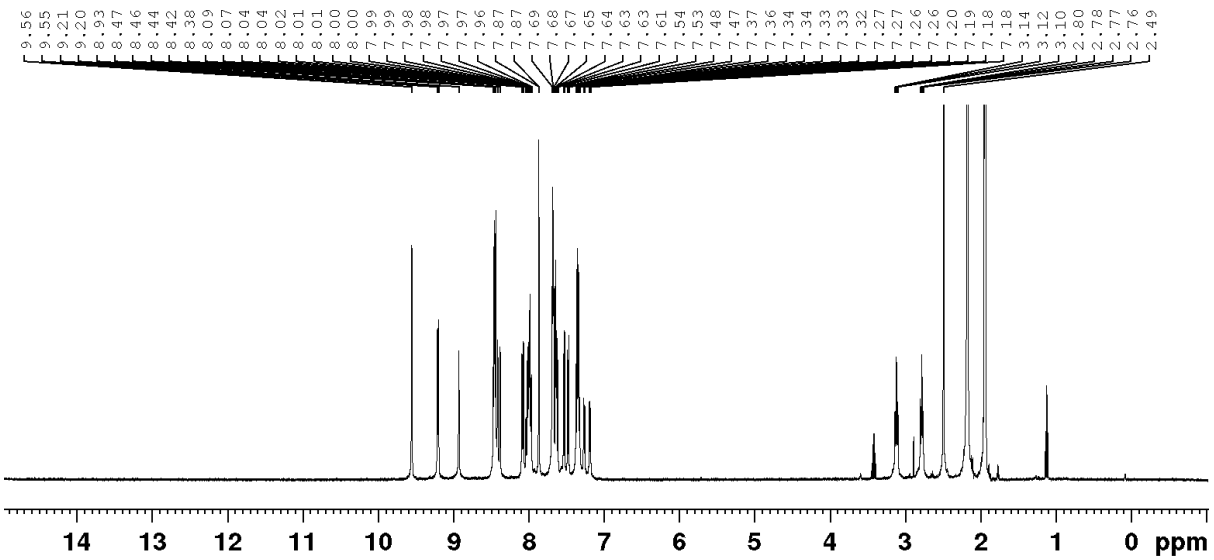

Figure S49: ^{1}H NMR (400 MHz, CD_3CN) spectrum $\mathbf{C}^{Ru(II)}$

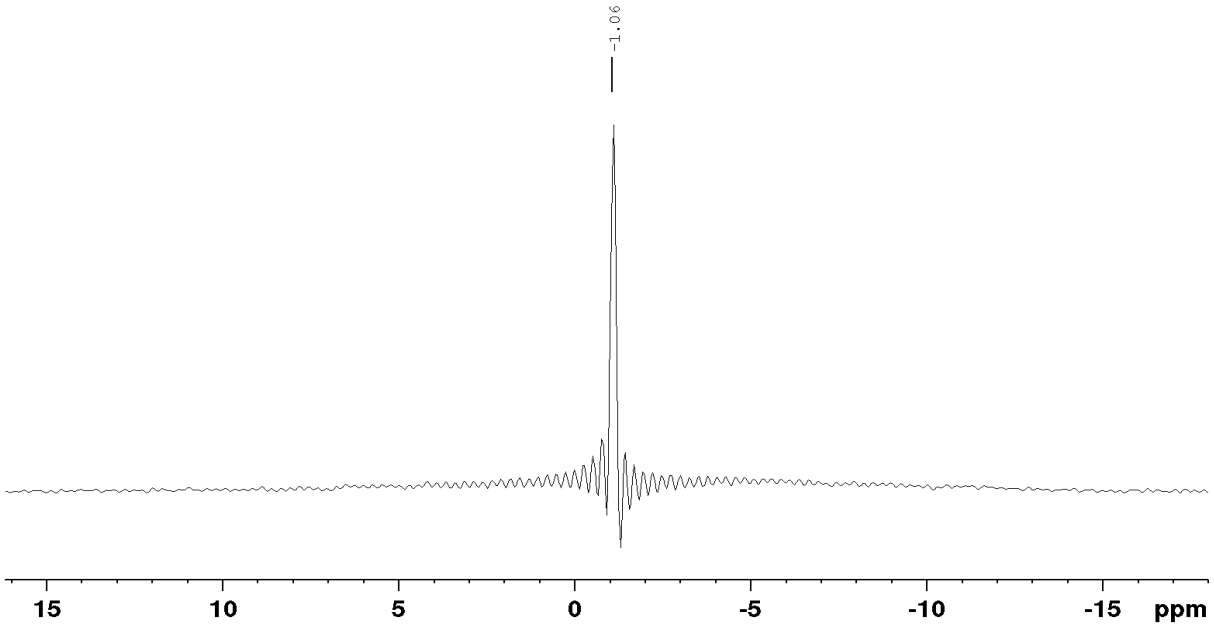

Figure S50 ^{11}B NMR (128 MHz, CD_3CN) spectrum of $\mathbf{C}^{Ru(II)}$

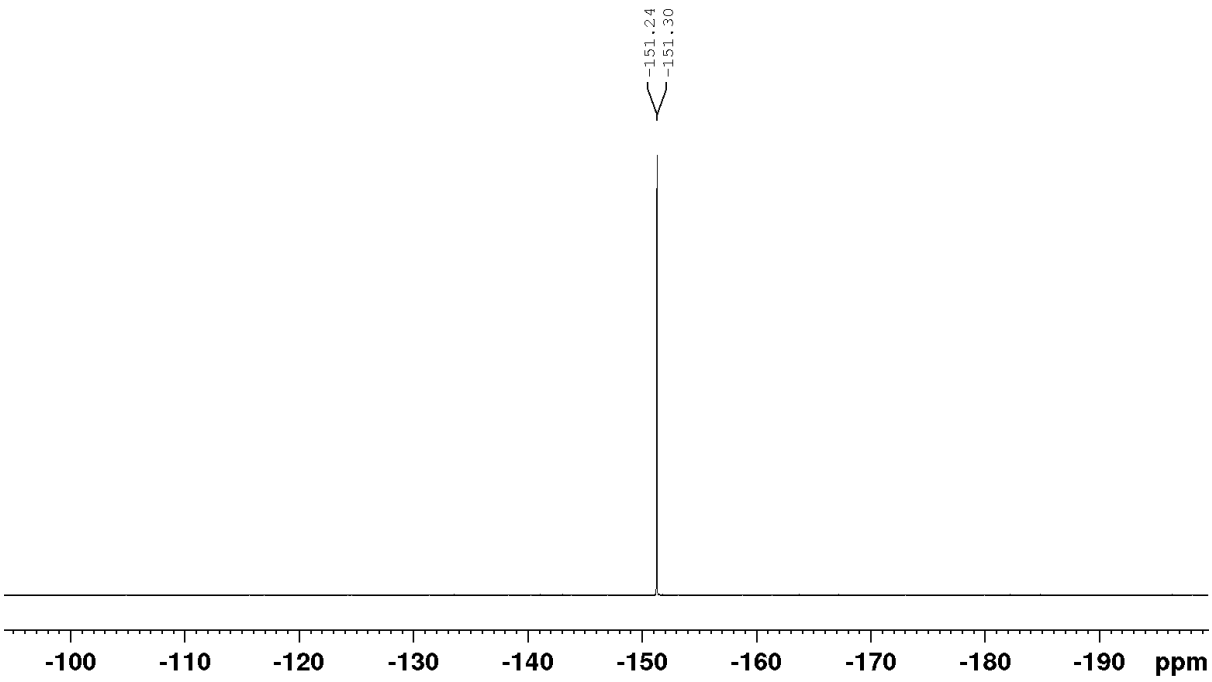

Figure S51: ^{19}F NMR (376 MHz, CD_3CN) spectrum of $\mathbf{C^{Ru(II)}}$

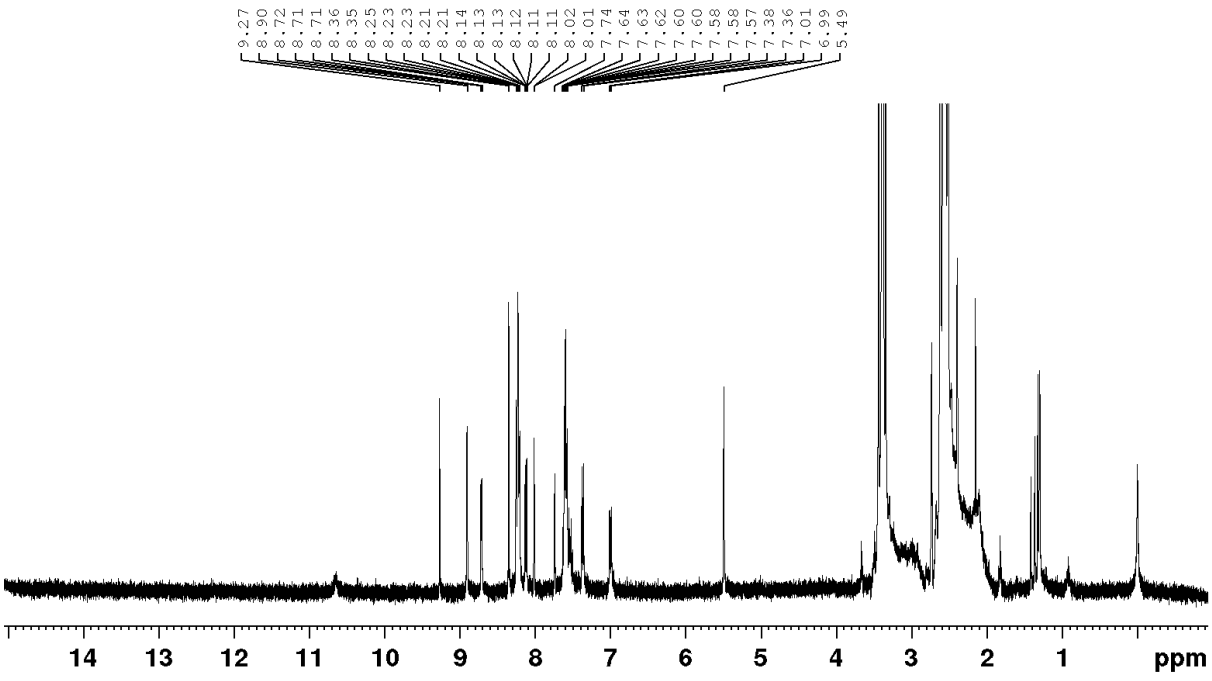

Figure S52 ^{1}H NMR (400 MHz, DMSO-d_6) spectrum of $\mathbf{L^{NIR}}$

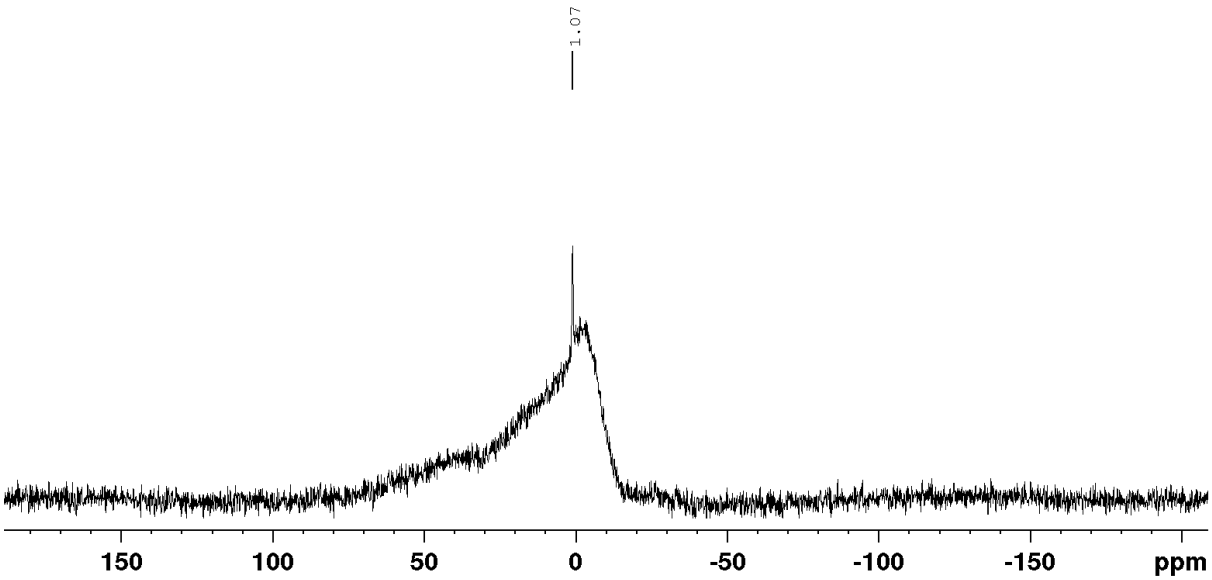

Figure S53: ^{11}B NMR (128 MHz, DMSO-d_6) spectrum of **L^{NIR}**

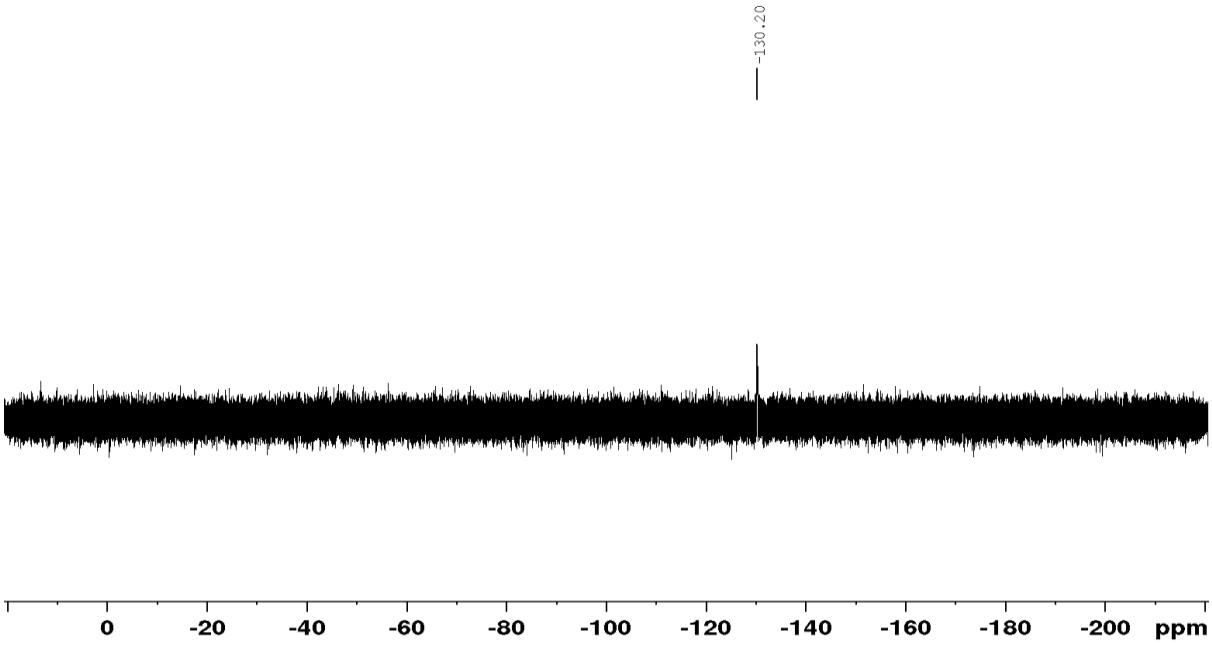

Figure S54: ^{19}F NMR (376 MHz, DMSO-d_6) spectrum of **L^{NIR}**

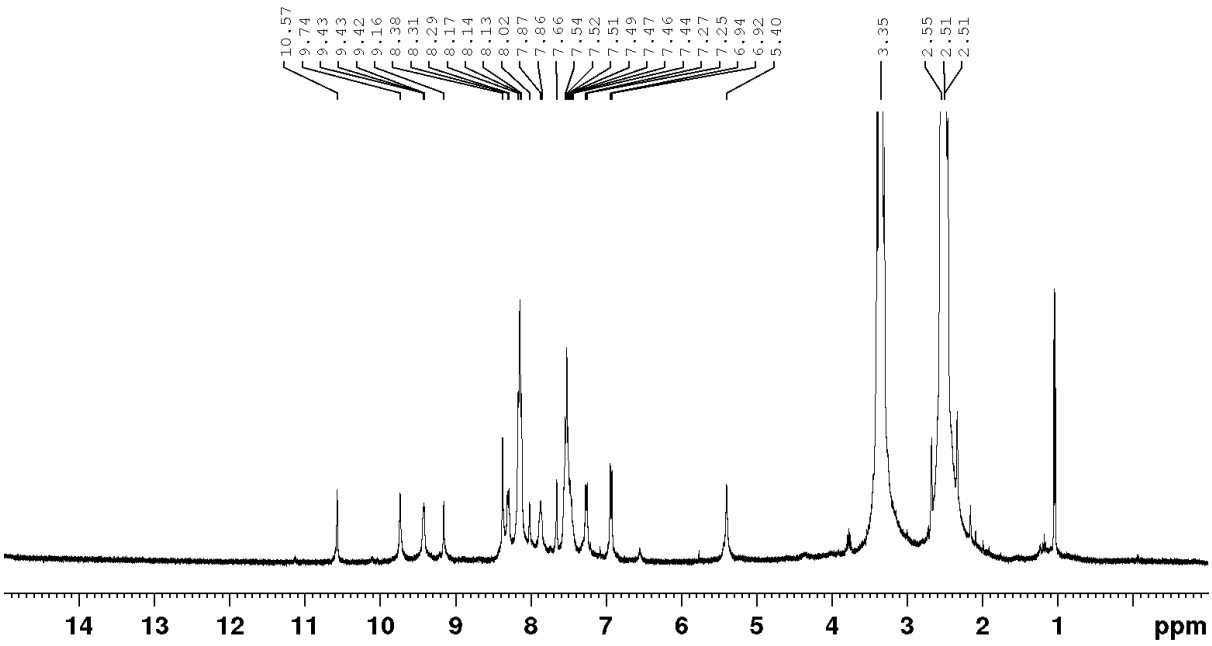

Figure S55 ^{1}H NMR (400 MHz, DMSO-d_6) spectrum of **C^{NIR}**

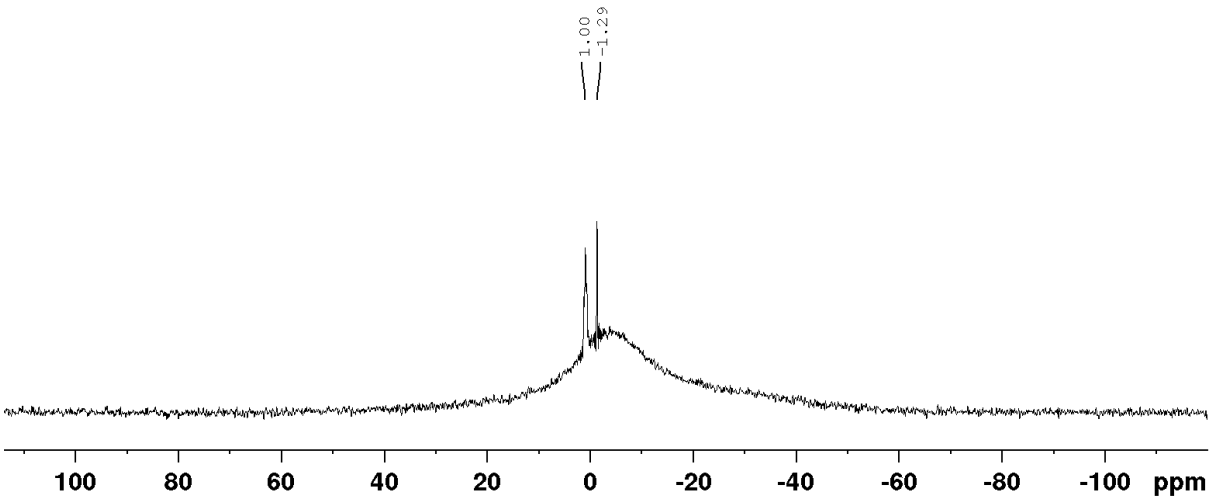

Figure S56: ^{11}B NMR (128 MHz, DMSO-d_6) spectrum of **C^{NIR}**

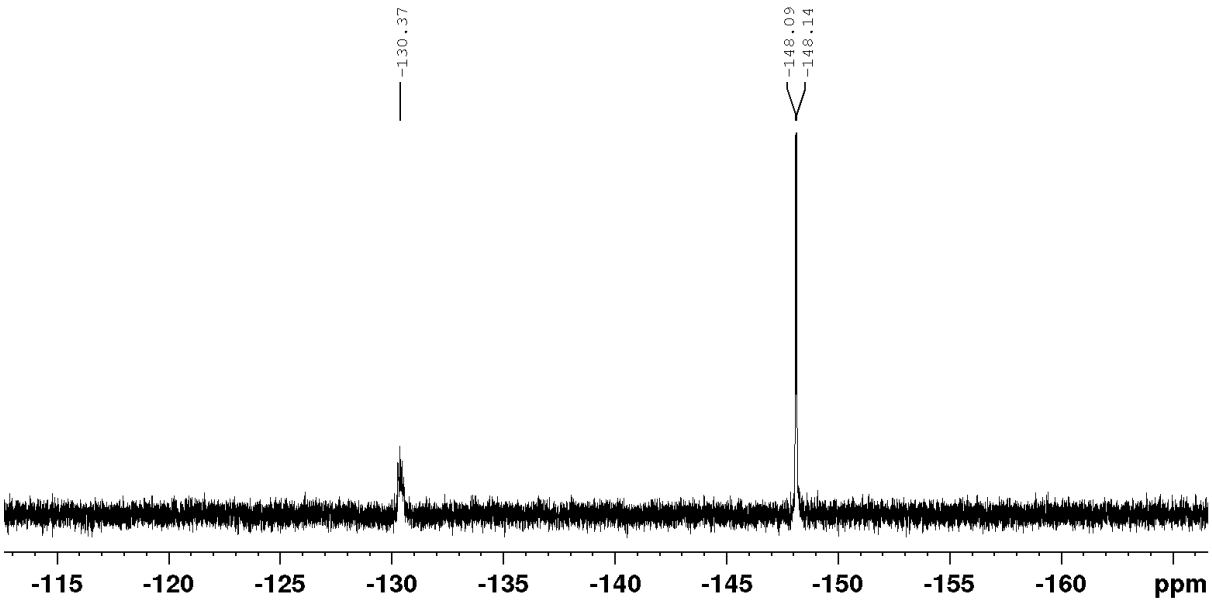

Figure S57: ^{19}F NMR (376 MHz, DMSO-d_6) spectrum of **L^{NIR}**

Chapter 8 Supporting information

Column chromatography was carried out using a Biotage Isolera™ Prime automated purification system, with ZIP KP 10 g silica gel cartridges, using the following solvent gradients. Solvent A: Hexane; solvent B: ethylacetate; solvent C: Methanol. Gradient A: A/B (0% - 100%, 30 column volumes (CV)), B/C (0 – 10%, 10 CV), B/C (10%, 10 CV). Gradient B: A/B (20% - 30%, 6 CV), A/B (30% - 75%, 15 CV), A/B (75%, 5 CV), A/B (75% - 100%, 5 CV), B/C (0% - 10%, 10 CV).

Synthesis of ligands L_{aq}1-7

3,5-bis(3-ethynylpyridine)-benzylalcohol (L^{CH2OH}):

3,5-dibromobenzylalcohol (1.00 g, 3.8 mmol, 1.0 eq.), 3-ethynylpyridine (1.16 g, 11.3 mmol, 3 eq.), CuI (72 mg, 0.4 mmol, 0.1 eq.), $Pd(PPh_3)_2Cl_2$ (264 mg, 0.4 mmol, 0.1 eq.) were added to a flame dried flask. Triethylamine (40 mL) was added and the suspension was stirred under nitrogen at 90°C for 24 h. Ethylacetate (100 mL) was added and the reaction mixture was filtered over Celite. The filtrate was concentrated *in vacuo*. The residue was dissolved in DCM and loaded onto silica gel before purification *via* chromatography (gradient A) to give the product as a white solid (828 mg, 2.67 mmol, 71% yield).

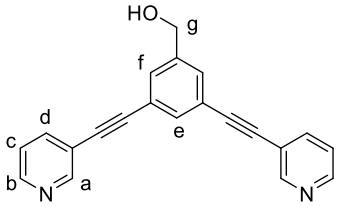

^{1}H NMR (400 MHz, DMSO-d_6): δ [ppm] 8.79 (d, J = 1.9 Hz, 2H, H_a), 8.62 (dd, J = 1.3 Hz, 4.8 Hz, 2H, H_b), 8.02 (dt, J = 1.9 Hz, 8.0 Hz, 2H, H_d) 7.69 (s, 1H, H_e), 7.61 (s, 2H, H_f), 7.50 (dd, J = 4.9 Hz, 8.0 Hz, 2H, H_c), 5.44 (t, J = 5.7 Hz, 1H, OH), 4.57 (d, J = 5.8, 2H, H_g).

^{13}C{^{1}H} NMR (101 MHz, DMSO-d_6): δ [ppm] 152.2 (C_a), 149.7 (C_b), 144.8, 139.2, 130.3, 124.2, 122.7, 119.6, 91.7 ($C_{alkynyl}$), 87.2 ($C_{alkynyl}$), 62.3, 31.2.

3,5-bis(3-ethynylpyridine)-4-benzylbromide (L^{CH2Br}):

3,5-bis(3-ethynylpyridine)-4-benzylalcohol (**L^{CH2OH}**) (200 mg, 0.6 mmol, 1.0 eq.), carbon tetrabromide (320 mg, 0.9 mmol, 1.5 eq.) and triphenylphosphine (200 mg, 0.7 mmol, 1.2 eq.) were added to a flame dried flask. Dry DCM (10 mL) was added and the solution was stirred in the absence of light, at room temperature, under nitrogen, for 4 h. The solution was loaded directly onto silica gel and purified *via* chromatography (gradient B) to give the product as a white solid (133 mg, 0.36 mmol, 56%).

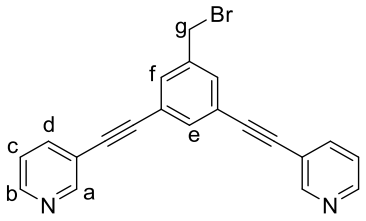

^{1}H NMR (400 MHz, $CDCl_3$): δ [ppm] 8.76 (d, J = 2.0 Hz, 2H, H_a), 8.57 (dd, J = 1.8 Hz, 4.8 Hz, 2H, H_b), 7.80 (dt, J = 1.9 Hz, 7.9 Hz, 2H, H_d), 7.65 (t, J = 1.4 Hz, 1H, H_e), 7.56 (d, J = 1.4 Hz, 2H, H_f), 7.30 (ddd, J = 0.8 Hz, 4.9 Hz, 7.9 Hz, 2H, H_c), 4.45 (s, 2H, H_g).

^{13}C{^{1}H} NMR (101 MHz, DMSO-d_6): δ [ppm] 152.2 (C_a), 149.9 (C_b), 143.4, 139.3 (C_e), 134.5, 133.1, 224.2, 123.4, 119.4, 91.1 ($C_{alkynyl}$), 88.1($C_{alkynyl}$), 32.7 (C_g).

3,5-bis(3-ethynylpyridine)-4-benzylazide (L^{CH2N3}):

3,5-bis(3-ethynylpyridine)-4-benzylbromide **L^{CH2Br}** (106 mg, 0.3 mmol, 1.0 eq.), and sodium azide (18 mg, 0.3 mmol, 1.0 eq.) were stirred in DMF (5 mL) at room temperature overnight. Excess water was added to quench to reaction. The resulting suspension was filtered, and the precipitate was taken up in 1:3 isopropanol/DCM (50 mL), dried over $MgSO_4$, filtered and the solvent removed *in vacuo*. The product was isolated via chromatography (gradient A) and the product was obtained as an off-white solid (74 mg, 0.2 mmol, 79%).

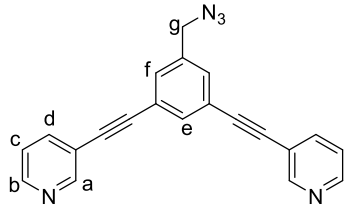

^{1}H NMR (400 MHz, $CDCl_3$): δ [ppm] 8.77 (s, 2H, H_a), 8.57 (d, J = 3.6 Hz, 2H, H_b), 7.80 (dt, J = 1.8 Hz, 7.9 Hz, 2H, H_d), 7.69 (t, J = 1.4 Hz, 1H, H_e), 7.48 (s, 2H, H_f), 7.29 (dd, J = 4.9 Hz, 7.8 Hz, 2H, H_c), 4.38 (s, 2H, H_g).

^{13}C{^{1}H} NMR (101 MHz, $CDCl_3$): δ [ppm] 171.3, 152.2, 149.8, 139.1, 136.5, 133.7, 133.1, 132.5, 132.0, 131.9, 91.4, 87.5, 66.5.

ESI-MS calc. for $C_{21}H_{14}N_5$ $[M+H]^+$: *m/z* = 336.1249; found 336.1244; δ = -1.5 ppm.

2-(acetoxymethyl)-6-((1-(3,5-bis(pyridin-3-ylethynyl)benzyl)-1H-1,2,3-triazol-4-yl)methoxy) tetra-hydro-2H-pyran-3,4,5-triyl triacetate (L_{aq}1):

The synthesis of ligand **L_{aq}1** was adapted from a previously reported procedure.[4] In details, 3,5-bis(3-ethynylpyridine)-4-benzylazide **L^{CH2N3}** (100 mg, 0.3 mmol, 1.0 eq.) was dissolved in a solution of 3:1 methanol: water (40 mL). Ascorbic acid (71 mg, 0.4 mmol, 1.3 eq.) and copper sulphate pentahydrate (7 mg, 0.03 mmol, 0.1 equiv.) were dissolved in distilled water (2.5 mL). Saturated NaOH aqueous solution (0.5 mL) was added to the aqueous copper sulphate solution and stirred for 10 min. The two solutions were combined before 2-propyl-tetra-O-acetyl-β-D-

glucopyranide was added and the resulting solution was left to stir at room temperature overnight. The reaction was monitored by TLC (1:1 Hex: EtOAc, R_f = 0.73) to ensure completion. Saturated $NH_4.OAc_{(aq)}$ (50 mL) was added to precipitate the product. The aqueous suspension was washed with ethyl acetate (4 x 50 mL). The combined organic phases were washed with brine and dried over $MgSO_4$. The solvent was removed *in vacuo* to give the product as an off white solid (182 mg, 0.25 mmol, 84%).

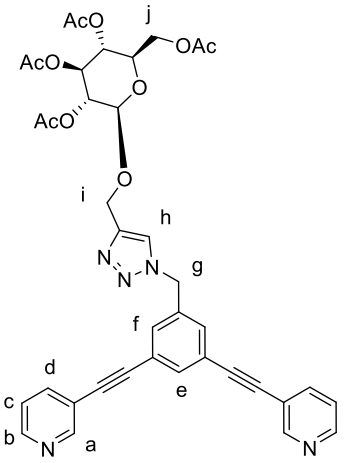

^{1}H NMR (400 MHz, $CDCl_3$): δ [ppm] 10.12 (s, 1H, H_h), 8.77 (d, J = 1.9 Hz, 2H, H_a), 8.60 (dd, J = 1.4, 4.9 Hz, 2H, H_b), 8.00 (dt, J = 1.7, 7.7 Hz, 2H, H_d), 7.48 (dd, J = 4.9, 7.9 Hz, 2H, H_c), 7.25 (t, J = 1.2 Hz, 1H, H_e), 7.02 (d, J = 1.3 Hz, 2H, H_f), 5.30 (t, J = 9.5, 1H, H_k), 4.96-4.87 (m, XH), 4.77 (dd, J = 8.0, 9.6 Hz, 2H, H_i) 4.38 (d, J = 2.5 Hz, 1H), 4.34 (d, J = 2.5 Hz, 2H), 4.27 (d, J = 2.6 Hz, 2H), 4.23 (d, J = 2.5 Hz, 1H), 4.22-4.25 (m, 2H), 2.02 (s, 3H, H_{OAc}), 2.00 (s, 3H, H_{OAc}), 1.98 (s, 3H, H_{OAc}), 1.94 (s, 3H, H_{OAc}).

^{13}C{^{1}H} NMR (101 MHz, DMSO-d_6): δ [ppm] 170.1 (C_{OAc}), 169.5 (C_{OAc}), 169.3 (C_{OAc}), 169.0 (C_{OAc}), 157.7, 151.8, 149.2, 138.7, 131.0, 125.4, 123.4, 119.0, 97.8, 91.3, 86.5, 79.2, 77.9, 72.0, 70.8, 70.6, 68.1, 61.6, 55.9, 20.5 (C_{OAc}), 20.4 (C_{OAc}), 20.4 (C_{OAc}), 20.3 (C_{OAc}).

ESI-MS calc. for $C_{36}H_{33}N_5O_8$ $[M-(CH_3COO)]^+$: *m/z* = 663.2329; found 663.4550.

2-((1-(3,5-bis(pyridin-3-ylethynyl)benzyl)-1H-1,2,3-triazol-4-yl)methoxy)-6-(hydroxymethyl)tetrahydro-2H-pyran-3,4,5-triol (L_{aq}2):

L_{aq}1 (135 mg, 0.18 mmol, 1 eq.) was dissolved in methanol (30 mL). To this solution was added Amberlite IRA 401 (OH^-) ion exchange beads (230 mg) and the reaction was stirred at room temperature for 16 h. The Amberlite beads were removed by filtration and the organic solution was concentrated *in vacuo*. Water (50 mL) was added to the colourless residue, and the resulting precipitate was filtered to afford the product as a white solid (61 mg, 0.11 mmol, 63%).

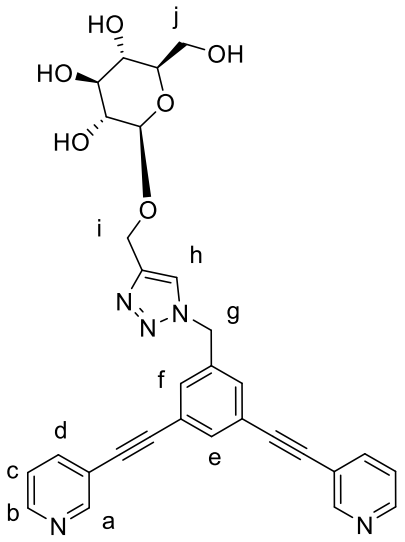

^{1}H NMR (400 MHz, DMSO-d_6/MeOD-d_4): δ [ppm] 8.79 (s, 2H, H_a), 8.62 (s, 2H, H_b), 8.28 (s, 1H, H_h), 8.05-7.98 (m, 2H, H_d), 7.80 (s, 1H, H_e), 7.68 (d, J = 1.2 Hz, 1H, H_f), 7.63 (d, J = 1.3 Hz, 1H, $H_{f'}$), 7.53-7.46 (m, 2H, H_c), 5.68 (s, 2H, H_g), 4.87 (d, J = 12.5 Hz, 1H, H_i), 4.66 (d, J = 12.5 Hz, 1H, $H_{i'}$), 3.72 (d, J = 11.8 Hz, 2H, H_j) 3.25-2.95 (m, 5H, $H_{Glucose}$).

^{13}C{^{1}H} NMR (101 MHz, $CDCl_3$): δ [ppm] 152.2, 149.9, 144.8, 139.2, 138.1, 134.2, 132.0, 125.1, 124.2, 123.3, 119.4, 102.7, 91.1, 87.9, 77.4, 77.2, 73.8, 70.6, 62.0, 61.6, 52.9, 52.3.

ESI-MS calc. for $C_{30}H_{28}N_5O_7$ $[M+H]^+$: *m/z* = 554.2039; found 554.3144.

Synthesis of ligands L_{aq}3 and L_{aq}4

3,5-bis(3-ethynylpyridine)-4-benzyl(thio-β-D-glucose tetraacetate) (L_{aq}3):

1-thio-β-D-glucose tetraacetate (104 mg, 0.3 mmol, 1.1 eq.) and bis-3,5-(3-ethynylpyridine)-4-benzylbromide (**L^{CH2Br}**) (97 mg, 0.3 mmol, 1.0 eq.) was dissolved in acetonitrile (6 mL) in a flame dried flask. Triethylamine (40 µL, 0.3 mmol, 1.1 eq.) was added and the solution was stirred for 3 h at reflux before being quenched with water. The reaction mixture was extracted with ethyl acetate (3 x 50 mL). The organic layer was dried over $MgSO_4$ and concentrated in vacuo. The residue was purified *via* chromatography (gradient A) to give the product as a yellow solid (160 mg, 0.22 mmol, 84% yield).

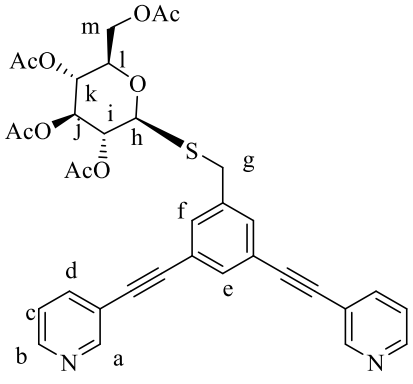

^{1}H NMR (400 MHz, $CDCl_3$): δ [ppm] 8.75 (dd, J = 0.8 Hz, 2.1 Hz, 2H, H_a), 8.55 (dd, J = 1.7 Hz, 4.9 Hz, 2H, H_b), 7.80 (dt, J = 1.9 Hz, 7.9 Hz, 2H, H_d), 7.63 (t, J = 1.5 Hz, 1H, H_e), 7.48 (d, J = 1.5 Hz, 2H, H_f), 7.29 (ddd, J = 1.0 Hz, 4.9, 7.9 Hz, 2H, H_c) 5.16 (d, J = 9.3 Hz, 1H, H_h), 5.11-5.04 (m, 2H, H_g), 4.35 (d, J = 10.0 Hz, 1H, H_l) 4.27-4.04 (m, 3H, H_i, H_j, H_k), 3.88 (m, 2H, H_m, $H_{m'}$), 3.68-3.62 (m, 1H, H_l).

^{13}C{^{1}H} NMR (101 MHz, $CDCl_3$): δ [ppm] = 169.6 (C_{Ac}), 169.1 (C_{Ac}), 168.4 (C_{Ac}), 168.4 (C_{Ac}), 151.3 (C_a), 147.9 (C_b), 137.5, 137.1, 132.7, 131.3, 122.4, 122.1, 118.9, 90.2 ($C_{alkynyl}$), 86.0 ($C_{alkynyl}$), 81.0, 74.9, 72.7, 68.7, 67.2, 61.1, 32.0 (C_g), 19.7 (C_{Ac}), 19.7 (C_{Ac}), 19.6 (C_{Ac}), 19.6 (C_{Ac}).

ESI-MS calcd. for $C_{35}H_{32}N_2O_9S$ $[M+H]^+$: *m/z* = 657.1907; found 657.1916; δ = 1.4 ppm.

3,5-bis(3-ethynylpyridine)-4-benzyl-thio-β-D-glucose (L_{aq}4):

L_{aq}3 (114 mg, 0.2 mmol, 1.0 equiv.) was dissolved in methanol (10 mL). To this solution was added Amberlite 401 OH- ion exchange beads (200 mg) and the reaction was stirred at room temperature overnight. The Amberlite beads were removed by filtration and the organic solution was concentrated *in vacuo*. Water (30 mL) was added to the colourless residue, and the resulting suspension was filtered to afford the product as a white solid (42 mg, 87 µmol, 51% yield).

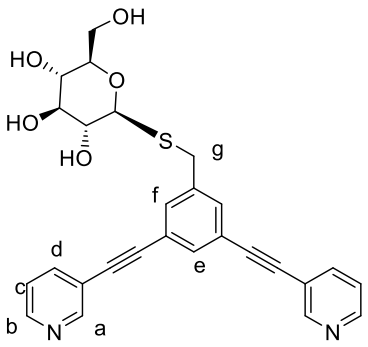

^{1}H NMR (400 MHz, MeOD-d_4): δ [ppm] 8.73 (dd, J = 0.9 Hz, 2.2 Hz, 2H, H_a), 8.54 (dd, J = 1.7 Hz, 5.0 Hz, 2H, H_b), 8.01 (dt, J = 2.0 Hz, 8.2 Hz, 2H, H_d), 7.67-7.63 (m, 3H, H_e, H_f), 7.48 (ddd, J = 0.9 Hz, 4.9 Hz, 8.0 Hz, 2H, H_c), 4.23-4.05 (m, 2H), 3.96-3.86 (m, 2H), 3.74-3.67 (m, 1H), 3.29-3.21 (m, 4H).

^{13}C{^{1}H} NMR (101 MHz, MeOD-d_4): δ [ppm] = 151.2, 148.1, 139.2, 132.6, 123.7, 123.0, 120.5, 91.3, 85.7, 80.8, 73.0, 70.2, 61.6, 56.9, 56.0, 54.9.

ESI-MS calcd. for $C_{27}H_{25}N_2O_5S$ $[M+H]^+$: *m/z* = 489.1484; found 489.1486; δ = 0.4 ppm.

Synthesis of 3,5-bis(3-ethynylpyridine)-1-(2-(2-methoxyethoxy)ethane)phenol (L_{aq}5)

3,5-bis(3-ethynylpyridine)phenol (L^{OH}) 3,5-dibromophenol (1.00 g, 4.0 mmol, 1.0 eq.), 3-ethynylpyridine (1.22 g, 11.9 mmol, 3.0 eq.), CuI (76 mg, 0.4 mmol, 0.1 eq.), $Pd(PPh_3)_2Cl_2$ (278 mg, 0.4 mmol, 0.1 eq.) were added to a flame dried round bottom flask under nitrogen. Triethylamine (40 mL) was added and the suspension was stirred at 90°C for 72 hours.

Ethylacetate (100 mL) was added and the reaction mixture was filtered over Celite. The filtrate was concentrated *in vacuo.* The residue was dissolved in DCM and loaded onto silica gel before purification via chromatography (gradient A) to give the product as a white solid (800 mg, 2.7 mmol, 68% yield).

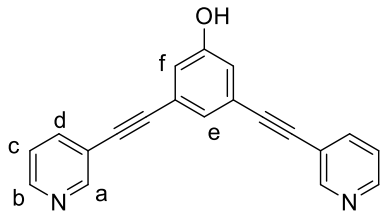

^{1}H NMR (400 MHz, DMSO-d_6): δ [ppm] 10.20 (b, 1H, H_{OH}), 8.77 (dd, J = 0.8 Hz, 2.2 Hz, 2H, H_a), 8.60 (dd, J = 1.7 Hz, 5.0 Hz, 2H, H_b), 7.99 (dt, J = 1.9 Hz, 7.8 Hz, 2H, H_d), 7.48 (ddd, J = 0.8 Hz, 4.9 Hz, 7.9 Hz, 2H, H_c), 7.24 (t, J = 1.1 Hz, 1H, H_e), 7.02 (d, J = 1.6 Hz, 2H, H_f).

^{13}C{^{1}H} NMR (101 MHz, DMSO-d_6): δ [ppm] 152.2 (C_a), 149.7 (C_b), 139.2, 125.7, 124.1, 123.8, 119.6, 119.4, 110.2, 91.8 (C_{alkyne}), 86.9 (C_{alkyne}).

ESI-MS calcd. for $C_{20}H_{13}N_2O$ $[M+H]^+$: *m/z* = 297.1028; found 297.1162; δ = 45 ppm.

3,3'-((5-(2-(2-methoxyethoxy)ethoxy)-1,3-phenylene)bis(ethyne-2,1-diyl))dipyridine (L_{aq}5):
3,5-bis(3-ethynylpyridine)-phenol (**L^{OH}**) (51 mg, 0.3 mmol, 1.0 eq.), and K_2CO_3 (46 mg, 0.6 mmol, 2 eq.) were dissolved in dry DMF (5 mL) and added to a flame dried RBF. 1-chloro-2-(2-methoxyethoxy)ethane (synthesized according to a previously reported procedure)[3] (61 mg, 0.4 mmol, 1.5 eq.) was added to this solution and the reaction was stirred at 90°C for 16 h under nitrogen. The reaction mixture was filtered over Celite and the solvent was removed *in vacuo*. The residue was taken up in DCM (50 mL) and washed with distilled water (3 x 30 mL) and brine (1 x 30 mL). The organic phase was dried over $MgSO_4$ and the solvent removed *in vacuo*. The crude residue was purified by chromatography (gradient A) to give the product as a yellow oil (366 mg, 0.17 mmol, 58%).

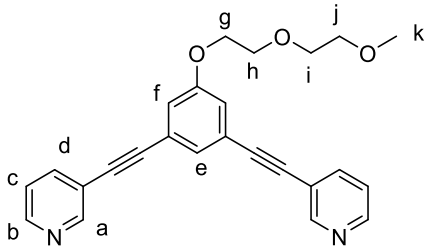

^{1}H NMR (400 MHz, MeOD-d_4): δ [ppm] 8.68 (s, 2H, H_a), 8.50 (d, J = 4.33 Hz, 2H, H_b), 7.94 (dt, J = 2.0 Hz, 2H, H_d), 7.43 (dd, J = 4.8, 8.0 Hz, 2H, H_d), 7.30 (s, 1H, H_e), 7.14 (s, 2H, H_f), 4.16 (t, J = 4.8 Hz, 2H, H_g), 3.83 (t, J = 4.4 Hz, 2H, H_h), 3.71-3.67 (m, 2H, H_i), 3.58-3.54 (m, 2H, H_j), 3.34 (s, 3H, H_k).

^{13}C{^{1}H} NMR (101 MHz, MeOD-d_4): δ [ppm] 158.8, 151.2, 148.1, 139.2, 127.0, 123.8, 123.7, 120.5, 118.2, 91.4 (C_{alkyne}), 85.6 (C_{alkyne}), 71.6 (C_g), 70.2 (C_h), 69.3 (C_i), 67.7 (C_j), 57.9 (C_k).

ESI-MS calcd. for $C_{25}H_{23}N_2O_3$ $[M+H]^+$: *m/z* = 399.1709; found 399.1799; δ = 22.5 ppm.

Synthesis of ligands L_{aq}6 and L_{aq}7

Synthesis of 2-(3,5-bis(pyridin-3-ylethynyl)phenyl)acetic acid (L_{aq}6)

Benzyl-(3,5-dibromophenylacetate) was synthesized according to a previously reported procedure.[2]

Benzyl-(3,5-bis(3-ethynylpyridine)-phenylacetate) ($L^{CH2COOBn}$):

A mixture of benzyl-(3,5-dibromophenylacetate) (370 mg, 1.0 mmol, 1.0 eq.), 3-ethynylpyridine (309 mg, 3.0 mmol, 3.0 eq.), $Pd(PPh_3)_2Cl_2$ (68.1 mg, 0.1 mmol, 0.1 eq.) and CuI (18.5 mg, 0.1 mmol, 0.1 eq.), was suspended in distilled triethylamine (15 mL) and stirred under a nitrogen atmosphere at 90°C. After 24 h, the reaction mixture was diluted with ethylacetate (50 mL) and filtered over glass-fritted funnel (por. 3). The solvent was removed under vacuum and the crude residue further purified by column chromatography (gradient A) to give the product benzyl-(3,5-bis(3-ethynylpyridine)-phenylacetate) (BnL1) as an off white solid (311 mg, 0.8 mmol, 75%).

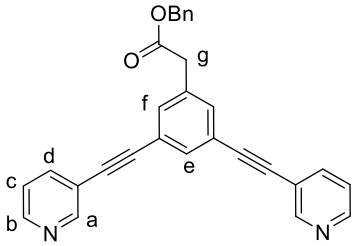

^{1}H NMR (400 MHz, DMSO-d_6): δ [ppm] = 8.80 (d, J = 1.4 Hz, 2H, H_a), 8.61 (dd, J = 1.6, 5.0 Hz, 2H, H_b), 8.12 (d, J = 1.6 Hz, 2H, H_f), 8.06 (t, J = 1.6, 1H H_e), 8.02 (dt, J = 1.8, 8.0 Hz, 2H, H_d) 7.64-7.35 (m, 7H, phenyl + H_c), 5.39 (s, 2H, H_g).

^{13}C{^{1}H} NMR (101 MHz, DMSO-d_6): δ [ppm] = 164.5, 152.3, 149.9, 139.3, 138.7, 136.1, 132.5, 131.9, 131.4, 129.2, 129.1, 128.8, 128.7, 124.1, 123.3, 119.2, 90.5, 88.6, 67.4.

ESI-MS calcd. for $C_{28}H_{19}N_2O_2$ $[M+H]^+$: *m/z* = 415.1447; found: 415.1448; δ = 0.2 ppm.

2-(3,5-bis(pyridin-3-ylethynyl)phenyl)acetic acid (L_{aq}6):

$L^{CH2COOBn}$ (768 mg, 1.8 mmol, 1 eq.) was dissolved in acetonitrile (50 mL). NaOH (211 mg, 5.4 mmol, 3.0 eq.) was dissolved in water (7 mL) and added to the organic solution. The reaction was stirred at 90°C for 5 h. The solution was cooled to room temperature and the solution was concentrated in vacuo (approx. 5 mL). The concentrated solution was acidified drop wise with concentrated HCl (~pH 5) and the resultant precipitate was collected by filtration. The solid was washed with cold ethyl acetate and diethyl ether to give the product as an off-white solid (442 mg, 1.3 mmol, 73%).

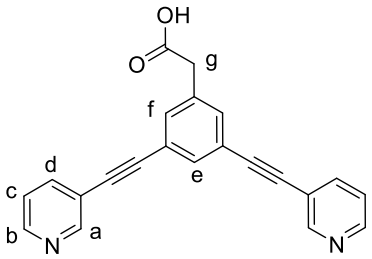

^{1}H NMR (400 MHz, $CDCl_3$): δ [ppm] 8.80 (s, 2H, H_a), 8.56 (d, J = 3.4 Hz, 2H, H_b), 7.83 (dt, J = 1.7 Hz, 8.0 Hz, 2H, H_d), 7.65 (t, J = 1.4 Hz, 1H, H_e), 7.55 (d, J = 1.3 Hz, 2H, H_f), 7.33 (dd, J = 4.7 Hz, 8.2 Hz, 2H, H_c), 3.70 (s, 2H, H_g).

^{13}C{^{1}H} NMR (101 MHz, DMSO-d_6): δ [ppm] 172.6 (C_{COOH}), 152.2 (C_a), 149.7 (C_b), 139.2 (C_e), 133.7, 132.7, 124.2, 122.7, 119.6, 91.6 (C_{Alkyne}), 87.4 (C_{Alkyne}).

ESI-MS calcd. for $C_{22}H_{14}N_2O_2$ $[M+H]^+$: *m/z* = 339.1134; found 339.1148; δ = 4.1 ppm.

Synthesis of Ligand 3-(3,5-Bis(3-ethynylpyridine)phenyl)-propionic acid (**L_{aq}7**)

Benzyl-(3-(3,5-dibromophenyl)propanoate) was synthesized according to a previously reported procedure.[2]

Benzyl-(3-(3,5-bis(3-ethynylpyridine)phenyl)-propanoate) ($L^{(CH2)2COOBn}$): A mixture of benzyl-(3(3,5-dibromophenyl)propanoate) (365 mg, 0.9 mmol, 1.0 eq.), 3-ethynylpyridine (284 mg, 2.8 mmol, 3.0 eq.), $Pd(PPh_3)_2Cl_2$ (64 mg, 0.1 mmol, 0.1 eq.), and CuI (19 mg, 0.1 mmol, 0.1 eq.), was suspended in distilled triethylamine (15 mL) and stirred under a nitrogen atmosphere at 90°C. After 24 h, the reaction mixture was diluted with ethyl acetate (50 mL) and filtered over glass-fritted funnel (por. 3). The solvent was removed in vacuo and the crude residue further purified by column chromatography (gradient A) to give the product benzyl-(3-(3,5-bis(3-ethynylpyridine)phenyl)propanoate) (**BnL2**) as an orange oil (236 mg, 0.5 mmol, 58%).

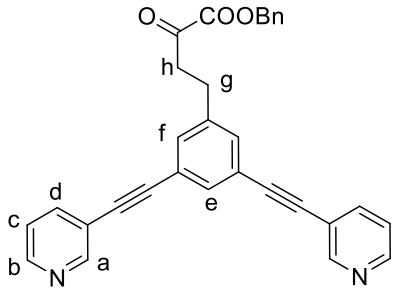

^{1}H NMR (400 MHz, DMSO-d_6): δ [ppm] = 8.80 (d, J = 1.4 Hz, 2H, H_a), 8.61 (dd, J = 1.6, 5.0 Hz, 2H, H_b), 8.12 (d, J = 1.6 Hz, 2H, H_f), 8.06 (t, J = 1.6 Hz, 1H, H_e), 8.02 (dt, J = 1.8, 8.0 Hz, 2H, H_d), 7.64-7.35 (m, 7H, phenyl, H_c), 5.39 (s, 2H, H_g).

^{13}C{^{1}H} NMR (101 MHz, DMSO-d_6): δ [ppm] = 164.5 (C_{COOH}), 152.3 (C_a), 149.9 (C_b), 139.3 (C_e), 138.7 (C_d), 136.1, 132.5, 131.9 (C_{phenyl}), 131.4 (C_{phenyl}), 129.2 (C_{phenyl}), 129.1 (C_{phenyl}), 128.8 (C_{phenyl}), 128.7 (C_{phenyl}), 124.1, 123.3, 119.2, 90.5 (C_{Alkyne}), 88.6 (C_{Alkyne}), 67.4.

ESI-MS calcd. for $C_{28}H_{19}N_2O_2$ $[M+H]^+$: *m/z* = 415.1447; found: 415.1448; δ = 0.2 ppm.

3-(3,5-Bis(3-ethynylpyridine)phenyl)-propionic acid (L_{aq}7): $L^{(CH2)2COOBn}$ (481 mg, 1.1 mmol, 1.0 eq.) was dissolved in acetonitrile (20 mL). NaOH (108 mg, 2.7 mmol, ~2.5 eq.) was dissolved in water (4 mL) and added to the organic solution. The reaction was stirred at 90°C for 5 h. The solution was cooled to room temperature and the solution was concentrated in vacuo (approx. 5 mL). The concentrated solution was acidified drop wise with conc. HCl (~pH 5) and the resultant precipitate was collected by filtration. The solid was washed with cold ethyl acetate and diethyl ether to give the product as an off-white solid (293 mg, 0.83 mmol, 75%).

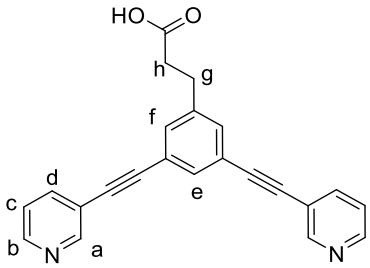

^{1}H NMR (400 MHz, $CDCl_3$): δ [ppm] 12.28 (s, 1H, H_i), 8.84 (d, J = 2.1 Hz, 2H, H_a), 8.67 (dd, J = 1.4 Hz, 4.8 Hz, 2H, H_b), 8.06 (dt, J = 1.7 Hz, 8.0 Hz, 2H, H_d), 7.70 (s, 1H, H_e), 7.61 (d, J = 0.9, 2H, H_f), 7.54 (dd, J = 4.9 Hz, 7.8 Hz, 2H, H_c), 2.93 (t, J = 7.4, 2H, H_h), 2.68 (t, J = 7.7, 2H, H_g).

^{13}C{^{1}H} NMR (101 MHz, DMSO-d_6): δ [ppm] 173.6 (C_{COOH}), 151.7 (C_a), 149.2 (C_b), 142.6, 138.7, 132.1, 132.0, 123.7, 122.4, 119.1, 91.3 (C_{Alkyne}), 86.8 (C_{Alkyne}), 34.6 (C_h), 29.7 (C_g).

ESI-MS calcd. for $C_{23}H_{17}N_2O_2$ $[M+H]^+$: *m/z* = 353.1290; found 353.1289; δ = -0.3 ppm.

General procedure for the synthesis of metallacages C_{aq}1-7

Synthesis of the cages was achieved by self-assembly. A solution of the palladium(II) nitrate dihydrate (2 eq.) and ligand (4 eq.) in DMSO was stirred at room temperature for 1 h. After precipitation by addition of acetone and diethylether, the solid was filtered and washed with cold acetone and diethyl ether to yield the cage compound as an off-white solid.

Cage C_{aq}1:

2-(acetoxymethyl)-6-((1-(3,5-bis(pyridin-3-ylethynyl)benzyl)-1H-1,2,3-triazol-4-yl)methoxy)tetrahydro-2H-pyran-3,4,5-triyl triacetate **(L_{aq}1)** (72 mg, 0.1 mmol, 4 eq.) and palladium(II) nitrate dihydrate (13 mg, 0.05 mmol, 2 eq.) were added to DMSO (5 mL) to form cage **C_{aq}1** (72 mg, 22 µmol, 86%).

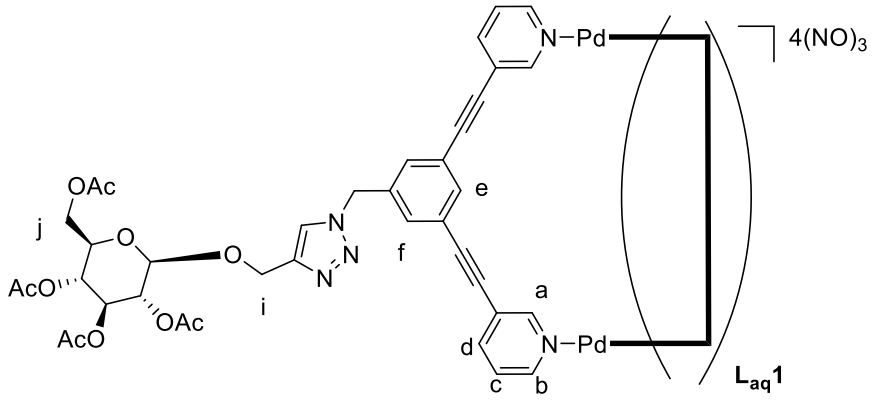

^{1}H NMR (400 MHz, DMSO-d_6): δ [ppm] 9.73 (s, 2H, H_a), 9.40 (s, 2H, H_b), 8.25 (d, J = 7.4 Hz, 2H, H_d), 8.16 (s, 1H, H_h) 7.90-7.78 (m, 2H, H_c), 7.72 (s, 1H, H_e), 7.67-7.61 (m, 2H, H_f), 5.67 (s, 2H, H_g), 5.32-4.39 (m, 5H, H_j-H_n), 4.25-3.81 (m, 2H, H_i).

ESI-MS calc. for $C_{152}H_{136}N_{20}O_{40}Pd_2NO_3$ $[M\text{-}3NO_3\text{-}4H]^{3+}$: *m/z* = 1053.2489; found: *m/z* = 1053.1826.

IR (ATR): [cm^{-1}] 412, 419, 473, 494, 617, 664, 718, 853, 1043, 1092, 1171, 1215, 1238, 1277, 1387, 1414, 1435, 1506, 1541, 1657, 1755.

Cage $C_{aq}2$:
2-((1-(3,5-bis(pyridin-3-ylethynyl)benzyl)-1H-1,2,3-triazol-4-yl)methoxy)-6-(hydroxymethyl)tetrahydro-2H-pyran-3,4,5-triol **($L_{aq}2$)** (55 mg, 0.1 mmol, 4 eq.) and palladium(II) nitrate dihydrate (13 mg, 0.05 mmol, 2 eq.) were added to DMSO (5 mL) to form cage **$C_{aq}2$** (38 mg, 14 µmol, 57%).

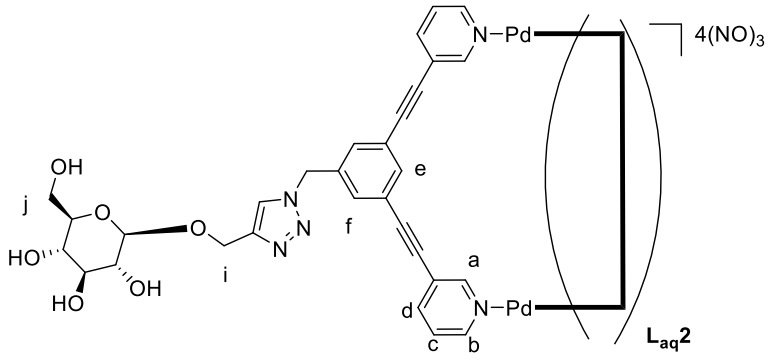

^{1}H NMR (500 MHz, DMSO-d_6): δ [ppm] 9.69 (s, 8H, H_a), 9.38 (s, 8H, H_b), 8.26 (s, 8H, H_d), 8.21 (s, 4H, H_h), 7.96 (s, 4H, H_e), 7.56 (s, 8H, H_f), 7.50 (dd, J = 4.8, 7.4 Hz, 8H, H_c), 5.73 (s, 8H, H_g), 5.76 (s, 8H, H_g), 5.05 (d, J = 5.4 Hz, 4H, H_{OH}), 4.97-4.91 (m, 12H, H_{OH}), 4.83 (d, J = 11.9 Hz, 4H, H_i), 4.65 (d, J = 11.9 Hz, 4H, $H_{i'}$), 3.74-3.63 (m, 8H, H_j) 3.22-2.90 (m, 20H, $H_{Glucose}$).

ESI MS calc. for $C_{120}H_{108}N_{20}O_{30}Pd_2NO_3$ $[M\text{-}3NO_3]^{2+}$: *m/z* = 1293.2848; found: *m/z* = 1293.1163.

IR (ATR): [cm^{-1}] 411, 687, 754, 808, 1020, 1070,1190, 1271, 1319, 1506, 1541, 1558, 1653, 1717, 2324, 2359, 3649, 3854.

Cage C_{aq}3:

3,5-bis(3-ethynylpyridine)-4-benzyl(thio-β-D-glucose tetraacetate) **(L_{aq}3)** (66 mg, 0.1 mmol, 4 eq.) and palladium(II) nitrate dihydrate (13 mg, 0.05 mmol, 2 eq.) were added to DMSO (5 mL) to form cage **C_{aq}3** (68 mg, 22 µM, 88%).

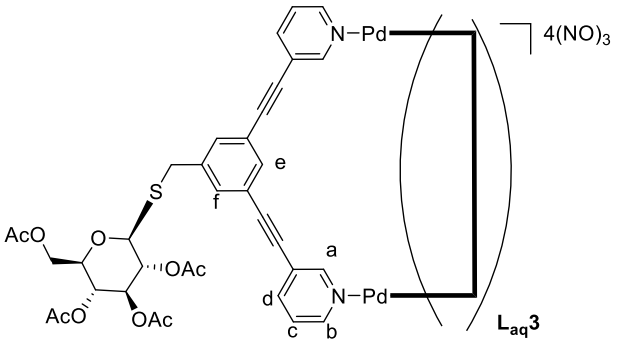

^{1}H NMR (400 MHz, DMSO-d_6): δ [ppm] 9.74 (d, J = 1.4 Hz, 2H, H_a), 9.39 (d, J = 5.7 Hz, 2H, H_b), 8.22 (d, J = 8.2 Hz, 2H, H_d), 7.83 (dd, J = 5.8, 7.8 Hz, 2H, H_c), 7.77 (s, 1H, H_e), 7.67 (s, 2H, H_f), 5.04-4.74 (m, 4H), 4.16-3.80 (m, 5H), 1.96-1.86 (m, 12H, H_{Ac}).

^{13}C{^{1}H} NMR (101 MHz, DMSO-d_6): δ [ppm] 170.4, 169.9, 169.7, 169.6, 153.4, 151.1, 132.5, 132.0, 131.9, 129.3, 129.2, 122.7, 122.2, 94.3, 85.5, 81.7, 74.7, 73.5, 70.0, 68.8, 62.6, 20.9, 20.8, 20.7.

ESI-MS Calc. for $C_{140}H_{128}N_8O_{36}S_4Pd_2N_2O_6$ $[M\text{-}2NO_3]^{3+}$: *m/z* = 988.8479; found: *m/z* = 988.8367.

IR (ATR): [cm^{-1}] 694, 814, 864, 937, 1024, 1061, 1105, 1194, 1227, 1258, 1420, 1456, 1506, 1541, 1558, 1578, 1636, 1684, 1717, 2222, 2328, 2342, 2359, 2822, 2874, 2924, 3734.

Cage C_{aq}4:

3,5-bis(3-ethynylpyridine)-4-benzyl(thio-β-D-glucose) **(L_{aq}4)** (49 mg, 0.1 mmol, 4 eq.) and palladium(II) nitrate dihydrate (13 mg, 0.05 mmol, 2 eq.) were added to DMSO (5 mL) to form cage **C_{aq}4** (41 mg, 17 µM, 68%).

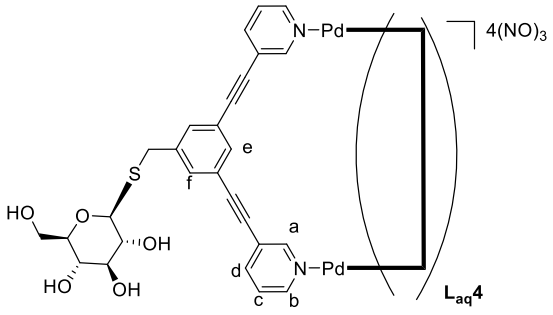

^{1}H NMR (400 MHz, DMSO-d_6): δ [ppm] 9.75 (s, 2H, H_a), 9.39 (d, J = 5.5 Hz, 2H, H_b), 8.23 (d, J = 8.4, 2H, H_d), 7.88-7.77 (m, 3H, H_c, H_e), 7.74 (s, 2H, H_f), 4.19-3.51 (m, 9H).

^{13}C{^{1}H} NMR (101 MHz, DMSO-d_6): δ [ppm] 153.3, 151.0, 143.2, 141.2, 134.5, 132.5, 132.0, 131.9, 129.3, 129.2, 127.8, 122.8, 122.1, 94.2, 85.5, 83.1, 81.7, 78.6, 77.2, 73.5, 70.6, 61.8, 61.7, 56.5.

ESI MS calc. for $C_{108}H_{92}N_8O_{20}S_4Pd_2NO_3$ $[M\text{-}3NO_3\text{-}4H]^{2+}$: 1113.1729; found: *m/z* = 1113.1669. Calc. for $C_{108}H_{92}N_8O_{20}S_4Pd_2$ $[M\text{-}4NO_3\text{-}4H]^{4+}$: *m/z* = 541.5934; found: *m/z* = 541.5928.

IR (ATR): [cm^{-1}] 413, 420, 457, 694, 814, 864, 945, 1024, 1061, 1105, 1194, 1227, 1258, 1314, 1339, 1420, 1456, 1506, 1541, 1558, 1578, 1636, 1684, 1717, 2222, 2342, 2359, 3628, 3649, 3821, 3838.

Cage C_{aq}5:
3,5-bis(3-ethynylpyridine)-1-(2-(2-methoxyethoxy)ethane)phenol **(L_{aq}5)** (40 mg, 0.1 mmol, 4 eq.) and palladium(II) nitrate dihydrate (13 mg, 0.05 mmol, 2 eq.) were added to DMSO (3 mL) to form cage **C_{aq}5** (30 mg, 16 µM, 83%).

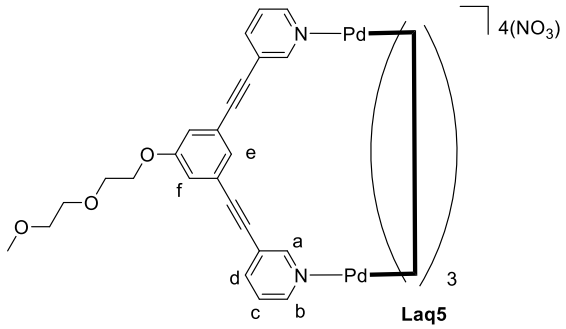

^{1}H NMR (400 MHz, DMSO-d_6): δ [ppm] 9.71 (s, 9.70, 8H, H_a), 9.37 (d, J = 5.0 Hz, 8H, H_b), 8.26 (d, J = 8.2, 8H, H_d), 7.81 (dd, J = 5.8, 7.9 Hz, 8H, H_c), 7.51 (s, 2H, H_e), 7.37 (s, 2H, $H_{e'}$), 7.30 (s, 4H, H_f), 7.07 (s, 4H, $H_{f'}$), 4.15 (t, J = 3.1 Hz, 8H, H_{PEG}), 3.20 (s, 8H, H_{PEG}), 2.89 (s, 8H, H_{PEG}), 2.73 (s, 8H, H_{PEG}). 2.50 (s, 12H, $H_{PEGmethyl}$)

^{13}C{^{1}H} NMR (101 MHz, DMSO-d_6): δ [ppm] 159.2, 153.4, 151.0, 143.2, 127.8, 123.3, 122.7, 120.0, 94.2, 85.4, 71.7, 70.2, 69.2, 68.3, 58.5, 40.9.

ESI-MS calc for $C_{100}H_{88}N_8O_{12}Pd_2N_2O_6$ $[M\text{-}2NO_3]^{3+}$: *m/z* = 644.4875; found: *m/z* = 644.4838. Calc for $C_{100}H_{84}N_8O_{12}Pd_2$ $[M\text{-}4NO_3\text{-}4H]^{4+}$: *m/z* = 451.6159; found: *m/z* =451.6234.

IR (ATR): [cm^{-1}] 694, 814, 864, 947, 1026, 1061, 1105, 1194, 1227, 1258, 1420, 1508, 1541, 1578, 1684, 1717, 2222, 2332, 2359, 2824, 2878, 2922.

Cage C_{aq}6:

3,5-bis(3-ethynylpyridine)-phenylacetic acid (**L_{aq}6**) (34 mg, 0.1 mmol, 4 eq.) and palladium(II) nitrate dihydrate (13 mg, 0.05 mmol, 2 eq were added to DMSO (3 mL) to form cage **C1.NO₃** (34 mg, 19 µmol, 76%).

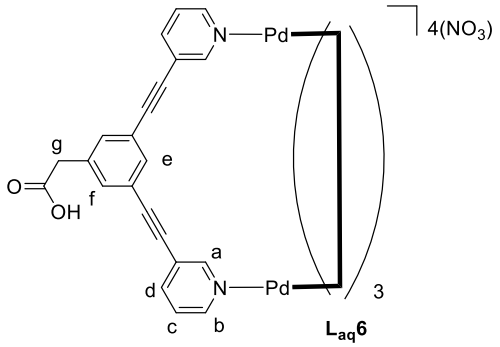

^{1}H NMR (400 MHz, DMSO-d_6): δ [ppm] 9.74 (s, 2H, H_a), 9.40 (d, J = 5.5 Hz, 2H, H_b), 8.26 (d, J = 7.9 Hz, 2H, H_d), 7.91-7.72 (m, 3H, H_c + H_e), 7.63 (s, 2H, H_f), 3.68 (s, 2H, H_g).

^{13}C{^{1}H} NMR (101 MHz, DMSO-d_6): δ [ppm] 172.4, 153.4, 151.0, 143.2, 137.6, 134.9, 127.8, 122.7, 122.0, 94.1, 85.5.

ESI-MS calc. for $C_{88}H_{60}N_8O_4Pd_2$ $[M\text{-}4O\text{+}4H]^{2+}$: *m/z* = 1506.2847; found 1506.3604.

IR (ATR): [cm^{-1}] 544, 687, 808, 872, 949, 1015, 1109, 1188, 1227, 1323, 1418, 1481, 1589, 1717, 2220, 2367, 2916, 3071.

Cage C_{aq}7:

3-(3,5-bis(3-ethynylpyridine)phenyl)-propionic acid (**L_{aq}7**) (35 mg, 0.1 mmol, 4 eq.) and palladium(II) nitrate dihydrate (13mg, 0.05 mmol, 2 eq.) were added to DMSO (5 mL) to form cage **C_{aq}7** (30 mg, 16 µM, 65%).

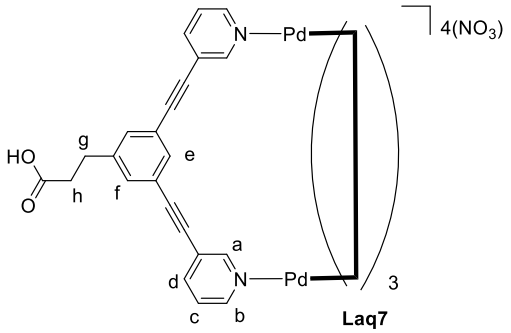

^{1}H NMR (400 MHz, DMSO-d_6): δ [ppm] 12.17 (bs, 4H, H_{COOH}), 9.72 (s, 8H, H_a), 9.38 (d, J = 5.6 Hz, 8H, H_b), 8.24 (d, J = 8.0, 8H, H_d), 7.82 (t, J = 7.5 Hz, 8H, H_c), 7.77 (s, 4H, H_e), 7.60 (s, 8H, H_f), 2.85 (t, J = 6.9 Hz, 8H, H_h), 2.55 (b, 8H, H_g).

IR (ATR): [cm^{-1}] 411, 689, 810, 864, 949, 1026, 1107, 1192, 1225, 1319, 1418, 1506, 1584, 1717, 1734, 2220, 2361, 3076.

NMR Spectra

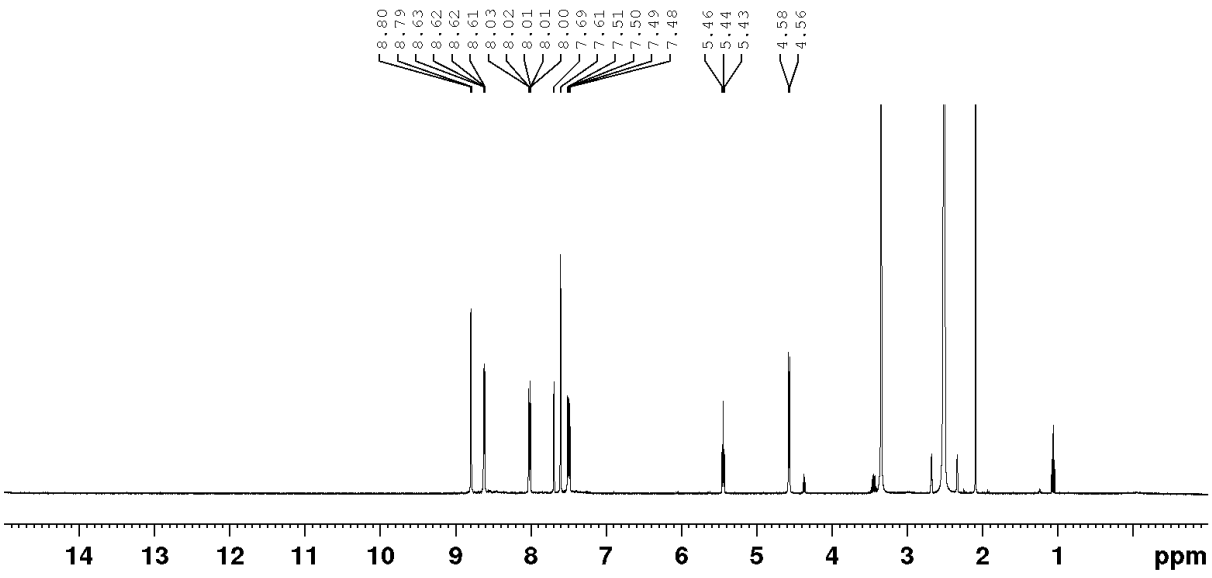

Figure S58: ^{1}H NMR spectra (400 MHz, DMSO-d_6) $\mathbf{L^{CH2OH}}$

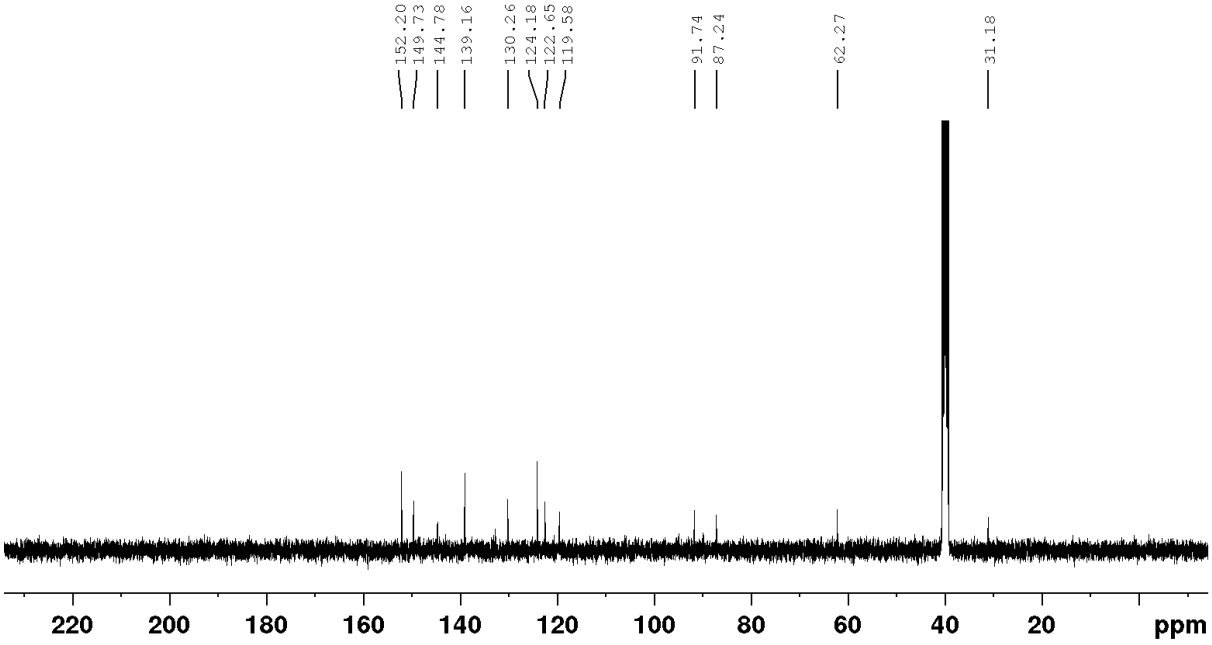

Figure S59: ^{13}C NMR spectra (101 MHz, DMSO-d_6) $\mathbf{L^{CH2OH}}$

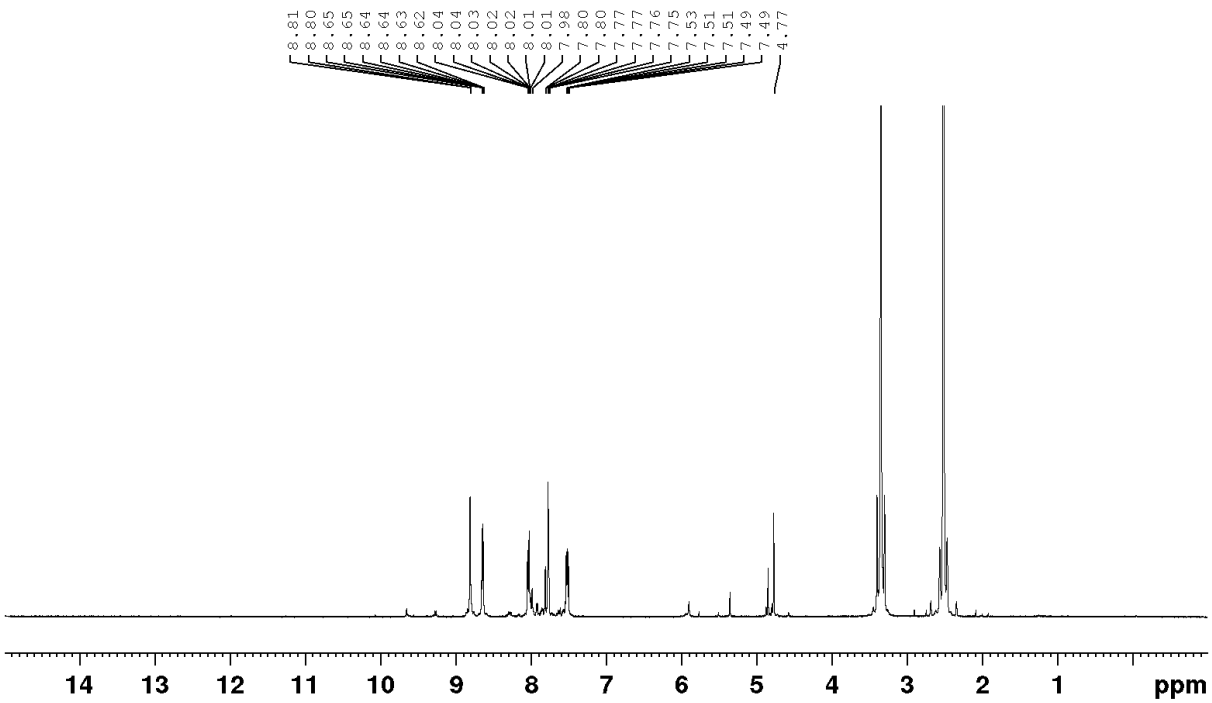

Figure S60 ^{1}H NMR (400MHz, DMSO-d_6) $\mathbf{L^{CH2Br}}$

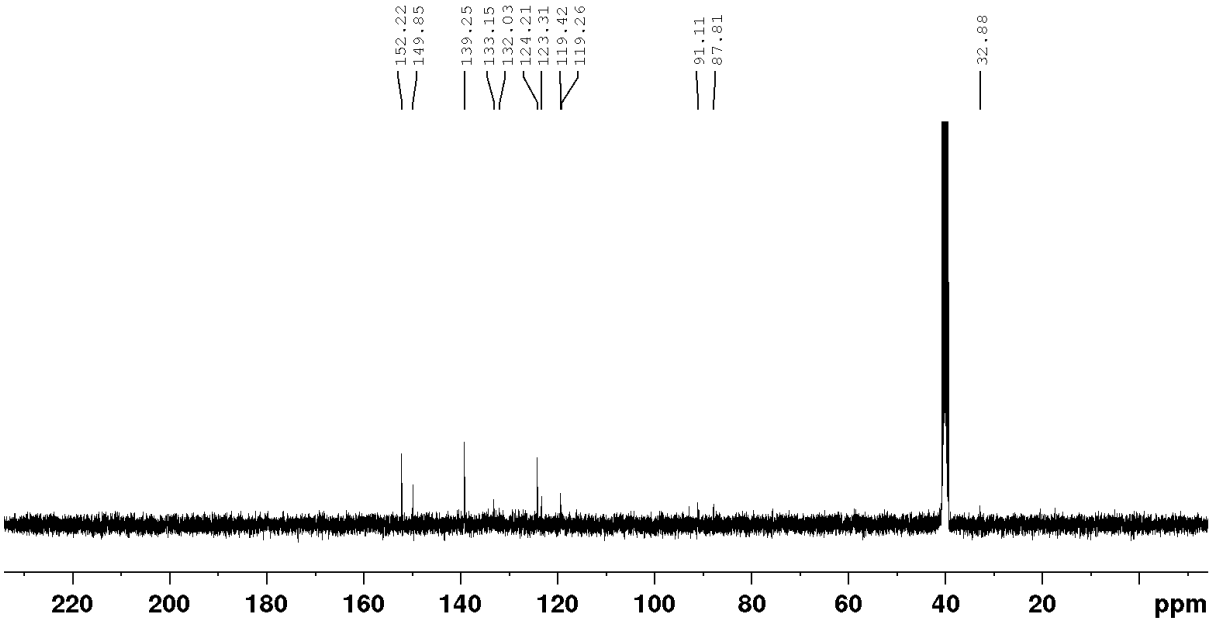

Figure S61 ^{13}C NMR (101MHz, DMSO-d_6) $\mathbf{L^{CH2Br}}$

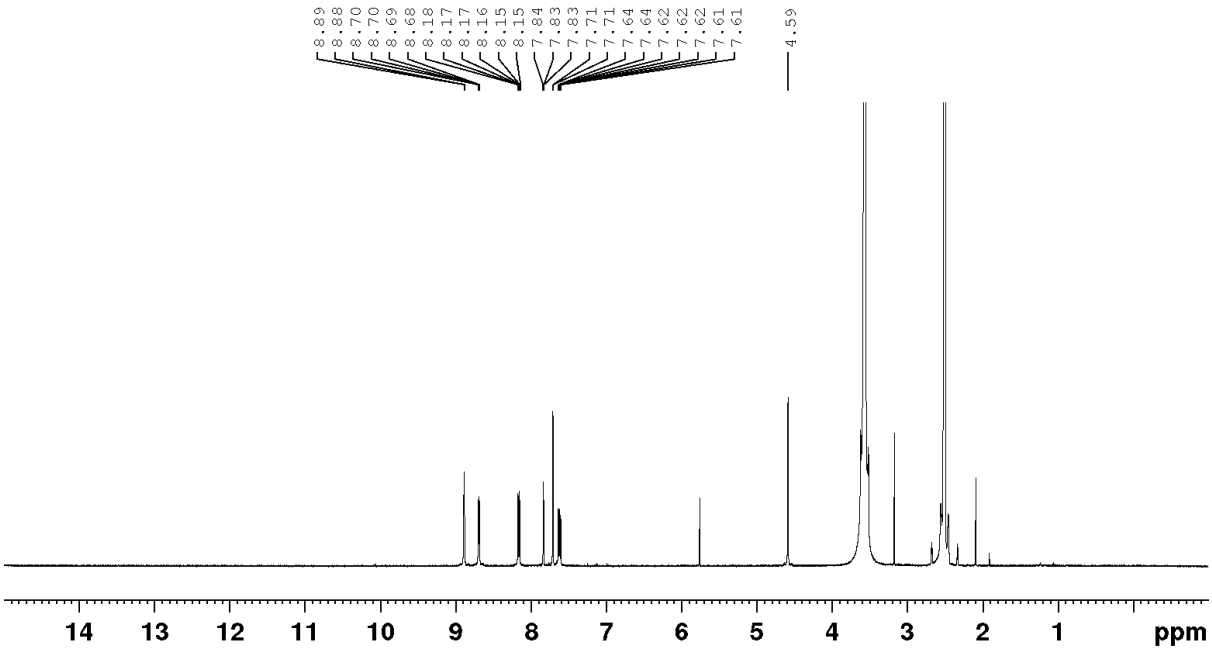

Figure S62 ^{1}H NMR (400 MHz, DMSO-d_6) $\mathbf{L^{CH2N3}}$

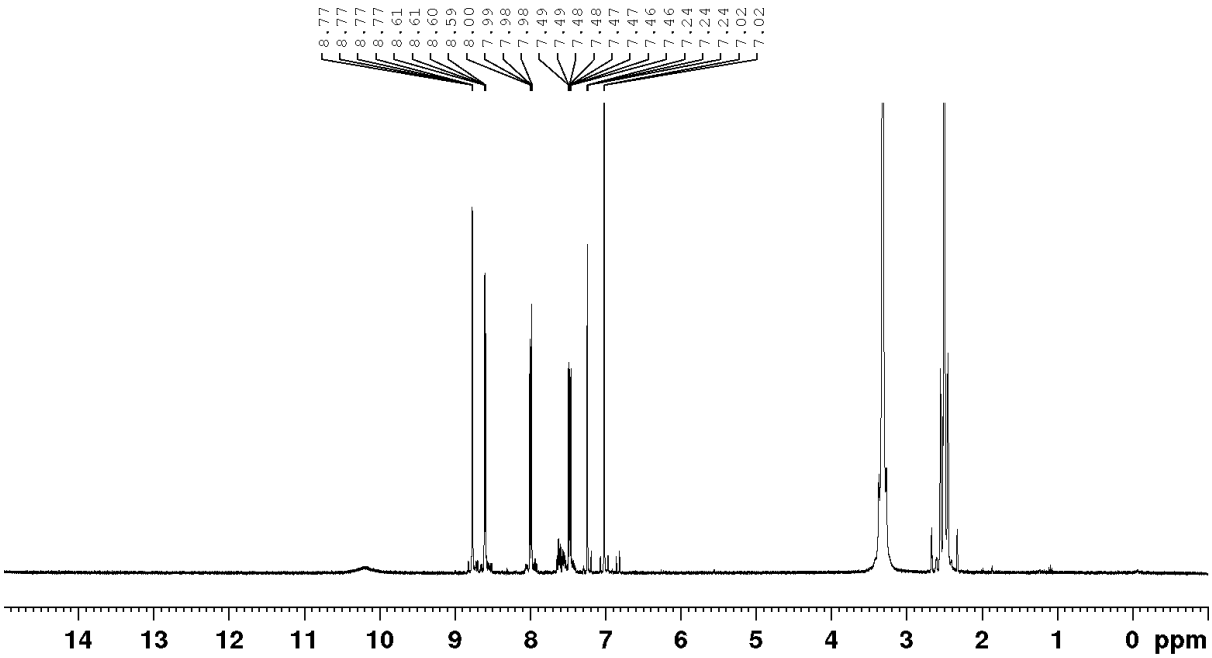

Figure S63 ^{1}H NMR (400 MHz, DMSO-d_6) $\mathbf{L^{OH}}$

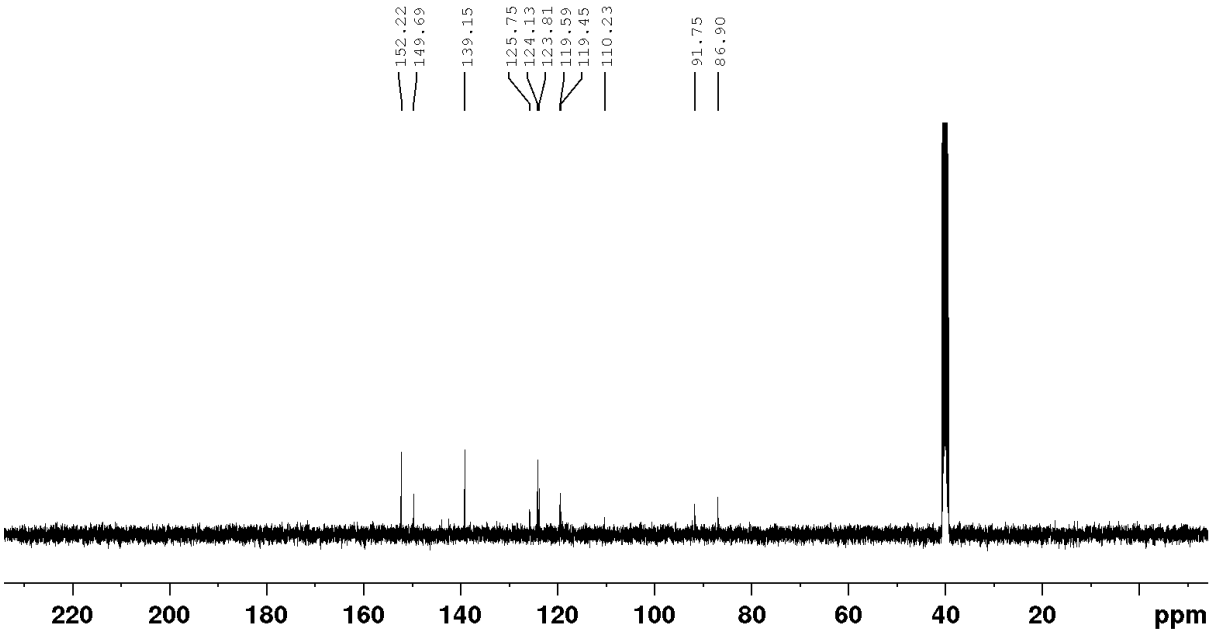

Figure S64 ^{13}C NMR (101 MHz, DMSO-d_6) **L^{OH}**

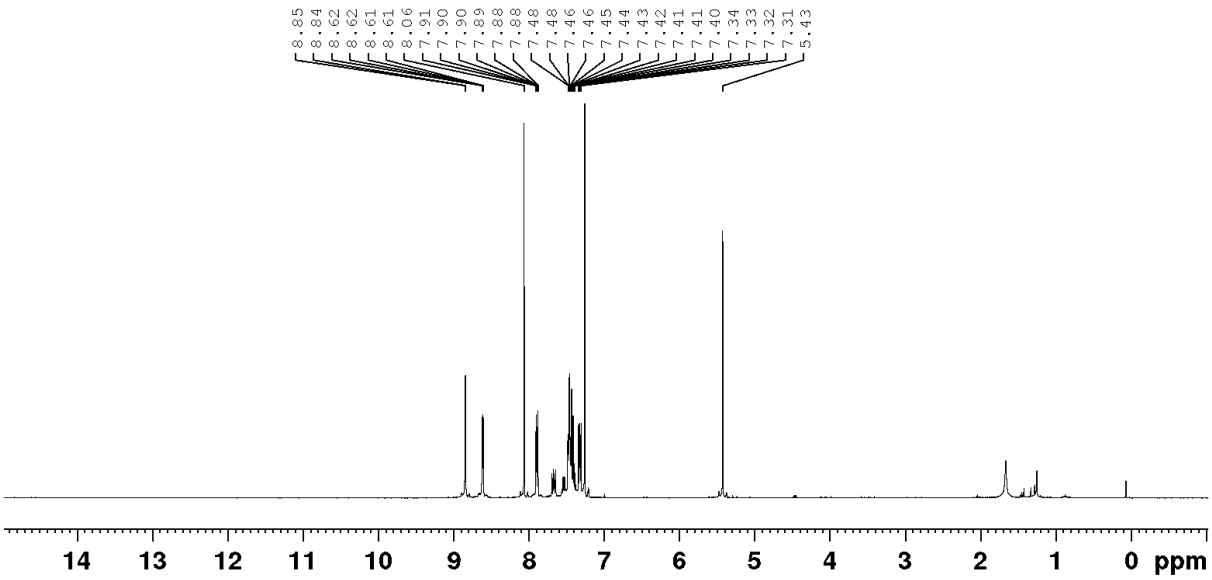

Figure S65 ^{1}H NMR (400 MHz, $CDCl_3$) **L^{CH2COOBn}**

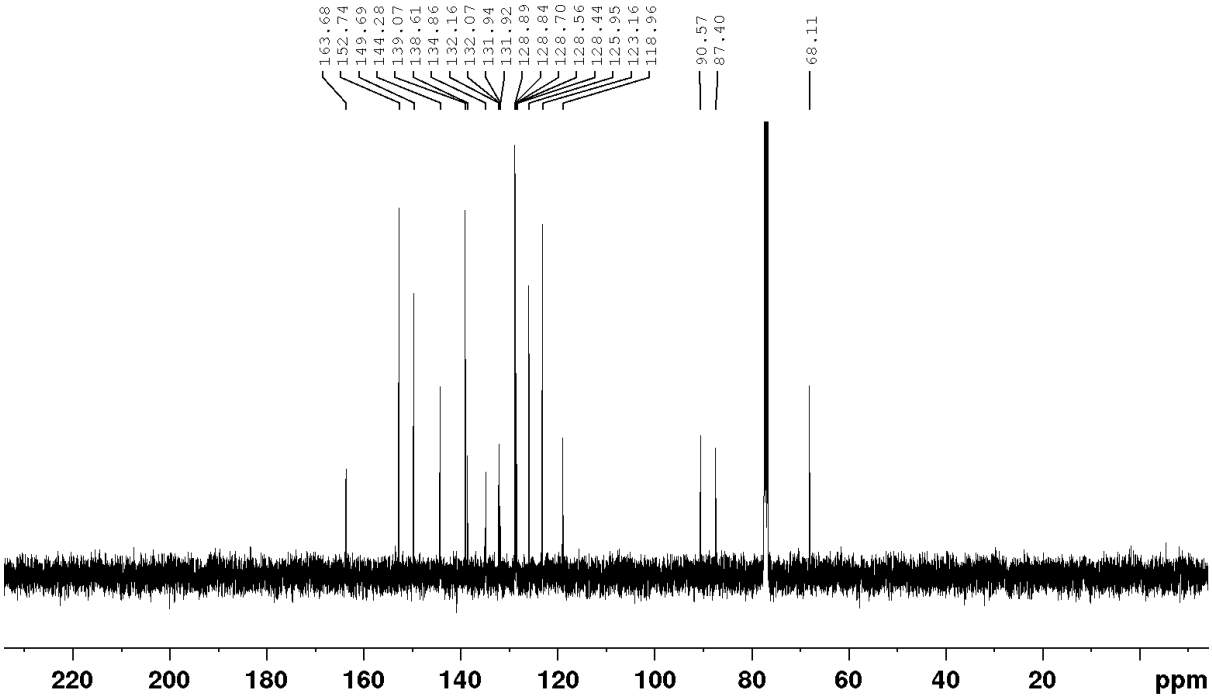

Figure S66 ^{13}C NMR (101MHz, $CDCl_3$) $\mathbf{L^{CH2COOBn}}$

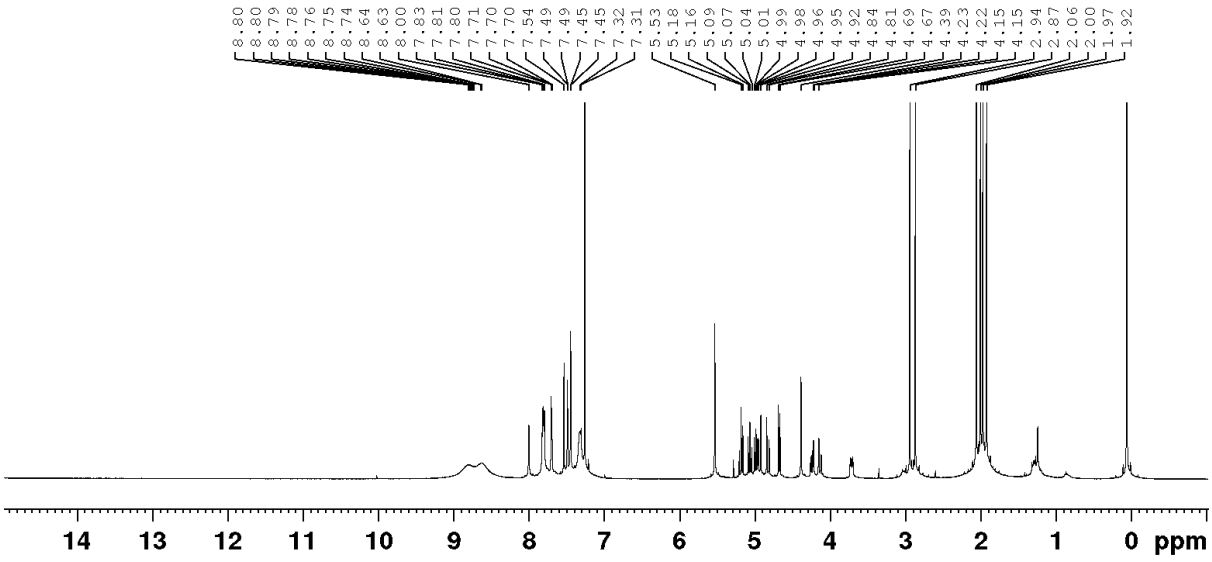

Figure S67: ^{1}H NMR (400 MHz, $CDCl_3$) spectra $\mathbf{L_{aq}1}$

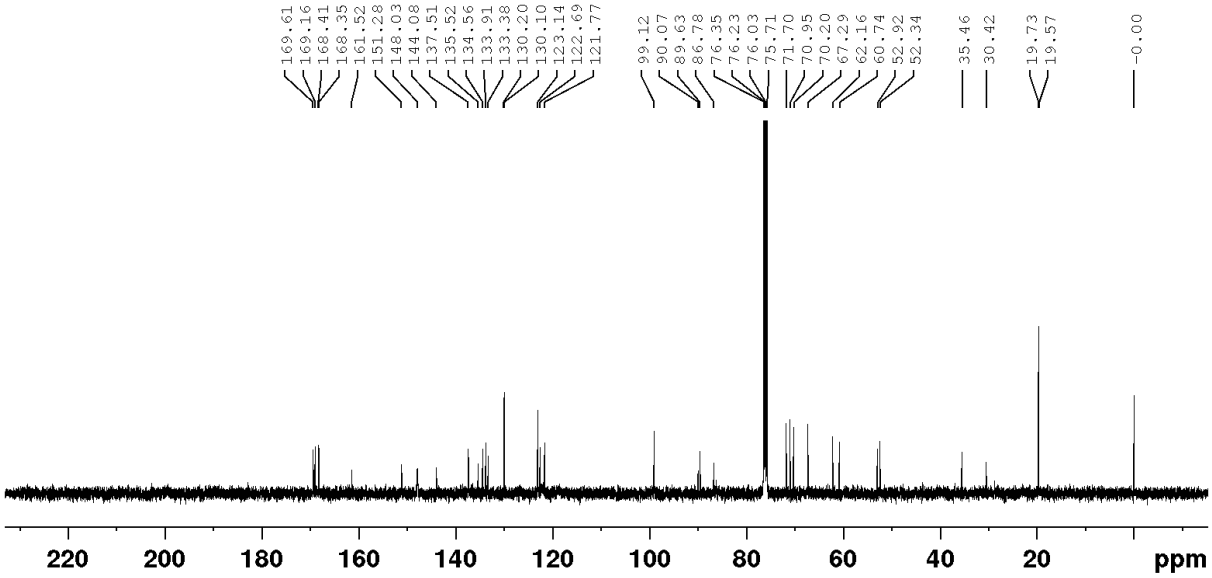

Figure S68: ^{13}C NMR (101 MHz, $CDCl_3$) $\mathbf{L_{aq}1}$

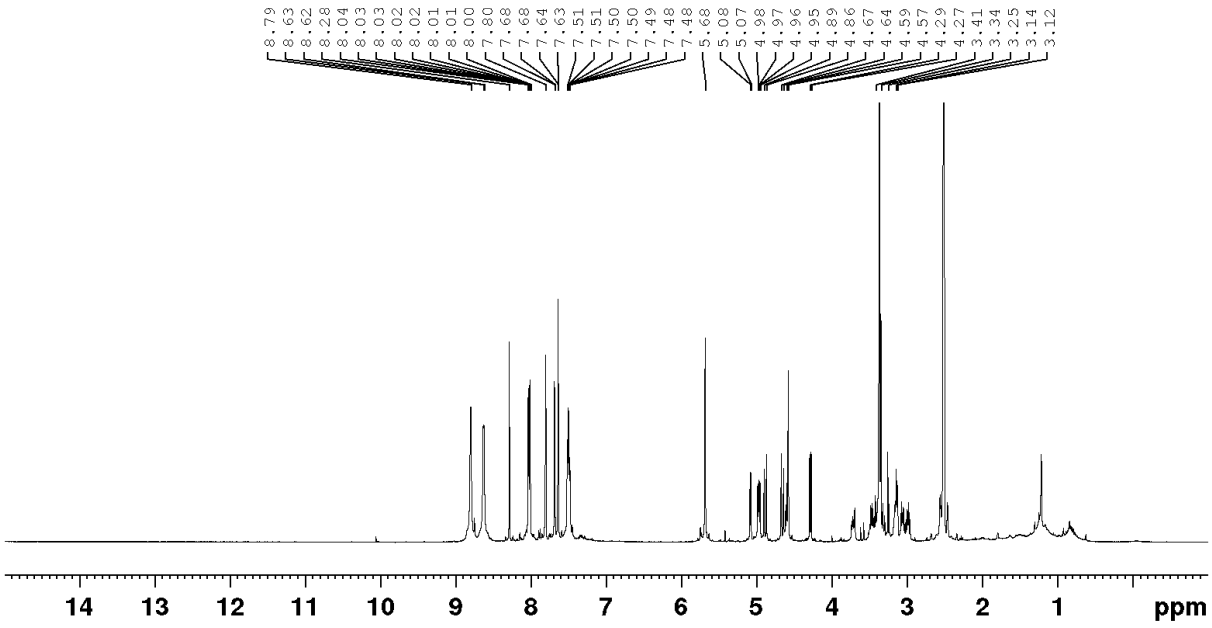

Figure S69 ^{1}H NMR (400 MHz, DMSO-d_6) $\mathbf{L_{aq}2}$

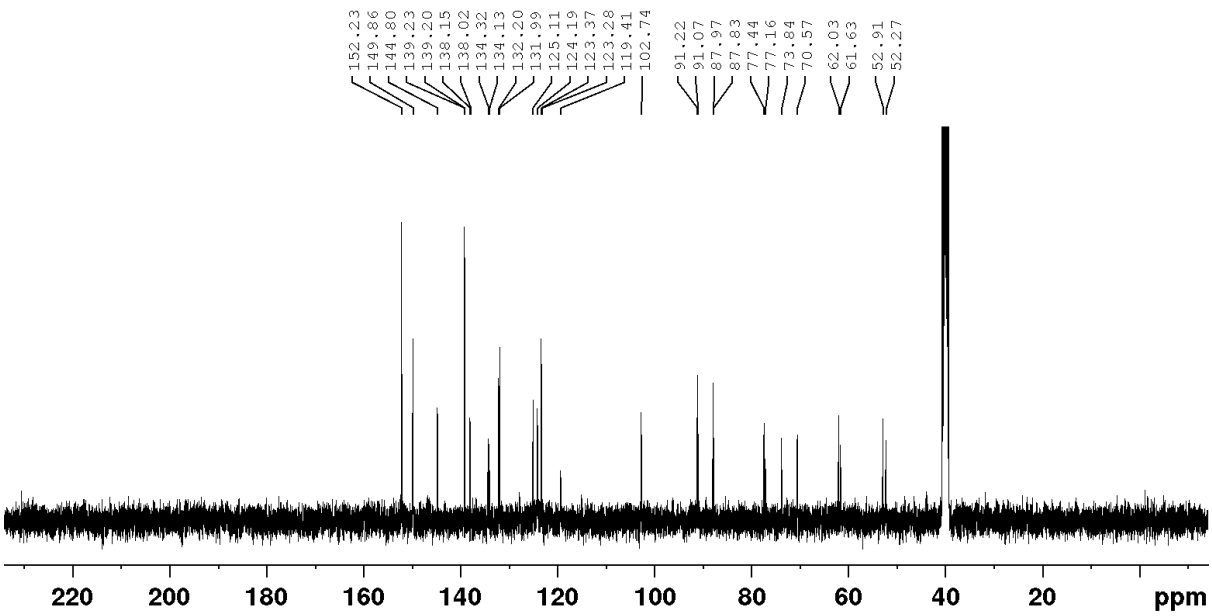

Figure S70 ^{13}C NMR (101 MHz, DMSO-d_6) $\mathbf{L_{aq}2}$

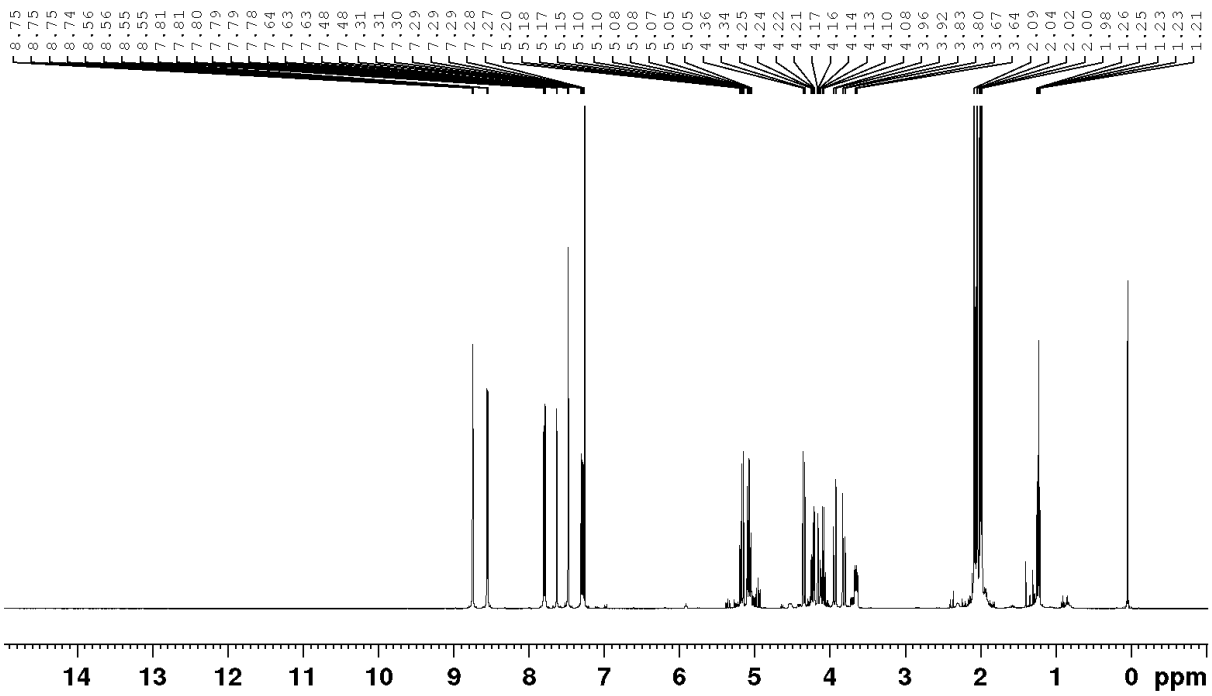

Figure S71: ^{1}H NMR (400 MHz, $CDCl_3$) spectrum of $\mathbf{L_{aq}3}$

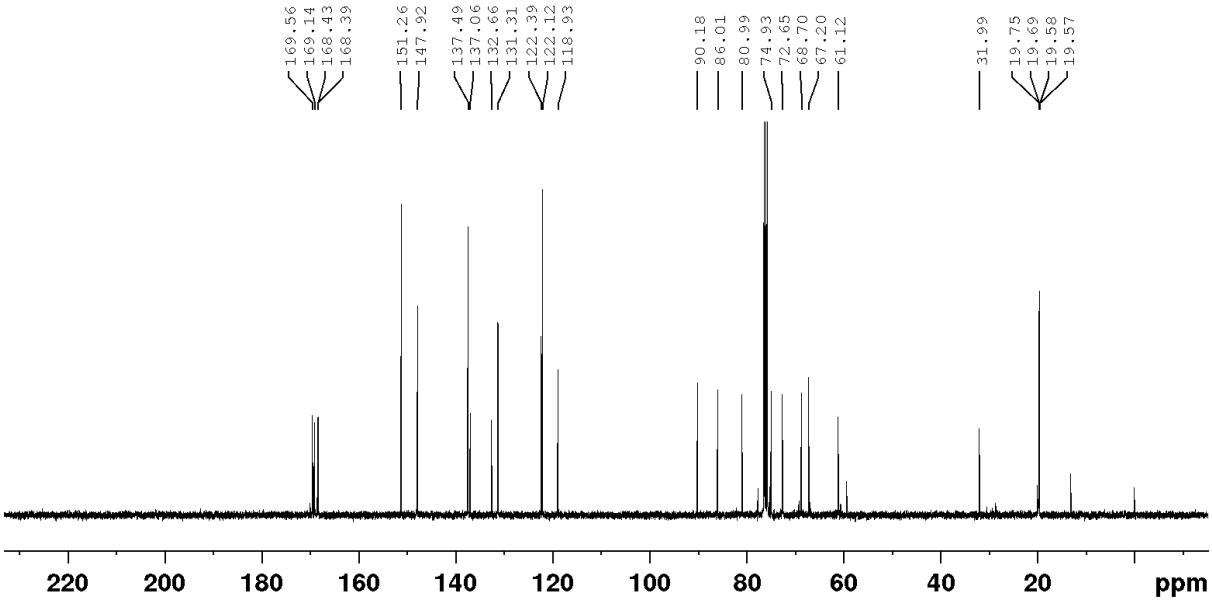

Figure S72: ^{13}C NMR (101 MHz, $CDCl_3$) spectrum of $\mathbf{L_{aq}3}$

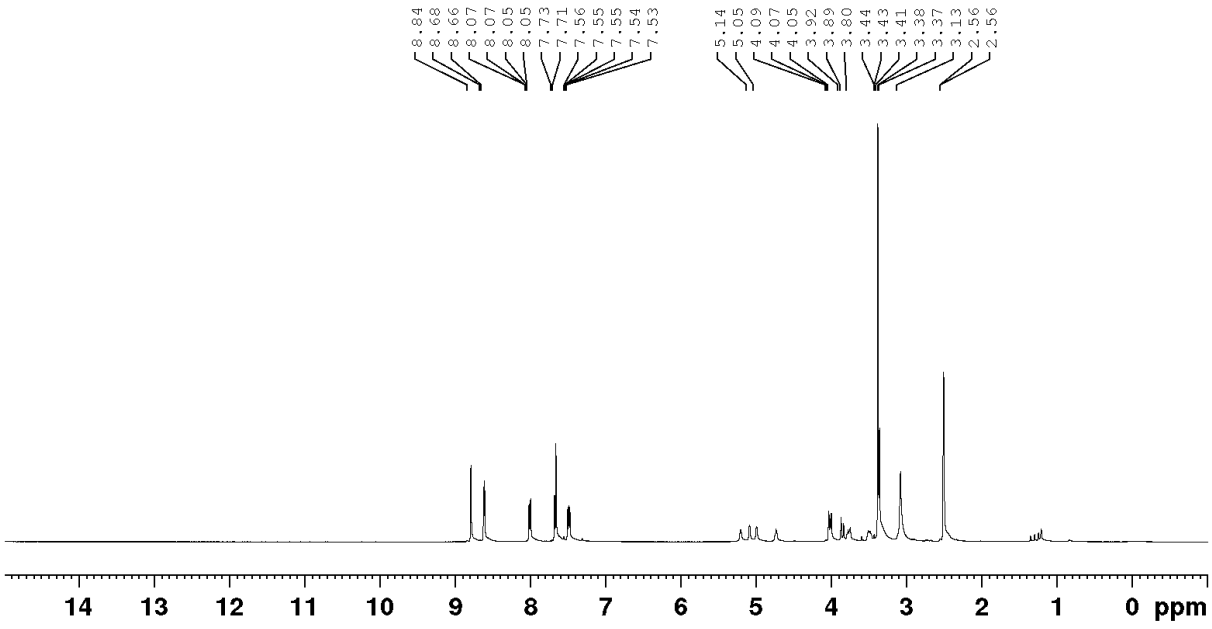

Figure S73: ^{1}H NMR (400 MHz, DMSO-d_6) of ligand $\mathbf{L_{aq}4}$

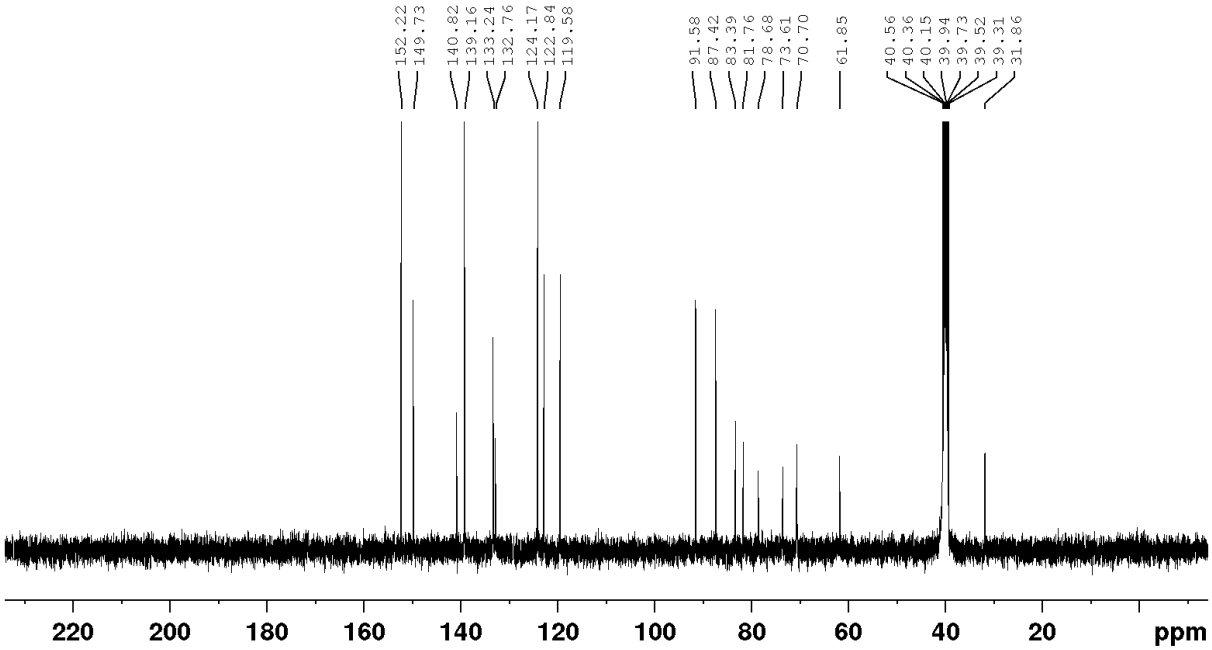

Figure S74: ^{13}C NMR (101 MHz, DMSO-d_6) of ligand $\mathbf{L_{aq}4}$

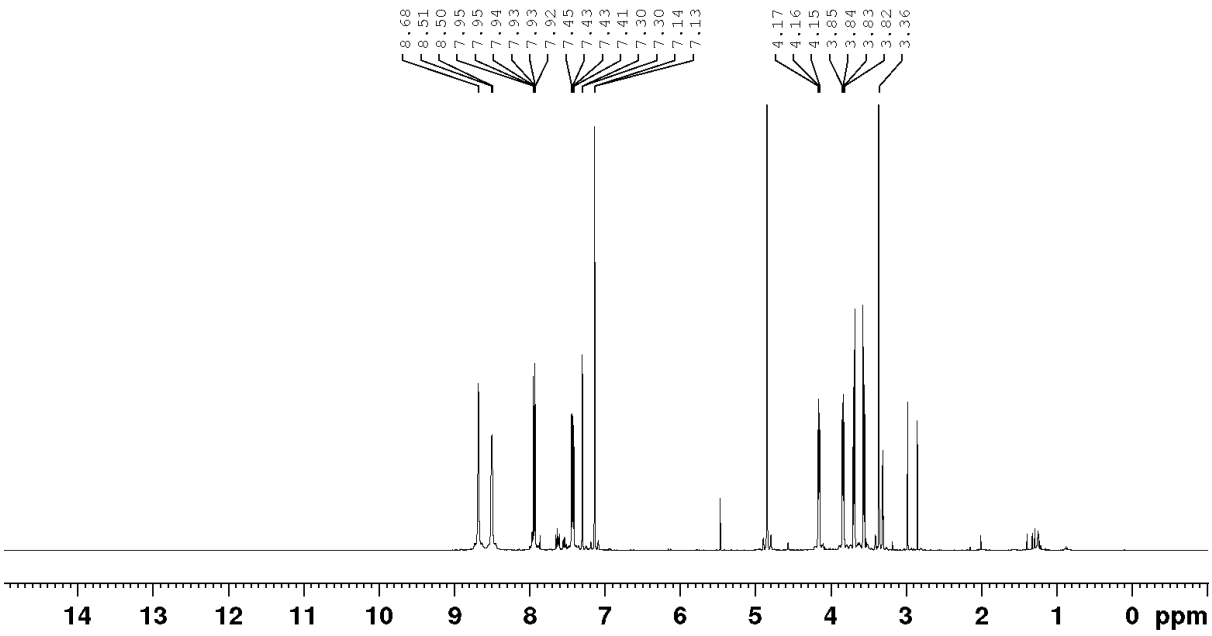

Figure S75: ^{1}H NMR (400 MHz, MeOD-d_4) spectrum $\mathbf{L_{aq}5}$

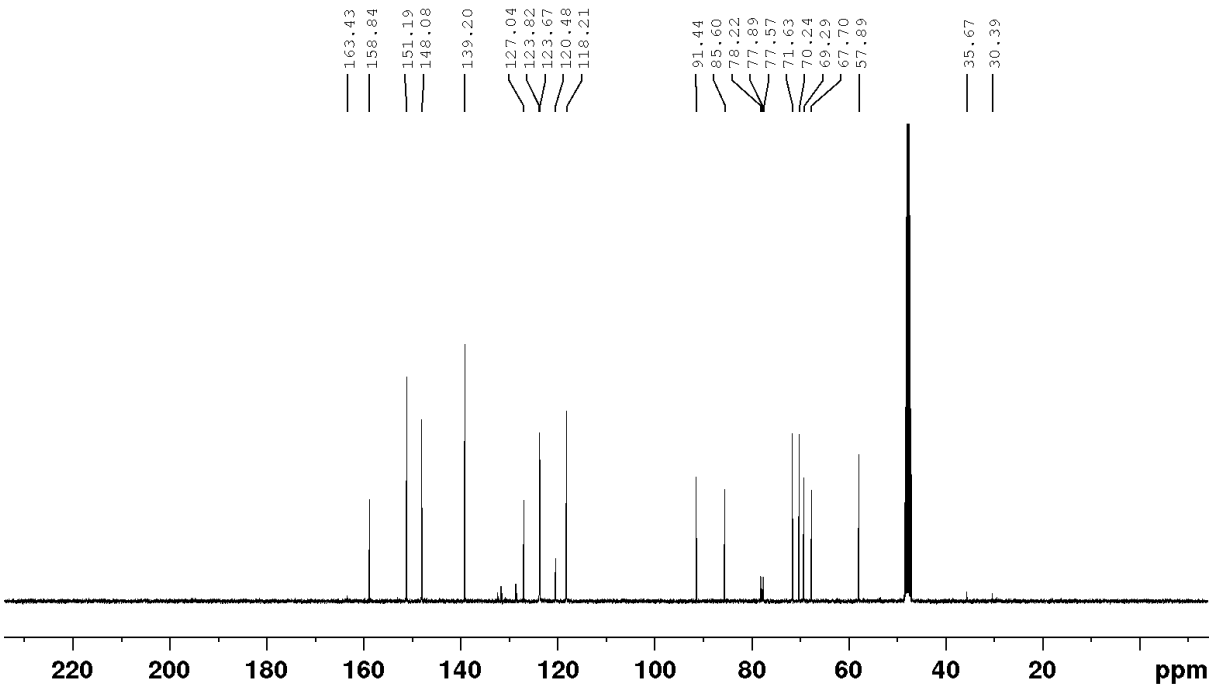

Figure S76: ^{13}C NMR (101MHz, MeOD-d_4) spectrum $\mathbf{L_{aq}5}$

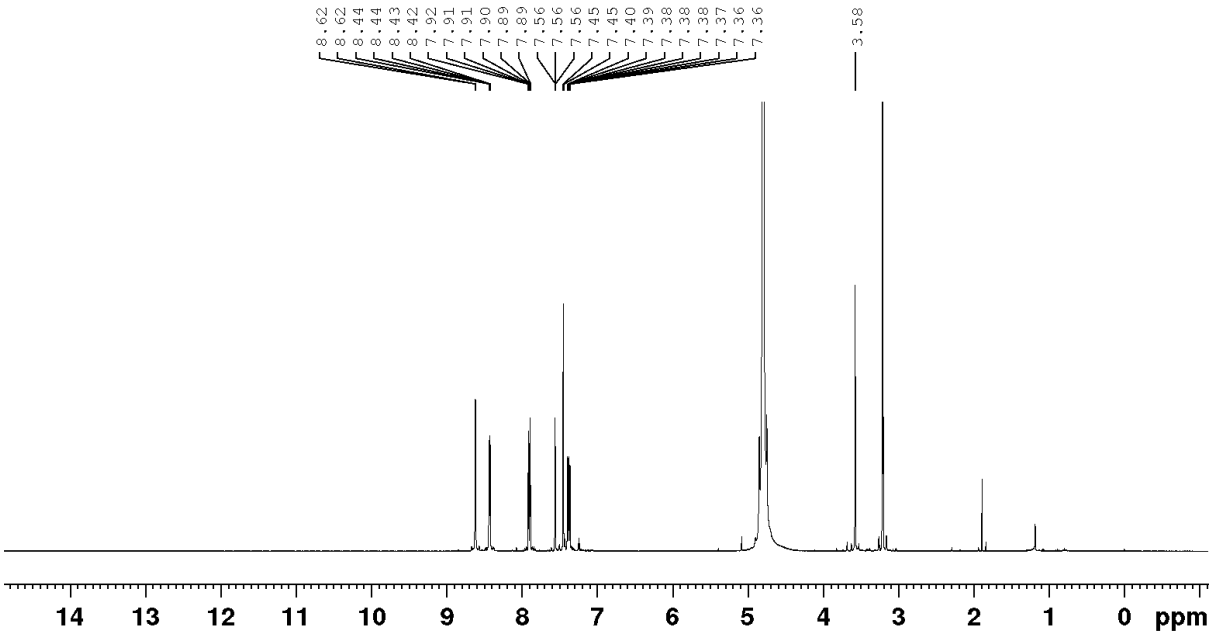

Figure S77: ^{1}H NMR (400 MHz, MeOD-d_4) spectrum $\mathbf{L_{aq}6}$

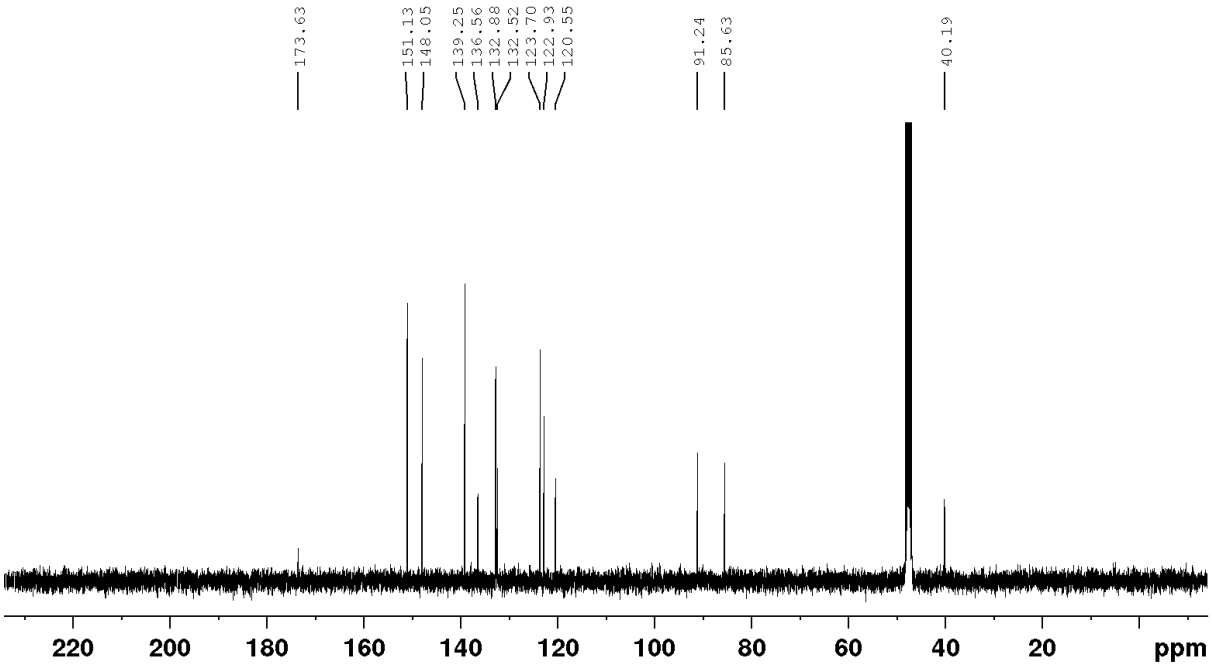

Figure S78: ^{13}C NMR (101 MHz, MeOD-d_4) spectrum $\mathbf{L_{aq}6}$

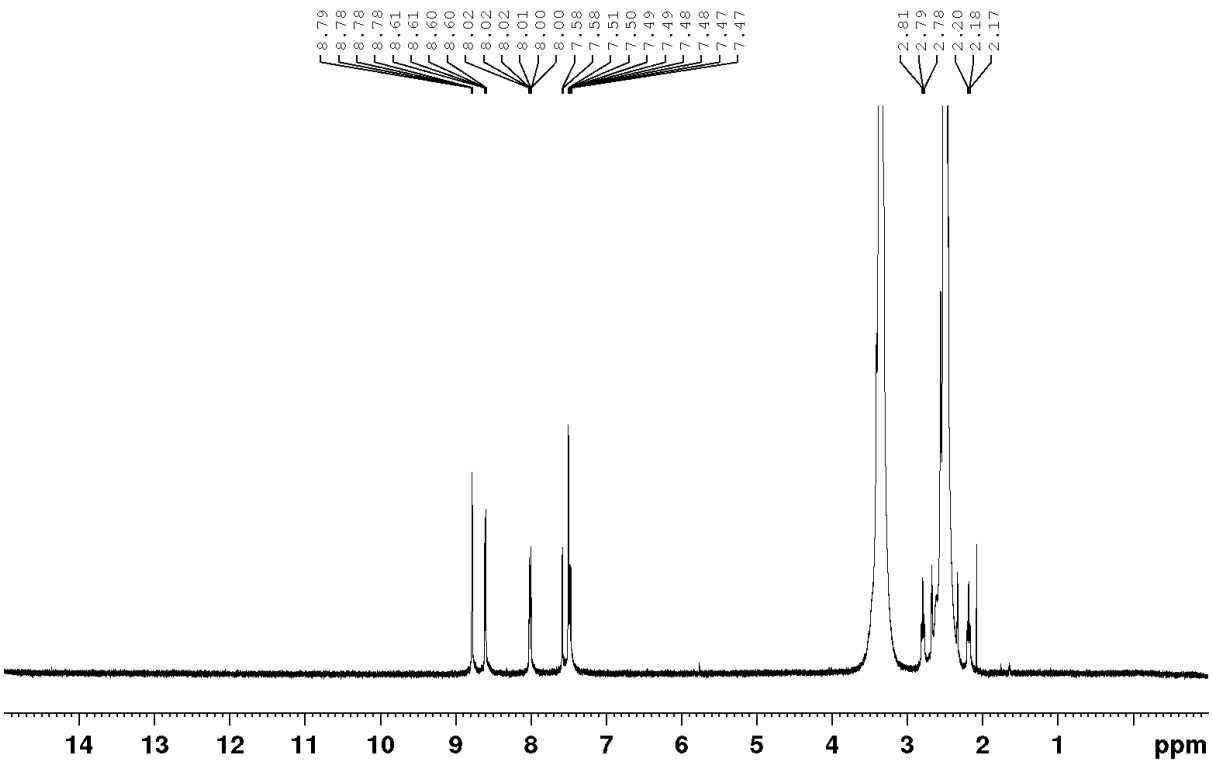

Figure S79: ^{1}H NMR (400 MHz, DMSO-d_6) of ligand $\mathbf{L_{aq}7}$

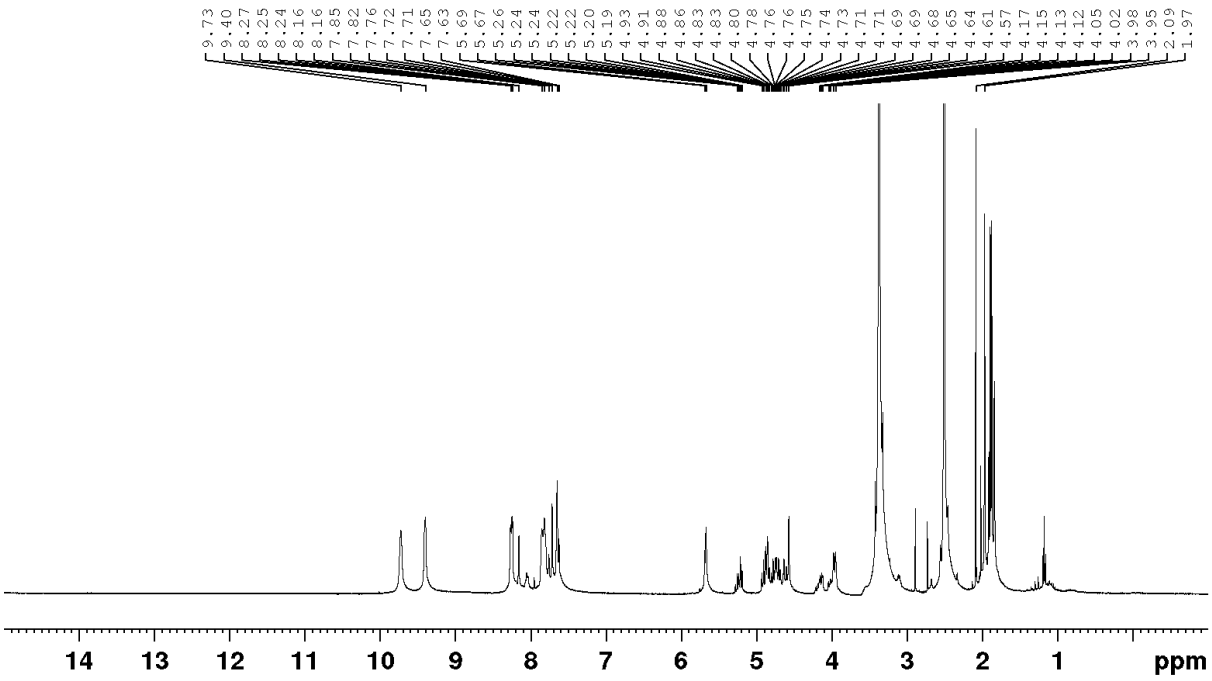

Figure S80: ^{1}H NMR (400 MHz, DMSO-d_6) spectra $\mathbf{C_{aq}1}$

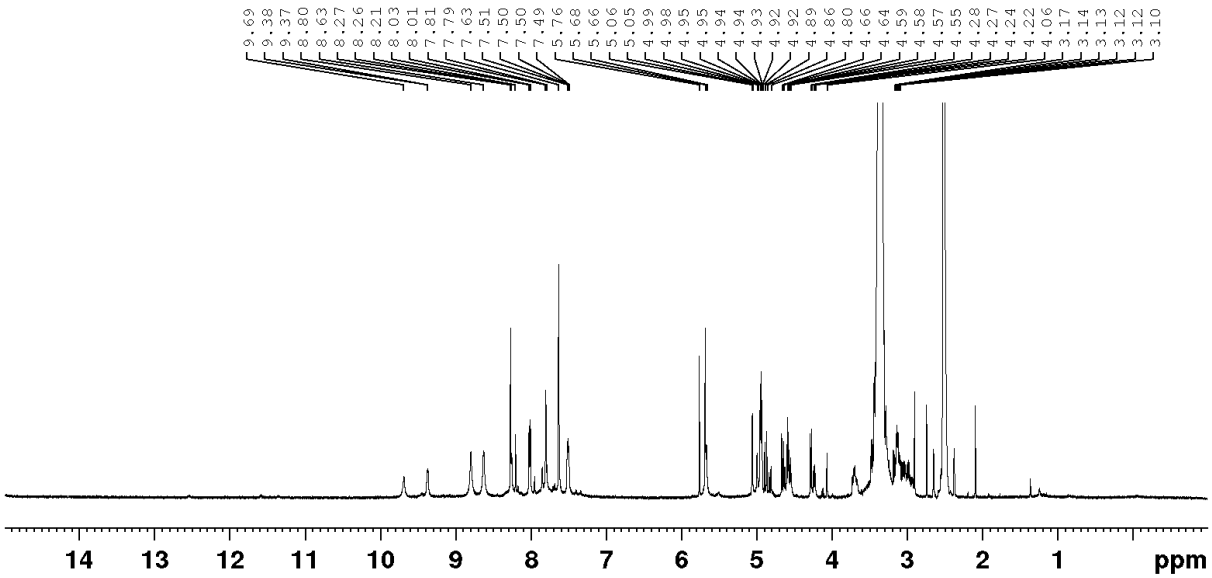

Figure S81: ^{1}H NMR (400 MHz, DMSO-d_6) spectra $\mathbf{C_{aq}2}$

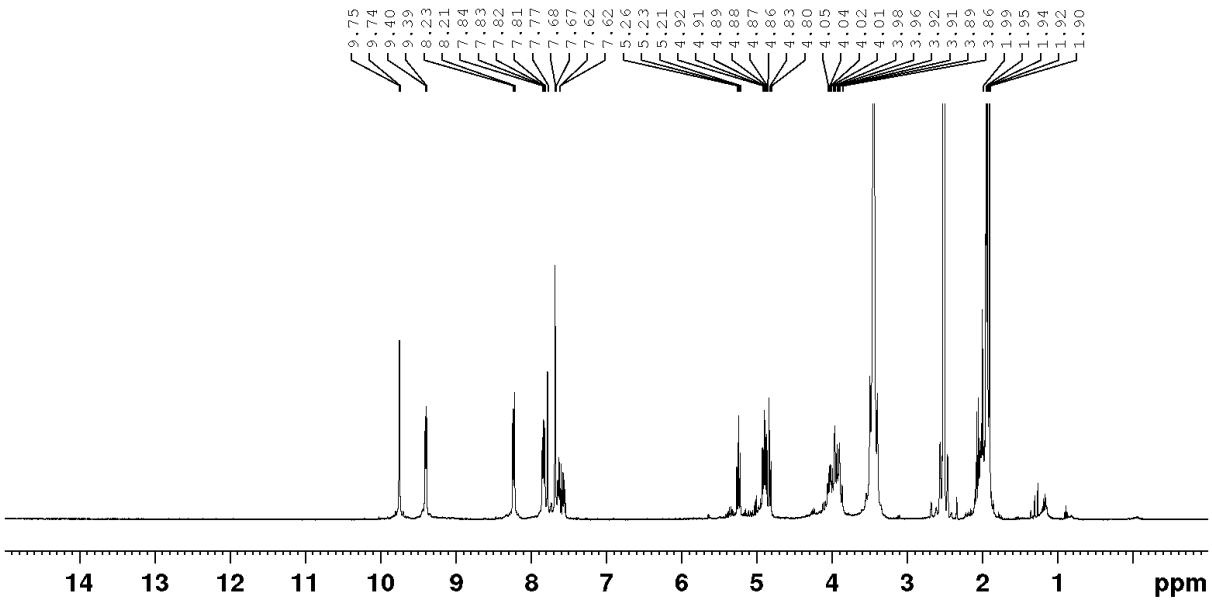

Figure S82: ^{1}H NMR (400 MHz, DMSO-d_6) spectra $\mathbf{C_{aq}3}$

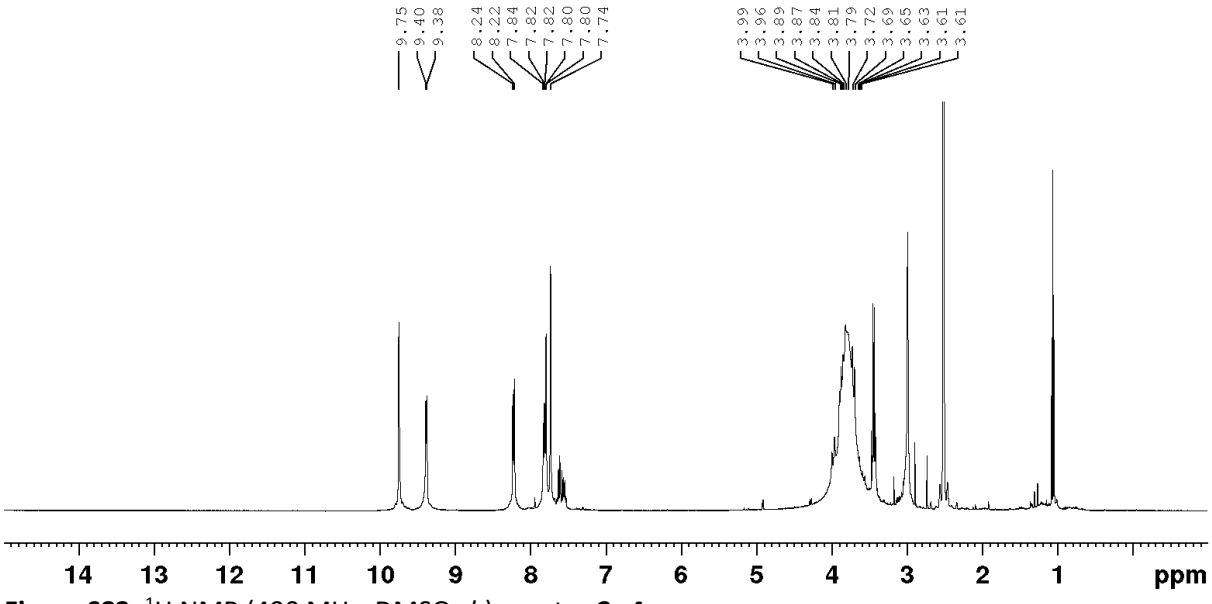

Figure S83: ^{1}H NMR (400 MHz, DMSO-d_6) spectra $\mathbf{C_{aq}4}$

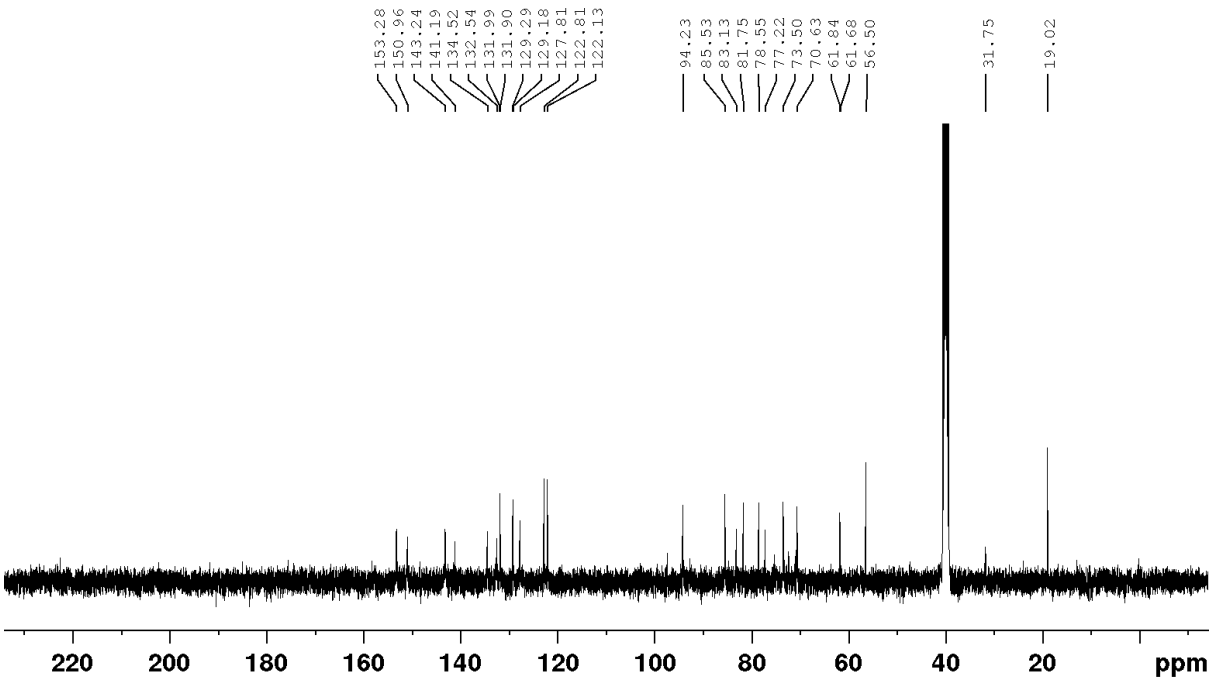

Figure S84: ^{13}C NMR (101 MHz, DMSO-d_6) spectra $\mathbf{C_{aq}4}$

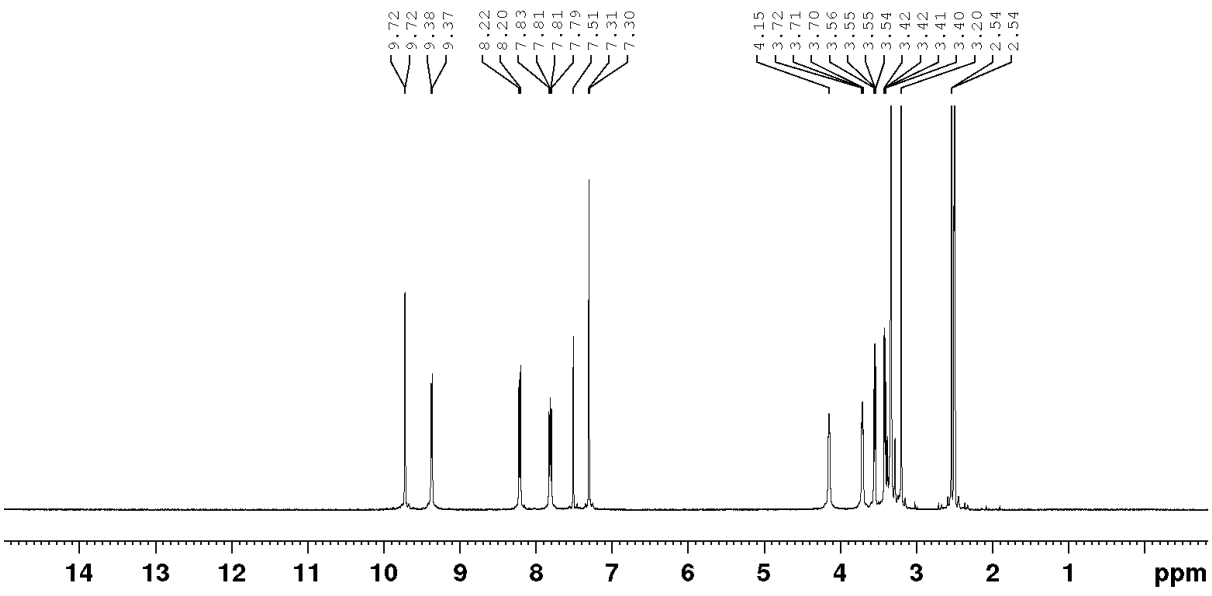

Figure S85: ^{1}H NMR (400 MHz, DMSO-d_6) spectra $\mathbf{C_{aq}5}$

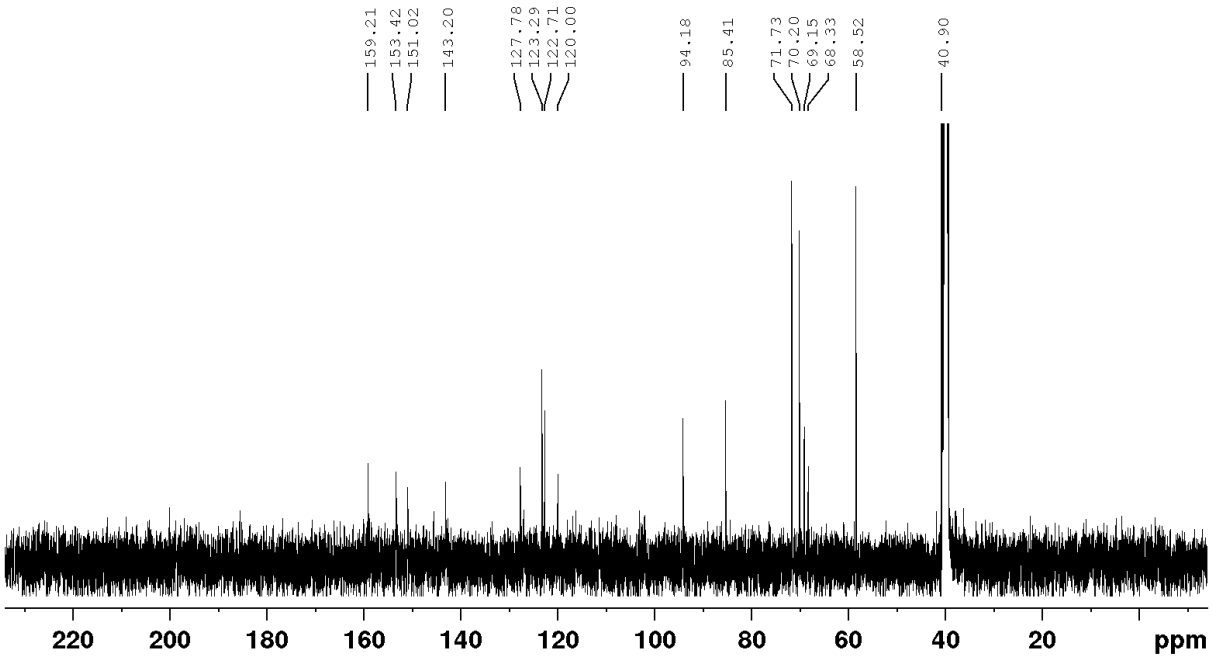

Figure S86: ^{13}C NMR (101 MHz, DMSO-d_6) spectra $\mathbf{C_{aq}5}$

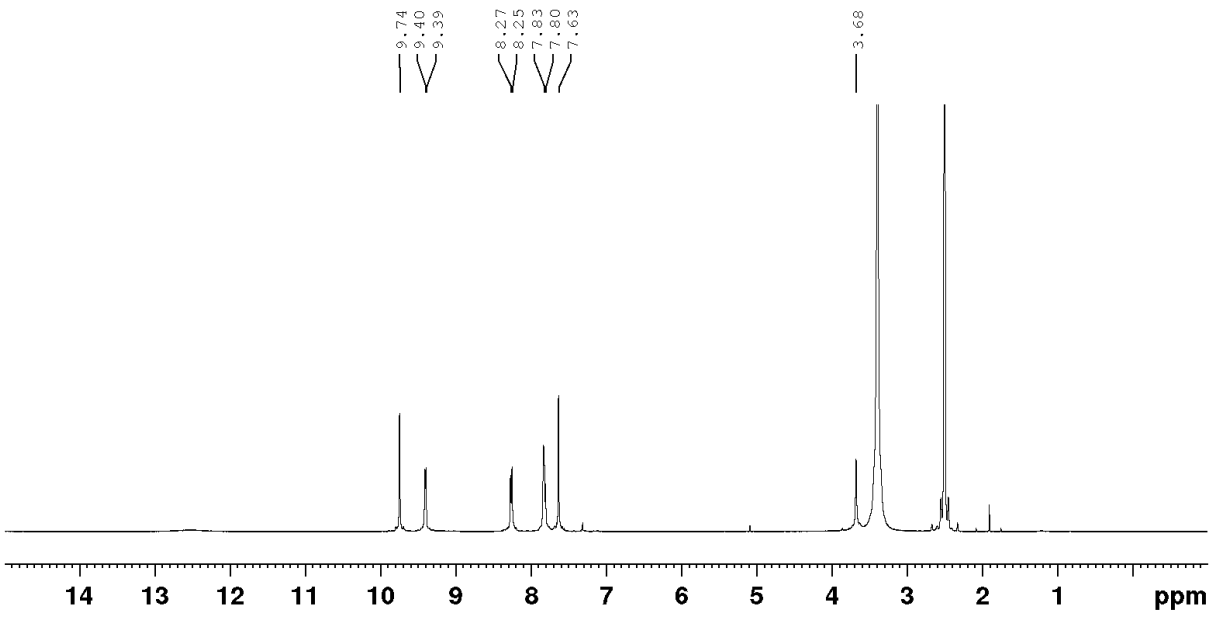

Figure S87: ^{1}H NMR (400 MHz, DMSO-d_6) spectra $\mathbf{C_{aq}6}$

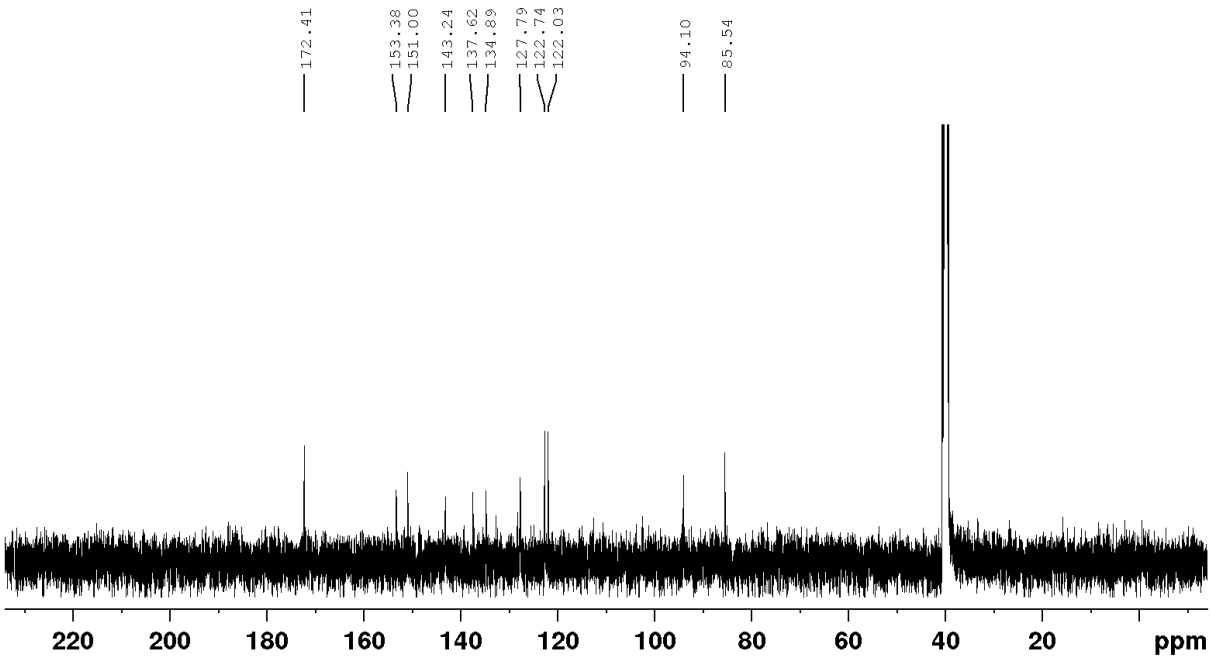

Figure S88: ^{13}C NMR (101 MHz, DMSO-d_6) spectra $\mathbf{C_{aq}6}$

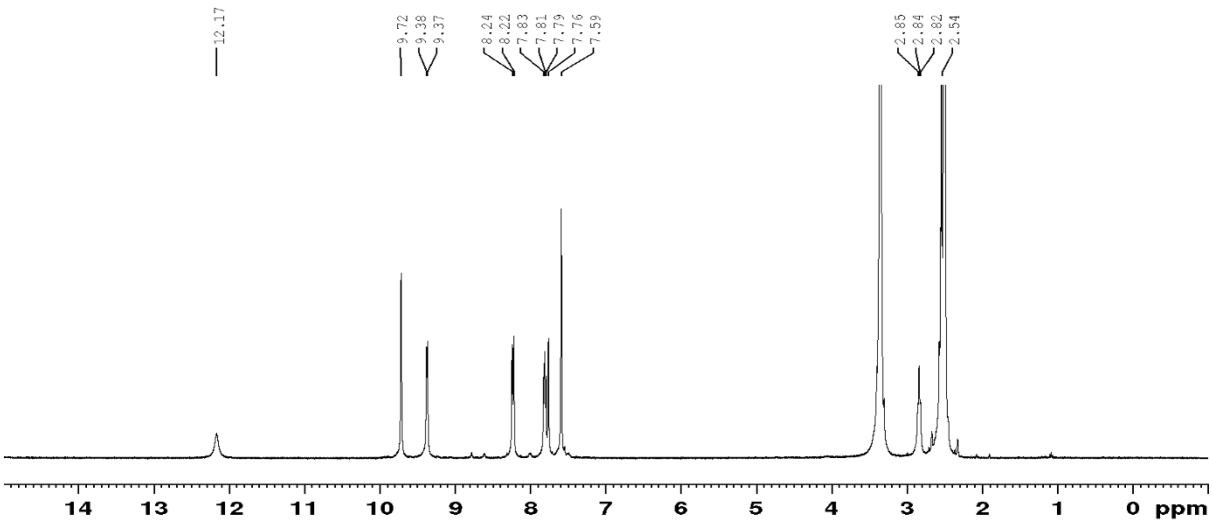

Figure S89: ^{1}H NMR (400 MHz, DMSO-d_6) spectra $\mathbf{C_{aq}7}$

Mass spectra isotopic patterns

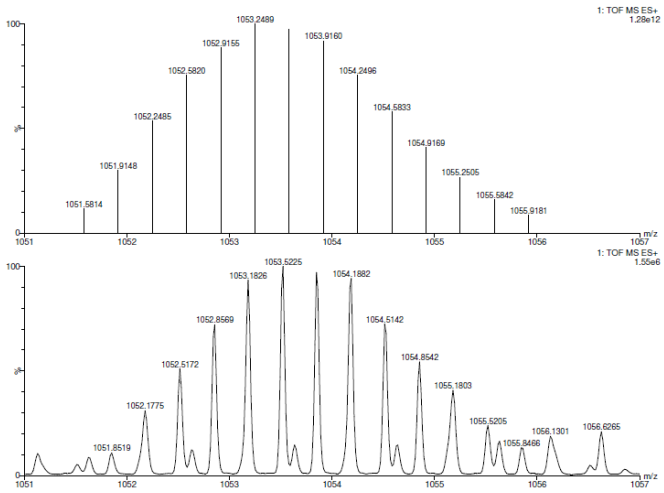

Figure S90. Comparison between the theoretical isotopic pattern (top) and the experimental isotopic pattern (bottom) of $[\mathbf{C_{aq}1}\text{-}3NO_3\text{-}4H]^{3+}$.

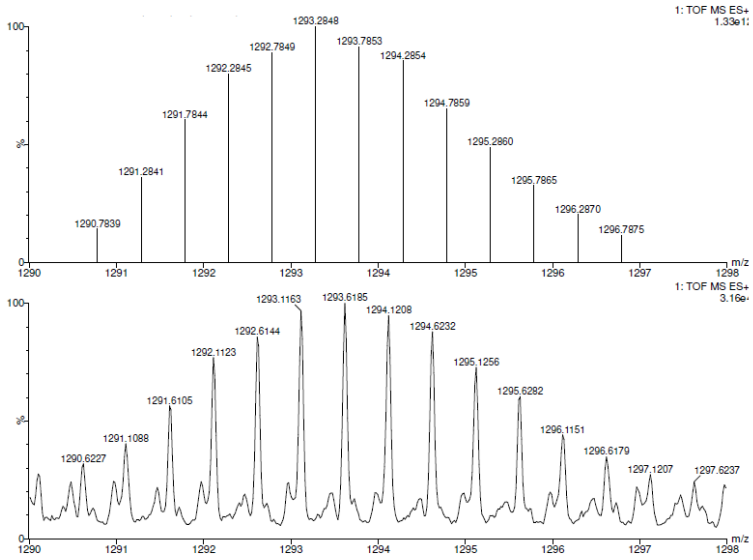

Figure S91: Comparison between the theoretical isotopic pattern (top) and the experimental isotopic pattern (bottom) of $[\mathbf{C_{aq}2}\text{-}3NO_3]^{2+}$.

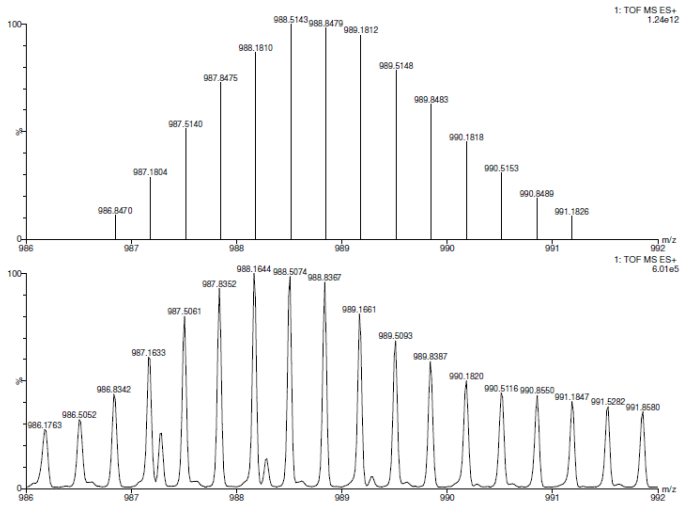

Figure S92. Comparison between the theoretical isotopic pattern (top) and the experimental isotopic pattern (bottom) of $[\mathbf{C_{aq}3}\text{-}2NO_3]^{3+}$

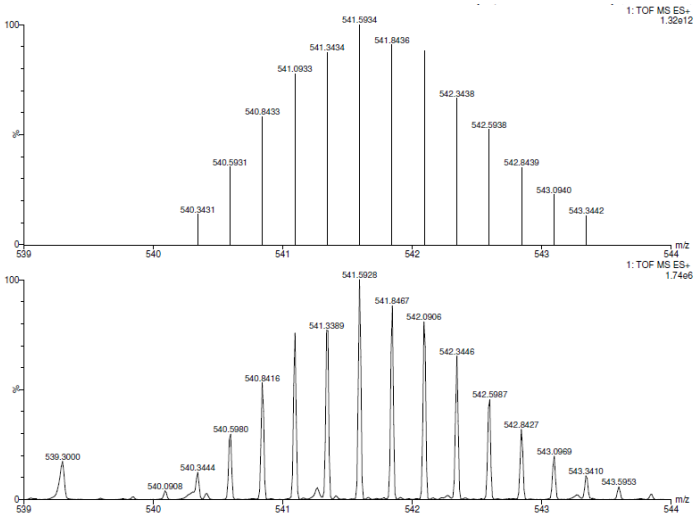

Figure S93 Comparison between the theoretical isotopic pattern (top) and the experimental isotopic pattern (bottom) of $[\mathbf{C_{aq}4}\text{-}3NO_3\text{-}4H]^{4+}$.

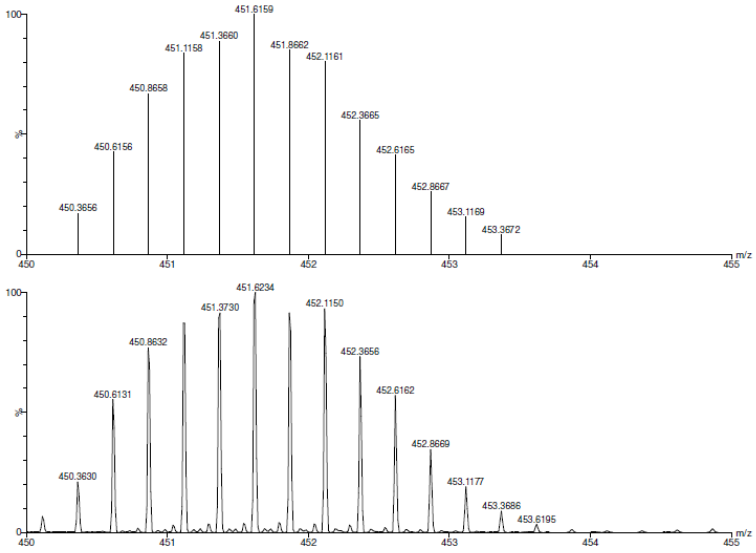

Figure S94. Comparison between the theoretical isotopic pattern (top) and the experimental isotopic pattern (bottom) of $[\mathbf{C_{aq}5}\text{-}4NO_3\text{-}4H]^{4+}$.

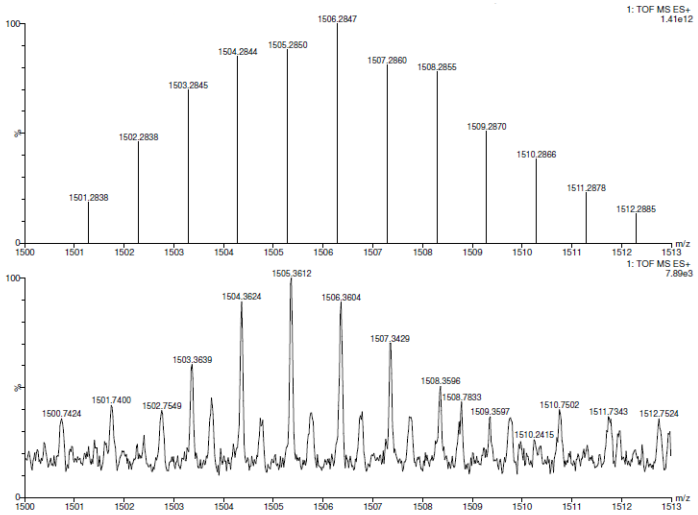

Figure S95. Comparison between the theoretical isotopic pattern (top) and the experimental pattern (bottom) of $[\mathbf{C_{aq}6}\text{-}4OH]^{2+}$.

Chapter 9: Supplementary Information

Column chromatography was carried out using a Biotage Isolera™ Prime automated purification system, with ZIP KP 10 g silica gel cartridges, using the following solvent gradients. Solvent A: Hexane; solvent B: ethylacetate; solvent C: Methanol. Gradient A: A/B (0% - 100%, 30 column volumes (CV)), B/C (0 – 10%, 10 CV), B/C (10%, 10 CV). Gradient B: A/B (20% - 30%, 6 CV), A/B (30% - 75%, 15 CV), A/B (75%, 5 CV), A/B (75% - 100%, 5 CV), B/C (0% - 10%, 10 CV).

Synthesis of ligands

*Synthesis of benzyl 3,5-bis(pyridin-3-ylethynyl)benzoate (**L^{E1}**) has been described in the supplementary of chapter 5*

3,5-bis(pyridin-3-ylethynyl)aniline (**L^{E2}**): 3,5-dibromoaniline (1.00 g, 4 mmol, 1.0 eq.), 3-ethynylpyridine (1.24 g, 12 mmol, 3 eq.), CuI (72 mg, 0.4 mmol, 0.1 eq.), $Pd(PPh_3)_2Cl_2$ (264 mg, 0.4 mmol, 0.1 eq.) were added to a flame dried flask. Triethylamine (30 mL) was added and the suspension was stirred under nitrogen at 90°C for 72 h. Ethylacetate (100 mL) was added and the reaction mixture was filtered over Celite. The filtrate was concentrated *in vacuo*. The residue was dissolved in DCM and loaded onto silica gel before purification *via* chromatography (gradient A) to give the product as a yellow solid (990 mg, 3.36 mmol, 84 % yield).

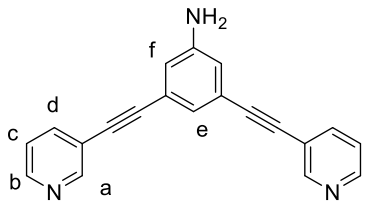

^{1}H NMR (400 MHz, $CDCl_3$): δ [ppm] = 8.75 (d, J = 1.6 Hz, 2H, H_a), 8.55 (dd, J = 4.9, 1.6 Hz, 2H, H_b), 7.79 (dt, J = 8.0, 1.8, 2H, H_d), 7.29 (ddd, J = 7.9, 4.8, 0.7 Hz, 2H, H_c), 7.15 (t, J = 1.3 Hz, 1H, H_e), 6.86 (d, J = 1.4 Hz, H_f), 3.76 (br, 2H, NH_2)

^{13}C NMR (101 MHz, $CDCl_3$): δ [ppm] = 152.3, 148.7, 146.5, 138.5, 125.3, 123.7, 123.1, 120.3, 118.2, 91.9, 86.0

ESI-MS (MeCN) calc. for $C_{20}H_{14}N_3[M+H]^+$: *m/z* = 296.1187; found 296.1258; ppm = 23.97

1,3-bis(pyridin-3-ylethynyl)benzene (L^{E3}): 1,3-dibromobenzene (1.00 g, 4.24 mmol, 1.0 eq.), 3-ethynylpyridine (1.31 g, 12.7 mmol, 3 eq.), CuI (72 mg, 0.4 mmol, 0.1 eq.), $Pd(PPh_3)_2Cl_2$ (264 mg, 0.4 mmol, 0.1 eq.) were added to a flame dried flask. Triethylamine (40 mL) was added and the suspension was stirred under nitrogen at 90°C for 24 h. Ethylacetate (100 mL) was added and the reaction mixture was filtered over Celite. The filtrate was concentrated *in vacuo*. The residue was dissolved in DCM and loaded onto silica gel before purification *via*

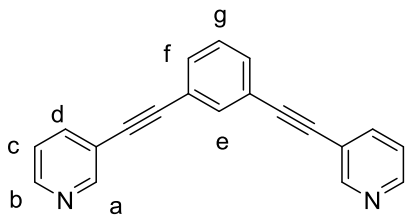

chromatography (gradient A) to give the product as a brown solid (712 mg, 2.54 mmol, 60 % yield).

^{1}H NMR (400 MHz, DMSO-d_6): δ [ppm] = 8.79 (d, J = 2.1 Hz, 2H, H_a), 8.61 (dd, J = 4.9, 1.6 Hz, 2H, H_b), 8.00 (dt, J = 8.0 Hz, 2H, H_d), 7.82 (t, J = 1.2 Hz, 1H, H_e), 7.66 (dd, J = 7.6, 1.6 Hz, 2H, H_f), 7.53 (t, J = 7.9, 2H, H_g), 7.48 (ddd, J = 7.8, 4.8, 0.76 Hz, 2H, H_c)

^{13}C NMR (101 MHz, DMSO-d_6): δ [ppm] = 152.2, 149.7, 139.2, 134.7, 132.5, 130.0, 124.2, 122.9, 119.6, 91.6, 87.5

ESI-MS (MeCN) calc. for $C_{20}H_{13}N_2[M+H]^+$: *m/z* = 281.1078; found 281.1172; ppm = 33.43

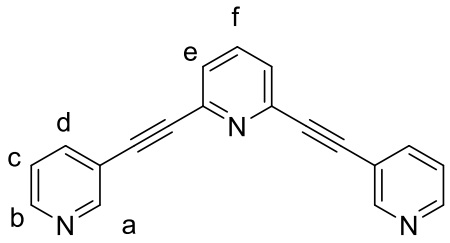

2,6-dibromopyridine (1.00 g, 4.22 mmol, 1.0 eq.), 3-ethynylpyridine (1.30 g, 12.7 mmol, 3 eq.), CuI (72 mg, 0.4 mmol, 0.1 eq.), $Pd(PPh_3)_2Cl_2$ (264 mg, 0.4 mmol, 0.1 eq.) were added to a flame dried flask. Triethylamine (40 mL) was added and the suspension was stirred under nitrogen at 90°C for 24 h. Ethylacetate (100 mL) was added and the reaction mixture was filtered over Celite. The filtrate was concentrated *in vacuo*. The residue was dissolved in DCM and loaded onto silica gel before purification via chromatography (gradient A) to give the product as a brown solid (865 mg, 3.08 mmol, 73 % yield).

^{1}H NMR (400 MHz, DMSO-d_6): δ [ppm] = 8.85 (s, 2H, H_a), 8.65 (d, J = 4.9 Hz, 2H, H_b), 8.09 (dt, J = 7.9, 1.7 Hz, 2H, H_d), 7.99 (t, J = 7.9 Hz, H_f), 7.75 (d, J = 8.0 Hz, 2H, H_e), 7.53 (ddd, J = 7.7, 4.8, 0.7 Hz, 2H, H_c)

^{13}C NMR (101 MHz, DMSO-d_6): δ [ppm] = 152.5, 150.3, 142.8, 139.6, 138.4, 127.9, 124.3, 118.8, 91.4, 86.3

ESI-MS (MeCN) calc. for $C_{19}H_{12}N_3[M+H]^+$: *m/z* = 282.1031; found 282.1104; ppm = 25.88

General procedure for cage synthesis

Synthesis of the cages was achieved by self-assembly. A solution of the palladium(II) nitrate dihydrate (2 eq.) or tetrakisacetonitrilepalladium(II) tetrafluoroborate and ligand (4 eq.) in DMSO was stirred at room temperature for 1 h. After precipitation by addition of acetone and diethylether, the solid was filtered and washed with cold acetone and diethyl ether to yield the cage compound as an off-white solid.

$\mathbf{C^{E1-4}}$ metallacage synthesis

$\mathbf{C^{E1}}$: benzyl 3,5-bis(pyridin-3-ylethynyl)benzoate (**$\mathbf{L^{E1}}$**) (40 mg, 96 µmol, 4 eq.) and $[Pd(MeCN)_4.2BF_4]$ (21 mg, 48 µmol, 2 eq.) were added to DMSO (3 mL) to form cage **$\mathbf{C^{E1}}$** (42

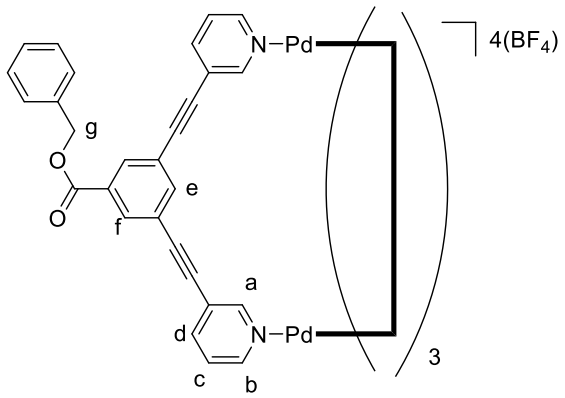

mg, 19 µM, 79 %).

^{1}H NMR (400 MHz, DMF-d_7): δ [ppm] = 9.88 (d, J = 1.7 Hz, 2H, H_a), 9.66 (dd, J = 5.9, 1.1 Hz, 2H, H_b), 8.44, (dt, J = 8.1, 1.4 Hz, 2H, H_d), 8.24 (d, J = 1.6 Hz, 2H, H_f), 7.95 (dd, J = 7.8, 5.9 Hz, 2H, H_c), 7.89 (t, J = 1.7 Hz, 1H, H_e), 7.55 – 7.35 (m, 5H, H_{phenyl}), 5.44 (s, 2H, H_g)

^{13}C NMR (101 MHz, DMF-d_7): δ [ppm] = 164.3, 153.8, 151.3, 143.6, 136.2, 133.4, 132.1, 128.8, 128.7, 127.8, 123.1, 123.0, 92.6, 86.2, 67.5

^{11}B NMR (128 MHz, DMF-d_7): δ [ppm] = -0.60

^{19}F NMR (376 MHz, DMF-d_7): δ [ppm] = -149.8

ESI-MS (MeCN) calc. for $C_{112}H_{72}N_8O_8Pd_2B_2F_8CH_3CNH_4$ $[M\text{-}2BF_4\text{+MeCN+4H}]^+$: *m/z* = 2088.4246; found 2088.3691

$\mathbf{C^{E2}}$: 3,5-bis(pyridin-3-ylethynyl)aniline (**$\mathbf{L^{E2}}$**) (40 mg, 136 µmol, 4 eq.) and $[Pd(MeCN)_4.2BF_4]$ (30 mg, 68 µmol, 2 eq.) were added to DMSO (5 mL) to form cage **$\mathbf{C^{E2}}$** (56 mg, 32 µM, 94 %)

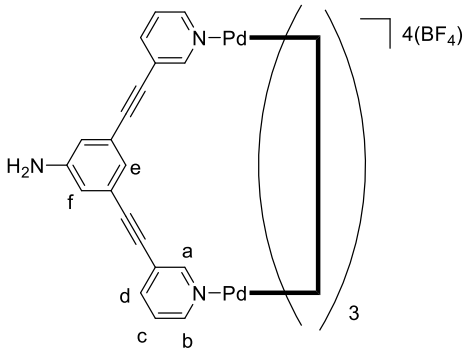

^{1}H NMR (400 MHz, DMF-d_7): δ [ppm] = 9.82 (s, 2H, H_a), 9.62 (dd, J = 5.9, 1.0 Hz, 2H, H_b), 8.31 (dt, J = 8.0, 1.5 Hz, 2H, H_d), 7.90 (dd, J = 7.80, 5.9 Hz, 2H, H_c), 6.98 (d, J = 1.3, 2H, H_f), 6.82 (s, 1H, H_e), 5.82 (br, 2H, NH_2)

^{13}C NMR (101 MHz, DMF-d_7): δ [ppm] = 153.3, 150.6, 150.1, 143.0, 127.6, 123.4, 122.3, 121.6, 118.0, 94.7, 83.6

^{11}B NMR (128 MHz, DMF-d_7): δ [ppm] = -0.81

^{19}F NMR (376 MHz, DMF-d_7): δ [ppm] = -150.3

ESI-MS (MeCN) calc. for $C_{80}H_{52}N_{12}Pd_2B_2F_8$ $[M\text{-}2BF_4]^+$: *m/z* = 1566.2617; found 1566.2549

C^{E3}: 3,5-bis(pyridin-3-ylethynyl)benzene (**L^{E3}**) (40 mg, 143 µmol, 4 eq.) and $[Pd(MeCN)_4.2BF_4]$

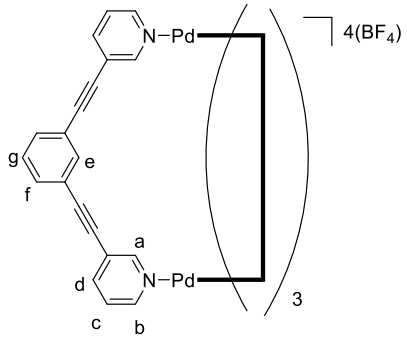

(32 mg, 71 µmol, 2 eq.) were added to DMSO (5 mL) to form cage **C^{E3}** (54 mg, 31 µM, 90 %)

^{1}H NMR (400 MHz, DMF-d_7): δ [ppm] = 9.85 (s, 2H, H_a), 9.64 (d, J = 5.7 Hz, 2H, H_b), 8.37 (d, J = 7.9 Hz, 2H, H_d), 7.94 (dd, J = 7.9, 5.8 Hz, 2H, H_c), 7.75 (d, J = 7.6 Hz, 2H, H_f), 7.69 (s, 1H, H_e), 7.63 (t, J = 7.6, 1H, H_g)

^{13}C NMR (101 MHz, DMF-d_7): δ [ppm] = 153.4, 150.9, 143.2, 133.9, 133.2, 130.1, 127.6, 123.1, 122.1, 93.6, 85.1

^{11}B NMR (128 MHz, DMF-d_7): δ [ppm] = -0.76

^{19}F NMR (376 MHz, DMF-d_7): δ [ppm] = -150.1

ESI-MS (MeCN) calc. for $C_{80}H_{48}N_8Pd_2B_2F_8CH_3CNH_4$ $[M\text{-}2BF_4\text{+MeCN+4H}]^+$: *m/z* = 1552.2764; found 1552.2233

C^{E4}: 1,6-bis(pyridin-3-ylethynyl)pyridine (**L^{E4}**) (40 mg, 143 µmol, 4 eq.) and $[Pd(MeCN)_4.2BF_4]$ (32 mg, 71 µmol, 2 eq.) were added to DMSO (5 mL) to form cage **C^{E3}** (46 mg, 31 µM, 77 %)

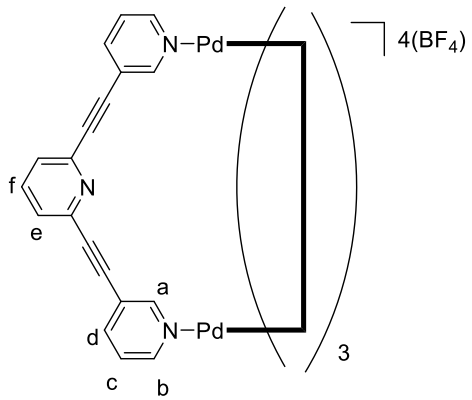

^{1}H NMR (400 MHz, DMF-d_7): δ [ppm] = 9.87 (d, J = 1.8, 2H, H_a), 9.67 (dd, J = 5.9, 1.2 Hz, 2H, H_b), 8.44 (dt, J = 8.1, 1.6 Hz, 2H, H_d), 8.08 (t, J = 7.8 Hz, 1H, H_f), 7.97 (dd, J = 7.7, 5.9 Hz, 2H, H_c), 7.83 (d, J = 7.85, 1H, H_g)

^{13}C NMR (101 MHz, DMF-d_7): δ [ppm] = 154.1, 151.7, 143.9, 142.5, 138.5, 128.7, 127.8, 122.6, 93.4, 83.7

^{11}B NMR (128 MHz, DMF-d_7): δ [ppm] = -0.72

^{19}F NMR (376 MHz, DMF-d_7): δ [ppm] = -150.4

ESI-MS (MeCN) calc. for $C_{76}H_{44}N_{12}Pd_2B_2F_8C_2H_6C_2N_2H_4$ $[M\text{-}2BF_4\text{+}2MeCN\text{+}4H]^+$: *m/z* = 1598.2836; found 1598.2034

Synthesis of $C^{E1}.NO_3$- $C^{E4}.NO_3$

$C^{E1}.NO_3$: benzyl 3,5-bis(pyridin-3-ylethynyl)benzoate (**L^{E1}**) (40 mg, 96 µmol, 4 eq.) and $[Pd(NO_3)_2.2H_2O]$ (13 mg, 48 µmol, 2 eq.) were added to DMSO (3 mL) to form cage **C^{E1}** (31 mg, 14.8 µM, 62 %).

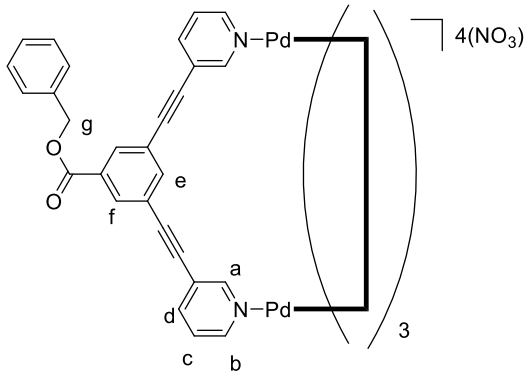

^{1}H NMR (400 MHz, DMF-d_7): δ [ppm] = 10.12 (d, J = 1.6 Hz, 2H, H_a), 9.73 (d, J = 5.6 Hz, 2H, H_b), 8.41 (dt, J = 8.1, 1.5 Hz, 2H, H_d), 8.23 (d, J = 1.6 Hz, 2H, H_f), 7.94 (s, 1H, H_e), 7.92 (dd, J = 8.1, 6.0 Hz, 2H, H_c), 7.55 – 7.35 (m, 5H, H_{phenyl}), 5.44 (s, 2H, H_g)

^{13}C NMR (101 MHz, DMF-d_7): δ [ppm] = 164.2, 154.0, 151.3, 143.3, 137.6, 136.0, 133.2, 131.9, 128.7, 128.5, 127.4, 123.0, 122.7, 92.4, 86.1, 67.3

ESI-MS (MeCN) calc. for $C_{112}H_{72}N_8O_8Pd_2NO_3CH_3CNH_2$ $[M\text{-}3NO_3\text{+}MeCN\text{+}2H]^{2+}$: *m/z* = 988.7024; found 988.6724

$C^{E2}.NO_3$: 3,5-bis(pyridin-3-ylethynyl)analine (**L^{E2}**) (40 mg, 136 µmol, 4 eq.) and $[Pd(NO_3)_2.2H_2O]$ (18 mg, 68 µmol, 2 eq.) were added to DMSO (5 mL) to form cage **$C^{E2}.NO_3$** (45 mg, 27.2 µM, 80

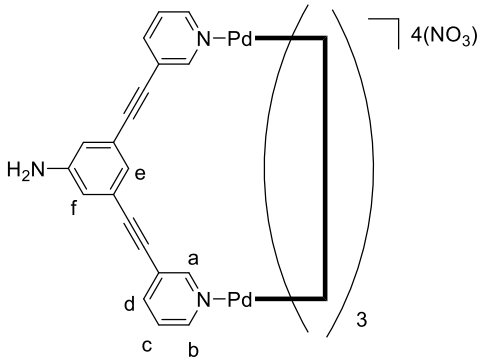

%).

^{1}H NMR (400 MHz, DMF-d_7): δ [ppm] = 10.02 (s, 2H, H_a), 9.65 (d, J = 5.6 Hz, 2H, H_b), 8.27 (d, J = 8.0, 2H, H_d), 7.86 (dd, J = 8.0, 5.9 Hz, 2H, H_c), 6.99 (s, 1H, H_e), 6.96 (s, 2H, H_f), 5.79 (s, 2H, NH_2)

^{13}C NMR (101 MHz, DMF-d_7): δ [ppm] = 154.7, 153.9, 150.6, 150.0, 142.8, 127.3, 123.4, 122.4, 118.0, 94.8, 83.6

C^{E3}.NO_3: 3,5-bis(pyridin-3-ylethynyl)benzene (**L^{E3}**) (40 mg, 143 µmol, 4 eq.) and $[Pd(NO_3)_2.2H_2O]$ (19 mg, 72 µmol, 2 eq.) were added to DMSO (5 mL) to form cage **C^{E3}.NO_3** (50

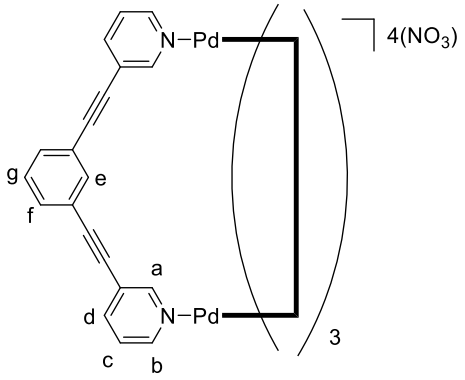

mg, 31.7 µM, 88 %).

^{1}H NMR (400 MHz, DMF-d_7): δ [ppm] = 10.09 (d, J = 1.7 Hz, 2H, H_a), 9.70 (dd, J = 5.8, 1.7 Hz, 2H, H_b), 8.33 (dt, J = 8.0, 1.5 Hz, 2H, H_d), 7.91 (dd, J = 7.9, 5.9 Hz, 2H, H_c), 7.76 (s, 1H, H_e), 7.72 (dd, J = 7.6, 1.5 Hz, 2H, H_f), 7.60 (t, J = 8.2 Hz, 1H, H_g)

^{13}C NMR (101 MHz, DMF-d_7): δ [ppm] = 154.0, 151.8, 151.1, 150.9, 143.8, 143.0, 142.6, 133.3, 128.9, 127.6, 123.2, 122.5, 122.4, 93.8, 85.2

ESI-MS (MeCN) calc. for $C_{80}H_{48}N_8Pd_2CH_3CNH$ $[M\text{-}4NO_3\text{+}MeCN\text{+}H]^{3+}$: *m/z* = 459.7562; found 459.7359

C^{E4}.NO_3: 3,5-bis(pyridin-3-ylethynyl)pyridine (**L^{E4}**) (40 mg, 143 µmol, 4 eq.) and $[Pd(NO_3)_2.2H_2O]$ (19 mg, 72 µmol, 2 eq.) were added to DMSO (5 mL) to form cage **C^{E4}.NO_3** (39 mg, 24.9 µM, 69%).

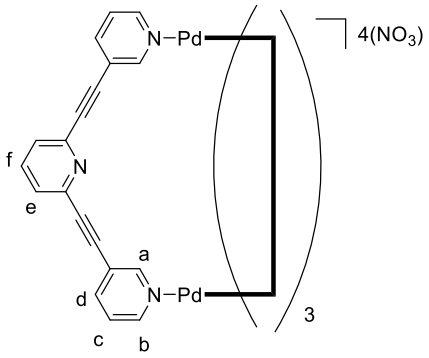

^{1}H NMR (400 MHz, DMF-d_7): δ [ppm] = 9.90 (d, J = 1.7 Hz, 2H, H_a), 9.74 (dd, J = 5.9, 1.1 Hz, 2H, H_b), 8.44, (dt, J = 8.0, 1.5 Hz, 2H, H_d), 8.07 (t, J = 7.6 Hz, 1H, H_f), 7.96 (dd, J = 7.9, 5.9 Hz, 2H, H_c), 7.84 (d, J = 7.8, 2H, H_e)

^{13}C NMR (101 MHz, DMF-d_7): δ [ppm] = 154.1, 151.8, 143.9, 142.5, 138.4, 128.8, 127.8, 122.5, 93.4, 83.7

ESI-MS (MeCN) calc. for $C_{76}H_{44}N_{12}Pd_2CH_3CNH$ $[M\text{-}4NO_3\text{+}MeCN\text{+}H]^{3+}$: *m/z* = 461.0832; found 461.0630

Encapsulation studies

^{1}H NMR encapsulation studies

The Pd_2L_4 cage (8 mg, 1.00 eq.) was dissolved in DMF-d_7 (1mL) and the ^{1}H-NMR (400 MHz, 64 scans) spectrum was recorded. Cisplatin (~2 mg, 2.00 eq.) was added and the yellow solution was stirred for 10 min. The ^{1}H NMR (400 MHz, 64 scans) spectrum of the sample was recorded and compared with the previous one.

^{19}F NMR encapsulation studies

The Pd_2L_4 cage (**C^{E1}-C^{E4}**) (8 mg, 1.00 eq.) was dissolved in DMF-d_7 (6M D_2O) (1mL) and the ^{19}F NMR (400 MHz, 64 scans) spectrum was recorded. Cisplatin (1.00 eq.) was added and the yellow solution was stirred for 10 min. The ^{19}F NMR (400 MHz, 64 scans) spectrum of the sample was recorded. The sample was removed and a further aliquot of cisplatin (1.00 eq.) was added to the solution. The sample was stirred for 10 min and a second ^{19}F NMR spectra was recorded and compared with the previous one.

NMR Spectra

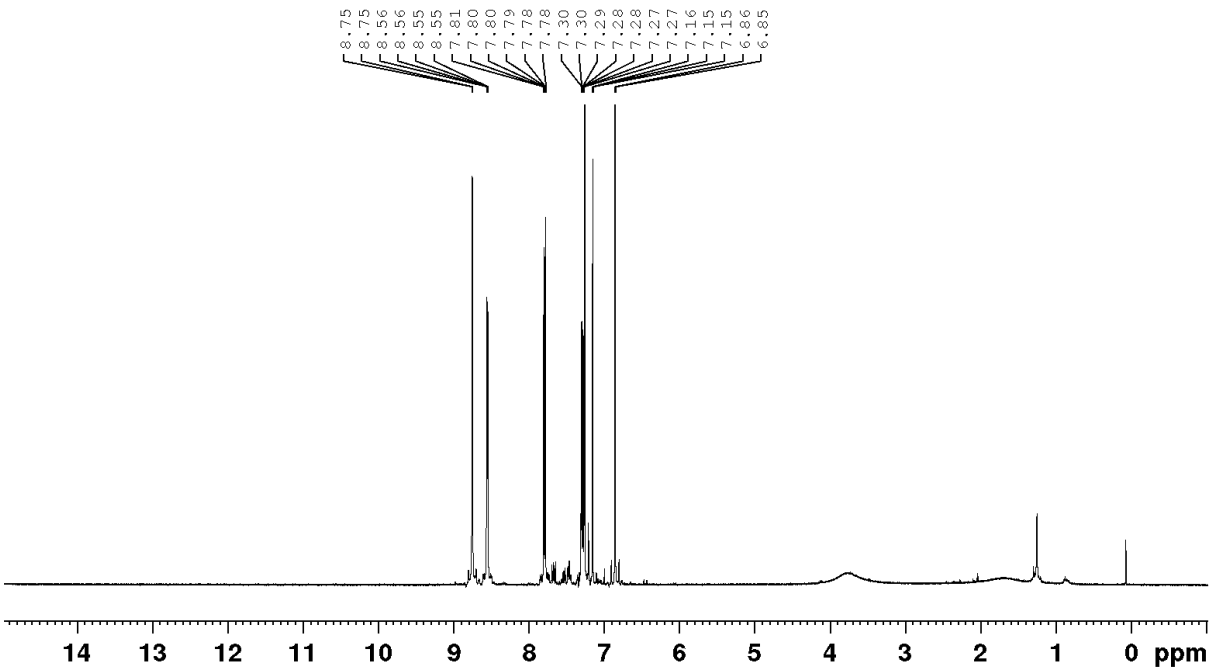

Figure S96: ^{1}H NMR (400 MHz, $CDCl_3$) spectrum of $\mathbf{L^{E2}}$

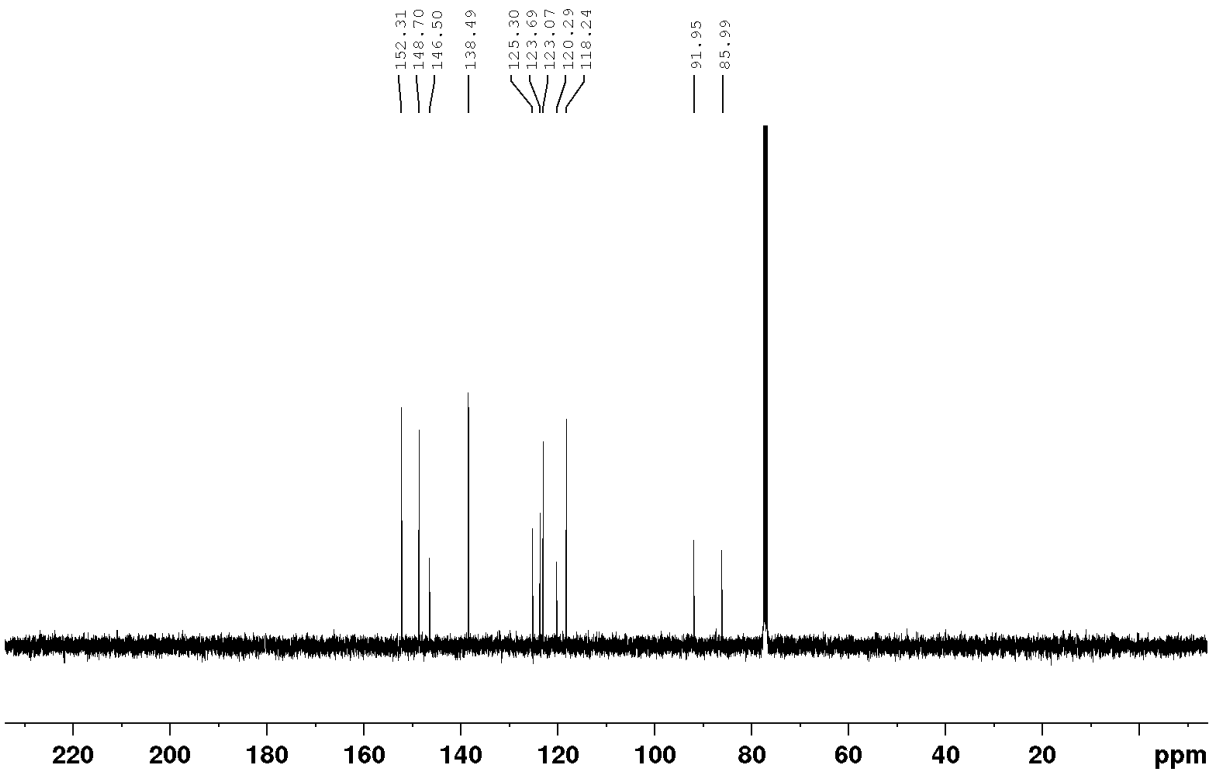

Figure S97: ^{13}C NMR (101 MHz, $CDCl_3$) spectrum of $\mathbf{L^{E2}}$

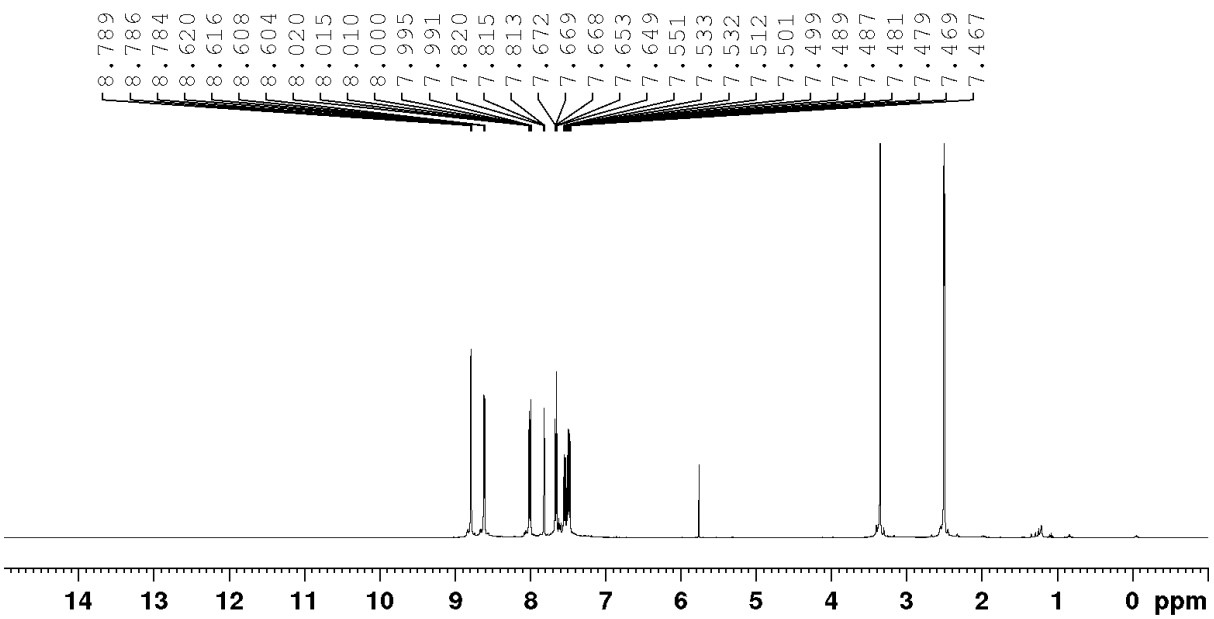

Figure S98: ^{1}H NMR (400 MHz, DMSO-d_6) spectrum of ligand **L^{E3}**

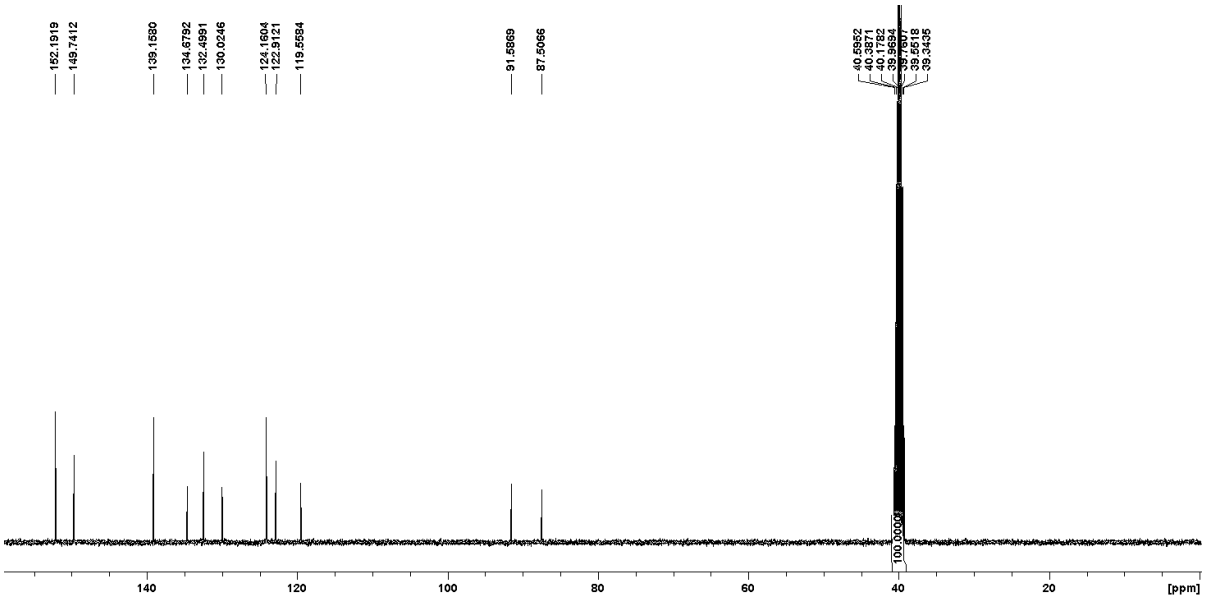

Figure S99: ^{13}C NMR (101 MHz, DMSO-d_6) spectrum of **L^{E3}**

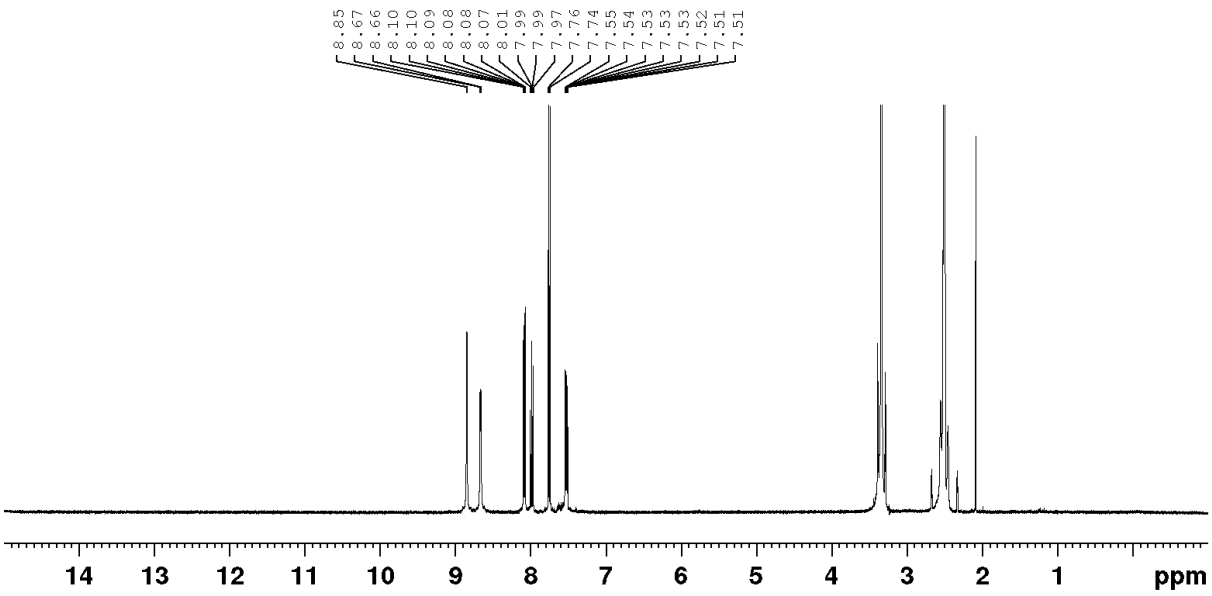

Figure S100 ^{1}H NMR (400 MHz, DMSO-d_6) spectrum of $\mathbf{L^{E4}}$

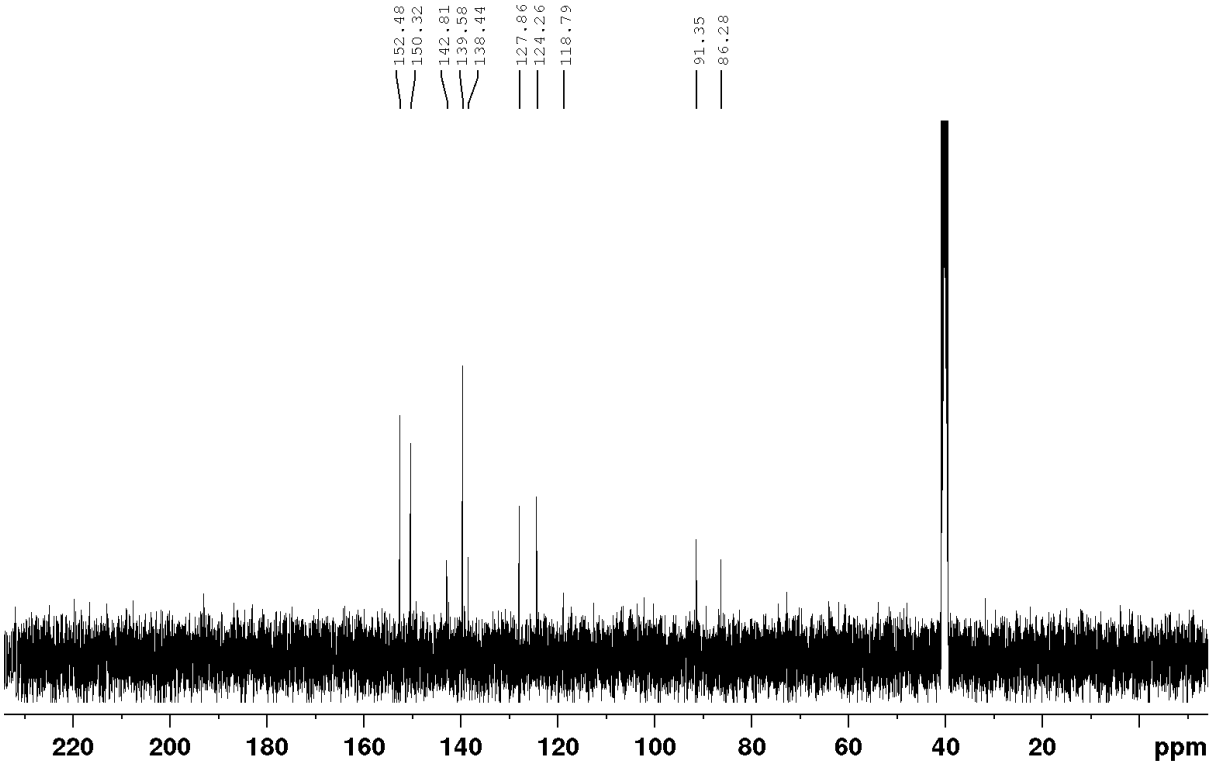

Figure S101 ^{13}C NMR (101 MHz, DMSO-d_6) spectrum of $\mathbf{L^{E4}}$

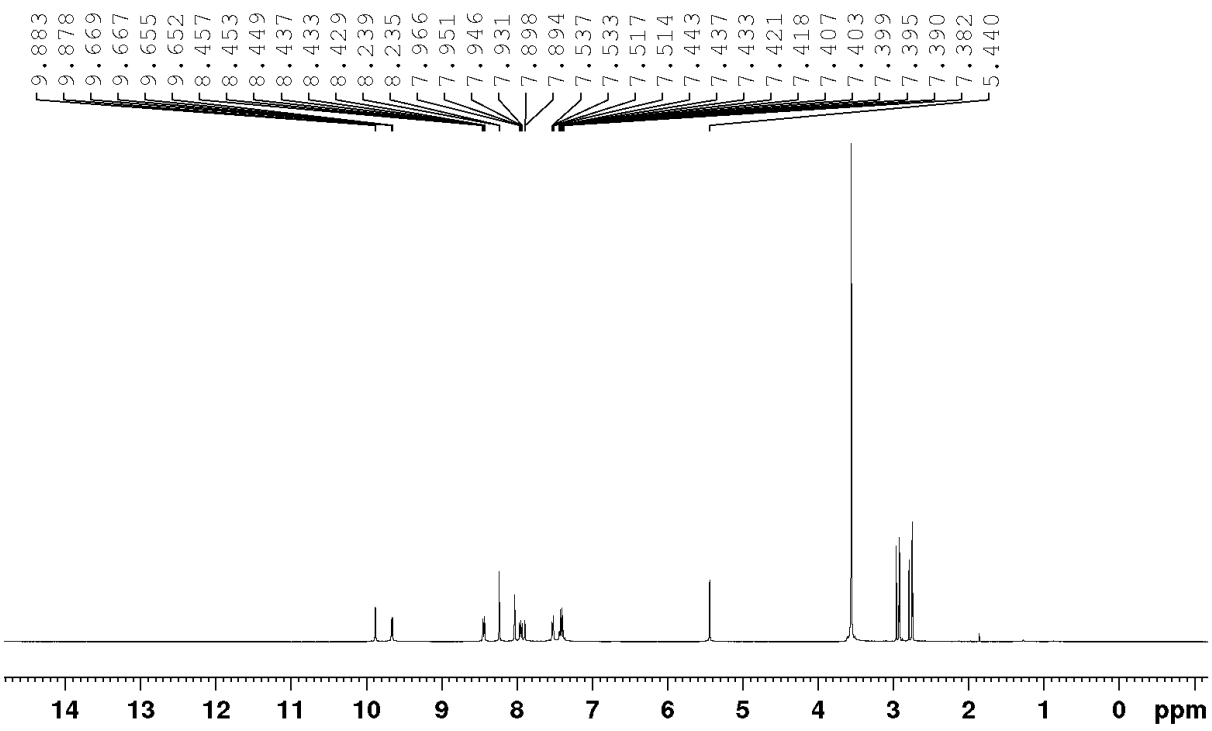

Figure S102 ^{1}H NMR (400 MHz, DMF-d_7) spectrum of $\mathbf{C^{E1}}$

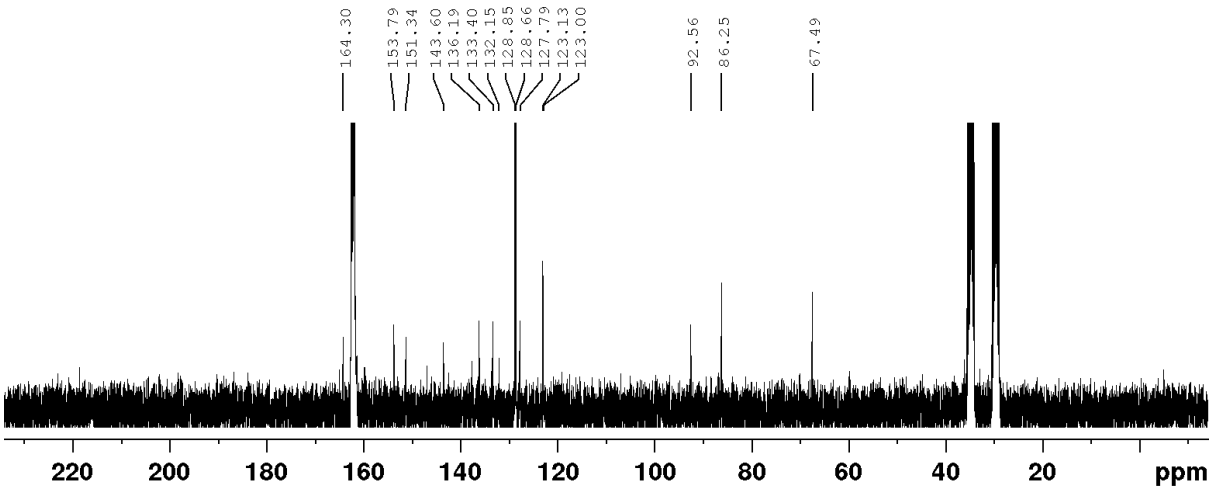

Figure S103 ^{13}C NMR (101 MHz, DMF-d_7) spectrum of $\mathbf{C^{E1}}$

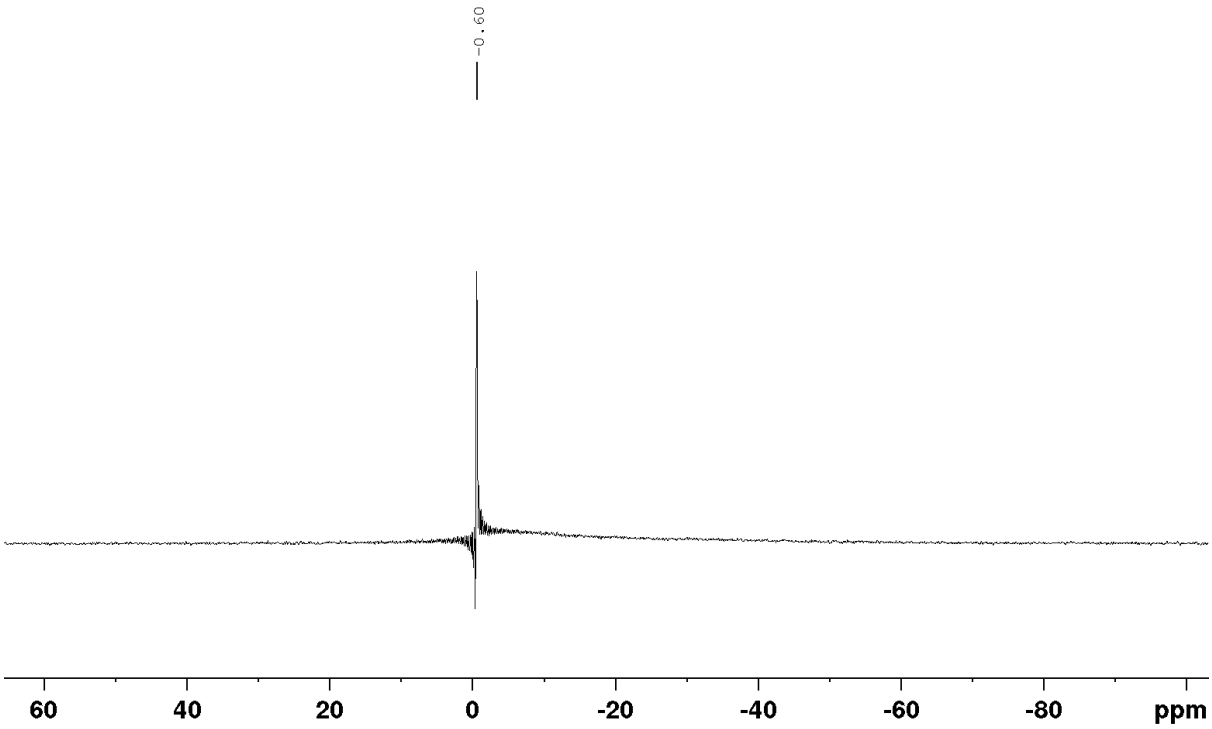

Figure S104 ^{11}B NMR (128 MHz, DMF-d_7) spectrum of $\mathbf{C^{E1}}$

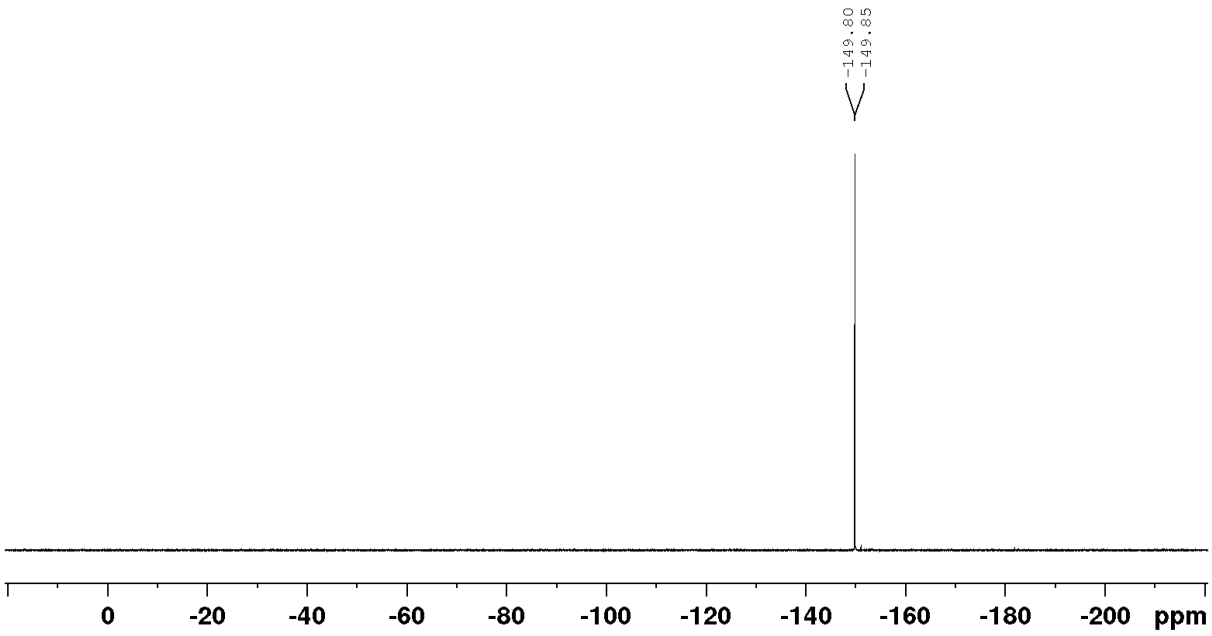

Figure S105 ^{19}F NMR (376 MHz, DMF-d_7) spectrum of $\mathbf{C^{E1}}$

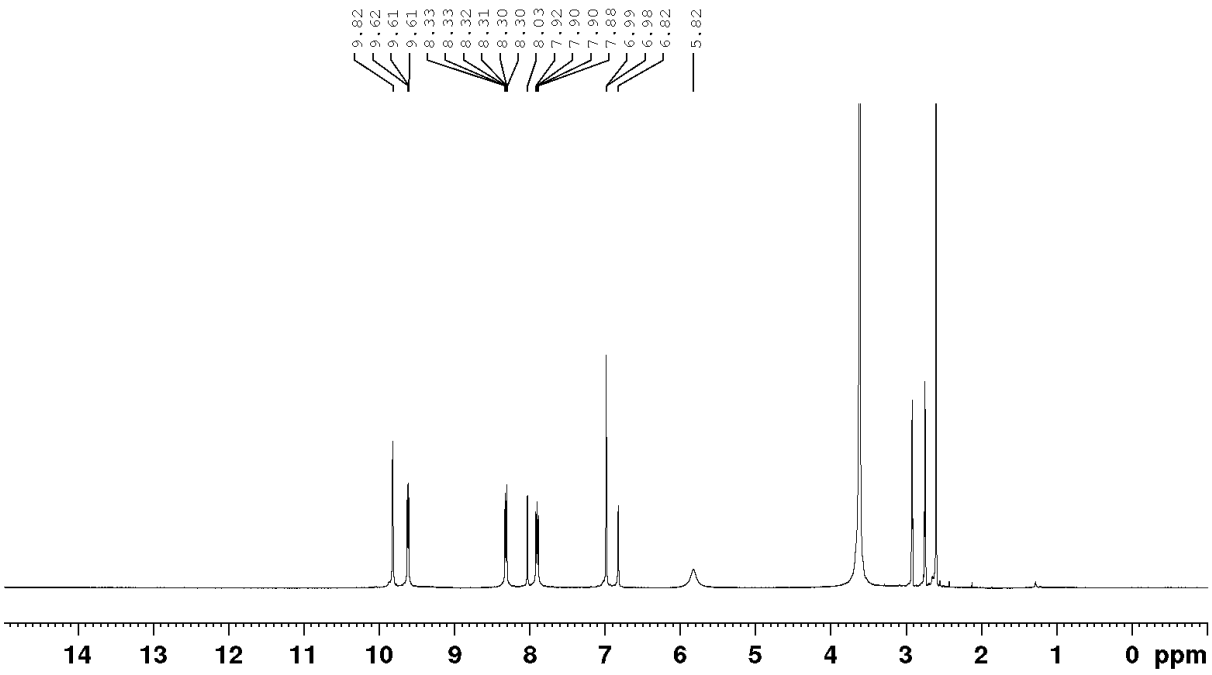

Figure S106: ^{1}H NMR (400 MHz, DMF-d_7) spectrum of $\mathbf{C^{E2}}$

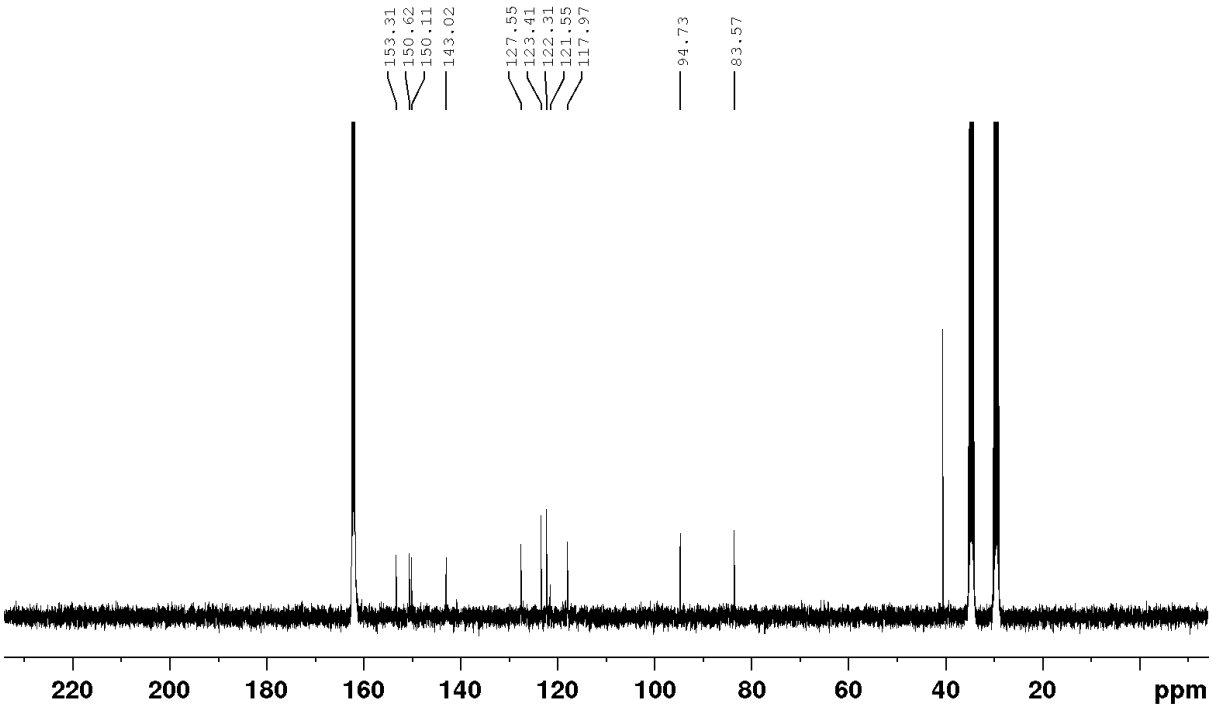

Figure S107 ^{13}C NMR (101 MHz, DMF-d_7) spectrum of $\mathbf{C^{E2}}$

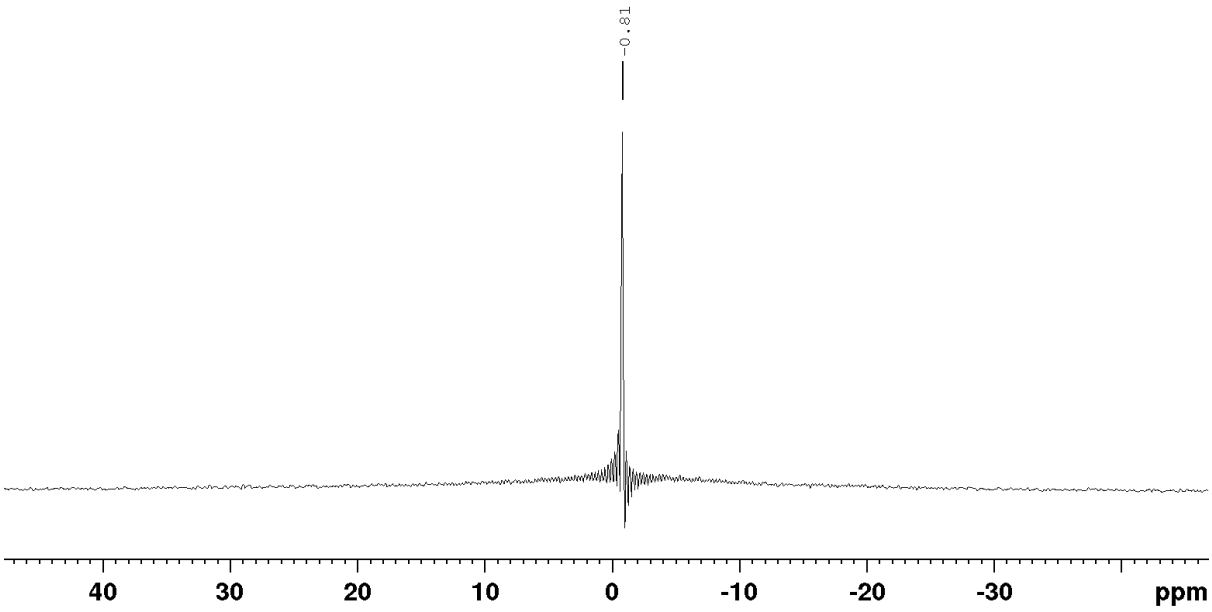

Figure S108 ^{11}B NMR (128 MHz, DMF-d_7) spectrum of $\mathbf{C^{E2}}$

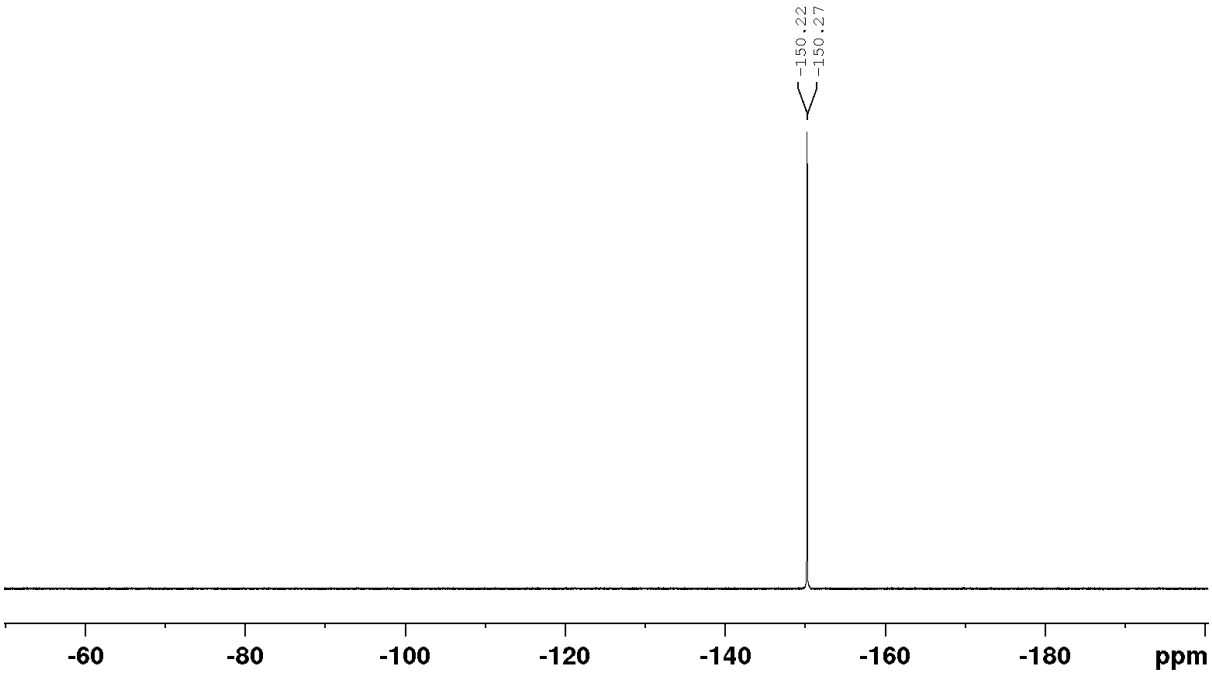

Figure S109 ^{19}F NMR (376 MHz, DMF-d_7) spectrum of $\mathbf{C^{E2}}$

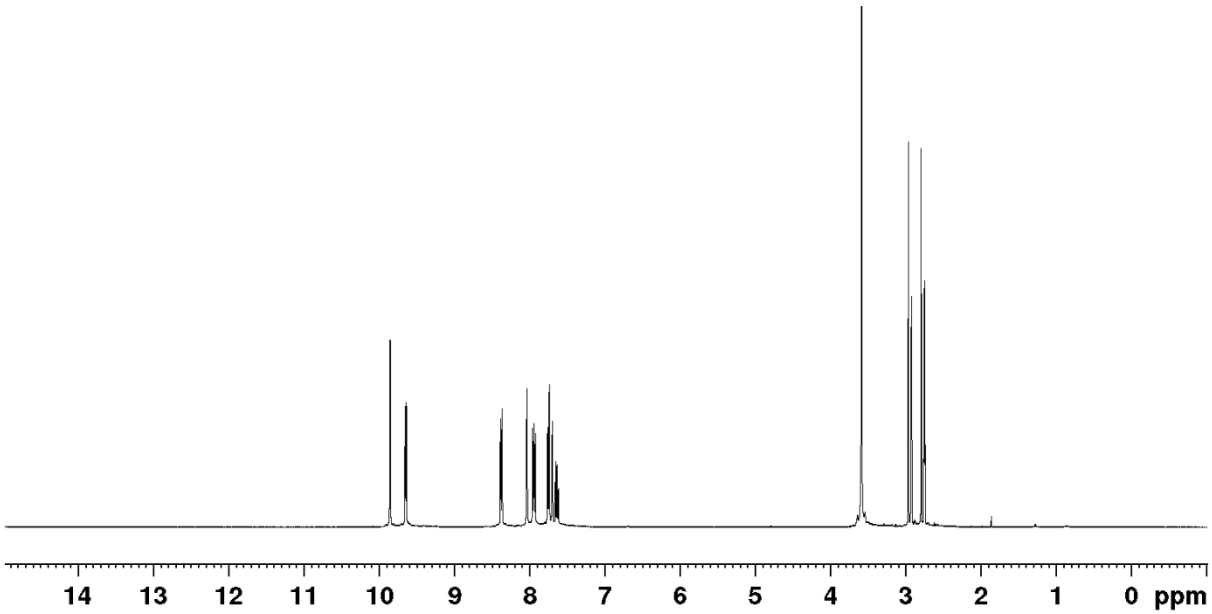

Figure S110: ^{1}H NMR (400 MHz, DMF-d_7) spectrum of **C^{E3}**

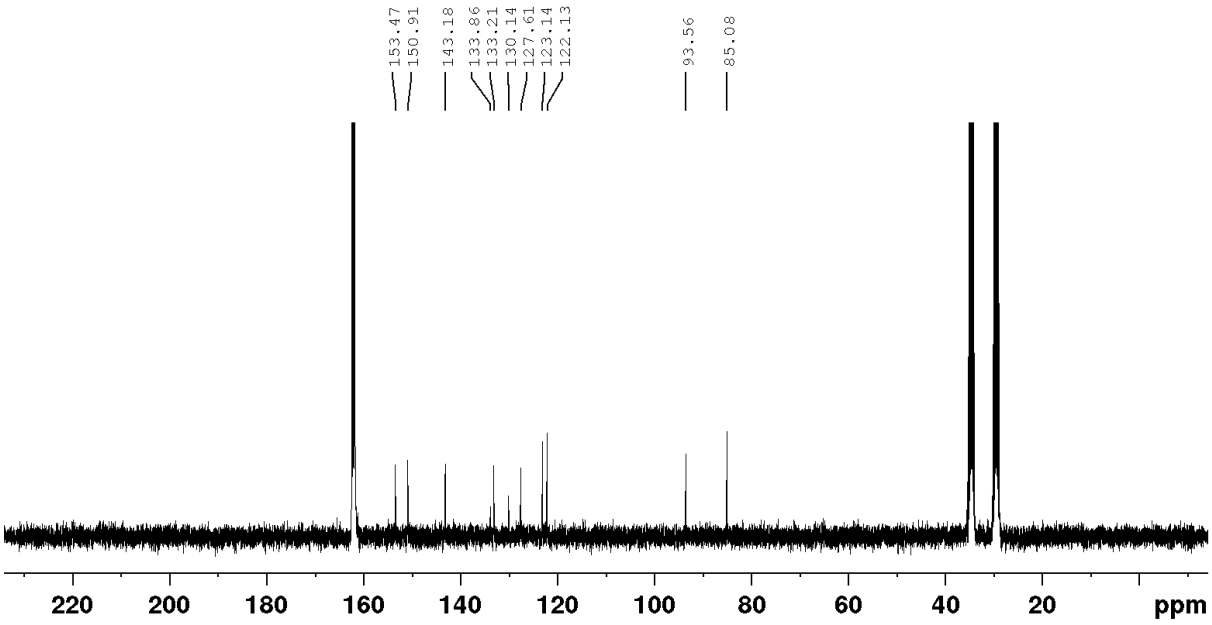

Figure S111 ^{13}C NMR (101 MHz, DMF-d_7) spectrum of **C^{E3}**

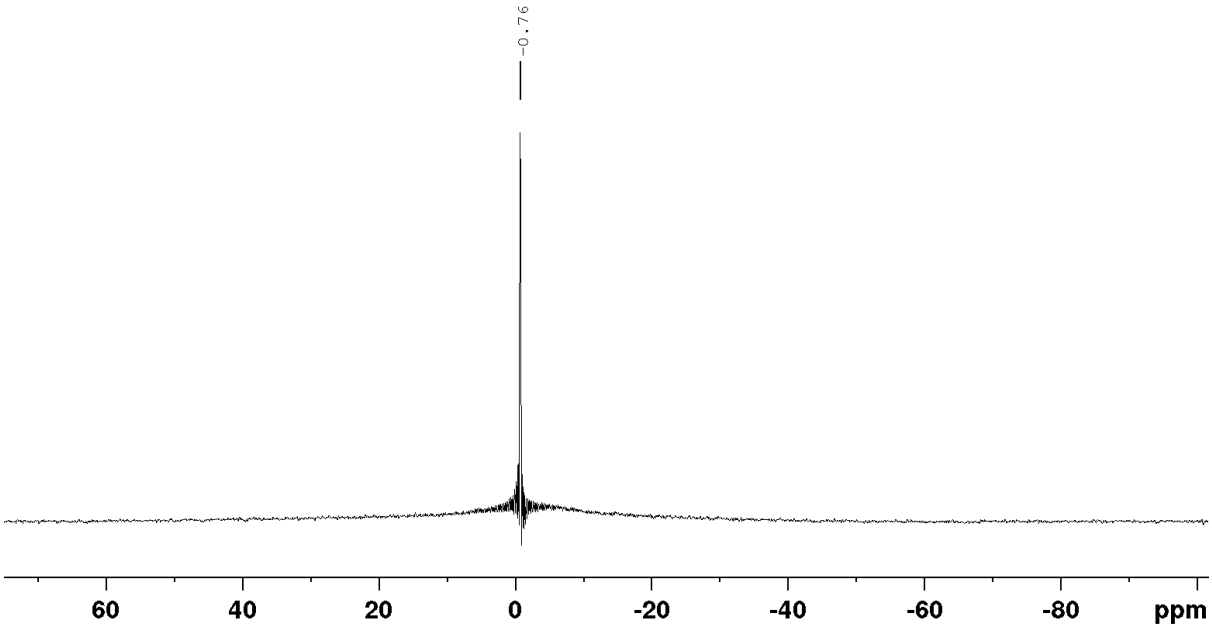

Figure S112 ^{11}B NMR (128 MHz, DMF-d_7) spectrum of **C^{E3}**

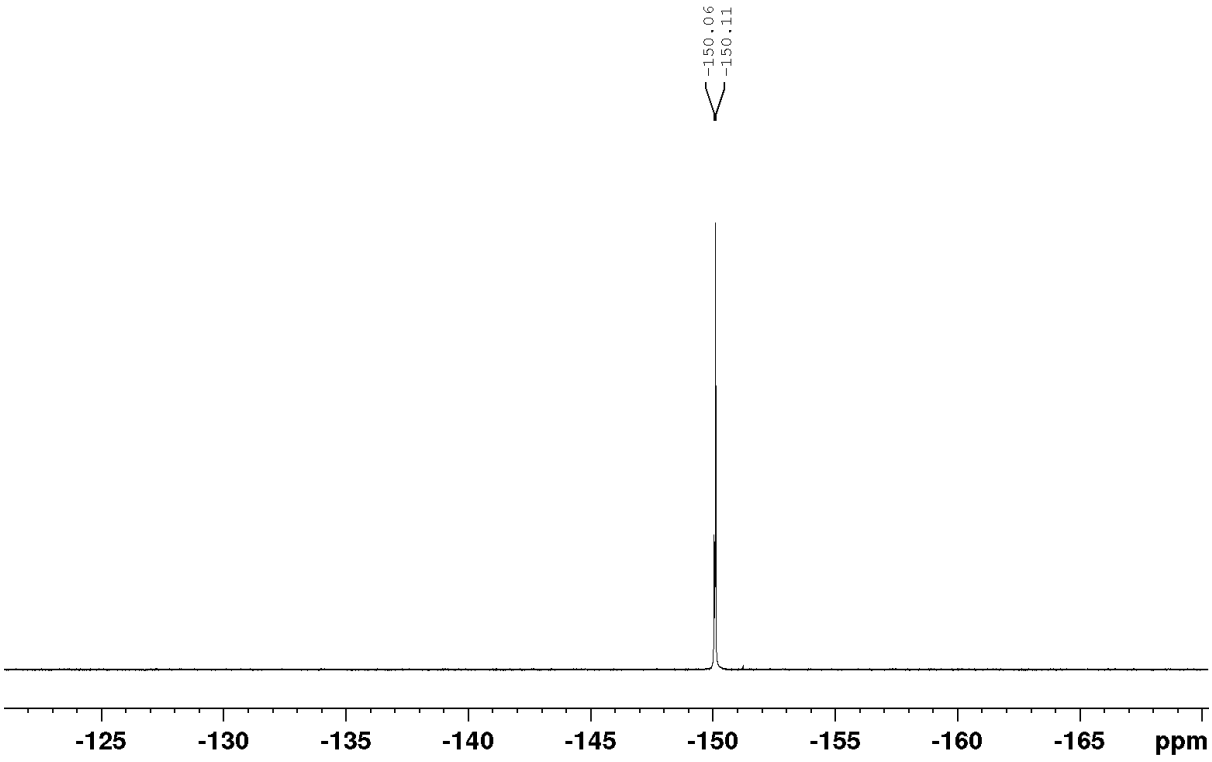

Figure S113 ^{19}F NMR (376 MHz, DMF-d_7) spectrum of **C^{E3}**

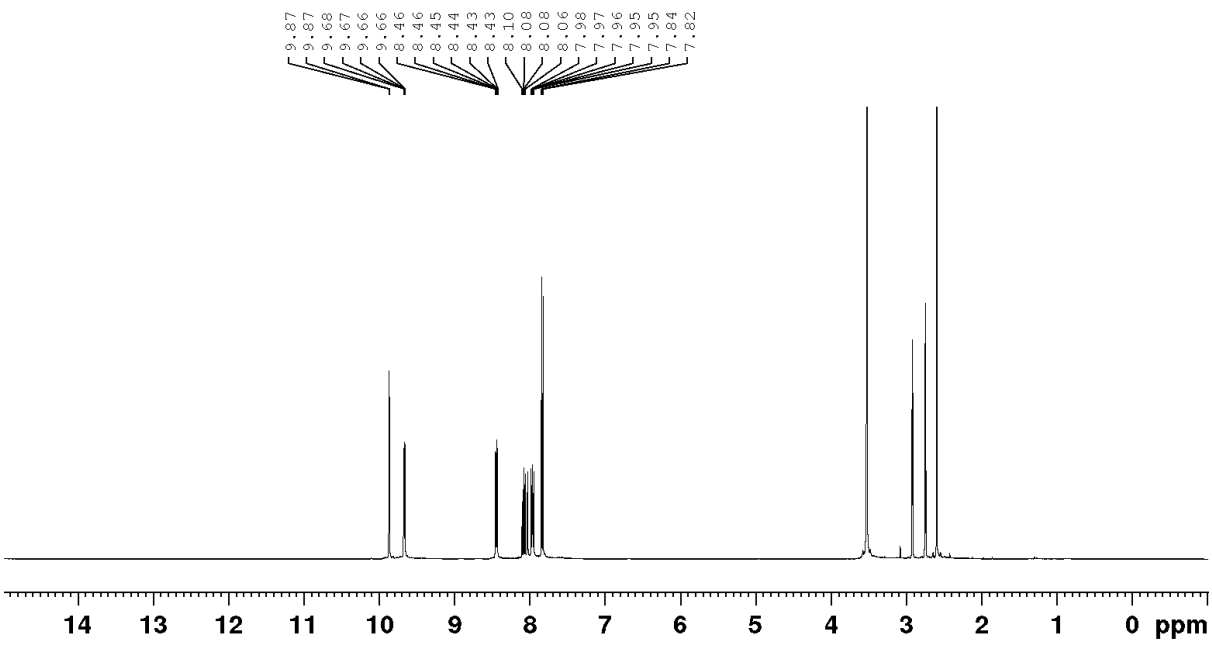

Figure S114: ^{1}H NMR (400 MHz, DMF-d_7) spectrum of $\mathbf{C^{E4}}$

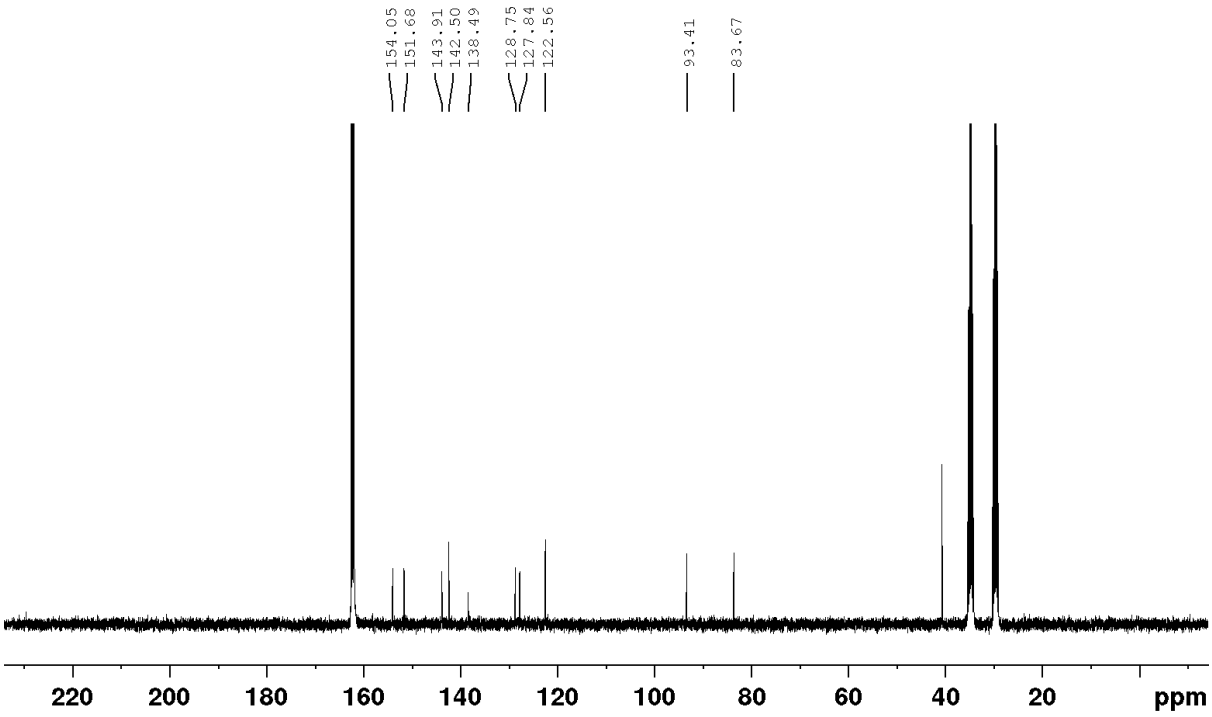

Figure S115 ^{13}C NMR (101 MHz, DMF-d_7) spectrum of $\mathbf{C^{E4}}$

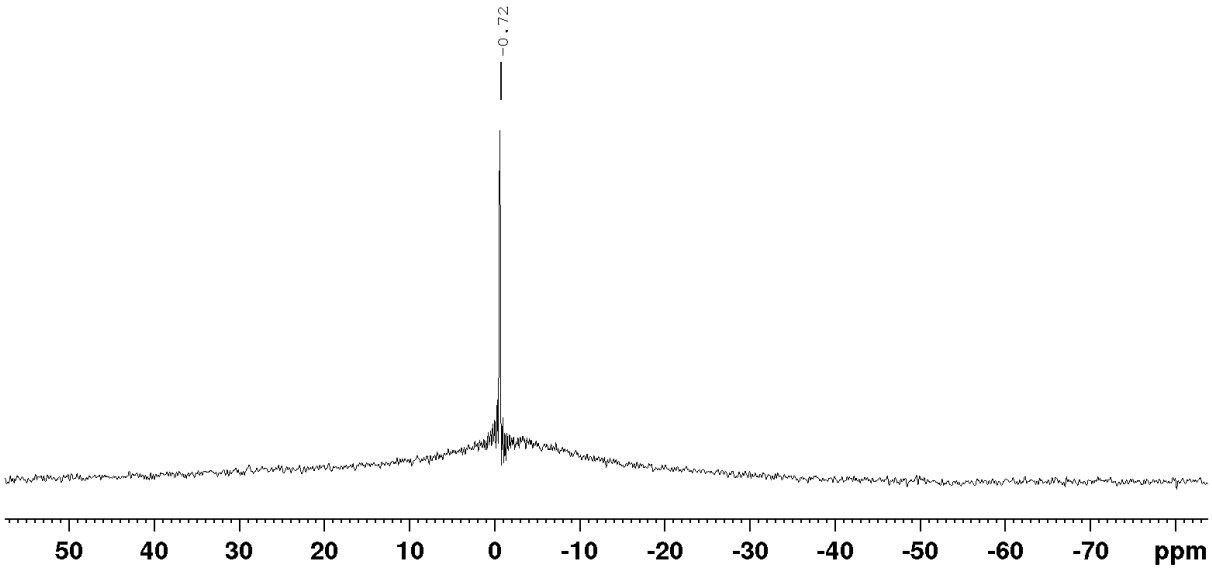

Figure S116 ^{11}B NMR (128 MHz, DMF-d_7) spectrum of $\mathbf{C^{E4}}$

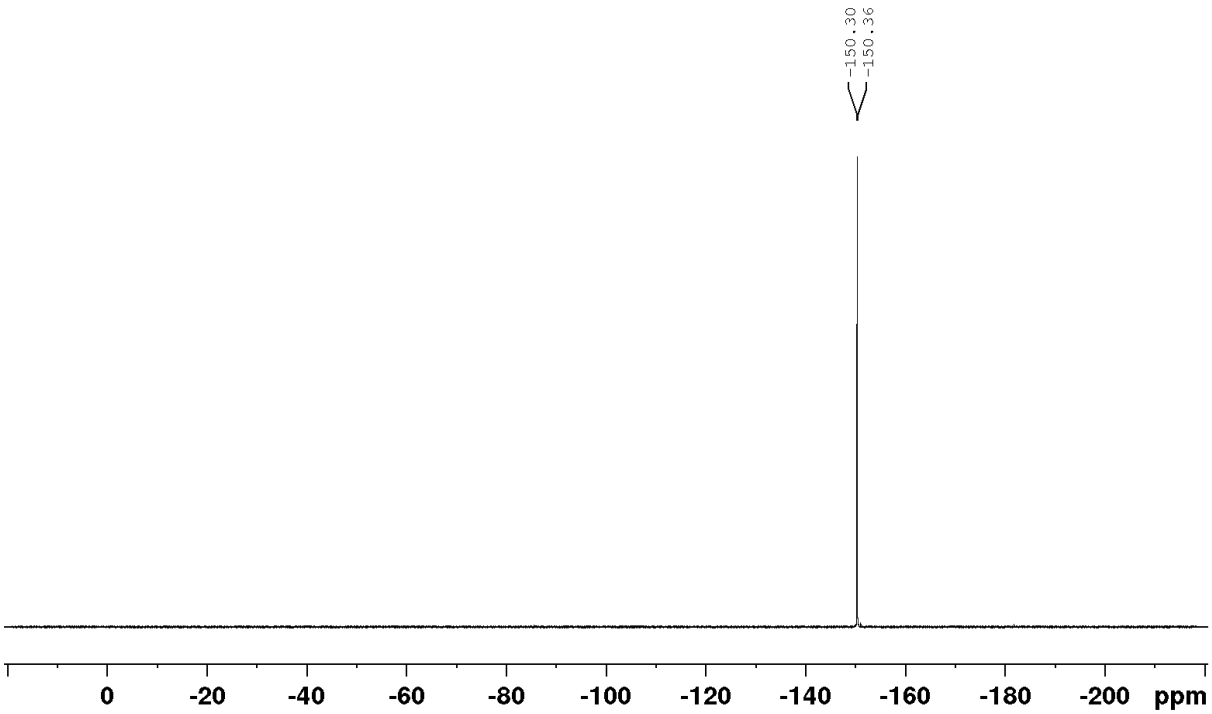

Figure S117 ^{19}F NMR (376 MHz, DMF-d_7) spectrum of $\mathbf{C^{E3}}$

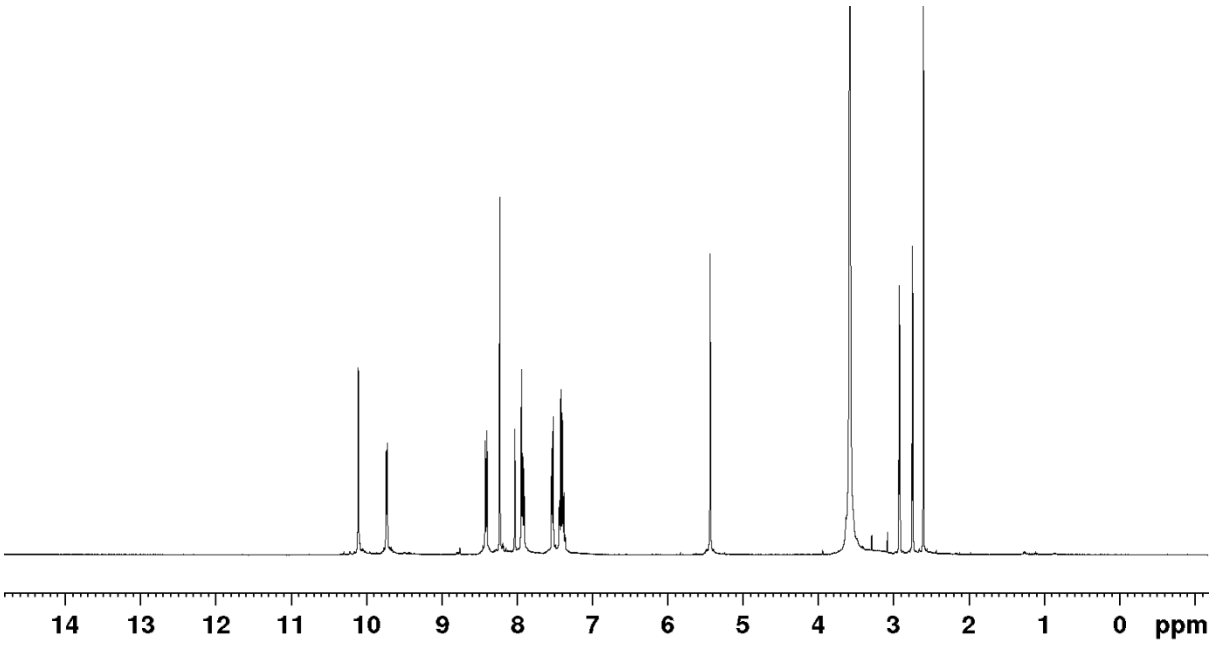

Figure S118: ^{1}H NMR (400 MHz, DMF-d_7) spectrum of $\mathbf{C^{E1}.NO_3}$

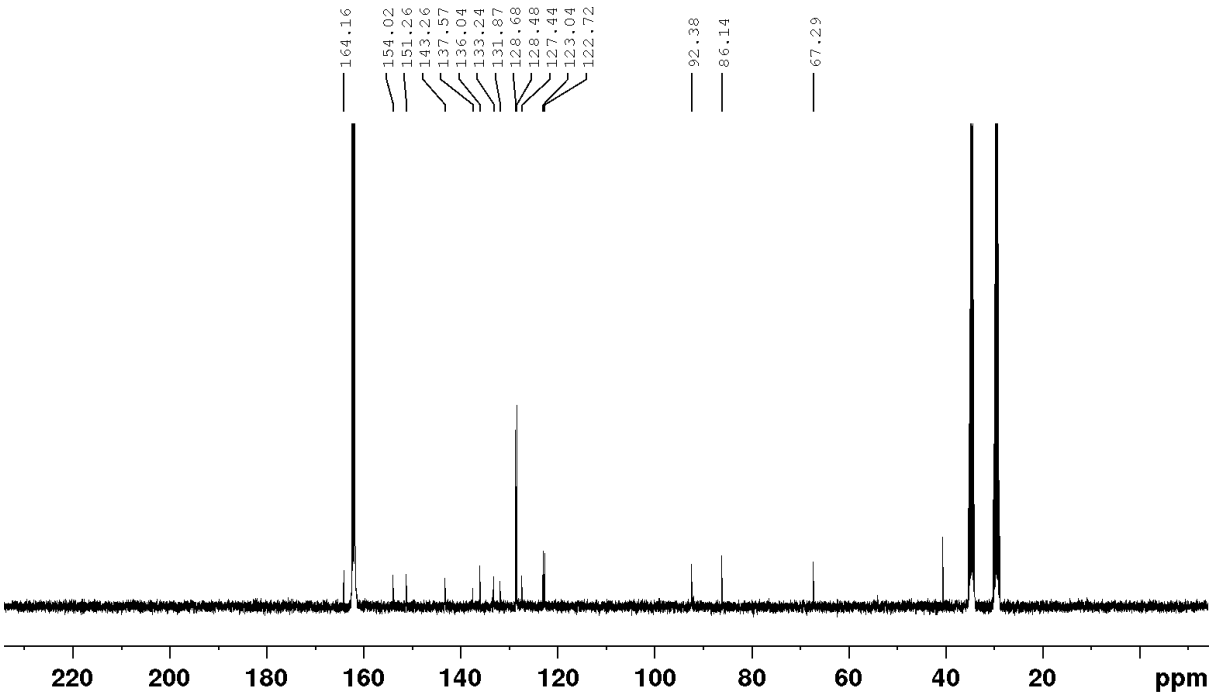

Figure S119^{13}C NMR (101 MHz, DMF-d_7) spectrum of $\mathbf{C^{E1}.NO_3}$

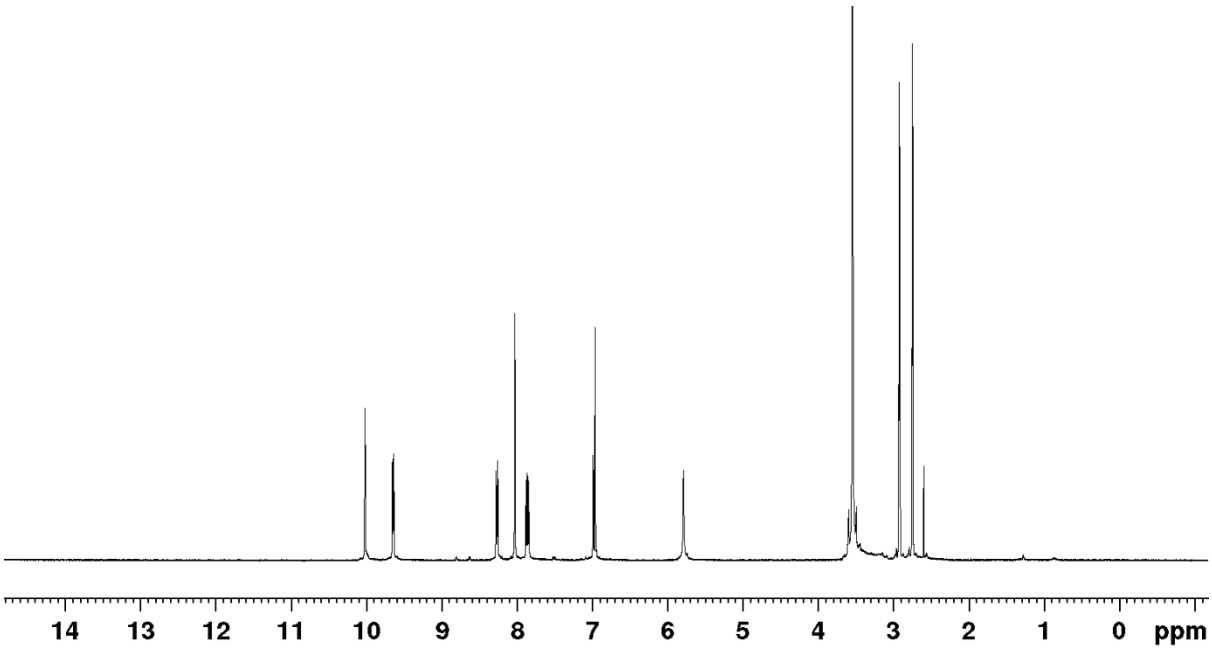

Figure S120: ^{1}H NMR (400 MHz, DMF-d_7) spectrum of **C^{E2}.NO_3**

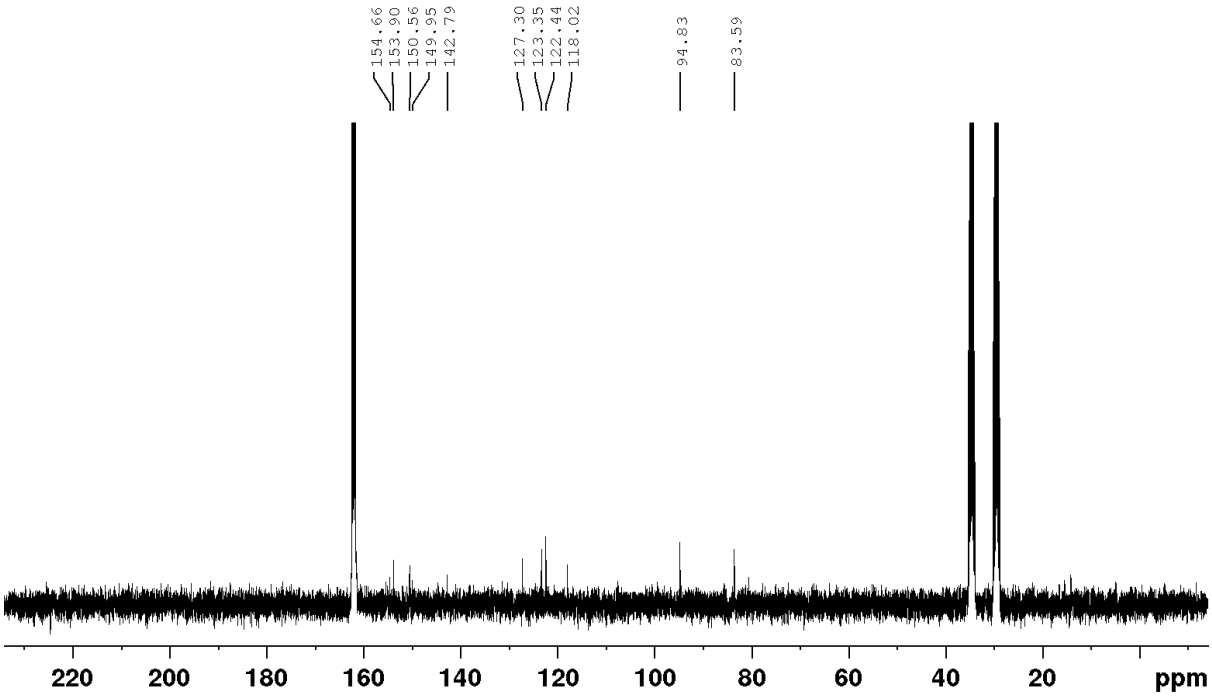

Figure S121 ^{13}C NMR (101 MHz, DMF-d_7) spectrum of **C^{E2}.NO_3**

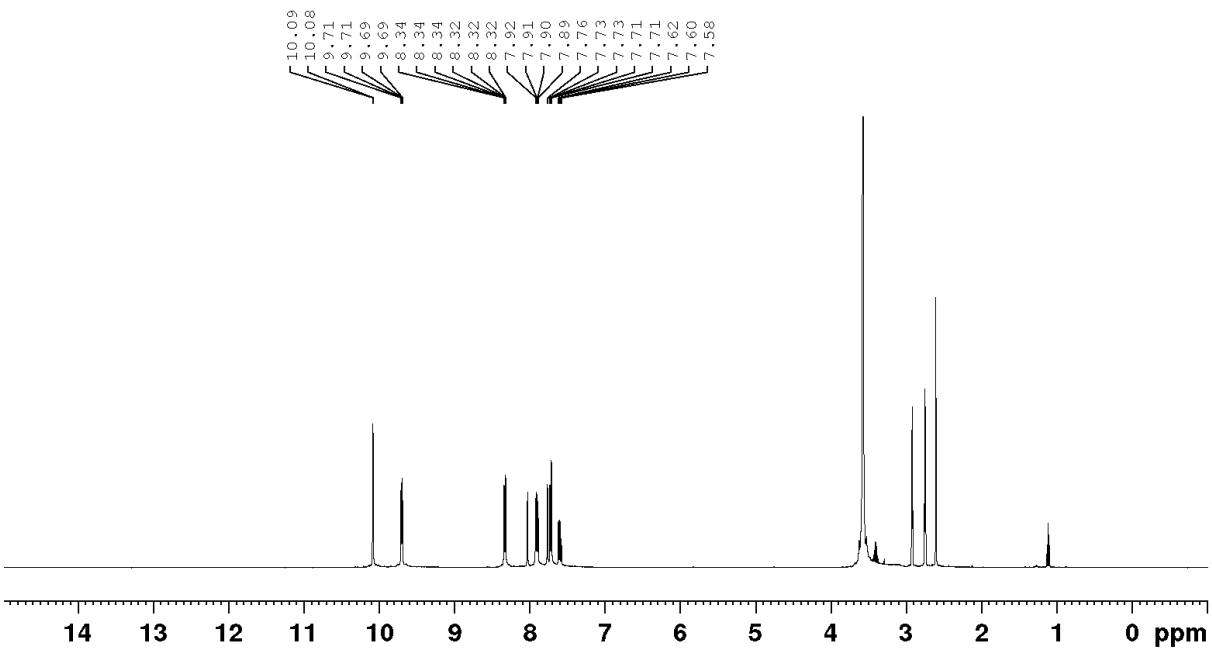

Figure S122: ^{1}H NMR (400 MHz, DMF-d_7) spectrum of $\mathbf{C^{E3}.NO_3}$

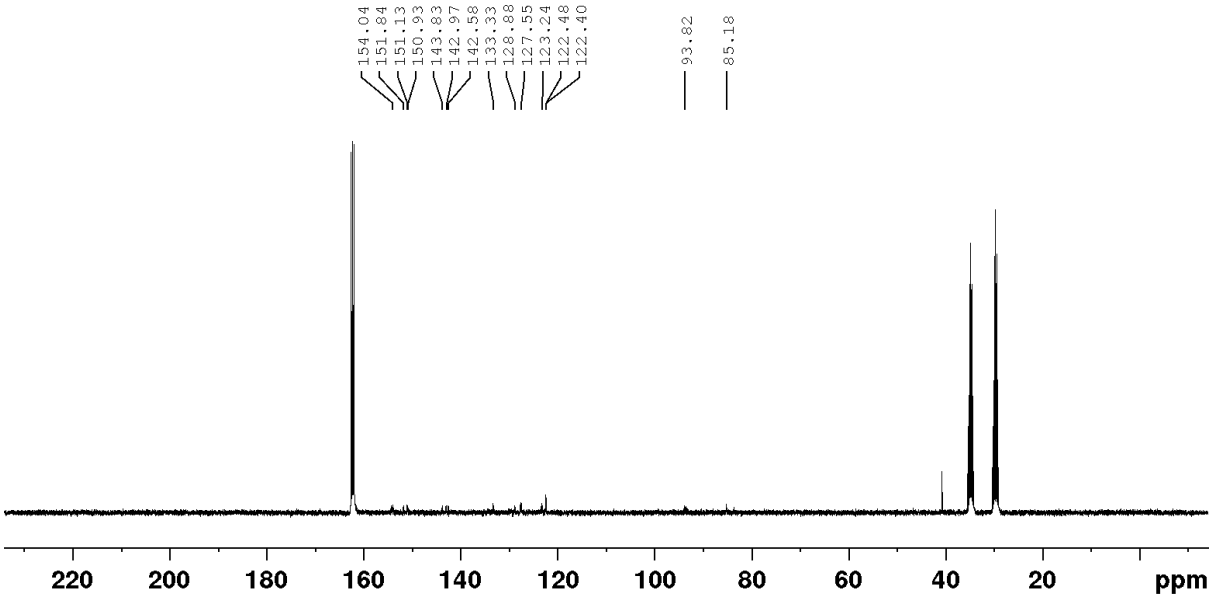

Figure S123 ^{13}C NMR (101 MHz, DMF-d_7) spectrum of $\mathbf{C^{E3}.NO_3}$

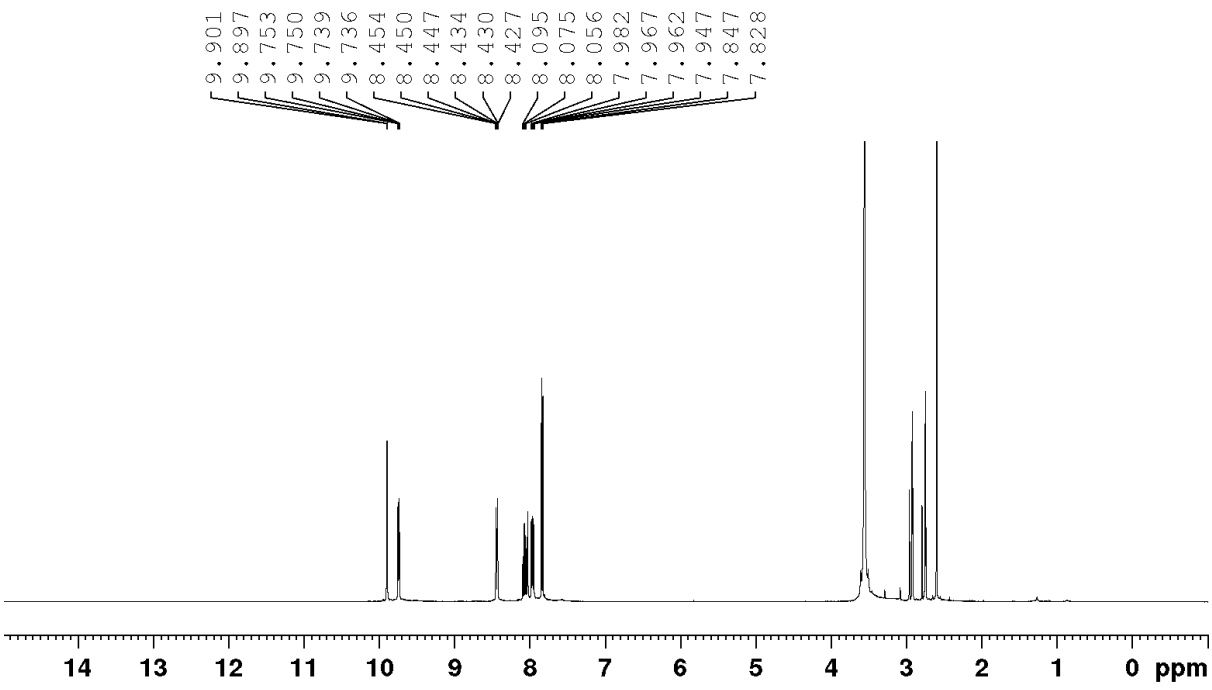

Figure S124: ^{1}H NMR (400 MHz, DMF-d_7) spectrum of $\mathbf{C^{E4}.NO_3}$

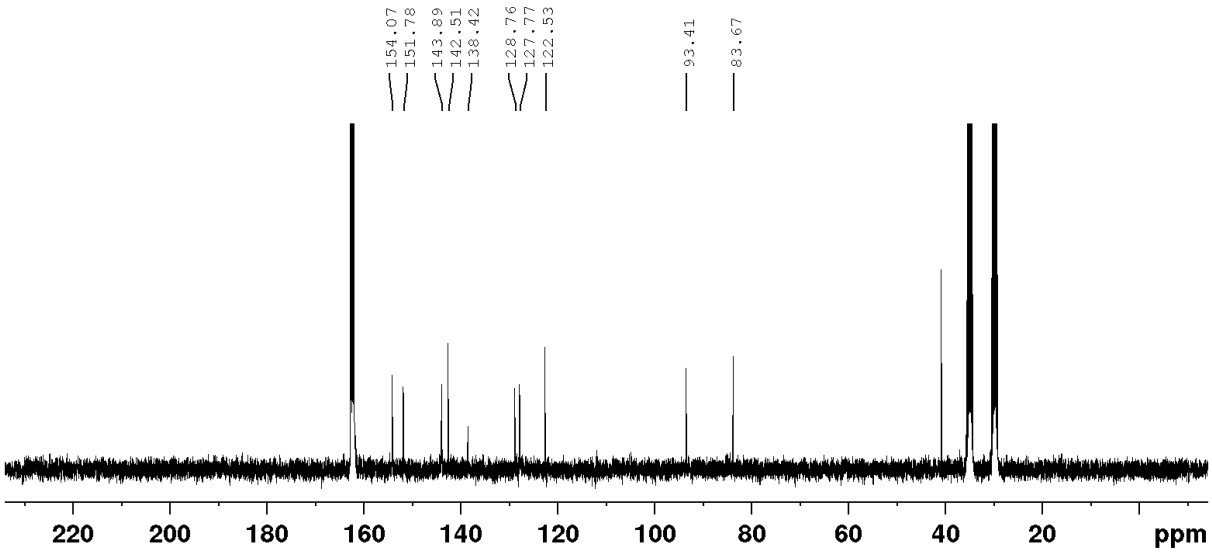

Figure S125 ^{13}C NMR (101 MHz, DMF-d_7) spectrum of $\mathbf{C^{E4}.NO_3}$

Mass spectra of C^{E1}-C^{E4} and $C^{E1}.NO_3$-$C^{E4}.NO_3$

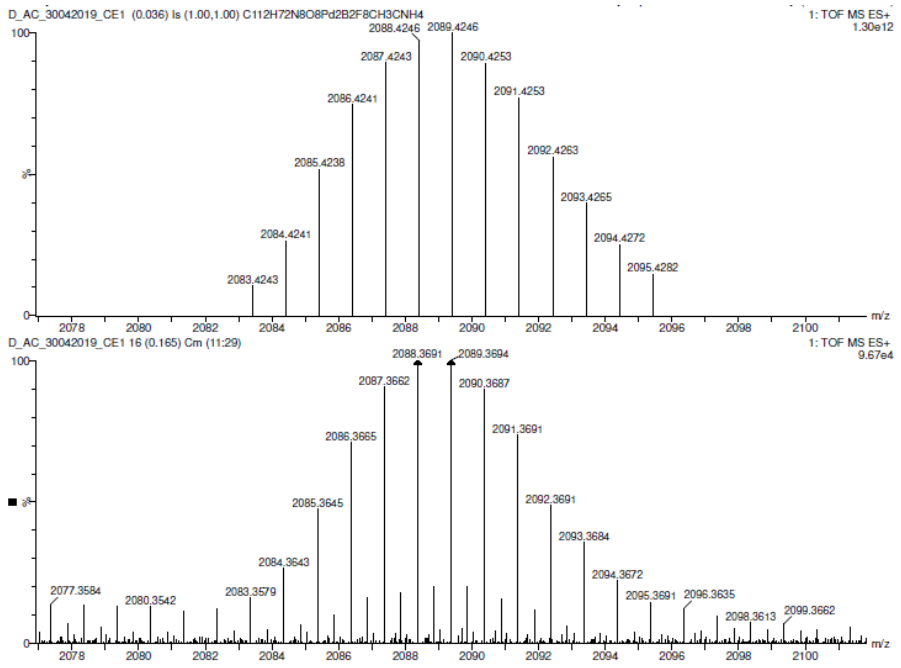

Figure S126. Comparison between the theoretical isotopic pattern (top) and the experimental isotopic pattern (bottom) of $[\mathbf{C}^{E1}\text{-}2BF_4\text{+MeCN+4H}]^+$

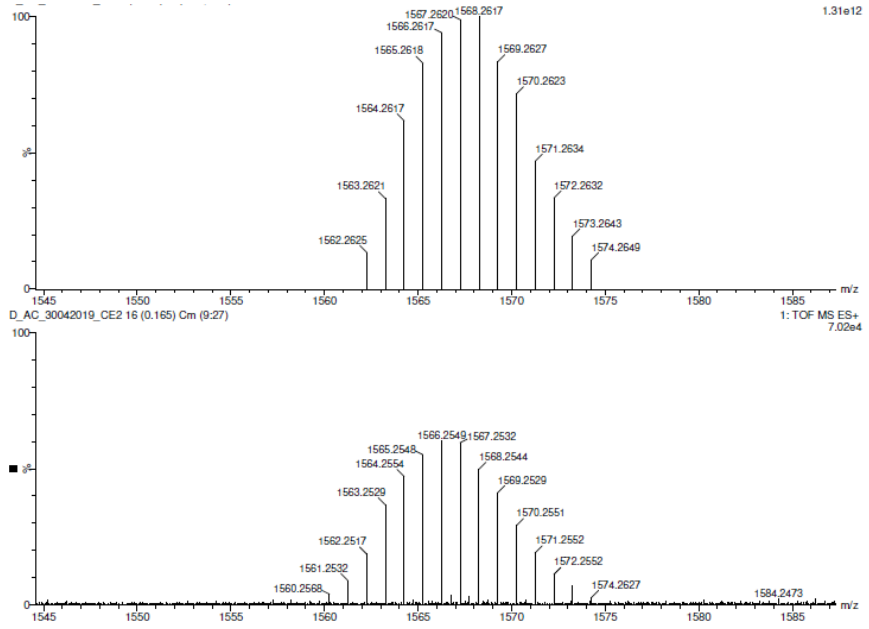

Figure S127. Comparison between the theoretical isotopic pattern (top) and the experimental isotopic pattern (bottom) of $[\mathbf{C}^{E2}\text{-}2BF_4]^+$

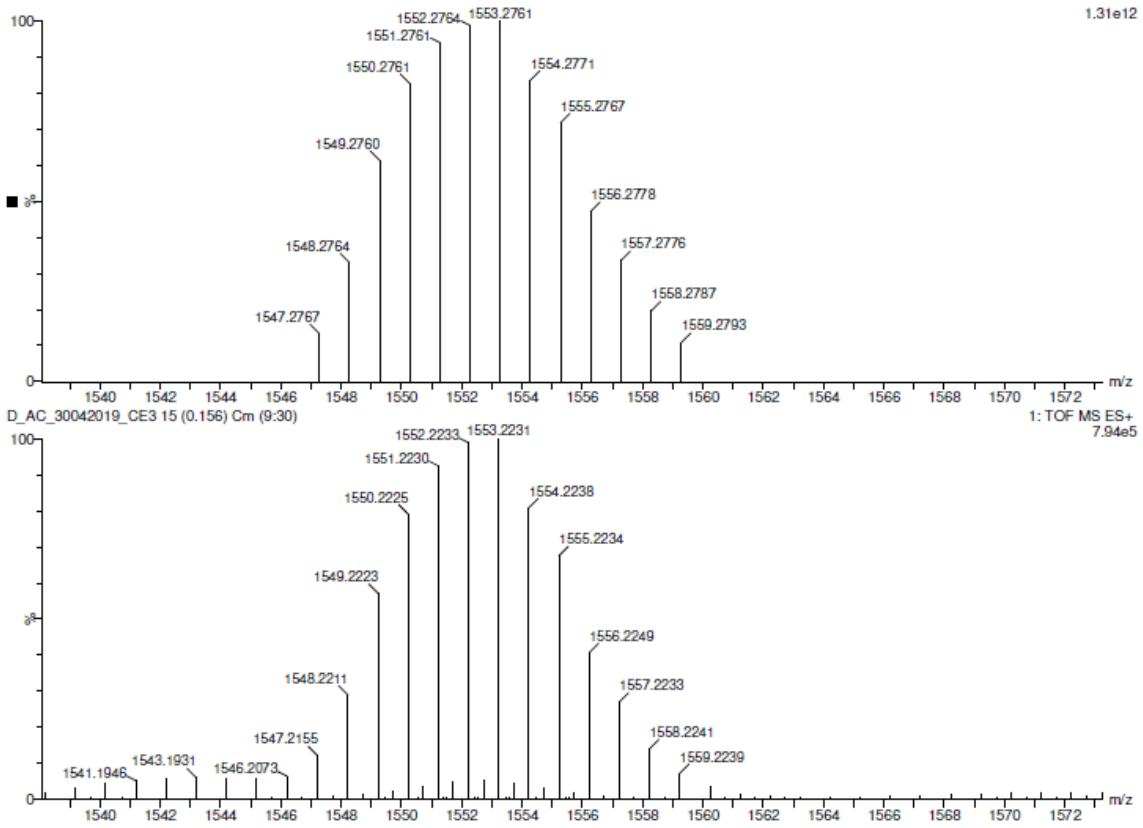

Figure S128. Comparison between the theoretical isotopic pattern (top) and the experimental isotopic pattern (bottom) of $[\mathbf{C}^{\mathbf{E3}}\text{-}2BF_4\text{+MeCN+4H}]^+$

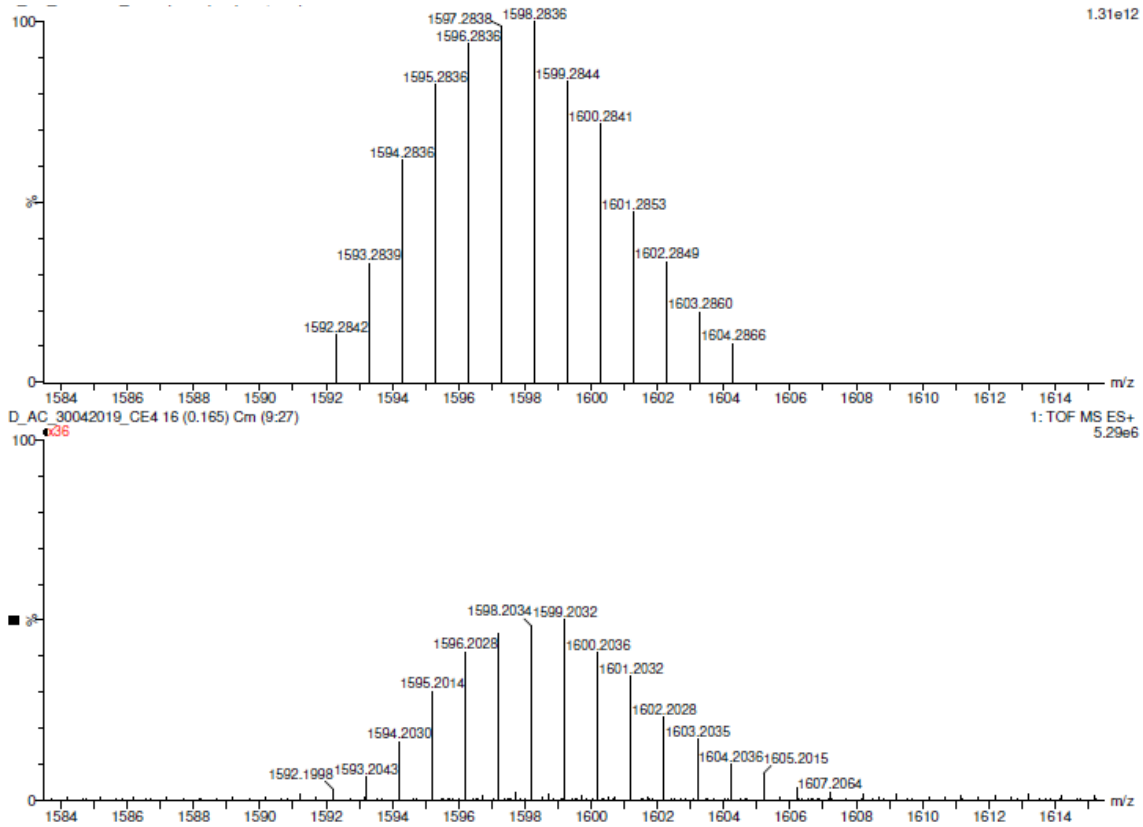

Figure S129. Comparison between the theoretical isotopic pattern (top) and the experimental isotopic pattern (bottom) of $[\mathbf{C}^{\mathbf{E4}}\text{-}2BF_4\text{+2MeCN+4H}]^+$

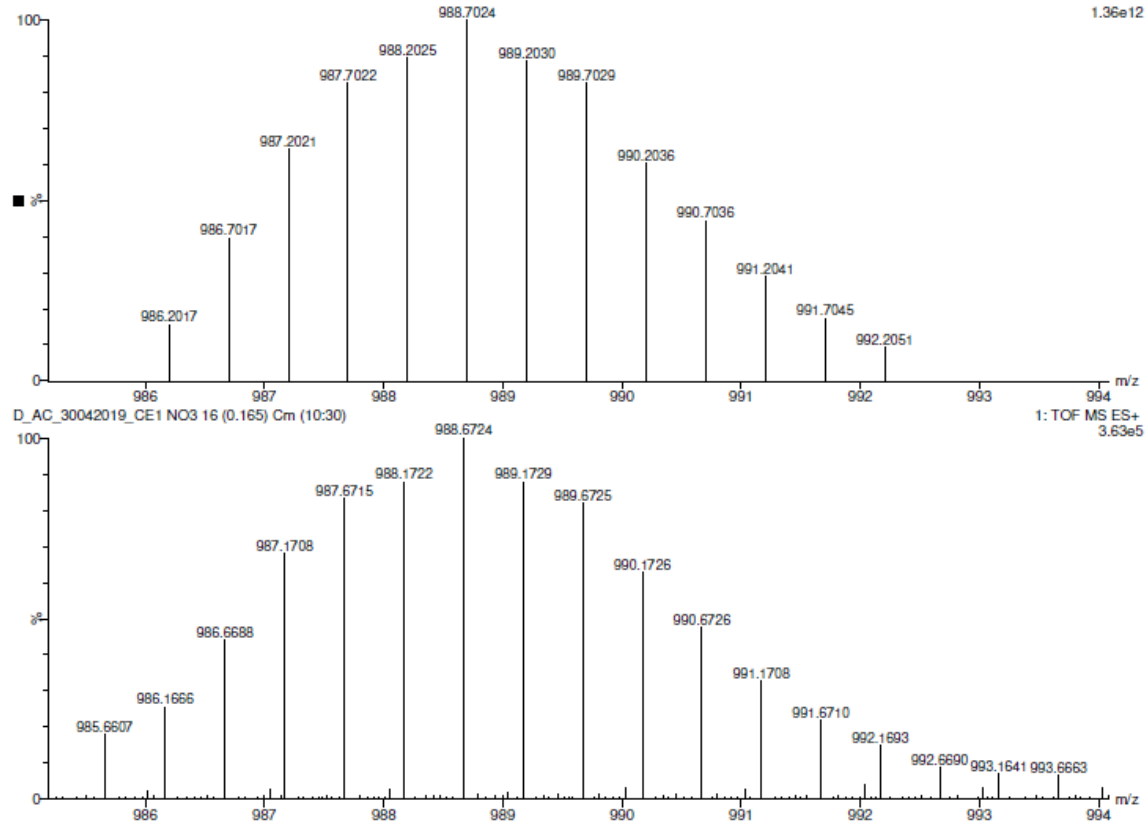

Figure S130. Comparison between the theoretical isotopic pattern (top) and the experimental isotopic pattern (bottom) of [$\mathbf{C^{E1}.NO3}$-3NO_3+MeCN+2H]$^{2+}$

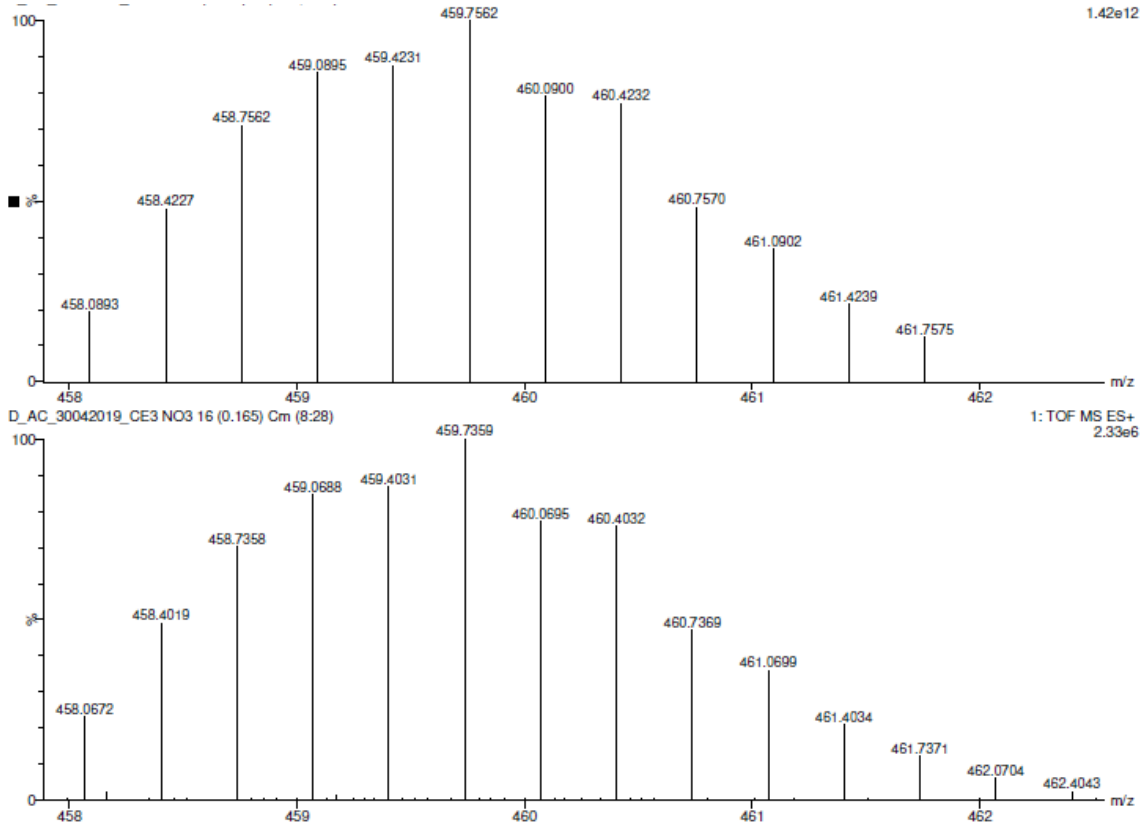

Figure S131. Comparison between the theoretical isotopic pattern (top) and the experimental isotopic pattern (bottom) of [$\mathbf{C^{E3}.NO_3}$-4NO_3+MeCN+H]$^{3+}$

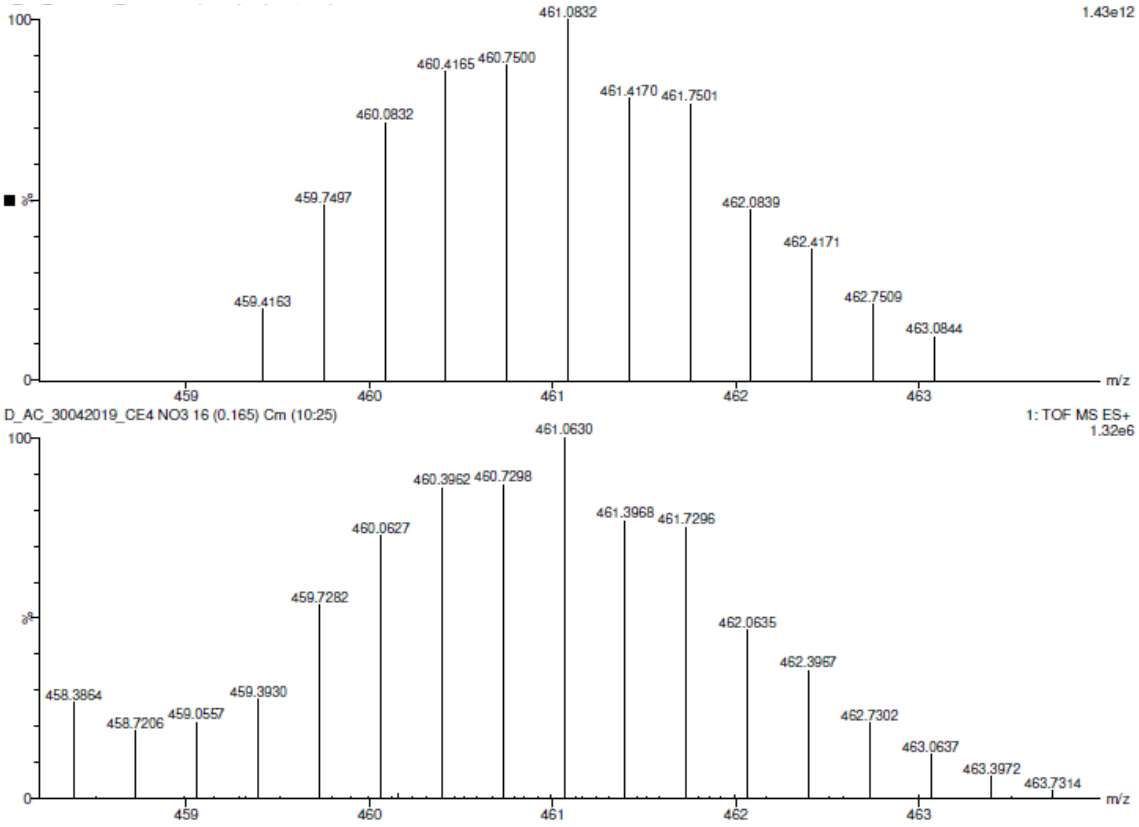

Figure S132. Comparison between the theoretical isotopic pattern (top) and the experimental isotopic pattern (bottom) of [$\mathbf{C^{E3}.NO_3}$-4NO_3+MeCN+H]$^{3+}$

References

1. Shewach, D. & Mitchell, B. Introduction to Cancer Chemotherapeutics. *Chem. Rev.* **109**, 2007–2009 (2009).

2. Thurston, D. E. Chemistry and pharmacology of anticancer drugs. 2007 (2007). doi:10.1038/sj.bjc.6604075

3. Perez, R. P. Cellular and molecular determinants of cisplatin resistance. *Eur. J. Cancer* **34**, 1535–1542 (1998).

4. Lebwohl, D. & Canetta, R. Clinical development of platinum complexes in cancer therapy: An historical perspective and an update. *European Journal of Cancer* **34**, 1522–1534 (1998).

5. Division, C., Products, E. & Electrode, P. Inhibition of Cell Division in Escherichia coli by Electrolysis Products from a Platinum Electrode. *Nature* **20**, 698–699 (1965).

6. Higby, D. J., Higby, D. J., Wallace, H. J., Albert, D. J. & Holland, J. F. Diaminodichloroplatinum: A phase I study showing responses in testicular and other tumors. *Cancer* **33**, 1219–1225 (1974).

7. Higby, D. J., Wallace, H. J., Albert, D. & Holland, J. F. Diamminodichloroplatinum in the chemotherapy of testicular tumors. *J. Urol.* **112**, 100–104 (1974).

8. Pinedo, H. M., Vendrik, C. P. J., Staquet, M. & Sylvester, R. Study of Cis-diammine-dichloro-platinum in advanced soft tissue sarcoma. *Eur. J. Cancer* **14**, 1149–1152 (1978).

9. Harrap, K. R. Preclinical studies identifying carboplatin as a viable cisplatin alternative. *Cancer Treat. Rev.* **12**, 21–33 (1985).

10. Martin A. Graham *et al.* Clinical Pharmacokinetics of Oxaliplatin: A critical review. *Clin. cancer Res.* **6**, 1205–1218 (2000).

11. Kenny, R. G. & Marmion, C. J. Toward Multi-Targeted Platinum and Ruthenium Drugs - A New Paradigm in Cancer Drug Treatment Regimens? *Chem. Rev.* **119**, 1058–1137 (2019).

12. Eljack, N. D. *et al.* Mechanisms of cell uptake and toxicity of the anticancer drug cisplatin. *Metallomics* **6**, 2126–2133 (2014).

13. Fuertes, M. A., Castilla, J., Alonso, C. & Pérez, J. M. Cisplatin Biochemical Mechanism of Action : From Cytotoxicity to Induction of Cell Death Through Interconnections Between Apoptotic and Necrotic Pathways. *Curr. Med. Chem.* 257–266 (2003).

14. Jamieson, E. R. & Lippard, S. J. Structure, Recognition, and Processing of Cisplatin−DNA Adducts. *Chem. Rev.* **99**, 2467–2498 (1999).

15. Yang, X. L. & Wang, A. H. J. *Structural studies of atom-specific anticancer drugs acting on DNA*. *Pharmacology and Therapeutics* **83**, (1999).

16. Payet, D., Gaucheron, F., Sip, M. & Leng, M. Instability of the monofunctional adducts in *cis* -[Pt(NH $_3$) $_2$ (*N7-N* -methyl-2-diazapyrenium)Cl] $^{2+}$;-modified DNA: rates of cross-linking reactions in *cis* -platinummodified DNA. *Nucleic Acids Res.* **21**, 5846–5851 (1993).

17. Nature, L. T. O. Letters to nature 100 3. *Nature* **378**, 1993–1995 (1995).

18. Ober, M. & Lippard, S. J. A 1,2-d(GpG) cisplatin intrastrand cross-link influences the rotational and translational setting of DNA in nucleosomes. *J. Am. Chem. Soc.* **130**, 2851–2861 (2008).

19. Pil, P. M. & Lippard, S. J. Protein HMG1 Specific Binding of Chromosomal to DNA Damaged by the Anticancer Drug Cisplatin. *Science (80-.).* **256**, 234–237 (2013).

20. Mu, D., Hsu, D. S. & Sancar, A. Reaction mechanism of human DNA repair excision nuclease. *J. Biol. Chem.* **271**, 8285–8294 (1996).

21. Johnstone, T. C., Suntharalingam, K. & Lippard, S. J. The Next Generation of Platinum Drugs: Targeted Pt(II) Agents, Nanoparticle Delivery, and Pt(IV) Prodrugs. *Chem. Rev.* **116**, 3436–3486 (2016).

22. Casini, A. & Reedijk, J. Interactions of anticancer Pt compounds with proteins: an overlooked topic in medicinal inorganic chemistry? *Chem. Sci.* **16**, 6511–6512 (2012).

23. Rose, M. C., Kostyanovskaya, E. & Huang, R. S. Pharmacogenomics of cisplatin sensitivity in non-small cell lung cancer. *Genomics, Proteomics Bioinforma.* **12**, 198–209 (2014).

24. Kelland, L. R. Preclinical Perspectives on Platinum Resistance. *Drugs* **59**, 1–8 (2000).

25. Speelmans, G., Staffhorst, R. W. H. M., Versluis, K., Reedijk, J. & De Kruijff, B. Cisplatin complexes with phosphatidylserine in membranes. *Biochemistry* **36**, 10545–10550 (1997).

26. Jordan, P. & Carmo-Fonseca, M. Molecular mechanisms involved in circadian clocks. *Cell. Mol. Life Sci.* **96**, 1229–1235 (2000).

27. Reedijk, J. Why does cisplatin reach guanine-N7 with competing S-donor ligands available in the cell? *Chem. Rev.* **99**, 2499–2510 (1999).

28. Ishikawa, T. & Ali-Osman, F. Glutathione-associated cis-diamminedichloroplatinum(II) metabolism and ATP-dependent efflux from leukemia cells. Molecular characterization of glutathione-platinum complex and its biological significance. *J. Biol. Chem.* **268**, 20116–20125 (1993).

29. Srinivasarao, M. & Low, P. S. Ligand-Targeted Drug Delivery. *Chem. Rev.* **117**, 12133–12164 (2017).

30. Wang, A. Z., Langer, R. & Farokhzad, O. C. Nanoparticle Delivery of Cancer Drugs. *Annu. Rev. Med.* **63**, 185–198 (2012).

31. Ait-Oudhia, S., Mager, D. E. & Straubinger, R. M. Application of pharmacokinetic and pharmacodynamic analysis to the development of liposomal formulations for oncology. *Pharmaceutics* **6**, 137–174 (2014).

32. Maria Laura Immordino, Franco Dosio & Luigi Cattel. Stealth liposomes: review of the basic science, rationale, and clinical applications, existing and potential. *Int. J. Nanomedicine* **1**, 297–315 (2006).

33. Yang, J. *et al.* Drug Delivery via Cell Membrane Fusion Using Lipopeptide Modified Liposomes. *ACS Cent. Sci.* acscentsci.6b00172 (2016). doi:10.1021/acscentsci.6b00172

34. Wang, A. Z., Langer, R. & Farokhzad, O. C. Nanoparticle Delivery of Cancer Drugs. *Annu. Rev. Med.* **63**, 185–198 (2012).

35. Danhier, F., Feron, O. & Préat, V. To exploit the tumor microenvironment: Passive and active tumor targeting of nanocarriers for anti-cancer drug delivery. *J. Control. Release* **148**, 135–146 (2010).

36. Matsumura, Y. & Maeda, H. A new concept for macromolecular therapeutics in cnacer chemotherapy: mechanism of tumoritropic accumulatio of proteins and the antitumor

agents Smancs. *Cancer Res.* **46**, 6387–6392 (1986).

37. Maeda, H., Wu, J., Sawa, T., Matsumura, Y. & Hori, K. Tumor vascular permeability and the EPR effect in macromolecular therapeutics: A review. *J. Control. Release* **65**, 271–284 (2000).

38. Danhier, F. To exploit the tumor microenvironment: Since the EPR effect fails in the clinic, what is the future of nanomedicine? *J. Control. Release* **244**, 108–121 (2016).

39. Wong, B. S. *et al.* Carbon nanotubes for delivery of small molecule drugs. *Adv. Drug Deliv. Rev.* **65**, 1964–2015 (2013).

40. Fratoddi, I., Venditti, I., Cametti, C. & Russo, M. V. Gold nanoparticles and gold nanoparticle- conjugates for delivery of therapeutic molecules. Progress and challenges. *J. Mater. Chem. B* **2**, 4204–4220 (2014).

41. Li, J. *et al.* Platinum(iv) prodrugs entrapped within multiwalled carbon nanotubes: Selective release by chemical reduction and hydrophobicity reversal. *Chem. Sci.* **3**, 2083–2087 (2012).

42. Yudasaka, M. *et al.* Nano-extraction and nano-condensation for C60 incorporation into single-wall carbon nanotubes in liquid phases. *Chem. Phys. Lett.* **380**, 42–46 (2003).

43. Maruyama, K. Intracellular targeting delivery of liposomal drugs to solid tumors based on EPR effects. *Advanced Drug Delivery Reviews* **63**, 161–169 (2011).

44. Vemuri, S. & Rhodes, C. T. Preparation and characterization of liposomes as therapeutic delivery systems: a review. *Pharm. Acta Helv.* **70**, 95–111 (1995).

45. Tarhini, A. A. *et al.* A phase I study of concurrent chemotherapy (paclitaxel and carboplatin) and thoracic radiotherapy with swallowed manganese superoxide dismutase plasmid liposome protection in patients with locally advanced stage III non-small-cell lung cancer. *Hum. Gene Ther.* **22**, 336–42 (2011).

46. Stathopoulos, G. P. & Boulikas, T. Lipoplatin Formulation Review Article. *J. Drug Deliv.* (2012). doi:10.1155/2012/581363

47. Robillard, M. S. *et al.* Solid-phase synthesis of peptide-platinum complexes using platinum-chelating building blocks derived from amino acids. *New J. Chem.* **29**, 220–225 (2005).

48. Robillard, M. S. *et al.* The first solid-phase synthesis of a peptide-Tethered platinum(II) complex. *Angew. Chemie - Int. Ed.* **39**, 3096–3099 (2000).

49. Damian, M. S., Hedman, H. K., Elmroth, S. K. C. & Diederichsen, U. Synthesis and DNA interaction of platinum complex/peptide chimera as potential drug candidates. *European J. Org. Chem.* 6161–6170 (2010). doi:10.1002/ejoc.201000677

50. Van Zutphen, S. *et al.* Combinatorial discovery of new asymmetric cis platinum anticancer complexes is made possible with solid-phase synthetic methods. *J. Inorg. Biochem.* **99**, 2032–2038 (2005).

51. Robillard, M. S. *et al.* Automated Parallel Solid-Phase Synthesis and Anticancer Screening of a Library of Peptide-Tethered Platinum(II) Complexes. *J. Comb. Chem.* **5**, 821–825 (2003).

52. Ndinguri, M. W., Solipuram, R., Gambrell, R. P., Aggarwal, S. & Hammer, R. P. Peptide targeting of platinum anti-cancer drugs. *Bioconjug. Chem.* **20**, 1869–1878 (2009).

53. Zhang, J. *et al.* CD13 inhibition enhances cytotoxic effect of chemotherapy agents.

Front. Pharmacol. **9**, 1–10 (2018).

54. Colombo, G. *et al.* Structure-activity relationships of linear and cyclic peptides containing the NGR tumor-homing motif. *J. Biol. Chem.* **277**, 47891–47897 (2002).

55. Möker, J., Salge-Bartels, U. & Thiem, J. Formation of glyco-functionalized platinum complexes by cross-metathesis and evaluation of their efficacy in inhibition of lung tumor cell lines. *J. Carbohydr. Chem.* **31**, 702–710 (2012).

56. Möker, J. & Thiem, J. Synthesis of novel gluco- and galacto-functionalized platinum complexes. *European J. Org. Chem.* 4842–4847 (2009). doi:10.1002/ejoc.200900691

57. Carlsson, J. *et al.* HER2 expression in breast cancer primary tumours and corresponding metastases. Original data and literature review. *Br. J. Cancer* **90**, 2344–2348 (2004).

58. Knight, W. A., Livingston, R. B., Gregory, E. J. & McGuire, W. L. Estrogen Receptor as an Independent Prognostic Factor for Early Recurrence in Breast Cancer. *Cancer Res.* **37**, 4669–4671 (1977).

59. Wang, X. & Guo, Z. Targeting and delivery of platinum-based anticancer drugs. *Chemical Society Reviews* **42**, 202–224 (2013).

60. Gandolfi, O., Blum, J. & Mandelbaum-Shavit, F. Antitumor steroidal-cis-platinum(II)-o-catecholato conjugates: preliminary evaluation on breast cancer MCF-7 cells. *Inorganica Chim. Acta* **91**, 257–261 (1984).

61. Dolman, R. C., Deacon, G. B. & Hambley, T. W. Studies of the binding of a series of platinum(IV) complexes to plasma proteins. *J. Inorg. Biochem.* **88**, 260–267 (2002).

62. An, S. S. *et al.* Investigation of the biological and anti-cancer properties of ellagic acid-encapsulated nano-sized metalla-cages. *Int. J. Nanomedicine* 227 (2015). doi:10.2147/ijn.s88289

63. Cook, T. R., Vajpayee, V., Lee, M. H., Stang, P. J. & Chi, K. W. Biomedical and biochemical applications of self-assembled metallacycles and metallacages. *Acc. Chem. Res.* **46**, 2464–2474 (2013).

64. Chakrabarty, R., Mukherjee, P. S. & Stang, P. J. Supramolecular coordination: Self-assembly of finite two- and three-dimensional ensembles. *Chem. Rev.* **111**, 6810–6918 (2011).

65. Cook, T. R. & Stang, P. J. Recent Developments in the Preparation and Chemistry of Metallacycles and Metallacages via Coordination. *Chem. Rev.* **115**, 7001–7045 (2015).

66. Schmidt, A., Casini, A. & Kühn, F. E. Self-assembled M 2 L 4 coordination cages : Synthesis and potential applications. *Coord. Chem. Rev.* **275**, 19–36 (2014).

67. Fujita, M. & Ogura, K. Supramolecular Self-Assembly of Macrocycles, Catenanes, and Cages through Coordination of Pyridine-Based Ligands to Transition Metals. *Bulletin of the Chemical Society of Japan* **69**, 1471–1482 (1996).

68. Gianneschi, N. C., Masar, M. S. & Mirkin, C. A. Development of a coordination chemistry-based approach for functional supramolecular structures. *Acc. Chem. Res.* **38**, 825–837 (2005).

69. Seidel, S. R. & Stang, P. J. High-symmetry coordination cages via self-assembly. *Acc. Chem. Res.* **35**, 972–983 (2002).

70. Fujita, M. *et al.* Molecular paneling via coordination. *Chem. Commun.* 509–518 (2001). doi:10.1039/b008684n

71. Yoshizawa, M., Tamura, M. & Fujita, M. Diels-Alder in Aqueous Molecular. *Science (80-.).* **312**, 251–255 (2006).

72. Zava, O., Mattsson, J., Therrien, B. & Dyson, P. J. Evidence for drug release from a metalla-cage delivery vector following cellular internalisation. *Chem. - A Eur. J.* **16**, 1428–1431 (2010).

73. Therrien, B., Süss-Fink, G., Govindaswamy, P., Renfrew, A. K. & Dyson, P. J. The "Complex-in-a-Complex" Cations [(acac)2M⊂Ru6(p-iPrC6H4Me)6(tpt)2(dhbq)3]6+: A Trojan Horse for Cancer Cells. *Angew. Chemie* **120**, 3773–3776 (2008).

74. Han, M., Engelhard, D. M. & Clever, G. H. Self-assembled coordination cages based on banana-shaped ligands. *Chem. Soc. Rev.* **43**, 1848–60 (2014).

75. Fleming, J. S., Mann, K. L. V, Psillakis, E. & Jeffery, J. C. Anion-Templated Assembly of a Supramolecular Cage Complex. *Angew. Chem. Int. Ed.* **1**, 1279–1281 (1998).

76. Turega, S. *et al.* Selective guest recognition by a self-assembled paramagnetic cage complex. *Chem. Commun.* **48**, 2752–2754 (2012).

77. Beissel, T., Powers, R. E. & Raymond, K. N. Symmetry-Based Metal Complex Cluster Formation. *Angew. Chemie Int. Ed. English* **35**, 1084–1086 (1996).

78. Tominaga, M. *et al.* Finite, spherical coordination networks that self-organize from 36 small components. *Angew. Chemie - Int. Ed.* **43**, 5621–5625 (2004).

79. Fujita, D. *et al.* Self-assembly of tetravalent Goldberg polyhedra from 144 small components. *Nature* **540**, 563–566 (2016).

80. Wang, X., Wang, X. & Guo, Z. Functionalization of Platinum Complexes for Biomedical Applications. *Acc. Chem. Res.* **48**, 2622–2631 (2015).

81. Holliday, B. J. & Mirkin, C. A. Strategies for the Construction of Supramolecular Compounds through Coordination Chemistry. *Angew. Chemie - Int. Ed.* **40**, 2022–2043 (2001).

82. Mishra, A. *et al.* Self-assembled supramolecular hetero-bimetallacycles for anticancer potency by intracellular release. *Chem. - A Eur. J.* **20**, 14410–14420 (2014).

83. Zheng, Y. R. *et al.* Mechanistic studies of the anticancer activity of an octahedral hexanuclear Pt(II) cage. *Inorganica Chim. Acta* **452**, 125–129 (2016).

84. McNeill, S. M. *et al.* Biologically active [Pd 2 L 4] 4+ quadruply-stranded helicates: stability and cytotoxicity. *Dalt. Trans.* **44**, 11129–11136 (2015).

85. Preston, D., McNeill, S. M., Lewis, J. E. M., Giles, G. I. & Crowley, J. D. Enhanced kinetic stability of [Pd 2 L 4] 4+ cages through ligand substitution. *Dalton Trans.* **45**, 8050–8060 (2016).

86. Dubey, A. *et al.* Anticancer potency and multidrug-resistant studies of self-assembled arene-ruthenium metallarectangles. *Chem. - A Eur. J.* **19**, 11622–11628 (2013).

87. Vajpayee, V. *et al.* Hexanuclear self-assembled arene-ruthenium nano-prismatic cages: potential anticancer agents. *Chem. Commun.* **47**, 5184–5186 (2011).

88. Vajpayee, V. *et al.* Self-assembled metalla-rectangles bearing azodipyridyl ligands: synthesis, characterization and antitumor activity. *Dalt. Trans.* **42**, 466–475 (2013).

89. Vajpayee, V. *et al.* Self-assembly of cationic, hetero- or homonuclear ruthenium(II) macrocyclic rectangles and their photophysical, electrochemical, and biological studies. *Organometallics* **30**, 6482–6489 (2011).

90. Vajpayee, V. *et al.* Coordination-driven self-assembly of ruthenium-based molecular-rectangles: Synthesis, characterization, photo-physical and anticancer potency studies. *Dalt. Trans.* **41**, 3046 (2012).

91. Gupta, G., Murray, B. S., Dyson, P. J. & Therrien, B. Synthesis, molecular structure and cytotoxicity of molecular materials based on water soluble half-sandwich Rh(III) and Ir(III) tetranuclear metalla-cycles. *Materials (Basel).* **6**, 5352–5366 (2013).

92. Mishra, A. *et al.* Anticancer potency studies of coordination driven self-assembled arene-Ru-based metalla-bowls. *ChemBioChem* **15**, 695–700 (2014).

93. Thota, S., Rodrigues, D. A., Crans, D. C. & Barreiro, E. J. Ru(II) Compounds: Next-Generation Anticancer Metallotherapeutics? *J. Med. Chem.* **61**, 5805–5821 (2018).

94. Dubey, A. *et al.* Anticancer Activity and Autophagy Involvement of Self-Assembled Arene-Ruthenium Metallacycles. *Organometallics* **34**, 4507–4514 (2015).

95. Dubey, A. *et al.* Investigation of the biological and anti-cancer properties of ellagic acid-encapsulated nano-sized metalla-cages. *Int. J. Nanomedicine* **10**, 227–240 (2015).

96. Kim, I. *et al.* Anticancer activities of self-assembled molecular bowls containing a phenanthrene-based donor and ru(II) acceptors. *Int. J. Nanomedicine* **10**, 143–153 (2015).

97. Moldrheim, E., Hannon, M. J., Meistermann, I., Rodger, A. & Sletten, E. Interaction between a DNA oligonucleotide and a dinuclear iron(II) supramolecular cylinder; an NMR and molecular dynamics study. *J. Biol. Inorg. Chem.* **7**, 770–780 (2002).

98. Malina, J., Hannon, M. J. & Brabec, V. DNA binding of dinuclear iron(II) metallosupramolecular cylinders. DNA unwinding and sequence preference. *Nucleic Acids Res.* **36**, 3630–3638 (2008).

99. Lewis, J. E. M., Gavey, E. L., Cameron, S. A. & Crowley, J. D. Stimuli-responsive Pd2L4 metallosupramolecular cages: towards targeted cisplatin drug delivery. *Chem. Sci.* **3**, 778–784 (2012).

100. Malina, J., Scott, P. & Brabec, V. Shape-selective recognition of DNA abasic sites by metallohelices: Inhibition of human AP endonuclease 1. *Nucleic Acids Res.* **43**, 5297–5306 (2015).

101. Malina, J., Hannon, M. J. & Brabec, V. Recognition of DNA bulges by dinuclear iron(II) metallosupramolecular helicates. *FEBS J.* **281**, 987–997 (2014).

102. Malina, J., Scott, P. & Brabec, V. Recognition of DNA/RNA bulges by antimicrobial and antitumor metallohelices. *Dalt. Trans.* **44**, 14656–14665 (2015).

103. Zhao, A. *et al.* Chiral metallohelices enantioselectively target hybrid human telomeric G-quadruplex DNA. *Nucleic Acids Res.* **45**, 5026–5035 (2017).

104. Hänsel-Hertsch, R., Di Antonio, M. & Balasubramanian, S. DNA G-quadruplexes in the human genome: detection, functions and therapeutic potential. *Nat. Rev. Mol. Cell Biol.* **18**, 279–284 (2017).

105. Hotze, A. C. G. *et al.* Supramolecular Iron Cylinder with Unprecedented DNA Binding Is a Potent Cytostatic and Apoptotic Agent without Exhibiting Genotoxicity. *Chem. Biol.* **15**, 1258–1267 (2008).

106. Cardo, L. & Hannon, M. J. Design and DNA-binding of metallo-supramolecular cylinders conjugated to peptides. *Inorganica Chim. Acta* **362**, 784–792 (2009).

107. Ducani, C., Leczkowska, A., Hodges, N. J. & Hannon, M. J. Noncovalent DNA-binding metallo-supramolecular cylinders prevent DNA transactions in vitro. *Angew. Chemie - Int. Ed.* **49**, 8942–8945 (2010).

108. Boer, D. R. *et al.* Self-Assembly of Functionalizable Two-Component 3D DNA Arrays through the Induced Formation of DNA Three-Way-Junction Branch Points by Supramolecular Cylinders. *Angew. Chemie Int. Ed.* **49**, 2336–2339 (2010).

109. Faulkner, A. D. *et al.* Asymmetric triplex metallohelices with high and selective activity against cancer cells. *Nat. Chem.* **6**, 797–803 (2014).

110. Brabec, V. *et al.* Metallohelices with activity against cisplatin-resistant cancer cells; does the mechanism involve DNA binding? *Chem. Sci.* **7**, 4407 (2013).

111. Therrien, B. Biologically relevant arene ruthenium metalla-assemblies. *CrystEngComm* **17**, 484–491 (2015).

112. Therrien, B. Discrete Metalla-Assemblies as Drug Delivery Vectors. *Nanomater. Drug Deliv. Imaging, Tissue Eng.* 145–166 (2013). doi:10.1002/9781118644591.ch4

113. Barry, N. P. E., Zava, O., Dyson, P. J. & Therrien, B. Synthesis, characterization and anticancer activity of porphyrin-containing organometallic cubes. *Aust. J. Chem.* **63**, 1529–1537 (2010).

114. Therrien, B. Drug Delivery by Water-Soluble Organometallic Cages. *Top Curr Chem* **319**, 35–55 (2012).

115. Burt, H. M. & Haxton, K. J. Polymeric Drug Delivery of Platinum-Based Anticancer Agents. *J. Pharm. Sci.* **98**, 2299–2316 (2009).

116. Svenson, S. & Tomalia, D. A. Dendrimers in biomedical applications - Reflections on the field. *Adv. Drug Deliv. Rev.* **57**, 2106–2129 (2005).

117. Brand, W. *et al.* Nanomedicinal products: A survey on specific toxicity and side effects. *Int. J. Nanomedicine* **12**, 6107–6129 (2017).

118. Casini, A., Woods, B. & Wenzel, M. The Promise of Self-Assembled 3D Supramolecular Coordination Complexes for Biomedical Applications. *Inorg. Chem.* **56**, 14715–14729 (2017).

119. Mattsson, J. *et al.* Drug delivery of lipophilic pyrenyl derivatives by encapsulation in a water soluble metalla-cage. *Dalton Trans.* **39**, 8248–55 (2010).

120. Barry, N. P. E., Zava, O., Dyson, P. J. & Therrien, B. Excellent correlation between drug release and portal size in metalla-cage drug-delivery systems. *Chem. - A Eur. J.* **17**, 9669–9677 (2011).

121. Zhao, D. *et al.* Surface functionalization of porous coordination nanocages via click chemistry and their application in drug delivery. *Adv. Mater.* **23**, 90–93 (2011).

122. Kishi, N. *et al.* Wide-ranging host capability of a PdII-Linked M 2L4 molecular capsule with an anthracene shell. *Chem. - A Eur. J.* **19**, 6313–6320 (2013).

123. Ahmedova, A. *et al.* Anticancer Potencies of Pt(II)-and Pd(II)-linked M2L4 Coordination Capsules with Improved Selectivity. *Chem. - An Asian J.* **11**, 474–477 (2016).

124. Ahmedova, A. *et al.* M2L4 coordination capsules with tunable anticancer activity upon guest encapsulation. *Dalton Trans.* **45**, 13214–13221 (2016).

125. McMorran, D. A. & Steel, P. J. The first coordinatively saturated, quadruply stranded helicate and its encapsulation of a hexafluorophosphate anion. *Angew. Chemie - Int. Ed.*

37, 3295–3297 (1998).

126. Li, H., Luo, J. & Liu, T. Modification of the Solution Behavior of Pd $_{12}$ L $_{24}$ Metal-Organic Nanocages via PEGylation. *Chem. - A Eur. J.* **22**, 17949–17952 (2016).

127. Schmidt, A. *et al.* Evaluation of New Palladium Cages as Potential Delivery Systems for the Anticancer Drug Cisplatin. *Chem. - A Eur. J.* **22**, 2253–2256 (2016).

128. Haubner, R., Finsinger, D. & Kessler, H. Stereoisomeric Peptide Libraries and Peptidomimetics for Designing Selective Inhibitors of the Alpha(V)beta(3) Integrin for a New Cancer Therapy. *Ang Chem Int Ed* **36**, 1375–1389 (1997).

129. Ikemi, M. *et al.* Peptide-coated, self-assembled M12L24 coordination spheres and their immobilization onto an inorganic surface. *Chem. Sci.* **1**, 68–71 (2010).

130. Fujita, D. *et al.* Protein encapsulation within synthetic molecular hosts. *Nat. Commun.* **3**, 1093 (2012).

131. Han, J. *et al.* Bioconjugation strategies to couple supramolecular Exo -functionalized palladium cages to peptides for biomedical applications. *Chem. Commun.* **53**, 1405–1408 (2017).

132. Schmidt, A., Hollering, M., Drees, M., Casini, A. & Kühn, F. E. Supramolecular exo-functionalized palladium cages: fluorescent properties and biological activity. *Dalton Trans.* **45**, 8556–8565 (2016).

133. Schmidt, A., Hollering, M., Han, J., Casini, A. & Kühn, F. E. Self-assembly of highly luminescent heteronuclear coordination cages. *Dalton Trans.* **45**, 12297–12300 (2016).

134. Kaiser, F. *et al.* Self-Assembled Palladium and Platinum Coordination Cages: Photophysical Studies and Anticancer Activity. *European Journal of Inorganic Chemistry* **2016**, 5189–5197 (2016).

135. Lewis, J. E. M., Elliott, A. B. S., McAdam, C. J., Gordon, K. C. & Crowley, J. D. 'Click' to functionalise: synthesis, characterisation and enhancement of the physical properties of a series of exo- and endo-functionalised Pd 2 L 4 nanocages. *Chem. Sci.* **5**, 1833–1843 (2014).

136. Lewis, J. E. M., John McAdam, C., Gardiner, M. G. & Crowley, J. D. A facile "click" approach to functionalised metallosupramolecular architectures. *Chem. Commun.* **49**, 3398 (2013).

137. Vardhan, H., Yusubov, M. & Verpoort, F. Self-assembled metal-organic polyhedra: An overview of various applications. *Coord. Chem. Rev.* **306**, 171–194 (2016).

138. Cook, T. R., Zheng, Y. R. & Stang, P. J. Metal-organic frameworks and self-assembled supramolecular coordination complexes: Comparing and contrasting the design, synthesis, and functionality of metal-organic materials. *Chem. Rev.* **113**, 734–777 (2013).

139. Ahmad, N., Younus, H. A., Chughtai, A. H. & Verpoort, F. Metal–organic molecular cages: applications of biochemical implications. *Chem. Soc. Rev.* **44**, 9–25 (2015).

140. Smulders, M. M. J., Riddell, I. a., Browne, C. & Nitschke, J. R. Building on architectural principles for three-dimensional metallosupramolecular construction. *Chem. Soc. Rev.* **42**, 1728–1754 (2013).

141. Harris, K., Fujita, D. & Fujita, M. Giant hollow MnL2n spherical complexes: structure, functionalisation and applications. *Chem. Commun.* **49**, 6703 (2013).

142. Ahmad, N., Chughtai, A. H., Younus, H. A. & Verpoort, F. Discrete metal-carboxylate self-assembled cages: Design, synthesis and applications. *Coord. Chem. Rev.* **280**, 1–27 (2014).

143. Barbour, L. J., Orr, G. W. & Atwood, J. L. An intermolecular (H2O)10 cluster in a solid-state supramolecular complex. *Nature* **393**, 671–673 (1998).

144. Amouri, H. *et al.* Host-guest interactions: Design strategy and structure of an unusual cobalt cage that encapsulates a tetrafluoroborate anion. *Angew. Chemie - Int. Ed.* **44**, 4543–4546 (2005).

145. Puig, E., Desmarets, C., Rager, M. N., Cooksy, A. L. & Amouri, H. Capturing a Square Planar Gold(III) Complex Inside a Platinum Nanocage: A Combined Experimental and Theoretical Study. (2018). doi:10.1021/acs.inorgchem.8b03272

146. Preston, D., Barnsley, J. E., Gordon, K. C. & Crowley, J. D. Controlled Formation of Heteroleptic [Pd $_2$ (L $_a$) $_2$ (L $_b$) $_2$] $^{4+}$ Cages. *J. Am. Chem. Soc.* **2**, jacs.6b05629 (2016).

147. Li, Y. *et al.* Hydrophobic metallo-supramolecular Pd2L4 cages for zwitterionic guest encapsulation in organic solvents. *Dalt. Trans.* **46**, 15204–15207 (2017).

148. Preston, D., Fox-Charles, A., Lo, W. K. C. & Crowley, J. D. Chloride triggered reversible switching from a metallosupramolecular [Pd 2 L 4] 4+ cage to a [Pd 2 L 2 Cl 4] metallo-macrocycle with release of endo- and exo-hedrally bound guests. *Chem. Commun.* **51**, 9042–9045 (2015).

149. Crowley, J. D., Preston, D. & Vasdev, R. A. S. Multicavity Metallosupramolecular Architectures. *Chem. - An Asian J.* (2017). doi:10.1002/asia.201700948

150. Chand, D. K., Biradha, K. & Fujita, M. Self-assembly of a novel macrotricyclic Pd(II) metallocage encapsulating a nitrate ion. *Chem. Commun.* 1652–1653 (2001). doi:10.1039/b104853h

151. Yue, N. L. S., Eisler, D. J., Jennings, M. C. & Puddephatt, R. J. Macrocyclic and lantern complexes of palladium(II) with bis(amidopyridine) ligands: Synthesis, structure, and host-guest chemistry. *Inorg. Chem.* **43**, 7671–7681 (2004).

152. Liao, P. *et al.* Two-component control of guest binding in a self-assembled cage molecule. *Chem. Commun.* **46**, 4932–4934 (2010).

153. Clever, G. H., Tashiro, S. & Shionoya, M. Inclusion of anionic guests inside a molecular cage with palladium(ii) centers as electrostatic anchors. *Angew. Chemie - Int. Ed.* **48**, 7010–7012 (2009).

154. Crowley, J. D. & Gavey, E. L. Use of di-1,4-substituted-1,2,3-triazole 'click' ligands to self-assemble dipalladium(ii) coordinatively saturated, quadruply stranded helicate cages. *Dalt. Trans.* **39**, 4035–4037 (2010).

155. Altaf, A. A. *et al.* Review on the Medicinal Importance of Pyridine Derivatives. *J. Drug Des. Med. Chem.* **1**, 1–11 (2015).

156. Kikuchi, S. A History of the Structural Theory of Benzene - The Aromatic Sextet Rule and Huckel's Rule. *J. Chem. Educ.* **74**, 194 (2009).

157. Best, S. JOAN RIBAS GISPERT Coordination chemistry Wiley-VCH, 2008, 600 pp. (paperback) ISBN-10 3-527-31802-X ISBN-13 978-3-527-31802-5. *Appl. Organomet. Chem.* **23**, 482–483 (2009).

158. De, S., Mahata, K. & Schmittel, M. Metal-coordination-driven dynamic heteroleptic architectures. *Chem. Soc. Rev.* **39**, 1555–1575 (2010).

159. Benkhäuser, C. & Lützen, A. Self-assembly of heteroleptic dinuclear metallosupramolecular kites from multivalent ligands via social self-sorting. *Beilstein J. Org. Chem.* **11**, 693–700 (2015).

160. Clever, G. H. & Punt, P. Cation-Anion Arrangement Patterns in Self-Assembled Pd2L4 and Pd4L8 Coordination Cages. *Acc. Chem. Res.* **50**, 2233–2243 (2017).

161. Fujita, M. *et al.* Self-assembly of ten molecules into nanometre-sized organic host frameworks. *Nature* **378**, 469–471 (1995).

162. Dalgarno, S. J., Power, N. P. & Atwood, J. L. Metallo-supramolecular capsules. *Coord. Chem. Rev.* **252**, 825–841 (2008).

163. Kishi, N., Li, Z., Yoza, K., Akita, M. & Yoshizawa, M. An M2L4 molecular capsule with an anthracene shell: Encapsulation of large guests up to 1nm. *J. Am. Chem. Soc.* **133**, 11438–11441 (2011).

164. Sonogashira, K., Tohda, Y. & Hagihara, N. A Convenient Synthesis of Acetylenes: Catalytic Substitutions of Acetylenic Hydrogen with Bromoalkenes, Iodoarenes and Bromopyridines. *Tetrahedron Lett.* **50**, 4467–4470 (1975).

165. Cassar, L. Synthesis of aryl- and vinyl-substituted acetylene derivatives by the use of nickel and palladium complexes. *J. Organomet. Chem.* **93**, 253–257 (1975).

166. Heck, R. F. Dicarboalkoxylation of Olefins and Acetylenes. *J. Am. Chem. Soc.* **94**, 2712–2716 (1972).

167. Dieck, H. A. & Heck, F. R. Palladium catalyzed synthesis of aryl, heterocyclic and vinylic acetylene derivatives. *J. Organomet. Chem.* **93**, 259–263 (1975).

168. Siemsen, P., Livingston, R. C. & Diederich, F. Acetylenic Coupling: A Powerful Tool in Molecular Construction. *Ang Chem Int Ed* **39**, 2632–2657 (2000).

169. Elangovan, A., Wang, Y. H. & Ho, T. I. Sonogashira coupling reaction with diminished homocoupling. *Org. Lett.* **5**, 1841–1844 (2003).

170. Chinchilla, R. & Na, C. The Sonogashira Reaction : A Booming Methodology in Synthetic Organic. *Chem. Rev.* **103**, 874–922 (2007).

171. Littke, F. A. & Fu, C. G. Palladium-Catalyzed Coupling Reactions of Aryl Chlorides. *Angew. Chemie Int. Ed.* **41**, 4176–4211 (2002).

172. Létinois-Halbes, U., Pale, P. & Berger, S. Ag NMR as a tool for mechanistic studies of Ag-catalyzed reactions: Evidence for in situ formation of alkyn-1-yl silver from alkynes and silver salts. *J. Org. Chem.* **70**, 9185–9190 (2005).

173. Richard O. Hynes. Integrins: Versatility, Modulation, and Signaling in Cell Adhesion. *Cell* **69**, 11–25 (1992).

174. Xiong, J. *et al.* Crystal structure of the extracellular segment of integrin alpha Vbeta3 in complex with an Arg-Gly-Asp ligand. *Science (80-.).* **296**, 151–155 (2002).

175. Xiong, J. P. *et al.* Crystal Structure of the Extracellular Segment of Integrin alpha Vbeta 3. *Science (80-.).* **294**, 339–345 (2001).

176. Xiong, J. P. *et al.* Crystal structure of the complete integrin αVβ3 ectodomain plus an α/β transmembrane fragment. *J. Cell Biol.* **186**, 589–600 (2009).

177. Nagae, M. *et al.* Crystal structure of α5β1 integrin ectodomain: Atomic details of the fibronectin receptor. *J. Cell Biol.* **197**, 131–140 (2012).

178. Zhu, J. *et al.* Closed headpiece of integrin αIIbβ3and its complex with an αIIbβ3-specific antagonist that does not induce opening. *Blood* **116**, 5050–5059 (2010).

179. Nieberler, M. *et al.* Exploring the role of RGD-recognizing integrins in cancer. *Cancers (Basel).* **9**, 1–33 (2017).

180. Hynes, R. O. Integrins : Bidirectional , Allosteric Signaling Machines In their roles as major adhesion receptors. *Cell* **110**, 673–687 (2002).

181. Wegener, K. L. *et al.* Structural Basis of Integrin Activation by Talin. *Cell* **128**, 171–182 (2007).

182. Gottschalk, K. E., Adams, P. D., Brunger, A. T. & Kessler, H. Transmembrane signal transduction of the αIIbβ3 integrin. *Protein Sci.* **11**, 1800–1812 (2002).

183. Müller, M. A. *et al.* The glycophorin A transmembrane sequence within integrin αvβ3 creates a non-signaling integrin with low basal affinity that is strongly adhesive under force. *J. Mol. Biol.* **425**, 2988–3006 (2013).

184. Mas-Moruno, C. *et al.* αvβ3- or α5β1-Integrin-Selective Peptidomimetics for Surface Coating. *Angew. Chemie - Int. Ed.* **55**, 7048–7067 (2016).

185. Takada, Y., Ye, X. & Simon, S. The integrins. *Genome Biol.* **8**, (2007).

186. Pierschbacher, M. D. & Ruoslahti, E. Cell attachment activity of fibronectin can be duplicated by small synthetic fragments of the molecule. *Nature* **309**, 3–6 (1984).

187. Desgrosellier, J. S. & Cheresh, D. A. Integrins in cancer: Biological implications and therapeutic opportunities. *Nat. Rev. Cancer* **10**, 9–22 (2010).

188. Sloan, E. K. *et al.* Tumor-specific expression of αvβ3 integrin promotes spontaneous metastasis of breast cancer to bone. *Breast Cancer Res.* **8**, 1–14 (2006).

189. Furger, K. A. *et al.* αvβ3 Integrin Expression Increases Breast Carcinoma Cell Responsiveness to the Malignancy-Enhancing Effects of Osteopontin 1 1 Grant 12078 from the Canadian Breast Cancer Research Initiative (A . F . C . and A . B . T .) A . L . A . is supported by the H. *Mol. cancer Res.* **1**, 810–819 (2003).

190. Katsamakas, S., Chatzisider, T., Thysiadis, S. & Sarli, V. RGD-mediated delivery of small-molecule drugs. *Future Med. Chem.* **9**, 579–604 (2017).

191. Plow, E. F., Pierschbacher, M. D., Ruoslahti, E., Marguerie, G. A. & Ginsberg, M. H. Tissue expression pattern of ABCG transporter indicates functional roles in reproduction of Toxocara canis. *Cell Biol.* **82**, 8057–8061 (1985).

192. Oldberg, A., Franzfn, A. & Heinegard, D. Cloning and sequence analysis of rat bone sialoprotein (osteopontin) cDNA reveals an Arg-Gly-Asp cell-binding sequence (cell adhesion/bone matrix proteins/glycosylation). *Biochemistry* **83**, 8819–8823 (1986).

193. Grant, D. S. *et al.* Two different laminin domains mediate the differentiation of human endothelial cells into capillary-like structures in vitro. *Cell* **58**, 933–943 (1989).

194. Suzuki, S., Oldberg, A., Hayman, E. G., Pierschbacher, M. D. & Ruoslahti, E. Complete amino acid sequence of human vitronectin deduced from cDNA. Similarity of cell attachment sites in vitronectin and fibronectin. *EMBO J.* **4**, 2519–24 (1985).

195. Aota, S. I., Nomizu, M. & Yamada, K. M. The short amino acid sequence Pro-His-Ser-Arg-Asn in human fibronectin enhances cell-adhesive function. *J. Biol. Chem.* **269**, 24756–24761 (1994).

196. Ruoslahti, E. & Pierschbacher, M. D. New Perspectives in Cell Adhesion: RGD and

Integrins. *Science (80-.).* **574**, 491–497 (1987).

197. Hegemann, J. D. *et al.* Rational improvement of the affinity and selectivity of integrin binding of grafted lasso peptides. *J. Med. Chem.* **57**, 5829–5834 (2014).

198. Hall, M. D., Mellor, H. R., Callaghan, R. & Hambley, T. W. Basis for Design and Development of Platinum(IV) Anticancer Complexes. *J. Med. Chem.* **50**, 3403–3411 (2007).

199. Böger, C. *et al.* Integrins αvβ3 and αvβ5 as prognostic, diagnostic, and therapeutic targets in gastric cancer. *Gastric Cancer* **18**, 784–795 (2015).

200. Schnell, O. *et al.* Expression of integrin αvβ3 in gliomas correlates with tumor grade and is not restricted to tumor vasculature. *Brain Pathol.* **18**, 378–386 (2008).

201. Harrell, J. C. *et al.* Endothelial-like properties of claudin-low breast cancer cells promote tumor vascular permeability and metastasis. *Clin. Exp. Metastasis* **31**, 33–45 (2014).

202. Sawada, K. *et al.* Loss of E-cadherin promotes ovarian cancer metastasis via α5-integrin, which is a therapeutic target. *Cancer Res.* **68**, 2329–2339 (2008).

203. Pisano, M. *et al.* In vitro activity of the αvβ3 integrin antagonist RGDechi-hCit on malignant melanoma cells. *Anticancer Res.* **33**, 871–880 (2013).

204. de Graaf, I. a M. *et al.* Preparation and incubation of precision-cut liver and intestinal slices for application in drug metabolism and toxicity studies. *Nat. Protoc.* **5**, 1540–51 (2010).

205. Jones, A. R. & Shusta, E. V. Blood-Brain Barrier Transport of Therapeutics via Receptor-Mediation. *Pharm. Res.* **24**, 1759–1771 (2007).

206. Guo, L., Ren, J. & Jiang, X. Perspectives on Brain-Targeting Drug Delivery Systems. *Curr. Pharm. Biotechnol.* **13**, 2310–2318 (2012).

207. Patel, M. M., Goyal, B. R., Bhadada, S. V, Bhatt, J. S. & Amin, A. F. Getting into the Brain. *CNS Drugs* **23**, 35–58 (2009).

208. Pardridge, W. M. Vector-mediated drug delivery to the brain. *Adv. Drug Deliv. Rev.* **36**, 299–321 (1999).

209. Yu, Y. J. *et al.* Boosting brain uptake of a therapeutic antibody by reducing its affinity for a transcytosis target. *Sci. Transl. Med.* **3**, (2011).

210. Muoio, V., Persson, P. B. & Sendeski, M. M. The neurovascular unit - concept review. *Acta Physiol.* **210**, 790–798 (2014).

211. Saidijam, M., Dermani, F. K., Sohrabi, S. & Simon, G. Efflux proteins at the blood – brain barrier : review and bioinformatics analysis analysis. *Xenobiotica* **0**, 1–27 (2018).

212. Avdeef, A. Physicochemical Profiling (Solubility, Permeability and Charge State). *Curr. Top. Med. Chem.* **1**, 277–351 (2005).

213. Lipinski, C. A., Dominy, B. W. & Feeney, P. J. *drug delivery reviews Experimental and computational approaches to estimate solubility and permeability in drug discovery and development settings*. *Advanced Drug Delivery Reviews* **23**, (1997).

214. Pardridge, W. M. Blood-brain barrier delivery. *Drug Discov. Today* **12**, 54–61 (2007).

215. Enerson, B. E. & Drewes, L. R. The rat blood-brain barrier transcriptome. *J. Cereb. Blood Flow Metab.* **26**, 959–973 (2006).

216. Pardridge, W. M. Drug and gene targeting to the brain with molecular Trojan horses. *Nat. Rev. Drug Discov.* **1**, 131–139 (2002).

217. Couch, J. A. *et al.* Addressing safety liabilities of TfR bispecific antibodies that cross the blood-brain barrier. *Sci. Transl. Med.* **5**, (2013).

218. Hervé, F., Ghinea, N. & Scherrmann, J.-M. CNS Delivery Via Adsorptive Transcytosis. *AAPS J.* **10**, 455–472 (2008).

219. Drin, G., Cottin, S., Blanc, E., Rees, A. R. & Temsamani, J. Studies on the internalization mechanism of cationic cell-penetrating peptides. *J. Biol. Chem.* **278**, 31192–31201 (2003).

220. Banks, W. A., Robinson, S. M. & Nath, A. Permeability of the blood-brain barrier to HIV-1 Tat. *Exp. Neurol.* **193**, 218–227 (2005).

221. Schwarze, S. R. *et al.* In vivo Protein Transduction : Delivery of a Biologically Active Protein into the Mouse In Vivo Protein Transduction : Detivery Protein of a into Biotogicatty Active the Mouse. *Adv. Sci.* **285**, 1569–1572 (2012).

222. Freire, J. M. *et al.* Nucleic acid delivery by cell penetrating peptides derived from dengue virus capsid protein: Design and mechanism of action. *FEBS J.* **281**, 191–215 (2014).

223. Freire, J. M. *et al.* Intracellular nucleic acid delivery by the supercharged dengue virus capsid protein. *PLoS One* **8**, (2013).

224. Neves, V. *et al.* Novel Peptides Derived from Dengue Virus Capsid Protein Translocate Reversibly the Blood-Brain Barrier through a Receptor-Free Mechanism. *ACS Chem. Biol.* **12**, 1257–1268 (2017).

225. Jaradat, D. M. M. Thirteen decades of peptide synthesis: key developments in solid phase peptide synthesis and amide bond formation utilized in peptide ligation. *Amino Acids* **50**, 39–68 (2018).

226. Kaiser, E. T., Colescott, R. L., Bossinger, C. D. & Cook, P. I. Color test for the Detection of Free Terminal Amino Groups in the Solid-Phase Synthesis of Peptides. *Anal. Biochem.* **34**, 595–598 (1970).

227. Terai, T. & Nagano, T. Small-molecule fluorophores and fluorescent probes for bioimaging. *J. Physiol.* **465**, 347–359 (2013).

228. Loudet, A. & Burgess, K. BODIPY Dyes and Their Derivatives: Syntheses and Spectroscopic Properties. *Chem. Rev.* **107**, 4891–4932 (2007).

229. Ulrich, G., Ziessel, R. & Harriman, A. The chemistry of fluorescent bodipy dyes: Versatility unsurpassed. *Angew. Chemie - Int. Ed.* **47**, 1184–1201 (2008).

230. Kamkaew, A. *et al.* BODIPY dyes in photodynamic therapy. *Chem. Soc. Rev.* **42**, 77–88 (2013).

231. Orofino-Pena, C. *et al.* Synthesis and properties of novel star-shaped oligofluorene conjugated systems with bodipy cores. *Beilstein J. Org. Chem.* **10**, 2704–2714 (2014).

232. Nepomnyashchii, A. B. & Bard, A. J. Electrochemistry and Electrogenerated Chemiluminescence of BODIPY Dyes. *Acc. Chem. Res.* **45**, 1844–1854 (2011).

233. Durantini, A. M., Heredia, D. A., Durantini, J. E. & Durantini, E. N. BODIPYs to the rescue: Potential applications in photodynamic inactivation. *Eur. J. Med. Chem.* **144**, 651–661 (2018).

234. Lu, H., MacK, J., Yang, Y. & Shen, Z. Structural modification strategies for the rational design of red/NIR region BODIPYs. *Chem. Soc. Rev.* **43**, 4778–4823 (2014).

235. Brizet, B. *et al.* Boron functionalization of BODIPY by various alcohols and phenols. *Org. Biomol. Chem.* **11**, 7729–7737 (2013).

236. Smith, N. W., Alonso, A., Brown, C. M. & Dzyuba, S. V. Triazole-containing BODIPY dyes as novel fluorescent probes for soluble oligomers of amyloid Aβ1-42 peptide. *Biochem. Biophys. Res. Commun.* **391**, 1455–1458 (2010).

237. Fischer, S. J., Benson, L. M., Fauq, A., Naylor, S. & Windebank, A. J. Cisplatin and dimethyl sulfoxide react to form an adducted compound with reduced cytotoxicity and neurotoxicity. *Neurotoxicology* **29**, 444–452 (2008).

238. Lewis, J. E. M. & Crowley, J. D. *Exo* - and *endo* -hedral interactions of counteranions with tetracationic Pd_2L_4 metallosupramolecular architectures. *Supramol. Chem.* **26**, 173–181 (2014).

239. Mei, J., Leung, N. L. C., Kwok, R. T. K., Lam, J. W. Y. & Tang, B. Z. Aggregation-Induced Emission: Together We Shine, United We Soar! *Chem. Rev.* **115**, 11718–11940 (2015).

240. Slominski, A., Tobin, D. J., Shibahara, S. & Wortsman, J. Melanin Pigmentation in Mammalian Skin and Its Hormonal Regulation. *Physiol. Rev.* **84**, 1155–1228 (2004).

241. Forman, H. J., Zhang, H. & Rinna, A. Glutathione: Overview of its protective roles, measurement, and biosynthesis. *Mol. Aspects Med.* **30**, 1–12 (2009).

242. Ntziachristos, V., Ripoll, J., Wang, L. V. & Weissleder, R. Looking and listening to light: The evolution of whole-body photonic imaging. *Nat. Biotechnol.* **23**, 313–320 (2005).

243. Descalzo, A. B., Xu, H. J., Shen, Z. & Rurack, K. Red/near-infrared boron-dipyrromethene dyes as strongly emitting fluorophores. *Ann. N. Y. Acad. Sci.* **1130**, 164–171 (2008).

244. Murtagh, J., Frimannsson, D. O. & O'Shea, D. F. Azide conjugatable and pH responsive near-infrared fluorescent imaging probes. *Org. Lett.* **11**, 5386–5389 (2009).

245. Walker, M. A. Improvement in aqueous solubility achieved via small molecular changes. *Bioorganic Med. Chem. Lett.* **27**, 5100–5108 (2017).

246. Altmann, P. J. & Pöthig, A. Pillarplexes: A Metal-Organic Class of Supramolecular Hosts. *J. Am. Chem. Soc.* **138**, 13171–13174 (2016).

247. David, S. E., Timmins, P. & Conway, B. R. Impact of the counterion on the solubility and physicochemical properties of salts of carboxylic acid drugs Impact of the counterion on the solubility and physicochemical properties of salts of carboxylic acid drugs. *Drug Dev. Ind. Pharm.* **9045**, 93–103 (2012).

248. Haynes, D. A., Jones, W. & Motherwell, W. D. S. Occurrence of Pharmaceutically Acceptable Anions and Cations in the Cambridge Structural Database. *J. Pharm. Sci.* **94**, 2111–2120 (2005).

249. August, D. P., Nichol, G. S. & Lusby, P. J. Maximizing Coordination Capsule–Guest Polar Interactions in Apolar Solvents Reveals Significant Binding. *Angew. Chemie - Int. Ed.* **55**, 15022–15026 (2016).

250. Leung, D. H., Bergman, R. G. & Raymond, K. N. Enthalpy-entropy compensation reveals solvent reorganization as a driving force for supramolecular encapsulation in water. *J. Am. Chem. Soc.* **130**, 2798–2805 (2008).

251. Wiester, M. J., Ulmann, P. A. & Mirkin, C. A. Enzyme mimics based upon supramolecular

coordination chemistry. *Angew. Chemie - Int. Ed.* **50**, 114–137 (2011).

252. Fernández-Vidal, M., White, S. H. & Ladokhin, A. S. Membrane partitioning: 'classical' and 'nonclassical' hydrophobic effects. *J. Membr. Biol.* **239**, 5–14 (2011).

253. Metherell, A. J., Cullen, W., Williams, N. H. & Ward, M. D. Binding of Hydrophobic Guests in a Coordination Cage Cavity is Driven by Liberation of "High-Energy" Water. *Chem. - A Eur. J.* **24**, 1554–1560 (2018).

254. Gilli, P., Ferretti, V., Gilli, G. & Borea, P. A. Enthalpy-entropy compensation in drug-receptor binding. *J. Phys. Chem.* **98**, 1515–1518 (1994).

255. Biedermann, F., Nau, W. M. & Schneider, H. J. The Hydrophobic Effect Revisited - Studies with Supramolecular Complexes Imply High-Energy Water as a Noncovalent Driving Force. *Angew. Chemie - Int. Ed.* **53**, 11158–11171 (2014).

256. Biedermann, F., Uzunova, V. D., Scherman, O. A., Nau, W. M. & De Simone, A. Release of high-energy water as an essential driving force for the high-affinity binding of cucurbit[n]urils. *J. Am. Chem. Soc.* **134**, 15318–15323 (2012).

257. Giernoth, R. Solvents and Solvent Effects in Organic Chemistry. 4th Ed. By Christian Reichardt and Thomas Welton. *Angew. Chemie Int. Ed.* **50**, 11289–11289 (2011).

258. Leavitt, S. & Freire, E. Direct measurement of protein binding energetics by isothermal titration calorimetry. *Biophys. methods* **11**, 560–566 (2001).

259. Freire, E., Mayorga, O. L. & Straume, M. Isothermal Tritation. *Anal. Chem.* **62**, (1990).

260. Ciana, L. Della, Hamachi, I. & Meyer, T. J. Synthesis of Side-chain Derivatives of 2,2'-bipyridine. *J. Org. Chem.* **54**, 1731–1735 (1989).